Proceedings

36th ASPE Annual Meeting

November 1-5, 2021

Renaissance Minneapolis Hotel, the Depot
Minneapolis, Minnesota, USA

American Society for
Precision Engineering

230 Washington Ave. Ext., Suite 101
Albany, NY 12203
518-463-8687

Proceedings of

The Thirty-Sixth Annual Meeting of the

American Society for Precision Engineering

November 1-5, 2021
Renaissance Minneapolis Hotel, the Depot
Minneapolis, Minnesota, USA

The American Society for Precision Engineering (ASPE) is a multidisciplinary professional and technical society concerned with research and development, design, manufacture and measurement of high accuracy components and systems. ASPE activities encompass relevant aspects of mechanical, electronic, optical and production engineering, physics, chemistry, and computer and materials science.

Membership is open to anyone interested in any aspect of precision engineering. Founded in 1986, ASPE provides a focus for a diverse but important community. Other professional organizations have covered aspects of precision engineering, always as a sideline to their principal goals. ASPE is based on the core of generic concepts necessary to achieve precision in any application; independent of discipline, ASPE intends to be the focus for precision technology – and to represent all facets from research to application.

The Annual Meeting has evolved into an international forum for the exchange of ideas and presentation of research results relating to precision engineering, metrology, controls and system integration. Precision engineers and scientists from private industry, government laboratories, and universities meet to learn about the latest developments and to exchange ideas about the future directions of these technologies.

ASPE – The American Society for Precision Engineering
230 Washington Avenue Ext., Suite 101, Albany, NY 12203
518.463.8687 ▪ www.aspe.net

Preface

This book comprises the proceedings of the 36th ASPE Annual Meeting. The contributions reflect the authors' opinions and are published as presented to ASPE, without change. Their inclusion in this publication does not necessarily constitute endorsement by the ASPE, or its editorial staff.

Individual readers of this book and nonprofit libraries acting for them are permitted to make fair use of the material contained in this book to be used in teaching or research; provided they copy said paper in total, as written by the author. Permission is granted to quote excerpts from the scientific or technical works in this book with proper acknowledgment of the source to include: The author's name, the book name, and the ASPE tag line. Reproduction of figures and tables is likewise permitted from the contents of this book, provided that the same acknowledgment of the same source and content is provided. Any other type reproduction, systematic copying or multiple reproduction of any material in this book is expressly prohibited except with the written permission of the ASPE editorial staff, addressed to the Society's headquarters.

ISBN 978-1-887706-79-4

2021

American Society for Precision Engineering
230 Washington Avenue Ext., Suite 101
Albany, NY 12203

Printed in the United States of America

Organizing and Technical Program Committee

Annual Meeting Chairperson
Don Martin, Martin Mason LLC

Technical Program Committee Chairpersons

Mr. Jim Nelson, 3M Company
Mr. Alexander Sohn, Facebook
Special Session on Replicated Optics

Prof. Michael A. Cullinan, The University of Texas at Austin
Micro-Nano Technologies

Dr. Jonathan D. Ellis, Clerio Vision, Inc.
Metrology Systems

Dr. Stephen J. Furst, Smart Material Solutions, Inc.
Precision Manufacturing

Prof. Richard K. Leach, University of Nottingham
Characterization

Mr. Adam Jaycox, Lawrence Livermore National Laboratory
Precision Design

Prof. David L. Trumper, Massachusetts Institute of Technology
Controls and Mechatronics

Tutorials Chair
Dr. Vivek G. Badami, Zygo Corporation

Exhibits Session Chair
Dr. Byron R. Knapp, Professional Instruments Company

Students and Young Members Chairs
Mr. Luis A. Aguirre, 3M Company
Prof. Stuart T. Smith, University of North Carolina – Charlotte

Scientific Review Committee

Luis A. Aguirre, 3M Company
Vivek G. Badami, Zygo Corporation
Dipankar Behera, University of Texas at Austin
Evgueni Bordatchev, National Research Council of Canada
Eric Buice, Lawrence Berkeley National Laboratory
Benjamin Bulla, son-x GmbH
Qunyi Chen, 3M Company
Shih-Chi Chen, Chinese University of Hong Kong
Liam G. Connolly, The University of Texas at Austin
Michael A. Cullinan, The University of Texas at Austin
Angshuman Deka, Richardson Grating, MKS Instruments, Inc.
Kevin Elliot, Corning Inc.
Jonathan D. Ellis, Clerio Vision, Inc.
Christopher Evans, University of North Carolina-Charlotte
Charlie Evertz, 3M Company
Massimiliano Ferrucci, National Institute of Standards & Technology
Stephen J. Furst, Smart Material Solutions, Inc.
Ken Heinz, Lawrence Livermore National Laboratory
Jonathan Hopkins, University of California – Los Angeles
Bradley H. Jared, University of Tennessee, Knoxville
Adam Jaycox, Lawrence Livermore National Laboratory
Byron R. Knapp, Professional Instruments Company
Ian Ladner, Lawrence Livermore National Laboratory
William Land II, Aerotech, Inc.
Richard K. Leach, University of Nottingham
Stephen J. Ludwick, Aerotech, Inc.
Dan Luttrell, Kriterion, LLC
Don Martin, Martin-Mason, LLC
Jimmie A. Miller, University of North Carolina-Charlotte
Joshua Montano, Los Alamos National Laboratory
Chris Morgan, Moore Nanotechnology Systems
Jim Nelson, 3M Company
Kang Ni, Apple Inc.
Robert Panas, Lawrence Livermore National Laboratory
Jon Pratt, National Institute of Standards & Technology
Suresh Kumar Ramasamy, Arris Composites
Deepak Ravindra, Micro-LAM, Inc.
Sourabh Saha, Georgia Institute of Technology
Tony L. Schmitz, University of Tennessee Knoxville
Lars Schoenemann, Leibniz-Institut für Werkstofforientierte Technologien - IWT
Richard Seugling, Lawrence Livermore National Laboratory
Hossein Shaninian, Micro-LAM, Inc.
Hongliang Shi, KLA
Stuart T. Smith, University of North Carolina–Charlotte
Alexander Sohn, Facebook
John S. Taylor, University of North Carolina-Charlotte
Adam Thompson, University of Nottingham
David L. Trumper, Massachusetts Institute of Technology

ASPE gratefully acknowledges the time and the effort given by the Organizing and Technical Program Committee and the Scientific Review Committee to bring the precision engineering community this program.

Contents

Preface ii

Organizing and Technical Program Committee ..... iii-iv

Table of Contents v

ASPE Lifetime Achievement Award vi

ASPE Distinguished Service Award vi

ASPE College of Fellows vii

ASPE Early Career Award vii

2021 Student Scholarship Recipients viii

Sustaining Corporate Sponsors ..... ix-xi

Corporate Sponsors xii

Technical Papers Index 1-10

Technical Papers 11-372

Author Index 373-375

ASPE Lifetime Achievement Award

Prof. Dr. Jan van Eijk

MICE bv

Prof. Dr. Jan van Eijk is a world leader in the development of high-precision mechatronics and a dedicated teacher committed to promoting and growing the mechatronic community. Prof. Dr. van Eijk began his career at the Philips Centre for Manufacturing Technology where he engrained the complementary practices of thoroughly understanding the fine technical details of each problem while articulating them in accessible descriptions that encouraged participation from the broader community. This deterministic approach to mechatronic system design is perhaps best exemplified by his contribution to the architecture of ASML's lithography tools. Prof. Dr. van Eijk continues to teach and promote these principles through his consulting company Mice bv, as a partner and trainer at the Mechatronics Academy, and through tutorials at ASPE and euspen meetings.

Jan van Eijk accepts the ASPE Lifetime Achievement Award as a representative of the Dutch community in precision engineering.

ASPE Distinguished Service Award

Prof. David L. Trumper

Massachusetts Institute of Technology

Prof. David L. Trumper joined the MIT Department of Mechanical Engineering in August 1993, and holds the rank of Professor. He received the B.S., M.S., and Ph.D. degrees from MIT in Electrical Engineering and Computer Science, in 1980, 1984, and 1990, respectively. Upon completing the Ph.D. degree, for three years he was an Assistant Professor in the Electrical Engineering Department at the University of North Carolina at Charlotte, working with Prof. Bob Hocken in the precision engineering group during the start-up of that program.

Dr. Trumper's research centers on the design of precision mechatronic systems, with a focus on the design of novel mechanisms, actuators, sensors, and control systems. He has conducted research in topics including precision motion control, high-performance manufacturing equipment, novel measurement instruments, biomedical and bioinstrumentation devices, and high-precision magnetic suspensions and bearings.

Dr. Trumper has been a member of ASPE since 1991, and has previously served on the board of directors and as ASPE President. He has also been co-chair of a series of six topical meetings on the Control of Mechatronic Systems, with the most recent meeting held in virtual format in May, 2020.

ASPE College of Fellows

Election to the ASPE College of Fellows is a highly prestigious honor that is intended to recognize and honor those exceptional members of the Society who have made outstanding contributions to the art and practice of Precision Engineering through original research, significant innovations, education and outreach, or service to the profession.

ASPE is proud to recognize the following individuals as new members of the College of Fellows:

Dannis M. Brouwer
University of Twente

Mark Stocker
Cranfield Precision, Division of Fives Landis Ltd.

ASPE Early Career Award

The ASPE benefits greatly from the infusion of energy and new ideas brought by members who are in the early stages of their career. The purpose of this award is to recognize outstanding technical contributions from this group, and to encourage them to continue to be active in the Society as they build their careers.

ASPE is proud to recognize the following individuals as receipients of the ASPE Early Career Award:

Michael A. Cullinan
The University of Texas at Austin

Nicholas W. Horvath
Lockheed Martin

2021 Scholarship Recipients

Graham J. Siddall ASPE Student Scholarship

The winner of the 2021 Graham J. Siddall ASPE Student Scholarship is Ian L. Heyman advised by Lei Zhou. This award includes the ASPE Annual Meeting registration fee and 4 tutorial fees.

With a 10-year student endowment, Graham Siddall recognizes a student scholar in the field of precision engineering. This prestigious award is valued at $1,000 and additionally will support the student winner in the form of waived conference and tutorial fees. Graham Siddall received his BS degree in Production Engineering and Management with First Class honors from the University of Nottingham in England. He received his M.Sc. and Ph.D. degrees in Natural Philosophy (Physics) in 1971 and 1975, respectively, working under the guidance of Professor R.V. Jones at the University of Aberdeen in Scotland.

ASPE Student Scholarships

ASPE is proud to award two student scholarships for the 36th Annual Meeting. This year's scholarship recipients are Zhidi Yang advised by Jonathan Hopkins and Hilary Johnson advised by Alex Slocum. The ASPE Student Scholarships include a waiver of the Annual Meeting registration fee and 4 tutorial fees.

ASPE 2021 Sustaining Corporate Sponsors

3M Company St. Paul, MN 55144 www.mmm.com	Aerotech, Inc. 101 Zeta Drive Pittsburgh, PA 15238 412-963-7470 www.aerotech.com
Ametek Precitech, Inc. 44 Blackbrook Road Keene, NH 03431 603-357-2511 www.precitech.com	ASM Pacific Technology Ltd. 20/F, Gateway ts, 8 Cheung Fai Road Tsing Yi, New Territories Hong Kong 852-2619 2000 www.asmpacific.com
Carl Zeiss Industrial Metrology 6250 Sycamore Lane North Maple Grove, MN 55369 763-744-2400 www.zeiss.com/metrology	Chardon Tool 115 Parker Court Chardon, OH 44024 440-286-6440 www.ChardonTool.com
Innolite Liebigstraße 20 52070 Aachen, Germany +49 241 4757080 innolite.de	Integrated Dynamics Engineering 68 Mazzeo Drive Randolph, MA 02368, USA 781-326-5700 www.ideworld.com

ASPE 2021 Sustaining Corporate Sponsors

Kern Precision, Inc.
1010 W Fullerton Ave, Unit E
Addison, IL 60101
331-979-0938
kern-microtechnik.com

Lion Precision
7166 4th Street North
Oakdale, MN 55128
651-484-6544
800-250-9297
www.lionprecision.com

Lawrence Berkeley National Laboratory
1 Cyclotron Road
MS: 46A-1123
Berkeley, CA 94720
510-486-4200
engineering.lbl.gov

MI-Partners
Habraken 1199
5507 TB Veldhoven, Netherlands
31-40-291-4920
Mi-Partners.nl

Moore Nanotechnology Systems, LLC
230 Old Homestead Highway
Swanzey, NH 03446
603-352-3030
www.nanotechsys.com

Micro-LAM, Inc.
5960 S. Sprinkle Rd,
Portage, MI 49002
269-288-4100
micro-lam.com

New Way Air Bearings
50 McDonald Boulevard
Aston, PA 19014
610-494-6700
Newwayairbearings.com

Physik Instrumente
16 Albert Street
Auburn, MA 01501
508-832-3456
PI-USA.us

ASPE 2021 Sustaining Corporate Sponsors

SPECIALTY COMPONENTS Specialty Components 14 Village Lane Wallingford, CT 06492 203-284-9112 Specialtycomponents.com	ASPE would like to thank our Sustaining Corporate Sponsors.

ASPE 2021 Corporate Sponsors

AVS US
126 Ridge Rd.
Ithaca, NY 14882
607-533-3521
www.a-v-s.us

Coherent Inc.
5100 Patrick Henry Drive
Santa Clara, CA 95054
1-800-527-3786
www.coherent.com

Corning, Inc.
Corning, NY 14831
607-974-3842
www.corning.com

Hummingbird Scientific
Williamette Dr. NE Lacey, WA
98516
360-252-2737
hummingbirdscientific.com

K & Y Diamond
2645 Diab
Laurent, Quebec H4S 1E7
Canada
514-333-5606
www.kydiamond.ca

Professional Instruments Company
7800 Powell Road
Hopkins, MN 55343
952-933-3315
www.airbearings.com

Tru-Stone Technologies
P.O. Box 430
Waite Park, MN 56387
320-251-7171
www.tru-stone.com

University of North Carolina-Charlotte
Center for Precision Metrology
9201 University City Blvd.
Charlotte, NC 28223-0001
704-687-8499
cpm.uncc.edu

Zygo Corporation
Laurel Brook Road
Middlefield, CT 06455-0448
860-347-8506
Toll-free: (800) ZYGO-NOW
www.zygo.com

ASPE would like to thank our Corporate Sponsors.

ASPE 2021 Annual Meeting
Oral Sessions

Session 1 – Optomechanical Sensing for Gravity, Acceleration, and Optical Power

Wednesday, November 3, 2021, 8:30 AM - 10:00 AM

Session Chairs:
Felipe Guzman, Texas A&M University
Jon Pratt, National Institute of Standards and Technology

1. **Four Challenges Met in the Development of Laser Metrology for the LISA Gravitational Wave Detector***
   Spero, R. (California Institute of Technology)

2. **An Electrostatic Force Balance as a Primary Standard to Measure High Laser Power by a Multiple Reflection System**
   Schulze, S.; Keck, L.; Rogers, K.; Simonds, B.; Artusio-Glimpse, A.; Williams, P.; Lehman, J. (National Institute of Standards and Technology); Seifert, F. (National Institute of Standards and Technology;University of Maryland); Newell, D. (National Institute of Standards and Technology); Theska, R. (Technische Universität Ilmenau); Schlamminger, S.; Shaw, G. (National Institute of Standards and Technology) **.....11**

3. **Membrane-based Optomechanical Accelerometry by a Multiple Reflection System**
   Chowdhury, M.D.; Agrawal, A.R.; Pluchar, C.M.; Wilson, D.J. (University of Arizona) **.....16**

4. **An Experiment to Test the Mechanical Losses of Different Bonding Techniques in Fused Silica**
   Carter, J.J. (Max Planck Institute for Gravitational Physics (Albert Einstein Institute); Institut für Gravitationsphysik der Leibniz Universität Hannover); Birckigt, P. (Fraunhofer Institute for Applied Optics and Precision Engineering; Institute of Applied Physics, Abbe Center of Photonics, Friedrich-Schiller-Universitat Jena, Albert-Einstein-Str.) Gerberding, O. (Institut für Experimentalphysik); Li, Q. (Institute of Applied Physics, Abbe Center of Photonics, Friedrich-Schiller-Universitat Jena, Albert-Einstein-Str.); Strüning, R. (Institut für Gravitationsphysik der Leibniz Universität Hannover); Ullsperger, T. (Max Planck Institute for Gravitational Physics (Albert Einstein Institute); Koehlenbeck, S.M. (Albert Einstein Institute); Institut für Gravitationsphysik der Leibniz Universität Hannover) **.....21**

***No Abstract Available**

5. **A New Spin on Kibble: A Self-Calibrating Torque Realization Device**
Comden, Z. (National Institute of Standards and Technology; University of Maryland); Schlamminger, S. (National Institute of Standards and Technology) Perera, C.W.; Seifert, F.; (National Institute of Standards and Technology; University of Maryland); Newell, D.; Hendricks, J.; Goldstein, B.; Chao, L. (National Institute of Standards and Technology) **27**

Session 2 – Precision Design

Wednesday, November 3, 2021, 10:30 AM - 12:00 PM

Session Chair:
Adam Jaycox, Lawrence Livermore National Laboratory

1. **Internal Feature Design for Increased Damping by Captured Powder**
Schmitz, T.L. (The University of Tennessee, Knoxville; Oak Ridge National Laboratory); Corson, G.; Compton, B. (The University of Tennessee, Knoxville); Gomez, M. (Oak Ridge National Laboratory) **32**

2. **Characteristics of Additively Manufactured Auxetic Materials for Spindle Vibration Mitigation**
Kim, J.; Hegde; H. (Texas A&M University); Kim, H. (Korea Institute of Industrial Technology; Korea Polytechnic University); Lee, C. (Texas A&M University) **37**

3. **High-speed Large-range Flexure-based Six-Axis Positioner**
Yang, Z.; Hopkins, J. (University of California, Los Angeles) **41**

4. **Improving Support Stiffness of Flexure Mechanisms by Statically Balancing**
de Jong, J.J.; Theans, S.; Epping; L.J.; Brouwer, D.M. (University of Twente) **45**

5. **Multi-Material Component Optimization via Hybrid Manufacturing**
Jared, B.H.; Miramontes, E.; Hamel; W.R.; Penney, J.; Schmitz, T.L. (The University of Tennessee, Knoxville); Robbins, J. (Sandia National Laboratories)..... **50**

6. **Design of the Mechanical System for the Quantum Electro-mechanical Metrology Suite**
Keck, L. (National Institute of Standards and Technology; Technische Universität Ilmenau); Schlamminger, S. (National Institute of Standards and Technology); Seifert, F. (National Institute of Standards and Technology; University of Maryland); Newell, D. (National Institute of Standards and Technology); Theska, R. (Technische Universität Ilmenau); Haddad, D. (National Institute of Standards and Technology) **54**

***No Abstract Available**

Session 3 – Micro Nano

Thursday, November 4, 2021, 8:30 AM - 10:00 AM

Session Chair:
Michael A. Cullinan, The University of Texas at Austin

1. **Accounting for Shrinkage in Functional Ceramic Structures Printed Through Two-Photon Polymerization**
   Cortes, J.; Mettry, M.; Worthington, M.; Chandrasekaran, S.; Panas, R.M. (Lawrence Livermore National Laboratory) **58**

2. **Design and Verification of a Lens Focus Module Based on a Bi-directional Thermoelectric Actuator**
   van den Buecken, N. (NTS-Group, Eindhoven University of Technology) **63**

3. **Large-Area Stitch-Free 3D Nano-Printing Based on Two-Photon Polymerization**
   Lu, W.; Shao, Q. (The Chinese University of Hong Kong); Chen, S. (The Chinese University of Hong Kong; Oxford-CityU Centre for Cerebro-Cardiovascular Health Engineering (CoCHE) **67**

4. **Testing for Torsion During Nanoindentation**
   Fan, C.; Smith, S.T. (The University of North Carolina at Charlotte) **72**

5. **Experimental Characterization of Heat Affected Zones for Fabricating Near-net Shaped Microscale Features**
   Behera, D.; Liao, A.; Cullinan, M.A. (The University of Texas Austin) **78**

6. **Precision Systems for a Conformable, Capillary-Driven, Continuous Roll-to-Roll Nanoimprint Lithography Process**
   Pandya, P.N.; Jain, A. (The University of Texas at Austin); Gilpin, R.; Baines, J. (E+R Group); Sreenivasan, S.V. (The University of Texas at Austin)..... **83**

Session 4 – Controls & Mechatronics

Thursday, November 4, 2021, 10:15 AM - 12:00 PM

Session Chair:
David L. Trumper, Massachusetts Institute of Technology

1. **Piezoelectric Shunt Damping in Cryogenic Conditions: Application to a Flexure-based Mechanism**
   Ambaum, N.; Vermeulen, J.P.M.B. (Eindhoven University of Technology); Mokrani, B. (ASML Netherlands) **89**

***No Abstract Available**

2. **Intelligent Online Scan Sequence Optimization for Uniform Temperature Distribution in Laser Powder Bed Fusion**
Okwudire, C.E.; Ramani, K.S.; He, C. (The University of Michigan) **97**

3. **Thermal Error Compensation for Large Machine Tools**
Ibabe, B.I.; Colinas-Armijo, N. (IDEKO); López de Lacalle, L.N. (EHU-UPV); Aguirre, G. (IDEKO) **102**

4. **Magnetically Levitated XYZ-Nanopositioning Sample for X-Ray Microscopy**
Heyman, I.; Ibrahim, M.; Zhou, L. (University of Texas at Austin) **108**

5. **Frequency-dependency and Coupled Dynamics of Near Field Acoustic Levitation Bearing**
Guo, P.; Wang, Y. (Northwestern University) **114**

6. **Contact-free, Electrostatically-levitated Reticle Handoff in Photolithography Tools***
Bhushan, B.M.; Trumper, D.L. (Massachusetts Institute of Technology)

7. **Active Control of High Frequency Regenerative Chatter Vibrations with Machine Tool Feed Drives**
Sencer, B.; Dumanli, A. (Oregon State University) **120**

Session 5 – Replicated Optics

Thursday, November 4, 2021, 1:30 PM - 3:00 PM

Session Chair:
Jim Nelson, 3M Company

1. **Single Point Diamond Turning of CVC SiC Using the Micro-LAM Process**
Shahinian, H.; Zhong, Y.; Turnbull, R.; Bodlapati, C.; Navare, J.; Mohammadi, H. (Micro-LAM, Inc.) **125**

2. **Simulation and Comparative Metrology of Diamond Dies, Metal Molds, and Replicated Microlens Arrays for Mass Fabrication**
Eaton, P. (North Carolina State University); Furst, S.J.; Cates, N.; Micklow, L. (Smart Material Solutions, Inc.); Pankow, M. (North Carolina State University) **130**

3. **Metrology of Ultra-High Precision Stamped Metallic Optical Mirrors for Photonics Packaging and Ultraviolet LED Applications**
Chen, Y.; Johnstone, R.; Hii, K.; Vallance R.R. (CudoForm, Inc.) **136**

***No Abstract Available**

4. **Precision in Roll-2-Roll Printed Electronics: Keynote**
Spaan-Burke, T.M.; van der Nolle, R.; de Vries, J.; Daneshkhah, B.; Felius, M.; Overschie, P.; Hannot S. (IBS Precision Engineering) **142**

5. **Single-Point Diamond Turning of Features with Large Azimuthal Slope**
Sohn, A.; Naples, N. (Facebook Reality Labs) **146**

Session 6 – Replicated Optics

Friday, November 5, 2021, 8:30 AM - 10:00 AM

Session Chairs:
Jonathan D. Ellis, Clerio Vision, Inc.
Richard K. Leach, University of Nottingham

1. **Qualitative Edge Topology Inspection and Interpretation by Enhanced Knife-Edge Interferometry**
Lee, C.; Wang, Z. (Texas A&M University) **152**

2. **The Effect of Motion Blur on Photogrammetric Measurements of a Robotic Moving Target**
Isa, M.A. (University of Nottingham); Leach, R.K. (University of Nottingham; Taraz Metrology); Branson, D.; Piano, S. (University of Nottingham) **155**

3. **Preliminary Study on Fluorescence Strobo-Stereoscopy for 3D Surface Imaging**
Guo, X.; Lee, C. (Texas A&M University) **161**

4. **Ultra-High-Speed Micromachining Spindle Metrology under Radial Loading Conditions**
Nahata, S.; Ozdoganlar, O.B. (Carnegie Mellon University) **165**

5. **Lateral Shift Mapping for Absolute Metrology of Acylindrical X-ray Telescope Mirrors**
Wisniewski, H.J. (The University of Arizona); Whalen, M.M; Heilmann, R.K.; Shattenburg, M.L. (Massachusetts Institute of Technology); Chalifoux, B.D. (The University of Arizona) **171**

6. **A Pilot Study on Uncertainty Analysis for Stereo-vision Photogrammetry**
Lifei, R. (The Hong Kong Polytechnic University; Zhejian University); Fai, C.C. (The Hong Kong Polytechnic University); Yanlong, C. (Zhejian University) Da, L. (The Hong Kong Polytechnic University); Jiangxin, Y.; Yanpeng, C. (Zhejian University) **178**

***No Abstract Available**

Session 7 – Precision Manufacturing

Friday, November 5, 2021, 10:30 AM - 12:00 PM

Session Chair:
Stephen J. Furst, Smart Material Solutions, Inc.

1. **Single Point Diamond Cutting of High-Aspect Ratio V-Grooves: Alternative Flank Cutting Strategy and Preliminary Burr Formation Analysis**
   Rangel, O.F.; Tutunea-Fatan, R. (Western University); Bordatchev, E.V. (National Research Council of Canada) **183**

2. **Tool Wear Evaluation Using a Constrained-motion Dynamometer**
   Gomez, M. (Oak Ridge National Laboratory); Schmitz, T.L. (Oak Ridge National Laboratory; University of Tennessee, Knoxville) **189**

3. **Integral Blade Rotor Milling Improvement by Physics-guided Machine Learning**
   Corson, G. (University of Tennessee, Knoxville); Karandikar, J. (Oak Ridge National Laboratory); Schmitz, T.L. (University of Tennessee, Knoxville; Oak Ridge National Laboratory) **193**

4. **A New Diamond Turning Model for Generating a Scratch-Free Surfaces in AL 6061 with Embedded Hard Particles**
   Ding, X.; Roblee, J. (AMETEK Precitech Inc.) **199**

5. **Ductile Cutting Regime in Diamond Milling of Monocrystalline Silicon**
   Groeb, M. (Kern Microtechnik GmbH; Technical University of Darmstadt); Fritz, M. (Kern Microtechnik GmbH); Groeb, J. (Independent Researcher); Ensinger, W. (Technical University of Darmstadt) **205**

6. **Ultrafast Laser Stress Figuring of Fused Silica Mirrors**
   Laverty, K.A.; Arnold, I.J.; Chalifoux, B.D. (University of Arizona) **211**

***No Abstract Available**

ASPE 2021 Annual Meeting
Poster Sessions

Wednesday, November 3, 2021, 3:30 PM – 5:00 PM
Thursday, November 4, 2021, 3:30 PM – 5:00 PM

1. **Fundamental Precision Limit of Frequency Measurement of Linear Harmonic Oscillators**
   Wang, M. (National Institute of Standards and Technology; University of Maryland); Zhang, R. (Worcester Polytechnic Institute); Ilic, R. (National Institute of Standards and Technology); Liu, Y. (Worcester Polytechnic Institute); Aksyuk, V.A. (National Institute of Standards and Technology) **215**

2. **CNC Machining and Metrology Training: ACE Program Update**
   Schmitz, T.L. (University of Tennessee, Knoxville; Oak Ridge National Laboratory); Cornelius, A.; Dvorak, J.; Nazario, J. (University of Tennessee, Knoxville); Betters, E. (University of Tennessee, Knoxville; Oak Ridge National Laboratory); Smith, S.; Blue, C. (Oak Ridge National Laboratory); Harmon, J.; Morrison, M.; Blevins, T.; Hopkins, J. (IACMI – The Composites Institute) **220**

3. **Optical Knife-edge Displacement Sensor Modeling**
   Zameroski, R. (University of Tennessee, Knoxville); Gomez, M. (Oak Ridge National Laboratory); Schmitz, T.L. (University of Tennessee, Knoxville; Oak Ridge National Laboratory) **221**

4. **Stability Analysis of a Constrained-motion Dynamometer**
   Gomez, M. (Oak Ridge National Laboratory); Schmitz, T.L. (University of Tennessee, Knoxville; Oak Ridge National Laboratory) **232**

5. **Tool Wear Evaluation Using a Constrained-motion Dynamometer**
   Gomez, M. (Oak Ridge National Laboratory); Schmitz, T.L. (University of Tennessee, Knoxville; Oak Ridge National Laboratory) **238**

6. **CNC Machining Considerations for WAAM Preforms**
   Dvorak, J.; Cornelius, A.; Corson, G.; Zameroski, R.; Jacobs, L.; Penney, J. (University of Tennessee, Knoxville); Schmitz, T.L. (University of Tennessee, Knoxville; Oak Ridge National Laboratory) **242**

7. **Surface Metrology of a DED Lens AM Part: Optical Microscope***
   Morgan, W.; Yazzie, J.; Wilson, W. (Navajo Technical University); Valdez, M.O.; Montano, J.D. (V&M Global Solutions LLC), Haliday, H.S.; Shanmugam, R.; Romani, M. (Navajo Technical University)

***No Abstract Available**

8. **Surface Metrology of a DED Lens AM Part: Contact Surface Profilometer***
Yazzie, J.; Morgan, W.; Wilson, W. (Navajo Technical University); Valdez, M.O.; Montano, J.D. (V&M Global Solutions LLC), Haliday, H.S.; Shanmugam, R.; Romani, M. (Navajo Technical University)

9. **Effects of Surface Treatments on ABS Mechanical Properties for Fused Filament Fabrication**
Shen, J.; Patterson, M.R.; Marshall, E.; Dvorak, J.; Romberg, S.; Compton, B. (University of Tennessee, Knoxville) Schmitz, T.L. (University of Tennessee, Knoxville; Oak Ridge National Laboratory) **248**

10. **A Prototype Contamination Inspection System for DUV/EUV Reticles**
Papadakis Ktistakis, I.; Pawlowski, M.E.; Walsh, J.; Loke, C.; Bendiksen, A.; Munden, R.; Roux, S. (ASML) **254**

11. **A Torsion Pendulum for Chip-scale Relative Gravimetry**
Pratt, J.R.; Schlamminger, S. (National Institute of Standards and Technology); Agrawal, A.R.; Wilson, D.J. (University of Arizona) **260**

12. **Optomechanical Inertial Sensors***
Guzman, F. (Texas A&M University)

13. **Remote Bayesian Updating for Milling Stability**
Karandikar, J. (Oak Ridge National Laboratory); Ramsauer, C.; Leitner, D. (University of Tennessee, Knoxville); Schmitz, T.L. (Oak Ridge National Laboratory; University of Tennessee, Knoxville); Bleicher, F. (University of Tennessee, Knoxville) **266**

14. **Accounting for Shrinkage in Functional Ceramic Structures Printed through Two-photon Polymerization**
Cortes, J.; Mettry, M.; Worthington, M.; Chandrasekaran, S.; Panas, R.M. (Lawrence Livermore National Laboratory) **271**

15. **Precision Stamp-based Thin-film Material Transfer System Using Soft-robotic Manipulation**
Ahn, S.; Zhou, L. (University of Texas at Austin) **276**

16. **Ductile Cutting Regime in Diamond Milling of Monocrystalline Silicon**
Groeb, M. (Kern Microtechnik GmbH; Technical University of Darmstadt); Fritz, M. (Kern Microtechnik GmbH); Groeb, J. (Independent Researcher); Ensinger, W. (Technical University of Darmstadt) **282**

***No Abstract Available**

17. **Milling Force Prediction Case Study for Non-standard Geometry Endmill Using Structured Light Scanning**
No, T. (University of Tennessee, Knoxville); Gomez, M. (Oak Ridge National Laboratory); Schmitz, T.L. (University of Tennessee, Knoxville; Oak Ridge National Laboratory) **288**

18. **Force-controlled Electrode Holder for Lathe-type Electrochemical Discharge Machine**
Furutani, K.; Tsuchiya, T. (Toyota Technological Institute) **294**

19. **In-process Machining Process Monitoring Based on Impedance Model of Dielectric Coating Layer at Tool-chip Interface**
Chun, H.; Kim, J.; Lee, C. (Texas A&M University) **298**

20. **Microfabrication and Experimental Investigation of Drag Reduction and Fouling Resistance Potential of Asymmetric Triangular Riblets**
Hamilton, B.W.; Tutunea-Fatan, R. (Western University); Bordatchev, E.V. (National Research Council of Canada); Farzaneh, A.; Hopkins, J.B. (University of California Los Angeles) **302**

21. **A set of Turing Complete Mechanical Logic Elements and a Simple Logic Circuit**
Sun, F.; Panas, R.M.; Bekker, L.; Pascall, A.J. (Lawrence Livermore National Laboratory) **308**

22. **A Dynamic Athermalization Approach for Precision Machine Designs***
Hijkoop, E.G.; Verbaan, K.; van Swaaij, S. (NTS-Group)

23. **Self-Sensing Hysteresis-Type Bearingless Motor**
Homiller, L.; Zhou, L. (University of Texas at Austin) **312**

24. **Time-domain Based Early Detection of Chatter Vibrations**
Bahtiyar, K.; Sencer, B. (Oregon State University) **317**

25. **Volumetric Two-Photon Polymerization Based on Computer-Generated Holograms**
Fu, Z. (The Chinese University of Hong Kong); Liu, K. (Tsinghau University); Wang, Y. (The Chinese University of Hong Kong; Centre for Perceptual and Interactive Illetelligence Ltd.); Chen, S. (The Chinese University of Hong Kong; Tsinghau University) **322**

26. **Parallel 3D Nanofabrication Using 1000 Programable Laser Foci**
Ouyang, W. (The Chinese University of Hong Kong); Han, F.; Chen, C. (The Chinese University of Hong Kong; Tsinghau University) **327**

27. **Control Co-design for Magnetically-suspended Stages with Light Weight and Flexible Structure**
Wu, J.; Zhou, L (University of Texas at Austin) **332**

***No Abstract Available**

28. **Study on Non-Axisymmetric 3D Curved Surface Turning by Driven-Type Rotary Tool Synchronized with Sprindle**
Ishizuka, A.; Morimoto, Y.; Hayashi, A.; Kaneko, Y.; Suzuki, N. (Kanazawa Institute of Technology) **338**

29. **Scaleable Positioning System for Minimal Time to Market and Low Cost***
van den Braber, R.; Verbaan, K. (NTS-Group)

30. **Innovation in Nanopositioning***
Raby, A.; Bartlett, G. (Prior Scientific Instruments Ltd.)

31. **Deep Learning Workflows for Dimensional Metrology with High-Resolution X-ray Computed Tomography**
Tekawade, A. (Argonne National Laboratory); Villarraga-Gomez, H. (Carl Zeiss Industrial Metrology, LLC); Andrew, M. (Carl Zeiss X-ray Microscopy, Inc.) Sforzo, B.A.; Kastengren, A.L.; Powell, C.F. (Argonne National Laboratory) **344**

32. **Design and Verification of a Planar, Flux-Steering Magnetic Actuator***
Anthis, A.F.; Trumper, D.L.; Hamer, T.T. (Massachusetts Institute of Technology)

33. **Advancing Throughput and Image Quality in 3D X-ray Microscopy by Deep Learning Reconstruction Techniques**
Villarraga-Gomez, H. (Carl Zeiss Industrial Metrology, LLC); Andreyev, A.; Andrew, M.; Bale, H.; Sanapala, R.; Terada, M.; Gu, A.; Johnson, B. (Carl Zeiss X-ray Microscopy, Inc.); Omlor, L. (Carl Zeiss, Inc.); Graf vom Hagen, C. (Carl Zeiss X-ray Microscopy, Inc.) **347**

34. **Design of a Polariscope Tool for the Evaluation of Strain in Roll-to-roll Nanofabrication**
Groh, B.T.; Connolly, L.G.; Cullinan, M.A. (University of Texas at Austin) **353**

35. **Optical Fiber Surface Probe Using Mechanically Modulated Fabry Perot Interferometer**
Shabahang, F.; Smith, S.T. (University of North Carolina at Charlotte) **355**

36. **Relaxed Uncertainty Dimensional Metrology for Assembly via Photogrammetry Using Open-Source Libraries**
Nawab, R.; Allen, A.D. (University of North Carolina at Charlotte); Lee, N. (Caterpillar Inc.) **360**

37. **Precision Design and Error Analysis of a Pump Variable Volute Mechanism**
Johnson, H.A.; Slocum, A.H. (Massachusetts Institute of Technology) **365**

38. **Interference Fit, Sub-Micron Piloted Tool Holder**
Arneson, D. (Professional Instruments Company) **370**

39. **Effect of Squeeze Film on Dynamics of an Air Bearing***
Knapp, B.; Arneson, D.; Oss, D. (Professional Instruments Company)

***No Abstract Available**

Technical Papers

An Electrostatic Force Balance as a Primary Standard to Measure High Laser Power by a Multiple Reflection System

Sven Schulze[1], Lorenz Keck[1], Kyle Rogers[1], Brian Simonds[1], Alexandra Artusio-Glimpse[1], Paul Williams[1], John Lehman[1], Frank Seifert[1,2], David Newell[1], René Theska[3], Stephan Schlamminger[1], Gordon Shaw[1]
[1]National Institute of Standards and Technology
Gaithersburg, MD, United States of America
[2]Joint Quantum Institute
University of Maryland
College Park, MD, United States of America
[3]Precision Engineering Group
Technische Universität Ilmenau
Ilmenau, Germany

INTRODUCTION

After the redefinition of the Internal System of Units (SI) in 2019, Planck's constant, *h*, defines the unit of mass, the kilogram, using absolute precision balances to generate very precise forces traceable to *h*. This eliminates the need for physical artifacts for mass calibrations and provides new opportunities in force measurements generally.

An application of great interest for metrologists is laser power calibration. A laser provides a defined force to a highly reflective surface. With the power P, the angle θ between the laser beam and the surface normal, and the speed of light, c, the photon momentum force F_L can be determined with

$$F_L = \frac{2P\cos\theta}{c}.$$

By using a high-power laser of $140\ kW$ and $\theta = 45\,°$ the photon pressure to an ideally reflective surface results in a force of approximately. $680\ \mu N$. The relative uncertainties of conventional calorimetric calibrations for lasers with high powers ($> 100\ W$) are in a range between 10^{-2} to 10^{-3}. Comparing this with reported uncertainties in precision mass measurements demonstrate uncertainties of 10^{-6} [5]. This suggests that there is great potential to improve laser power measurement using these precision balances to measure photon pressure forces traceable to *h*.

Performing a measurement with lower uncertainty than the state of the art requires a relative expanded uncertainty of $< 0.1\,\%$ for a measurement of approximately $680\ \mu N$ of laser photon pressure force. For measuring small forces with a small uncertainty, electrostatic force balances are recommended as shown in Figure 1Figure 1:. This is mainly because a Kibble balance requires either the measurement of an extremely small voltage for the flux integral characterization, or an extremely small current during force measurement for the forces of interest to laser power calibration. For this reason, we favor an electrostatic balance over a Kibble balance for this measurement.

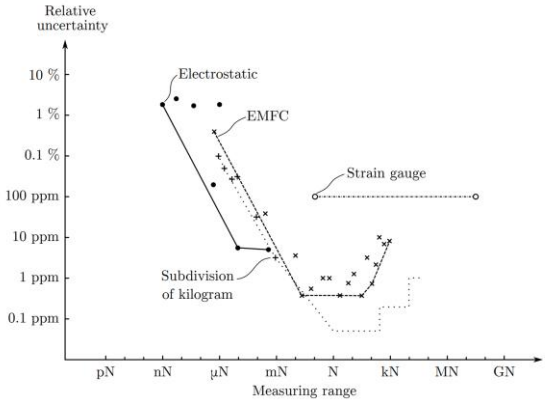

Figure 1: Shows the achievable uncertainty in the specified force measurement range for commercial electrostatic and electromagnetic (EMFC) balances. Adapted from [1]

For the final laser power measurement, a custom laser system is being designed. The High Amplification Laser pressure Optics (HALO) [2] is used to passively amplify the laser pressure force from an incoming $10\ kW$ beam using 14 reflections on a sensing mirror, which is attached to an electrostatic force balance.

THEORY OF THE ELETROSTATIC FORCE BALANCE

The principle of operation of an electrostatic force balance is visually demonstrated in Figure 2: Simple sketch of the working principle in an electrostatic balance: 1 - balance mechanism, 2 - flexure pivots, 3 - highly reflective mirror, 4 - capacitor with outer and inner electrode, 5 - laser interferometer, 6 - laser beam under test.Figure 2. A balance mechanism based on a flexure design supports the inner electrode of a cylindrical capacitor. Also, a mirror is supported with the free moving member of the mechanism. In the weighing mode, the laser force F_L acts upon the mirror and is compensated with the electrostatic force F_{el} by adjusting the voltage V at the capacitor according to the following equation (excluding the surface potential for the sake of simplicity)

$$F_L = F_{el} = \frac{1}{2}\frac{\mathrm{d}C}{\mathrm{d}x}V^2.$$

$\frac{\mathrm{d}C}{\mathrm{d}x}$ describes the capacitance gradient, which is measured in an independent balance mode called “capacitance gradient mode”. Here, the balance is deflected, and the capacitance, C, monitored for different balance positions with a capacitance bridge.

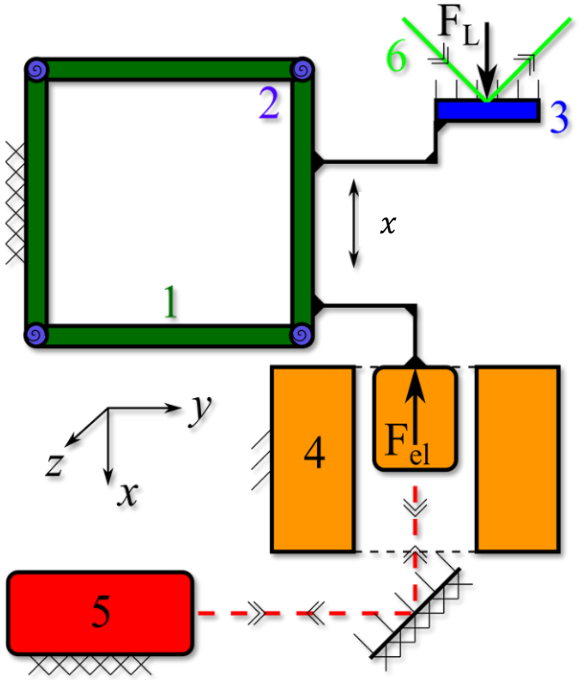

Figure 2: Simple sketch of the working principle in an electrostatic balance: 1 - balance mechanism, 2 - flexure pivots, 3 - highly reflective mirror, 4 - capacitor with outer and inner electrode, 5 - laser interferometer, 6 - laser beam under test.

BALANCE SETUP

A new electrostatic balance has been designed and is currently being characterized at NIST. The balance design consists of a new monolithic flexure mechanism [3], a cylindrical capacitor, a Fabry Perot interferometer, and a new control system. A photo of the new balance setup can be seen in Figure 3. The new mechanism is based on parallel four bar linkage kinematics with adjustable counterweights and employs an inverted pendulum to reduce the stiffness of the mechanism to approximately $0.045\ N/m$. Theoretically, the stiffness could continuously be further reduced.

The control system is based on a PID loop and allows for customizing the control parameters for different balance settings.

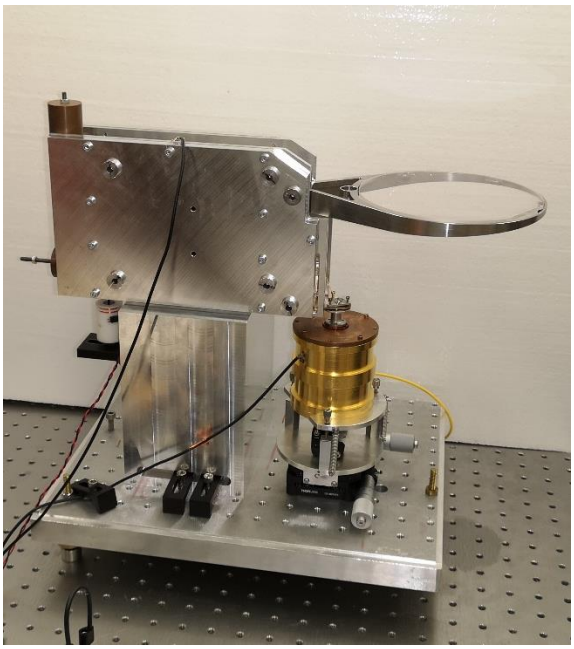

Figure 3: The new electrostatic force balance for photon momentum measurement at NIST.

PRELIMINARY MEASUREMENTS

We conducted a series of measurements in order to characterize the balance capabilities and verify that the balance setup can measure with the required relative uncertainty. The measurements are briefly introduced below.

Capacitance gradient

We measured the capacitance gradient of the balance to ensure that the gradient is linear and stable over a certain time interval. Therefore, the mechanism is deflected and returned to its initial position by using an external coil. The deflection

is stepped into 5 steps up and 5 steps down and is repeated 20 times over a total time interval of 14 hours.

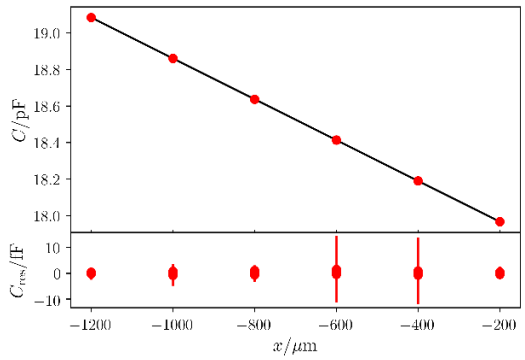

Figure 4: Capacitance gradient measurement for the new balance. The upper plot shows the capacitance data over the balance deflection, and the lower plot shows the fitting residuals for a second order polynomial fit.

The gradient is approximately $1.2\ pF/mm$, but the true value for a measurement depends on the alignment of the inner electrode with respect to the outer electrode [4]. The gradient needs to be measured before or after a measurement to make sure that alignment has not changed. In general, it shows good linearity as expected from the cylindrical capacitor usually employed in electrostatic force balances at NIST.

Resolution of the balance

In a further step we measured the resolution of the new balance. The Allan variance was calculated for two time series measurements of electrostatic force. In both cases, the balance was covered with a draft shield and left undisturbed during data collection.

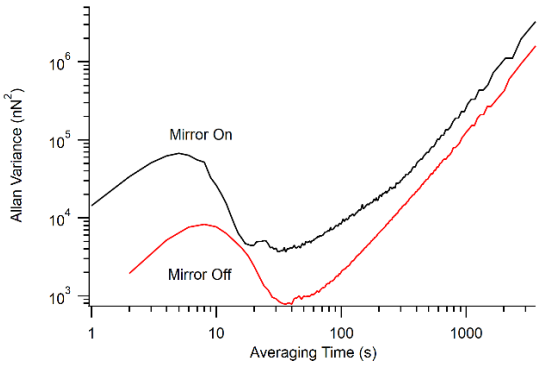

Figure 5: Allan Variance plot for the new balance. The balance was kept in an equilibrium position with the capacitor force acting. The setup was draft shielded, and we did both a measurement with the mirror, and without the mirror.

There is a clear difference in the measurements depending on whether the mirror was attached to the balance. The minimum in the Allan deviation (calculated from the square root of the variance) occurred at approximately $30\ nN$ after 40 seconds of averaging time when the mirror was not attached, and at approximately $60\ nN$ after 60 seconds of averaging when the mirror was attached. The $15\ cm$ diameter mirror blank is susceptible to unpredictable external forces from air currents and other disturbances inside the draft shield. It should be noted, however, that for longer averaging times especially, temperature fluctuations can cause long term drift due to thermomechanical expansion of the balance mechanism.

Stiffness and Hysteresis of the mechanics

Flexure mechanisms play an important role in precision balances due to their virtually infinite resolution. However, it must be said, that flexure systems show hysteresis due to anelastic effects from the material that is being bent.

We conducted a stiffness measurement on the balance by stepwise deflecting the mechanism up and down using the electrostatic force of the capacitor. Figure shows the result of a stiffness measurement. Here, the mechanism is deflected and returned to its initial position by using the capacitor. The deflection occurs in 5 steps up and 5 steps down and is repeated 20 times over a total time interval of 25 hours. The residuals of the stiffness plot indicate the stiffness is stable over that time.

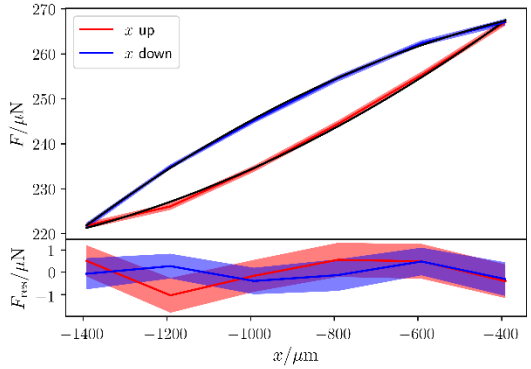

Figure 6: Stiffness measurement at the new balance setup. The inverted pendulum was adjusted such that the stiffness yields approximately. 0.045 N/m. We see a hysteresis in the measurement caused by anelastic aftereffects in the flexures. This hysteresis is on the order of $10\ \mu N$ *for a travel of* $1\ mm$.

More measurements on the balance hysteresis will be done in order to characterize this phenomenon more thoroughly and to make a certain statement that this will not limit our measurement accuracy. Previous experience with other

electrostatic force balances suggests that $10\,\mu N$ hysteresis over $1\,mm$ of balance deflection should not present a limitation in the measurement precision [5] provided that transient deflections from the balance null position can be kept reasonably small.

Coupler rotation

We designed the balance such that the mirror axis (equal to force application axis) is offset from the capacitor force axis. This was done to make sure that none of the laser power transmitting through the mirror can heat any of the balance components. This feature introduces a corner loading error because the free end of the mechanism translates linearly only in an ideal system [3]. The impact of the corner loading error depends on the parasitic rotation of the free end, which is why we measured this rotation around all three axes. The measurement was conducted with an autocollimator and a plane mirror put on the free end while moving the balance.

According to the theory in [3] for the corner loading analysis, the measurements show that we do not have to correct for this error since the relative magnitude of the effect is below a threshold of 10^{-4}. Note that the rotation around the x axis, φ_x does not contribute to this error, because this describes a rotation around the force measurement axis. Therefore, the mechanism is deflected and returned to its initial position by using the capacitor. The deflection is repeated 20 times over a total time interval of 5 days.

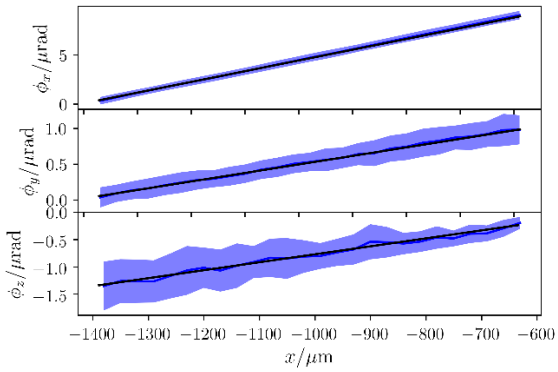

Figure 7: Rotation of the free end of the parallel four bar linkage measured with an autocollimator and a flat mirror placed on the free end while moving up and down.

Test run with a $5\,mg$ E1 mass

The timeseries data in Fig. 8 show electrostatic force during a weighing experiment. A commercial class E1 $5\,mg$ reference mass (tolerance of $3\,\mu g$) was placed onto and removed from the balance manually while electrostatic force required to maintain a null position was recorded. When the mass is on the balance, electrostatic force decreases to maintain the null position. This change in electrostatic force is equal to the weight of the test mass. The force was averaged for 60 seconds before, during, and after the mass placement on the balance, with approximately 60 seconds allowed for the balance control loop to equilibrate to its new static force. The average of the balance forces with the mass off was subtracted from the balance force with the mass on to determine the differential force due to the reference mass. The trial was repeated 5 times yielding a mass value of $4.990\,mg$ with a standard deviation of $0.011\,mg$ using local gravitational acceleration.

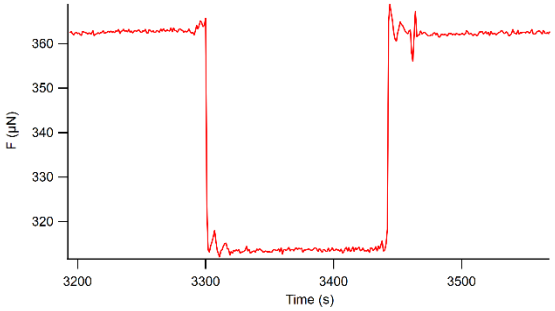

Figure 8: Typical measurement signal of the E1 $5mg$ mass measurement with the new electrostatic force balance.

Although the statistical uncertainty represented by the standard deviation of the measurement results is sufficiently large to consider the mass determined with the electrostatic force balance equivalent to the nominal mass value of the reference, it is worth noting that the accuracy of the current measurement may be limited by the capacitance bridge used to determine $\frac{dC}{dx}$. The values of capacitance during the gradient determination varied between approximately $18\,pF$ and $19\,pF$. The resolution of the bridge used in this work is $0.01\,pF$. For the capacitance gradient measurement, the $1\,pF$ change can therefore only be determined with a relative accuracy of approximately $1\,\%$. In this context, the $0.2\,\%$ relative difference between the mass determined from electrostatics and the nominal value of the reference would be reasonable to expect. The use of a higher-precision capacitance bridge may further improve comparisons with other reference forces.

CHALLENGES & SOLUTION APPROACES

The measurement of this high laser power comes with some particular challenges that we want to address briefly.

(1) Air currents around the large mirror cause a noticeable amount of force noise. We will enclose the balance and the mirror with a draft shield and only leave the top of the mirror where the test laser beam is incident.

(2) The balance hysteresis should be kept as low as possible. For this, we want to make sure that the balance does ideally not deflect when the laser beam is applied. The approach here is to take advantage of the digital system and ramp the laser power up. Also, implement a feedforward structure in the control system to simultaneously apply the right electrostatic force to the balance while the laser is ramped up will minimize deviation from the null position.

(3) We expect noise and drifts due to thermal power induced in the balance components from absorbed heat in the mirror and scattering reflections. For keeping this effect small, we want to minimize the integration time in a measurement, and optimize the thermal characteristics of the balance enclosure.

CONCLUSIONS & OUTLOOK

Most of the hard- and software components for the new electrostatic force balance for laser power measurement at NIST have been developed. Next, we expect to conduct the first measurement of a laser force provided by the HALO laser system.

From a laser system design perspective, we aim for new developments to improve the laser collimation to reduce the size of the mirror attached to the balance and therefore, the weight of the mirror. This development could help to further reduce measurement uncertainty from air currents in the future.

DISCLAIMER

This article is authored by employees of the U.S. federal government and is not subject to copyright. Commercial equipment and materials are identified in order to adequately specify certain procedures. In no case does such identification imply recommendation or endorsement by the National Institute of Standards and Technology, nor does it imply that the materials or equipment identified are necessarily the best available for the purpose.

REFERENCES

[1] R. Marangoni, “Traceable Multicomponent Force and Torque Measurement”, Dissertation, Technische Universitaet Ilmenau, 2019

[2] Alexandra B. Artusio-Glimpse, “High amplification laser-pressure optic enables ultra-low uncertainty measurements of optical laser power at kilowatt levels”, 17 August 2021

[3] L. Keck, G. Shaw, R. Theska and S. Schlamminger, "Design of an Electrostatic Balance Mechanism to Measure Optical Power of 100 kW", *IEEE Trans. Inst. and Meas.*, vol. 70, pp. 1-9, 2021

[4] Julian Stirling, Gordon A Shaw, “Realising traceable electrostatic forces despite non-linear balance motion” Meas. Sci. Technol. 28, March/02/2017

[5] G.A. Shaw, J. Stirling, J.A. Kramar, A. Moses, P. Abbott, R. Steiner, A. Koffman, J.R. Pratt, Z.J. Kubarych, "Milligram mass metrology using an electrostatic force balance", *Metrologia*, vol. 53, pp. A86, 2016

MEMBRANE-BASED OPTOMECHANICAL ACCELEROMETRY

Mitul Dey Chowdhury[1], Aman R. Agrawal[1], Christian M. Pluchar[1], and Dalziel J. Wilson[1,2]

[1]Wyant College of Optical Sciences, University of Arizona, Tucson, Arizona, USA

[2]Department of Physics, University of Arizona, Tucson, Arizona, USA

OPTOMECHANICAL ACCELEROMETERS

Optomechanical accelerometers employ a mechanical resonator as a test mass and an optomechanical interferometer for displacement-based readout. The sensitivity of the readout can be enhanced by coupling the mechanical resonator to an optical cavity. Advantages of cavity optomechanical systems over electromechanical accelerometers include quantum-noise-limited displacement readout (enabling thermal-noise-limited acceleration sensitivity), high bandwidth (limited by cavity response time), in-situ calibration (using the optical wavelength as a ruler), and radiation-pressure actuation of motion (for tailoring or stabilizing the mechanical susceptibility of the test mass). Numerous optomechanical platforms have been explored in the past decade, based on photonic crystals [1], whispering gallery mode resonators such as microtoroids, and Fabry-Pérot cavities [2] coupled to tethered or levitated test masses with frequencies varying from 10 Hz to 100 kHz, and sensitivities to thermal (Brownian) noise ranging from 10 $\mathrm{n}g_0/\sqrt{\mathrm{Hz}}$ to 10 $\mu g_0/\sqrt{\mathrm{Hz}}$ ($g_0 = 9.81\ \mathrm{m/s^2}$). Despite this progress, platforms that meet the unique technical demands of optomechanical accelerometry – in particular, the ability to monolithically integrate a relatively large and compliant test mass with an optical microcavity – remain an open line of investigation.

ACCELEROMETER DESIGN

We propose a simple and scalable platform for optomechanical accelerometry based on a pair of vertically integrated silicon nitride (Si_3N_4) membranes with different stiffnesses, forming an optical cavity (Fig. 1).

In addition to the generic strengths of all modern optomechanical devices, membranes made of stoichiometric Si_3N_4 possess a set of compelling

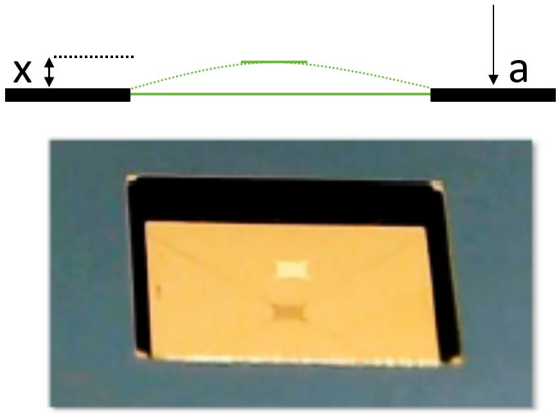

FIGURE 1. Vertically integrated optomechanical accelerometer based on a pair of 100 nm-thick Si_3N_4 membranes with different stiffnesses. The top membrane is in a trampoline geometry, comprising a [insert dimensions] pad rigidly attached to a silicon chip with four tethers. The bottom membrane is square, affixed to the same chip.The width of the membrane window is 2.5 mm. The two masses also form an etalon.

features motivating this design. Among them are the ability to achieve ultra-high quality factors – approaching 1 billion [3] – using phononic engineering; the ability to tune resonance frequencies using optical radiation pressure, thermal, and electrostatic forces; parts-per-million optical loss; and the ability to operate as a high reflectivity mirror by photonic crystal patterning. Another advantageous feature of Si_3N_4 membranes specific to accelerometry is their quality factor (Q) versus mass (m) scaling: due to an effect called dissipation dilution, the Q of tensily stressed membranes increases with area, enabling large $Q \times m$ factors (yielding low thermal acceleration) in a relatively compact form factor (in one dimension).

Traditionally, membrane accelerometers must be integrated as part of a separate optical cavity that amplifies the probe light (when its wavelength is tuned close to the cavity's resonance), enhancing

the sensitivity of displacement-readout by the cavity's finesse ($\mathcal{F}$). Our monolithic design (Fig 1.) overcomes the technical challenges of aligning separate optomechanical components and precludes long-term mechanical drift between them. Furthermore, monolithic cavity accelerometers are a prerequisite for proposed membrane-based dark matter detectors [4].

DEVICE CHARACTERIZATION

As a demonstration, we have studied the optical and mechanical properties of the device shown in Fig. 1, consisting of a trampoline monolithically suspended above a square membrane on opposite sides of a 200 μm silicon chip. (Devices were fabricated using standard photolithography and KOH wet-etching steps for a Si_3N_4 trampoline [5] but etching only from the trampoline side.)

Optically, the pair of reflective membranes forms an etalon (of 200 μm average mirror-separation), which may be probed in transmission (employed here) or in reflection. The transmittance (ratio of transmitted optical power to the incident power) as a function of wavelength was used to characterize the finesse of the optical cavity (Fig. 2). From the sweep, we inferred $\mathcal{F} \approx 2$.

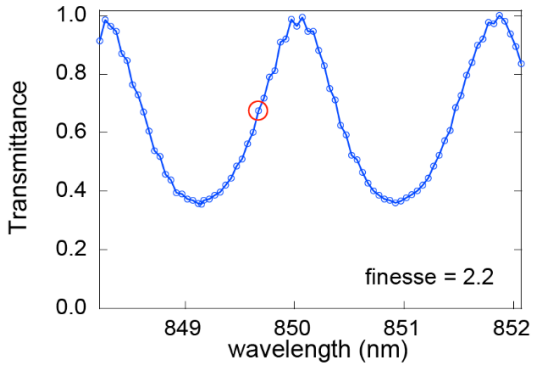

FIGURE 2. The device forms a low-finesse optical cavity. An ECDL beam at normal incidence was wavelength-swept around a central wavelength of 850 nm to obtain the transmission fringes. 849.7 nm (highlighted in red) was chosen as the probe wavelength for "side-of-the-fringe" operation in transmission.

An acceleration applied to the chip results in a displacement of the trampoline ($m \approx 10\,ng$, design mechanical resonance frequency, $\omega_0 \approx 2\pi \times 40\,\mathrm{kHz}$) relative to the stiffer square membrane ($m \approx 1\,\mu g$, $\omega_0 \approx 2\pi \times 180\,\mathrm{kHz}$). The motion is imprinted onto the phase of the intracavity light field, thereby leading to changes in the transmitted amplitude. This interferometric aspect of the optical cavity implies that the resulting power fluctuations can be directly measured by a photodetector to infer the displacement of the test mass (as an alternative to optical homodyne detection, which is sensitive to phase differentials as opposed to amplitude fluctuations of the transmitted light). In this direct detection scheme, the displacement is maximally transduced to a transmittance change for probe wavelengths such as 849.7 nm (our choice, highlighted in Fig. 2) that ensure "side-of-the-fringe" operation.

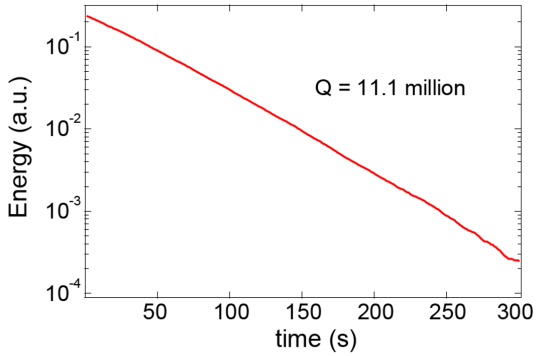

FIGURE 3. Energy ringdown (exponential decay) to measure the mechanical quality factor of the fundamental trampoline mode.

The displacement, and subsequently, acceleration can be inferred by taking a power spectral density (PSD) of the detected signal, which is used to characterize the mechanical susceptibility (χ) of the test mass to external accelerations:

$$|x(\omega)| = |\chi(\omega)||\,a(\omega)|, \qquad \chi(\omega) = \frac{1}{(\omega_0^2 - \omega^2) + \frac{2i\omega\omega_0}{Q}}, \tag{1}$$

determined by the resonance frequency (ω_0) and mechanical damping rate (ω_0/Q). Operating in a vacuum chamber at 10^{-7} mbar, the spectrum was investigated for peaks at the expected resonances, arising from the thermally driven motion (thermal acceleration $a_{th} = \sqrt{4k_B T\omega_0/mQ}$) of the trampoline. The fundamental mode was found to be 39.77 kHz. The area under the PSD peak corresponds to the thermal energy of the oscillator at

room temperature ($T = 300\ K$): $< x^2 > = k_B T / m\omega_0^2$, and is used to calibrate the signal from voltage units to displacement units.

Ringdown measurements were used to obtain the Q factor of the trampoline (Fig. 3): the device was excited briefly at resonance using an external piezoelectric drive, and the area under the resonance peak was monitored as a function of time. The time taken by the oscillator to relax to thermal equilibrium is of the order of Q/ω_0, the inverse of the damping rate. The ringdown measurement confirmed an ultra-high Q of ≈ 11 million. The magnitudes of ω_0 and Q fully characterize the acceleration susceptibility, which is used via equation (1) to convert the measured displacement of the trampoline to acceleration.

Accelerometer Sensitivity

Mechanical-resonator-based accelerometers amplify acceleration signals by a factor of Q on resonance, including thermal-noise induced Brownian motion which fundamentally limits the sensitivity of the device. As shown in Fig. 4(b), the thermal noise floor corresponds to an acceleration sensitivity of ($\mathrm{a}_{th} = \sqrt{4\mathrm{k_B T}\omega_0/\mathrm{mQ}} \approx 0.6\ \mu g_0/\sqrt{Hz}$), attained only at resonance.

The bandwidth of the accelerometer corresponds to the frequency range over which the thermal motion of the test mass is resolved. This is determined by laser shot noise, which adds displacement imprecision (x_{imp}) to the readout as a function of the available optical power (P), as $x_{\mathrm{imp}} \propto 1/\sqrt{P}$. In practice, the performance of the accelerometer is limited by the etalon's low finesse ($\mathcal{F} \approx 2$), which is a measure of the enhancement of the incident power by the cavity. As shown in Fig. 4(a), we have achieved a shot-noise-limited displacement sensitivity of $x_{\mathrm{imp}} \approx 6 \times 10^{-15}\mathrm{m}/\sqrt{\mathrm{Hz}}$ for a side-of-the-fringe measurement with 1.5 mW of near-infrared (849.7 nm) transmitted optical power, corresponding to a thermal-noise-limited bandwidth of 1 kHz near resonance, and a broadband sensitivity of $\omega^2 x_{\mathrm{imp}} \approx 30\ \mu g_0/\sqrt{\mathrm{Hz}}$. Broadband thermal sensitivity for the same optical power could be achieved by increasing the finesse to $\mathcal{F} \sim 100$, well within the proven performance of photonic crystal mirrors [6].

Radiation Pressure Actuation

We highlight the virtues of the high rigidity and radiation-pressure-driven manipulation available to the dual-membrane platform by using feedback cooling to enhance a weak stochastic acceleration measurement.

To effect feedback, a secondary laser beam (650 nm, 100 μW) was introduced for radiation pressure actuation. The auxiliary beam was intensity-

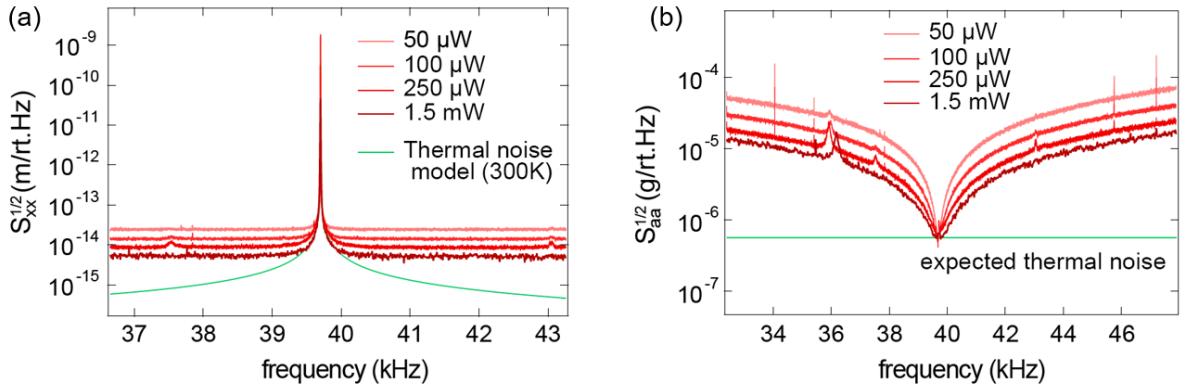

FIGURE 4. (a) Displacement measurements (S_{xx}: displacement PSD) for varying transmitted powers demonstrating that the broadband sensitivity is enhanced by increasing optical power (alternately, increasing finesse); (b) acceleration sensitivity (S_{aa}: acceleration PSD) inferred from (a) via equation (1), showing increased bandwidth with increasing power. For all measurements, the accelerometer was probed in transmission by direct detection.

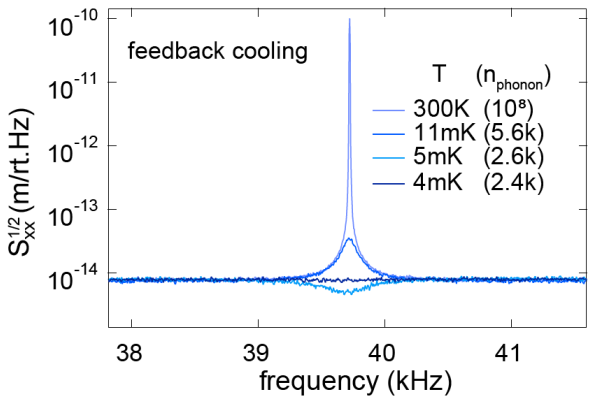

Figure 5. Radiation pressure feedback cooling of thermal motion from room temperature (300 K) down to the imprecision noise floor, corresponding to a minimum temperature of 4 mK or 2.4×10^3 phonons ($n_{phonon} = k_B T/\hbar\omega_0$). Increasing the feedback gain decreases temperature until the imprecision floor is reached. Increasing the gain further leads to squashing of the apparent mechanical motion beyond the shot-noise limit. This corresponds to re-heating the mechanical mode to 5 mK.

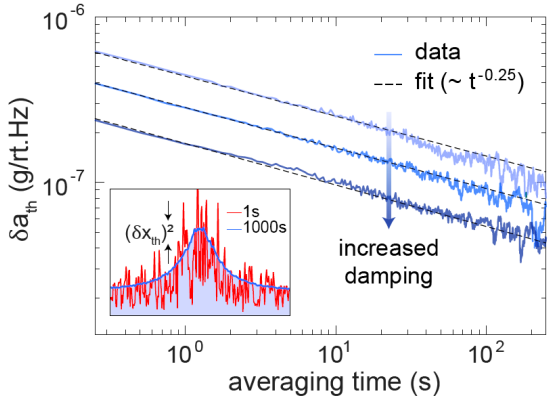

FIGURE 6. Uncertainty in the inferred acceleration (from an estimate of the thermal energy) as a function of time, for different feedback gains. Reducing thermal noise also reduces the variance in the thermal noise more quickly. Inset: Reduction in the variance in the thermal noise peak, after averaging the spectrum for 1000 seconds.

modulated in proportion to the velocity of the resonator, inferred by phase-shifting the displacement signal from the 850 nm probe beam. As shown in Fig. 5, the fundamental trampoline mode was cooled from 300 K to 4 mK, limited by the shot noise imprecision of the measurement.

Cooling of the thermal motion enhances the resolution of incoherent accelerations impinging upon the test mass [7][8]. The energy imparted by incoherent or stochastic forces such as thermal noise is estimated from the area under the resonance peak. As highlighted in the inset in Fig. 6, averaging the spectrum over longer integration times is a strategy to reduce the uncertainty in this estimation. Equivalently, this is also achieved by feedback cooling. Despite cold-damping both thermal and non-thermal motion, feedback cooling helps signal resolution by reducing the integration time required to achieve a target variance in the energy estimate. To demonstrate this principle, the area beneath the thermal peak at 40 kHz is averaged over 200 seconds for different feedback gains. Statistics from multiple measurements showed that the variance in the energy estimate reduces linearly with increased integration time, so that the standard deviation in inferring

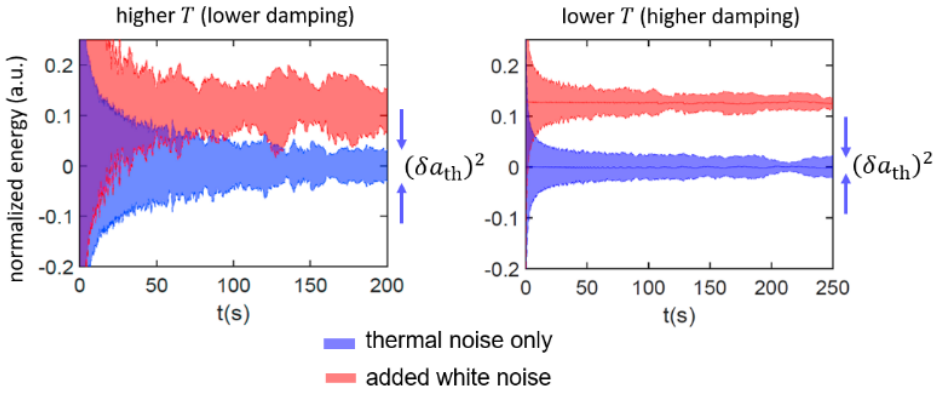

Figure 7. Energy in excess of thermal energy contributing to the resonance peak, as a function of integration time. The shaded regions indicate the uncertainty bounds in the estimation. The external white noise drive in each case carries the same average energy. For lower damping, it takes longer to resolve the added white noise from a fluctuation in the thermal noise (longer overlap in shaded regions).

the acceleration scales as $\delta a \sim t^{-0.25}$. We observed that for the largest damping rate, a stochastic acceleration as small as $50\, ng_0/\sqrt{\mathrm{Hz}}$ could be resolved after 200 seconds.

Additionally, we verified the resolution-enhancement of non-thermal incoherent forces by applying an external white noise drive using a piezo, for two separate values of feedback gain. As shown in Fig. 7, cold-damping to lower temperatures helps resolve the added noise faster.

CONCLUSION AND OUTLOOK

We have presented a compact, monolithic cavity optomechanical platform based on two vertically integrated silicon nitride membranes with different stiffnesses. We showed that the accelerometer achieved thermal-noise-limited sub-μg_0 sensitivity over 1 kHz bandwidth at resonance, and shot-noise-limited broadband sensitivity. Radiation pressure was used to feedback-cool the thermal motion of the trampoline from room temperature to 4 mK, which enabled the resolution of incoherent accelerations at the level of $50\, ng_0/\sqrt{\mathrm{Hz}}$ within minutes of signal integration.

Looking forward, we envision a $\mathcal{F} \sim 100$ (by patterning a photonic crystal structure onto the test mass), centimeter-scale membrane optomechanical accelerometer operating in a 4 K cryostat in order to achieve sub-$ng_0/\sqrt{\mathrm{Hz}}$ acceleration measurement. This system will operate close to the quantum limit, and will allow searches for fundamental weak forces produced by ultralight dark matter and spontaneous waveform collapse.

ACKNOWLEDGEMENTS

This work is supported by NSF Grant No. ECCS-1945832.

REFERENCES

[1] Krause AG, Winger M, Blasius TD, Lin Q, Painter O. A high-resolution microchip optomechanical accelerometer. Nature Photonics. 2012 Nov;6(11):768-72.

[2] Guzman F, Kumanchik LM, Spannagel R, Braxmaier C. Compact fully monolithic optomechanical accelerometer. arXiv preprint arXiv:1811.01049. 2018 Oct 16.

[3] Ghadimi AH, Fedorov SA, Engelsen NJ, Bereyhi MJ, Schilling R, Wilson DJ, Kippenberg TJ. Elastic strain engineering for ultralow mechanical dissipation. Science. 2018 May 18;360(6390):764-8.

[4] Manley J, Chowdhury MD, Grin D, Singh S, Wilson DJ. Searching for vector dark matter with an optomechanical accelerometer. Physical Review Letters. 2021 Feb 10;126(6):061301.

[5] Reinhardt C, Müller T, Bourassa A, Sankey JC. Ultralow-noise SiN trampoline resonators for sensing and optomechanics. Physical Review X. 2016 Apr 1;6(2):021001.

[6] Moura JP, Norte RA, Guo J, Schäfermeier C, Gröblacher S. Centimeter-scale suspended photonic crystal mirrors. Optics express. 2018 Jan 22;26(2):1895-909.

[7] Gavartin E, Verlot P, Kippenberg TJ. A hybrid on-chip optomechanical transducer for ultrasensitive force measurements. Nature nanotechnology. 2012 Aug;7(8):509-14.

[8] Pontin A, Bonaldi M, Borrielli A, Cataliotti FS, Marino F, Prodi GA, Serra E, Marin F. Detection of weak stochastic forces in a parametrically stabilized micro-optomechanical system. Physical Review A. 2014 Feb 28;89(2):023848.

AN EXPERIMENT TO TEST THE MECHANICAL LOSSES OF DIFFERENT BONDING TECHNIQUES IN FUSED SILICA

Jonathan J. Carter[1,2], Pascal Birckigt[3,4], Oliver Gerberding[5], Qingfeng Li[4], Rick Strüning[2], Tobias Ullsperger[4], and Sina M. Koehlenbeck[1,2]
1 Max Planck Institute for Gravitational Physics (Albert Einstein Institute), Callinstraße 38, 30167 Hannover, Germany
2 Institut für Gravitationsphysik der Leibniz Universität Hannover, Callinstraße 38, 30167 Hannover, Germany
3 Fraunhofer Institute for Applied Optics and Precision Engineering, Albert-Einstein-Str. 7, 07745 Jena, Germany
4 Institute of Applied Physics, Abbe Center of Photonics, Friedrich-Schiller-Universität Jena, Albert-Einstein-Str. 15, 07745 Jena, Germany
5 Institut für Experimentalphysik, Luruper Chaussee 149, 22761 Hamburg, Germany

ABSTRACT
High-purity glasses are used for their low optical and mechanical loss, which makes them an excellent material for oscillators in optical systems, such as inertial sensors. Complex geometries often require the assembly of multiple pieces of glass and their permanent bonding. One common method is hydroxide catalysis bonding, which leaves an enclosed medium layer. This layer has different mechanical properties to the bulk glass around it. The higher mechanical loss of this layer makes it more susceptible to displacement noise originating from the conversion of energy from oscillation to heat and vice versa. Therefore, other methods are needed to bond together glass assemblies. To investigate this, we have set up an experiment to measure the mechanical losses of several different types of bond commonly used in fused silica manufacturing, namely; plasma activated direct bonding, hydroxide catalysis bonding, laser welding, and adhesive bonding. In this paper we present the experimental design and show initial results of the first test sample.

INTRODUCTION
Intrinsic thermal noise is a limit to the performance of many high precision optomechanical devices [1]. Via the fluctuation dissipation theorem, the thermal noise is directly linked to the mechanical dissipation of the device. To prevent additional loss channels, many optomechanical measurement devices are constructed monolithically [2, 3]. One-piece constructions can be impractical, and complex components must then be assembled from multiple parts due to their geometry and size [4]. There are now a wide variety of glass bonding techniques available to construct quasi-monolithic assemblies, such as optical contacting and hydroxide catalysis bonding. The associated losses, in particular of hydroxide catalysis bonding [5, 6], have been studied in the course of the construction of the advanced Laser Interferometer Gravitational-Wave Observatories (aLIGO). Others, such as plasma activated direct bonding [7], have no measurements of their intrinsic losses in the literature to the authors' knowledge.

This paper details work ongoing to measure the mechanical losses of several fused silica bonding techniques. The production process, manufacturing of the test samples, and the experiment to measure he mechanical Quality factor, Q, are detailed, as well as results from the first tested sample.

MICRO-OSCILLATOR DESIGN
A micro-oscillator with bonding interfaces in key locations was designed for this experiment. The Q factor is related to the mechanical loss angle, ϕ by

$$Q = \frac{1}{\phi}. \tag{1}$$

By measuring the Q factor, and understanding all loss terms, it is possible to infer what contribution is due to the bonding interface itself.

Our device design is shown in FIGURE 1. It takes inspiration from work by Guzmán et al. [8], who

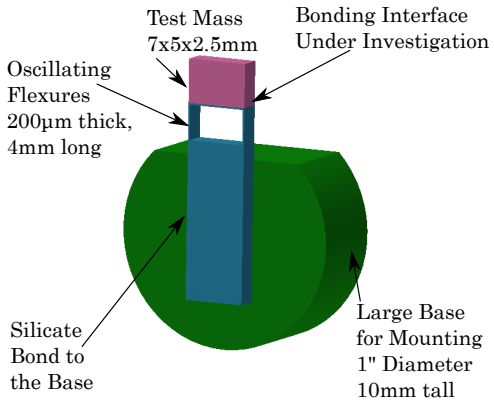

FIGURE 1. The test sample design. There are three separate glass parts depicted in green, blue and violet. The large round base, in green, is attached to the flexure piece, in blue, via silicate bonding. This bonding interface is necessary, but not under investigation, as it is far from any oscillating parts. The flexure piece is attached to the test mass, in violet, at a distance of 200 µm *from the flexures. This connection is created with the bonding technique under investigation. In the case of monolithic control samples, there is no bonding interface here, but bulk glass. The flexure piece uses a parallelogram geometry to oscillate in plane.*

showed that a device using parallelogram flexure structures can make for a high Q factor oscillation along one spatial direction. The bonding interface between two fused silica parts are varied between the bonding techniques listed in a separate section below.

The bonding surfaces is located in the top part of the assembly, between the test mass and the flexure piece. As this part is only held up by glass flexures of 200 µm thickness, it is able to move with respect to the base. The flexures are bent by the oscillation which induce stress along their length and in the corners of the base and test mass. The bonding surface is as close as possible to this deformation induced stress, thus contributing a loss channel and lowering the Q factor of the oscillation.

Finite Element Analysis (FEA) with COMSOL Multiphysics was used to analyse the oscillations as well as the induced stress in the design. It was found that the first eigen mode was a horizontal motion at approximately 2.1 kHz. This is the mode desired and excited during measurements of the Q factor. A second, vertical mode occurs at

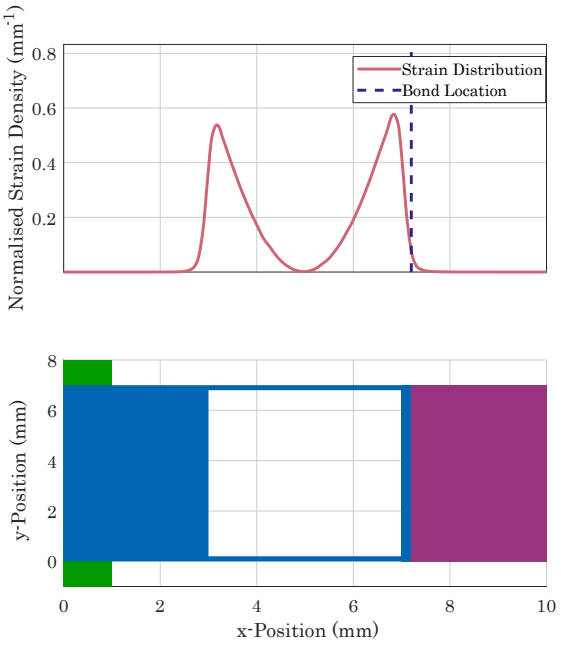

FIGURE 2. Normalised ratio of strain energy distribution across the geometry estimated by FEA. The strain distribution peaks in the corners of the oscillating part and decaying rapidly as it disperses into the bulk. The location of the bonding surface is shown with the dashed line and is as close as possible to the flexures to maximise strain across the bonding interface.

5.1 kHz. This is undesired, but as it is more than a factor of two above in frequency and orthogonal, cross contamination is expected to be low. The next modes occur in the tens of kHz and are all rotational. These are assumed to be too high in frequency to interfere with the measurement.

FEA is also used to measure the strain energy distribution across the flexure elements. This is necessary for two aspects, the first is estimating the contribution of the material effect to the Q factor of the oscillator, the second is for calculating the energy in the bonding interface and so derive its actual loss coefficient. The distribution of strain energy was simulated by applying a fixed extension on the test mass and simulating how the strain energy distribution changed in segments along the length of the flexures. This was then normalised with the total strain energy in the system to produce FIGURE 2.

The leading limiting source of loss in the design is from the material itself which we will describe with its respective Q factor Q_{Mat}. This term can

be subdivided further into bulk and surface loss. Bulk loss is the loss in the volume of the oscillator intrinsic to the material it is made from. As such, the experiment uses a low loss Corning 7980-0F fused Silica with an intrinsic Q factor of 1.1×10^7 as measured by [16].

Surface loss can be understood in a similar manner to bulk loss. At the surface of the oscillator damage occurs that breaks the regular structure and allows contaminates to penetrate in the material acting as an additional loss source. This leads to an understanding of a low loss bulk with a surface layer of depth, d_s, with a higher loss. The associate Q factor can be described mathematically as

$$\frac{1}{Q_\mathrm{Mat}} = \phi_\mathrm{Bulk} + \phi_\mathrm{Surf}\, d_\mathrm{s} \frac{\int_S \epsilon^2(\vec{r})\mathrm{d}S}{\int_V \epsilon^2(\vec{r})\mathrm{d}V}, \qquad (2)$$

where ϕ is the loss angle in the bulk and surface layer respectively, and ϵ is the strain energy density. Gretarsson et al. [17] made measurements of some of these factors in the late 90s. This estimated the approximate contribution ϕ_Surf as 10^{-5} and a d_s of 1 µm. Although these values depend heavily on the treatment of samples, we assume it to be comparable. Substituting in values from FIGURE 2 gives a Q_Mat of 9×10^6.

Contributions to the Q factor from thermoelastic damping, Q_TED, can be estimated using the Zener approximation. By following the method of Lifshitz [18], an estimated contribution of Q_TED as 2×10^7 is reached for this design. The contribution of Akheizer loss, see [19] for details, is also very similar with $Q_\mathrm{ph-ph}$ of 2×10^7. Air pressure damping is minimised by performing the tests under vacuum, leaving only frictional losses as the unknown loss term. As this does not belong to the sample itself, we can estimate the theoretical limit of the Q factor of this oscillator design as 4.5×10^6.

Several samples of each bonding technique have now been produced and are ready for testing. An exemplary sample is shown in FIGURE 3. In addition, several devices with no bonding interface, i. e., monolithically, were produced, which act as a reference for the bonded samples.

All samples were produced from double-side polished cylindrical pieces of CORNING 7980-0F fused silica 1" in diameter round plates. The sample manufacturing steps are shown in FIGURE 4.

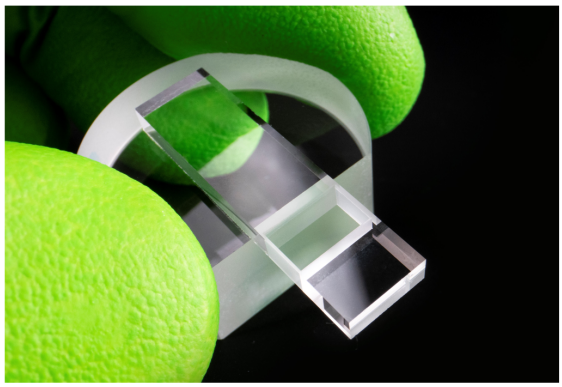

FIGURE 3. Photo of an exemplary test sample.

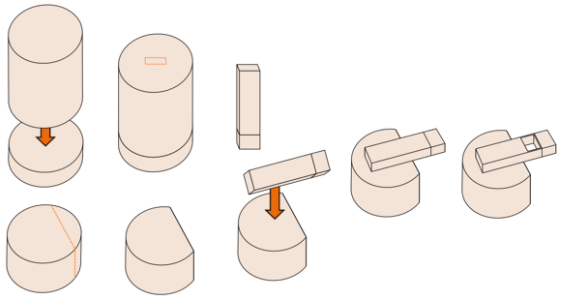

FIGURE 4. Schematic manufacturing steps for producing the test samples. Firstly, two round plates are joined using a certain bonding technique. Then, it is cut into cuboids via diamond sawing, which are then carefully polished from all sides. Meanwhile, a segment of another round plate is cut off to form the base. The cuboid is joined with the base. Finally, laser ablation is applied using an ultrashort pulsed laser.

As a final manufacturing step, the thin flexures were exposed by precise micro-machining using an ultrashort pulsed laser system, TruMicro5070. Starting from the backside of the cuboid, the focused laser pulses were scanned across the whole rectangular area except of the thin flexures at the edges. During the layer-wise ablation process the focal position was continuously moved up to realise taper-free cuts, leaving flexible elements of only 200 µm width.

BONDING TECHNIQUES

This section describes the various joining techniques for fused silica pieces under investigation ranging from simple gluing to glass welding.

Hydroxide Catalysis Bonding

Hydroxide-catalysis bonding, also called silicate bonding, is a form of bonding between glass surfaces invented by Gwo et al. at Stanford [11].

It has been used extensively in the gravitational wave community because of its low mechanical loss and high strength and so is well studied [5, 6, 12]. The bonding process uses two polished, flat surfaces of silica based glass. One surface is treated with a hydrous solution, here a sodium silicate solution, then, the other surface is put into contact. During curing, the solution forms long siloxane chains. After the water has evaporated, these interact and tangle together forming a strong, highly stiff interlayer [13].

Adhesive Bonding

Adhesive bonding is a broad term used to describe any bonding method with an organic glue as medium between the two surfaces. In this specific case, Epotec 301-2 was used. While this is the least promising bonding technique in terms of thermal noise performance, it is the simplest bonding technique. Knowing what level of thermal noise this bonding can achieve is therefore of broad interest to the community.

Plasma Activated Bonding

Plasma activated bonding, which is a low-temperature direct process, is performed by optically contacting two clean, highly polished, highly flat surfaces. Surfaces are prepared via chemical cleaning and a plasma-activation step. After contacting, a force of several kPa is applied. Then, a process of thermal annealing converts the resulting hydrogen bonds into strong covalent bonds, making a stable interface [9, 10]. As direct bonding yields a high-strength, interlayer-free interface, it is perhaps the most promising bonding technique in terms of thermal noise performance.

Ultrashort Pulse Laser (USP) Glass Welding

In USP glass welding, the lasers have a wavelength to which the glass is transparent. Significant energy input can only be established via nonlinear absorption, e.g. multiphoton ionisation, when high intensity, of order hundreds of $\mathrm{TW\,cm^{-2}}$, is reached by tight focusing. When two glass surfaces are brought together and the laser beam is focused at the interface, the glass near the focal volume is melted across the interface so that a new joint is formed. Here, the melting points are placed on a grid with a distance of $50\,\mu\mathrm{m}$. More details are given in [14]. Previous studies have investigated the mechanical loss of this bonding technique and found it to be less than the surface loss of their tested samples and thus was not detectable [15].

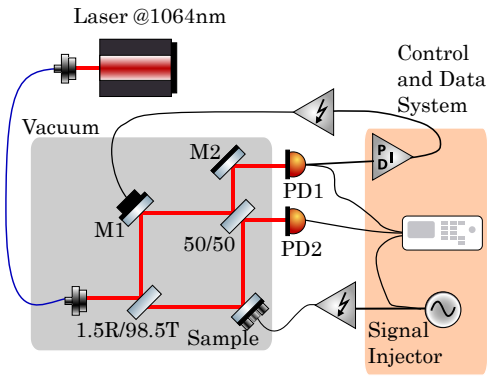

FIGURE 5. Left: The experimental schematics of the interferometer used to test the samples. The experiment uses laser light from at $1064\,\mathrm{nm}$ *laser. This is sent onto a breadboard in vacuum via optical fibre feedthroughs. It is coupled out and send into Mach Zehnder interferometer. The power is not distributed evenly, but rather via a* $1.5/98.5$ *beamsplitter to compensate for the low reflectivity of fused silica. M1 is driven by a controller to keep the interferometer at the operating point, which is the mid-fringe. The sample is in a custom mount attached to a shear-piezo which is driven allowing for a measure of its transfer function.*

EXPERIMENT

In order to measure the Q factor of the samples, two things are needed, a way to excite motion and a way to measure the samples response. A piezo element attached to the mount of the oscillator can do the former. As the device is made of optical grade fused silica, an interferometer can do the later.

The interferometer is a homodyne interferometer in a Mach Zehnder configuration, as shown in FIGURE 5. A piezo driven mirror in one arm keeps the interferometer on the mid fringe operating point, ensuring a linear response of the interferometer readout. A shear-piezo mounted under the sample causes excitation for measurement of the mechanical response of the oscillator.

After setting up the experiment in a vacuum environment, the first step was to measure the background noise of the interferometric readout. For this purpose, we used a device that was shaped like the test pieces but had no bending geometry, allowing it to remain a rigid piece. It was found that there were no significant resonance peaks in the region of interest, and a noise floor of $1 \times 10^{-11}\,\mathrm{mHz^{-1/2}}$ was achieved.

RESULTS & DISCUSSION

The first sample under test was one of the monolithic reference samples with bending flexures. Since no loss channel from a bond is present this will give the intrinsic loss of the sample material and geometry and the experimental set-up.

An excitation signal was applied to the shear-piezo, driving the sample across Fourier frequencies from 2 kHz to 4 kHz. The displacement of the test mass was recorded with the interferometer and the transfer function from the driving displacement to the test mass displacement was calculated. The amplitude of the transfer function was then fit with the model of a simple damped harmonic oscillator, given by

$$\tilde{X} = \left| \frac{\omega_0^2}{\left(-\omega^2 + {\omega_0}^2 + \frac{i\omega_0\omega}{Q}\right)} \right|, \qquad (3)$$

where ω_0 is the natural angular frequency, and $\tilde{X}$ is the magnitude of the frequency response to stimulation. The fit was done using MATLABs Nlinfit function. The result of this fit is shown in FIGURE 6.

The Q factor is 257.7, three orders of magnitude below where it is expected to be. The cause of the discrepancy is unknown, though there are two ideas that are being investigated. The first is that contaminants had entered the flexures. There is also some concerns that the largely unknown term of frictional loss are limiting the measurements. Alternatives to the currently used clamp are being investigated. It is hoped that improving the rigidity of the clamp will lead to less differential motion and so less friction.

CONCLUSIONS

This paper reports ongoing efforts to measure the mechanical loss intrinsic to several bonding techniques commonly used in fused silica manufacturing.

A mechanical oscillator geometry has been designed for the purpose of measuring the loss in bonding interfaces. The oscillator design has a promising theoretical Q factor and artificially induced loss channel to measure the bonding interfaces. Several test pieces have been produced. By using interferometry, a means of measuring the Q factor of the sample has been achieved. This will in turn allow for an estimation of the mechanical loss due to the bond. However, the Q factor of the substrate is not what it is expected to be. There are several reasons this could be the case and ongoing investigations seek to answer why.

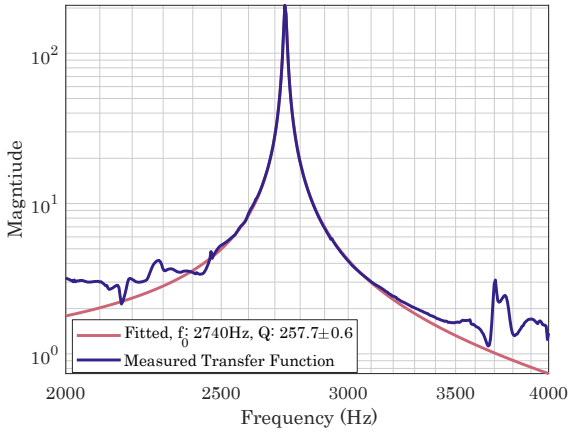

FIGURE 6. The fit and measured absolute transfer function of monolithic sample 13. The peak location has a deviation of 30% from the value predicted by FEA simulation. As the resonance frequency is strongly dependent on flexure thickness the difference is mainly attributed to the small variations in thickness seen along the flexures.

Overall the experiment still has promise to produce measurements of the mechanical loss of several in glass bonding techniques. By knowing this, larger fused silica glass assemblies can be made, without being limited by thermal noise. It is hoped that this will prove valuable information both to the specific field of gravitational wave astronomy and the broader glass optomechanical sensor design field as a whole.

ACKNOWLEDGEMENTS

We would like to thank Prof. Dr. Gerhard Heinzel, Prof. Dr. Benno Willke, Prof. Dr. Uwe Zeitner, Dr.-Ing. Stefan Risse, and Dr. Harald Lück for their continuing support of the project and are gratefully for their advice and ideas.

This project was supported by the Max Planck and Fraunhofer Institute Cooperation ”High-QG”.

REFERENCES

[1] Zhou F et al. Broadband thermomechanically limited sensing with an optomechanical accelerometer. Optica, 2021: https://doi.org/10.1364/OPTICA.413117

[2] Cumming AV et al. Design and development of the advanced LIGO monolithic fused silica

suspension. Classical and Quantum Gravity, 2012: https://doi.org/10.1088/0264-9381/29/3/035003

[3] Bellouard Y et al. Integrating optics and micro-mechanics in a single substrate: a step toward monolithic integration in fused silica. Optics Express, 2005: https://doi.org/10.1364/OPEX.13.006635

[4] Carter J et al. A high Q, quasi-monolithic optomechanical inertial sensor. 2020 IEEE International Symposium on Inertial Sensors and Systems (INERTIAL) Society, 2020: https://doi.org/10.1109/inertial48129.2020.9090085

[5] Smith J et al. Mechanical loss associated with silicate bonding of fused silica. Classical and Quantum Gravity, 2003: https://doi.org/10.1088/0264-9381/20/23/007

[6] Cunningham L et al. Re-evaluation of the mechanical loss factor of hydroxide-catalysis bonds and its significance for the next generation of gravitational wave detectors. Physics Letters A, 2010: https://doi.org/10.1016/j.physleta.2010.07.049

[7] Shari N et al. Chemical free room temperature wafer to wafer direct bonding. Journal of The Electrochemical Society, 1995: https://doi.org/10.1149/1.2048440

[8] Guzmán Cervantes F et al. High sensitivity optomechanical reference accelerometer over 10 kHz. Applied Physics Letters, 2014: https://doi.org/10.1063/1.4881936

[9] Kalkowski G et al. Optical contacting of low-expansion materials. Optical Manufacturing and Testing IX. Proc. SPIE, 2011: https://doi.org/10.1117/12.894382

[10] Tan CM, Yu W, and Wei J. Comparison of medium-vacuum and plasma-activated low-temperature wafer bonding. Applied Physics Letters, 2006: https://doi.org/10.1063/1.2185467

[11] Gwo DH. Ultraprecision bonding for cryogenic fused-silica optics. Cryogenic Optical Systems and Instruments VIII (Vol. 3435, pp. 136-142). International Society for Optics and Photonics, 1998: https://doi.org/10.1117/12.323731

[12] Rowan S, et al. Mechanical losses associated with the technique of hydroxide-catalysis bonding of fused silica. Physics Letters A, 1998: https://doi.org/10.1016/s0375-9601(98)00533-7

[13] van Veggel AA, et al. Hydroxide catalysis bonding of silicon carbide. Journal of the European Ceramic Society, 2008: https://doi.org/10.1016/j.jeurceramsoc.2007.06.002

[14] Richter S, Nolte S, and Tünnermann A. Ultrashort pulse laser welding. A new approach for high-stability bonding of different glasses. Phys. Procedia, 2012: https://doi.org/10.1016/j.phpro.2012.10.073

[15] Harry G et al. Mechanical loss of laser-welded fused silica fibers. Review of Scientific Instruments, 2006: https://doi.org/10.1063/1.2170075

[16] Numata K et al. Intrinsic losses in various kinds of fused silica. Classical and Quantum Gravity, 2001: https://doi.org/10.1063/1.2170075

[17] Gretarsson AM and Harry GM. Dissipation of mechanical energy in fused silica fibers. Review of Scientific Instruments, 1999: https://doi.org/10.1063/1.1150040

[18] Lifshitz R and Roukes ML. Thermoelastic damping in micro-and nanomechanical systems. Physical Review B, 2000: https://doi.org/10.1103/physrevb.61.5600

[19] Nawrodt R et al. Investigation of mechanical losses of thin silicon flexures at low temperatures. Classical and Quantum Gravity, 2013: https://doi.org/10.1088/0264-9381/30/11/115008

A NEW SPIN ON KIBBLE: FIRST MEASUREMENTS WITH A SELF-CALIBRATING TORQUE REALIZATION DEVICE

Zane Comden[1,2], Stephan Schlamminger[1], Charles Waduwarage Perera[1,2], Frank Seifert[1,2], David Newell[1], Jay Hendricks[1], Barbara Goldstein[1], Leon Chao[1]
[1]National Institute of Standards and Technology, Gaithersburg, MD
[2]University of Maryland, College Park, MD

INTRODUCTION

After the 2019 redefinition of the International System of Units (SI), torque no longer needs to be traceable to a calibrated weight suspended from a known lever arm. Specifically, a modification of the Kibble principle used for realizing the kilogram allows for direct realization of torque via electrical measurements traceable to the revised SI [1]-[3].

For small torque lower than 1 cN m, the process of balancing small mass artifacts required to calibrate fragile transducers is difficult, burdensome, and often irreproducible. A recent NIST/US Air Force collaborative effort to design, construct and characterize a self-calibrating electromechanical system mainly consisting of a tabletop sized rotating electromagnet aimed at generating 1 mN m to 1 N m with 0.1% accuracy for directly calibrating torque tools is currently under development. This instrument, the Electronic NIST Torque Realizer (ENTR), is intended to re-route the SI standards dissemination chain from mechanical standards to electrical standards, empowering calibration facilities ranging from military to research and industry to directly realize torque for themselves.

OPERATIONAL THEORY

The realization of torque is achieved via a conversion of the traditionally linear Kibble principle to a rotational frame. In the linear version, a round coil is translated vertically through a fixed magnet system. In the rotational version, a magnet system spins against a fixed D-shaped coil. Here, this process requires two modes of operation: spin mode (eq. 1) and torque mode (eq. 2)

$$V = BLr\dot{\phi} \quad (1) \qquad \tau = BLrI \quad (2)$$

where V is the induced voltage in the coil from the spinning magnet, B is the magnetic flux density of the magnetic circuit, L is the total length of the radial wire segments of the coil, r is the distance between the axis of rotation and the center of each wire segment, $\dot{\phi}$ is the angular velocity, τ is the torque, and I is the electrical current. Strictly speaking, V, τ and B are all functions of the angle ϕ of the magnet ranging from 0° to 360° and to simplify the notation, we set $\beta(\phi) = B(\phi)Lr$. Thus, a simpler way to depict eqs. 1 and 2 would be

$$V(\phi) = \beta(\phi)\dot{\phi} \quad (3) \qquad \tau(\phi) = \beta(\phi)I \quad (4)$$

In spin mode, $V(\phi)$ is mapped out repeatedly as the rotating magnet spins continuously at $\dot{\phi}$ allowing for $\beta(\phi)$ to be calculated for a large number of ϕ values. In torque mode, the magnet is servoed to a desired angle ϕ_1 by injecting a current I into the coil. The torque $\tau(\phi_1)$ can then be calculated by multiplying the measured current with the $\beta(\phi)$ imported from spin mode, or explicitly:

$$\tau(\phi) = \frac{IV(\phi)}{\dot{\phi}} \qquad (5)$$

MECHANICAL DESIGN

At the heart of ENTR is a set of two ring magnets capable of rotation. A pair of commercial NdFeB axially magnetized rings were each sliced in half using a waterjet cutter. Half the semi circular rings were flipped upside down, paired back with the original half, and placed onto mild steel yokes for guiding the magnetic flux. The yokes were fixed to a rigid shaft such that the two magnet sets were oriented in attraction and the slits between the top and bottom magnets were aligned, see Fig. 1. Two ZrO_2 radial ball bearings constrain the rotation of the shaft. A study was conducted comparing the internal friction of multiple commercial bearings and ZrO_2 was chosen for its lowest friction properties within the study group. The lower bearing is set into a base plate for the rotary shaft to rest on, and the upper bearing is held in place by a bracket which attaches to the base plate, see Fig. 2. A precision machined tapered ring built into the bottom yoke provides

a surface for mounting a Renishaw RESM[1] optical rotary encoder.

The initial iteration of the instrument used a stainless steel angle bracket to hold the top bearing in place and aluminum hex standoffs for supporting the coil. However, the stray magnetic field near the air gap lightly interacted with the nearby metallic surfaces, causing eddy current damping during spin mode. Thus, these components were replaced with 3D printed versions made from PLA plastic as shown in Fig. 4 - 5. Furthermore, at the time of writing, the desired Renishaw rotary encoder has been on backorder by the manufacturer, so a temporary, lower performance encoder was affixed to the rotary shaft above the top bearing in order to conduct initial measurements.

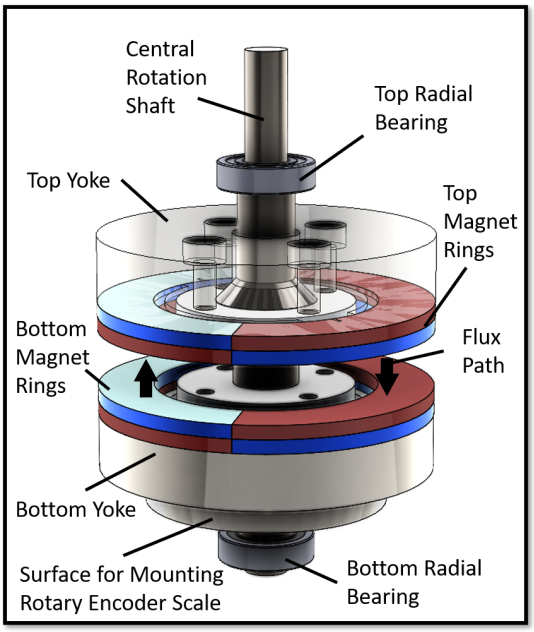

Fig. 1: 3D CAD model of rotational components. Top magnetic yoke made transparent for easier visibility and magnet polarities shaded red/blue for clarity. A stainless steel stepped shaft is constrained by the inner racers of two ZrO_2 ceramic bearings. Two mild steel yokes are mounted onto flanges on the shaft and four half ring magnets are attached to the yokes. Each pair has opposite polarity per yoke and the two magnet assemblies are oriented in attraction. The bottom yoke is machined with a tapered ring for centering the encoder scale.

[1]Certain commercial equipment, instruments, and materials are identified in this paper in order to specify the experimental procedure adequately. Such identification is not intended to imply recommendation or endorsement by the National Institute of Standards and Technology, nor is it intended to imply that the materials or equipment identified are necessarily the best available for the purpose.

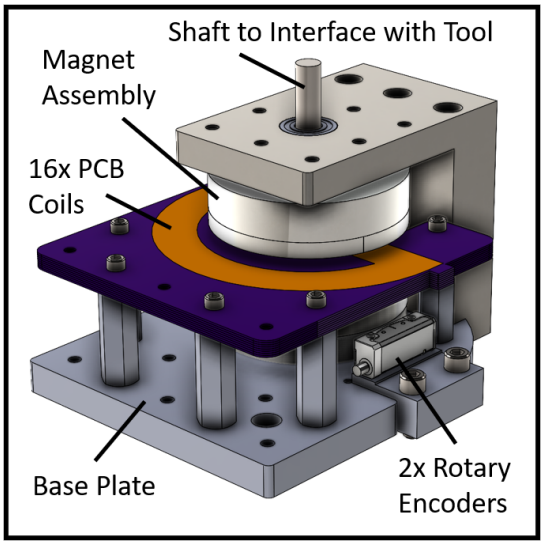

Fig. 2: CAD model of full ENTR assembly with mounting components and locations for future rotary encoder readheads.

COIL DESIGN

To generate a torque, the straight segments of a D-shaped coil interact with the magnetic field generated inside the gap between the two magnet pairs. Due to the irregular geometry, the coil was fabricated on a printed circuit board (PCB) as opposed to the traditional method of wire winding. This method of constructing coils has proven advantageous due to ease of manufacturing, low cost, and thus mass producible in the future.

Every 0.8 mm thick PCB is double sided, each containing 33 turns. The cross sectional dimensions of each trace are 0.36 mm by 0.71 mm and each trace is separated by 0.125 mm. A stack of 8 PCBs results in a total of 528 turns and rests on plastic hex standoffs such that the stack sits vertically centered between the magnets. The total coil resistance measured was approximately 120 Ω, see Fig. 3.

OPERATION

A statement regarding the accuracy of each measurand cannot be made at the time of this writing. Thus, instead of realizaing a calibrated torque derived from the measured $\beta(\phi)$ from spin mode, we have chosen to independently calculate and compare the $\beta(\phi)$ from each mode, $\beta_S(\phi)$ and $\beta_\tau(\phi)$ as an indicator of initial ENTR performance.

EXPERIMENT 1

Spin Mode

In spin mode, the rotating magnet system is driven at relatively constant angular velocity

Fig. 3: CAD model of the top side of a single 0.8 mm thick PCB. A total of 33 turns are printed on each side. At the top of the PCB are two bare copper pads, allowing for stacking and soldering in series. A stack of 8 PCBs with 528 turns has a total resistance of about 120 Ω.

$\dot{\phi} \approx 3$ rad/s via a constant stream of compressed air. In order to determine $\beta_S(\phi)$, simultaneous measurements of the rotation angle ϕ of the magnet system as well as the induced voltage V through the coil must be taken as the magnet spins. A square wave signal generated by an I/O counter/timer PCI card serves as as a clock to synchronize the start of each measurement as well as a hardware trigger for taking each V and ϕ data point. The voltage is measured with a Keysight 34465A multimeter and the angle with a US Digital E2 encoder for this initial measurement campaign.

Because each ϕ measurement is coupled with a timestamp, the time derivative between each pair of points yields the angular velocity of the magnet $\dot{\phi}$. The last voltage point taken is dropped to account for the one fewer $\dot{\phi}$ points compared to the number of ϕ points. The measured V values are then divided by their corresponding $\dot{\phi}$ values resulting in a $\beta_S(\phi)$. Here, ENTR undergoes 42 magnet revolutions or 3988 data points and the calculated $\beta_S(\phi)$ = 0.2405 T m^2 at ϕ = 92°. The $\beta_S(\phi)$ values were fit with a second order polynomial in the range of 50-130 degrees with a standard deviation of the residuals of 0.21%.

Torque Mode

In torque mode, the coil is disconnected from the voltmeter and connected to a Rigol DP832 programmable voltage source to drive current as the intended current source for this instrument has not yet been acquired. Once current flows, the magnets rotate counterclockwise until the two slits separating the two magnet rings are aligned with the straight segments of the coil, i.e. the static equilibrium point where $\tau = 0$, in our case approximately where $\phi = 0$ or 180°.

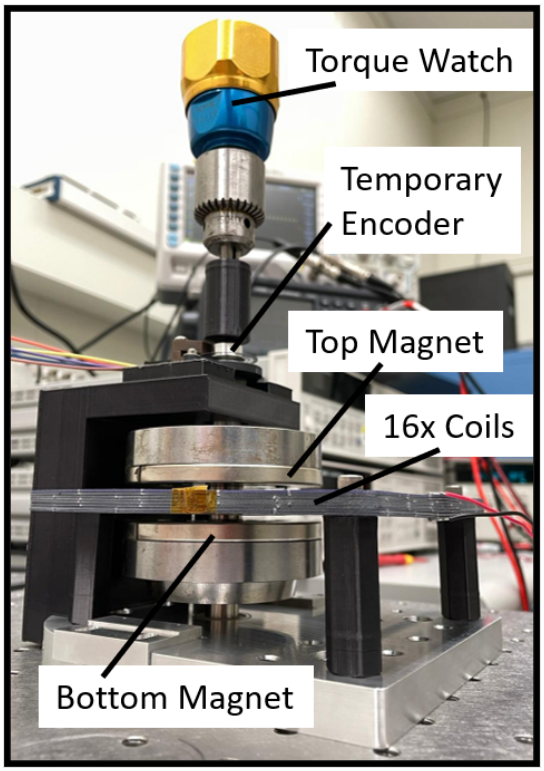

Fig. 4: ENTR in vertical orientation. A torsion spring based Waters Industry analogue torque watch [0 - 2.4 in oz (as displayed on the dial)] is attached to the central shaft of ENTR. A torque generated by ENTR is counterbalanced with the torque watch held static by hand to compare.

Here, a low range [0- 2.4 in oz] torque watch is attached via a coupler to the top of the central shaft as shown in Figs. 4-5. The voltage source is set statically to 6 V, or the equivalent of 50.86 mA through the coil. The torque watch is rotated clockwise by hand against the ENTR torque direction and held at a new equilibrium position ϕ = 92° where the analog torque watch reading of τ = 1.80 in oz (13 mN m) is measured. At the moment, we have not acquired a high precision, calibrated torque standard, such as a small torque transducer, thus the reason for relying on an uncalibrated antique torque watch originally purchased secondhand for reverse engineering purposes. An informal calibration using a mass on lever arm indicates the torque watch reads high by 4.31%. Given these measurements and after applying the torque watch correction, the torque mode

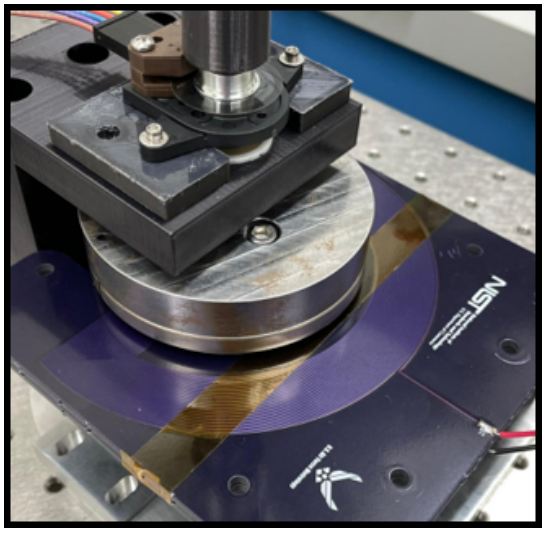

Fig. 5: Top view of ENTR showing upper magnet assembly, PCB coil, and rotary encoder.

$\beta_\tau(\phi) = 0.240\,\mathrm{T\,m^2}$.

As mentioned before, the actual intended use for this absolute realization instrument will be to import the spin mode $\beta_S(\phi)$ into torque mode to calculate $\tau(\phi)$ but this exercise is a necessary step for confirming both modes are in agreement and characterizing the performance of this instrument.

EXPERIMENT 2

SPIN MODE

Due to the inaccuracy and low resolution of the torque watch paired with the challenges of calibrating it properly, ENTR has been flipped by 90 degrees and operated with the shaft horizontal such that a torque generated by a gravitational mass can be directly applied, bypassing the need for the torque watch as shown in Fig. 6. Similar to Experiment 1, spin mode is driven by compressed air. The $\dot{\phi}$ varies more within each revolution due to minor imbalances in the rotating assembly having a greater impact compared to the vertical orientation. The spin mode measurement of $\beta_S(\phi)$ presented here undergoes 49 magnet revolutions or 3967 data points and the calculated $\beta_S(\phi)$ = 0.2411 T m^2 at ϕ = 95°. A fit in the same manner as Experiment 1 was performed, giving a standard deviation of the residuals of 0.18%.

TORQUE MODE

Utilizing a precision machined aluminum balance beam rigidly mounted on axis to the ENTR shaft, a mass is suspended from one end of the beam via copper wire, measured on an analytical balance to be 10.16 g including the wire. Though the wire is far from straight when hanging, the center of mass of the suspended assembly self-aligns vertically to the center of the connection point. The effective lever arm is measured with a Mitutoyo digital caliper with a precision of 10 μm to be 85.79 mm.

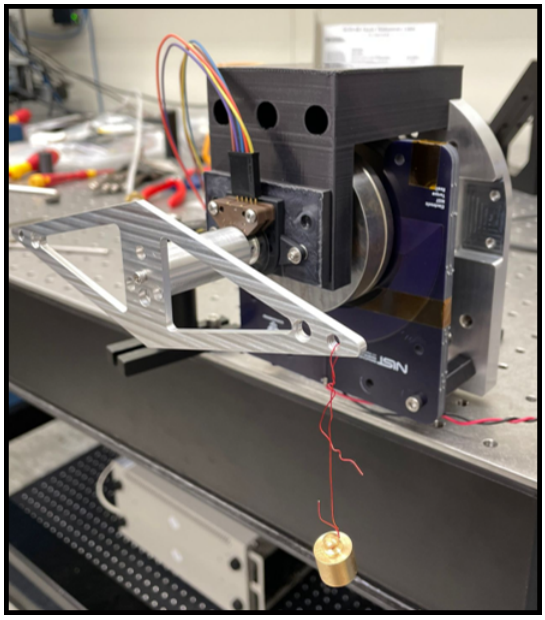

Fig. 6: ENTR oriented in the horizontal direction. The balance beam is servo controlled to 1.66 rad relative to the zero index and deemed to be horizontal, i.e. the torque generated by the gravitational mass is maximum. The hanging assembly is measured to be 10.16 g on a 85.79 mm lever arm.

For Experiment 2, the voltage source is swapped out for a programmable power supply allowing closed loop control of the balance beam's rotation angle. The horizontal beam position is measured at 95° relative to the encoder zero index and the current is read using an Agilent 3458A multimeter.

RESULTS & DISCUSSION

The results of this first comparison between $\beta_S(\phi)$ and $\beta_\tau(\phi)$ show excellent agreement, a promising outcome for utilizing a suite of uncalibrated instrumentation and electronics. By flipping ENTR on its side and bypassing the need for a torque watch, we are able to measure $\beta_\tau(\phi)$ more precisely by directly applying a traditional torque generated by a gravitational mass over a lever arm. Fig. 7 shows the $\beta_S(\phi)$ profile over one revolution, sampled 3967 times over 49 rotations. Fig. 8 (Top) indicates a zoomed in view of the profile from 50° to 130° with a second order fit and Fig. 8 (Bottom) shows the residuals between the raw data and fit. The relative standard deviation

of the residuals is approximately 0.19%. The results of Experiment 2 are:

$$\beta_S(95^\circ) = 0.2411\,\mathrm{T\,m^2}$$
$$\beta_T(95^\circ) = 0.2409\,\mathrm{T\,m^2}$$

The difference between the $\beta(\phi)$ values are 0.08%, marginally below the target uncertainty of 0.1%. Though the accuracy of the measurements are unknown at the moment, the independent agreement between the two modes brings confidence towards the initial performance of this torque realization instrument.

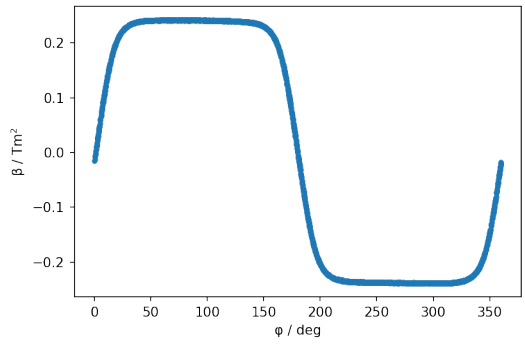

Fig. 7: Experiment 2 spin mode $\beta_S(\phi)$ profile over 360° with ENTR in the horizontal orientation. Profile is comprised of 49 sweeps, 3967 data points.

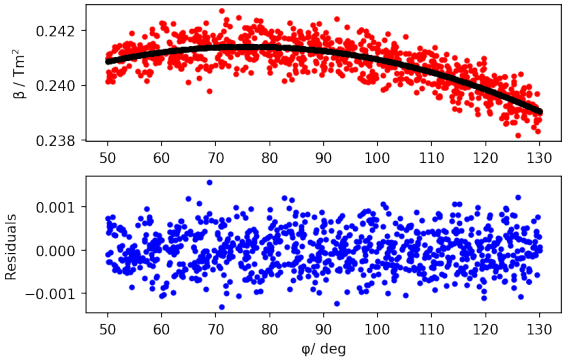

Fig. 8: (Top) $\beta_S(\phi)$ profile from 50° to 130° plotted in red with a 2nd order polynomial fit in black where $\beta_S(95^\circ) = 0.2411\,\mathrm{T\,m^2}$. (Bottom) Residuals of the 2nd order fit. Standard deviation is 0.19%.

Here, we have shown a crude, early prototype of ENTR that can already compare to the performance of a commercial torque watch. In the near future, we plan to improve measurement results through installation of higher quality components and refine the data analysis/acquisition procedure. We hope to have a complete measurement with a full uncertainty budget by the end of the year.

ACKNOWLEDGMENTS

This project has been made possible by the NIST PREP in partnership with the University of Maryland. The authors would like to thank the members of the Fundamental and Applied Electrical Measurement Groups at NIST; In particular, Associate Researcher Lorenz Keck, and Dr. Stefan Cular for their advice and assistance through discussion.

References

[1] D Haddad *et al* "Measurement of the Planck constant at the National Institute of Standards and Technology from 2015 to 2017," *Metrologia*, vol. 54, 633-641, 2017.

[2] L Chao *et al* "The Design of an Instrument to Realize Small Torque at NIST," *NCSL International and CPEM Conference Proceedings*, 2020.

[3] A Nishino *et al* "Design of a new torque standard machine based on a torque generation method using electromagnetic force," *Meas. Sci. Technol.* 28 025005, 2017.

INTERNAL FEATURE DESIGN FOR INCREASED DAMPING BY CAPTURED POWDER

Gregory Corson[1], Brett Compton[1], Michael Gomez[2], and Tony Schmitz[1,2]
[1]Mechanical, Aerospace, and Biomedical Engineering
University of Tennessee, Knoxville
Knoxville, TN 37996, USA
[2]Manufacturing Science Division
Oak Ridge National Laboratory
Oak Ridge, TN 37830, USA

INTRODUCTION

This paper describes the design of internal features for powder bed fusion (PBF) printed structures with captured feedstock powder. The designs are tailored to increase damping and, therefore, dynamic stiffness for additively manufactured components. Additive manufacturing (AM) has gained global attention and is being implemented across multiple industries and disciplines. It enables complex internal and external geometries, a reduced number of components, and material minimization in comparison to parts produced by sole machining from wrought blanks. In the PBF process, an energy source is used to scan and fuse planar cross-sections of the design geometry as consecutive feedstock powder layers are exposed. Prior research has shown that intentional retention of powder within a PBF structure can provide significant energy dissipation, or damping, as compared to solid, monolithic counterparts [1–3]. Increased damping serves to improve dynamic stiffness which increases fatigue life and machinability of AM components. Other research has shown that the mode shapes of structures with captured powder can be modified through the inclusion of internal supports [4].

This research studied the effect of free-standing internal features and the potential for increased damping through their interaction with retained feedstock powder using PBF. Four designs were studied with the same nominal external geometries, 100 mm long rectangular posts with 30 mm by 20 mm cross-sections. The internal geometries included: solid and powder cores with {no ribs, ribs normal to long edge (for shear damping), ribs normal to short edge (for compression damping)}. The modal damping ratios for dominant vibration modes for each design were extracted from free-free boundary condition modal impact testing. The inclusion of feedstock powder and internal features produced damping ratio increases by factors of 26 to 28 over the solid geometry.

DESIGN

Features were incorporated inside structures with the same external dimensions and nominal core of captured powder. Unlike previous research, the designs focused on free-standing, solidified internal features (i.e., free to move relative to the external structure). These designs were intended to add damping through captured powder interaction without significant detriment to the static stiffness. Computer aided design (CAD) and finite element analysis (FEA) were performed using SOLIDWORKS™. The FEA simulations were used to guide the design process by observing the free-free vibrational behavior of the solidified post. Figure 1 shows the identical external dimensions for design. Figure 2 shows the first free-free bending mode shape for the solid post with a natural frequency of 6392 Hz. The mode shape agreed with FEA predictions and provided the motivation for the internal structure designs. Similar agreement with FEA predictions was observed for modes from these designs.

[2] Notice: This manuscript has been authored by UT-Battelle, LLC, under contract DE-AC05-00OR22725 with the US Department of Energy (DOE). The US government retains and the publisher, by accepting the article for publication, acknowledges that the US government retains a nonexclusive, paid-up, irrevocable, worldwide license to publish or reproduce the published form of this manuscript, or allow others to do so, for US government purposes. DOE will provide public access to these results of federally sponsored research in accordance with the DOE Public Access Plan (http://energy.gov/downloads/doe-public-access-plan).

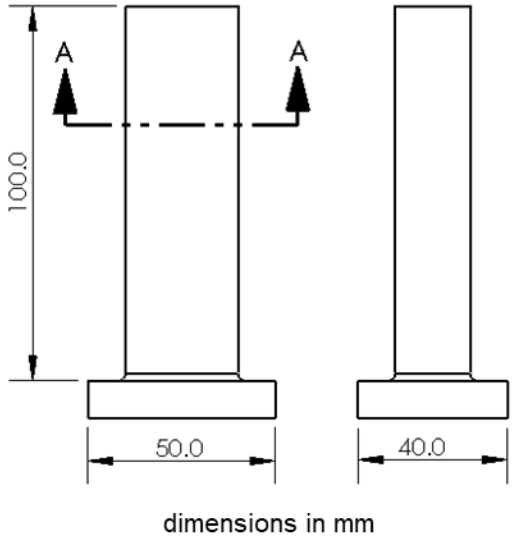

FIGURE 1. External geometry of PBF posts and section A-A location in Figure 4.

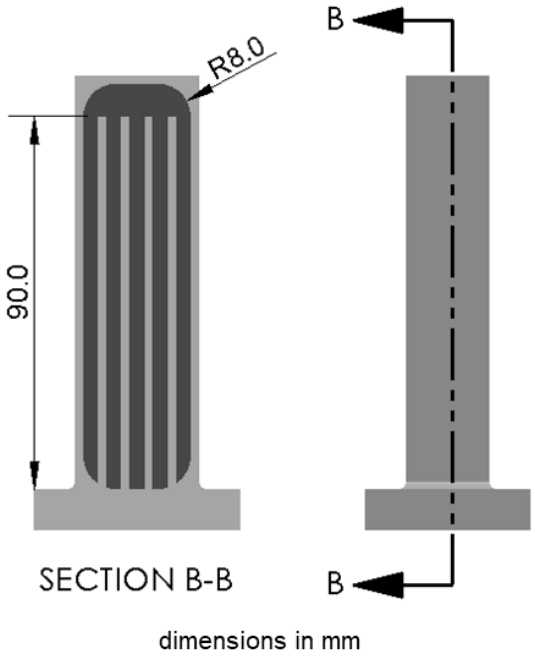

FIGURE 3. Internal view of shear rib design. Vibration test direction was into the page.

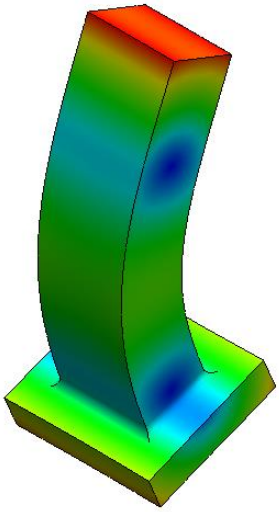

FIGURE 2. First free-free bending mode shape for solid post with 6392 Hz natural frequency.

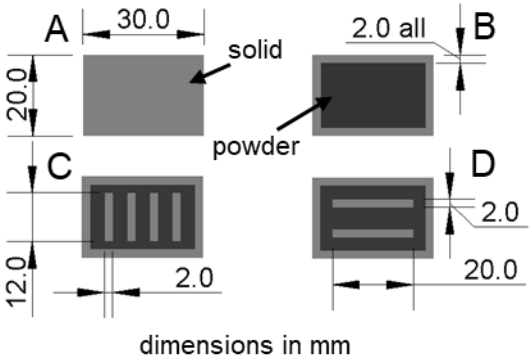

FIGURE 4. Post section A-A from Figure 1: A) solid; B) powder only; C) shear (shear damping); and D) normal (compression damping).

Figures 3 and 4 display the internal geometries of the different designs. The first two designs (A and B in Figure 4) are simple: solid and captured powder. The second two designs include internal, free standing ribs that are not attached to the surrounding walls. As the name suggests, the "shear" ribs were intended to shear the flow of powder as the external structure was excited at its first free-free bending mode shape; see Figure 2. This obstruction in the powder flow of the powder was expected to add damping. The "normal" ribs were oriented normal to the excitation direction and therefore provided

powder compression during motion in the first free-free bending mode shape. The intent of this design was to “squeeze” the powder and support or recruit additional powder that was not excited in the no-rib, captured powder design. As shown in Figure 3, the normal and shear clamped-free ribs protruded from the base with a height of 90 mm and were surrounded by the captured powder. Additionally, 8 mm internal fillets were included to assist the printing process; see Figure 3.

EXPERIMENTAL SETUP

The structures were fabricated by laser PBF using a Concept Laser M2 Cusing with stainless steel 316L powder produced by Praxair Surface Technologies. The powder size distribution was {15-45} µm with a spherical morphology and was produced by gas atomization.

The frequency response function (FRF) was measured for each printed structure using impact, or tap, testing, where a modal hammer (PCB model 086C04) was used to excite the structure and a low-mass accelerometer (PCB model 352C23) was used to measure the vibration response. The direct FRF, where the hammer and accelerometer are spatially co-located, was measured at the central, top edge of each beam as shown in Figure 5. The structures were placed on soft foam pads to approximate free-free boundary conditions.

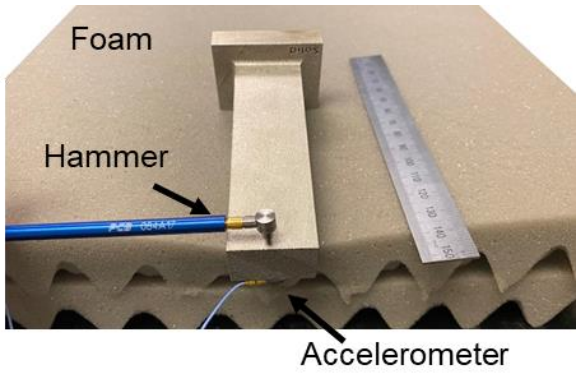

FIGURE 5. Free-free boundary condition tap testing setup for PBF posts.

RESULTS AND DISCUSSION

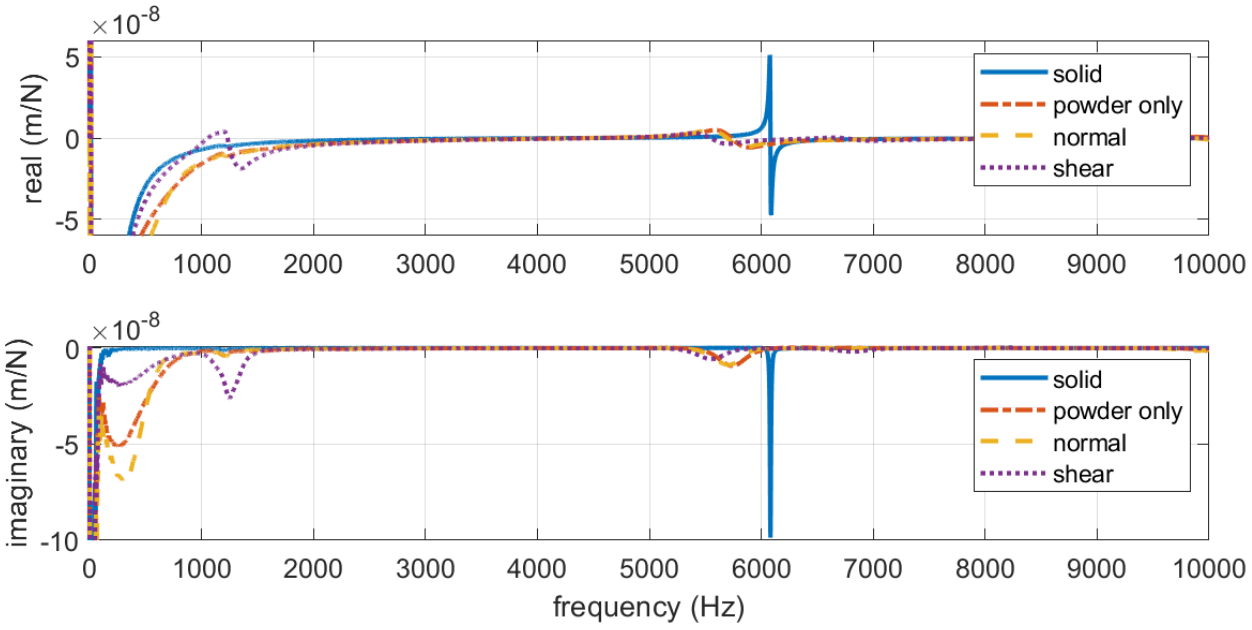

FIGURE 6. Direct FRFs for PBF posts.

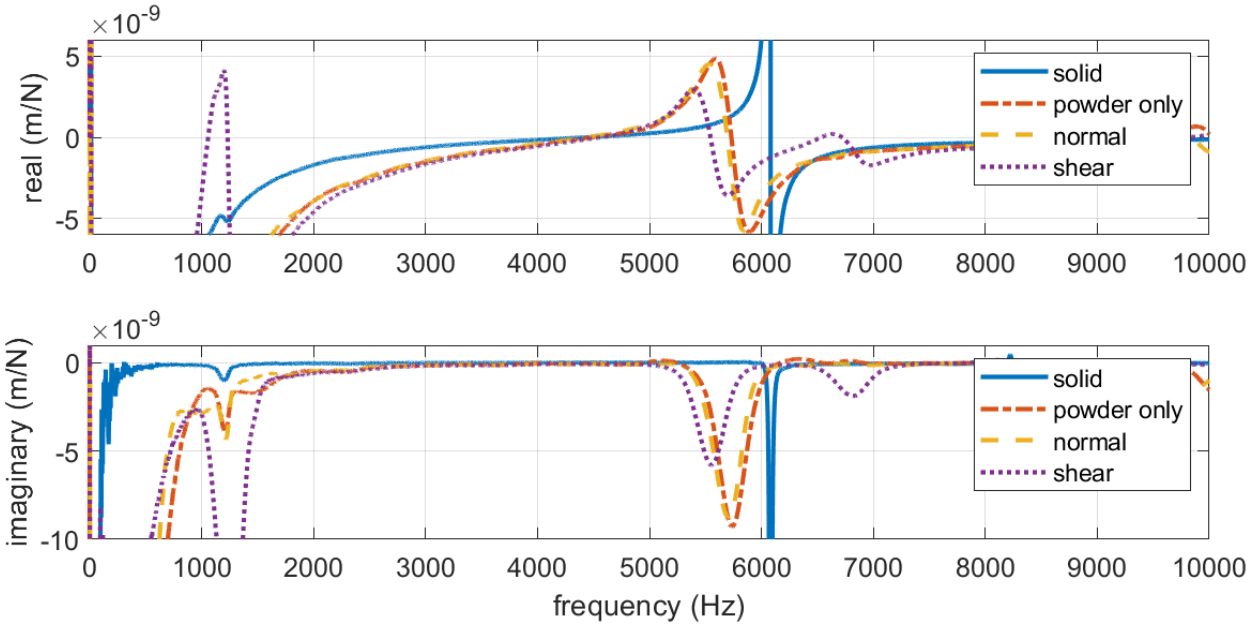

FIGURE 7. Zoomed view of Figure 6 to highlight the direct FRF measurements of PBF posts containing captured powder.

TABLE 1. Best-fit modal parameters for the PBF posts.

Design	Mode	f_n (Hz)	k_q (N/m)	m_q (kg)	ζ_q
solid	1	6082	5.03×10^9	3.45	0.001
powder only	1	5741	2.06×10^9	1.58	0.026
normal	1	5708	2.10×10^9	1.63	0.027
shear	1	5555	3.15×10^9	2.58	0.028
	2	6820	1.23×10^{10}	6.71	0.022

Figure 6 shows the direct FRF measurements for each of the PBF posts (free-free boundary conditions). The solid post's first natural frequency is observed at 6082 Hz, similar to the FEA prediction of 6392 Hz. This demonstrates that the foam foundation provides a reasonable free-free boundary conditions approximation. As expected, the solid post was lowly damped; this is shown by the sharp peaks in both the real and imaginary parts of the complex-valued FRF. The larger peak heights for the solid post's response also show that this structure provides much lower dynamic stiffness than the geometries with captured powder.

Figure 7 shows the FRFs for the posts with captured powder in more detail. The peak heights for the posts with captured powder are significantly smaller than the solid post. The natural frequencies are also lower. The captured powder post response peaks in Figure 7 are also significantly wider, indicating the captured powder provides considerable damping and increased dynamic stiffness.

The modal parameters for each FRF were obtained by a peak picking fitting procedure [5]; the results are listed in Table 1, where f_n is natural frequency, k_q is modal stiffness, m_q is modal mass, and ζ_q is the modal damping ratio. The modal damping ratio for the solid post is 0.001, or 0.1%. This is anticipated for metallic, monolithic components.

Table 1 shows that the captured powder provided an increase in damping by factors of 26 to 28 as compared to the solid post. The shear rib configuration provided increased modal stiffness and damping as compared to the normal ribs and powder-only posts. There is also a second mode for the shear rib design at 6820 Hz. An FEA investigation into the dynamic nature of the clamped-free internal geometry predicted a

natural frequency near 6700 Hz in the excitation direction of the external structure. Figure 8 displays the corresponding clamped-free mode shape for the shear ribs. This mode resembles the traditional second mode shape for a clamped-free (cantilever) uniform cross-section beam.

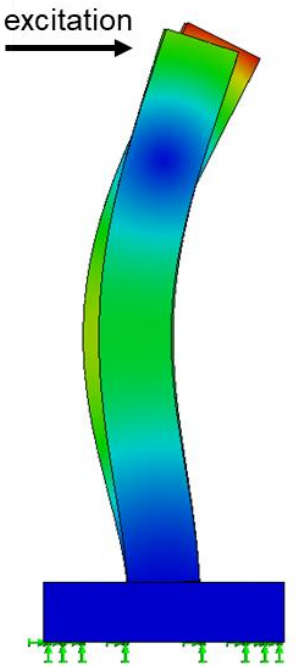

FIGURE 8. Clamped-free mode shape for shear ribs.

The 6820 Hz mode for the shear rib (mode 2 in Table 1) demonstrates that the dynamics of internal features contribute to the dynamics of the entire structure. This provides insight into future design possibilities.

CONCLUSIONS

This paper investigated the use of intentional captured powder during powder bed fusion printing of prismatic structures to increase damping and, therefore, dynamic stiffness. Finite element analysis was used to predict the natural frequencies and mode shapes for free-free boundary conditions. Internal features were proposed to provide additional energy dissipation through increased powder interaction. The post designs were printed and free-free tap testing was used to identify modal parameters, which were compared for each design. It was shown that captured powder and internal features provided significant damping and increased dynamic stiffness. It was also shown that the dynamics of internal free-standing features could be used to tailor the dynamic response of the overall structure.

ACKNOWLEDGEMENTS

The authors would like to acknowledge Chris Ledford and Ryan Duncan for their assistance. This research used resources of the Manufacturing Demonstration Facility, a DOE Office of Energy Efficiency & Renewable Energy (EERE) User Facility at Oak Ridge National Laboratory.

REFERENCES

[1] Schmitz T, Betters E, West J. Increased damping through captured powder in additive manufacturing. Manuf Lett 2020;25:1–5. https://doi.org/10.1016/j.mfglet.2020.05.003.

[2] Schmitz T, Gomez M, Ray B, Heikkenen E, Sisco K, Haines M, et al. Damping and mode shape modification for additively manufactured walls with captured powder. Precis Eng 2020;66:110–24. https://doi.org/10.1016/j.precisioneng.2020.07.002.

[3] Scott-Emuakpor O, George T, Runyon B, Holycross C, Langley B, Sheridan L, et al. Investigating Damping Performance of Laser Powder Bed Fused Components With Unique Internal Structures. Vol. 7C Struct. Dyn., Oslo, Norway: American Society of Mechanical Engineers; 2018, p. V07CT35A020. https://doi.org/10.1115/GT2018-75977.

[4] Gomez M, Corson G, Heikkenen E, Sisco K, Haines M, Schmitz T. Biologically-inspired rib designs for captured powder damping in additive manufacturing. Manuf Lett 2021:7.

[5] Schmitz TL, Smith KS. Mechanical Vibrations: Modeling and Measurement. Second edition. Cham: Springer; 2021.

CHARACTERISTICS OF ADDITIVELY MANUFACTURED AUXETIC MATERIALS FOR SPINDLE VIBRATION MITIGATION

Jungsub Kim[1], Himanshu Hegde[1], Hyo-Young Kim[2, 3], and ChaBum Lee[1]
[1]J. Mike Walker '66 Department of Mechanical Engineering
Texas A&M University
College Station, TX, USA

[2]Manufacturing System R&D Group
Korea Institute of Industrial Technology
Cheonan-si, Chungnam-do, South Korea

[3]Department of Mechatronics Engineering
Korea Polytechnic University
Siheung-si, Gyeonggi-do, South Korea

ABSTRACT
This paper introduces novel spindle holders made of additively manufactured auxetic materials for spindle vibration mitigation. Unlike conventional spindle vibration suppression methods using anti-vibration tool holders or software-based dampers, auxetic under cycle loading, providing sufficient stiffness and compactness. The re-entrant hexagon-type auxetic structures commonly used in the auxetic design were fabricated by additive manufacturing (AM) process using titanium and carbon fiber-reinforced polymer (CFRP) feedstocks. Static and dynamic behaviors of two auxetic structures were characterized by finite element analysis (FEA) and were experimentally identified by characterizing stiffness, damping, frequency response function, and vibration power transmissibility, and those results were compared with those of control group to quantitatively characterize how auxetic materials impact on spindle vibration mitigation. As a result, the CFRP auxetic material-based spindle holder had high damping characteristics and showed approximately a 15 dB decrease in the spindle vibration magnitude compared to the control group. Therefore, the advancement of AM technology will enable further development of auxetic structures toward the tooling in advanced manufacturing.

INTRODUCTION
Additive manufacturing (AM) is a highly attractive process for manufacturing near-net-shape and complex components that can be difficult to fabricate using subtractive and formative manufacturing processes with low cost and waste [1-2]. Thus, AM can make it possible to create nearly any geometric form like hollow spaces, honeycomb, filling, internal cooling channels, negative drafts, and so on [3-4].
Meanwhile, auxetic materials as typical honeycomb materials have received tremendous attention due to their excellent performance such as lightweight, high toughness, shear resistances, and excellent acoustic and energy absorption properties. In particular, the study on auxetic material has more interests due to negative Poisson's ratio (NPR). Because the auxetic material with NPR typically possess enhanced toughness, shear resistance and energy absorption properties [5]. However, it is limited and difficult to fabricate the auxetic material using subtractive and formative manufacturing processes.
Therefore, many researchers have studied characteristics of auxetic materials manufactured using AM which can fabricate components with complex and near-net shape. Alomarah et al. investigated the compressive properties of auxetic materials fabricated by AM process like multi-jet fusion (MJF) process. Four auxetic structures such as re-entrant chiral auxetic structure, re-entrant, tetra chiral, and anti-tetra chiral structure were manufactured, and then the comparative study was conducted experimentally and numerically [6]. Lvov et al. conducted the combination of theoretical calculations, computer simulations, and experimental evaluation of NPR for re-entrant auxetic structure printed by fusion deposition modeling (FDM) process. As a result, it was shown that the printed auxetic structures can be used as dampers due to energy absorption [7].

Quan et al. demonstrated the manufacturing of carbon fiber-reinforced polymer (CFRP) auxetic structure using FDM process. And then, a combined experimental analytical and numerical approach was employed to investigate the compressive properties of printed CFRP auxetic structure compare with pure polylactic acid (PLA) auxetic structure. It was found that adding CFRP to an auxetic structure led to a dramatic increase in compressive stiffness and energy absorption [8]. Boldrin et al. evaluated the modal and structural dynamics response of auxetic structure [9]. In addition, many studies related to static and dynamic characteristics of auxetic material fabricated by AM processes have been examined for their applicability to academies and industry.

In this paper, auxetic materials were designed and fabricated for spindle vibration mitigation. Titanium (Ti) and CFRP base feedstocks were employed to fabricate auxetic structures by AM process like powder bed fusion (PBF) and FDM. This paper performs FEA and experimental investigation (stiffness, damping, frequency response function, vibration power transmissibility) of base structure (no auxetic) and dependent auxetic structures (Ti and CFRP auxetic).

DESIGN AND FABRICATION

The auxetic material-based spindle holders were designed and fabricated by AM process using Ti and CFRP feedstocks. Ti having high strength to density ratio of any metallic element and corrosion-resistant was used to fabricate the Ti auxetic holder by PBF printer (DMP Flex 350, 3D Systems). Ti which is a spherical Ti-6Al-4V powder having an average particle size of 30 μm was used as feedstock, and it has a tensile strength of 1,000 MPa and tensile modulus of 105 GPa. The Ti auxetic holder was fabricated under conditions like laser power of 145 W and scanning speed of 1,000 mm/s. And CFRP having high strength, low density, and vibration resistance was also employed to manufacture the CFRP auxetic holder by fused deposition modeling (FDM) printer (Mark 2, Markforged). Onyx which is micro carbon fiber-filled nylon was used as feedstock and it has a tensile strength of 800 MPa and tensile modulus of 60 GPa. The CFRP auxetic holder was manufactured under conditions including layer thickness of 100 μm, feed speed of 500 mm/s and extruding temperature of 250 ℃. The successfully fabricated Ti and CFRP auxetic holders can be seen in Figure 1. The diameter, height, length, width, and angle of Ti and CFRP auxetic holders were measured by a vernier caliper (CD-6" ASX, Mitutoyo) and the measured results are summarized in Table 1. As a result, the Ti and CFRP auxetic holders had a dimension error of 3.96% compared with the computer-aided design (CAD) model, and critical defects such as crack, pore, and warping were not created in the AM process.

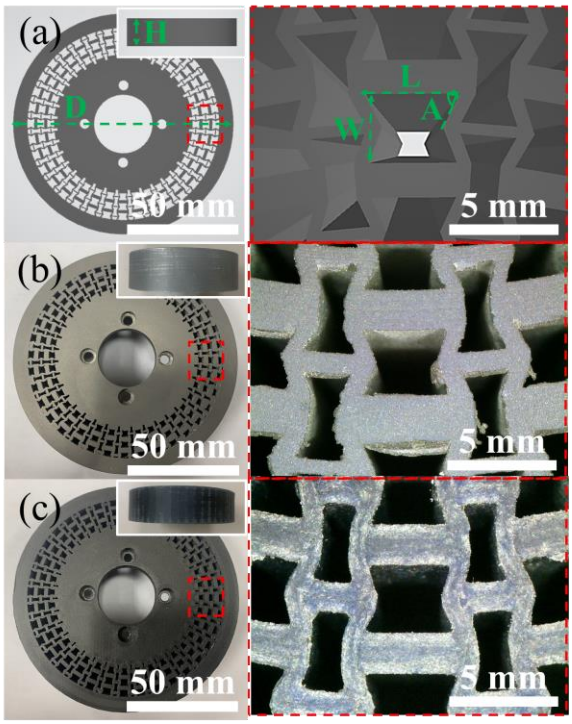

FIGURE 1. Fabricated auxetic material-based spindle holders: (a) CAD model, (b) Ti and (c) CFRP auxetic holders.

TABLE 1. Measured dimension of fabricated auxetic material-based spindle holders

	CAD Model	**Ti Auxetic**	**CFRP Auxetic**
Diameter (mm)	100.00	99.48	99.84
Height (mm)	25.00	24.94	25.44
Length (mm)	3.50	3.21	3.35
Width (mm)	3.00	2.74	2.54
Angle (°)	70.00	71.45	72.40

STATIC AND DYNAMIC CHARACTERISTICS

Stiffness and damping

The finite element analysis (FEA) was performed by using Ansys software package to characterize the static and dynamic behaviors of the auxetic holders. The simulation model is

shown in Figure 2a. The outer surface was fixed and the input conditions like static and impulse forces were applied on the two mount holes. To perform the stiffness simulation, the static forces of 0 ~ 100 N were applied along the X-direction and the X-axis displacement of the mount holes was measured, as shown in Figure 2b. And the free-vibration simulation was also performed. A force of 2 N was applied along X-direction for a duration of 0.1 ms and the X-direction acceleration response was measured.

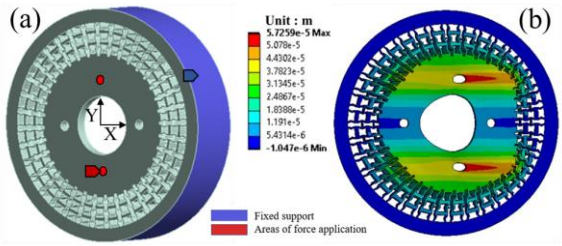

FIGURE 2. Finite element analysis of auxetic material based-spindle holders: (a) FEM model and (b) simulation results (force-displacement relationship upon 100 N).

To identify the stiffness and damping of the auxetic holders, the stiffness and free-vibration test were carried out to compare with the FEA results. The X-axis displacement of the shuttle attached to the auxetic holder was measured by applying the static forces of 0 ~ 100 N along the X-direction to the shuttle. The applied force and the corresponding displacement were measured by a capacitive sensor (CS) (HPC-40 & 4100-SL, Capacitec) and a force sensor (FS) (4577A1C1, Kistler), respectively. And then, the stiffness was calculated using measured force and displacement. As a result, it was found that the stiffness of Ti and CFRP auxetic holders: 28.25 N/μm and 1.75 N/μm by FEA and 27.24 N/μm and 1.62 N/μm by experiment, as shown in Figure 3a. And there were 3.6% and 7.4% discrepancies between the FEA results and the stiffness test for the Ti and CFRP auxetic holders, respectively. In addition, the damping was calculated through the free-vibration test was conducted using an accelerometer (ACC) (2222C, Endevco). Raw data from the free-vibration test were obtained by hammering the attached shuttle with the ACC attached in X-direction. As shown in Figure 3b, it was found that the damping and natural frequency of Ti and CFRP auxetic holders were estimated to be ζ 0.0019, ζ 0.0724, and ω_n 5,625 Hz, ω_n 1,257 Hz, by FEA, respectively. Damping ratio and natural frequency were measured by free-vibration test: ζ 0.0037, ζ 0.0544 and 5,600 Hz, ω_n 1,256 Hz, by experiments, respectively. There were 24.1% and 12.4% discrepancies between the FEA result and the free-vibration test for the Ti and CFRP auxetic holders, respectively.

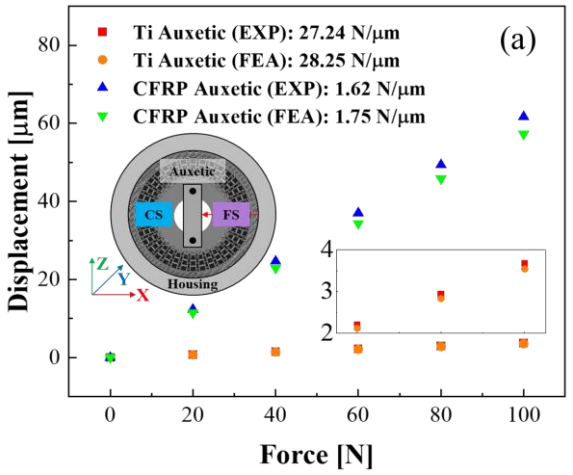

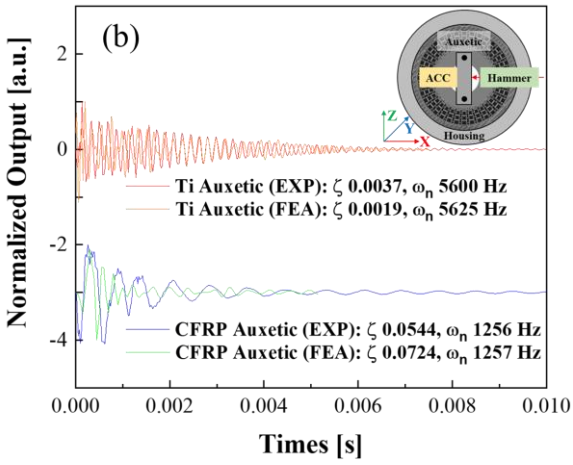

FIGURE 3. Dynamic characteristics of auxetic material-based spindle holders: (a) stiffness and (b) damping.

Vibration power transmissibility

The hammering test was carried out to investigate the vibration power transmissibility of the auxetic holders. One Acc was attached to the spindle housing and the other ACC was attached to the shuttle attached to the spindle holder. And then, the attached shuttle was

tapped using the hammer which was connected to the dynamic signal analyzer (DSA) (35670a, Agilent). The DSA was used to collect and analyzed the input force and vibration signals from both the auxetic holder and housing. As a result, it was found that both Ti and CFRP auxetic holders mitigated high-frequency vibration compared to the case of spindle holders with no auxetic material, as shown in Figure 4. Especially, the CFRP auxetic holder decreased the vibration by approximately 1.5 dB over the wide frequency range.

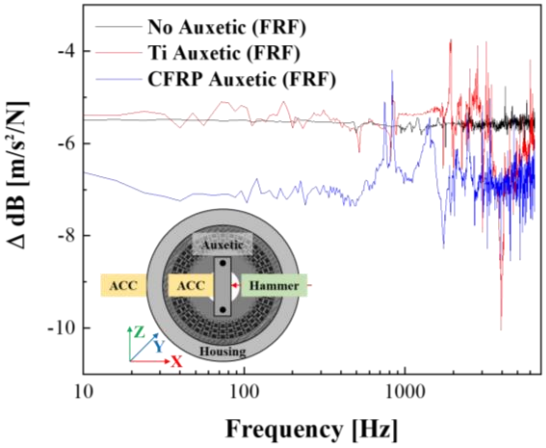

FIGURE 4. Vibration power transmissibility of auxetic material-based spindle holders.

CONCLUSION

In this paper, the auxetic materials for spindle vibration mitigation were designed, fabricated, and validated. The auxetic materials having complex geometry were fabricated using AM process. And then, the static and dynamic behaviors of the Ti and CFRP auxetic holders were investigated by FEA and experiments related to the stiffness, damping, and vibration power transmissibility. As a result, the Ti and CFRP auxetic holders can suppress the spindle vibration over the wide frequency range. Therefore, the auxetic holders will enable spindle vibration mitigation. For future work, dynamic material models of the auxetic materials and their corresponding vibration effects will be theoretically studied.

ACKNOWLEDGEMENT

This research has been supported by Korea Institute of Industrial Technology (KITECH, Project No. JE200016, Development of robotic machining state monitoring and process technology for improving product quality) and Ministry of Trade, Industry and Energy (KEIT, Project No. 20011498, Robotic CFRP-metal mechanical joining and adhesive bonding process for future automotive applications).

REFERENCES

[1] Wong, K. V., and Hernandez, A., “A review of additive manufacturing,” International scholarly research notices, 2012.

[2] Gibson, I., Rosen, D. W., Stucker, B., and Khorasani, M., “Additive manufacturing Technologies,” vol. 17, Cham, Switzerland: Springer, 2021.

[3] Vayre, B., Vignat, F., and Villeneuve, F., “Designing for additive manufacturing,” Procedia CIrP, vol. 3, pp. 632-637, 2012.

[4] Gao, W., Zhang, Y., Ramanujan, D., Ramani, K., Chen, Y., Williams, C. B., and Zavattieri, P. D., “The status, challenges, and future of additive manufacturing in engineering,” Computer-Aided Design, vol. 69, pp. 65-89, 2015.

[5] Alderson, A., and Alderson, K. L., “Auxetic materials,” Proceedings of the Institution of Mechanical Engineers, Part G: Journal of Aerospace Engineering, vol. 221, no. 4, pp. 565-575, 2007.

[6] Alomarah, A., Ruan, D., Masood, S., and Gao, Z., “Compressive properties of a novel additively manufactured 3D auxetic structure,” Smart Materials and Structures, vol. 28, no. 8, 085019, 2019.

[7] Lvov, V. A., Senatov, F. S., Stepashkin, A. A., Veveris, A. A., Pavlov, M. D., and Komissarov, A. A., “Low-cycle fatigue behavior of 3D-printed metallic auxetic structure,” Materials Today: Proceedings, vol. 33, pp. 1979-1983, 2020.

[8] Quan, C., Han, B., Hou, Z., Zhang, Q., Tian, X., and Lu, T. J., “3D printed continuous fiber reinforced composite auxetic honeycomb structures,” Composites Part B: Engineering, vol. 187, 107858, 2020.

[9] Boldrin, L., Hummel, S., Scarpa, F., Di Maio, D., Lira, C., Ruzzene, M., and Patsias, S., “Dynamic behaviour of auxetic gradient composite hexagonal honeycombs,” Composite Structures, vol. 149, pp. 114-124, 2016.

High-speed Large-range Flexure-based Six-Axis Positioner

Zhidi Yang and Jonathan Hopkins
Department of Mechanical and Aerospace Engineering
University of California, Los Angeles
Los Angeles, CA, USA

ABSTRACT
This paper introduces a new flexure-based high-precision six-axis positioner, called the hexblade positioner, that can simultaneously achieve combinations of high speeds and large ranges overall all six degrees of freedom. A geometry optimizer is used in conjunction with a custom-developed analytical tool to quantitatively generate plots of the design's complete performance capabilities. The results of the optimization show that the hexblade positioner is well suited for high-precision applications where large normalized ranges and high speeds (i.e., high natural frequencies) are simultaneously desired. Such applications include deposition-nozzle positioners that enable rapid high-resolution 3D printing in harsh, high-vibration environments. An optimal version of the hexblade design is fabricated and frequency-sweep data is collected to characterize its dynamic capabilities.

HEXBLADE POSITIONER DESIGN
The hexblade positioner, shown in two different views in Fig. 1a,b, was designed using the freedom and constraint topologies (FACT) approach [1-3] using the steps provided in Hopkins and McCalib [1] for achieving decoupled actuation. The positioner consists of a rigid motion stage joined to two different but similar sets of three identical decoupled actuation limbs [1] arranged in an axisymmetric configuration. Each decoupled actuation limb consists of a bent-blade flexure that joins the positioner's stage to an intermediate rigid body. This intermediate rigid body is joined to another rigid body by two traditional blade flexures, which lie on parallel planes that are perpendicular to the axis of the bent-blade-flexure's crease as shown by the dashed blue lines in Fig. 1c. The last rigid body in the serial chain of flexures is mechanically grounded as indicated by the hatched black lines drawn in Fig. 1c. A high-precision contact-free linear voice coil motor, labeled actuator in Fig. 1a, is positioned between the two blade flexures so that the motor can impart a force on the intermediate rigid body at a location halfway down the length of the blade flexures to minimize the intermediate body's parasitic motion error as it moves.

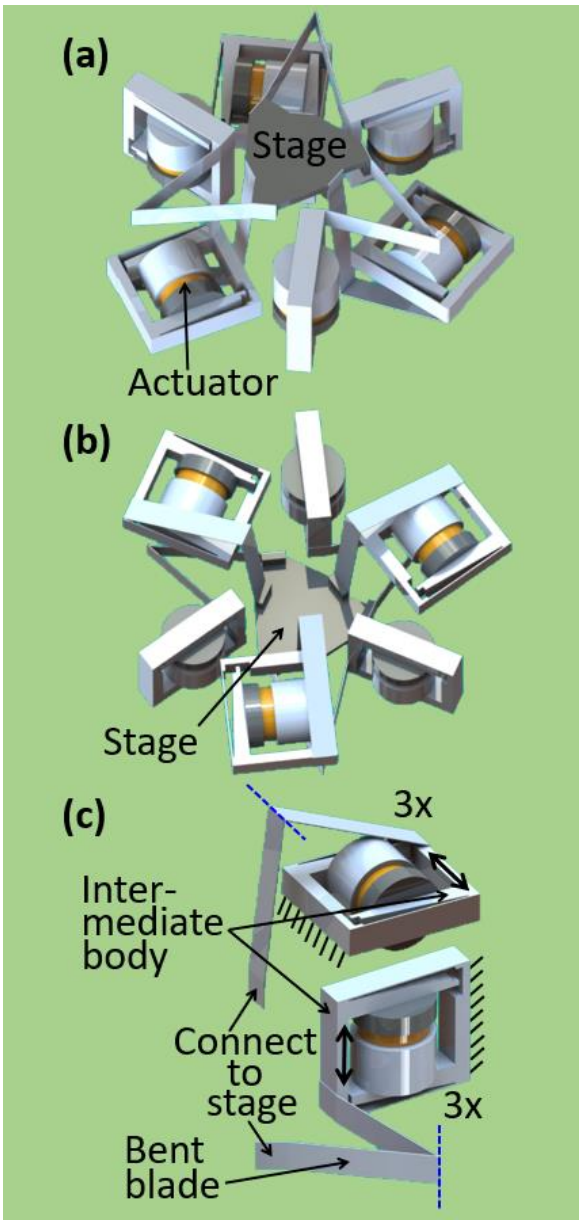

FIGURE 1. (a), (b) Two different views of the hexblade positioner design. (c) Two different but similar sets of the three identical decoupled actuation limbs [1] that constitute the design.

The parallel blade flexures constitute each decoupled actuation limb's actuator bearing [1], which serves the purpose of guiding the translational motion of the linear voice coil motor (shown as a black translation arrow in Fig. 1c) and ensures that its outer cylindrical magnet and its inner copper coil remain aligned over the actuator's stroke. Note that the actuator's heavier magnet half is attached to the grounded rigid body so that the positioner is required to accelerate as little mass as possible for achieving high speeds. The bent-blade flexures constitute the decoupled actuation limbs' decoupling flexures [1], which decouple their corresponding actuator from the motions induced by the other five actuators in the system. Thus, although the bent-blade flexures stiffly pass the translation motion of their actuators along their crease's axis to the system's stage to successfully drive it, if any of the other actuators in the system drive the stage, the bent-blade flexure will deform to minimize the effect of those stage motions on the bent-blade flexure's corresponding actuator.

ANALYTICAL OPTIMIZATION

We created a custom analytical tool that enables the construction of twist-wrench stiffness [4] and mass [5] matrices of general flexure systems. We then constructed these matrices for the hexblade six-axis positioner design as functions of its geometric parameters. Using these matrices, we were able to rapidly calculate the natural frequencies of different geometric versions of the design. We also used the stiffness matrices in conjunction with other custom-developed constraint functions to calculate the maximum range achieved by the design's stage along each of its six DOFs. The largest displacement achieved by the design's stage without any bodies or elements colliding, yielding, or buckling or that is achieved at the actuators' maximum load output or stroke is considered the design's maximum range along its corresponding DOF. A normalized range, R, was thus able to be calculated for any version of the hexblade design by considering the maximum range along all six of its DOFs according to

$$R = \sqrt{\frac{w_1 x_{trans}^2 + w_2 y_{trans}^2 + w_3 z_{trans}^2 + w_4 x_\theta^2 + w_5 y_\theta^2 + w_6 z_\theta^2}{X^2 + Y^2 + Z^2}} \quad (1)$$

where x_{trans}, y_{trans}, and z_{trans}, are the maximum linear displacements along the x, y, and z-axes respectively, x_θ, y_θ, and z_θ, are the maximum angular rotations about the x, y, and z-axes respectively, and the parameters X, Y, and Z are the lengths of the sides of the smallest rectangular box inside of which the respective designs could fit. The parameters, w_1, w_2, w_3, w_4, w_5, and w_6, are all weighting factors that are set according to the priority of each DOF for specific applications.

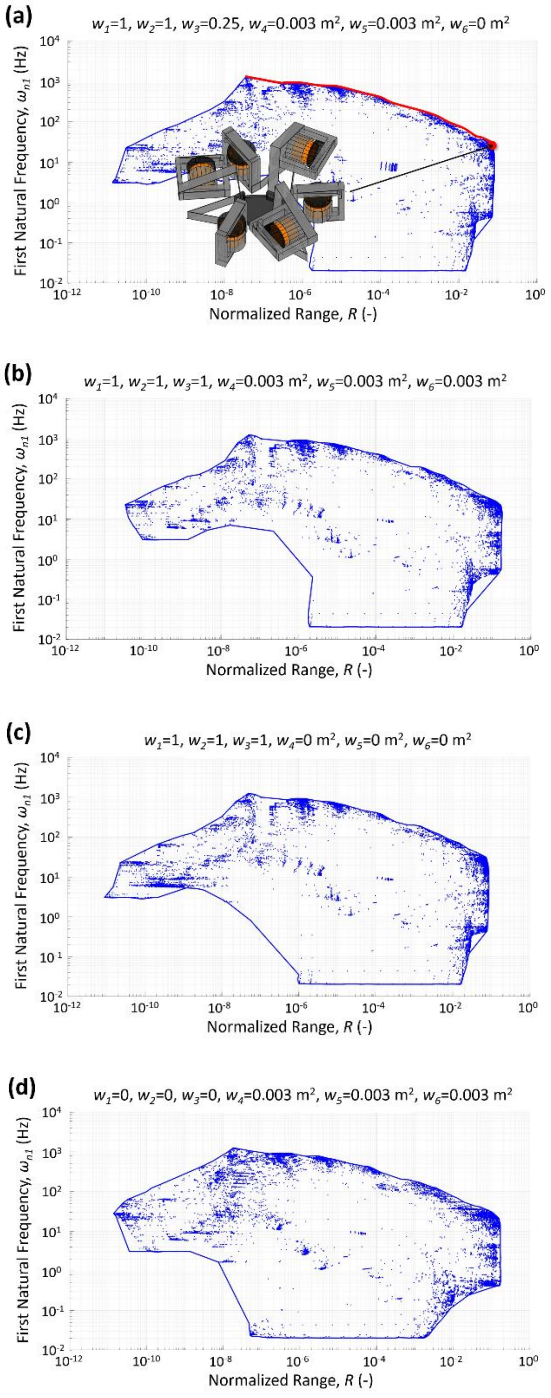

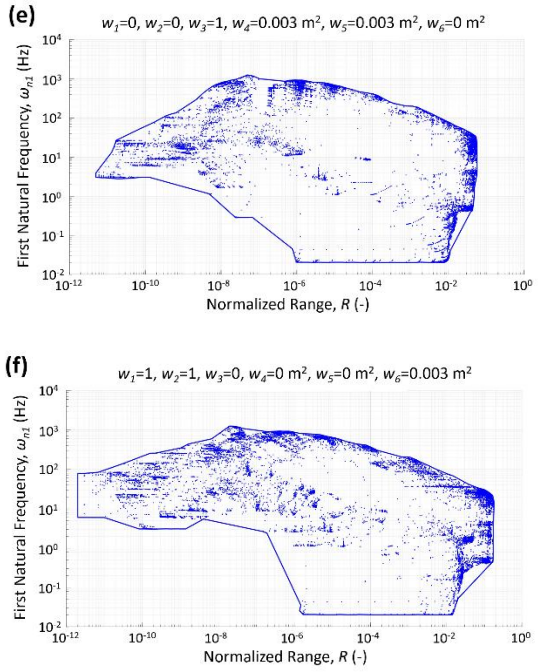
(e)
w_1=0, w_2=0, w_3=1, w_4=0.003 m², w_5=0.003 m², w_6=0 m²
First Natural Frequency, ω_{n1} (Hz)
Normalized Range, R (-)
(f)
w_1=1, w_2=1, w_3=0, w_4=0 m², w_5=0 m², w_6=0.003 m²
First Natural Frequency, ω_{n1} (Hz)
Normalized Range, R (-)

FIGURE 2. (a)-(f) Performance capability plots of the hexblade positioner design for six different combination of weighting factors, w_1-w_6.

We used the boundary learning optimization tool (i.e., BLOT) [6] to perform a parametric sweep on the hexblade design to identify its performance boundaries for various combinations of the weighting factors specific to various applications of interest (Fig. 2). Note from the plots of Fig. 2 that each blue dot corresponds to a single parametric version of hexblade design. Each design's first natural frequency, ω_{n1}, is shown plotted on the y-axis of each plot and is closely related to the speed with which the design's stage can be driven. The normalized range, R, of each design is shown plotted on the x-axis and is a single representative number of the design's overall range capabilities considering all six DOFs simultaneously according to the weighting factors defined.

The regions within the blue solid boundaries shown in the plots of Fig. 2 represent the complete performance capabilities of the hexblade design for various combination of weighting factors, and can thus be used to identify their corresponding optimal versions of the design. Consider the plot of Fig. 2a, for example, which was generated using weighting factors that were tuned to the application for which the hexblade positioner was designed (i.e., a 3D printer's deposition-nozzle positioner that enables rapid high-resolution printing in harsh, high-vibration environments). The optimal versions of the hexblade design for that specific application lie along the red portion of the boundary shown in Fig. 2a. Among those optimal designs, the design version that favors range over speed is shown in Fig. 2a, which is also the design shown in Fig. 1. Note that the design shown in Fig. 2a was generated using our custom MATLAB tool—not a commercial computer-aided design (CAD) package.

FREQUENCY SWEEP DATA

We fabricated and assembled the optimized version of the hexblade design shown in Fig. 2a. A photo of the fabricated design is shown in Fig. 3a. Reflective pearl markers were attached to the design's stage so that 4 Vicon cameras fixed to a surrounding frame (Fig. 3b) could track the locations and orientations of the design's stage as it is actuated by its voice-coil actuators. The actuators were used to sweep the design's stage along the x-axis from 1 Hz to 80 Hz and the 4 Vicon cameras recorded the resulting frequency sweep data provided in Fig. 3c.

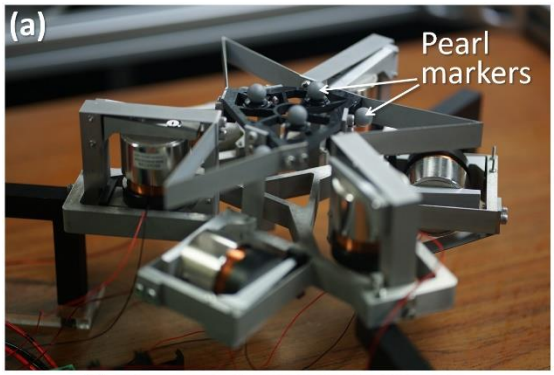

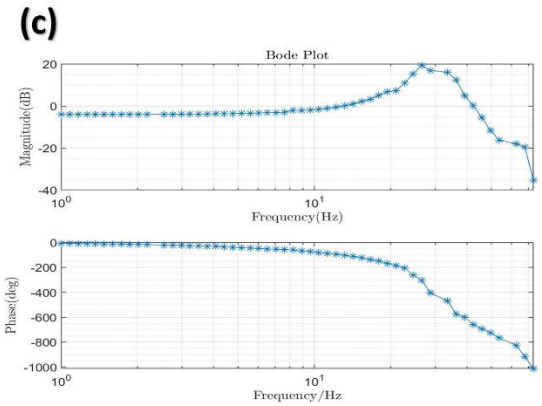

FIGURE 3. (a) Fabricated version of the optimal hexblade design shown in Fig. 2a. (b) Four Vicon cameras fixed to an aluminum frame measure the location and orientation of the design's actuated stage. (c) Experimentally measured Bode plot of the design when its stage was driven with a translation along the x-axis.

CONCLUSION

In this paper we present a new six-axis precision positioner, called the hexblade positioner, that utilizes bent-blade flexures to achieve large ranges of deformation at high speeds. Although it was designed to enable high-resolution 3D printing in dynamic environments, the positioner is a competitor to other high-precision flexure-based six-axis positioners such as the popular Stewart Platform design [7]. Analytical tools were created to analyze the performance capabilities (i.e., the natural frequencies and normalized ranges) of any geometric version of the hexblade positioner. These tools were used in conjunction with other optimization tools to generate cloud plots that represent the design's complete performance capabilities. These plots were used to identify optimal versions of the hexblade topology. An optimal version of the design that favors large range over high speed was fabricated and tested. A frequency sweep is conducted to demonstrate the design's dynamics performance along its x-axis.

ACKNOWLEDGEMENTS

This work was funded by the Defense Advanced Research Projects Agency (DARPA) under Award Number: HR00112010002. Program Office William Carter is gratefully acknowledged along with our grant collaborators Prof. Rob Candler and Prof. Pirouz Kavehpour at UCLA.

REFERENCES

[1] Hopkins JB, McCalib Jr D. Synthesizing multi-axis flexure systems with decoupled actuators. Precision Engineering. 2016 Oct 1;46:206-20.

[2] Hopkins JB, Culpepper ML. Synthesis of multi-degree of freedom, parallel flexure system concepts via Freedom and Constraint Topology (FACT)–Part I: Principles. Precision Engineering. 2010 Apr 1;34(2):259-70.

[3] Hopkins JB, Culpepper ML. Synthesis of multi-degree of freedom, parallel flexure system concepts via freedom and constraint topology (FACT). Part II: Practice. Precision Engineering. 2010 Apr 1;34(2):271-8.

[4] Hopkins JB, Lange KJ, Spadaccini CM. Designing microstructural architectures with thermally actuated properties using freedom, actuation, and constraint topologies. Journal of Mechanical Design. 2013 Jun 1;135(6):061004.

[5] Hopkins, J.B., Song, Y., Wang, S., Behbahani, A.H., Josefson, I., "Optimal Actuation of Dynamically Driven Serial and Hybrid Flexure Systems," *Proc. of the ASME IDETC/CIE*, Buffalo, NY, August 2014

[6] Hatamizadeh, A., Song, Y., Hopkins, J.B., 2018, "Optimizing the Geometry of Flexure System Topologies Using the Boundary Learning Optimization Tool (BLOT)," Mathematical Problems in Engineering, 2018(1058732): 14 pages

[7] Dasgupta, B., Mruthyunjaya, T.S., 2000, "The Stewart Platform Manipulator: A Review", *Mech. and Mach. Theory*, 35:1: pp. 15-40.

IMPROVING SUPPORT STIFFNESS OF FLEXURE MECHANISMS BY STATICALLY BALANCING

Jan J. de Jong, S. Theans, L.J. Epping, and Dannis M. Brouwer

Precision Engineering, University of Twente, Enschede, The Netherlands

ABSTRACT

Static balance eliminates the actuation stiffness of flexure mechanisms and thereby reduces the motor effort and unwanted heat production. However, this typically comes at the cost of lowered support stiffness and stroke. This paper aims to show that the maximum stresses in the flexures may be reduced as well by static balance. Therefore, thicker flexures can be used, paradoxically leading to an increased support stiffness by static balance. In a case study of a parallel flexure mechanism we shown an increased support stiffness of 11%, while the measured actuation stiffness reduces by more than 95%. This shows that a tradeoff between actuation and support stiffness is avoidable.

INTRODUCTION

In high-precision applications, flexure mechanisms allow for predicable, highly accurate motion as their flexural elements bend with virtually no friction, wear or play. However, flexure mechanisms have a limited stroke and loadbearing capacity due to the build-up of stress concentrations. This leads to material fatigue and restricts the flexure thickness [1]. Furthermore, a static force is needed for deflection, potentially heating up the actuators which leads to undesired thermal expansion [2]. Moreover, the inherent actuation stiffness is undesired when high force sensitivity is required, for example in passive vibration isolation systems [3].

Static balancing aims to eliminate this actuation stiffness by addition of negative stiffness elements [4], [5] and/or by preloading the original flexure mechanism [6], [7]. This makes the potential energy constant and the total stiffness (close to) zero over the stroke of the mechanism. Several negative side effects might be associated to this preload, such as a lowered load carrying capacity and a lowered support stiffness and consequently a reduced the dynamic performance.

This paper will show that the tradeoff between support and actuation stiffness can be turned into a win-win situation. When a flexure is preloaded appropriately, it will bend more uniformly over its length, reducing the maximum stress. This in turn allows for thicker flexures and hence an increased support stiffness. This principle is applied to a statically balanced parallel flexure guide and is shown through simulations and measurements.

METHODS

Static balance by constant preload

A parallel flexure guide is an elementary flexure mechanism used to guide linear motion (Figure 1). The mechanism consist of two leaf flexures that constrain the shuttle to pure translational motion.

Such a mechanism can be statically balanced by a compressive preload F_p. This preload induces a negative geometric stiffness as the shuttle moves over an ark due to kinematic shortening. When this negative stiffness compensates the flexures' inherent stiffness, the actuation stiffness becomes zero. In this case the balance force is found from the Euler's buckling load

$$F_b = 2\pi^2 \frac{EI}{l^2} \quad (1)$$

in which E, is the Young's modulus, I the area moment of inertia and l the length of the flexure.

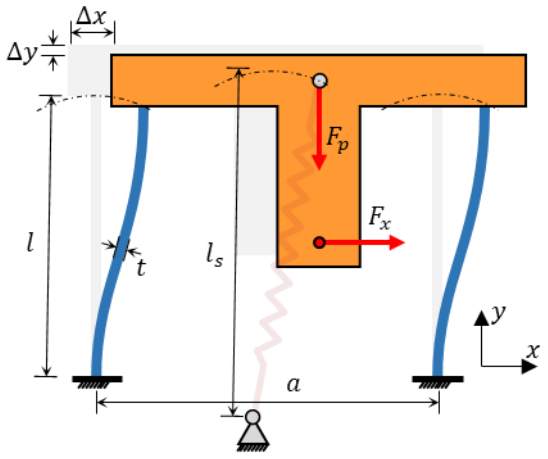

Figure 1. Schematic description of parallel flexure guide. The red dot indicates the center of compliance where the actuation force applies.

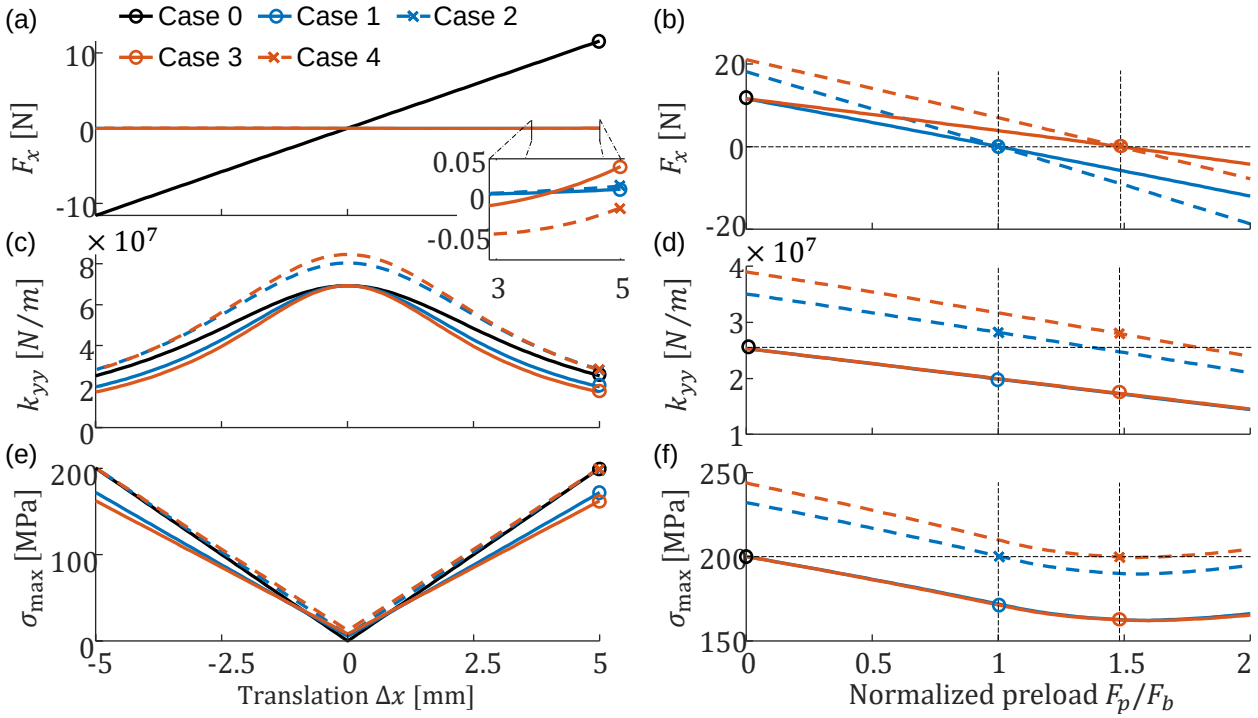

Figure 2. The actuation force F_x (a and b), support stiffness k_{yy} (c and d) and maximum stress σ_{max}(e and f) as a function of translation Δx (a, c, and e) and of increasing preload (b, d, and f). The solid lines correspond to the unbalanced (black), preload balanced (blue) and spring balanced (red) cases with original thickness whereas the dashed lines indicate the cases with increase thickness The circles and crosses indicate the corresponding operating points of the five cases. Note that the preload (horizontal axis, left) is normalized with the buckling force F_b of each case.

Static balance by spring load

In order to apply this balancing preload, we attach a pretensioned helical spring between the shuttle and the base. This results in a position-dependent orientation of the spring force that causes an increase in actuation stiffness. In turn, this requires more pretension F_s to balance

$$F_s \approx \frac{12 l_s}{12 l_s - \pi^2 l} F_b \qquad (2)$$

in which l_s is the pretensioned length of the balancing spring.

Approach

To show that balancing can improve the support stiffness of flexure based mechanisms, we first investigate the influence of balancing on a) the actuation force F_x, b) the in-plane support stiffness in the y-direction k_{yy} and c) the maximum stress $\sigma_{\max}$ and stress distribution. By using flexible multibody simulation software we compare five cases as defined in Table *2*. Two types of simulations are performed: I) simulation over the full stroke with a constant preload and II) with increasing preload at maximum deflection. We compare the constant preload cases with spring load balancing. The baseline simulation parameters are found in Table 1. Based on these simulations we then present a balanced parallel flexure guide to demonstrate the reduction of actuation stiffness.

RESULTS

In this section the results of the simulations and measurements will be discussed. We start with the effect of a constant preload (case 1, and 2) on the actuation stiffness, support stiffness and stress distribution. Thereafter, the influence of a spring (case 3 and 4) will be discussed and finally the results of the demonstrator are given. The main findings are depicted in *Figure 2* and *Table 2*.

Actuation stiffness

Figure 2 a and b show that preload reduces the actuation force needed to deflect the stage. The system is statically balanced when the preload is increased to $F_p = F_b$. The actuation force at full deflection is then less than $0.02\,\mathrm{N}$, which is around 0.01% of its unbalanced value. Beyond this balancing preload, the actuation stiffness

Table 1. The parameters used in the simulation.

Name	Symbol	Value	Unit
Max. deflection	Δx	5.0	mm
Shuttle width	a	90	mm
Flexure length	l	87	mm
Flexure width	w	30	mm
Flexure thickness (baseline - case 0)	t_0	0.5	mm
Young's modulus	E	200	GPa
Stress limit	$\sigma_{\lim}$	200	MPa
Spring length	l_s	210	mm
Spring stiffness	k_s	0.81	N/mm

becomes negative. An actuator is then needed to keep the stage in place.

Support stiffness

Figure 2 c) shows that the support stiffness significantly drops at deflection, as is common with flexure mechanisms. Additionally, the support stiffness worsens significantly due to the balancing preload (*Figure 2 d*). For example case 1 loses 21% of its support stiffness. This undesired reduction is explained by the negative geometric stiffness that acts in the support directions as well.

Stress distribution

Figure 2 e) shows a linear trend between stress and deflection, whereas *Figure 2 f)* shows that increasing preloads leads to a reduction of the maximum stress in the flexures up to about $F_p = 1.5\ F_b$. For even higher preloads, the maximum stress starts increasing again. For a balancing preload F_b this leads to a stress reduction of 14 % for case 1 (*Figure 2 e* and *f*, and *Table 2*).

Figure 3 shows that preload lowers the stresses at the fixtures but increases the stresses elsewhere. This indicates that the curvature of bending is more evenly distributed over the flexure, avoiding local stress concentrations.

Table 2. The thickness t, support stiffness k_{yy} and the maximum stress σ_{max} for the five cases.

Name [Unit]		t [mm]	k_{yy} [kN/mm]	$\sigma_{\max}$ [MPa]
0) Unbalanced	(t_0)	0.50	25.3	200
1) Preload balanced	$(t_1 = t_0)$	0.50	20.0	171
2) Preload balanced	$(t_2 > t_0)$	0.58	28.2	200
3) Spring balanced	$(t_3 = t_0)$	0.50	17.4	163
4) Spring balanced	$(t_4 > t_0)$	0.61	28.0	200

Improving support stiffness

This load-induced stress reduction allows for thicker flexures to be used as the material stress limit are not yet reached. This in turn results in a higher support stiffness. In case 2 the thickness is increased by 16%, leading to a support stiffness improvement of 11% compared to the unbalanced case (case 0) and 41% compared to the balanced case with the original flexures (case 1). See *Table 2* for the exact values.

The influence of a balancing spring

As mentioned earlier, the preload can be increased beyond F_b while still lowering the stresses. This is fortunate when balancing with a spring, since geometric effects induced by the spring require higher balancing preload (*Eq. (2)* and *Figure 2 b*). Case 4 shows that for a spring length of $l_s = 2.5l$ and a corresponding preload of $F_s = 1.48\ F_b$, the thickness can be increased by 22 %. This results in a statically balanced mechanism with an 11% higher support stiffness when compared to the unbalanced case (case 0) and a 61% higher support stiffness when compared to the spring balanced case that uses the original flexures thickness (case 3).

Measurements on a demonstrator

To show that static balance of a parallel flexure guide is obtained, we measured the natural

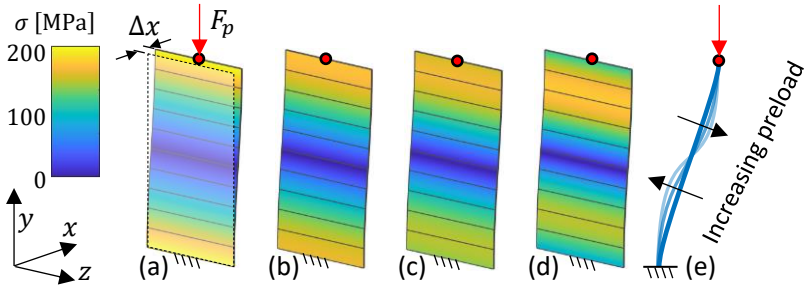

Figure 3. Stress distribution over a curved flexure for increasing preloads (a) no preload $F_p = 0$, (b) balancing preload $F_p = F_b$, (c) minimum stress preload $F_p = 1.5\ F_b$, (d) overloading preload $F_p = 2.5\ F_b$. The exaggerated effect of preload on the curvature of the flexure is shown in (e). The red dot indicates the force application point.

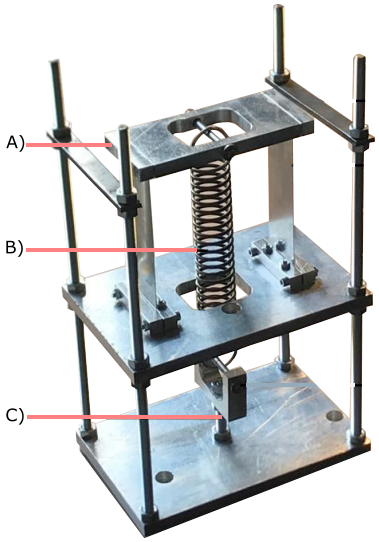

Figure 4. A statically balanced parallel flexure guide. The actuation stiffness of the shuttle A) is reduced by a pretensioned helical spring B). An adjustment screw C) allows for fine-tuning of the pretension.

frequency of oscillation of a demonstrator subjected to increasing pretension (*Figure 4*).

Figure 5 shows a similar trend in the reduction of the natural frequency for simulation and experimental data. The difference in values may be explained by unmodeled mass, slightly thicker flexures or a variation in spring parameters. The change in natural frequency indicate an actuation stiffness reduction of more than 95%.

CONCLUSION

This research shows that static balance may aid the efficiency and the supporting capacity of flexure mechanisms. Paradoxically, the balancing preload may lead to an improved (off-axis) support stiffness as the stress concentrations are reduced such that thicker flexures may be used. In a parallel flexure guide these thicker flexures lead to an 11% support stiffness increase in when compared to the unbalanced case and a 61% increase when compared to the balanced case with original flexure thickness.

On the one hand this indicates that the trade-off between support and actuation stiffness can be overcome. On the other hand it shows that the effect of preload on stress cannot be neglected when designing these types of statically balanced mechanisms.

Measurements on a demonstrator confirm an actuation stiffness reduction of more than $95\ \%$.

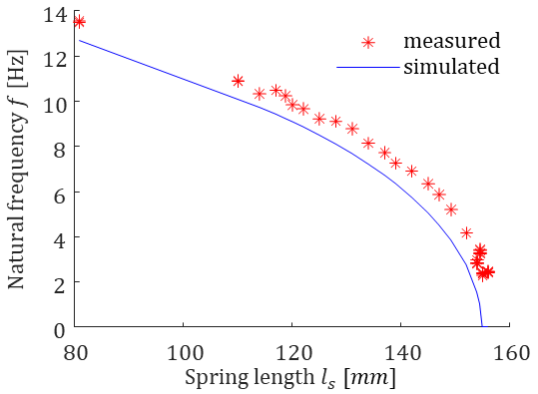

Figure 5. The natural frequency corresponding to the intendent motion direction of the demonstrator for increasing spring tension.

REFERENCES

[1] M. Naves, D. M. Brouwer, and R. G. K. M. Aarts, “Building block-based spatial topology synthesis method for large-stroke flexure hinges,” *J. Mech. Robot.*, vol. 9, no. 4, pp. 1–9, 2017.

[2] Q. Yang, S. Bi, and T. Liu, “Static balancing of flexural pivots with two symmetrically arranged pre-compressing springs,” in *IOP Conference Series: Materials Science and Engineering*, 2020, vol. 892, no. 1.

[3] R. V. Jones, “Some uses of elasticity in instrument design,” *J. Sci. Instrum.*, vol. 39, no. 5, pp. 193–203, 1962.

[4] J. van Eijk and J. F. Dijksman, “Plate spring mechanism with constant negative stiffness,” *Mech. Mach. Theory*, vol. 14, no. 1, pp. 1–9, 1979, doi: 10.1016/0094-114X(79)90036-3.

[5] P. R. Kuppens, M. A. Bessa, J. L. Herder, and J. B. Hopkins, “Compliant Mechanisms That Use Static Balancing to Achieve Dramatically Different States of Stiffness,” *J. Mech. Robot.*, vol. 13, no. 2, pp. 1–6, 2021.

[6] F. M. Morsch and J. L. Herder, “Design of a Generic Zero Stiffness Compliant Joint,” *Proc. ASME Des. Eng. Tech. Conf.*, vol. 2, no. June, pp. 427–435, 2011.

[7] E. G. Merriam and L. L. Howell, “Non-dimensional approach for static balancing of rotational fl exures,” *MAMT*, vol. 84, pp. 90–98, 2015.

[8] K. Hoetmer, G. Woo, C. Kim, and J. Herder, “Negative stiffness building blocks for statically balanced compliant mechanisms: Design and testing,” *J. Mech. Robot.*, vol. 2, no. 4, 2010.

[9] G. J. Simitses and D. H. Hodges, “Introduction and fundamentals,” in *Fundamentals of Structural Stability*, 2006, pp. 3–18.

MULTI-MATERIAL COMPONENT OPTIMIZATION VIA HYBRID MANUFACTURING

Bradley H. Jared[1], Eduardo Miramontes[1], William R. Hamel[1], Joshua Penney[1], Tony L. Schmitz[1], Joshua Robbins[2]

[1]Mechanical, Aerospace and Biomedical Engineering
The University of Tennessee
Knoxville, TN
[2]Computational Sciences and Math
Sandia National Laboratories
Albuquerque, NM

The timely fabrication of large, complex metallic structures is a persistent challenge for America's industrial base. Delivery schedules for large parts, i.e one to two feet cube and larger, are routinely defined in months and years; introducing unacceptable risk and cost for most products. On-going work is addressing these challenges through the development of a large-scale hybrid metal manufacturing system, Figure 1, which combines multi-material metal inert gas (MIG) deposition, fringe projection metrology, part handling and five-axis machining. MIG deposition is performed using a Fronius dual-wire cold metal transfer (CMT) welding head mounted to a Kuka KR50 six-axis robotic manipulator with 2.5m reach. Metrology of parts is performed using a GOM ATOS-Q 8M with a fixed focal lens configuration providing a 350mmx260mm field of view and a nominal image resolution of 100μm. The part is moved between the deposition and metrology stations using a Kuka KP2-HV rotary-tilt stage mounted onto a Kuka KL4000 linear stage. Parts are moved from the rotary-tilt-linear positioner into a Haas UMC 750 five-axis machining center using a Kuka KR250 robot with 2.7m reach.

The resulting hybrid manufacturing cycle introduces design opportunities for complex, multi-material part topographies that provide improved throughput, accuracy and performance over conventional components. Current work is exploring the design space for large, high aspect ratio part geometries using first principles and Sandia National Laboratories' Plato Analyze topology optimization (TO) software platform,

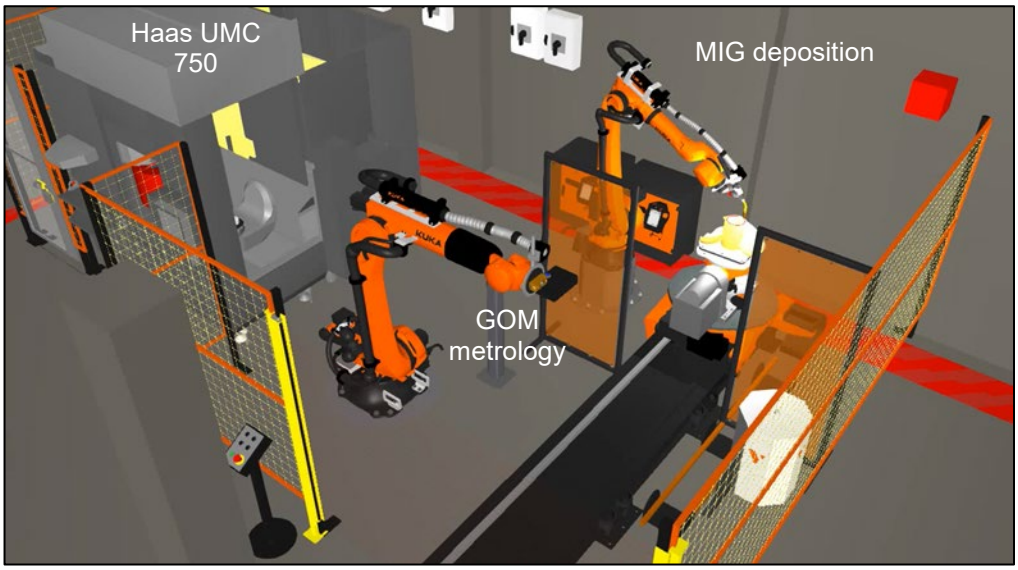

Figure 1. Large-scale hybrid manufacturing cell integrating wire-arc deposition, fringe projection metrology and five-axis machining.

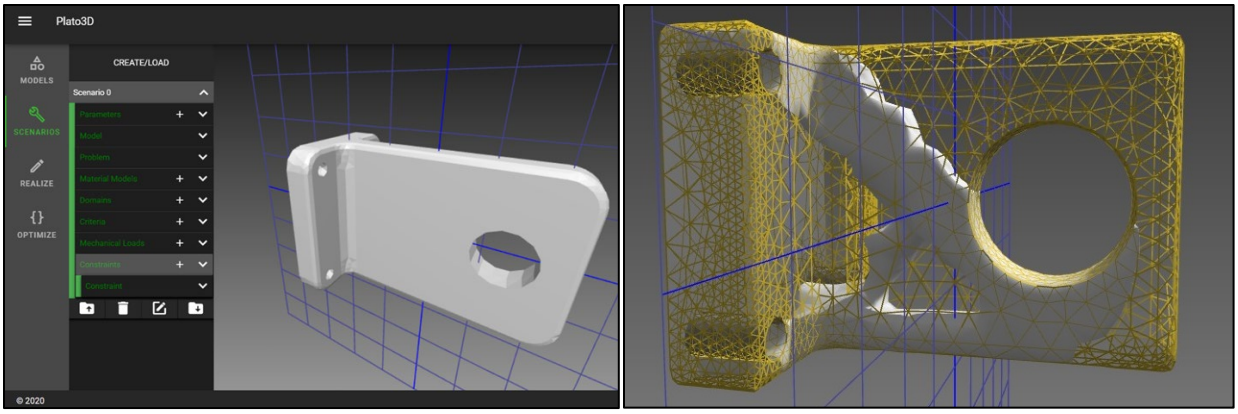

Figure 2. Sandia's Plato Analyze GUI interface and design volume (left) with resulting optimized bracket geometry (right).

Figure 2. Plato is a powerful and flexible research platform that has facilitated direct collaboration with developers exploring new optimization capabilities pertinent to large-scale structures and complex operating environments.

Initial work is using compliance minimization to reduce material use and fabrication time for large structures under load. The design process starts with a solid model representation, ex. Solid Works, that is converted into a tetrahedron mesh saved as an Exodus file using Coreform Cubit. Meshing is a critical step as element size directly influences the accuracy and fidelity of the optimization, as well as the number of computation cycles required to perform the optimization. Design analyses are constrained to elastic material response, so that elastic modulus and Poisson's ratio are the only required material inputs. Stainless steel was utilized as the material exemplar for the optimization presented herein.

Design intent is focused on high-aspect ratio geometries that combine solid, exterior thin-walls with complex internal structures. The objective is to design structures printed with a nominally constant exterior wall thickness. The dual-wire capabilities of the Fronius CMT head then facilitates the fabrication of interior structures that leverage a different material and/or a different wire diameter for finer resolution features. This wall / core configuration is relatively simple to construct in Cubit. In Plato, optimizations are then performed establishing the wall geometry as a fixed material block, while optimization is performed using only the core volume, Figure 3. Load constraints involve fixing displacements on one end and a uniform 30MPa pressure load applied downward to the top surface, Figure 4.

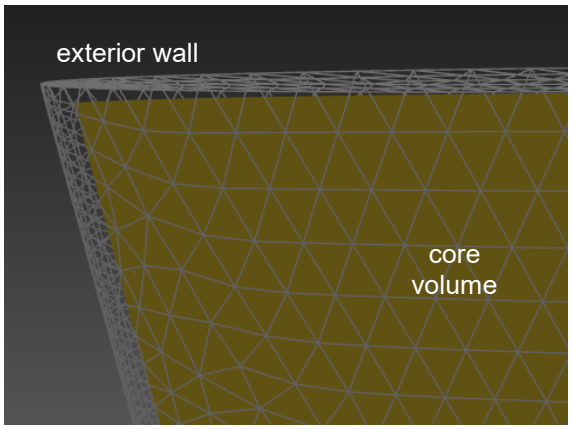

Figure 3. Plato design optimization representations showing the fixed, external wall (transparent mesh) and the internal core volume (yellow mesh volumes).

Since mesh resolution is critical in resolving feature geometries, the average voxel size generated in Cubit was roughly 170µm, producing a model with approximately 2.15 million mesh elements. The core volume represented 95% of original total, so that the sold wall represented 5% of the original total volume. During optimization, the core volume was then constrained to be 50% of its original volume, or 47.5% of total original structure.

Figure 5 shows the resulting optimized geometry. From a simple cantilever beam-bending model, stresses are highest near the fixed displacement constraint and the exterior surfaces. Accordingly, Plato located solid material at the fixed root of the geometry. Intuitively, ribbed structures were also formed along the length of the interior core, perpendicular to the load direction.

Initial design boundaries were not informed by

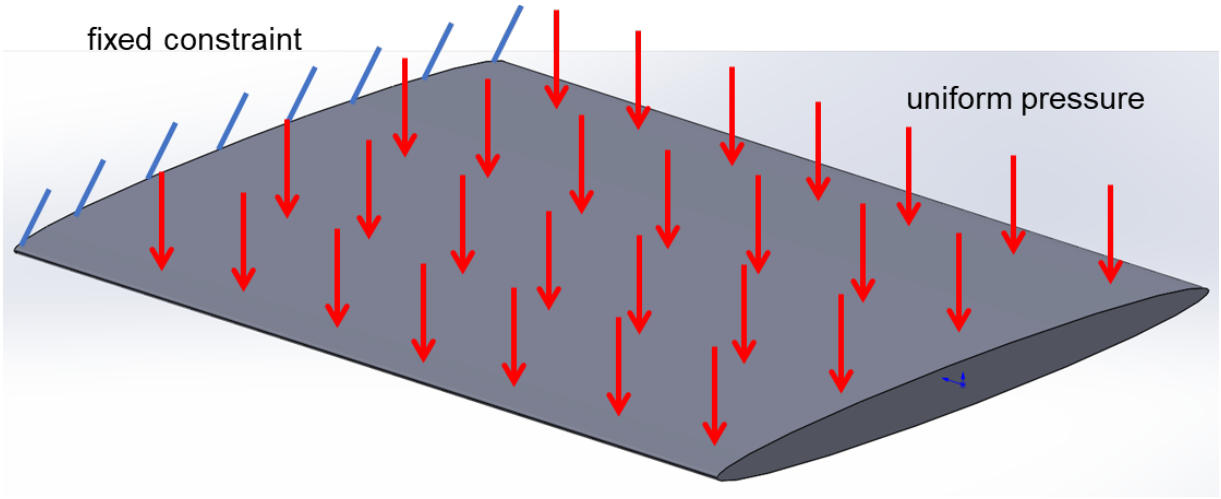

Figure 4. Geometry and load conditions for a simple, 120mm wide, 140mm long and 8mm thick ellipsoid.

Figure 5. Resulting optimized geometry for the ellipsoid, looking down on the loaded face. The fixed displacement constraints of the geometry are represented on the left end.

manufacturing constraints as one intent of the work is to quantify manufacturing research opportunities and needs. Design concepts are intended for demonstration, however, using the new large-scale hybrid metal manufacturing system. Realized part constructions will be informed and constrained by the hybrid manufacturing system's capabilities. Feature resolution, build angle and material interfaces are commonly limited in additive manufacturing, and will be considered in on-going work. The overlap of desired design topographies and manufacturing capabilities remains indeterminant, but will be quantified during prototype fabrication cycles. Future work will also examine the use of Pareto curves to balance design stiffness and maximum principal stresses to generate mass minimized designs. Further, different load scenarios will be performed using point and non-uniform distributed loads on top and bottom surfaces.

ACKNOWLEDGMENTS

This work relates to Department of Navy award (Award Number N00014-20-1-2836 in collaboration with Oregon State University)

issued by the Office of Naval Research. The United States Government has a royalty-free license throughout the world in all copyrightable material contained herein. Any opinions, findings, and conclusions or recommendations expressed in this material are those of the author(s) and do not necessarily reflect the views of the Office of Naval Research.

DESIGN OF THE MECHANICAL SYSTEM FOR THE QUANTUM ELECTRO-MECHANICAL METROLOGY SUITE

Lorenz Keck[1,3], Stephan Schlamminger[1], Frank Seifert[1,2], David Newell[1], René Theska[3], and Darine Haddad[1]
[1]Fundamental Electrical Measurements Group
National Institute of Standards and Technology
Gaithersburg, MD, United States of America
[2]Joint Quantum Institute
University of Maryland
College Park, MD, United States of America
[3]Precision Engineering Group
Technische Universität Ilmenau
Ilmenau, Germany

INTRODUCTION

At the National Institute of Standards and Technology (NIST), a new Kibble balance for the "Quantum Electro-Mechanical Metrology Suite" (QEMMS) is being designed. The QEMMS will be used to realize the unit of mass from 10 g to 100 g with a targeted absolute expanded uncertainty of 2 µg. For this purpose, multiple sub-systems need to be envisioned. Here, we focus on the design of the balance mechanism, and on its integration in an overarching balance setup.

THEORY OF THE KIBBLE BALANCE

In the Kibble balance the weight of a test mass is compensated by a counter force provided by a coil-magnet system. Two modes of operation are necessary in order to conduct an absolute measurement of mass: the weighing mode, and the velocity mode. In the latter, a coil attached to the balance mechanism is moved vertically with velocity v through the field of a magnet and induces a voltage V in the coil. The velocity is measured with an interferometer and the voltage is recorded with a voltmeter. It follows with Faraday's law

$$V = -\frac{\partial \Phi}{\partial z} v,$$

where Φ is the magnetic flux and z the axis of movement.

The actual weighing takes place in a static mode of operation, the weighing mode. Here, the coil's position is maintained constant using a feedback control that adjusts the force between the coil and magnet. The expression for this mode is derived by equating the weight of a test mass m with the force provided by the coil-magnet system. It is

$$mg = -\frac{\partial \Phi}{\partial z} I,$$

where g is the local gravitational acceleration, and I the electric current through the coil.

Combing the equations for the two modes of operation, and eliminating $\partial\Phi/\partial z$ yields the Kibble balance equation

$$mgv = IV.$$

From the last equation and considering the two modes of operation we see that the Kibble balance performs a (virtual) comparison between electrical and mechanical power, which was captured in its original name "watt balance". In today's literature, however, watt balance is superseded by "Kibble balance" to honor its inventor Dr. Bryan Kibble [1].

A NEW BALANCE MECHANISM

The main objectives of the new balance design are to reduce the complexity of the control systems required for precise operation, and to keep the mechanical design simple. Kibble balances at NIST traditionally use auxiliary electrostatic and -magnetic servos to achieve the trajectory control. Here, however, the vertical trajectory of the coil should be achieved with flexure pivots, which provide the following two functions:
(1) suspending the necessary components, e.g., a mass pan, the coil, a counterweight, and optical systems, and
(2) defining the coil trajectory in the velocity mode.

The most important aspects regarding the design of the new flexure mechanism are mentioned here:
(1) In the velocity mode, the coil should travel in a vertical trajectory without horizontal motion.
(2) The main pivot should support 15 kg of load and simultaneously deflect ± 7 ° to allow for the execution of both the velocity and the weighing mode. This angle corresponds to a vertical coil travel of ± 30 mm.
(3) The stiffness of the flexure mechanism has to be lower than 0.1 Nm^{-1}, and should ideally be continuously adjustable even below that. Also, it should be constant along the travel, and stable over time.
(4) The hysteretic force of the typical mass placement should ideally be equivalent to 0.1 µg or lower in order to allow for a measurement with the required uncertainty.

Thus, the main flexure should be as thin as possible, and a material with low anelastic loss needs to be selected. Wire electrical discharge machining, precision grinding, or highspeed milling allow for minimal flexure thicknesses of ca. 0.05 mm. At first, a kinematic structure needs to be synthesized. This structure typically consists of a sub-component for balancing and one for guiding of the coil. The sub-component for balancing is usually either a beam, or a wheel. Both designs find application in existing Kibble balances, e.g., at NIST (wheel), and at the National Research Council in Canada (NRC) (beam) [2].
Furthermore, a dedicated guiding mechanism to the beam/wheel structure constrains the motion of the coil as vertical as possible. Therefore, the guiding subcomponent is connected to the beam/wheel such that the mechanism becomes a system with 1 degree of freedom (DOF) as demonstrated with black boxes in Figure 1. If carefully designed, the structure shown in Figure 2 can fulfill the 4 requirements listed earlier. In addition, it has the following features:
(1) The guiding mechanism does not increase the horizontal footprint of the beam/wheel.
(2) The guiding mechanism produces a linear output motion.
(3) The design is symmetric, and purely planar.

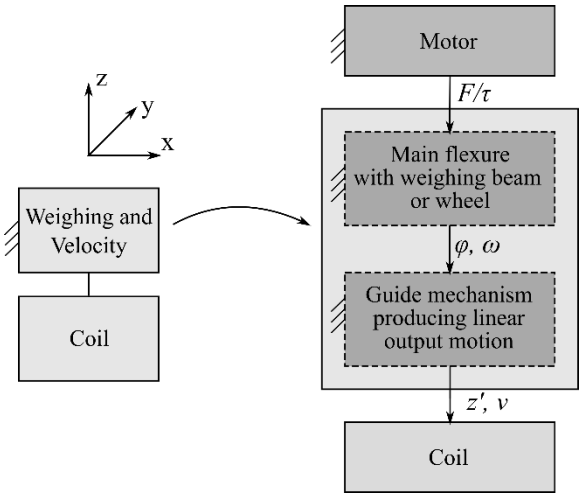

Figure 1: The integrated balance mechanism suspending the coil in the weighing and the velocity mode. Note that the "Motor" only drives the balance in the velocity mode. Here, z' is the motion coordinate of the coil, v is the velocity, φ is the deflection angle of the main pivot, and ω the angular velocity. Furthermore, F and τ denote the input force/torque to the mechanism in the velocity mode.

Especially the main flexure pivot, the balancing system (beam or wheel), and the guiding mechanism require attention during design.

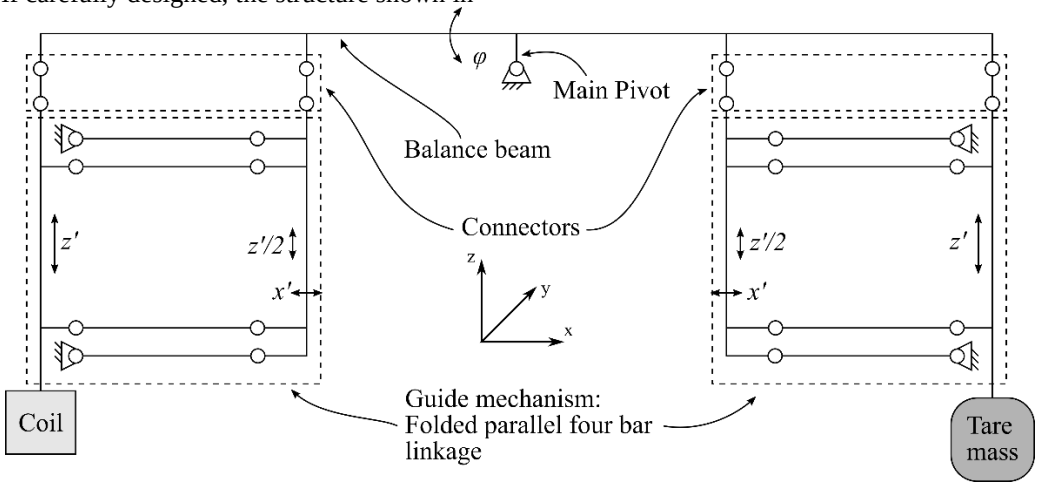

Figure 2: Kinematic structure of the new mechanism for the Kibble balance in the QEMMS. The kinematics is based on a folded parallel four bar linkage where the motion is constrained to 1 DOF (z') applying an external linkage which simultaneously serves as balance beam. Note that the balance beam here is only for demonstration purposes. This can be changed with a wheel where the connectors are bands rolling off of a round surface while moving.

MAIN PIVOT

The main flexure pivot was designed with the objective to keep the stress in the flexure low even when the fully loaded balance is deflected in the velocity mode. This is important in order to maintain a sufficient safety factor in the material for lifecycle strength of the pivot. We are using a hard tempered Copper Beryllium C17200 alloy due to its high yield strength (ca. 1000 MPa) and its low anelastic loss coefficient [3]. In the fully deflected balance situation during the velocity mode, the flexure is bent by 7 °. For a simple flexure strip, finite element analysis (FEA) shows a high stress concentration at the bottom end of the thin flexure region. For a strip with 5 mm length, 10 mm width, and $0.05 - 0.12$ mm in minimal thickness, FEA shows a maximum equivalent stress of $1400 - 2400$ MPa, which the selected material cannot resist, especially not over many years of operation. Also, conventional circular notch hinges as applied in weighing cells are not capable of resisting the induced stress: The maximum equivalent stress for a 10 mm wide hinge with minimal notch height 0.05 mm, and a notch radius of 3 mm is approximately 1000 MPa.

With the objective to reduce the notch effect in this region, other FEA series were conducted based on the parameters in Figure 3.

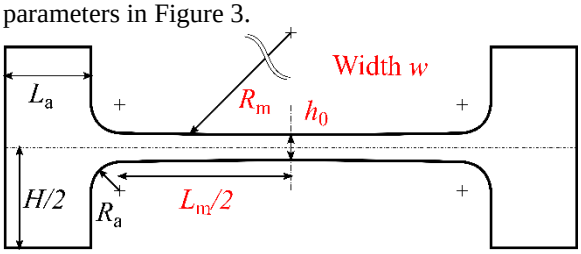

Figure 3: Parameters in the new flexure pivot design. The geometry is similar to a conventional notch hinge, but the notch radii R_m are made large to distribute the stress in the deflected flexure state over a larger area. The red parameters are relevant for parameter studies. The black parameters are fixed, because they do not have significant impact to the result.

We can see from Figure 4 that a flexure contour with a large radius in the flex region can reduce the stress in the material significantly. We think this is because the stress in the material is distributed more evenly over a larger area than in a flexure strip or a conventional circular hinge.

Deriving from the stress plot in Figure 4, and considering the theory of flexure strips in [4], the upper half region of the flexure strip could be made solid to stiffen up the flexure against deformation in other directions but without compromising the stress reducing parameters and the low elastic stiffness.

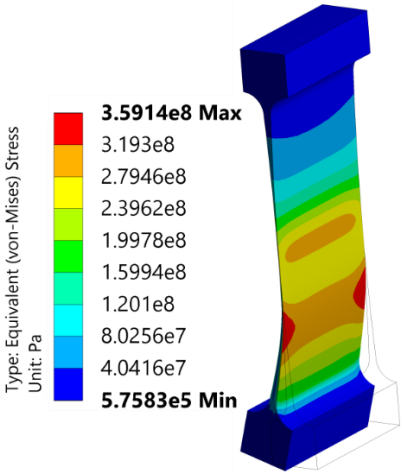

Figure 4: Deformation is exaggerated by a factor of 2.3. 3D FEA equivalent stress plot in the main flexure. The parameters (in mm) with respect to Figure 3 were: L_a – 3, R_a – 1.5, R_m – 200, h_0 – 0.05, L_m – 20, H – 5, w – 10. The top of the flexure was fixed, and a mass of 15 kg was suspended by the lower end at the flexure. A rotational displacement of 7° was introduced at the lower end. The maximum equivalent stress has reduced to 359 MPa and occurs near the center towards the bottom of the region with length L_m in Figure 3. The notch height at the flex point is ca. 120 µm.

WHEEL OR BEAM

One of the questions in the design of the balance mechanism is whether to use a beam or a wheel as the balancing component. Since both were already applied in Kibble balance mechanisms it seems intuitive that both options could similarly be used here as well.
There are noticeable differences in application paired with a one-dimensional guiding mechanism. The differences are demonstrated below using a beam balance as an example. They are mainly caused by the horizontal force acting upon the final stage of the guiding mechanism while deflecting the system.

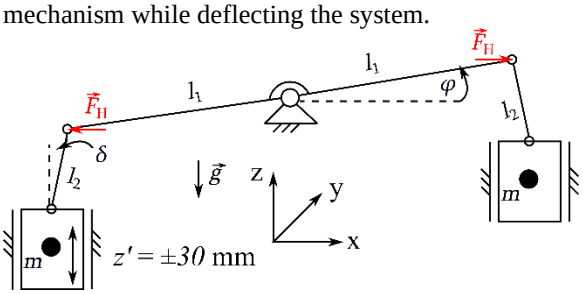

Figure 5: Simplified rigid schematics of the new Kibble balance mechanism with a balancing beam: l_1 – length for a beam arm, l_2 – length of the connector to the guide, m – mass suspended with the beam on the main and countermass site, F_H – parasitic horizontal force to the balance beam. The guide mechanism is shown as a simplified block.

In Figure 5, however, we can see, that there is a horizontal force acting upon the balance beam while deflecting the main pivot about the negative y axis with φ. The force F_H depends on the angle δ which

furthermore depends on φ, and on the weight of the supported masses m, i.e.,

$$F_{\mathrm{H}}(\varphi) = mg\frac{l_1}{l_2}\left(\frac{\varphi^2}{2}\right),$$

using the Taylor series for the cosine truncated after the second order.

This causes a moment M around the main pivot with a lever arm $z' = l_1\varphi$, i.e.,

$$M(\varphi) = 2mg\frac{l_1^2}{l_2}\left(\frac{\varphi^3}{2}\right),$$

which shows a third order dependency of the parasitic moment M on the deflection angle φ.

Assuming that the linear, elastic part of the stiffness in a flexure mechanism can be entirely compensated with, e.g., an inverted pendulum, this system shows a quadratic stiffness K from the parasitic moment according to

$$K = \frac{dM}{d\varphi} = 2mg\frac{l_1^2}{l_2}\left(\frac{3\varphi^2}{2}\right).$$

In high precision mass comparators where the null position is maintained during the whole measurement procedure, this quadratic stiffness term does not usually matter because it is infinitely small around the null position. However, the term becomes highly dominant during the velocity mode travel in a Kibble balance: Considering reasonable values for $m = 6\,\mathrm{kg}$, $g = 9.81\,\mathrm{N \cdot kg^{-1}}$, $l_1 = 250\,\mathrm{mm}$, $l_2 = 100\,\mathrm{mm}$, and $\varphi = 7°$ yields a stiffness at the end of a velocity mode sweep of $K = 1.64\,\mathrm{Nm \cdot rad^{-1}}$, which is equivalent to a linear stiffness of ca. $26\,\mathrm{Nm^{-1}}$. The non-linear stiffness paired with this high value would cause the requirement for a relatively large motor to drive the balance in the velocity mode, and makes a precise velocity control of the balance more challenging.
Additionally, the horizontal force F_{H} acts upon the guiding mechanism, which is also a flexure system, and, therefore, yields a non-linear deformation in the flexures along the travel. This causes the trajectory to become non-linear.
One could think of compensating the horizontal force in a beam balance with auxiliary compensation systems, but this additional complexity is not desired in the compact new version of a Kibble balance mechanism we are about to design.

However, since the issue of the horizontal force can be solved by replacing the beam with a wheel, we move forward by employing a wheel balance with a flexure pivot in the center, and multifilament bands rolling off of the wheel surface. Note that geometrical deviations and misalignments of the position of the wheel are of minor influence compared to the systematic parasitic motion of a balance beam and can thus be neglected.

CONCLUSIONS

In this article, we described how decisions in the design of key components for the new mechanism in the Kibble balance of the QEMMS have evolved. We found a flexure pivot geometry that keeps the stress in the loaded and deflected flexure 3 times lower than the yield strength of the material. Also, the advantage of a wheel balance compared to a beam balance in combination with a guiding mechanism was shown.

DISCLAIMER

This article is authored by employees of the U.S. federal government and is not subject to copyright. Commercial equipment and materials are identified in order to adequately specify certain procedures. In no case does such identification imply recommendation or endorsement by the National Institute of Standards and Technology, nor does it imply that the materials or equipment identified are necessarily the best available for the purpose.

REFERENCES

[1] Kibble B. A Measurement of the Gryomagnetic Ratio of the Proton by the Strong field Method. J.H. Sanders, A.H. Wapstra (Eds.), Atomic Masses and Fundamental Constants, vol 5, Plenum Press, New York (1976), pp. 545 – 551.

[2] Robinson I., Schlamminger S. The watt or Kibble balance: a technique for implementing the new SI definition of the unit of mass. Metrologia 53, A46-A74, 2016.

[3] Quinn T. The beam balance as an instrument for very precise weighing. Measurement Science and Technology 3, 141-159, 1992.

[4] Speake C. Anelasticity in flexure strips revisited. Metrologia 55, 114-119, 2018.

ACCOUNTING FOR SHRINKAGE IN FUNCTIONAL CERAMIC STRUCTURES PRINTED THROUGH TWO-PHOTON POLYMERIZATION

John Cortes[1], Magi Mettry[1], Matthew Worthington[1], Swetha Chandrasekaran[1], Robert Panas[1]
[1]Lawrence Livermore National Laboratory
Livermore, California, USA

INTRODUCTION

Advances in additive manufacturing during the last decade or two have revolutionized the way highly complex devices are both designed and manufactured at all scales. Geometries that were previously considered impossible to manufacture are now commonly printed through several methods and materials. Additive manufacturing creates the opportunity to manufacture highly intricate 3-dimensional structures using a single, highly repetitive process, one layer at a time.

Although most of that work has focused on macro-scale printing processes with plastics (and more recently, metals and composites), a significant scientific push has been made to also develop processes in the micron and sub-micron scale [1, 2, 3]. These advances have been advantageous for fields such as MEMS/NEMS, microfluidics and micro-scale optical systems.

Two-photon Polymerization (2PP) is one of the technologies that has allowed for development of 3D-printed microstructures. Two-photon Polymerization utilizes femtosecond laser pulses with two-photon absorption to generate features using a wide variety of photon-activated photoresists and resins with a resolution as high as 100 nm [4]. The print resolution of 2PP processes is determined by the exposure dose to the smallest polymerized volume. This dose can be finely tuned by both the pulse energy and the scanning speed [5] used during the writing step. Other parameters such as layer distance, hatching distance and number of scans per layer can also be implemented to tune the dose and material response more precisely.

Most of these resins result in polymer structures which are limited in their application due to their poor mechanical properties. However, the use of ceramic resins has recently been developed for 2PP processes [6, 7]. They generally come in the form of polymer-derived ceramics (PDC) and are highly tuneable based on their molecular compositions. While these resins feature much more favourable mechanical properties, they tend to shrink anywhere from 30-55% during post-processing [8, 9]. This may not be desirable and difficult to design for in precise MEMS/NEMS applications, therefore it is crucial that this shrinkage be fully understood and accounted for in structures that may require assembly and precise placement.

In this work, we study the shrinkage of 2PP-printed silicon oxycarbide (SiOC) disk microstructures that feature strain relief structures. These are meant to keep these micro-disks centered and aligned for assembly purposes. This type of procedure could be useful in the assembly process of many MEMS devices, such as micromirrors, which require precise positioning between capacitance-driven paddles and the mirrors [10].

METHODS

The two-photon printing process was carried out in a commercially available NanoScribe GmbH Photonic Professional GT laser lithography system at LLNL's Advanced Manufacturing Laboratory (AML). This device features a TOPTICA laser with a wavelength of 780 nm and a pulse duration of approximately 100 fs. The lens used was a Zeiss 63x1.4NA oil DIC M27. A single-side polished silicon chip measuring approximately 1 cm by 1 cm was treated by 3-(Trimethoxysilyl)propyl methacrylate (Silane) for 5 minutes at 90 °C to aid with print adhesion.

After the treatment, the silicon chip was cleaned with IPA. A drop of the custom polymer-derived ceramic (PDC) resin was applied to the polished side of the silane-treated silicon chip. The structures were printed up-side-down using "dip-in laser lithography." The printed structure was then developed by submerging it in a beaker of propylene glycol monomethyl ether acetate (PGMEA) overnight.

After full development, the sample was dried using a Microscopy Sciences 3100 critical point

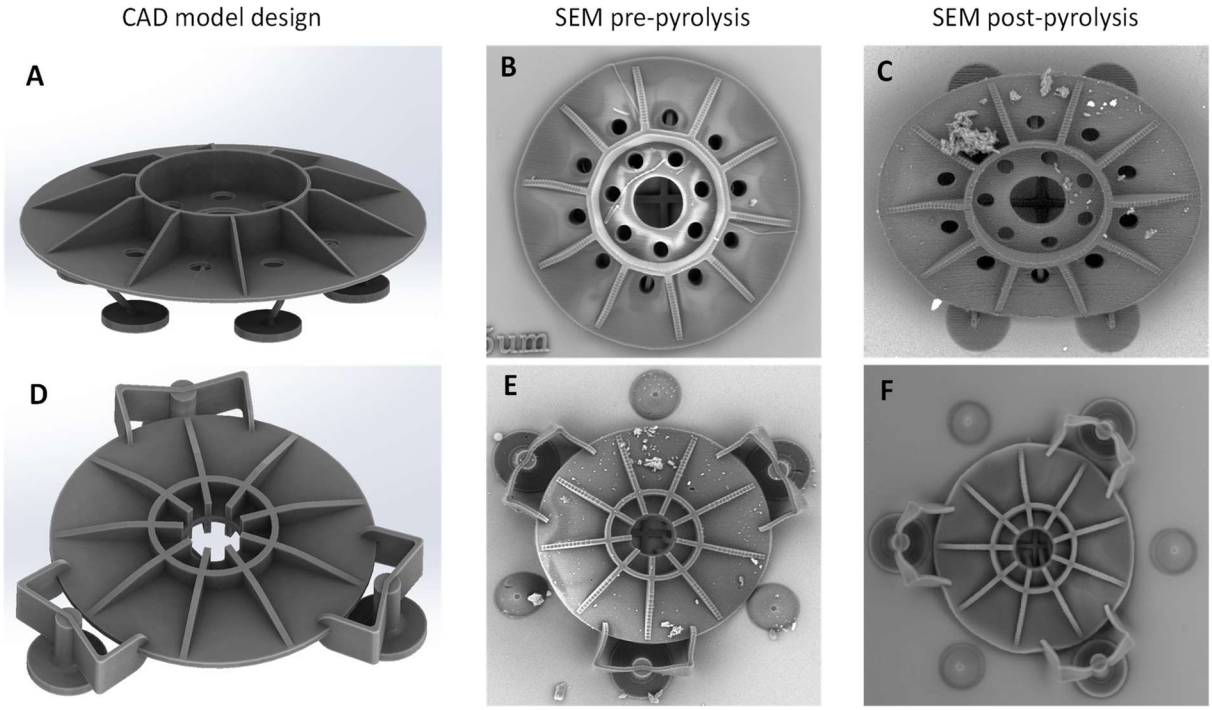

FIGURE 1. A) CAD model of a 120 µm diameter disk with six self-centering stress relief legs. B) SEM image of the disk before the pyrolysis step. C) SEM image of the disk after pyrolysis after 35% isotropic shrinkage. D) CAD model of a 120 µm diameter disk with three self-centering stress relief blades. E) SEM image of the disk before the pyrolysis step. F) SEM image of the disk after pyrolysis after 38% isotropic shrinkage.

drying system. After critical-point-drying, the samples were pyrolyzed in an oven in a nitrogen atmosphere at temperatures of 250° C, 400° C, 600° C and 1000° C, each step for an hour. The sample was then allowed to cool down to room temperature at a rate of 5° C per min. The samples were then characterized using a Phenom XL benchtop scanning electron microscope (SEM).

RESULTS

We have designed and fabricated 120.0 µm wide, 2.5 µm thick suspended disks that feature two different types of self-centering strain relief legs that are designed to account for the shrinkage that is characteristic of 2PP-printed ceramic materials. These types of strain-relief structures are necessary for ceramic prints because the shrinkage generally causes the print to delaminate from the surface as it contracts.

The two different designs are shown in figure 1. The first design (panels A, B, C) features legs that accommodate the shrinkage by rotating underneath the disk about the anchor base and act as a pin joint. Each individual leg features two "pinch points" that flatten the otherwise circular legs to promote bending towards the center axis of the disk.

The legs themselves are 3.0 µm in diameter but are reduced to a width of 1.5 µm at the pinch points. This design is effective in guiding the disk's outer edge towards the center axis as it shrinks. Though the shrinkage of these pre-ceramic resins is known to be mostly isotropic in nature, variations in thickness and feature type could cause misalignment during shrinkage. Adding these engineered strain-relief legs accounts for those potential variations.

The second design (panels D, E, F) features a set of three, 2.0 µm thick, 10.0 µm tall vertical blades that bend inward as the main disk structure shrinks. The blades are anchored by a 6.0 µm thick post which is designed to be rigid, with minimal bending. Both of these designs are able to accommodate shrinkages as high as 50% before mechanical failure.

More importantly, these strain relief structures have been shown to not only accommodate for

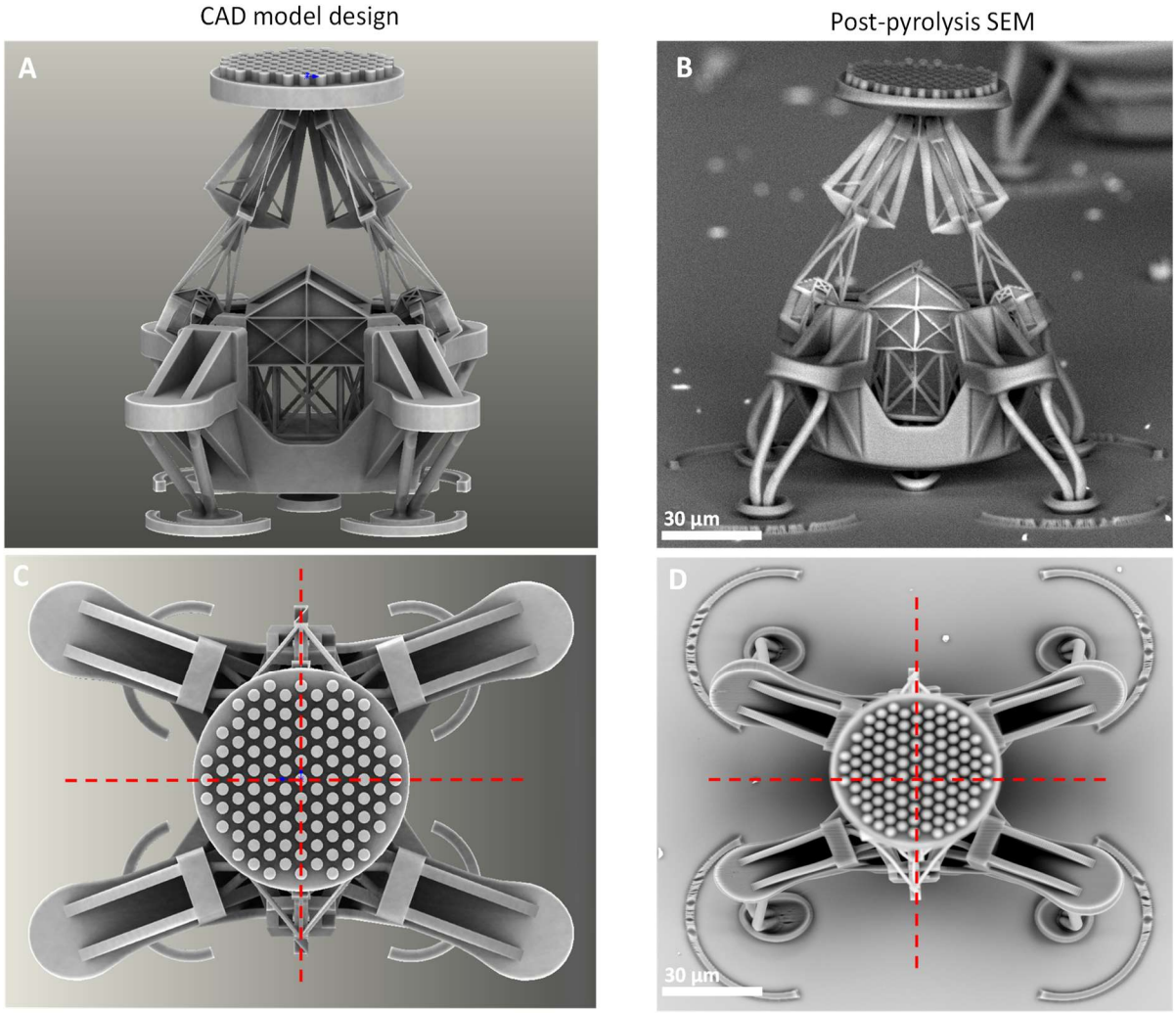

FIGURE 2. A) Side view of the CAD model of a functional MEMS component within a self-centering structure with four stress relief legs. B) Side view SEM image of the structure after shrinking during the pyrolysis step. C) Top view of the CAD model of a functional MEMS component within a self-centering structure with four stress relief legs. D) Top view SEM image of the structure after shrinking showing the centered alignment.

the shrinkage in the ceramic material, but they also keep the centerline of the disk within an acceptable range for precision assembly. Each ceramic print features a crosshair at the base in the center, so that the shift from the center axis can be fully characterized. We found that even though the disks themselves shrink as much as 40%, the centerline of the disks remain within approximately 3 µm of their starting position when measured from above through SEM imaging. Out of the 20 total disks that were printed (10 of each strain relief structure type), the maximum deviation was 3.5 µm. seven out of the twenty disks shifted less than 1 µm from their centerline, though they displayed shrinkage of about 35%-40%.

These structures were printed with optimized parameters to minimize the amount of shrinkage. The power input to each voxel ranged from 35% to 45% (of the maximum 150 mW produced by the Nanoscribe laser) with scan speeds ranging from 6,000 µm/s to 8,000 µm/s. In addition to these parameters, each individual voxel was printed with a multi-pass approach which energized each layer after a brief pause. The layer-to-layer distance was kept at a constant 100 nm. Similarly, the lateral hatching distance was maintained at a constant 300 nm.

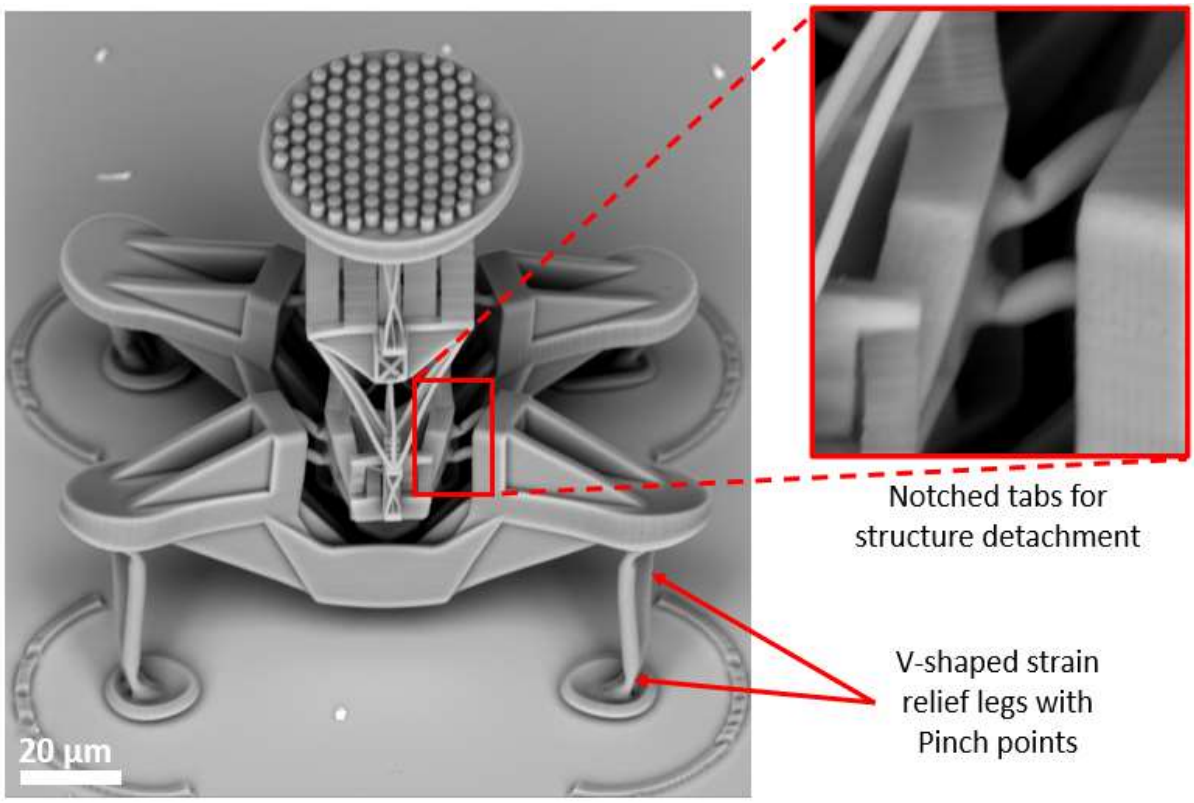

FIGURE 3. SEM image of a complex MEMS micromirror leg printed on a strain-relief structure. The structure features four sets of flexible legs that guide the central structure during shrinkage and ensure that it remains aligned with its center axis during the process. The leg and strain relief structure are connected by 8 notched linkages, which are designed to mechanically fail when the MEMS leg is pulled in the upward direction.

The multi-pass approach resulted in the maximum amount of cross-linking in the material before the critical point drying and pyrolysis steps, which contribute to the overall shrinkage of the structure. Testing found that doing two passes per voxel produced the least amount of shrinkage while producing accurate prints.

Adding more passes slightly decreased shrinkage by about 5%, but there is a significant sacrifice in print quality and accuracy to the designed model. Phantom features can be created as the laser's focal point changes due to the voxels being crosslinked from previous passes. This can be more problematic on functional prints that have small, sub-micrometer features whose performance depends on model to print accuracy.

CASE STUDY: MEMS MICROMIRRORS

We turned our focus on testing one the strain-relief approaches for functional devices as well, not just static disks. Figure 2 shows the strain-relief approach being applied to a set of legs meant for a functional MEMS micro-mirror device. In this application, four sets of V-shaped "pinched" legs are implemented to not only keep the functional structured centered, but also to minimize potential rotation during shrinkage. The legs themselves are 2 µm in diameter and are reduced to 1 µm at the pinch point. There is also an additional attachment point at the bottom of the structure in the center in the structure

These highly complex devices were printed and processed using the same approach as for the disks. The design shows that even highly complex structures can remain centered during shrinkage with this approach. We take advantage of the fact the shrinkage is both linear and isotropic. Specifically, we were able to

consistently produce structures that are aligned within 2 μm of their designed center axis. Being able to maintain this level of alignment is very important for this specific set of legs, since they will eventually be integrated into a large micromirror array that will feature hundreds of legs that must be aligned to micrometer scale for the whole device to work properly.

The leg itself is detachable through a set of pop-out tabs that have small notches on them, as shown in Figure 3. This allows the central support structure (which is maintained centered by the strain relief legs) to remain in place while the stamp procedure is performed. A similar process is outlined in [10] for an array featuring seven mirrors with 2PP-printed polymer legs. These ceramic legs would allow these types of MEMS micro-mirrors to have an increased range of motion at even higher frequencies.

CONCLUSION AND FUTURE WORK

This work shows a path towards integrating ceramic-based, 2PP-printed structures with functional devices that would benefit from the improved mechanical properties. One of the current barriers to this integration and wider implementation is the amount of shrinkage that the preceramic resins display. We propose to account for that shrinkage with the use of engineered strain relief support structures, which contain the functional structure within them and maintain it centered within an acceptable range for assembly.

The next step of this project is to test the detachable structures for stamping and assembly. We will then move to test multiple structures at one time and perform single and double-stamp procedures to assemble functional structures into pre-determined positions. Future research will also explore the possibility of developing new resin recipes to produce ceramic prints that do not shrink as much during pyrolysis.

ACKNOWLEDGEMENTS

This work was performed under the auspices of the U.S. Department of Energy by Lawrence Livermore National Laboratory under Contract DE-AC52-07NA27344 (LLNL-CONF-826753) and supported by LDRD 19-ERD-018.

REFERENCES

[1] Saha, et al. “Scalable Submicrometer Additive Manufacturing.” Science, vol. 366, no. 6461, 2019, pp. 105–109.

[2] Chu, et al. “Centimeter Height 3D-Printing with Femtosecond Laser Two-Photon Polymerization.” Advanced Materials Technologies, vol. 3, no. 5, 2018, p. 1700396.

[3] Ngo, Kashani, Imbalzano, Nguyen and Hui. “Additive manufacturing (3D printing): A review of materials, methods, applications and challenges.” Composites Part B: Engineering, vol. 143 (2018).

[4] Zheng, Kurselis, El-Tamer, Hinze, Reinhardt, Overmeyer and Chichkov. “Nanofabrication of High-Resolution Periodic Structures with a Gap Size Below 100 nm by Two-Photon Polymerization.” Nanoscale Res Lett., vol. 14, 134 (2019).

[5] Ovsianikov et al. “Two Photon Polymerization of Polymer–Ceramic Hybrid Materials for Transdermal Drug Delivery.” Int. J. Appl. Ceram. Technol. 2007, vol. 4, issue 1, p. 22–29.

[6] Cui, et al. “Additive Manufacturing and Size-Dependent Mechanical Properties of Three-Dimensional Microarchitected, High-Temperature Ceramic Metamaterials.” Journal of Materials Research, vol. 33, no. 3, 2018, pp. 360–371.

[7] Eckel, et al. “Additive Manufacturing of Polymer-Derived Ceramics.” Science, vol. 351, no. 6268, 2015, pp. 58–62.
Polymerization.” Nanoscale Res Letters, vol. 14, 134 (2019).

[8] Brigo, Schmidt, Gandin, Michieli, Colombo and Brusatin. “3D Nanofabrication of SiOC Ceramic Structures.” Adv. Sci. 2018, vol. 5, 1800937.

[9] Bauer et al. “Additive Manufacturing of Ductile, Ultrastrong Polymer-Derived Nanoceramics.” Matter, vol. 1, no. 6, 2019, p. 1547-1556.

[10] Hopkins, et al. "A High-Speed Large-Range Tip-Tilt-Piston Micromirror Array." Journal of Microelectromechanical Systems, vol. 26, no. 1, pp. 196-205, Feb. 2017.

DESIGN AND VERIFICATION OF A LENS FOCUS MODULE BASED ON A BI-DIRECTIONAL THERMOELECTRIC ACTUATOR

Nick van den Beucken
Development and Engineering, Master Thesis
NTS-Group, Eindhoven University of Technology
Eindhoven, Noord-Brabant, The Netherlands

INTRODUCTION

In today's high-tech industry applications silicon wafers are the basis for manufacturing integrated circuits (IC's). When producing IC's an important aspect is the height profile of the die on the wafer. To measure this height profile white light interferometry is used, which contains a lens focus module. To enable accurate computation of the height profile, or more precise, to retrieve phase information from the light, the position demands on this lens focus module are very stringent. It typically has to make several steps of about 60 nm, but once in position it needs to maintain that exact position; it has to stay within 0.1 nm for 0.2 s.

Existing commercially available lens focus modules consists of a straight guide and a piezoelectric based actuator. The incorporated straight guides are typically based on a parallelogram using flexure hinges. This module has a stroke up to 100 µm and is driven by a piezo stack with a stroke increase ratio of 1:5. Due to the way this ratio is mechanically established the vertical eigenfrequency is limited to be around 200 Hz with an objective lens of 0.2 kg. This vertical eigenfrequency needs to be increased in order to be less sensitive for external disturbances and thereby better maintain position. Another issue is caused by the amplifier noise that is present in the system. A piezo stack typically has a high bandwidth, which makes the actuator susceptible to 1/f noise from the electronics required to drive it. This implies a low noise level in positioning.

To overcome above limitation, a new actuator concept was investigated, which makes use of the thermal expansion principle. Due to the thermal inertia this actuation concept should function as a low-pass filter and therefore the high frequency noise will not be converted into a vertical translation. This principle has been demonstrated in 2018 by P.M. v.d. Hoogenhof [1]. The limitation of this concept is the way the actuator must return to its initial state, namely by passive convection of heat to the surrounding. The shortcomings in the work from 2018 are resolved by application of Peltier elements to heat up a metal beam and use the thermal elongation for the displacement step of the objective lens. The advantage of Peltier elements is the reversibility, it could be used in two directions (heating and cooling) by switching the direction of the electrical current, which makes it a bi-directional actuator.

A Matlab model was developed to predict the performance of the actuator and to investigate the influence of design variables (e.g. thermal resistance, actuator thickness) which are important for optimizing the actuator design. A lumped system analysis is performed, which means that it is assumed that the temperature inside each of the defined thermal capacitances is homogeneous (see Figure 1). A new design for the straight guide mechanism was made to increase the first eigenfrequency to approximately 1000 Hz. Testing and verification of the actuator was performed by building a test set-up (see Figure 2) and running experiments.

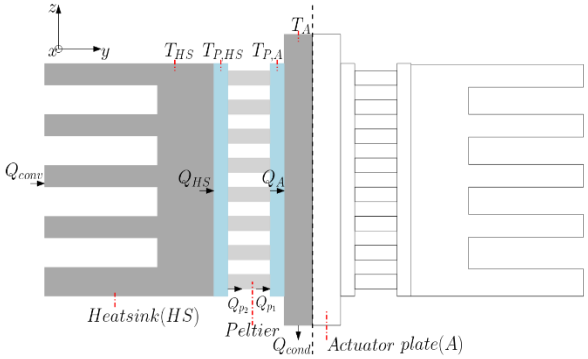

FIGURE 1. Schematic overview of the bi-directional thermoelectric actuator, which consists of an actuator plate, two Peltier elements and two heatsinks. The Peltier element is connected to the other parts by a glue, which introduces a thermal resistance. It is a symmetric design, represented by the dotted line in the figure.

(a)

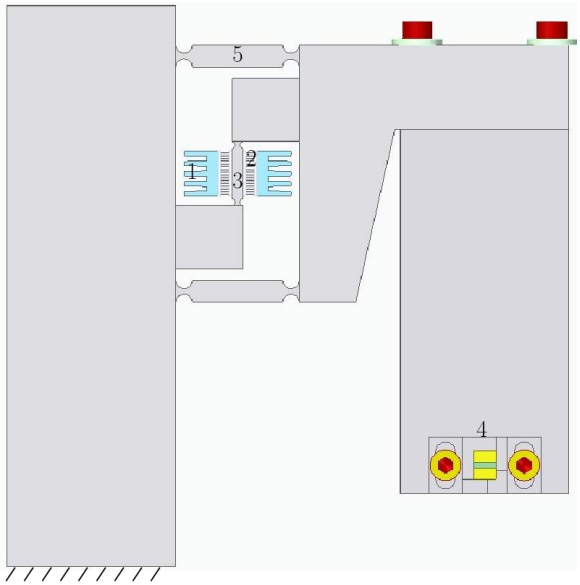

(b)

FIGURE 2. (a) The thermal actuator positioned in the straight guide mechanism; 1. heatsink 2. Peltier element 3. actuator plate 4. linear encoder scale positioned on the point of interest 5. leafsprings of the flexure parallelogram and (b) experimental set-up, zoom in of the thermal actuator and the straight guide mechanism.

Lens Focus Module

To reduce the complexity and costs the mechanical design for the lens focus module is based on a monolithic flexure parallelogram. One actuator is positioned in the module such that the actuation is in the center of compliance of the leafsprings. The displacement of the straight guide is measured as a function of time with high accuracy, using a linear encoder.

This encoder uses a scale with a stripe pattern for a total measuring range of 1 mm. The optical resolution of the applied encoder is 250 nm which enables interpolation down to 62.5 pm when using a 12 bits interpolator.

Experiments

The developed thermo-mechanical model in Matlab can be used to predict the actuator behaviour. The open loop model validation is done by comparing measurements with the outcome of the model for the same electrical DC currents. This is shown in Figure 3 where the measured step response of two different DC currents is plotted together with the corresponding model results. The model fits the measured data very well in the first second. For the high DC current small deviations can be observed in the first 0.2 s. These could be explained by uncertainty in the thickness of the glue layer. As input for the thermal model this was estimated at 0.15 mm. Furthermore delay time differences within the first 0.1 s can also be explained by the lumped mass assumption in the thermal model.

Differences between the model calculations and the measurements in longer time experiments > 1 s (see Figure 3a) can be explained due to slow heating up and thus expansion of the straight guide mechanism. The model calculates the elongation of the actuator plate. Because the linear encoder measures the displacement at a different position in the mechanism, a counter working additional displacement occurs caused by the thermal energy leakage from the actuator to the straight guide.

(a)

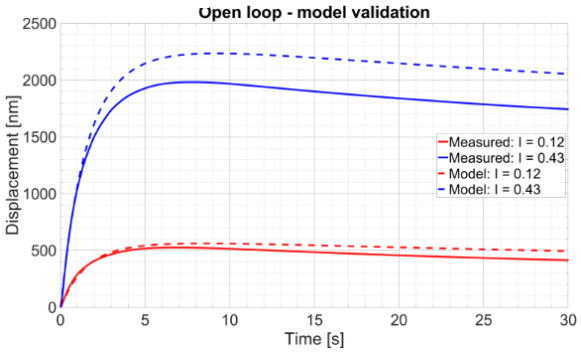

(b)

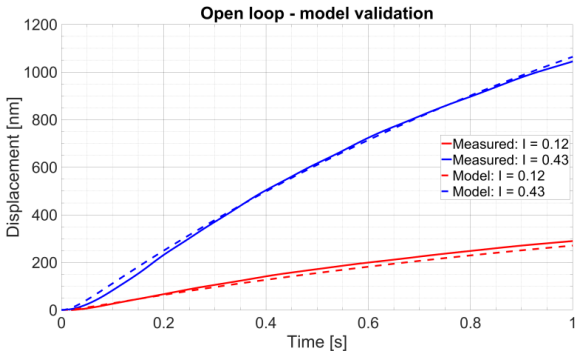

FIGURE 3. The thermo-mechanical model is validated with the open loop measurements. (a) the first 30 seconds of the step responses and (b) zoom in of the first second.

A PID controller with feedforward was developed for the closed loop measurements. A step response was performed to determine the characteristics of the actuator in combination with the straight guide. The result of the closed loop controller for a first order setpoint response is shown in Figure 4. In the error plot the system characteristics is represented, the peak-to-peak (6 sigma) steady-state error is equal to 0.8 nm with a settling time of about 0.3 s.

(a)

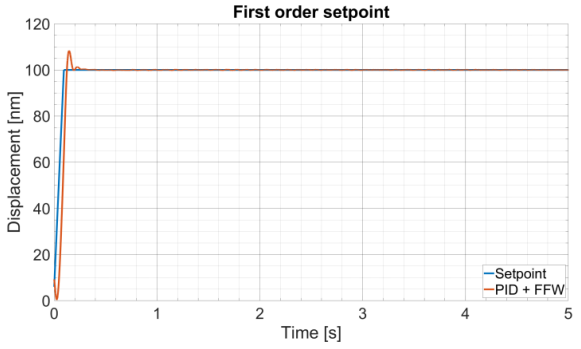

(b)

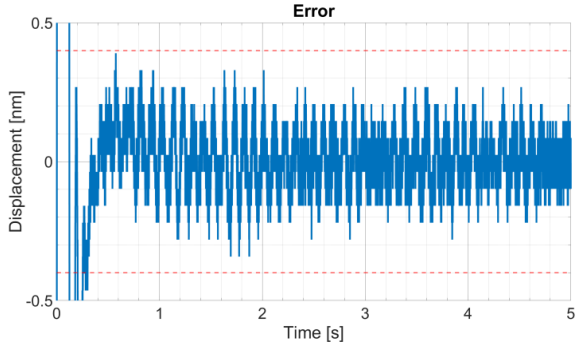

FIGURE 4. Response of the system to a first order setpoint, the set-up was positioned on an optical table with active isolator leg bundles. (a) displacement of the lens focus module and (b) zoom in of the error signal of the system.

For the intended application the actuator should be able to make seven steps of 50 - 80 nm. The response of the trajectory and the corresponding error plot is shown in Figure 5. The actuator is able to follow the trajectory and shows the same error plot for each step. In the error plot the red boundaries are plotted at ± 0.4 nm. The controller is able to keep the error within these boundaries for the trajectory reference signal. Only the settling time increases, from 0.3 s to 0.7 s in step 7.

(a)

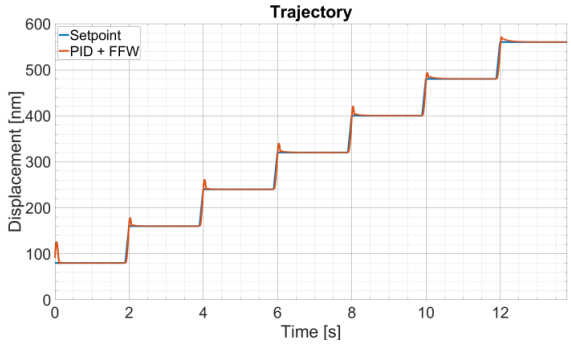

(b)

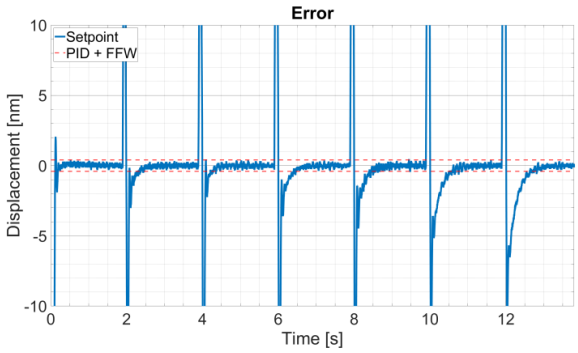

FIGURE 5. Response of the system to a trajectory setpoint. (a) displacement of the lens focus module and (b) error signal of the system.

Next steps: Reduce settling time, measure frequency response, identify fundamental performance limit of this actuator (when becomes electronics-noise dominant again).

REFERENCES

[1] P.M. v.d. Hoogenhof, “Design of a thermally actuated objective lens focus system”, Master’s thesis, TU/e, 2018.

LARGE-AREA STITCH-FREE 3D NANO-PRINTING BASED ON TWO-PHOTON POLYMERIZATION

Wanping Lu[1], Qi Shao[1], and Shih-Chi Chen[1,2*]
[1]Department of Mechanical and Automation Engineering
The Chinese University of Hong Kong
Shatin, N.T., Hong Kong SAR, China
[2]Oxford-CityU Centre for Cerebro-Cardiovascular Health Engineering (CoCHE),
Hong Kong Science Park, N.T., Hong Kong SAR, China
[*]Email: scchen@mae.cuhk.edu.hk

In this paper, we present a new method to eliminate stitching errors during large-area two-photon polymerization (TPP) printing for the digital micromirror device (DMD)-based TPP fabrication system by synchronizing the scanning holograms in the DMD and the moving XYZ stage, i.e., the moving laser foci will never move out of the DMD workspace during fabrication. To demonstrate the efficacy of the method, we have fabricated large-scale complex 2D and 3D structures in a continuous fashion without stitching, including a 3D woodpile structure, 3D bending rail, and different metamaterial structures. The results show our method can produce seamless large-scale 3D structure with 100 nm resolutions for both single-focus and multi-focus fabrication processes, generating impact to the nanotechnology and photonics community.

INTRODUCTION

TPP is the most precise 3D printing process, realized based on the nonlinear two-photon absorption effect that occurs at the focal region of a femtosecond laser. As such, arbitrarily complex 3D structures can be created by serially scanning the laser focus achieving sub-200 nm resolution. Owing to its high resolution, TPP has found a wide range of applications in photonics and nanotechnology etc. For example, TPP has been used to fabricate metasurface structures, biomedical scaffolds, and photonic crystals [1-3]. Presently, practical applications of the TPP technology, i.e., low-cost large-area printing, is largely limited by its low fabrication rate and fabrication errors, i.e., stitching errors.

Recently, our team has developed two unique TPP fabrication methods based on DMDs, i.e., holography-based multi-focus TPP fabrication [4, 5] and femtosecond projection two-photon lithography (FP-TPL) [6], which substantially improve the fabrication rate by two orders of magnitude, i.e., 100 mm^3/hr with a resolution of 140 nm. Although the speed and precision have been improved, stitching errors are still unavoidable due to the limited precision of the sample stage and object volume shrinkage after photopolymerization, which has been a common issue for all nanofabrication systems when printing a structure larger than a system's work volume.

In this work, we address this issue by synchronizing the scanning holograms displayed on the DMD and the moving XYZ stage, i.e., the moving laser foci will never move out of the DMD workspace.

OPTICAL SETUP

Figure 1 presents the optical configuration of the DMD-based TPP system, where the laser source is an 80 MHz Ti:Sapphire femtosecond laser (Chameleon Vision S, Coherent) with a central wavelength of 800 nm, and a pulse width of 75 fs. First, a train of optics, including a blazed transmission grating (T-1400-800, 1400 lines/mm, Lightsmyth), high reflectivity mirrors (M1 - M3), and 4-f system (L1 and L2; f_{L1} = 80 mm, f_{L2} = 250 mm) are introduced to pre-compensate the negative angular dispersion induced by the DMD. After the DMD, a spatial filter selects the -1st order diffraction beam, which contains the encoded wavefronts. Lastly, a 4-f system, i.e., L4 (f = 54 mm) and the objective (CFI Plan Fluor 40×, N.A. = 1.3, Nikon) relays the scanning laser to the photoresin. To monitor the fabrication process in situ, an imaging module, sharing the objective, is built around the fabrication platform including a fiber-based Kohler illumination system, a dichroic mirror and a CCD camera. A precision XYZ stage (V-551 4B/2B, Physik Instrumente) positions the sample for continuous fabrication.

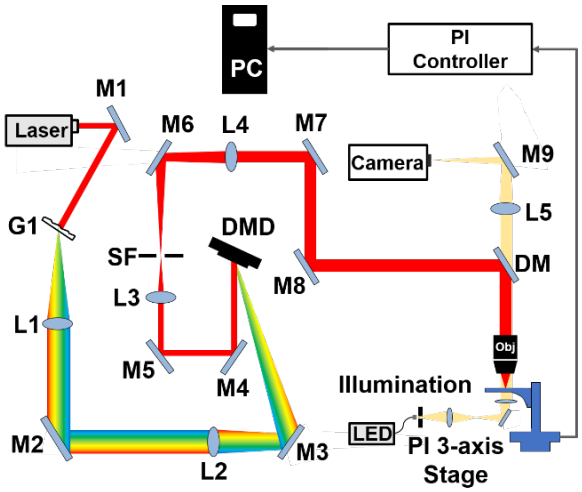

FIGURE 1. Optical configuration of the DMD-based 3D printing system; L1-L5, lenses; M1-M9, high-reflectivity mirrors; G1, grating; SF, spatial filter; DM, dichroic mirror; Obj, objective lens.

STITCH-FREE 3D PRINTING

Stitching is an unavoidable process for the DMD TPP system (or any 3D printing system) when the designed structure is larger than the workspace of the laser scanning system, i.e., the sample stage is held stationary during printing while the laser scans over the DMD workspace, i.e., 60 x 120 x 200 μm^3. After completion, the sample stage moves to the next volume for processing. For photopolymerization-based 3D printing, e.g., TPP, stitching errors are mainly attributed to (1) the volume shrinkage after photopolymerization and (2) positioning errors of the sample stage, which result in geometric errors and non-uniform index distribution in printed structures, e.g., lens or 3D scaffolds, which compromise the quality and performance of the printed structure.

To address the issue, we propose a stitch-free nano-printing process, i.e., the sample stage is continuously moving during the DMD fabrication processes such that the volume to be printed is continuously fed to the laser processing area until the entire structure is completed, a concept inspired from the Infinite Field of View (IFOV) of Aerotech. To realize this, the DMD and sample stage are synchronized via a PXI controller (National Instruments), where the stage is commanded to move at a constant speed (i.e.., 5 - 10 μm/s) while the laser foci are scanning at 22.7 kHz. The synchronization process is shown in Fig. 2. To synchronize the motion between the DMD scanner and the XYZ stage and to ensure continuous fabrication with a limited DMD memory, the DMD memory is divided into two parts, the first part for displaying (i.e., scanning) the loaded holograms, and the second part for loading the next scanning hologram sequence. After the first hologram sequence (i.e., 30,000 holograms) is loaded, PXI Port1 sends out a pulse signal to initiate the printing process. In parallel, PXI Port2 and Port3 send out pulse sequences to respectively control the DMD and XYZ stage, which are operated in the trigger mode. When the hologram sequence stored in the first part completes scanning, the second part of the DMD memory immediately takes over the scanning process; and at the same time the first part of the DMD memory is cleared, followed by loading the next set of holograms. This process alternates and repeats until the fabrication process ends. Each sequence contains 30,000 binary holograms. To avoid the accumulation of motion errors from the time lag between switching hologram sequences (i.e., a few milliseconds), the trigger signal, which has a period of T (e.g., 10 - 15 sec), is resent to the DMD and XYZ stage after every hologram loading cycle to synchronize their motions again.

On the other hand, to compensate the displacement introduced by the moving stage during printing, the coordinates of each laser focus and fabrication trajectory are pre-calculated and converted into binary holograms automatically via a custom-developed program.

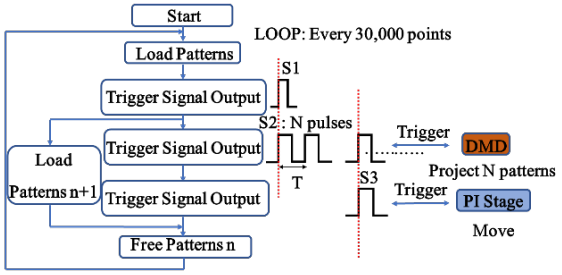

FIGURE 2. Flow chart for synchronizing the DMD and XYZ stage motion to realize stitch-free large area printing.

FABRICATION RESULTS

In this section, we present the TPP fabrication results of large-scale 2D and 3D structures to demonstrate the efficacy of the stitch-free algorithm. First, we fabricate large-scale 2D metasurface structures, including a micro-pillar array for anti-reflection applications and split ring resonator (SRR) structures for photonic applications.

Figure 3 presents a large-area micro-pillar array, fabricated by the conventional stitching approach (Fig. 3A) and stitch-free appraoch (Fig. 3B). Each pillar has a diameter of 1.7 μm; the distance between adjacent pillars are 3.2 μm. In Fig. 3A, one can clearly observe the stitching errors among each printed area with a size of 35 × 26 μm^2 due to sample stage positioning errors. In contrast, in Fig. 3B no stitching errors have been observed over the entire array which has a size of about 250 × 250 μm^2. From the zoom-in view, we can confirm the pillar array are precise and uniform.

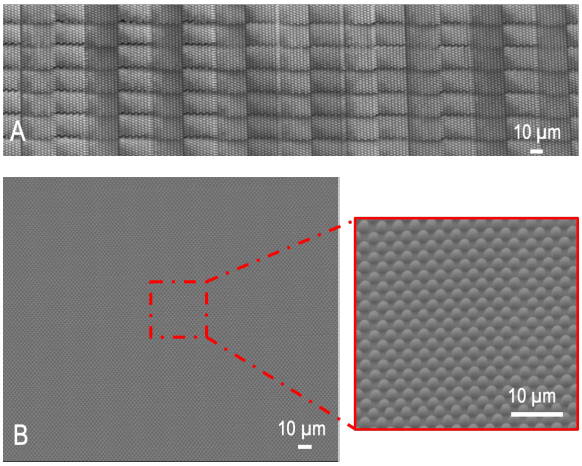

FIGURE 3. SEM images of the micro-pillar array: A. Conventioanl process; B Stitch-free process.

Figure 4 presents a large-scale 2D SRR structure, i.e., "u" array, with a size of 450 × 500 μm^2. Notably, to increase the fabrication rate we applied three laser foci for parallel printing in combination with the stitch-free algorithm. From the results, we can confirm that the stitching errors have been entirely eliminated and the stitch-free algorithm can be directly applied to the DMD for both single- and multi-focus random-access scanning.

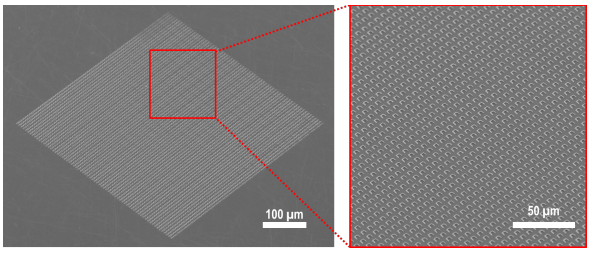

FIGURE 4. SEM image of the 2D SRR structure, fabricated by three-focus random-access scanning.

LAEGE-SCALE 3D STRUCTURES

Next, we present the fabrication results of 3D structures. Figure 5 presents a large-area woodpile structure for 3D cell culture applications, fabricated by both the conventional stitching approach (Fig. 5A) and stitch-free appraoch (Fig. 5B) for comparison. In Fig. 5A, a 510 × 510 × 6 μm^3 woodpile structure is printed via 17 × 17 = 289 stitches, where stitching errors due to positioning errors can be clearly observed in the zoom-in view, which is expected. In Fig. 3B, a large-area, i.e., 500 × 500 × 10 μm^3, woodpile structure is continuously printed via the stitch-free approach. From the zoom-in view, we can confirm the woodpile structure is uniform without any visible stitching errors. Figure 5C and 5D present isometric views of the woodpile structures in Fig. 5A and 5B respectively, which confirm again the woodpile structure printed via the stitch-free algorithm in Fig. 5B has no visible defects in both lateral (in-plane) and axial (out-of-plane) directions.

Figure 6 presents a 3D bending rail with a total length of 450 μm, fabricated via the stitch-free algorithm. The zoom-in view confrims the stitching errors have been eliminated. Notably, owing to the advantage of random-access scanning, during fabrication the laser focus does not need to scan over empty spaces without structures, but directly follows the twisting rail in 3D, which helps minimizing the fabrication time (i.e., 360 sec). In contrast, to fabricate this structure, conventional point-scanning systems has to adopt a layer-by-layer fabrication strategy, which can generate stitching errors in both lateral and axial directions.

It is worth to note that stitching errors due to volume shrinkage have not been observed in our results. This is because the continuous fabrication eliminates the wait time for moving the sample during which the laser writing is halted. Since printing is no longer interrupted, the volume shrinkage effect is distributed evenly across the structure, rather than concentrated at the junction of the two stitched parts. On the other hand, in comparison to IFOV, since the scanning holograms do not have inertia-induced dynamic errors, the resulting algorithm is able to produce seamless large-scale 3D structure with better precision for both single-focus and multi-focus fabrication processes.

To demonstrate the printing resolution, Figure 7 presents the fabrication results of a binary phase

supercritical lens (Fig. 7A) and metalens (Fig. 7B) for visible light applications, which requires a precision of 100 nm. The maximum radius of the phase supercritical lens is 19.8 μm with 44 concentric rings. Among them, 22 rings have a phase of π and the width of the ring is 500 nm; another 22 rings have a phase of 0 and the widths of the ring vary between 300 - 500 nm. In Fig. 7B, the radius of the metalens is 20 μm; and the minimum radius of a single pillar unit is designed to be 400 nm; the heights of the pillar vary between 2.5 to 3 μm.

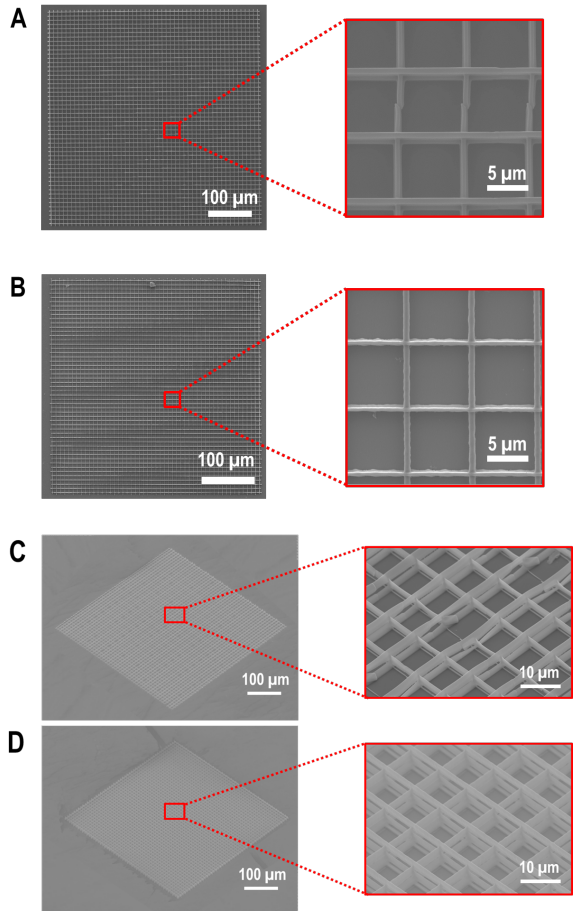

FIGURE 5. SEM images of the woodpile structure: A and C. Conventional process; B and D. Stitch-free process.

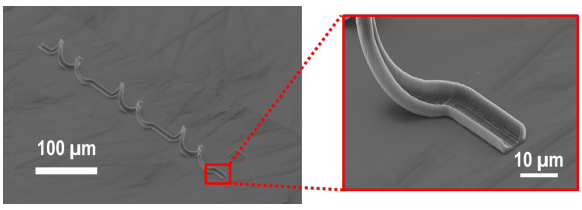

FIGURE 6. SEM images of the 3D bending rail structure.

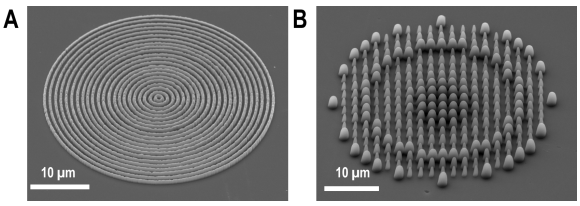

FIGURE 7. SEM images of the phase supercritical lens (A) and metalens (B) structures.

CONCLUSION

In conclusion, we have presented a new stitch-free printing method for the DMD-based TPP fabrication system. Based on the method, large-scale 2D and 3D structures have been fabricated in a continuous fashion, which entirely eliminates the stitching errors; in addition, the size of the object to be printed is only limited by the range of the sample positioner. The stitch-free algorithm has been used in combination with both single- and multi-focus random-scanning, demonstrating 100 nm printing resolution and high-speed nanofabrication. The stitch-free method can readily be applied to other fabrication systems, e.g., FP-TPL, to enhance the fabrication results. The high-precision and high-speed DMD-based TPP fabrication system may find important applications in the fields of nanotechnology, biotechnology and photonics.

ACKNOWLEDGMENT

This work partially supported by the Oxford-CityU Centre for Cerebro-Cardiovascular Health Engineering (CoCHE) under the Innovation and Technology Fund; HKSAR Research Grants Council (RGC), General Research Fund (GRF), 14203020.

REFERENCES

[1] Maigyte L, Purlys V, Trull J, et al. Flat Lensing in the Visible Frequency Range by Woodpile Photonic Crystals. Optics Letters. 2013; 38(14):2376-2378.

[2] Richter B, Hahn V, Bertels S, et al. Guiding Cell Attachment in 3D Microscaffolds Selectively Functionalized with Two Distinct Adhesion Proteins. Advanced Materials. 2017; 29(5):1604342.

[3] Qu J, Kadic M, Naber A, et al. Micro-structured Two-component 3D Metamaterials with Negative Thermal-expansion Coefficient from Positive Constituents. Scientific Reports. 2017; 7(1):1-8.

[4] Geng Q, Wang D, Chen P, Chen S. Ultrafast Multi-focus 3-D Nano-fabrication based on

Two-photon Polymerization. Nature Communications. 2019; 10: 2179.
[5] Geng Q, Gu C, Cheng J, Chen S, Digital Micromirror Device-based Two-photon Microscopy for Three-dimensional and Random-access Imaging. Optica. 2017; 4(6): 674-677.
[6] Saha SK, Wang D, Nguyen VH, Chang Y, Oakdale JS, Chen S. Scalable Submicrometer Additive Manufacturing. Science. 2019; 366(6461): 105-109.

TESTING FOR TORSION DURING NANOINDENTATION

Chunjie Fan[1], Stuart T. Smith[1]
[1]Center for precision metrology
The University of North Carolina at Charlotte

ABSTRACT

The goal of this study is to measure any torsional forces during nanoindentation. Phenomena occurring during indentation, such as phase transformations, dislocation pile-up, slip plane behavior (shear band), anisotropic material properties (including plasticity), composites, laminate multilayers, and structured materials (3D Nano scribe micro additive materials) might produce torsional forces during nano-indentation.

To facility this study, instrumentation has been designed and fabricated to be able to control indents with forces ranging from 10 mN to 1000 mN. As the indent load is increased, the penetration depth of the indenter is measured using capacitance sensing capable of measuring indent depths of up to 10000 nm with a resolution of better than 5 nm. The indenter is mounted on an air-bearing with the indenter tip centered to better than 10 µm. A rotary encoder mounted on the spindle of the air-bearing has a resolution of 1 µrad without filtering.

It has been observed that while most metals spanning a large range of hardness values have similar force-displacement characteristics. And different types of materials have different load-penetration curves. To validate the measurement result from this instrument, the hardness of copper was measured to have a bulk hardness of 370 MPa that is comparable with a value of 390 MPa determined from published literature. Throughout all of the measurements, no rotation was observed with the singular exception of silicon under loads that resulted in a substantial brittle fracturing.

INTRODUCTION

Nanoindentation is used in research communities and industries for evaluating surface and near sub-surface performance characteristics: surface hardness of materials, tribological properties, coating quality, dislocation stresses, strain hardening effects, fracture toughness, thin film deposited layers, polymer viscoelastic and material creep behavior [1-3]. Engineers are interested in the surface hardness because this is a major factor that influences wear (i.e. machines typically fail since wear over time) and indicates issues with materials processing. Furthermore, in-situ nanoindentation tests with further sensing of the indent region have enabled the study of mechanical, biological, thermal, and electrical properties by continuously measuring the reaction force and penetration depth under control environment conditions.

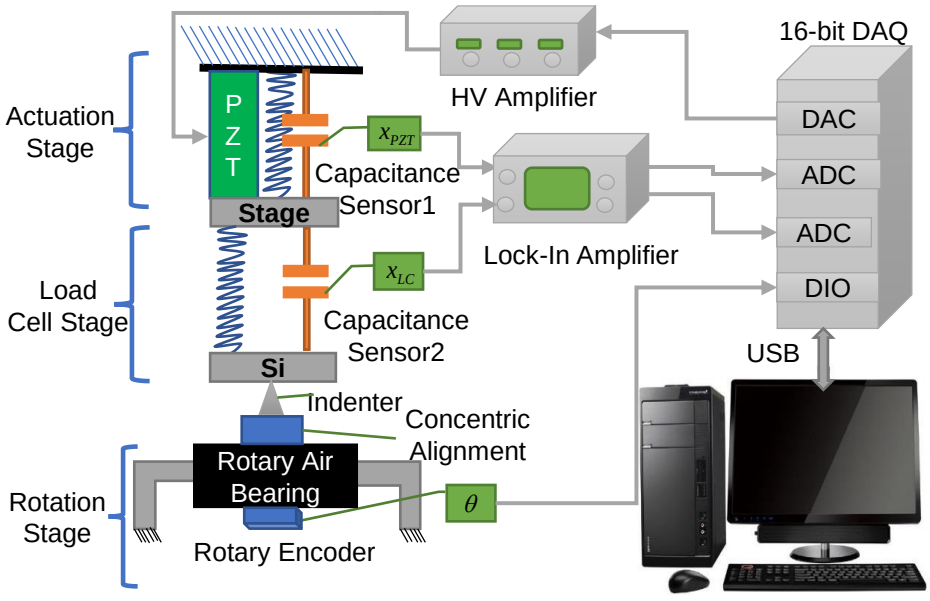

Figure 1. Basic structure of nano-indentation system.

The changes in electrical properties (insulator to conductor transition under high pressure) and phase transformation (i.e. cubic diamond structure to beta silicon for a single crystal silicon during nano-indentation) [4-5] are also detected during nano-indentation test. As an example of possible anisotropic behavior, the single crystal silicon has an alpha diamond cubic structure, however once the applied pressure is above 12.5 GPa, the structure will be compressed to a beta-silicon structure that resembles a flattening of the original structure. This transition was shown in research conducted at Colorado State University by Ian L. Spain [8] using diamond anvil cells. Nano-indentation tests have the capability to measure force, in sub-micro-newton resolution, and displacement, with sub-nanometer to nanometer resolution, but do not have the capability to measure twisting force [1-8].

Experimental facility

The experimental apparatus shown in Figure 2 indicates major features of the new instrument.

Apparatus

(1) A precision micrometer stage to adjust the position of the nano-indentation system relative to the indenter and air bearing assembly.

(2) A piezoelectric actuated stage to push the indenter into the sample.

A new nano-indentation system has been created that includes a high voltage (HV) amplifier, an actuation stage, a load-cell stage, a rotation stage, a lock-in amplifier, and LabVIEW control software with data acquisition (DAQ). A block diagram indicating major components of the nano-indentation system is showing in Figure 1. The technique involves an actuation process to apply a load, and a load-cell to transfer the load to the indenter. The piezoelectric actuation stage and load-cell stage will generate displacements that are measured by capacitance gages. The signals of these capacitance gages are transmitted to a lock-in amplifier and transformed into signals that can be calibrated to determine displacement. The rotary stage (rotary air-bearing supporting the indenter) can freely rotate, and the rotation angle is measured to determine the presence of rotational (torsional) moments.

(3) A load-cell stage to measure the load and the displacement.

(4) A concentric alignment apparatus to maintain the diamond indenter tip and the rotary stage axis of the air bearing in the same line.

(5) A coarse and fine adjustment tip alignment mechanism on the rotary air bearing and a precision rotary encoder to measure the change in angle.

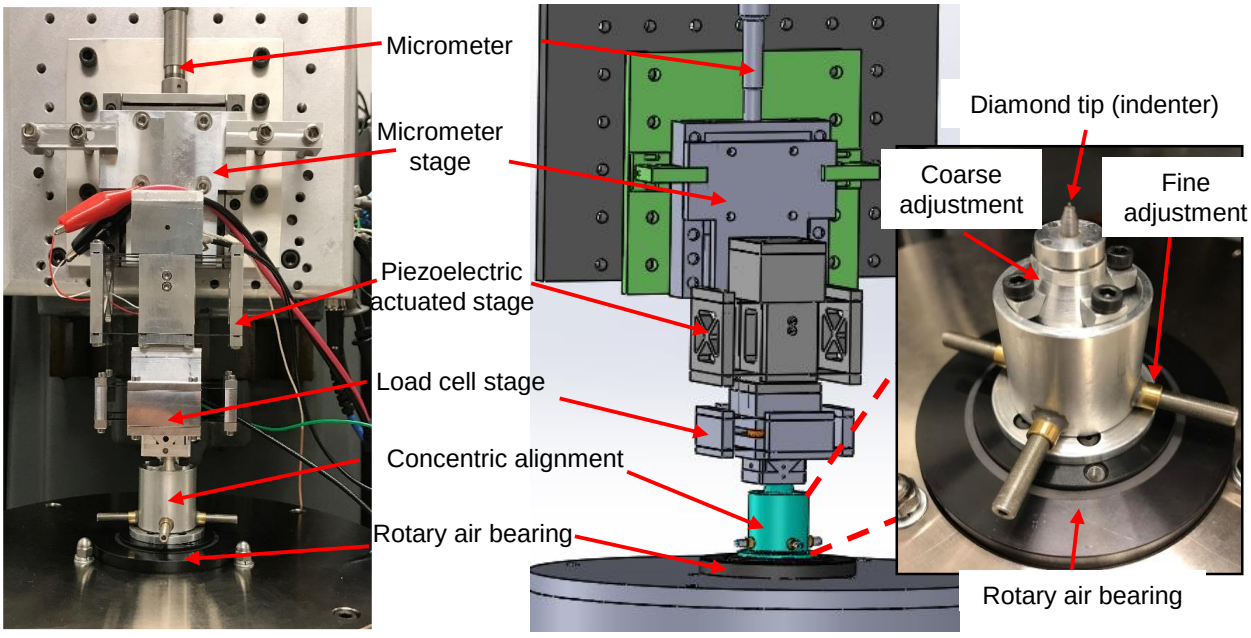

Figure 2. Experimental facility showing relations between concentric alignment, actuation, and load sensing mechanisms.

The entire rotary system was mounted on the XY table of a Moore measuring machine for testing. The rotary stage includes a rotary air bearing, a concentric apparatus (centering adjustment) and a rotary encoder. The rotary air bearing (Precision Instruments air bearing 30-62792-073A) is used to provide precise angular measurements. To achieve the alignment of the indenter tip with the rotary axis of the bearing, a coarse and fine adjustment mechanism is used to locate the indenter tips to be coincident with the rotation axis of the air bearing. A microscope is used to observe the alignment of the indenter to the rotation axis of the bearing. Load-cell spring stiffness and the displacements of components are calibrated. The load-cell has a stiffness of ~100 kN/m, and the frame loop has a system stiffness around 5000 kN/m. Indenter forces are determined by load-cell and loads are calculated by the multiplication of calibrated stiffness and the displacement.

A 20 kHz sinusoidal signal generated from the lock-in amplifier was sent to the balance line driver (DRV135), then two 180 phase shift signals are sending to a fixed capacitor and the self-made varying capacitor, shown in Figure 3. A combination of previous capacitance sensor is sending through a buffer (AD630) and sending back to the lock-in amplifier. The lock-in amplifier will use this signal and the internal referenced sine wave to measure the changing amplitude of this signal.

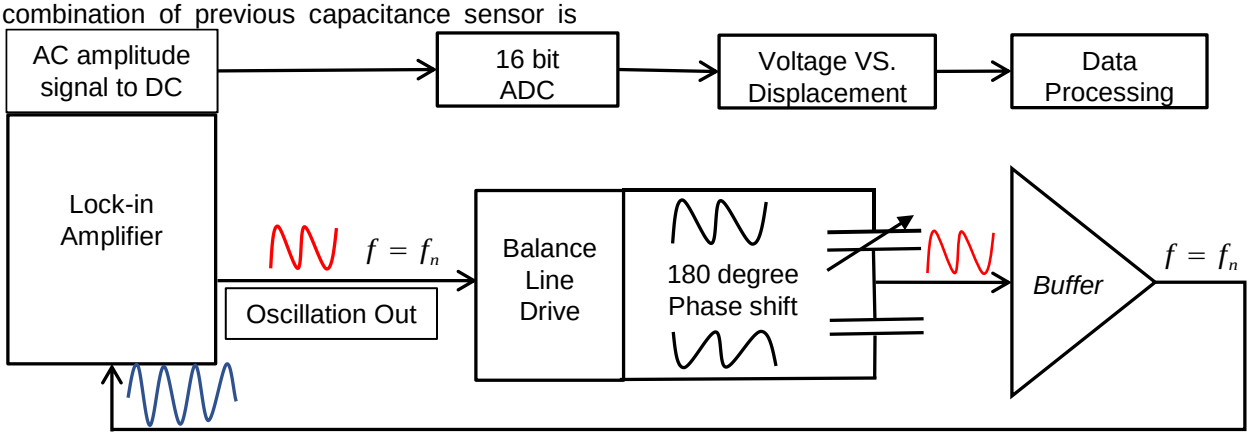

Figure 3. Block diagram of signal process for nano-indentation.

EXPERIMENTAL PROCEDURE

An open loop triangle ramp signal is applied to the actuator stage to move the specimen surface towards and away from the indenter. The block diagram shown in Figure 4 indicates all of the components involved in the control and measurements during an indent cycle. A 16-bit ADC will record the changing amplitude signal and transfer this voltage signal to displacement or force value. LabVIEW and myRIO controller are used to determine the amplitude and velocity of the ramp signal that is transferred to an external 16-bit DAC. Information and controls of both ADC and DAC are communicated using four SPI buses. The 16-bit DAC outputs have a linear fitting curve that reference to the Keithley digital multimeter (DMM model 2010) with a gain of 0.99790951 has R-square value of 0.99999999. The ADC inputs have a linear fitting curve that reference to the DMM with a gain of 0.9866782 and an R-square value of 0.9999991.

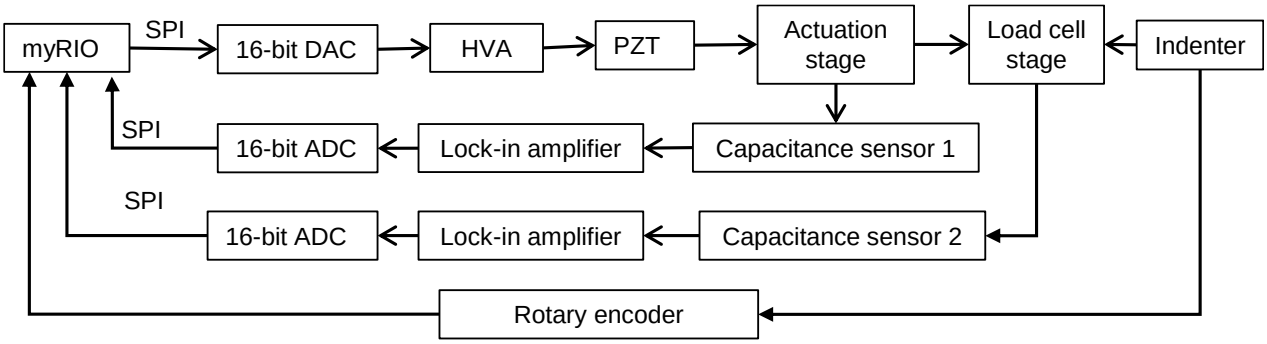

Figure 4. Bock diagram for the PZT driven actuator stage.

The control voltage of this 16-bit DAC for the PZT driver is from 0 to 10 V range. This voltage controls the high voltage amplifier driver that has a gain of 15. Changes in the length of the PZT will drive the actuation stage forward or backward. Since the load-cell stage is in series with the actuation stage, it is moving with the actuation stage moving platform. When the load-cell stage contacts the indenter, there will be a reaction that, in turn, induces a displacement of the load-cell stage. Two capacitance sensors record the displacement of both the actuation stage and the load-cell stage and the resulting changes in signals from each sensor are demodulated using Lock-in amplifiers (Perkin Elmer instruments 7265 DSP and 7280 DSP). Simultaneously with these measurements, the rotary encoder is recorded to measure any rotational movement of the indenter.

PRELIMINARY RESULTS

Performance characteristics to be measured include: the noise analysis (noise sources), actuator stage and load-cell stage calibration, stability testing and estimated uncertainty budgets of the system. The stability test shows the capacitance sensors of the actuation stage has 3 nm variance, and the load-cell stage has 5 nm variance in 10 minutes. Temperature sensors show the environment, and the instrument has a temperature of 20 ± 0.1°C. Table 1 shows the results from the stability test for 10 minutes.

Table 1. The measurement results from stability testing over 10 minutes period.

Uncertainty	Load-cell stage stability u	Actuator stage stability u
Noise (f_{nyq} = 5 Hz) non-contact	5 nm (standard deviation)	3 nm (standard deviation)
Noise (f_{nyq} = 5 Hz) in contact	7 nm (standard deviation)	3 nm (standard deviation)

PERFORMANCES TESTING

The actuation stage has a 16 µm range and the load-cell stage has a range of 10 µm (1 N). The tilt angle of the actuation stage during translation is within 0.05 arc sec in this 16 µm range. Rotary encoder has 1 µrad rotary resolution, the stability of the rotary air-bearing is ~ 4 µrad in 10 minutes. A boxcar averaging filter is used for increasing the resolution to 0.01 µrad during stability test.

To determine the torsional force to overcome the 'static friction' of the air-bearing, a mass of 1 gram was suspended on a thread length 0.35 m. This mass was contacted with a horizontal arm at a distance of about 25 mm from the bearing axis. Translation of the top support of the pendulum is used to create a torque about the axis of the bearing. From these experiments, it was observed that the static torque is greater for one direction of rotation. In one direction, the maximum static torsional force to drive the rotary air bearing is about 1.7 mN, which at a moment arm of 25 mm corresponds to a torque of 42 µN·m. The torque required to initiate motion in the other direction was below the resolution of the measurement, that is approximately 0.7 µN·m. The reason for the directionality of the static torsional friction is not known. Table 2 shows the performance of the nanoindentation instrument.

Table 2. The performance of the nanoindentation.

Performance	Actuation (0.1 Hz)	Load-cell (0.1 Hz)	Air bearing	Initial torque (µN·m)
Range	16000 nm	10000 nm	660000 CPR	0.7 (CW) 42 (CCW)
Resolution	4 nm	4 nm (0.4 mN)	0.01 µrad	0.7

DISCUSSION

There are a wide variety of material studies that can derive information from micro/nano-scale indentation analysis, for materials ranging from metals and alloys (Steel, Al, Cu, Zi) to plastics (Polyethylene), structural materials (3D nano scribe additive manufacturing), and crystal materials (Si, Ge, Silica). All these materials have been tested and a comprehensive set of results are including in [10]. During nanoindentation

process, the load-cell stage records the force between the indenter tip and the specimen. The maximum load force happens at the maximum penetration depth for the loading process. During unloading process, a constant slope range (~25% of the unloading curve), can be typically observed from the load and penetration curve. Atomic force microscope imaging of NiP amorphous sample after indentation test at a load of 100 mN using a diamond Berkovich indenter, shown in Figure 5.

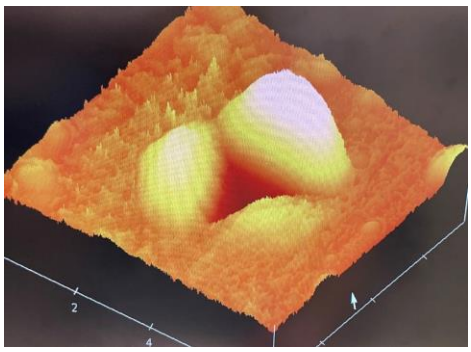

Figure 5: AFM imaging of NiP amorphous after indentation test at a load of 100 mN.

The nanoindentation result for single crystal silicon were plotted out in the following Figure 6. Rotation angle was detected only during macroscopic catastrophic fracturing for single crystal silicon with a load up to 0.75 N, as shown in the Figure 7. Several samples, like aluminum, copper, single crystal silicon, single crystal Germanium, and amorphous nickel phosphorous, were used for the rotational measurement during nano-indentation as shown in reference [10]. From the measurement results, no rotational effects were observed in crystalline and amorphous metals, semi-conductors (Si, Ge), ceramic, PZT ceramic, CFRP, PTFE, and insulators.

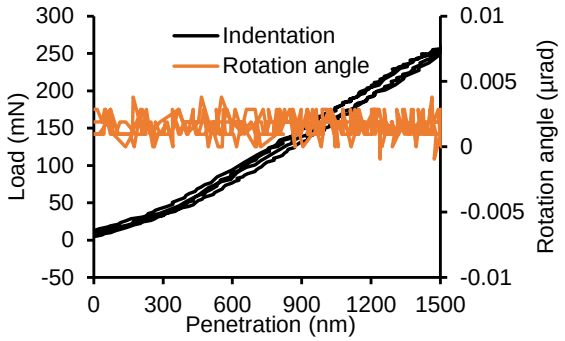

Figure 6: Penetration depth and load between the indenter and Single crystal silicon. Rotation angle during nanoindentation is plotting out at the second vertical axis.

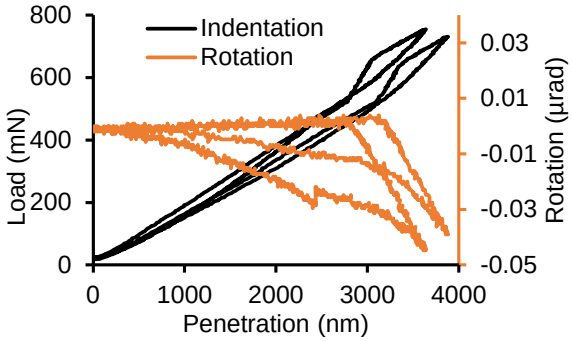

Figure 7: Penetration depth and load between the indenter and Single crystal silicon. Rotation angle during nanoindentation is plotting out at the second vertical axis.

Figure 8 is a nanoindentation measurement of pure copper, and the displacement and load during nanoindentation is plotting out. Figure 9 shows the hardness values is calculated around 370 MPa that is comparable with the annealed pure copper hardness values (390 MPa) [9].

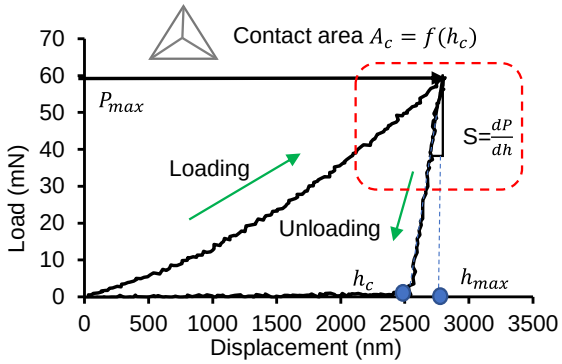

Figure 8: A nanoindentation measurement of pure copper to record the displacement and load curves.

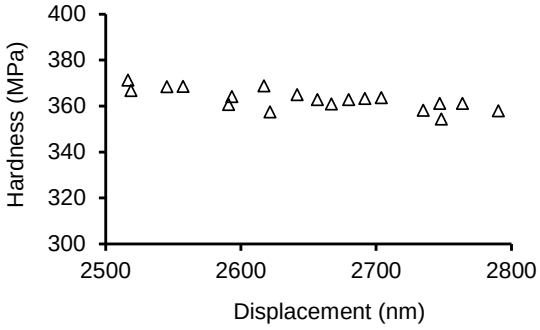

Figure 9: Hardness values of the pure copper sample is calculated and compensated with frame stiffness showing values around 370 MPa from 2.8 μm to 2.5 μm displacement range.

CONCLUSION

The contribution of the nanoindentation instrument is to create a new method to measure torsion effects during nano-indentation. A novel nano-indentation machine with rotary function is designed and built. This novel nanoindentation instrument has a piezo actuation stage, load-cell stage, and rotary stage with rotary air-bearing. The actuation stage supplies the driven displacement to push the indenter to the sample surface. The load-cell will measure the force between the actuation stage and the indenter, which is coaxial with the rotary stage. The point of contact is estimated when the load-cell begins to vary corresponding to a force between the indenter and the sample surface.

The hard material, particularly the brittle materials, like Si and Ge, produce a substantially elastic response at low load values. PTFE, on the other hand, shows continued plastic deformation with duration of indent that is characteristic of viscoelastic materials. CFRP, during unloading process, maintains the force during the initial portion of the unload cycle, resulting in an "S" shape unloading curves. Reasons for this are not clear although it is noted that the specimens came in the form of plates that are difficult to bond to the dovetail specimen platform and may not be as flat as the other specimens. The effect of pushing the predominantly elastic fibers of CFRP into the polymer substrate may also contribute to this unusual plot.

From the measurement results, no rotational effects were observed in crystalline and amorphous metals, semi-conductors (Si, Ge), ceramic, PZT ceramic, CFRP, PTFE, and insulators. Indent plots for all these materials can be found in reference [10]. In our studies, the affecting factors for this nanoindentation research include, thermal drift of the sample and the instrument, the initial penetration depth of the indentation process, instrument compliance, piling-up and sinking-in situation during indentation, surface roughness or residual stress of the sample, and indenter alignments.

This nano-indentation could be extended to scratching and ploughing behavior for the plastic deformation research. Three-dimensional force and torque measurements may provide additional insights into deformation processes.

REFERENCES

[1] Fischer-Cripps, A.C., 2006. "Critical review of analysis and interpretation of nanoindentation test data". Surface and coatings technology, 200(14-15), pp.4153-4165.

[2] Li, X. and Bhushan, B., 2002. "A review of nanoindentation continuous stiffness measurement technique and its applications". Materials characterization, 48(1), pp.11-36.

[3] Tabor, D., 1970. "The hardness of solids". Review of physics in technology, 1(3), p.145.

[4] Ruffell, S., Sears, K., Bradby, J.E. and Williams, J.S., 2011. "Room temperature writing of electrically conductive and insulating zones in silicon by nanoindentation". Applied Physics Letters, 98(5), p.052105.

[5] Dong, Z. and Song, Y., 2011. "Novel Pressure-Induced Structural Transformations of Inorganic Nanowires". In Nanowires-Fundamental Research. InTech.

[6] Asif, S.S., Wahl, K.J. and Colton, R.J., 1999. "Nanoindentation and contact stiffness measurement using force modulation with a capacitive load-displacement transducer". Review of scientific instruments, 70(5), pp.2408-2413.

[7] B. K. Nowakowski, D. T. Smith, S. T. Smith, L. F. Correa, and R. F. Cook (2013) "Development of a precision nanoindentation platform - Rev. Sci. Instrum". 84, 075110 (2013); doi: 10.1063/1.4811195

[8] Ian L. Spain, "New physics with the diamond-anvil cell". Semiconductors at high pressure. Contemporary physics, Volume 28, 1987.

[9] D. Tabor. "The hardness of metals". OUP Press, Appendix VI, page 167.

[10] C. Fan. "Controlling force and displacement: Instrumentation design and application in thermal actuation and nanoindentation". Ph.D. thesis, UNC Charlotte, 2021.

Experimental Characterization of Heat Affected Zones for Fabricating Near-net Shaped Microscale Features

Dipankar Behera[1], Aaron Liao[1], and Michael A. Cullinan[1]
[1]Department of Mechanical Engineering
The University of Texas Austin
Austin, TX, United States of America

INTRODUCTION

Most of the conventional metal additive manufacturing (AM) processes today are becoming increasingly applicable the aerospace, biomedical and electronics industry because of their ability to handle complex macroscale architectures. However, the commecially available AM tools have resolutions to the order of 100s of microns which is higher to the required feature sizes in several microscale applications. Consequently, there is a gradual shift towards developing metal AM techniques with micron and sub-micron level accuracies to replace multi-step and expensive subtractive manufacturing processes[1]. The microscale selective laser sintering tool (μ-SLS) developed at The University of Texas at Austin aims to fabricate sub-5 μm features with a high throughput with primary applications in the packaging back-end of a semiconductor fab [2].

In a powder fusion processes like selective laser sintering/melting (SLS/M), a focused laser beam is applied on selective regions in the layers of particles to produce a sintered 3D part. However, the dimensional accuracy of these parts is severely affected because of material shrinkage and laser heat affected zones. Laterally, heat affected zones can be defined as a symmetric area with its centroid coincident on the center of the laser beam's spot. Several researchers have explored in-situ and post-sintering monitoring methods to understand and evaluate the heat affected zones, and correct for purely based on the process parameters of the machine. However, the current state-of-the-art in SLS/M does not yield satisfactory part accuracies for a wide range of geometries, and is typically defined for a given machine.

The μ-SLS process starts with the positioning of the substrate under a nanoparticle dispense system, followed by the translation of the dispensed bed under a projection mirror-based optical system for sintering. The process is then repeated to fabricate layer-by-layer 3D parts. A critical auxiliary step includes the alignment of the sample under the dispense and optical subsytems to achieve submicron accuracy and repeatability in the positioning which is achieved by the long-range XY-nanopositioning stage. From the perspective of μ-SLS tool, the need to achieve near-net shaped features during a single-shot exposure is critical to avoid additional post-processing steps. This work proposes an experimental framework to capture and monitor the sintering process using a thermal camera and develop experimental models that can predict the nominal geometric correction required along with the processing window to achieve the desired feature shape.

THERMAL CAMERA SETUP

Figure 1 shows the physical embodiment of the thermal imaging camera (FLIR A655x series) setup on the Microscale Selective Laser Sintering (μ-SLS) tool. A close-up higher magnification lens interfaced with the IR sensor allows for an effective resolution of ~25 μm features. The thermal camera is fixtured at a shallow angle of ~15 degrees from the substrate plane to capture the process in situ. The key challenge in developing this setup involves aligning the optical path to obtain high resolution images.

Additionally, the sintering exposure times are in the 10s of milliseconds depending on the projected area and laser irradiance, which means that the thermal camera setup needs to capture enough frames per second to develop an accurate model of the process. Lastly, the emmissivity of the area under laser changes as the sintering progresses, which introduces additional challenges in processing the images to capture how the heat spreads.

EXPERIMENTAL FRAMEWORK

The first step involves alignment and focusing of the thermal camera nominally around the spot area. The camera is fixtured on a universal mount to access all multiple degrees of freedom during the alignment and focusing steps. Next, monochrome images of several different patterns with varying areas are projected on the substrate coated with Ag nanoparticle ink. The process is continuously recorded using the thermal camera. The individual frames are then transformed using the Matlab Image Processing Toolbox to acquire projected images. The sintered samples are then measured under an optical profilometer or scanning electron microscope and further processed to characterize their areal accuracy and the heat affected zones. The key variable in these steps include – different feature geometries, varying laser irradiance (obtained by varying laser power and pulse characteristics) and changing emissivities during the sintering process.

PRELIMINARY RESULTS

A primary source of error is in defining the transformation matrix for the projected thermal image, which needs to be done after realignment of the thermal camera for varying patterns. This was done by considering a 500 micron circle which shows up as an ellipse in the actual thermal camera image as shown in Figure 2a. First, the ellipse is transformed using an affine transformation matrix (ATM). Next, the circle Hough transform (CHT) based feature extraction algorithm is used to identify the closest ATM that yields a circle for a given CHT sensitivity parameter of 0.9. Figure 2b shows the transformed circle. The reliance on the CHT to find the transformed image gives an ATM for individual frames and if the thermal camera position or the spot location has not been changed, the same matrix can be used to transform other complex patterns captured by the thermal camera as well. Figure 2c shows the preliminary image of the transformed thermal camera image of a 'double-I' pattern as obtained using the thermal camera.

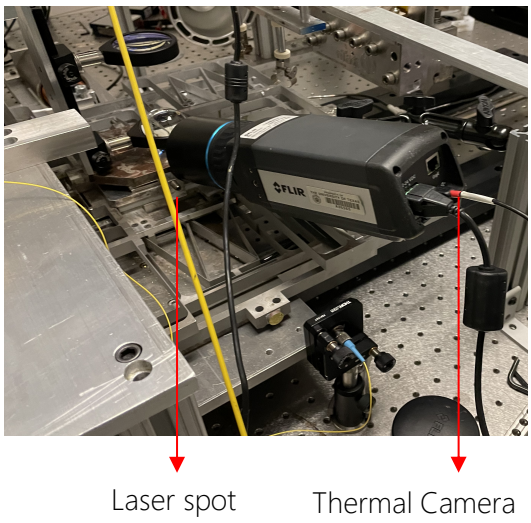

Figure 1 Design embodiment of the thermal camera setup on the current μ-SLS setup.

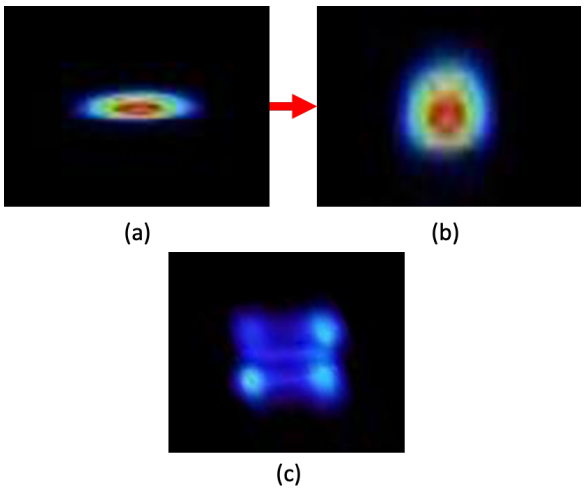

Figure 2 Transformed thermal image of the sample while sintering 'I' shapes

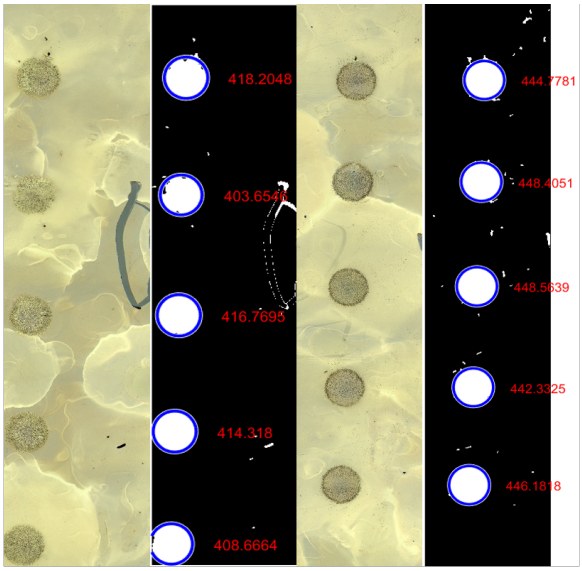

Figure 3 Transformed thermal image of the sample while sintering 'I' shapes

Next, the 500 micron circles are sintered on the substrate with gradually increasing powers. After sintering, the excess ink with removed and the samples are dried, and a Keyence VKX-1000 optical profilometer is used to get images of the parts. To measurement of the diameter from the profilometer image is somewhat manual. Therefore, these images are processed and the CHT algorithm is used to find the best circle. Based on the scale factor obtained from the profilometer, the diameters of the circles are calculated. Figures 3a and 3b shows the optical profilometer image and processed image. of the sintered 500 micron circles for a lower irradiance (~12W/cm^2), while Figures 3c and 3d show the corresponding processed and images for a circle with a higher irradiance (~39 W/cm^2). The multiple circles in each subfigure correspond different spots for the same irradiance. As it can be seen from the images, the mean diameter of the circles as obtained in Figure 3a is 414.49±3.63 μm, while that in Figure 3c is 456.48±6.92 μm. The increase in diameters as the irradiance increases is expected. However, the actual diameters are not beyond 500 μm, which is where truly the HAZs start to affect our parts.

Figure 4 shows the progression of the circles as captured by the thermal camera. Since the thermal camera is continously recording the images, the first image is considered the first shot of laser where the bed started heating up. Despite the close up IR lens, the the projected DMD image covers a small area of the thermal camera sensor. The temperature range on the thermal image acquisition software (ResearchIR by FLIR) have been adjusted to denoise the images and spots show in Figure 4 have been scaled and resized. In figure 4, the laser is effectively on for all the spots where a reddish region can be seen, which indicates a higher temperature. However, it must be noted that all these images show the all the points in the measured area having the same emissivity, which introduces additional complexity to the analysis. As the part sinters, the emissivity of the sintered area changes as phase change from liquid to solid occurs. Additionally it also changes with the

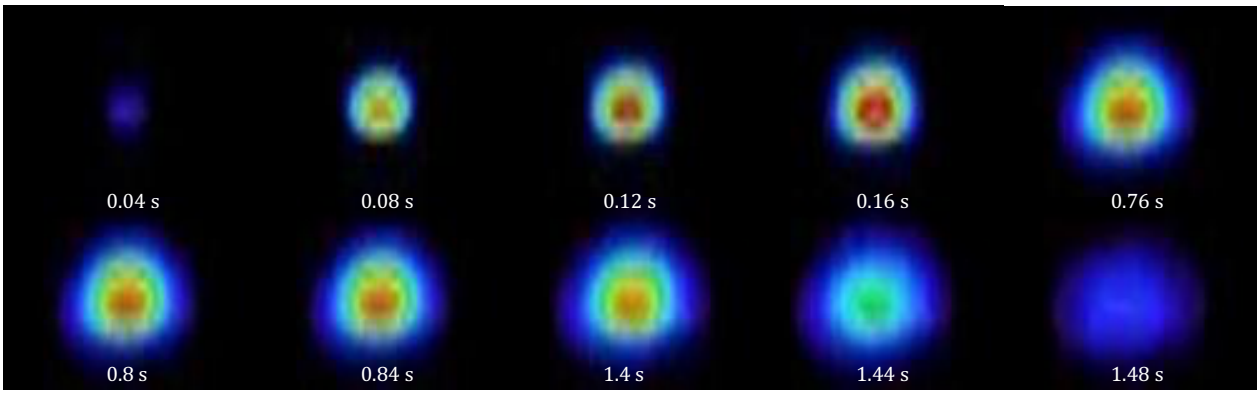

Figure 4 Transformed thermal image of the sample while sintering 'I' shapes

degree of sintering, and the surface roughness of the parts as they are forming. However, if nominally the sintered area is defined based on the pixel to length ratios in the thermal camera, the heat spread around it could inform crucial information about how the HAZs grow.

Figure 5 shows the raw counts of the frame along the center shown in Figure 4, corresponding to 0.16 s. A line plot of the raw radiometric data across the center of the circle was examined to gain insight into the conditions/temperatures at which sintering occurs. The points highlighted on the graph correspond to the measured diameter and center of the circle. Since the spatial resolution of the camera is 25um/pxl, pixel values were interpolated from the original data to get the count values. This helps us compare the thermal data to the optical profilometer.

Figure 6 shows the raw radiometric count data for each frame. This shows the temperature read by the camera at the two points at the edge of the circle during the frames at which the laser is on and then some after it turns off (frame 34 onwards) after the heat dissipates into the surrounding medium. However, for the frames where the laser is on and as the substrate is heating up, the counts/temperature should rise but due to the emissivity change as each frame progresses we see a gradual dip in the raw counts.

CONCLUSIONS AND FUTURE WORK

An experimental and analysis framework for understanding how HAZs spread in microscale selective laser sintering process was presented in this work. The approach shown here can be used to develop a model that can be applied to other geometries depending and validated by comparing the optical image with the temperature bands. The key limitation of the current study is that the emissivity change is not accounted for, which doesn't give an accurate representation of how the heat spreads in the sintering region. Therefore, further work is needed to account for the phase change and corresponding emissivity change to understand the growth of the HAZs more accurately and compare with thermal simulation models.

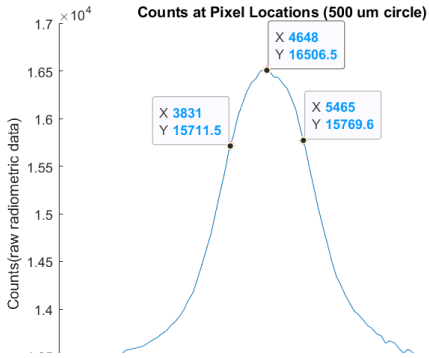

Figure 3 Transformed thermal image of the sample while sintering 'I' shapes

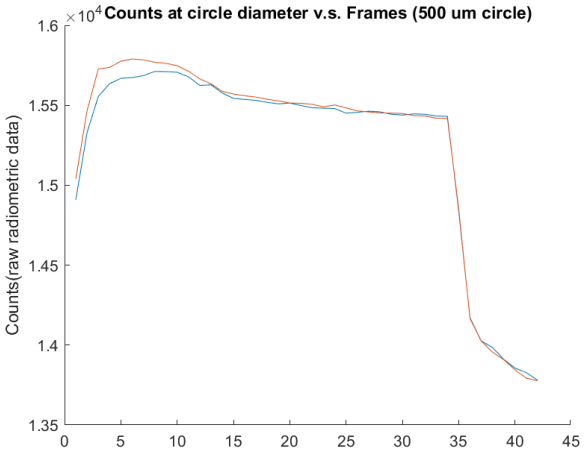

Figure 3 Transformed thermal image of the sample while sintering 'I' shapes

REFERENCES

[1] L. Hirt, A. Reiser, R. Spolenak, and T. Zambelli, "Additive Manufacturing of Metal Structures at the Micrometer Scale," *Adv. Mater.*, vol. 29, no. 17, 2017.

[2] Roy, N.K., Behera, D., Dibua, O.G. et al. A novel microscale selective laser sintering (μ-SLS) process for the fabrication of microelectronic parts. Microsyst Nanoeng 5, 64 (2019). https://doi.org/10.1038/s41378-019-

0116-8

PRECISION SYSTEMS FOR A CONFORMABLE, CAPILLARY-DRIVEN, CONTINUOUS ROLL-TO-ROLL NANOIMPRINT LITHOGRAPHY PROCESS

Parth N. Pandya[1], Anant Jain[1], Richard Gilpin[2], Josh Baines[2] and S.V. Sreenivasan[1]
[1]NASCENT Center
The University of Texas at Austin
Austin, Texas, USA
[2]E+R Group
Accrington, Lancashire, United Kingdom

INTRODUCTION

An alternative approach to roll-to-roll nanoimprint lithography is being developed which eliminates the use of an embossing roller. This paper describes a machine designed to implement a capillary-driven, conformable, and continuous, roll-to-roll nanoimprint lithography process with a flexible template and transfer sub-50 nm features on a flexible substrate film with a sub-50 nm residual layer thicknesses (RLT) while maintaining a throughput of up to 5 m/min that is typically achievable in commercial roll-to-roll nanoimprint tools. Applications in display devices, nanophotonics and microelectronics can see enhanced performance by reducing feature sizes obtained in roll-to-roll nanoimprint lithography. In a specific example of flexible displays with transparent metal mesh electrodes, reducing RLT to sub-50 nm allows RLT etch which can significantly improve transmission, sheet resistance and haze improving its commercial viability.

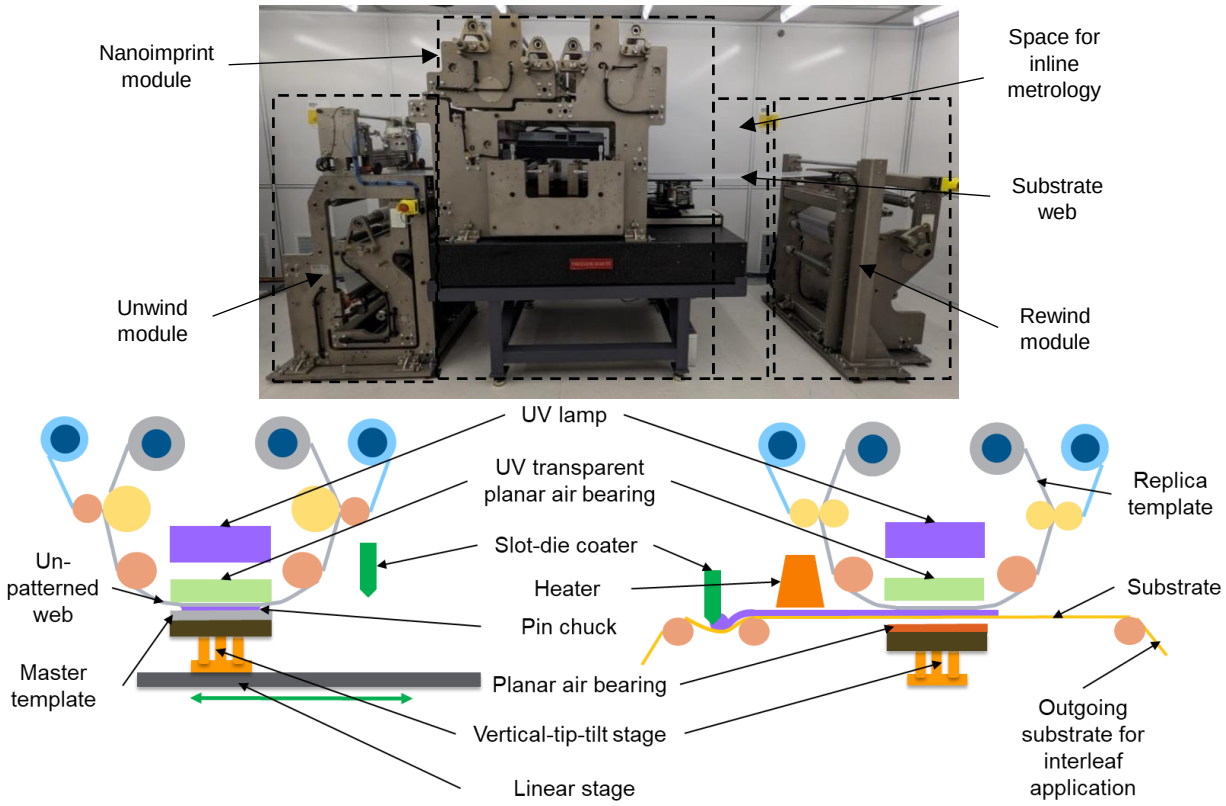

FIGURE 1. Nanoscale roll-to-roll replication tool (top). Schematic of Nanoimprint module used for replica template fabrication (bottom left). Schematic of Unwind, Nanoimprint and Rewind module used for continuous roll-to-roll nanoimprint lithography (bottom right).

SYSTEMS AND PROCESSES

The nanoscale roll-to-roll replication (nR3) tool is shown in Figure 1. It consists of an Unwind module, Nanoimprint module and a Rewind module. The Unwind and Rewind modules have been designed and built by Emerson and Renwick Ltd. A flexible substrate is conveyed from the Unwind module supply roller to the Rewind module take-up roller with control over tension, speed and sidelay along with interleaf removal and application. The Unwind module includes a tensioned-web-over-slot die coater which can deposit <1um wet films of UV curable imprint resist solutions. Upon evaporating the solvent from the coated films, <100 nm liquid resist films can be achieved.

The Nanoimprint module can be used as a standalone system to fabricate a flexible replica template from a rigid master template. Along with the Unwind and Rewind modules, the Nanoimprint module can transfer patterns from the flexible replica template to the flexible substrate. The Nanoimprint module consists of the following subsystems: replica template web handling, vertical-tip-tilt stage, horizontal linear stages, substrate and template chucks (or conveyers) and UV exposure. The template web is held in a roll-to-roll configuration between supply and take-up rollers with control over speed, tension, sidelay and interleaf removal and application. The template web motion is synchronized with the substrate via electronic gearing. The horizontal free span of the template web is the imprint zone where capillary action enables nanoimprinting over a planar region.

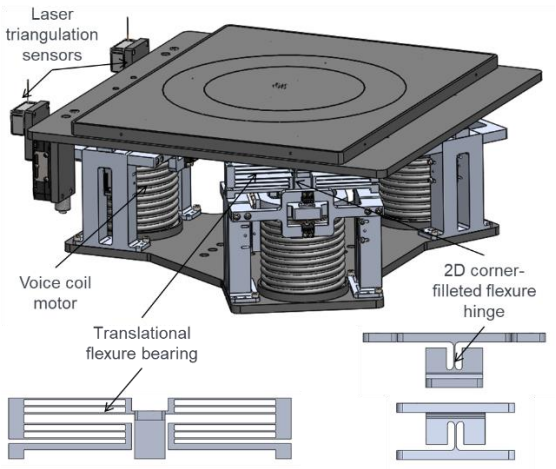

FIGURE 2. Voice coil motor-driven flexure stage with vertical-tip-tilt degrees of freedom.

A voice coil motor driven flexure bearing stage with vertical-tip-tilt degrees of freedom is used to align the substrate with the template in the planar imprint zone while sustaining the contact forces generated during imprinting. As shown in Figure 3, a translational flexure bearing constrains the voice coil motor in the vertical direction. A 2D flexure hinge acts as a ball joint and provides the angular tip and tilt degrees of freedom. Optical encoders are used for position feedback of the voice coil motors. Laser triangulation sensors mounted on the vertical-tip-tilt stage are used to measure the gap between the substrate and the template in the imprint zone and ensure parallelism.

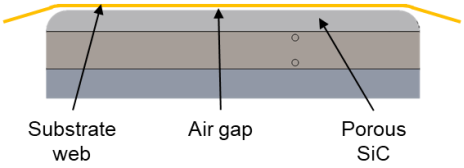

FIGURE 3. Substrate side vacuum preloaded planar air bearing.

The vertical-tip-tilt stage can carry a pin chuck to mount a rigid master template in the case of replica template fabrication. For continuous nanoimprinting from the replica template web to the substrate web, a vacuum preloaded planar air bearing is mounted on the vertical-tip-tilt stage to enable contactless conveying of the substrate web. As shown in Figure 3, the porous SiC supplies positive air pressure to the web to avoid any scratching during web motion. Preload is mainly applied using vacuum with an additional tension component pulling the substrate web towards the planar air bearing face.

A UV transparent vacuum preloaded planar air bearing is used to convey the template web in a contactless manner while allowing room for UV curing of the liquid imprint resist in the imprinting zone as shown in Figure 4. A porous SiC zone on the perimeter of the imprint zone provides positive air pressure for contactless conveying. Preload is applied via vacuum and an additional web tension component pulling the template web towards the planar bearing face. This template side air bearing can also be used to chuck the template web in place by switching off the positive air pressure. The central region of the UV transparent planar air bearing forms a cavity with the template web. Pressuring this cavity allows for out-of-plane curvature control of the template

web and enables lamination of the template web over the substrate web (or the master template).

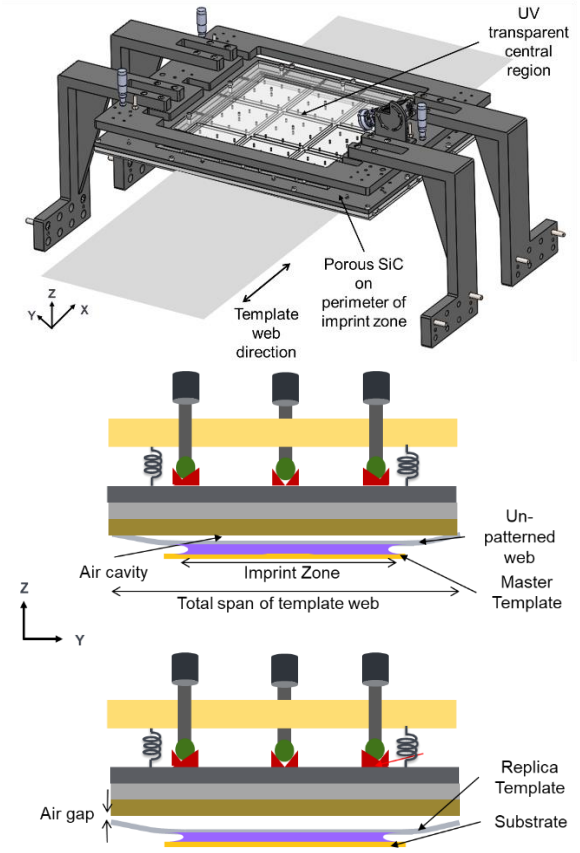

FIGURE 4. UV transparent vacuum preloaded planar air bearing w.r.t web direction (top). Depiction of usage in replica template fabrication (middle) and usage in continuous roll-to-roll nanoimprint lithography (bottom)

In the replica template fabrication process, the master template is a patterned Gen 2 glass that is mounted on a pin chuck being carried by the vertical-tip-tilt stage and the linear XY stages. An un-patterned web is mounted on the nanoimprint module rollers. A film of resist is deposited on the master template via slot-die coating or inkjets or a combination of both. The master template is aligned with the flat region of the un-patterned web while minimizing parallelism errors. The web is chucked in position by turning off the air pressure in the porous region of the air bearing. A ramp cavity pressure is applied which initiates a point contact of the un-patterned web with the master template with the resist film in between. Contact is detected by measuring the current consumption of the voice coil motors while holding position. As the cavity pressure increases, the point contact expands to an area contact and finally laminates the un-patterned web over the master template. This method of lamination ensures no bubbles are entrapped in the liquid film. Subsequently, the patterned liquid resist is UV cured which solidifies the patterns. The cavity pressure is then reduced with a ramp function while simultaneously lowering the voice coil stage which separates the master template from the replica template web. The imprint resist is more wetting towards the web material compared to the glass master and therefore, separates cleanly. The transferred patterns on the replica template web are encapsulated with an oxide layer.

In the process of pattern transfer from the replica template web to the substrate web, the substrate web is mounted on the Unwind-Rewind modules and a slot-die coater deposits an imprint resist solution followed by evaporation of solvent. A planar vacuum preloaded air bearing mounted on the vertical-tip-tilt stage conveys the substrate web. The template web is synchronized with the substrate web and conveyed over the UV transparent air bearing. The horizontal spans of the replica template web and substrate web in the imprint zone are aligned to minimize parallelism errors. The template web cavity is always pressurized. As the substrate web with the deposited resist enters the planar imprint zone, the replica template web makes a line contact with the substrate web and the liquid resist in between. As both the substrate and template webs move downstream, the line contact develops into an area contact and capillary action fills the nanoscale patterns in the template web with the resist material. A line scan UV lamp is used to cure the resist. The substrate and template web paths downstream of the imprint zone are matched for defect-free separation. An interleaf film is applied on the substrate after it exits the imprint zone.

SUBSYSTEM MODELLING AND CONTROLS

In the vertical-tip-tilt stage, the translational flexure bearings have a stiffness of 11 N/mm each and a range of motion (ROM) of ±5 mm calculated via classical beam theory and verified with FEA. The on-axis stiffness and angular ROM of the 2D flexure hinge are 1.374 Nm/rad and ±4.1 degrees respectively and are calculated as shown in [1] and verified with FEA. Off-axis stiffness and parasitic errors were calculated and verified with FEA. Holding 2 of the voice coil motors stationary, a vertical displacement of +5

mm in the 3rd voice coil motor (which also leads to a +1 degree angular change in the 2D flexure hinge) leads to a parasitic error of 95 um in the horizontal direction (1.9% coupling ratio). Note that a large mm-scale vertical displacement is not applied when the template is in contact with the contact. Large displacement flexures were designed to accommodate varied substrate geometries. The voice coil motors are actuated via transconductance amplifiers and a PID controller which gives a sub-50 nm precision under the expected imprint loads. The plant is modelled as a linear system

$$F_c - kz - c\dot{z} - F_l = m\ddot{z} \quad (1)$$

where F_c is the PID controlled voice coil motor force, k is the combined on-axis stiffness of the flexure bearings, c is the electromagnetic damping in the voice coil motor, m is the moving mass, F_l is the imprint load and z is the vertical displacement.

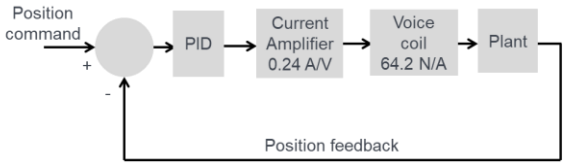

FIGURE 5. Vertical-tip-tilt stage position control loop diagram

Web tension is controlled via speed adaptation. Every span of web has independent tension control with one roller being the master driver (independent roller) and the other roller controlled to maintain the desired speed and tension. As shown in Figure 6, web tension is measured with load cells and the necessary speed adaptation of the controlled roller is formulated by PID gains. An internal Siemens controller achieves the desired speed which acts a control input to the plant model. A tension precision of ±0.5N and speed precision of 1 encoder count (corresponding to 3 um linear displacement) is achieved. The plant is given by

$$l\frac{dT}{dt} = AE(v_c - v_0) \quad (2)$$

where l is the span of the web between the independent and controlled roller, A is the cross-section area of the web, E is the Young's modulus of the web, v_c is the linear speed of the controlled roller and v_0 is the linear speed of the independent roller. Note that the effect of nonlinear terms is negligible and therefore, they have been excluded from the plant model.

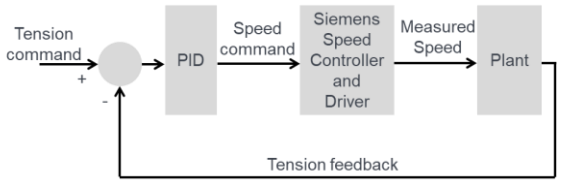

FIGURE 6. Web tension control loop diagram

The UV transparent vacuum preloaded planar air bearing is supplied with a ramp cavity pressure enabling the template web to gradually make contact with the substrate (or the master template). Based on [2], the cavity pressure required to go from point contact (or line contact) to complete area contact over the entire imprinting region is proportional to the gap is as follows.

$$P_c = \frac{2gT}{(l_s - l_i)^2} \quad (3)$$

where P_c is the cavity pressure, g is the gap between the template and the substrate, T is web tension per unit width, l_s is the total span of the template web and l_i is the length of the imprint zone. In the case of replica template fabrication, the web is chucked in place and cavity pressure is sustained since there is no outlet for cavity pressure to escape. In the case of continuous R2R nanoimprinting, there is an air gap between the template web and the vacuum preload perimeter area. For a given cavity pressure and thin air gaps, the leakage flow rate through the air gap is calculated as follows based on shear flow between plates

$$U_{out} = \frac{(P_c - P_a)bh_0^3}{12\mu l_0} \quad (4)$$

where U_{out} is leakage flow rate, P_c is the cavity pressure, P_a is cavity pressure, μ is viscosity of air, l_0, b, h_0 are length, breadth and width of the air gap. As long as cavity inlet flow rate is sufficiently large than leakage rate, the cavity pressure should be sustained. Since smaller air gaps produce lower leakage, preload via web tension or vacuum becomes important.

Compared to a polished wafer, flexible substrates typically have undesirable nanotopography as shown in Figure 7. These micron-scale variations over mm-scale pitches may potentially hinder

capillary-driven lamination and entrap air bubbles between the template web and the liquid resist film. Capillary driven lamination of one surface onto another is feasible when the surface adhesion energy per unit width (γL) of the laminated film is greater than the additional elastic energy stored in the membrane [3, 4]. γ is the surface energy of the interface and L is nanotopography pitch. In the case of a tensioned web, elastic energy per unit width is produced by inducing deformation against web tension ($\sim T\delta^2/L$) and against bending stiffness of the web ($\sim Et^3\delta^2/(12(1-\nu^2)L^3)$). T is web tension per unit width, δ is nanotopography depth variation, L is nanotopography pitch, E is Young's modulus of web material and ν is Poisson's ratio. For an exemplary polycarbonate web with nanotopography pitch of 1 mm and depth variation of 1 um (worst case scenario), it is seen that the additional elastic energy in the tensioned web required to overcome this nanotopography and form a laminated film without bubble entrapment is orders of magnitude lower than the adhesion energy of the web-resist interface. This indicates that the undesirable nanotopography of the flexible web material can be overcome to form uniform defect-free films.

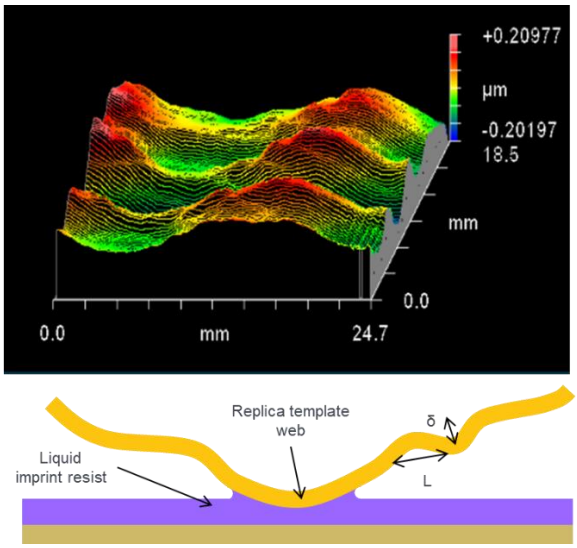

FIGURE 7. Topography of a polycarbonate web measured with Zygo optical profilometer (top). Schematic of replica template web with topography pitch and depth variation (bottom)

EFFECTS OF SUBSYSTEM UNCERTAINTIES ON PROCESS OUTPUTS

The main objective of quantifying effect of uncertainties in the template and substrate handling subsystems is ensure that there is no out-of-plane separation and in-plane shear between the template and the substrate during the continuous imprinting process and minimizing the effects of these uncertainties on process output parameters like RLT, pattern defects and lateral pattern dimensions. As shown in Figure 8, out-of-plane loss of contact can occur when the variations in pneumatic pressure and web tension. For nm-scale thin films, capillary stiction force can be significant as shown below which aids in holding the template-liquid resist-substrate film stack together.

$$\Delta P = \frac{2\gamma\, cos\alpha}{h} \qquad (5)$$

where γ is the surface tension of the liquid resist, α is the contact angle with the webs, h is the liquid film thickness and ΔP is the pressure difference required to overcome capillary stiction forces. The factors contributing to external pressure acting against capillary stiction in trying to create out-of-plane separation are vacuum preload, tension preload and weight of the web. For a nanometer-scale thin film, these factors are orders of magnitude lower than capillary stiction. Another undesirable effect of pressure variation could be variations in the RLT. Using the formula in [5], it is seen that even producing a 5% change in the thickness of nm-scale liquid film in the imprinting duration requires pneumatic pressure orders of magnitude greater than atmospheric pressure. Hence, any variations in RLT will depend mainly on coating non-uniformity and on web nanotopography to some extent. A precision pressure regulator with a repeatability of <40 Pa is used to pressurize the cavity.

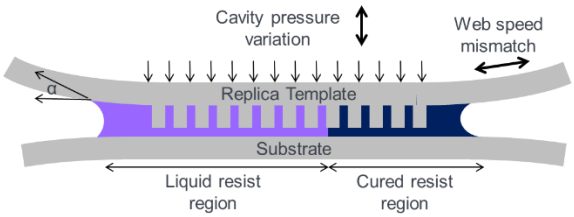

FIGURE 8. Schematic of replica template and substrate webs with web speed mismatch and cavity pressure variation.

In order to prevent in-plane shear between the template and substrate webs, adequate precision is required in speed synchronization and individual web tensions. A mismatch in linear displacement or elongation of one web w.r.t another can cause potential in-plane shear in the

patterned region of imprint zone thereby creating defects. Based on web tension repeatability of ±0.5N, speed matching precision of ±3 um per servo period of 0.5 milliseconds and roller runout errors of 10 um, it is expected that a mismatch of <50um linear displacement is expected to be present in the web in the planar imprint region at any given time. In a hypothetical scenario where the substrate and templates are perfectly rigid plates in contact with each other with a liquid resist film in between, a 50 um displacement mismatch between them would cause shear failure of the cured resist patterns. In the case of flexible webs, total linear elongation is comprised of elastic elongation in the free span of the web and elastic elongation in the laminated span of the web. In the free span of the web, longitudinal web stiffness ($\sim AE/l_s$) determines elongation where A is cross-section area of the web, E is the Young's modulus of the web and l_s is the length of the free span. In the laminated region of the web, resistance to elongation is mainly provided by bending stiffness ($\sim nE_pI_p/h_p^3$) and shear stiffness ($\sim nG_pA_p/h_p$) of the cured pattern where n is the number of cured patterns in the laminated region, E_p is the Young's modulus and G_p is the shear modulus of the solid resist material, h_p is the pattern height, A_p is the cross-sectional area and I_p is the area moment of inertia in the bending direction. For a mm-scale area of cured resist, the ratio of web stiffness to cured resist stiffness is $<10^{-6}$. Hence, a 50 um mismatch in web displacements is essentially taken up by free span elongation.

CONCLUSIONS AND FUTURE WORK

A method of performing continuous, roll-to-roll nanoimprint lithography was presented in this paper along with the design and control of the various subsystems in the nR3 tool. Understanding interfacial nanoscale fluid phenomena was crucial in determining the precision requirements of the subsystems in order to achieve sub-50 nm RLT and sub-50 nm pattern dimensions. The process described here can overcome the use of an embossing roller and extend the resolution limits achieved in R2R-NIL by exploiting the capillary action of nanometer-scale thin films. The nR3 tool is currently in the final stages of testing and process work is expected to begin by mid-November.

ACKNOWLEDGEMENTS

This work was performed at the University of Texas at Austin NASCENT Center. NASCENT Center is a nanosystems engineering research center funded by the National Science Foundation. We thank the National Science Foundation (NSF) (Grant Numbers EEC-1160494).

REFERENCES

[1] Lobontiu N, Paine JS, Garcia E, Goldfarb M. Corner-filleted flexure hinges. J. Mech. Des.. 2001 Sep 1;123(3):346-52.

[2] Xu D, Liechti K. Analytical and experimental study of a circular membrane in adhesive contact with a rigid substrate. International journal of solids and structures. 2011 Oct 1;48(20):2965-76.

[3] Py C, Reverdy P, Doppler L, Bico J, Roman B, Baroud CN. Capillarity induced folding of elastic sheets. The European Physical Journal Special Topics. 2009 Jan;166(1):67-71.

[4] Singhal S. Jet and coat of adaptive sustainable thin films. 2012.

[5] Ahn SH, Guo LJ. Large-area roll-to-roll and roll-to-plate nanoimprint lithography: a step toward high-throughput application of continuous nanoimprinting. ACS nano. 2009 Aug 25;3(8):2304-10.

PIEZOELECTRIC SHUNT DAMPING IN CRYOGENIC CONDITIONS: APPLICATION TO A FLEXURE-BASED MECHANISM

N. Ambaum[1], J.P.M.B. Vermeulen[1], and B. Mokrani[2]
[1]Department of Mechanical Engineering
Control Systems Technology group – Mechatronic Systems Design
Eindhoven University of Technology
Eindhoven, The Netherlands
[2]Mechatronics Department
ASML Netherlands
Veldhoven, The Netherlands

INTRODUCTION

The high demand for semiconductor chips further pushes the limits regarding productivity of lithography systems. This translates, among others, into a search for more powerful electromagnetic linear and planar motors that are used to accelerate and accurately position the substrate (wafers) and the mask (reticle) relative to each other. Recently, first feasibility studies have been conducted to demonstrate the potential of using superconducting magnets as a replacement of Neodymium magnets in a wafer stage planar motor. It was shown that an increase in magnetic field density by a factor $6-8$ is feasible [1,2].

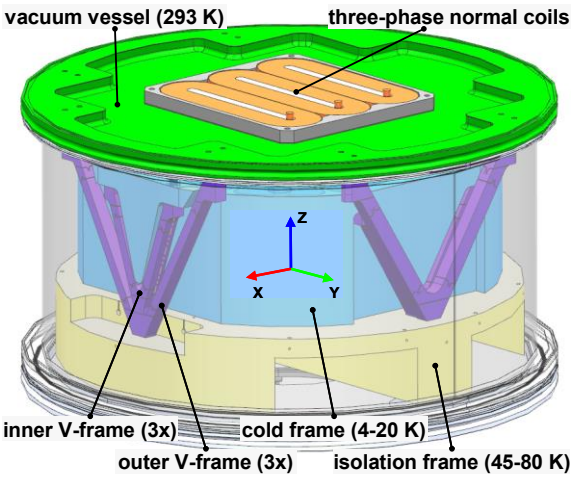

FIGURE 1. Demonstrator of a superconducting magnet plate for application in a planar motor in a vacuum environment. The three-phase normal coils are magnetically levitated at the top side.

Superconducting magnetic coils in high-performance motors need to operate at cryogenic temperatures, which prescribes an appropriate high-stiffness fixation and thermal isolation. Moreover, cryostats generally operate in vacuum and have poor heat extraction efficiency. Thermomechanical and electrical material properties like thermal conductivity, thermal expansion, Young's modulus and electric conductivity are known to change significantly compared to room temperature.

A demonstrator of a superconducting magnet plate for application in a planer motor was build [2] as depicted in FIGURE 1 and FIGURE 2, where the three-phase normal conducting moving coils are magnetically levitated above the vacuum vessel. The superconducting part consists of three masses, interconnected via flexure-based V-frames (struts) to provide a kinematic support. The cold frame (in blue) is holding the superconducting coils at $4-20\,\mathrm{K}$. The cold frame is connected via three pairs of double hinged struts (inner V-frames) to the isolation frame (in yellow), which acts as a thermal shield and is cooled down to $45\ -80\,\mathrm{K}$. The isolation mass is connected via outer V-frames to the vacuum vessel, which operates at room temperature.

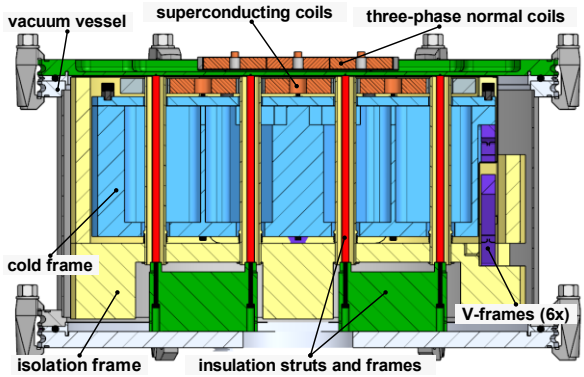

FIGURE 2. Cross section of demonstrator. The superconducting coils are mechanically fixated to the cold frame (blue) and thermally isolated via an isolation frame (yellow) from the environment.

The supporting V-frames should accurately support the superconducting magnets (within $10\ \mu\text{m}$ tolerances), and create a thermal barrier for heat influx at the same time. This implies a trade-off between mechanical stiffness and thermal isolation in the lithography system. It also implies undesired internal dynamics of the cryostat, with very lightly damped vibration modes.

This paper investigates the potential of piezoelectric shunt damping under cryogenic temperatures. Eddy current damping is briefly discussed. For the particular application of the superconducting magnet plate, the aim is to fulfil the dynamic specifications in terms of natural frequency f_n and modal damping ζ of TABLE 1.

TABLE 1. Dynamic specifications for the cold frame and the isolation frame in the cryostat at $10\ K$ and $80\ K$ respectively.

	Isolation frame	Cold frame
T	$80\ \text{K}$	$10\ \text{K}$
f_n	$50 - 500\ \text{Hz}$	$500 - 1000\ \text{Hz}$
ζ	$5 - 10\%$	$1 - 2\%$

DAMPING AT CRYOGENIC CONDITIONS

High tech systems, operating at cryogenic conditions, inherently have very little damping. Due to the very low temperatures, most traditional passive damping solutions are unsuitable or inefficient. Moreover, in view of the relatively poor efficiency to remove heat at cryogenic temperatures, interfaces to the environment are typically designed to have a high thermal resistance, hence poor (frictional) damping properties. For repeatability reasons, the aforementioned kinematic supporting V-frames for the cold frame and the isolation frame, are made monolithic, resulting in very little (material) damping with a typical loss factor $\eta = 0.001$ [3]. This loss factor even reduces under cryogenic conditions, as material damping decreases with temperature [4].

Furthermore, viscoelastic dampers, known to be effective under room temperature conditions, do not work at cryogenic temperature. Due to its temperature dependence, rubber material loses its viscoelastic properties and becomes brittle at low temperature, leading to negligible loss factors. Viscous fluids, as applied in hydraulic dampers, would simply freeze at cryogenic temperatures. In the next section, two potential damping solutions at cryogenic conditions are addressed, viz. eddy current damping and piezoelectric shunt damping.

Eddy current damping

Motion of a current conductor relative to a magnetic field causes eddy currents, resulting in a resistive damping force proportional to the original motion. In cryogenic applications, particularly aerospace related, eddy current damping (ECD) is put forward as a viable solution [5,6,7]. More recently, ECD is also studied for magnetic levitation systems [8,9]. For both application areas, ECD shows to be a suitable damping method for relatively low temperatures down to $15 - 80\ \text{K}$.

The ECD performance benefits greatly from the increased electric conductivity (σ) of copper at low temperatures, which is a factor 1000 larger at $10\ \text{K}$ compared to room temperature [10]. The enhanced conductivity proportionally translates into an increased damping ratio, i.e. $\zeta \propto \sigma$ [11]. However, this relation neglects the conductor thickness limitations and the absence of mutual inductance. These assumptions are not valid for high thermal conductivity and at relatively high frequencies, as the penetration depth of eddy currents reduces significantly and the mutual inductance can no longer be ignored. This results in significantly lower damping performance.

For the aforementioned application, ECD is unsuitable as a passive damping solution due to the marginal increase in conductivity at $80\ \text{K}$ (only a factor 10), along with the limited penetration depth and the high critical damping (d_{crit}). Its implementation would require an unrealistically large magnet-conductor set-up.

Piezoelectric shunt damping

Embedding a piezoelectric transducer into a structure enables the transformation of its mechanical energy into electrical energy. The transformed energy can be then dissipated in simple passive circuits, in the form of resistive and resistive-inductive shunts, or even more complex semi-active circuits [12][13].

Piezoelectric shunt damping techniques have already been widely studied for room temperature but are rather unexplored for cryogenic conditions. Although it has already been demonstrated that piezoelectric properties are not significantly impacted by temperature change [14], the damping performance potential under cryogenic conditions is rather unknown. Indeed,

the piezoelectric strain, at cryogenic temperatures, is in the order of ~30% of the strain at room temperature [15,16], which suggests a moderate decrease of the piezoelectric effect at low temperatures. This makes the piezoelectric shunt damping a potential solution for the cryostat.

THEORY OF RL SHUNT DAMPING

Consider the single degree of freedom piezoelectric system of FIGURE 3, shunted in series on a resistor R and an inductor L. The related dynamics are governed by the following EQUATIONS for the mechanical and electrical behaviour respectively:

$$M\ddot{x} + K_a x = \frac{d_{33}K_a}{C(1-k_c^2)}Q \qquad (2)$$

$$L\ddot{Q} + R\dot{Q} + \frac{1}{C(1-k_c^2)}Q = \frac{d_{33}K_a}{C(1-k_c^2)}x \qquad (3)$$

Here M is the mass, x is the displacement, Q is the electrical charge, K_a is the piezoelectric transducer stiffness with short-circuited electrodes, C is the capacitance with free-free mechanical boundary condition, d_{33} is the piezoelectric constant, and k_c^2 is the electromechanical coupling factor $(k_c^2 < 1)$, it quantifies the ability of the transducer to convert mechanical energy into electrical energy and vice versa.

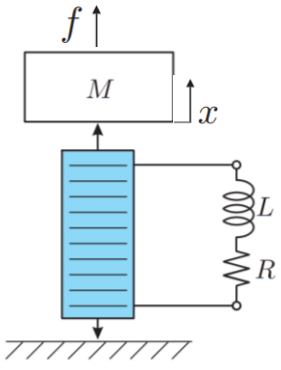

FIGURE 3. Single degree of freedom piezoelectric system shunted in series on a resistor R and an inductor L.

The system of FIGURE 3 that consists of two coupled oscillators, is now tuned such that the electrical oscillator is able to absorb the vibration energy of the mechanical oscillator. We define the resonance frequency ω_e and the modal (relative) damping ζ_e of the electrical circuit as:

$$\omega_e = \frac{1}{\sqrt{LC(1-k_c^2)}} \quad \text{and} \quad \zeta_e = \frac{1}{2\omega_e}\frac{R}{L} \qquad (4)$$

The piezoelectric transducer, which is shunted on the inductor L and the resistor R, behaves in a way very similar to a tuned mass damper system. The resistor is used to dissipate the absorbed energy, and can be mounted, either in series or in parallel. Depending upon the frequency content of the disturbance, the tuning is typically done in two ways, viz. through equal peak design or via maximal damping [17,18]. The two methods are further elaborated below.

a) Equal peak design:

The RL circuit is typically tuned to minimize the H_∞ norm (i.e. the maximum) of the frequency response function (FRF) from external force f to the displacement x of the mass. This design is usually referred to as the equal peak design as it results in two peaks with equal amplitude, as shown in the FRF of FIGURE 4 (red line). In order to maximize the energy absorption, the inductor L is tuned such that the optimal electrical resonance frequency ω_e^* matches the mechanical resonance frequency Ω_i. In this case, the optimal tuning frequency ω_e^* and damping ζ_e^* are:

$$\frac{\omega_e^*}{\Omega_i} = 1 \quad \text{or} \quad \frac{\omega_e^*}{\omega_i} = \frac{1}{\sqrt{1-k_c^2}} \qquad (5)$$

and

$$\zeta_e^* = \sqrt{3/8}k_c \qquad (6)$$

where Ω_i and ω_i are the resonance frequencies of the targeted mode i with open-electrodes, and short-circuited electrodes respectively. The equal peak design is the most commonly used.

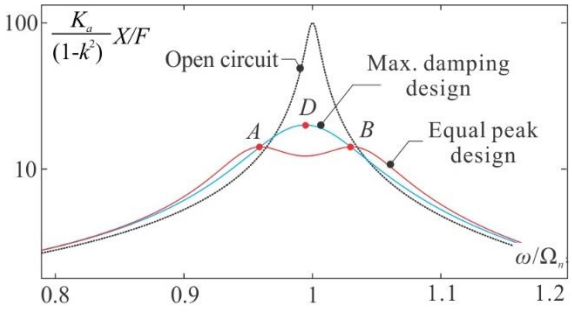

FIGURE 4. FRF of a single degree of freedom piezoelectric system without (black) and with (red and blue) RL shunt tuned to the mechanical resonance.

b) Maximum damping (stability) design

As an alternative, the RL circuit can be tuned to maximize the amount of damping of the targeted mode, and thus, the stability of the system. The optimal tuning of the RL circuit is achieved by choosing the electrical resonance frequency ω_e^* such that:

$$\frac{\omega_i \omega_e^*}{\Omega_i} = 1 \quad \text{or} \quad \frac{\omega_e^*}{\omega_i} = \frac{1}{1-k_c^2} \tag{7}$$

and the electrical damping ζ_e^* as:

$$\zeta_e^* = k_c \tag{8}$$

The above tuning equations merely depend on four measurable parameters: the inherent piezoelectric capacitance C, the resonance frequencies of the targeted mode with open and short-circuited electrodes, Ω_i and ω_i respectively, and the electromechanical coupling factor k_c. Therefore, the aforementioned tuning rules apply directly to any piezoelectric structure, provided these four tuning parameters are available. Note also that for a multi-degree of freedom system, the generalized electromechanical coupling factor K_i, associated with a specific mode i, should be used instead of k_c, which is defined as:

$$K_i^2 = 1 - \frac{\omega_i^2}{\Omega_i^2} \tag{9}$$

This generalized electromechanical coupling factor K_i scales with the electromechanical coupling factor k_c (material part), and the fraction of strain energy ν_i in the transducer (structural part):

$$K_i^2 = \frac{k_c^2}{1-k_c^2}\nu_i \tag{10}$$

Note that the coupling factor k_c is a material property, and depends on three temperature dependant piezoelectric properties: (i) the piezoelectric constant $d_{33}(T)$, (ii) the dielectric constant $\varepsilon_{33}^T(T)$, and (iii) the elastic compliance $s^E(T)$, such that [20]:

$$k_c(T) = \frac{d_{33}(T)}{\sqrt{\varepsilon_{33}^T(T) s^E(T)}} \tag{11}$$

Any change of the environmental temperature will result into a change of the coupling factor k_c, and thus the shunt damping performance.

Finally, for both tuning methods of the electrical circuit, the maximum achievable damping performance scales linearly with the generalized electromechanical coupling factor K_i, and thus, with the piezoelectric material property k_c and with the square root of the modal fraction of strain energy in the piezo, as shown by EQUATION. (10). Next, the sensitivity of the RL shunt damping to temperature change is investigated.

Cryogenic properties

To asssess the damping performance at cryogenic temperatures, the change of the electromechanical coupling factor $k_c(T)$ and fraction of strain energy ν_i need to be assessed. The former is quite straightforward, the latter, however, is more complicated as it depends on the location of the transducer in the structure and the shape of the damped mode.

Compared to room temperature, the electromechanical coupling factor k_c decreases by 13% at 80 K, and 22% at 4 K (see TABLE 2). The effect on the damping performance is expected to be of the same order of magnitude, following from EQUATION. (10). On the other hand, the fraction of strain energy depends on the relative compliance of the piezoelectric transducer in the structure, and thus can be optimized by design. The change in elastic compliance at 80 K of the Ti6Al4V V-frames is -10% according to [19], while the change in elastic compliance of the PZT-5A transducer is about -20%, as shown in TABLE 2. This results in a negligible change of modal density of strain energy ν_i, and thus a negligible effect on the damping performance. Moreover, since the fraction of strain energy or modal density of strain energy is a design parameter, the designer can optimise the mechanical properties and the piezoelectric transducer for specific operating temperatures.

TABLE 2. Electromechanical coupling factor and elastic compliance of multilayer ceramic PZT for various temperatures [20,21].

T	293 K	80 K	4 K
k_c [–]	0.67	0.58	0.52
s^E [$\mu m^2/N$]	18.5/17.1	15/14.3[1]	13.7/9.71[1]

[1] Obtained by interpolation based on [21].

EXPERIMENTAL IMPLEMENTATION

Six piezoelectric transducers are implemented in the demonstrator setup, as part of the outer V-frames, which connect the isolation frame to the vacuum vessel (see FIGURE 5). The cold frame is removed from the test setup. The transducer location is based on the highest fraction of strain energy for the particular vibration modes to be damped. Multilayer ceramic PZT material was chosen based on the coupling factor k_c and availability. The geometry was chosen such that the longitudinal stiffness of the transducer is equal to the V-frame stifness, thereby balancing the fraction of strain energy v_i to the reduction of compliance in the system (in order to conserve the resonance frequencies within an acceptable range). Depending on the application, further optimization might be feasible.

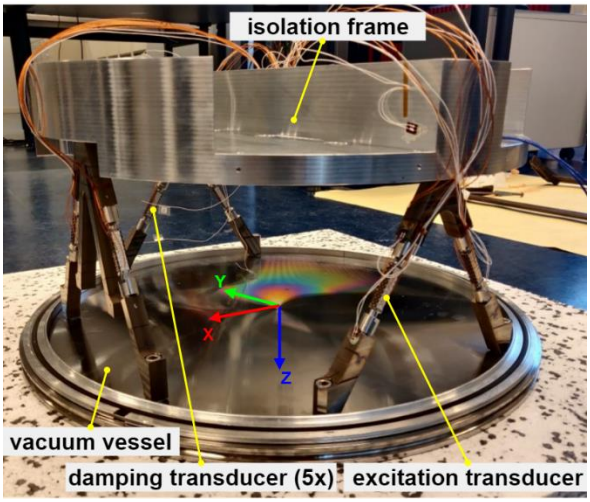

FIGURE 5. Test setup for cryogenic damping experiments with piezoelectric transducers implemented as part of the V-frames that support the isolation frame to the vacuum vessel (only partly visible). The cold frame is removed.

One of the six transducers is used as excitation source (sine sweep). Two accelerometers (PCB 351B41) are used to measure the acceleration of the cold frame in horizontal and vertical direction (X and Z). To facilitate the tuning of the shunt components, a variable synthetic inductor (Antoniou circuit [22]) is used together with a variable resistance. The temperature is measured by thin film resistance temperature detectors (IST p1k0.232.6w) in the V-frame at both sides of the transducers.

The setup is cooled to $77\ \mathrm{K}$ using liquid nitrogen as shown in FIGURE 6. During slowly heating up towards room temperature, the system identification and damping measurements are performed at specific temperatures. A thermal time constant of $< 10\ \mathrm{K/h}$ is realized by enclosing the setup with a $50\ \mathrm{mm}$ layer of thermal isolation.

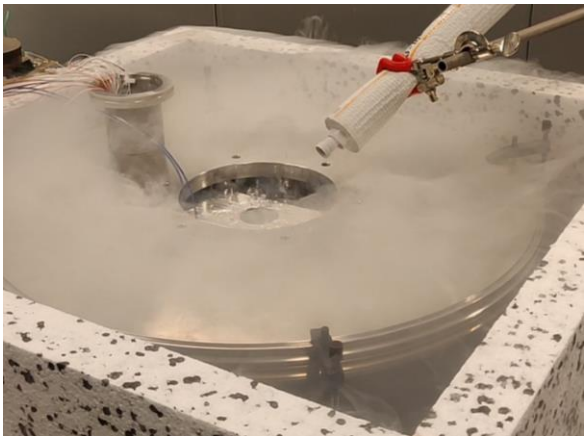

FIGURE 6. Isolated test set up filled up with liquid nitrogen for cooling down to cryogenic temperatures.

For damping a particular mode, the effectiveness of the various piezoelectric transducers is determined beforehand, based on the highest fraction of strain energy via FEA. The main targeted mode is in X- direction (see FIGURE 5) in the range of $150 - 200\ \mathrm{Hz}$.

Shunt damping at room temperature

First, the resonance frequencies of the targeted mode, $\Omega_i = 1013.5\ \mathrm{rad/s}$ and $\omega_i = 994.0\ \mathrm{rad/s}$, are obtained from the measured response with, respectively, open- and short circuited electrodes (of the five available transducers as they act altogether as a single transducer). Then, the generalized electromechanical coupling factor K_i, associated to the targeted mode is obtained from EQUATION. (9), $K_i = 20\%$.

This results in a theoretically maximum obtainable modal damping for the targeted mode, assuming an equal peak design [23], of $\zeta_i = K_i/2 = 10\%$. The inherent modal damping of the open- circuited system is found to be $\zeta_n = 1.2\%$ (the undamped situation); it is calculated from the FRF with open electrodes using the Full Width Half Power method.

Next, the shunt damping is implemented by connecting a RL circuit to the most effective piezoelectric transducer. It is tuned by setting the electrical eigenfrequency ω_e equal to the open-circuited eigenfrequency Ω_i, followed by iteratively tuning the resistance for best

attenuation. The obtained result is shown in FIGURE 7. The damped response has an attenuation of 12.3 dB compared to the open-circuited response, corresponding to a modal damping $\zeta_{att} = 7.5\%$ (for an equivalent 1-DoF system [23]). This value is lower than the maximum obtainable damping because only the most effective transducer is connected, instead of all five available transducers.

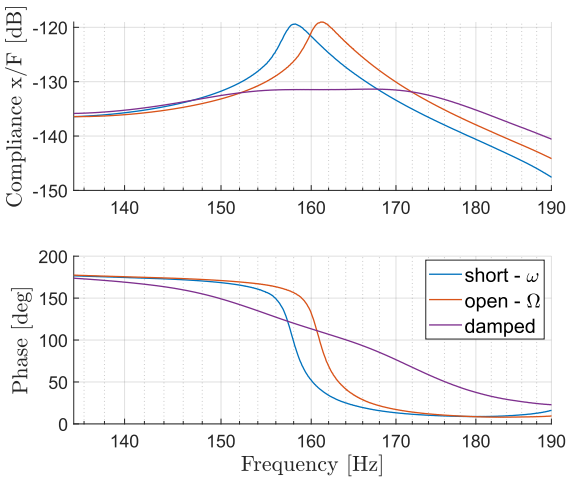

FIGURE 7. Measured FRFs at 293 K for short- and open circuited electrodes (undamped), and with the tuned RL-shunt connected (damped).

Shunt damping at cryogenic temperatures

The experiment is repeated for temperatures in the range of 77 K – 205 K. The generalized coupling factor is shown as a function of temperature in FIGURE 8, while the natural damping and the realized damping are shown in FIGURE 9.

TABLE 3. Measured maximum obtainable modal damping using all 5 transducers, and realized damping based on 1 transducer.

T [K]	ζ_d [%]	ζ_{att} [%]
293	10.2	7.5
200	10.3	7.5
100	9.0	6.6
80	8.5	6.3

The damping values at various temperatures are shown in TABLE 3. A small decrease in piezoelectric damping is observed at 80 K relative to room temperature of only 16.7% for the maximum obtainable damping ζ_d and 16.0% in realized damping ζ_{att}. This is in line with the previously observed decrease of 13% in electromechanical coupling factor k_c.

With a realized damping $\zeta_{att} = 6.3\%$ compared to the natural damping $\zeta_n = 0.6\%$ it is shown that piezoelectric shunt damping is a feasible damping solution at temperatures in the range of 80 K – 293 K.

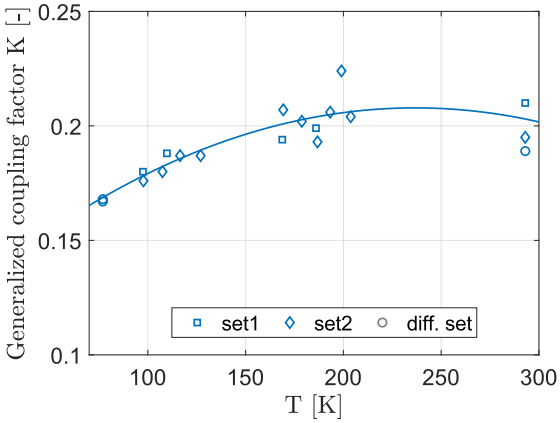

FIGURE 8. Experimental results: Measured generalized coupling factor vs. temperature. Each set represents measurements performed on the same day.

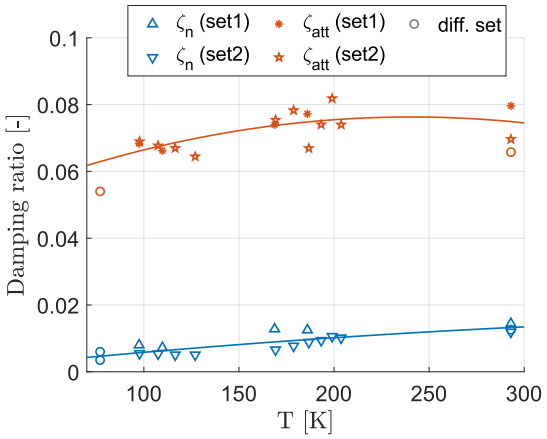

FIGURE 9. Experimental results: Measured piezoelectric damping vs. temperature: inherent modal damping (ζ_n) without shunt, and realized damping with a single transducer (ζ_{att}). Each set represents measurements performed on the same day.

CONCLUSION

In this paper, piezoelectric shunt damping is proven to be a feasible solution to provide passive damping in cryogenic conditions, specifically in a flexure-based superconducting magnet plate support. The piezoelectric properties related to the damping performance slightly decrease with respect to room temperature, in the order of 15%, in line with the similarely small decrease in the

electromechanical coupling factor k_c. By implementing piezoelectric transducers with an optimized resistive inductive RL-shunt in a superconducting magnet plate demonstrator setup, a damping increase from $\zeta_n = 1.4\%$ to $\zeta_{att} = 7.5\%$ at room temperature was found. At $80\ \mathrm{K}$ a damping increase from $\zeta_n = 0.6\%$ to $\zeta_{att} = 6.3\%$ is obtained. It can be concluded that piezoelectric shunt damping provides significant damping at cryogenic temperatures and only has a small decrease in performance compared to room temperature.

Although it was found that eddy current damping cannot provide the required damping performance at $80\ \mathrm{K}$, it is recommended to further study the potential for applications with a different operating frequency/temperature.

REFERENCES

[1] Koolmees, H. B., Bruyn, B. J. H. de, Vermeulen, J. P. M. B., Jansen, J. W., Lomonova, E. A., On the Performance Potential of Superconducting Linear and Planar Motors, Proc. of the 17th EUSPEN International Conference, Hannover, Germany, May 2017.

[2] Koolmees H.B. A superconducting magnet plate: for a planar motor application. PhD Thesis, Eindhoven University of Technology; 2020

[3] Lakes R. S. High Damping Composite Materials : Journal of Composite Materials. 2002; 36(03) :287–97.

[4] Levine M. B., White C., Material damping experiments at cryogenic teamperatures. Proceedings of Optical Materials and Structures Technologies, SPIE's 48th Annual Meeting; 2003 Aug. 4-7; San Diego, California, United States. SPIE, 2003; 5179: 165.

[5] Gunter E. J., Humpris R. R., Design study of magnetic eddy current dampers for application to cryogenic turbo-machinery. University of Virginia; 1983 Dec. Report No.:UVA/528210/MAE84/101, Contractor Report: NASA Grant NAG-3-263.

[6] Cunningham R. E. Passive Eddy-Current Damping As a Means of Vibration Control in Cryogenic Turbomachinery. Lewis Research Center, Cleveland, Ohio. NASA Tech Paper 2562, 1986 Feb.

[7] NASA TechPort. Cryogenic Vibration Damping Mechanisms for Space Telescopes and Interferometers [Internet]. California: Jet Propulsion Laboratory; 2005 Available from: https://techport.nasa.gov/view/5809.

[8] Zheng J., Deng Z., Zhang Y., Wang W., Wang S., Wang J., Performance improvement of high temperature superconducting maglev system by eddy current damper. IEEE Transaction Applied Superconductivity. 2009 Jul; 19(3):2148–51.

[9] Jiang ZF, Gou XF. Eddy damping effect of additional conductors in superconducting levitation systems. Physica C: Superconductivity and its Applications. 2015, Sep.; 519:112–7.

[10] Janssen Precision Engineering. Cryogenic (4K...293K) Material Properties [Internet]. Available from: https:www.jpe-innovations.com/precision-point/cryogenic-material-properties/

[11] Sodano H. A., Bae J. S., Inman D. J., Keith Belvin W., Concept and model of eddy current damper for vibration suppression of a beam. Journal of Sound and Vibration. 2005, Jan.; 288 (4–5):1177–96.

[12] Gripp J. A. B., Rade D. A., Vibration and noise control using shunted piezoelectric transducers: A review. Mechanical Systems and Signal Processing. 2018, Apr.; 112:359–83.

[13] Marakakis K., Tairidis G. K., Koutsianitis P., Stavroulakis G. E., Shunt piezoelectric systems for noise and vibration control: A review. Front Built Environement. 2019, May; 5:64.

[14] Jaffe H., Piezoelectric Ceramics. Journal of American Ceramic Society. 1958, Nov; 41(11): 494–8.

[15] Taylor R. P., Nellis G. F., Klein S. A., Hoch D. W., Fellers J., Roach P., et al. Measurements of the material properties of a laminated piezoelectric stack at cryogenic temperatures. AIP Conference 2006, Mar; 824 (2006): 200–7.

[16] Jiang, X., Cook, W. B., & Hackenberger, W. S. (2009, September). Cryogenic piezoelectric actuators. In *Astronomical and Space Optical Systems* (Vol. 7439, p. 74390Z). International Society for Optics and Photonics.

[17] Asami T., Nishihara O., Baz A. M., Analytical Solutions to H∞ and H2 Optimization of Dynamic Vibration Absorbers Attached to Damped Linear Systems. Journal of Vibration and Acoustics, 2002 Mar; 124(2):284–95.

[18] Soltani P., Kerschen G., Tondreau G., Deraemaeker A., Piezoelectric vibration damping using resonant shunt circuits: an exact solution. Smart Materials and Structtures, 2014; 23(12):125014.

[19] Naimon E. R., Weston W. F., Ledbetter HM. Elastic properties of two titanium alloys at low temperatures. Cryogenics (Guildf). 1974, May; 14(5): 246–9.

[20] Zhang X. L., Chen Z. X., Cross L. E., Schulze W. A., Dielectric and piezoelectric properties of modified lead titanate zirconate ceramics from 4.2 to 300 K. Journal of Material Science, 1983; 18(4): 968–72.

[21] Sabat R. G., Mukherjee B. K., Ren W., Yang G., Temperature dependence of the complete material coefficients matrix of soft and hard doped piezoelectric lead zirconate titanate ceramics. Journal of Applied Physics. 2007, Mar; 101(6).
[22] Antoniou A., Naidu K. S., Modeling of a Gyrator Circuit. IEEE Transaction of Circuit Theory. 1973, Sept; 20(5): 533-40.
[23] Mokrani, B. Piezoelectric Shunt Damping of Rotationally Periodic Structures. Ph.D. Thesis, Universite Libre de Bruxelles, Brussels, Belgium, January 2015.
[24] Ambaum, N., Passive damping for a flexure-based mechanism in cryogenic conditions, M.Sc. Thesis, Eindhoven University of Technology, March 31, 2021

INTELLIGENT ONLINE SCAN SEQUENCE OPTIMIZATION FOR UNIFORM TEMPERATURE DISTRIBUTION IN LASER POWDER BED FUSION

Keval S. Ramani, Chuan He and Chinedum E. Okwudire
Department of Mechanical Engineering
The University of Michigan
Ann Arbor, MI

OVERVIEW

Metal parts produced from laser powder bed fusion (LPBF) suffer from residual stress and deformations due to nonuniform temperature distribution. An intelligent online scan sequence optimization for uniform temperature distribution is explored in this study. The layer in LPBF is subdivided into stripes or islands, and the sequence for laser scanning is determined optimally. The optimization is based on the finite differences method and a control theoretic approach. Preliminary results using a simple stripe scan pattern show that the proposed approach improves temperature uniformity as compared to popular heuristic scan sequences in the literature.

BACKGROUND AND MOTIVATION

LPBF is a type of additive manufacturing process that builds a part layer-by-layer, by using a high-power laser source to melt a spread layer of (metallic) powder on top of the previously printed layers. Although this process enables the fabrication of freeform geometries with near-fully dense microstructure, and intricate features with very fine resolution, it suffers from various dimensional and microstructural defects [1]. Thermal abnormalities predominantly degrade the quality of a fabricated part. Therefore, controlling the thermal evolution of the process is the key factor in diminishing these thermal abnormalities [2].

Scanning strategy, e.g., laser power, scan speed, hatch spacing, scan pattern and scan sequence, are often selected by round-robin testing, trial and error, or heuristics, to control the thermal evolution of the process. Laser power and scan speed are the elements of scanning strategy often controlled online [3]–[5].

One element of scanning strategy that has received relatively little attention is scan sequence. Scan sequence refers to the order in which a specific in-fill pattern is scanned. For example, two of the most commonly used scan patterns in practice are simple stripe and island, shown in Fig. 1. Scan sequence in these examples could mean the order in which each line in the simple stripe pattern is scanned or the order in which each island in the island pattern is scanned. The order in which the islands are scanned affects temperature distribution significantly [6], [7]. To determine optimal scan sequence for island scan patterns, heuristic methods and genetic algorithm are used [8]. However, a major weakness of the heuristic optimization strategies is that they are purely geometric. They do not utilize a thermal model, rather they try to make temperature uniform by maximizing the distance between the exposure-island and previously printed islands. Moreover, to our best knowledge, there has been no attempt to optimize or control scan sequence online using physics-based thermal models combined with real-time measurements of temperature distribution.

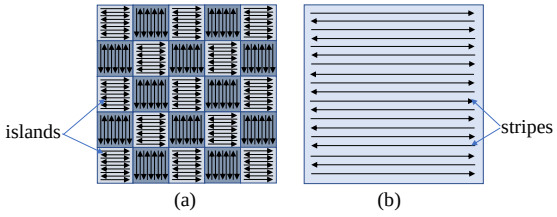

FIGURE 1. Two common scan patterns for a layer in LPBF (a) islands, (b) stripes

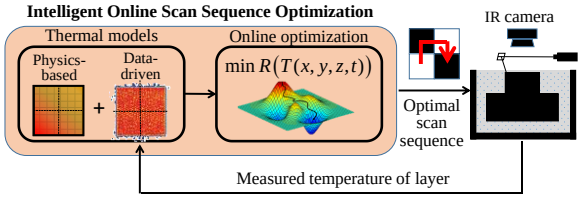

FIGURE 2. Flowchart for the intelligent online scan sequence optimization framework

Our research seeks an intelligent approach that uses physics-based thermal models and feedback from sensors to determine optimal scan sequence online, layer-by-layer [9]. This vision will be achieved in two phases (see Fig. 2):

- Phase I: Physics-based scanning
- Phase II: Physics-based and data-driven scanning

Phase I (see Fig. 2) of this research will focus on developing a physics-based temperature distribution model which can then be used for combinatorial optimization to find an optimal scan sequence. The goal of modelling is to develop a reasonably accurate and computationally efficient thermal model. The goal of Phase II (see Fig. 2) will be to complement the model-based strategy in Phase I with data-driven learning to mitigate the effect of uncertainty, nonlinearity and parameter variation. This study focuses on Phase I of the above vision. The temperature evolution is modelled using the finite difference method (FDM). Based on the temperature model, a computationally efficient optimization based on control theory is used to select a scan sequence that minimizes a thermal uniformity metric.

FINITE DIFFERENCE MODEL

The heat conduction equation can be modeled using FDM as

$$\frac{T(i+1,j,k,l)+T(i-1,j,k,l)-2T(i,j,k,l)}{\Delta x^2}+\frac{T(i,j+1,k,l)+T(i,j-1,k,l)-2T(i,j,k,l)}{\Delta y^2}+\frac{T(i,j,k+1,l)+T(i,j,k-1,l)-2T(i,j,k,l)}{\Delta z^2}+\frac{u(i,j,k,l)}{k_t}=\frac{1}{\alpha}\frac{T(i,j,k,l+1)-T(i,j,k,l)}{\Delta t} \quad (1)$$

where Δx, Δy and Δz are the dimensions of the element cuboid (see Fig. 3), i, j and k are the spatial indices of the elements, l is the temporal index (i.e., $t = l\Delta t$), Δt is the time step and $T(i,j,k,l)$ is the temperature of element located at (i,j,k) at time l. Rearranging (1) gives the state equation

$$\mathbf{T}(l+1)=\mathbf{AT}(l)+\mathbf{Bu}(l) \quad (2)$$

where $\mathbf{T}(l)$ is the state vector comprising of temperatures of all elements at time l, $\mathbf{A}$ is the state matrix, $\mathbf{B}$ is the input matrix and $\mathbf{u}(l)$ denotes the power input to the elements at time l. This study, without loss of generality, assumes that the top and bottom surfaces experience convection (with an ambient temperature T_a, see Fig. 3) and the remaining four faces are insulated (e.g., due to the presence of un-sintered powder around them).

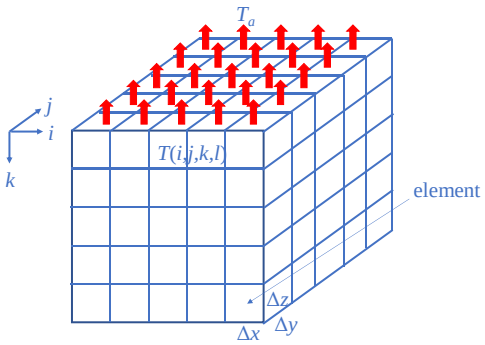

FIGURE 3. Finite difference model

Our FDM model assumes that the laser heat on an element acts at the center of the element. The number of time steps spent on an element can be approximated as

$$n_c \approx \frac{\Delta x}{v_s \Delta t} \quad (3)$$

The corresponding state equation for heating of an element can then be written as

$$\mathbf{T}(l_c+1)=\mathbf{A}_c\mathbf{T}(l_c)+\mathbf{b}_c;\quad \mathbf{A}_c \triangleq \mathbf{A}^{n_c};\ \mathbf{b}_c \triangleq \sum_{m=0}^{n_c-1}\mathbf{A}^m\mathbf{Bu}(m);\ l_c = n_c l \quad (4)$$

Different from Eq. (2), the state-space model of Eq. (4) has a sampling interval of $n_c\Delta t$. Similarly, this idea can be extended to any feature (e.g., stripe or island) of a scan pattern to obtain a feature-level state-space representation given by

$$\mathbf{T}(l_p+1)=\mathbf{A}_p\mathbf{T}(l_p)+\mathbf{b}_p;\quad \mathbf{A}_p \triangleq \mathbf{A}^{n_p};\ \mathbf{b}_p \triangleq \sum_{m=0}^{n_p-1}\mathbf{A}^m\mathbf{Bu}(m);\ l_p = n_p l \quad (5)$$

SCAN SEQUENCE OPTIMIZATION

The thermal history of each feature (stripe or island) of a scan pattern can be computed using Eq. (5) and the feature selector state-space equation can be expressed as

$$\mathbf{T}(l_p+1)=\mathbf{A}_p\mathbf{T}(l_p)+\begin{bmatrix}b_{p1} & b_{p2} & \dots & b_{pm}\end{bmatrix}\begin{bmatrix}u_{p1}\\ u_{p2}\\ \vdots\\ u_{pm}\end{bmatrix} \quad (6)$$

where l_p and $\mathbf{A}_p$ are the equivalent time and state matrix to heat a feature. The vectors b_{p1}, b_{p2}, …, b_{pm} represent the effect of heating features 1, 2, …, m, respectively. The binary variables u_{p1}, u_{p2}, …, u_{pm} are selected to ensure that only one feature is heated at a time, i.e., only one among u_{p1}, u_{p2}, …, u_{pm} is selected to be one and the rest are zero. The selection is done such that at the

end of heating each feature, the following metric is minimized

$$R(l_p) = \sqrt{\frac{\sum_{i,j,k}\left(T\left(i,j,k,l_p\right) - T_{avg}\left(l_p\right)\right)^2}{n_e T_m^2}} \tag{7}$$

where $T_{avg}(l_p)$ is the average temperature of elements $T(i,j,k,l_p)$ at time l_p, n_e is the number of elements and T_m is the melting temperature of the material.

Notice that $R(l_p)$ is a function of state vector $\mathbf{T}(l_p)$ and can be expressed as

$$\begin{aligned} &R(l_p) = \left\|\mathbf{C}_{eq}\mathbf{T}(l_p)\right\|_2; \\ &\mathbf{C}_{eq} = \frac{1}{\sqrt{n_e}T_m}\left[\mathbf{I} - \frac{\mathbf{1}\mathbf{1}^T}{n_e} \quad \mathbf{0}\right] \end{aligned} \tag{8}$$

where $\mathbf{I}$ is the identity matrix, $\mathbf{1}$ is a row vector whose elements are all equal to 1, and $\mathbf{0}$ is null matrix used to account for any elements of $\mathbf{T}(l_p)$ that are not needed to calculate $R(l_p)$ – e.g., T_a. The optimization problem can be formulated as

$$\begin{aligned} &\min_{\mathbf{u}_{eq}(l_p)}\left(R(l_p+1) = \left\|\mathbf{C}_{eq}\mathbf{T}(l_p+1)\right\|_2\right) \\ &\text{s.t.}\ \ \mathbf{T}(l_p+1) = \mathbf{A}_{eq}\mathbf{T}(l_p) + \mathbf{B}_{eq}\mathbf{u}_{eq}(l_p) \end{aligned} \tag{9}$$

where $\mathbf{A}_{eq} = \mathbf{A}_p$, the columns of $\mathbf{B}_{eq}$ represent corresponding vectors $\mathbf{b}_p$ (see Eq. (6)) for each feature and $\mathbf{u}_{eq}(l_p)$ is a vector comprising of only one element equal to 1 and all other elements equal to 0. The location of 1 in $\mathbf{u}_{eq}(l_p)$ represents the column of $\mathbf{B}_{eq}$ and hence the feature to be scanned. The objective of the optimization problem can be written as

$$\begin{aligned} &\left\|\mathbf{C}_{eq}\mathbf{T}(l_p+1)\right\|_2^2 \\ &= \left\|\mathbf{C}_{eq}\mathbf{A}_{eq}\mathbf{T}(l_p) + \mathbf{C}_{eq}\mathbf{B}_{eq}\mathbf{u}_{eq}(l_p)\right\|_2^2 \\ &= \mathbf{u}_{eq}^T(l_p)\mathbf{B}_{eq}^T\mathbf{C}_{eq}^T\mathbf{C}_{eq}\mathbf{B}_{eq}\mathbf{u}_{eq}(l_p) \\ &\quad + 2\mathbf{T}^T(l_p)\mathbf{A}_{eq}^T\mathbf{C}_{eq}^T\mathbf{C}_{eq}\mathbf{B}_{eq}\mathbf{u}_{eq}(l_p) \\ &\quad + \mathbf{T}^T(l_p)\mathbf{A}_{eq}^T\mathbf{C}_{eq}^T\mathbf{C}_{eq}\mathbf{A}_{eq}\mathbf{T}(l_p) \end{aligned} \tag{10}$$

The third term of the summation is independent of $\mathbf{u}_{eq}(l_p)$, thus does not affect the optimization. The vector $\mathbf{u}_{eq}(l_p)$ has one element equal to 1 and all others equal to 0 which results in only the diagonal terms of $\mathbf{B}_{eq}^T\mathbf{C}_{eq}^T\mathbf{C}_{eq}\mathbf{B}_{eq}$ affecting the summation. Hence, the optimization problem can be formulated as

$$\begin{aligned} &\min_i \lambda_i \\ &\text{s.t.}\ \ \boldsymbol{\lambda} = \underbrace{diag(\mathbf{B}_{eq}^T\mathbf{C}_{eq}^T\mathbf{C}_{eq}\mathbf{B}_{eq})}_{\boldsymbol{\Gamma}} \\ &\qquad + \underbrace{2\mathbf{B}_{eq}^T\mathbf{C}_{eq}^T\mathbf{C}_{eq}\mathbf{A}_{eq}}_{\boldsymbol{\Lambda}}\mathbf{T}(l_p) \end{aligned} \tag{11}$$

where λ_i are elements of $\boldsymbol{\lambda}$. Since $\boldsymbol{\Gamma}$ and $\boldsymbol{\Lambda}$ are known a priori, they can be pre-computed offline.

Starting from time l_p = 0 with known $\mathbf{T}(0)$, determining the optimal scan sequence at any given time step l_p is as follows: (i) calculate the vector $\boldsymbol{\lambda}$ from Eq. (11) and determine the index i corresponding to its smallest element; (ii) select the optimal feature at time l_p that minimizes $R(l_p+1)$ by entering 1 as the element of $\mathbf{u}_{eq}(l_p)$ corresponding to index i; (iii) calculate the optimal thermal distribution $\mathbf{T}(l_p+1)$ using the state equation in Eq. (5); (iv) advance to time l_p+1 and repeat the process from (i).

SIMULATION RESULTS

For this case study, an area of 5.0 cm by 5.0 cm is scanned in the middle of a plate with a length of 7.6 cm, a width of 7.6 cm and a thickness of 1.0 mm. The area to be scanned is divided into 250 bidirectional stripes. The parameters for the thermal model are $\Delta x = \Delta y = 200\ \mu$m (a stripe comprises of 250 elements), k_t = 24 W/mK, α = 6.689×10^{-6} m^2/s, T_m = 1928 K, v_s = 0.6 m/s and Δt = 0.333 ms. The laser power and initial temperature are 200 W and 293 K, respectively. There is no heat transfer across the *xz* and *yz* planes on the sides of the plate, whereas the top and bottom *xy* planes experience convection with h = 20W/m^{2}K to the ambient environment, assumed to be at a constant temperature of T_a = 293 K. Along the *z*-axis, two layers are considered. The first layer (the layer being heated) has a thickness of 200 μm and the second layer has a thickness of 800 μm.

Figure 4 shows the temperature uniformity metric defined in Eq. (7) as a function of the number of stripes scanned. The proposed optimal scan sequence shown in Figure 5, performs much better than sequential (1,2,3,...,250), alternate (1,3,5,...249,2,4,...,250) and out-to-in (1,250,2,249,...125,126) approaches. The proposed approach improves the mean value of R by 3.3, 2.1 and 2.2 times, as compared to the sequential, alternate and out-to-in approaches, respectively. Also, the proposed approach improves the standard deviation of R by 1.8, 1.1 and 1.3 times, as compared to the sequential, alternate and out-to-in approaches, respectively. This fact is confirmed by Figure 6 which shows the thermal distribution of four approaches at four instances- after 62, 124, 186 and 250 stripes are scanned. It takes 2 seconds for online computation of the optimal scan sequences, using radial basis functions to simplify the computations.

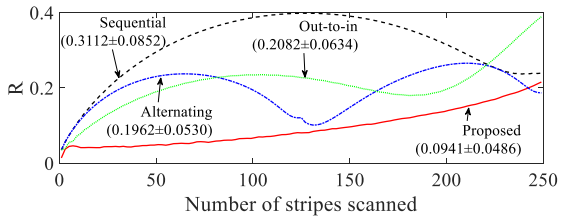

FIGURE 4. Thermal uniformity metric (*R*) for different scan sequences as a function of number of stripes scanned. The numbers in parenthesis show the mean ± standard deviation of R for each scan sequence.

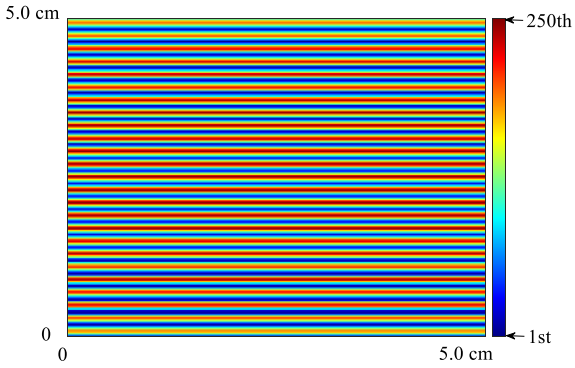

FIGURE 5. Pictorial depiction of proposed optimal scan sequence; the shade of color of each stripe indicates the order in which it is scanned.

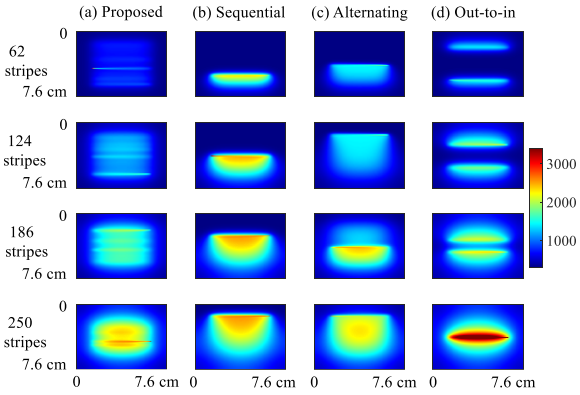

FIGURE 6. Temperature distribution at four instances during the scanning process. The temperatures denoted by the color bars are in Kelvin

The temperature values shown in Fig. 6 are higher than realistic values because of several assumptions made while formulating the FDM model. For example, neglecting latent heat, assuming the laser is a point source, material properties such as conductivity and diffusivity are constant, etc. Future research shall focus on an FDM model and optimization approach without using these assumptions.

CONCLUSION

The LPBF AM process is gaining popularity for producing metallic parts. However, the quality of LPBF parts deteriorates significantly if the temperature evolution is non-uniform. Hence, a lot of research has focused on monitoring and control of the temperature field.

Optimization of the scan sequence has received very little attention in the literature. This study focuses on a control theoretic approach for achieving intelligent online scan sequence optimization. A linear state-space thermal model of the LPBF process is formulated using the finite difference method. Using optimal control theory, the next feature (island or stripe) to be scanned in the sequence is determined such that a temperature uniformity metric is minimized at the end of scanning the feature. This greedy optimization process is repeated till all features in the layer are scanned.

The current model assumes that the laser source is concentrated at a point and the material properties such as conductivity and diffusivity do not vary with location or temperature. Also, the effect of latent heat is not considered. Future work will focus on incorporating these effects in the model and optimizing the scan sequence. The developed approach will be implemented experimentally on a PANDA 11 open-architecture LPBF machine available at the University of Michigan [9].

REFERENCES

[1] A. Bauereiss, T. Scharowsky, and C. Korner, “Defect Generation and Propagation Mechanism during Additive Manufacturing by Selective Beam Melting,” *J. Mater. Process. Technol.*, vol. 214, no. 11, pp. 2522–2528, 2014.

[2] G. Tapia and A. Elwany, “A Review on Process Monitoring and Control in Metal-based Additive Manufacturing,” *J. Manuf. Sci. Eng.*, vol. 136, no. 6, 2014.

[3] J.-P. Kruth, J. Duflou, P. Mercelis, J. Van Vaerenbergh, T. Craeghs, and J. De Keuster, “On-line Monitoring and Process Control in Selective Laser Melting and Laser Cutting,” in *Proceedings of the 5th Lane Conference, Laser Assisted Net Shape Engineering*, 2007, pp. 23–37.

[4] S. Berumen, F. Bechmann, S. Lindner, J.-P. Kruth, and T. Craeghs, “Quality Control of Laser-and Powder Bed-based Additive Manufacturing (AM) Technologies,” *Phys.*

Procedia, vol. 5, pp. 617–622, 2010.

[5] X. Wang, C. S. Lough, D. A. Bristow, R. G. Landers, and E. C. Kinzel, “A Layer-to-layer Control-Oriented Model for Selective Laser Melting,” in *2020 American Control Conference (ACC)*, 2020, pp. 481–486.

[6] C. Li, C. Fu, Y. Guo, and F. Fang, “A Multiscale Modeling Approach for Fast Prediction of Part Distortion in Selective Laser Melting,” *J. Mater. Process. Technol.*, vol. 229, pp. 703--712, 2016.

[7] L. Mugwagwa, D. Dimitrov, S. Matope, and I. Yadroitsev, “Evaluation of the Impact of Scanning Strategies on Residual Stresses in Selective Laser Melting,” *Int. J. Adv. Manuf. Technol.*, vol. 102, no. 5–8, pp. 2441–2450, 2019.

[8] E. Malekipour, “Innovative Tessellation Algorithm for Generating More Uniform Temperature Distribution in the Powder-bed Fusion Process,” *Master’s Thesis Purdue Univ.*, 2018.

[9] K. S. Ramani, E. Malekipour, and C. E. Okwudire, “Toward Intelligent Online Scan Sequence Optimization for Uniform Temperature Distribution in LPBF Additive Manufacturing,” in *Proceedings of the MSEC 2021 Manufacturing Science and Engineering Conference*, 2021.

THERMAL ERROR COMPENSATION FOR LARGE MACHINE TOOLS

Beñat Iñigo[1], Natalia Colinas-Armijo[1], Luis N. López de Lacalle[2] and Gorka Aguirre[1]
[1]Design and Precision Engineering
IDEKO
Elgoibar, Basque Country, Spain
[2]Department of Mechanical Engineering
EHU-UPV
Bilbao, Basque Country, Spain

INTRODUCTION

Thermal errors represent one of the main error sources regarding the volumetric accuracy of machine tools. Thermal error compensation is a relatively low-cost solution to improve the accuracy of machine tools by estimating in real time the instantaneous error and compensating it in the control of the machine.

A large amount of research efforts have been focused on developing robust and effective compensation solutions [1]. Most of the efforts have been focused on the effect of localized heat sources (e.g. spindle bearings), but distributed effects, such as the variation of the ambient temperature on large structural components, have received much less attention.

Temperature sensors are usually located next to the heat sources for an indirect estimation of the generated heat. This is a valid approach for localized heat sources but distributed effects can be more complex, as no clear heat source may be located. This aspect becomes more important in large machine tools, where the effect of the ambient variations can be comparable to those generated by local heat sources. A wide variety of methods have been proposed to address the challenge of optimal sensor positioning. Some methods are based on statistical analysis of the measured temperatures, clustering signals according to different criteria [2], while others are based on system information provided by simulations models [3], but again, criteria adapted to distributed thermal effects are needed.

A thermal error compensation solution for local and distributed thermal effects in large machine tools is proposed. Temperature sensor positioning and identification of the compensation model will be carried out by Proper Orthogonal Decomposition (POD) based reduction and stablished optimal sensor placement procedures. A milling machine column is taken as a case study and the compensation model is validated with additional simulations. Finally, an intuitive approach is described based on a graphic interpretation of the sensor placement procedure.

OPTIMAL SENSOR PLACEMENT FOR POD BASED COMPENSATION MODEL

The goal of Model order reduction (MOR) applied to thermomechanical systems is to obtain a modal basis $\boldsymbol{\Phi}$ so that the relevant information of the system, in this case the temperature field, can be described by few dominant modes

$$\boldsymbol{T} \approx \boldsymbol{\Phi} \cdot \hat{\boldsymbol{T}} \quad (1)$$

where $\boldsymbol{T}$ represents the temperature field and $\hat{\boldsymbol{T}}$ represents the coefficients multiplying each mode at a given instant. The goal of optimal sensor placement procedures is to select a few number of nodes/sensors ($\boldsymbol{T_s}(t)$) that can successfully estimate the coefficients $\hat{\boldsymbol{T}}(t)$ at each moment.

$$\hat{\boldsymbol{T}} = \boldsymbol{A} \cdot \boldsymbol{T}_s \quad (2)$$

Once the temperature field has been estimated, the deformation field can be calculated using the thermoelastic coupling matrix to compensate displacement at any given point.

Proper orthogonal decomposition

Proper Orthogonal Decomposition is a MOR technique where a reduced modal basis is obtained, so that the relevant information of a large system of order n can be captured by a few r dominant modes ($r << n$).
POD relies on the reduction of the system

outcome instead of the system itself. For the case of thermomechanical systems, the goal is to reduce a matrix formed by sequential vector results at different time instants (t_1 to t_p) with the temperature field information $\boldsymbol{T}(t)$. These vectors are called snapshots, obtained from either simulations or experimental measurements, and they form the snapshot matrix $\boldsymbol{T}$ of nxp dimension describing the evolution of the thermal field:

$$\boldsymbol{T} = [\, \boldsymbol{T}(t_1)\ \boldsymbol{T}(t_2)\ \ \ldots\ \boldsymbol{T}(t_p)\,] \tag{3}$$

An orthonormal basis can be obtained applying the singular value decomposition to matrix $\boldsymbol{T}$:

$$\boldsymbol{T} = \boldsymbol{U} \cdot \boldsymbol{S} \cdot \boldsymbol{V}^* \tag{4}$$

In eq. (4) the matrix $\boldsymbol{U}$ of dimension nxn is an orthonormal basis that describes the spatial variation of the thermal field according to each mode. The matrix $\boldsymbol{S}$ contains the singular values λ, ordered from highest to lowest, and thus, hierarchically classifying the modes from the most to the least dominant. By selecting the first r dominant modes, the reduced modal base $\boldsymbol{\Phi}_{nxr}$ is obtained from the first r columns of $\boldsymbol{U}_{nxn}$ matrix. This reduced basis can be used to obtain a compensation model by selecting a subset n_s of nodes/sensors where the temperature will be registered at each new time step [4]. Thermal field is then estimated according to equations (1) and (2).

Optimal sensor selection

Several techniques have been proposed to optimally select the subset of nodes n_s to be measured [5]. According to [6] these techniques can be classified in three categories regarding to the sequence of the placement strategy: backward, forward and simultaneous strategies. In this work a backward and a forward strategy are compared, described in [7,8] and [6] respectively.

In order to obtain the transformation matrix A (see eq. (2)), which describes how the selected nodes and modes are related, a least square problem is inferred from eq. (1). Instead of the full vector $\boldsymbol{T}_{[nx1]}$, only the measured temperatures $\boldsymbol{T}_{s\,[nsx1]}$ are considered, with the corresponding rows of the modal basis $\boldsymbol{\Phi}_{s\,[nsxr]}$. Equation (5) is solved by least squares minimization, as shown in eq. (6):

$$\boldsymbol{T}_s = \boldsymbol{\Phi}_s \cdot \widehat{\boldsymbol{T}} \tag{5}$$

$$\widehat{\boldsymbol{T}} = (\boldsymbol{\Phi}_s{}^T \boldsymbol{\Phi}_s)^{-1} \boldsymbol{\Phi}_s{}^T \cdot \boldsymbol{T}_s \tag{6}$$

To ensure that the solution of eq. (6) is unique, i.e. $\boldsymbol{\Phi}_s$ has full rank, the number of nodes needs to (at least) match the number of modes that want to be inferred ($s \geq r$).

In the forward technique, nodes are selected in sequential order so that in each step the trace of the covariance matrix from (6) is minimized.

$$min\ \ trace((\boldsymbol{\Phi}_s{}^T \boldsymbol{\Phi}_s)^{-1}) \tag{7}$$

From 1 to r nodes/modes, one node is selected at each iteration, as the ones already selected remain fixed. This means that at step j, j-1 sensors are already fixed. The combinations between the fixed nodes and each of the remaining are evaluated and the one with the minimum covariance is selected. Therefore, the selection of the nodes on previous steps will condition the selection of the following ones. As $s \geq r$ condition must be fulfilled, only the first j modes are considered in each step.

In the backward strategy, the selection starts with the whole subset of nodes and one of them is eliminated at each step. The method of effective independence (EI) proposed by [5] is adopted in this case. The method consists on computing the following matrix:

$$\boldsymbol{E} = \boldsymbol{\Phi}_{ns0xm} \boldsymbol{F}^{-1} \boldsymbol{\Phi}_{s0xm}{}^T \tag{8}$$

where F is the Fisher Information Matrix (FIM)

$$\boldsymbol{F} = \boldsymbol{\Phi}_{s0xm}{}^T \cdot \boldsymbol{\Phi}_{ns0xm} \tag{9}$$

Each diagonal element of E represents the fractional contribution of the corresponding node to the orthogonality of the modal basis, and therefore the one with lowest value is eliminated from the node set. The elimination procedure is repeated until s nodes are left.

When the number of nodes s is relatively low, the forward approach is faster, as only s steps are need, while in the backward approach s_0-s nodes must be eliminated. However, the backward approach allows to consider the information of all r modes when evaluating the EI, while the forward approach can only consider the first j modes.

COLUMN MODEL

A finite element model of a milling machine column is used as a case study. The model is shown in FIGURE 1FIGURE 1. All relevant parameters of the FE model are summarized in TABLE 1.

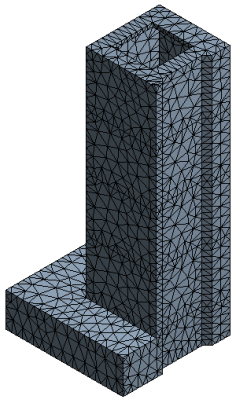

FIGURE 1. FE model of the column.

TABLE 1. FE model properties

Property	Value	Units
Nodes	16764	
Elements	8316	
Material	Structural Steel	
Thermal Conductivity	60.5	W / m·ºC
Specific Heat	434	J / kg·ºC

LOAD CASES

Two local heat sources are defined in the lower and upper opposite sides of the column and all the external surfaces exchange heat by convection with the varying environment. Local heat sources represent typical heat loads on a milling machine with possible origins in heat generated by ball screws or the main spindles. In order to obtain and validate the compensation model two different simulation are defined. Transient thermomechanical simulations are carried out under following conditions:

- Training load case: The local heat sources are introduced as steps of 300W and 200W respectively, at different time intervals. The ambient temperature variation consist on a sine with ±2ºC and 24h period.

- Testing load case: The local heat sources location remains unchanged, but steps are randomly varied every 0.5h between 0, 25, 50, 75 and 100% of their maximum amplitude. Environment variation consist on a sine of ±3ºC and 24h period with 4h delay with respect to the training cycle.

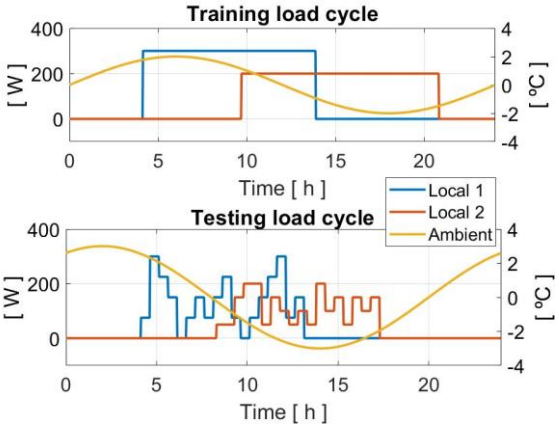

FIGURE 2. Training and testing load cycles for model identification and validation.

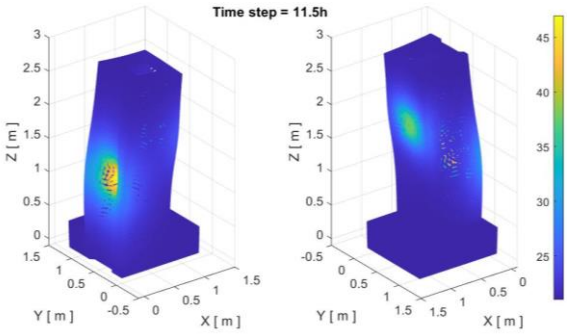

FIGURE 3. Snapshot of the training load cycle at time 11.5h. Temperature is represented by color map. Deformation amplified by 1000X. Front (left) and back (right) views are shown.

Load cycles are shown in FIGURE 2. FIGURE 3 shows thermal field and deformation at a specific time step.

COMPENSATION MODEL/RESULTS

In this section the training load case defined in the previous section will be used to obtain the compensation model, applying POD and optimal sensor placement procedures described in previous sections. Then, the compensation model will be applied in the testing load cycle to evaluate the prediction capability of the model.

The snapshot matrix of temperatures, described in eq. (3), is obtained from the simulation of the training load cycle. The matrix is reduced according to the process described in previous sections, so that the majority of the information

can be captured with few dominant modes. Increasing the number of modes will improve the temperature estimation, and thus, the predicted deformation, but requires more nodes to be measured, as the number must be at least equal to the number of modes. Considering a realistic number of temperature sensors that can be placed in a real machine, selection of the first 2 to 10 modes are analyzed, with the corresponding 2 to 10 node selection.

Temperature field is obtained from the temperature measurements of the selected nodes (see equations (1) and (2)) and the deformation field is calculated using the thermoelastic coupling matrix. In order to test the validity of the resulting compensation model, simulated and estimated displacements are compared. FIGURE 4 shows the rms of the residual error for every node from 2 to 10 modes/nodes.

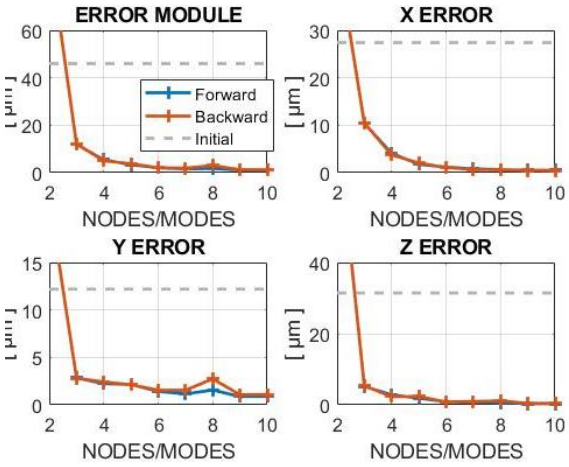

FIGURE 4. Error RMS from 2 to 10 nodes/modes for forward (blue) and backward (red) node selection.

As it can be observed, the compensation model is not capable to predict the error with only 2 modes and nodes, where the error after compensation is bigger than the initial value. From 3 modes/nodes on, the prediction is more accurate, and converges rapidly. After 6 modes, the improvement on adding successive nodes is almost negligible. The error module with 3 nodes is reduced to a 26% of the initial value. With 6 and 10 nodes, this value is reduced to 4.5% and 3% respectively. FIGURE 5 shows the error over 24h test load case of a single node, where model prediction can be observed for different number of nodes.

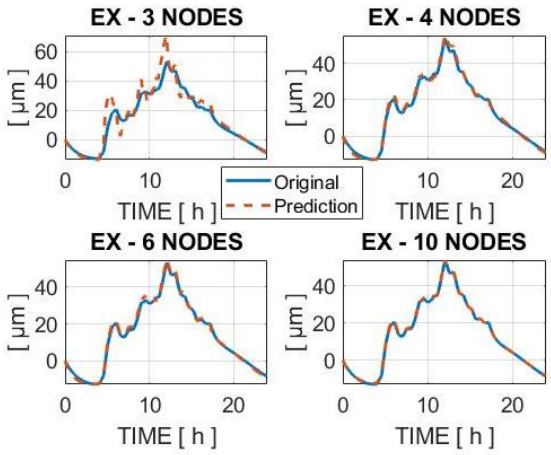

FIGURE 5. Original error (blue) and predicted (red) in X direction of a node for different number of modes/nodes.

The backward and forward method leads to very similar results. FIGURE 6 and FIGURE 7 show the node selection for the forward and backward methods respectively.

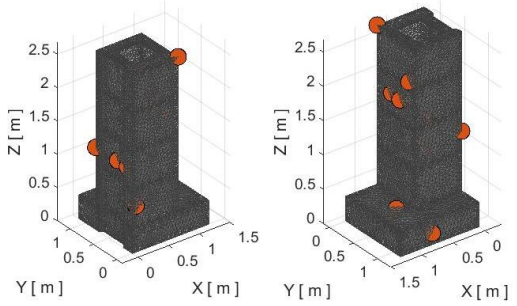

FIGURE 6. Forward selection for 10 number of modes/nodes.

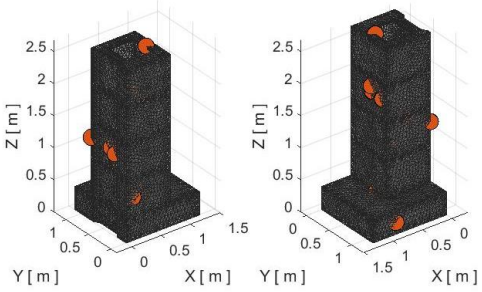

FIGURE 7. Backward selection for 10 number of modes/nodes.

Node selection varies slightly between them, but they are still located in similar zones with respect to the influence of the thermal loads. In both cases, 2 or 3 sensors are located next to the local heat areas, as the others show a more disperse setup, where the ambient temperature

can be captured without much of the local heat influences.

According to the results and the characteristics of the training and testing load cycles, can be said that once the model is fed up with sufficient thermal modes and nodes, it shows a good behavior against load frequency, relative amplitude and relative phase changes.

ROBUSTNESS ANALYSIS

In this section an intuitive and visual approach is presented to provide a better understanding of the underlying process of node selection, on both backward and forward methods, and evaluate how sensible the compensation model is to a sensor misplacement comparing to the automatic selection shown in FIGURE 6 and FIGURE 7.

Graphic representation of forward node selection is shown in *FIGURE 8* for the first 6 steps. At each step nodes are colored according to the metric described in eq. (7), where white zones represent lower values, and therefore, nodes more likely to be chosen. As in previous section the nodes were automatically selected (the one with the minimum value), the graphic approach shows a whole zone with nodes with a similar score. As expected, in the first 2 steps the highlighted zones roughly correspond to the application area of the local loads 1 and 2 respectively. The third one shows areas far away of their influence, where ambient temperature variation can be properly captured. Steps 3 and 4 show a secondary ring-shaped area around local heats. From step 5 on, areas around local loads alternate with ones under environmental influence.

To validate this approach, a manual/graphic node selection is carried out, selecting the nodes directly from the plots shown in *FIGURE 8*, according to the user visual criteria. Error comparison from 2 to 10 nodes is shown in FIGURE 9, comparing automatic and manual forward selection. Distances between manually selected nodes and the automatic ones has varied 270mm in average, showing that variety of nearly optimal sensor location are plausible as long as they are located in previously mentioned areas. Very similar results are obtained.

A similar approach has been taken with the backward modal selection. This time nodes are eliminated according to the metric in eq. (8) while the elimination process is shown to the user at each step.

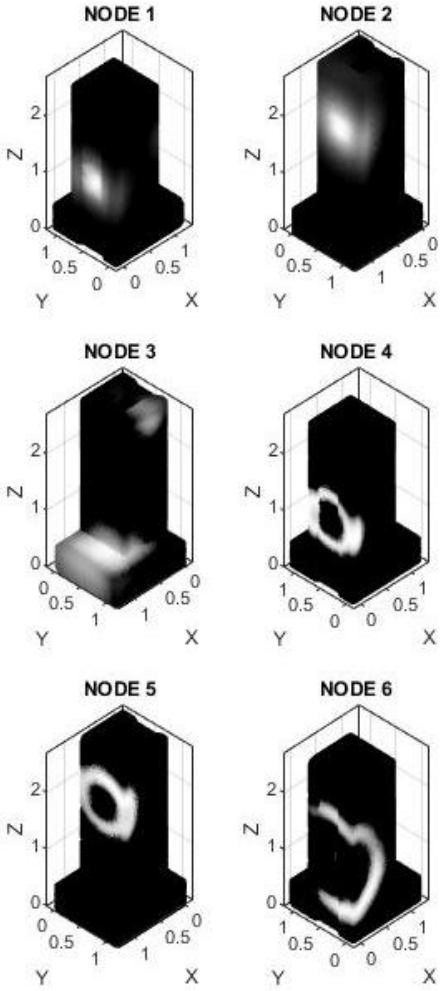

FIGURE 8. Graphic representation of the forward node selection for the first 8 steps. White color represents the zones with the best score according to eq. 7.

After enough nodes have been eliminated (e.g. 90%) remaining areas can be identified as optimal zones where the nodes should be placed. In FIGURE 10 backward elimination step is shown after 10300 out of 11500 nodes have been discarded. Nodes in local load areas still remains, as well as an are similar to the step 3 in forward selection, influenced by the environment. Part of the rings around local heat areas (similar to step 4 and 5 in forward) can also be appreciated. Node selection is validated comparing it to the automatic backward selection, where similar results are achieved.

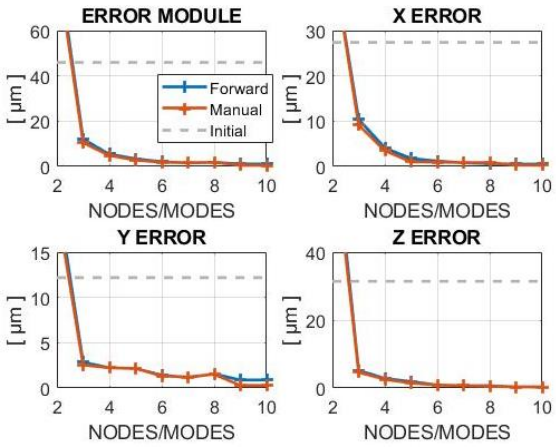

FIGURE 9. Error RMS from 2 to 10 nodes/modes for forward (blue) and backward (red) node selection.

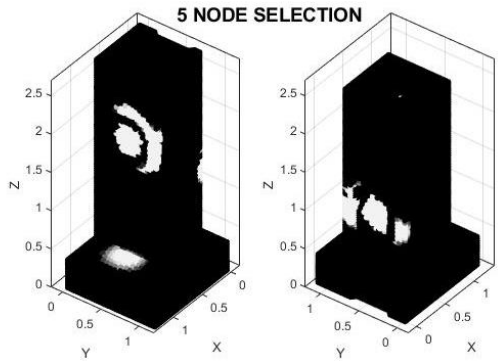

FIGURE 10. Graphic representation of backward elimination method for 5 node locations. Eliminated nodes are represented in black, remaining nodes in white/grey.

CONCLUSIONS

POD model order reduction technique and optimal sensor placement algorithms have been applied to a large machine tool component under local and environmental loads. The compensation model has shown good prediction capacity under relative load changes in amplitude, phase and frequency. The results suggest that this methodology has great potential as a compensation strategy in real machine tool components when the main thermal sources are known. Backward and forward selection strategies have shown very similar results with no substantial differences.

Graphic interpretation of the selection process shows that both methods reach to a similar optimal areas where the sensors should be placed. Graphic representation can help to understand the selection process and visualize optimal zones in a more general way. This provides a useful tool to evaluate the cost/benefit of adding an extra sensor or changing location of an actual one due to other practical restrictions.

REFERENCES

[1] Mareš M, Horejš O, Havlík L. Thermal error compensation of a 5-axis machine tool using indigenous temperature sensors and CNC integrated Python code validated with a machined test piece. Precision Engineering. 2020 Nov; 66: p. 21–30.

[2] Yoganathan D, Kondepudi S, Kalluri B, Manthapuri S. Optimal sensor placement strategy for office buildings using clustering algorithms. Energy and Buildings. 2018 Jan; 158: p. 1206–1225.

[3] Koevoets AH, Eggink HJ, van der Sanden J, Dekkers J, Ruijl TAM. Optimal sensor configuring techniques for the compensation of thermo-elastic deformations in high-precision systems. In 2007 13th International Workshop on Thermal Investigation of ICs and Systems (THERMINIC); 2007 Sep. p. 208–213.

[4] Antoulas AC, Sorensen D. Aproximation of Large-Scale Dynamical Systems: An Overview. International Journal of Applied Mathematics and Computer Science. 2001 Oct; 11.

[5] Kammer DC. Sensor placement for on-orbit modal identification and correlation of large space structures. Journal of Guidance, Control, and Dynamics. 1991 Mar; 14: p. 251–259.

[6] Benner P, Herzog R, Lang N, Riedel I, Saak J. Comparison of model order reduction methods for optimal sensor placement for thermo-elastic models. Engineering Optimization. 2019 Mar; 51: p. 465–483.

[7] Liu K, Yan RJ, Guedes Soares C. Optimal sensor placement and assessment for modal identification. Ocean Engineering. 2018 Oct; 165: p. 209–220.

[8] Colinas-Armijo N, Iñigo B, Lacalle L, Aguirre G. Optimal temperature sensor placement for error compensation of distributed thermal effects. In International Conference on Thermal Issues in Machine Tools; 2021 Apr.

MAGNETICALLY LEVITATED XYZ PRECISION SAMPLE STAGE FOR NEXT-GENERATION X-RAY MICROSCOPY

Ian Heyman, Malek Ibrahim, Lei Zhou
Walker Department of Mechanical Engineering
University of Texas at Austin, TX, USA

INTRODUCTION

Micro/nano-positioning is a key enabling technical capability for a variety of applications such as MEMS inspection, wafer scanning, micro-/nano-machining and additive manufacturing, and scanning probe microscopes. One example application of nanopositioning stages is the X-ray microscope system, such as the VelociProbe [1], which has excellent positioning accuracy and vibration isolation. In the next generation APS-U PtychoProbe scanning system, larger samples need to be accommodated and improved scanning speeds are required, as shown in Table 1 and Figure 1. This demand for extreme positioning performance with long motion stroke in all translational degrees of freedom (DOFs) necessitates innovation in the design and development of precision motion solutions.

Through the years, a number of studies have investigated different designs of precision motion stages, which can be categorized into four groups according to their bearing mechanisms: roller element bearing stages [2, 3], air bearing stages [4, 5], flexure stages [6, 7], and magnetically-levitated (maglev) stages [8, 9]. However, almost all prior stage designs have limitations that can obstruct their performance as a sample stage in next-generation microscopes. Roller element bearing stages are robust and low-cost, however they typically suffer from stick-slip friction which can limit their precision. Air bearing stages eliminate mechanical friction and have excellent performance, however they cannot operate in vacuum. Flexure stages use compliant mechanisms to achieve frictionless motion and have demonstrated excellent performance in nanopositioning systems, however they typically have limited motion range and tend to consume relatively large system volume to achieve compliance in multiple DOFs. Maglev stages have advantages including excellent motion performance, long motion stroke, vacuum compatibility, and compact packaging, which makes them promising for the target application. However, prior designs of maglev stages typically aim at long-stroke planar motion, and most cannot provide sufficient travel range in all DOFs. This motivates new design of maglev stages that can satisfy the requirements shown in Table 1, thereby enabling next-gen X-ray probes with unprecedented scanning speed and accuracy.

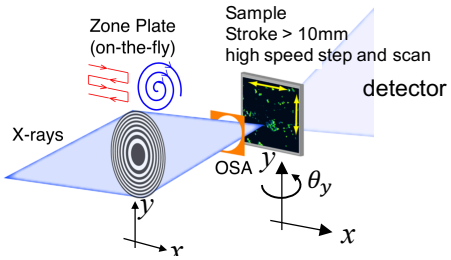

FIGURE 1. Diagram of the motion system in an X-ray microscope. Figure from [1].

TABLE 1. Sample stage motion performance requirement between Velociprobe [1] and the next-generation PtychoProbe.

Specification	Velociprobe [1]	PtychoProbe
Motion Range	15 µm in XYZ	10 mm in XYZ
Stage Speed	–	7 mm/s
Position Accuracy	2 nm in XY	1.25 nm in XY
In-vacuum	No	Yes

This paper presents the design and prototyping for a novel long-stroke, high-speed XYZ maglev precision positioning stage. Our proposed stage presents a magnetic design with a stator which generates uniform magnetic field in a large air gap of around 10 mm, and uses Lorentz force for active control of magnetic levitation and motion. Such a magnetic design can provide uniform force generation over long-stroke displacement, which simplifies the controller design needed to achieve high motion performance. We have constructed a prototype maglev stage according to the design. Finite element (FE) simulation results validate the proposed stage design.

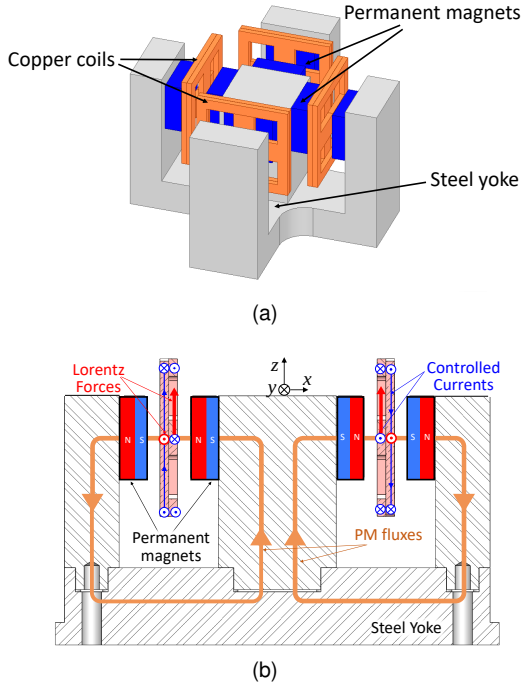

FIGURE 2. Operating principle of the proposed long-stroke Lorentz-force magnetically-levitated XYZ precision positioning stage. (a) Concept diagram. (b) Cross-section diagram of magnetic design.

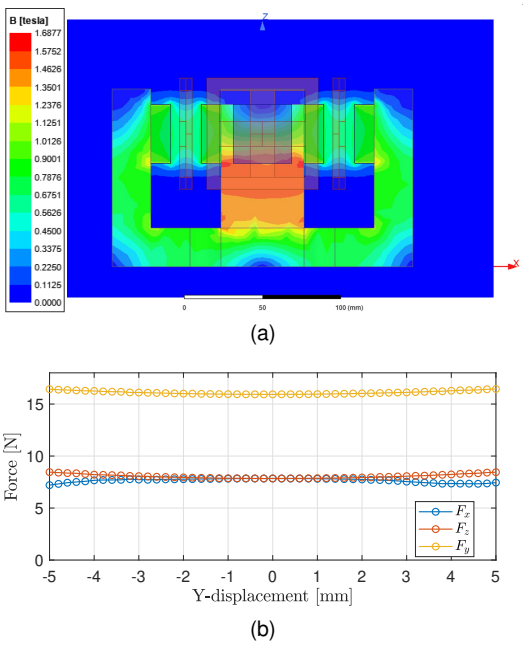

FIGURE 3. (a) Flux density distribution simulated by magnetic finite element method. (b) Simulated forces as stage moves over 10 mm. Uniformity within 10%.

OPERATING PRINCIPLE

Figure 2 shows the operating principle of our proposed maglev sample stage design. Fig. 2a shows a concept diagram, and Fig. 2b shows a cross-section diagram of the stage's magnetic structure including the magnetic fluxes and force generations. The proposed stage is mainly comprised of a stator and a moving stage. The stator consists of a steel yoke and 8 permanent magnets (PMs) magnetized in the radial direction. With the magnetic design shown in Fig. 2b, the stator forms a largely uniform magnetic field in the air gaps. The moving stage consists of 8 coils excited by independently controlled currents. When the coils are energized with these controlled currents, Lorentz forces can be generated to the stage which actively stabilize the stage's magnetic suspension in all 6 DOFs and enable long-stroke motion in the 3 translational DOFs.

MODELING AND SIMULATIONS

This section presents the analytical models and numerical simulations that we have created to predict the stage's performance.

Analytical Modeling: We assume that the air gap magnetic fluxes generated by the stator are uniform with a magnitude of B_g, and only the center branch of the coils is contributing to the force generation. The number of turns of each coil is N, and the length of the magnet is l_m. Then the k-directional Lorentz force generated on the coil at j position on the stage can be calculated as

$$F_k^j = NB_g l_m i_k^j,$$

where F_k^j is the Lorentz force in the k-direction generated by coil at j position, i_k^j is the current that generates F_k^j, $j = \pm x$ or $\pm y$, and $k = x, y, z$. We also define T_{k0} as the k-directional torque imposed on the stage in the centered position.

The total forces and torques on the moving stage can then be calculated as

$$\sum F_x = F_x^{+y} + F_x^{-y},$$
$$\sum F_y = F_y^{+x} + F_y^{-x},$$
$$\sum F_z = F_z^{+x} + F_z^{-y} + F_z^{+x} + F_z^{-x},$$
$$\sum T_x = T_{x0} + (F_z^{+x} + F_z^{-x})\Delta y + (F_y^{+x} + F_y^{-x})\Delta z,$$
$$\sum T_y = T_{y0} + (F_z^{+y} + F_z^{-y})\Delta x + (F_x^{+y} + F_x^{-y})\Delta z,$$
$$\sum T_z = T_{z0}.$$

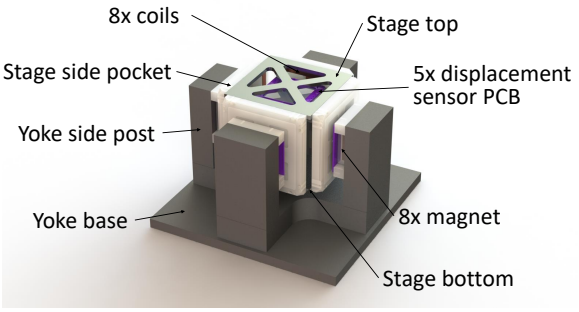

FIGURE 4. The final full sample stage assembly, rendered in SolidWorks CAD with the stage box levitating.

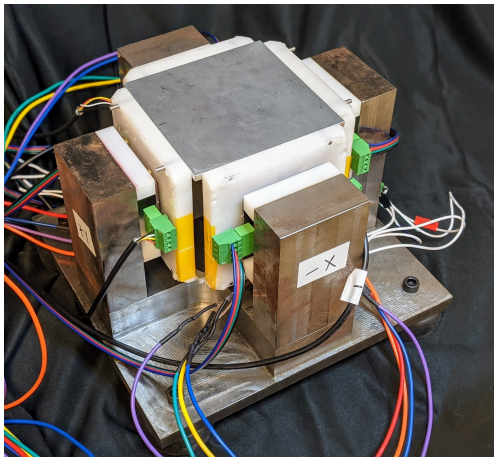

FIGURE 5. Photograph of the maglev stage prototype.

Numerical Modeling: We conducted the magnetic FE simulation for the stage using Ansys Maxwell (Ansys, Inc., USA). The results are illustrated in Figure 3. Here, Figure 3(a) shows the simulated flux density distribution generated by the stator only, and Figure 3(b) shows the simulated force on the motion stage as the stage is moved in the lateral direction by 10 mm when the corresponding force-generation coil is excited by a current of 2 A. Data show that the stage's force generation in all translational directions are largely uniform within the stage's entire motion stroke, which validates the feasibility of the design.

HARDWARE DESIGN AND PROTOTYPING

Figure 4 shows a CAD model of the prototype of the proposed maglev precision positioning stage design, and Figure 5 shows a photograph of the prototype system. The maglev stage system is comprised of a stator assembly, a moving stage, sensing circuits, driving electronics, and a feedback control system.

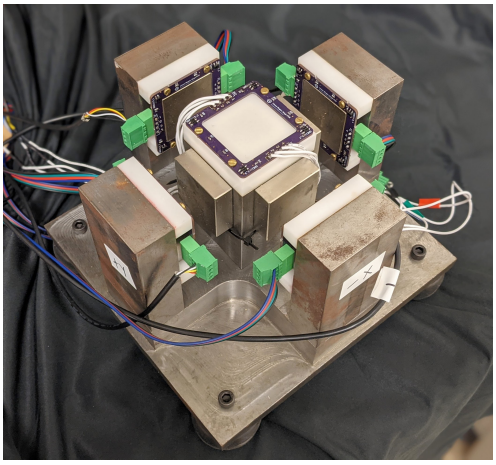

FIGURE 6. Photograph of the stator assembly.

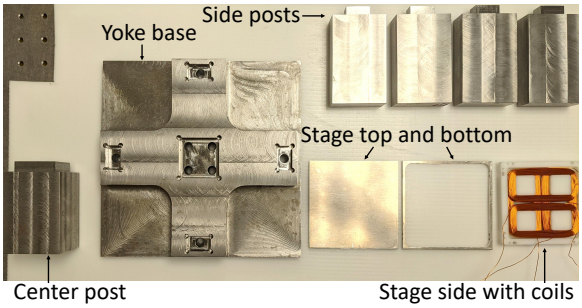

FIGURE 7. Photograph of manufactured parts for stator assembly and moving stage.

Figure 6 presents a photo of the stator assembly, which consists of a stator yoke made of 1018 low carbon steel (Westbrook Metals, Austin, TX), 8 neodymium PMs of grade N42 and dimensioned 1.5"x1.5"x.5" (K&J Magnetics), and hand-machined PCB spacers made of Delrin acetal (DuPont). The stator yoke is comprised of one yoke base, one center post, and four side posts (as shown in Fig. 7). There is a PM adhered to each face of the steel center post (four total) and steel side posts (four total) with Loctite AA326 adhesive. Each surface to which a magnet is mounted was first prepared using Loctite SF7649 primer. Above and below each of the side post magnets, a Delrin spacer was adhered with Vibra-TITE VC-3 Threadmate. The purpose of the Delrin spacer is to allow the PCB-mounted optical displacement sensors to read the moving stage position in their optimal operating range. The PCBs are fixed to the spacers with brass screws to avoid magnetic flux interruption, and are detailed in Fig. 9.

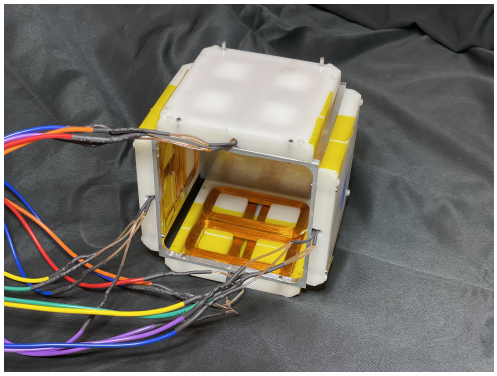

(a)

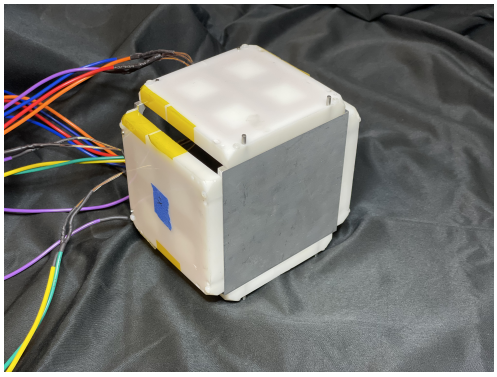

(b)

FIGURE 8. Photos of the moving stage from (a) the bottom and (b) the top.

Figure 8 presents two views of the moving stage, which consists of four stage sides with embedded actuator coils, one stage top, and one stage bottom frame (Figure 7). The stage top and bottom are made of 6061-T6 aluminum alloy, and the stage side structures are made of rigid photopolymer resin (Formlabs Rigid 4000 resin printed in a Formlabs Form 3 stereolithography printer). Two actuation coils are arranged in the pocket of each stage side, and are arranged in different orientations to generate forces in two different directions. The coils are made of epoxy-coated, self-bonding magnetic copper wires of AWG 24 (MWS Wire Industries), and were fabricated by hand winding the magnetic wire on a custom-machined aluminum bobbin. Each coil has 160 turns. Each coil was then subjected to 6A of current for 10 minutes to cure the epoxy coating.

To measure the stage's motion in all 6 DOFs, we designed and fabricated 5 printed circuit boards (PCBs). Each PCB holds 4 reflective-type optical displacement sensors (QRE 1113 from On Semiconductor), one on each corner of the PCB, as

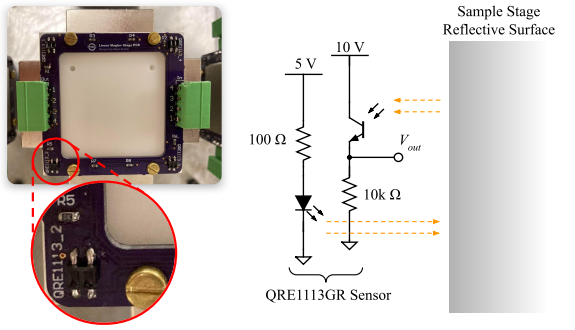

FIGURE 9. Photograph of the optical sensor PCB used for this work, along with the circuit diagram of the QRE1113GR Sensor from ON Semicon-

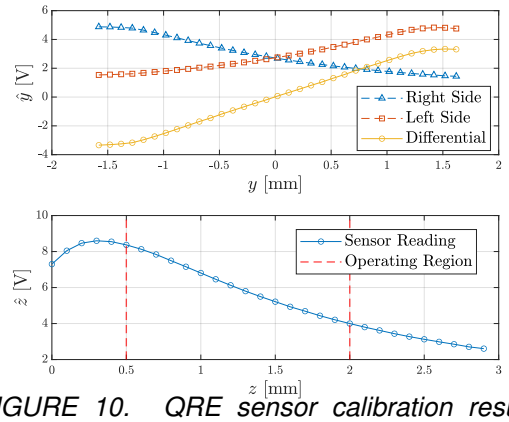

FIGURE 10. QRE sensor calibration results. Here, $\hat{y}$ and $\hat{z}$ refer to the voltage output produced by the sensors. Calibration was also performed in the x-direction, but the result was omitted here because the calibration output was effectively identical to that of the y-direction.

shown in Figure 9. The sensor consists of an infrared LED and a phototransistor facing the same direction. As shown in Figure 9, the infrared LED shines an infrared beam on a surface of the moving stage, and the phototransistor detects the reflected light. Consequently, the voltage output of the phototransistor will be correlated to the distance between the sensor and the reflective surface. Four sensor PCBs are mounted on the side posts of the stator assembly, and one PCB is mounted on the top of the stator's center post. With this sensor arrangement, the stage's motion in all DOFs is detectable, where the x and y directional displacement are measured differentially, while the z-directional stage displacement is measured only by the sensors on the top of the center post. Figure 10 shows the calibration data of the sensors in the y and z directions. It can be observed that the data are largely linear with respect to the stage's displacement in the corre-

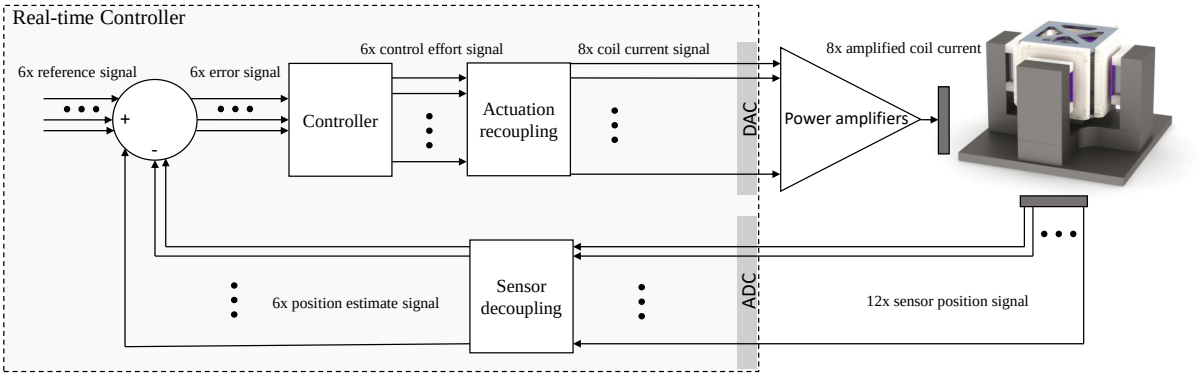

FIGURE 11. Block diagram of the system.

sponding motion direction.

Figure 11 illustrates the feedback loop of the system. The 12 position signals gathered by the reflective sensors - 4 differential signals for the x-direction, 4 differential signals for the y-direction, and 4 signals for the z-direction - are sent directly from the PCBs to the analog input channels of the realtime controller. These signals are converted from voltage to millimeter measurements using calibration data to the estimated stage displacements in x, y, z, θ_x, θ_y, θ_z directions. These estimated displacement signals are then compared to the reference position, and the resulting error signals are sent into a lead-lag type of PID controller of the form of

$$C(s) = K_p(1 + \frac{1}{T_i s})(\frac{\alpha\tau s + 1}{\tau s + 1}),$$

where K_p is the proportional gain, T_i is the integral time constant, α is the lead controller constant, and τ is the lead time constant. The outputs of the controllers are recoupled to their respective coils and output through the analog output channels of the realtime controller current command. The current command signals are then amplified by 8 channels of audio power amplifiers (OPA549, Texas Instruments) before being sent to the moving stage coils. We are currently implementing the control algorithm shown in Figure 11 in a CompactRIO realtime controller (National Instruments), where the main control loop will be operating at a sampling rate of 5 kHz. Figure 12 shows a photograph of the overall system, including the amplifiers and controllers.

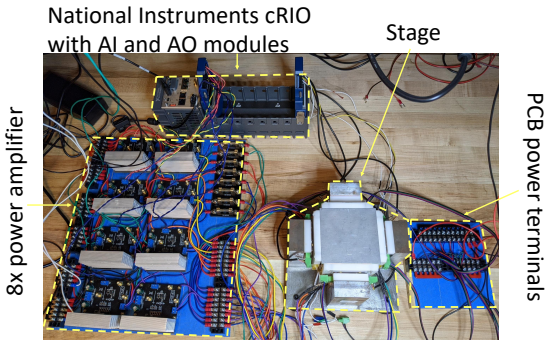

FIGURE 12. Photo of system connection.

CONCLUSION AND FUTURE WORK

In this paper, an overview of the design, model, and prototyping process for a novel long-stroke, high speed XYZ maglev precision positioning stage is presented. The FE simulation of the stage's performance shows the feasibility of the stage design, and a prototype of the proposed maglev precision motion stage has been manufactured and is ready to begin testing. A feedback control system for the stage is currently being built and stage levitation and controller tuning will commence in the coming weeks. Future works include: (1) Experimentally test the motion performance of the prototype stage and comparing the results to existing technology and target performance, and (2) Designing and implementing gravity compensation for the moving stage to reduce power consumption.

REFERENCES

[1] Deng J, Preissner C, Klug JA, Mashrafi S, Roehrig C, Jiang Y, et al. The Velociprobe: An ultrafast hard X-ray nanoprobe for high-resolution ptychographic imaging. Review of Scientific Instruments. 2019;90(8):083701.

[2] Dong X, Yoon D, Okwudire CE. A novel approach for mitigating the effects of pre-rolling/pre-sliding friction on the settling time of rolling bearing nanopositioning stages using high frequency vibration. Precision Engineering. 2017;47:375–388.

[3] Shen JC, Yan CC. Sliding-Mode Tracking Control of a Precision Stage. In: Applied Mechanics and Materials. vol. 284. Trans Tech Publ; 2013. p. 2325–2329.

[4] Chung TT, Chu CH, Fan KC, Yen JY, Szu KI. Development of a nano-positioning planar motion stage. In: 2010 2nd International Conference on Mechanical and Electronics Engineering. vol. 1. IEEE; 2010. p. V1–122.

[5] Torralba M, Valenzuela M, Yagüe-Fabra J, Albajez J, Aguilar J. Large range nanopositioning stage design: A three-layer and two-stage platform. Measurement. 2016;89:55–71.

[6] Shu D, Lai B, Kearney S, Anton J, Liu W, Maser J, et al. Design and test of precision vertical and horizontal linear nanopositioning flexure stages with centimeter-level travel range for x-ray instrumentation. In: Optomechanical Engineering 2017. vol. 10371. International Society for Optics and Photonics; 2017. p. 103710C.

[7] Li CX, Gu GY, Yang MJ, Zhu LM. Design and analysis of a high-speed XYZ nanopositioning stage. In: 2015 International Conference on Manipulation, Manufacturing and Measurement on the Nanoscale (3M-NANO). IEEE; 2015. p. 229–234.

[8] Zhou L, Trumper DL. Magnetically Levitated Linear Stage With Linear Bearingless Slice Hysteresis Motors. IEEE/ASME Transactions on Mechatronics. 2020;26(2):1084–1094.

[9] Zhang Z, Menq CH. Six-axis magnetic levitation and motion control. IEEE Transactions on robotics. 2007;23(2):196–205.

FREQUENCY-DEPENDENCY AND COUPLED DYNAMICS OF NEAR FIELD ACOUSTIC LEVITATION BEARING

Yaoke Wang[1] and Ping Guo[1,*]

[1] Department of Mechanical Engineering, Northwestern University, Evanston, USA

INTRODUCTION

Near field acoustic levitation (NFAL) utilizes structural vibration and squeeze motion of a thin air film to achieve non-contact support. It could potentially lead to simple and miniaturized designs of precision instruments with the premise of low friction and zero backlash [1, 2]. Though NFAL bearings have the potentials to achieve adequate stiffness for the application in positioning stages and other precision instruments, their quasi-static and dynamic characteristics are unclear at the moment, which needs to be systematically investigated for the industrial application of NFAL.

To analytically predict the dynamic response of an NFAL bearing, models focused on the slow dynamics of NFAL have been developed to study the temporal evolution of levitation height [3, 4]. However, these models are not eligible to be applied in the real-time prediction of system performance due to the highly nonlinear and coupled partial differential equations to be solved. To explicitly quantify levitation force in NFAL, a method to solve the Reynolds equation using separation of variables is proposed [5], which focuses on the temporally and spatially averaged levitation force. To estimate the dynamic and quasi-static performance of NFAL bearings from purely analytical solutions, we proposed a stiffness model under the assumption of high-frequency excitation [6]. The proposed model characterizes NFAL with two distinct stiffness variables: a dynamic stiffness that governs the real-time fluctuation of the levitated object and an effective stiffness that governs the time-averaged levitation position. This stiffness model can effectively predict the quasi-static and disturbance response of NFAL bearings using pure analytical solutions without solving any differential equations or relying on experimental calibrations.

Though our proposed stiffness model [6] is an effective tool for predicting the dynamic characteristics of NFAL bearings, it ignores real-time height fluctuation of the levitated object, which might be of critical importance in applications where a delicate object is levitated (e.g., silicon wafers and photovoltaic cells). To further investigate the coupled dynamics of NFAL, we extend our original stiffness model by considering both the effects of dynamic stiffness on the fluctuation of levitated objects and the effective stiffness governing the air film dynamics in the prediction of levitation height and force.

In this paper, real-time vibration of the levitated object is incorporated into the new mass-air stiffness model by superimposing the vibration amplitudes and phase delays between the driving surface and levitated object over the time-averaged evolution of levitation height. It is found that the levitation force and the excitation frequency will no longer follow a monotonically increasing relationship. When excited at a low frequency, due to the existence of dynamic stiffness, the levitated object and the driving surface vibrate approximately in phase, resulting in an offset of the squeeze motion or reduced levitation force. When approaching a critical frequency, the air-mass system of the bearing resonates. As a result, the phase delay between vibrations of the levitated object and the driving surface starts to increases rapidly, thus amplifying the squeeze motion amplitudes and levitation force.

Experiments are designed and carried out to verify the new stiffness model. It is found that the proposed model is capable to predict the nonlinear transition of levitation height and air film thickness at different excitation frequencies. It is also concluded that a critical frequency exists following our theoretical prediction, below which no levitation occurs. The results presented may provide additional insights and guidance for future NFAL system design.

* Corresponding author: Ping Guo. Email: ping.guo@northwestern.edu
First Author: Yaoke Wang. Email: yaokewang2020@u.northwestern.edu

MASS-AIR STIFFNESS MODEL OF NFAL

In our previous study [6], an NFAL system utilizes a nonlinear spring to represent the mechanical performance of the air film between the driving surface and levitated object, as shown in FIGURE 1(a). Here, a circular plate at the bottom provides the cyclic squeeze motion to the air film driven by a piezo actuator. The resultant squeeze motion generates a positively biased pressure fluctuation in the air film to provide a non-contact support force, which is coined as near field acoustic levitation (NFAL). A levitated object is assumed to be static at an average levitation height $\bar{h}$ under high-frequency excitation. The real-time air film thickness h can be represented by:

$$h(t) = \bar{h} - \tilde{h}(t) = \bar{h} - A_{mp} sin(2\pi f t) \quad (1)$$

where $\tilde{h}(t)$ is the periodic variation of $h(t)$ with an amplitude of A_{mp} and a frequency f. In the original stiffness model, the vibration amplitude of the driving surface is equal to the squeeze amplitude of the air film. Similarly, the real-time levitation force $F(t)$ experienced by the levitated object can be separated by a time-averaged term and a dynamic term as

$$F(t) = \bar{F} + F_{amp} \sin(2\pi f t) \quad (2)$$

where $\bar{F}$ is the time-averaged levitation force and F_{amp} is the amplitude of the dynamic reaction force. By linearizing the Reynolds equation for the air film hydrodynamics, these two force components can be approximated by

$$\begin{cases} F_{amp} = \dfrac{\pi R^2 p_a \Phi_f}{\bar{h}} A_{mp} \\ \bar{F} = \dfrac{\pi R^2 p_a \Phi_f}{2\bar{h}^2} A_{mp}^2 \end{cases} \quad (3)$$

where R is the radius of the circular surface and p_a is atmospheric pressure. Here, Φ_f is a frequency correction coefficient which can be represented by

$$\Phi_f = \alpha \tanh\left(\frac{f}{f_{ref}}\right), \qquad 0 < \alpha < 1 \quad (4)$$

where α is a constant usually ranging from 0.8 to 1, which sets the maximum efficiency of an NFAL system. f_{ref} is a reference frequency defining the convergence rate of Φ_f to α, so when the excitation frequency is large enough, the levitation force will be independent of the excitation frequency.

By comparing the dynamic reaction force and the periodic variation of air film thickness, we can derive a dynamic stiffness that connects two as

$$k = \frac{\pi R^2 p_a \Phi_f}{\bar{h}} \quad (5)$$

By taking the derivative of the time-averaged force $\bar{F}$ with respect to the average levitation height $\bar{h}$, we can derive an effective stiffness can as

$$K = \frac{d\bar{F}}{d\bar{h}} = \frac{\pi R^2 p_a \Phi_f}{\bar{h}^3} A_{mp}^2 \quad (6)$$

Thus, in an NFAL system, the dynamic stiffness k relates the excitation amplitude to the dynamic force amplitude, while the effective stiffness K governs the time-averaged force-displacement relationship, which reveals the quasi-static properties of NFAL.

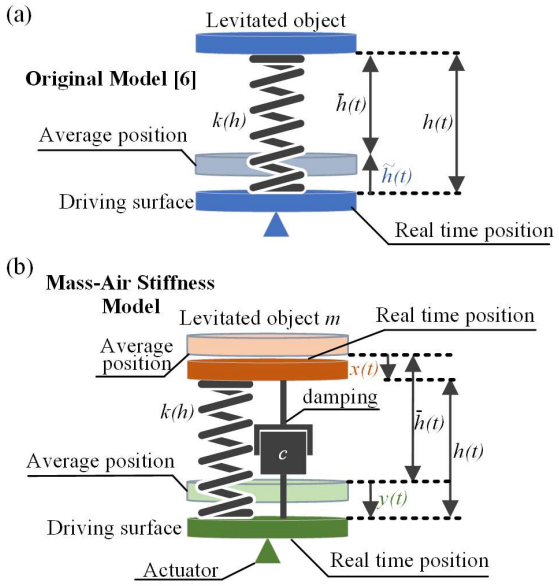

FIGURE 1. Comparison between the (a) original and (b) new mass-air stiffness models.

The effectiveness of this original NFAL stiffness model has been validated with experiments in our previous study, making it useful for the performance prediction in many common application scenarios; however, the prediction error will dramatically increase when the model is used to predict the levitation height of lightweight objects, at low excitation frequencies, or in a low levitation height condition. The original stiffness model was derived under two assumptions. (1) The height fluctuation of levitated objects is ignored due to the high vibration amplitude attenuation at high excitation frequencies, and (2) the effect of air damping is negligible in the

prediction of quasi-static levitation height. As a result, the vibration amplitude from the driving surface is equal to the change of air film thickness, while the dynamic responses from the air damping and levitated object vibration are ignored.

To address the challenges identified above, in this study, we further extend to a mass-air stiffness model, which removes the restrictions of the above two assumptions. The model takes into account the dynamic fluctuation of the levitated object and damping effects, as shown in Figure 1(b). This new mass-air stiffness model will not only improve the prediction accuracy, but also be able to predict some unique frequency-dependent behaviors, which have not been explained in any previous studies.

In the new mass-air stiffness model, the vibration of the levitated object is considered. So its motion, y, is related to the motion of the driving surface, x, by the following equation

$$k'y + C_d\dot{y} + m\ddot{y} = k'x + C_d\dot{x} \tag{7}$$

The driving surface provides a harmonic squeeze motion to the air film, defined by $x=X_{amp}\sin(2\pi ft)$. k' denotes the new dynamic stiffness with its definition updated as

$$k' = \frac{\pi R^2 p_a \Phi_f\left(\frac{A_{mp}}{X_{amp}}\right)}{\bar{h}} \tag{8}$$

An amplitude correction term A_{mp}/X_{amp} is introduced to reflect that the true squeeze amplitude of the air film, which represents the real-time variation of the upper and lower surface vibration as $A_{mp}=||x(t)-y(t)||$.

The damping coefficient, C_d, is empirically defined according to [5] as

$$C_d = \frac{3\pi R^4 \eta}{2\bar{h}^3} \tag{9}$$

where η is the dynamic viscosity of air film. By applying the Laplace transform to the equations of motion, we can derive the expression of the squeeze amplitude of the air film as

$$\frac{A_{mp}}{X_{amp}} = \left|\frac{4\pi^2 f^2 m}{k' - 4\pi^2 f^2 m + 2\pi f C_d \omega j}\right| \tag{10}$$

To investigate how the air-film-dynamics-induced vibration of the levitated object affects the dynamic behaviors of an NFAL system, Eq. (10) is numerically solved with the parameters listed in Table 1.

TABLE 1. Parameters for dynamic simulation.

m (g)	α	R (mm)
1.3	0.9	12.7
f_{ref} (kHz)	X_{amp} (μm)	$\bar{h}$ (μm)
3	1	40

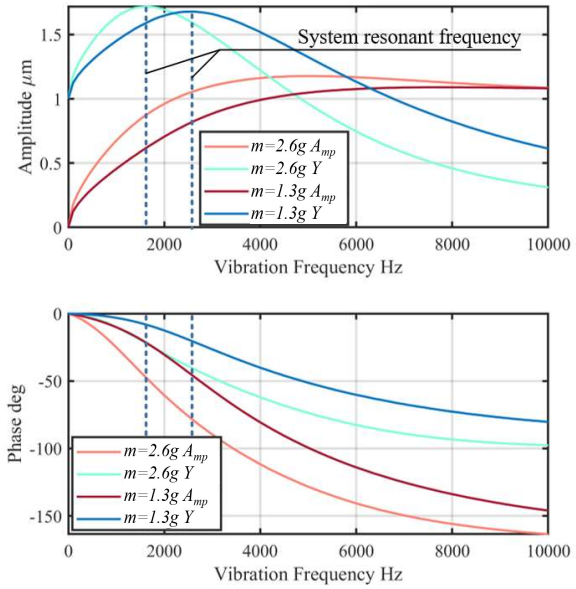

FIGURE 2. Frequency responses of the air film and levitated object.

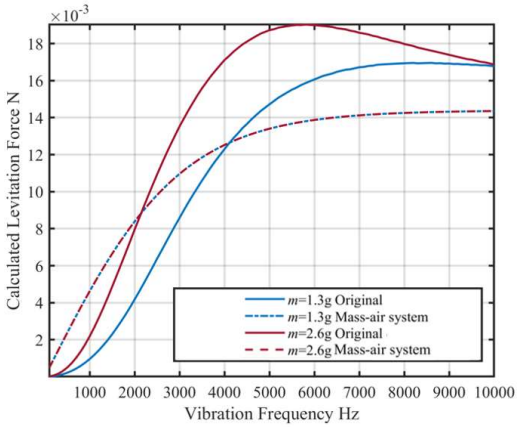

FIGURE 3. Simulated time-averaged levitation force on the levitated object

The simulated frequency responses of the air film and levitated object is shown in FIGURE 2. The phase difference between the motion of the

levitated object and the squeeze motion of air film is close to 0 at a low-frequency range. This reveals that at a low excitation frequency, the actual squeeze motion amplitude to the air film is much smaller than the vibration amplitude of the driving surface, because the levitated object follows the movement of the driving surface. As the frequency increases, a resonant vibration occurs at the levitated object, where the entire mass-air system resonates. It is around this frequency that the squeeze motion amplitude of the air film increases and stays constant as the excitation frequency further increases.

The change of air film thickness is the root cause of levitation force. We calculate the change of levitation force based on the squeeze motion of air film thickness for different excitation frequencies, as shown in Figure 3. The results are compared between the new mass-air stiffness model and the original model. According to the results shown in FIGURE 3, the levitation force is dependent on the object mass, which has not been considered in the original dynamic model. In addition, the new model is able to capture the air-mass resonance, where a significantly larger levitation force is predicted than that obtained from the original model.

The results of this simulation reveal the importance of vibration frequency to the performance of NFAL systems. When the excitation frequency is much lower than the system resonant frequency, the levitated object tends to follow the motion of the driving surface, so that the actual vibration amplitude of the air film is severely reduced. Our predicted levitation force is much smaller than the predicted value from the original model at low frequencies as shown in Figure 3. As the excitation frequency increases, the levitated object can no longer follow the motion of the driving surface, increasing the phase difference between the two motions as well as the actual squeeze amplitude of the air film. When the phase difference exceeds 90°, as shown in Figure 2(b), the actual squeeze amplitude may even exceed the vibration amplitude of the driving surface, thus amplifying the levitation force.

In addition, by comparing the frequency responses and predicted levitation for objects with different masses, it can be found the performance is mass-dependent due to the inclusion of air-mass interactions in the new model, which has not been revelaed by previous studies.

EXPERIMENTAL RESULTS

To further validate the proposed mass-air stiffness model for NFAL. An experiment setup similar to that in [6] is developed to evaluate the dynamic performance of a miniaturized NFAL system. The range of experimental conditions is summarized in Table 2. The excitation frequency starts from 1 kHz up to 9 kHz, while the excitation amplitude from the piezo actuator is set from 0.5 μm to 1 μm. The upper limit of the excitation frequency and amplitude is set by the current capacity of the piezo amplifier, piezo stack life, and the resonant frequencies of the mechanical structure. We also make sure that a pure translational motion is applied to the driving surface and no structural resonance is excited (to be not confused with the air-mass system resonance) within the testing range.

TABLE 2. Experimental parameters.

f (kHz)	X_{amp} (μm)	m (g)
1, 1.1, …, 9	0.75, 1	1.35

In the experiment, the vibration amplitude and phase of the levitated object, as well as its levitation height, are measured by a *Polytec* laser vibrometer and recorded by an *NI* PXIE-6366 data acquisition card. The phase difference is calculated with respect to a reference signal, which is the pre-amplified voltage signal driving the piezo actuator.

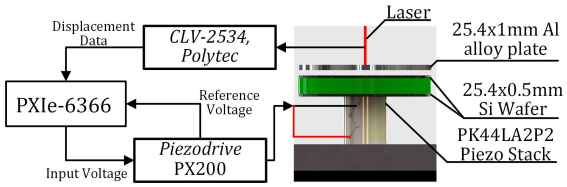

FIGURE 4. Experimental setup [6].

The most intuitive method to validate the new mass-air dynamic model with obtained experimental data is to compare the experimental results of air film squeeze amplitude A_{mp} and levitation height $\bar{h}$ with those calculated from the proposed model at different frequencies. The levitation height is calculated by using a time-averaged force balance equation as

$$\bar{h} = \sqrt{\frac{\pi R^2 p_a \Phi_f \left(\frac{A_{mp}}{X_{amp}}\right)}{2mg}} A_{mp} \tag{11}$$

where A_{mp} can be determined using the frequency response derived in Eq. (10).

The damping coefficient C_d is determined using a reference levitation height at h_{ref} = 30 μm since the actual damping ratio cannot be infinitely large for a very small levitation height as shown in Eq. (9). By solving Eqs. (9-11), we can derive the relationship between the levitation height and excitation frequency *f*-$\bar{h}$, as well as the relationship between the air film squeeze motion amplitude and excitation frequency *f*-A_{mp}. We compare *f*-$\bar{h}$ *and f*-A_{mp} curves from the model-derived and experimental results for two different driving amplitudes in Figure 5.

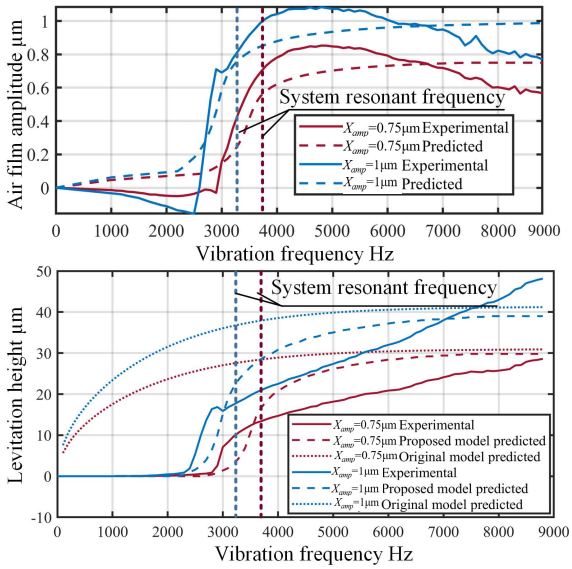

FIGURE 5. Comparison of the (a) levitation height and (b) squeeze motion amplitude of the air film from the predicted and experimental results.

Based on the observation from FIGURE 5, the proposed model is able to predict a unique resonant frequency shown in dotted lines respectively for X=0.75 μm and 1 μm at which the squeeze motion amplitude and the levitation height start to dramatically increase due to a "resonance" of the air-mass system. It can also predict the general trend of levitation height and squeeze amplitude at larger frequencies. The predicted results deviate from the experimental results at high frequencies due to the large error in the estimation of the damping coefficient C_d. The damping coefficient might not be simply described by Eq. (9) for a wide frequency/levitation height range.

In addition, through the above theoretical modeling and corresponding experimental studies, an existing misunderstanding of NFAL is addressed. The previous models, including our original stiffness model, assume that the squeeze motion amplitude of the air film is exactly that of the driving surface. Under this condition, the levitation height should have been gradually increased starting from 0 Hz. While for both experimental results and predictions from the new air-mass model in Figure 5, the levitation height only starts to rapidly increase when the excitation frequency is approaching the resonant frequency of the air-mass system. In fact, the levitation force is jointly affected by motions from the driving surface and levitated object. By increasing the excitation frequency, the NFAL system not only stiffens the air film as demonstrated in Eqs. (3) and (4), but also creates a phase difference between motions from the driving surface and levitated object, which in turn affects the levitation force.

CONCLUSION

To predict the nonlinear dynamic behaviors of NFAL, such as frequency-dependent effects, where previous models cannot address, a mass-air stiffness model is proposed. It takes into account the effects of vibration of the levitated object and air damping. By numerical analysis and experimental verification, it is found that the proposed model can effectively predict the air-mass resonance and its influence on the levitation force and height, which has not been reported by previous studies. In addition, it also shows that the influence of frequency on the performance of NFAL is sophisticated. On the one hand, it affects the stiffness of the air film; while at the same time, it affects the frequency response of the levitated object, especially for a lightweight object, which in turn influences the actual squeeze amplitude of the air film. The non-linear dynamic behaviors and frequency-dependent effects of NFAL should be considered when designing a new NFAL bearing system.

ACKNOWLEDGMENTS

This research was supported by the start-up fund from McCormick School of Engineering, Northwestern University, Evanston, IL, USA.

REFERENCES

[1] Hashimoto Y, Koike Y, Ueha S. Near-field acoustic levitation of planar specimens using flexural vibration. J Acoust Soc Am. 1996;100(4):2057–61.

[2] Shi M, Feng K, Hu J, Zhu J, Cui H. Near-field acoustic levitation and applications to bearings: a critical review. Int J Extrem Manuf. 2019;1(3):032002.

[3] Minikes A, Bucher I. Coupled dynamics of a squeeze-film levitated mass and a vibrating piezoelectric disc: numerical analysis and experimental study. J Sound Vib. 2003;263(2):241–68.

[4] Ilssar D, Bucher I. On the slow dynamics of near-field acoustically levitated objects under High excitation frequencies. J Sound Vib. 2015;354:154–66.

[5] Minikes A, Bucher I, Haber S. Levitation force induced by pressure radiation in gas squeeze films. J Acoust Soc Am. 2004;116(1):217–26.

[6] Wang Y, Guo P. Stiffness modeling for near field acoustic levitation bearings. Appl Phys Lett. 2021;118(20):204102.

ACTIVE CONTROL OF HIGH FREQUENCY REGENERATIVE CHATTER VIBRATIONS WITH MACHINE TOOL FEED DRIVES

Alper Dumanli and Burak Sencer
School of Mechanical, Industrial and Manufacturing Engineering
Oregon State University
Corvallis, Oregon, USA

INTRODUCTION

Chatter vibrations have been a limiting factor for attaining larger material removal rates (MRR) in turning for decades [1]. They originate due the flexibilities (resonances) in the workpiece-machine-tooling structure and by the regeneration effects [1,2]. Overall process-machine interaction can be modelled by a delay differential equation (DDE), and chatter-free cutting conditions are selected from Stability Lobe Diagrams (SLDs). Nevertheless, practical spindle speeds in turning are lower and when structural resonances are at high frequency, conventional SLDs have densely packed narrow lobes that cannot be used to maximize MRRs [2].

The overreaching goal has been to exceed stability limitations in turning, and it can be attained by shaping SLDs in two major ways; firstly, regeneration effect is targeted through process parameter selection such as exploiting process damping [3], optimizing tool geometry/posture [4], or by spindle speed variation (SSV) [2]. These efforts shape SLDs locally to create stable pockets to reach higher MRRs and designed to work on a pre-determined spindle speed region.

Another approach focuses on dampening structural resonances by passive or active systems [2,6-10]. Increasing modal damping lifts SLDs up, which delivers moderate stability increase over a wider spindle speed range. Tuned-mass-dampers (TMD), or tools with friction dampers [2] are widely used in practice, and their robustness can be enhanced semi-actively [8,9]. However, fully active systems are much more effective since they can dampen multiple modes [7], integrate within machine elements [9], and even realized by using machine's existing feed drives [10]. A fundamental requirement for effective active damping is that targeted resonances must lie within the control bandwidth of the actuator or feed drive system, which limits their practical usage to dampen modes within ~200Hz range [2,10]. Control algorithms based on direct velocity [6,8] or acceleration feedback [10] are widely used. However, when low frequency resonances are damped actively, the lightly damped high frequency modes becomes destabilized. Therefore, loop shaping based tuning should be practiced [10], or model-based techniques such as H∞, μ-synthesis or delayed feedback [7,11,12] are employed. Still, fundamental limitation of modal damping-based chatter control techniques is that they rely on servo control bandwidth, which cannot be widened enough to dampen high frequency modes.

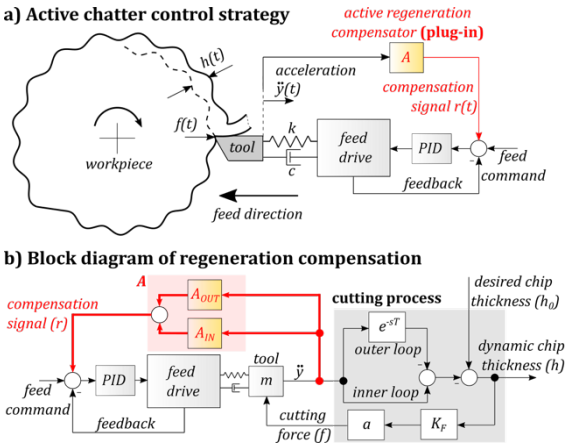

FIGURE 1: Regenerative turning process and proposed compensator structure

This paper presents an active chatter vibration control strategy for machine tool feed drives to improve the material removal rates in turning. As opposed to the injecting modal damping by servo loop shaping [5-10], proposed controller is designed to achieve *process loop shaping*, which focuses on controlling regenerative machining process dynamics using machine tool feed drives. This approach brings two major advantages over state of the art. Firstly, core cause of chatter; regeneration effects are suppressed, which allows local shaping of SLDs to significantly increase MRR. Secondly, it

allows control of high frequency chatter that is beyond the position bandwidth of feed drives. Figure 1a depicts the proposed scheme. Proposed controller is designed as an add-on compensator (filter) strapped around the existing low-bandwidth servo controller to suppress chatter vibrations. Thus, both low frequency position control and high frequency chatter mitigation are achieved jointly. Following sections explain design, parameter tuning and experimental validation of proposed approach in orthogonal (plunge) turning.

DESIGN OF THE PROCESS CONTROLLER

Figure 1 illustrates the well-known dynamics of orthogonal turning [1,2] with a flexible tool assembly carried by a feed drive system. Dynamic chip thickness $h(s)=L\{h(t)\}$ and feed forces $f(s)$ generated by current vibration of the tool tip $y(s)$ and the one left on part surface in previous spindle revolution, $e^{-sT}y(s)$:

$$y(s)=h_0-[y(s)-e^{-sT}y(s)],\quad f(s)=K_F a h(s) \tag{1}$$

where s is the Laplace operator, T is the spindle (delay) period, h_0 is intended (static) chip thickness, K_F is the cutting force coefficient, and a is width (depth) of cut. Cutting forces excite the flexible structure and produce current vibrations as:

$$y(s)=G(s)f(s)=K_F a\left(h_0-[y(s)-e^{-sT}y(s)]\right) \tag{2}$$

where $G(s)$ is the transfer function of the flexible tooling system. Laplace operator (s) is dropped from signals and functions in the remainder, and Equation (2) is expressed in transfer function form as:

$$\frac{y}{h_0}=\frac{K_F aG}{1+aK_F G\left(1-e^{-sT}\right)}=\frac{K_F aG}{1+aL_P} \tag{3}$$

where the $L_P=K_F G(1-e^{-sT})$ term in Equation(3) is the so-called "*process loop transmission*" dynamics with a being the process gain.

Block diagram of proposed control scheme is given in Figure 1b. As shown, an add-on compensator (filter) is designed that injects a position compensation signal r based on the tool vibration measurement y. The idea is to design the compensator A to shape the process loop transmission L_p and maximize its gain margin. Notice that $A=A_{IN}+A_{OUT}$ has 2 parts. A_{IN} is designed to suppress the effect of inner modulation and A_{OUT} is designed to target the outer modulation.

With the introduction of ARC signal r, the augmented tool tip and process dynamics can be derived from Equation(2) and Figure 1b as:

$$\begin{aligned} y &= Gf + AT_T y \\ &= K_F aG\left[h_0 - y\left(1-e^{-sT}\right)\right] + \left(A_{IN}+A_{OUT}\right)T_T y \end{aligned} \tag{4}$$

where $T_T=y/r$ is the tool tip tracking transfer function of feed drive system, which is typically governed by a low-bandwidth industrial PID controller. Equation 4 can be put in a transfer function form as:

$$\frac{y}{h_0}=\frac{K_F aG}{1+\underbrace{\left(K_F aG-A_{IN}T_T\right)}_{\substack{\text{inner modulation}\\ \text{cancellation}}}-\underbrace{\left(K_F aGe^{-sT}+A_{OUT}T_T\right)}_{\substack{\text{outer modulation}\\ \text{cancellation}}}} \tag{5}$$

Design of the (A_{OUT})

A_{OUT} is designed to suppress the effect of outer modulation. Notice from Equation (5) that if A_{OUT} could be ideally chosen as:

$$A_{OUT}=-K_F aGT_T^{-1}e^{-sT} \tag{6}$$

effect of outer regeneration is completely cancelled. a is the desired stable depth of cut, and G is the disturbance response of tool/feed drive system, which can be measured by tap-testing. However, the inverse of higher-order closed-loop tracking dynamics, T_T^{-1} term, cannot be realized on a practical system due to servo phase losses and non-minimum phase zeros [6,10]. Therefore, its delayed realization, $T_T^{-1}e^{-sT}$ term in Equation (6) is considered. The idea is to approximate $-T_T^{-1}e^{-sT}$ by an N^{th} order FIR filter within a meaningful frequency band $\omega\in[\omega_1,\omega_M]$:

$$\begin{aligned} P_{OUT} &= p_1 z^{-T_1/T_s}+p_2 z^{-T_2/T_s}+\cdots+p_N z^{-T_N/T_s} \\ &\approx -T_T^{-1}e^{-sT},\quad z=e^{sT_s} \end{aligned} \tag{7}$$

with T_s being position loop sampling time. Frequency band [ω_1, ω_M] is selected to confine chatter frequency by setting $\omega_1=\omega_n$ and ω_M is set reasonably larger. Notice that the delay T is known at a given spindle (cutting) speed, $T=60/n$. Filter delays $T_1\ldots T_N$ are selected centered around that spindle period $[T_1\ldots T_N]\leftrightarrow[T-2\pi/\omega_1\ldots T+2\pi/\omega_1]$ to ensure causal inversion of T_T. Finally, gains of the FIR filter $p_1\ldots p_N$ are determined to minimize its fitting discrepancy from system inverse, $\min||P_{OUT}+T_T^{-1}e^{-sT}||$ by:

$$\min_{p_1\cdots p_N}\left(\begin{aligned}&\operatorname{Re}\left\{P_{OUT}\left(j\omega\right)T_T\left(j\omega\right)+e^{-j\omega T}\right\}^2\\&+\operatorname{Im}\left\{P_{OUT}\left(j\omega\right)T_T\left(j\omega\right)+e^{-j\omega T}\right\}^2\end{aligned}\right) \tag{8}$$

$$\text{for all } \omega\in\left[\begin{array}{cc}\omega_1 & \omega_M\end{array}\right]$$

which can be put in a matrix-vector form as:

$\min_{\mathbf{p}=p_1\cdots p_N} \left\|\mathbf{Ap}+\mathbf{v}\right\|_2^2$, where:

$$\mathbf{A}=\begin{bmatrix} \mathrm{Re}\left\{e^{-j\omega_1 T_1}T_T(j\omega_1)\right\} & \cdots & \mathrm{Re}\left\{e^{-j\omega_1 T_N}T_T(j\omega_1)\right\} \\ \vdots & \ddots & \vdots \\ \mathrm{Re}\left\{e^{-j\omega_1 T_1}T_T(j\omega_M)\right\} & \cdots & \mathrm{Re}\left\{e^{-j\omega_1 T_N}T_T(j\omega_M)\right\} \\ \mathrm{Im}\left\{e^{-j\omega_1 T_1}T_T(j\omega_1)\right\} & \cdots & \mathrm{Im}\left\{e^{-j\omega_1 T_N}T_T(j\omega_1)\right\} \\ \vdots & \ddots & \vdots \\ \mathrm{Im}\left\{e^{-j\omega_1 T_1}T_T(j\omega_M)\right\} & \cdots & \mathrm{Im}\left\{e^{-j\omega_1 T_N}T_T(j\omega_M)\right\} \end{bmatrix}$$

$$\mathbf{v}=\begin{bmatrix} \cos(\omega_1) & \cdots & \cos(\omega_M) & \sin(\omega_1) & \cdots & \sin(\omega_M) \end{bmatrix}^T$$

(9)

where M is the frequency resolution. Equation (9) is a convex optimization (least squares fitting) problem, which can be solved efficiently to determine FIR gains, and A_{OUT} is implemented as:

$$A_{OUT}=K_F a G P_{OUT} \qquad (10)$$

Design of A_{IN} Compensator

The A_{IN} compensator is designed to further increase a_{lim} around a targeted spindle speed by cancelling the effect of inner modulation. To cancel the inner modulation terms (see Equation (5)), A_{IN} is selected in the form of:

$$A_{IN}=-K_F a G \hat{T}_T^{-1} P_{IN} \qquad (11)$$

where $\hat{T}_T^{-1}$is an approximate, causal inverse of feed drive's tracking dynamics, which neglects non-minimum phase zeros. Design of the P_{IN} filter in Equation(11) is critical. Like the design of A_{OUT} compensator, P_{IN} is selected as simple K^{th} order FIR filter:

$$P_{IN}=q_0+q_1 z^{-1}+\cdots+q_K z^{-K},\quad z=e^{sT_s} \qquad (12)$$

whose parameters $q_0 \ldots q_K$ are determined to maximize a_{lim} by minimizing the real part of process loop transmission. Based on Equation (11), this parameter search is set as an optimization problem:

$$\min_{q_0\cdots q_K}\left(\frac{1}{a_{\lim}}\right) \quad \text{subject to:}$$

$$-\mathrm{Re}\left\{\begin{array}{l} \underbrace{\left(K_F G-\underbrace{K_F G T_T \hat{T}_T^{-1} P_{IN}}_{A_{IN}T_T/a}\right)}_{\text{Inner modulation}} - \\ \underbrace{\left(K_F G e^{-sT}+T_T A_{OUT}/a\right)}_{\text{Outer modulation}} \end{array}\right\} \le \frac{1}{a_{\lim}} \qquad (13)$$

Above optimization problem has two key elements. Firstly, the objective function tries to minimize $1/a_{lim}$, whereas its only constraint tries to keep the negative real part of loop transmission below that. Therefore, optimal filter parameters are sought that maximizes gain margin of the process by pushing the real crossing of process loop transmission to right-hand side of the complex plane. This parameter search is governed by Equation (13), and it is in fact a convex optimization problem that can be solved conveniently using linear programming to determine the best filter parameters. With the P_{IN} filter determined from Equation (13) proposed ARC design, $A=A_{OUT}+A_{IN}$ is implemented from Equations (10) and (11) as shown in Figure 1b.

EXPERIMENTAL VALIDATION

The experimental turning system setup used in validating proposed active chatter avoidance strategy is shown in Figure 2. Orthogonal tube cutting experiments are conducted on a Al6061 workpiece with a carbide insert, yielding roughly K_F=~1338 [N/mm^2]. A Dytran 3035B1G accelerometer with 10 [mV/g] sensitivity is used to measure the tooling dynamics G, and Figure 4b shows measured and fitted FRFs. Notice that due to slender tool shank, the tooling system suffers from a dominant mode at ~2.57 [kHz].

As shown, the tool (shank) is fed to the workpiece by a piezo actuated feed drive system in this setup. Details of the drive system can be found in [13]. The actuator assembly contains an internal displacement sensor, which allows tuning a dedicated collocated PID controller with a maximum tracking bandwidth of 1[kHz] shown in Figure 2c (see blue line, x/r). The sampling frequency of the real-time control system is set to 50 [kHz]. Tool tip tracking transfer function (T_T=y/r) is measured by integrating the tool tip acceleration measurements and shown in Figure 4c.

Proposed active control algorithm ARC is first designed to suppress chatter due to the dominant mode at ~2.57 [kHz] (See Figure 2b) by selecting the target frequency band as $\omega \in$[2500, 2800] [Hz]. The objective is to open up a stable pocket at around n=1800 [rpm]. FIR filter orders of A_{IN} and A_{OUT} are set as N=20, K=5. Note that in realization of ARC, tool tip vibrations (y) are estimated from integrating accelerometer measurements and high-pass filtering with 250[Hz] cut-off.

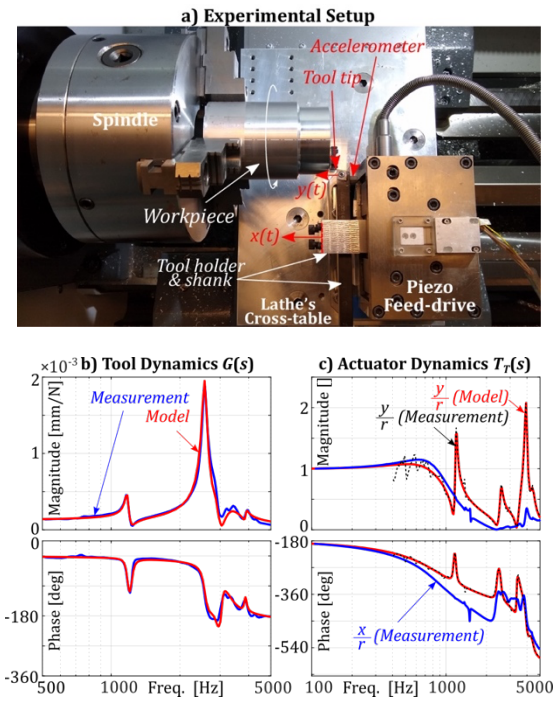

FIGURE 2: Experimental setup and its dynamic characterization.

Figure 3 shows the original and shaped process dynamics by ARC. As shown in Figure 3a, A_{OUT} eliminates ripples due to the regeneration effect, and A_{IN} further minimizes the negative real part of process loop transmission. This improves the gain margin of the process significantly. It is also evident from Figure 3b that process loop transmission is squeezed and pushed to the right-hand side of complex plane and the -1 point by the help of ARC.

Next, SLDs are plotted in Figure 4a. As shown, due to high frequency resonance (~2.57[kHz]), the original stability lobes are very tight, and asymptotic stability limit is below ~0.5[mm]. However, when ARC is used, stability is drastically improved around the desired 1800[rpm]. Widths of cut up to ~2[mm] can be cut stably providing 4× improvement in productivity. Tube cutting experiments (plunge turning) at a feedrate of 4[μm/rev] are conducted. As shown, workpieces with 0.5-1.75[mm] wall thicknesses are machined free of chatter with a smooth surface finish by the help of the proposed ARC design.

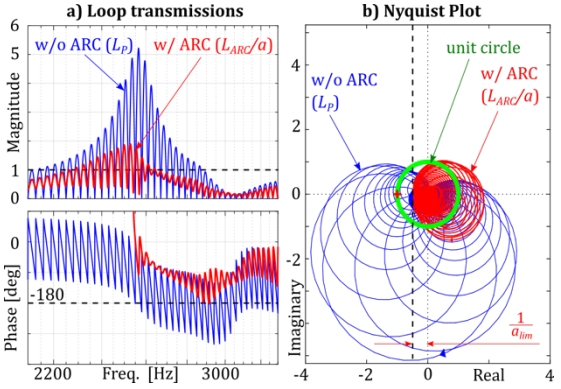

FIGURE 3: Experimental setup and its dynamic characterization.

Figure 4b shows the effect of ARC when it is switched on during machining at 1.75mm width. When ARC is turned on at ~2.5[sec], chatter vibrations at 2.66[kHz] are quickly dampened, and the process is stabilized. More importantly, ARC suppresses chatter vibrations originating from a mode beyond feed drive positioning bandwidth (~1[kHz]). This provides great flexibility since drive's servo controller can be designed separately and safely for positioning, and ARC is activated to suppress chatter when needed. Note that to take advantage of ARC for high frequency chatter avoidance, drives must be able to respond to at least small (micron level) position commands at that high frequency.

Lastly, ARC is implemented to create lobes at different spindle speeds such as at 1000 and 1400[rpm] to showcase its flexibility and robustness to increase MRR on demand in Figure 5. As shown, ARC can be tuned to create large stability lobes at various speeds. In comparison, delayed feedback control [12] can only provide minor improvement and requires tedious manual gain tuning.

CONCLUSIONS

The objective of this paper was to design a controller to exceed bandwidth limitation of conventional feed drive systems in actively controlling high frequency chatter vibrations. Regenerative chatter vibrations occurring at 2.66kHz are attenuated by a feed drive system that has <1kHz closed-loop bandwidth (2.5× lower). Stability lobes are shaped to realize 4× higher MRR in a desired cutting speed range. Proposed compensator can be used jointly with an existing servo control to utilize machine tool feed drives for active high frequency chatter control. Or, it can be implemented stand-alone on an active damper system such as in inertial actuators [5-10], which broadens its impact for

various machine tools and use scenarios. Implementation in other chatter-experiencing machining processes remains to be a future research topic.

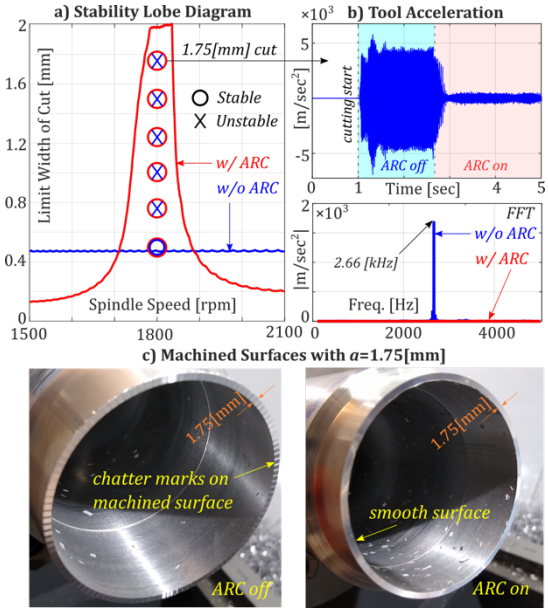

FIGURE 4: Validation of the proposed controller at 1800[rpm]

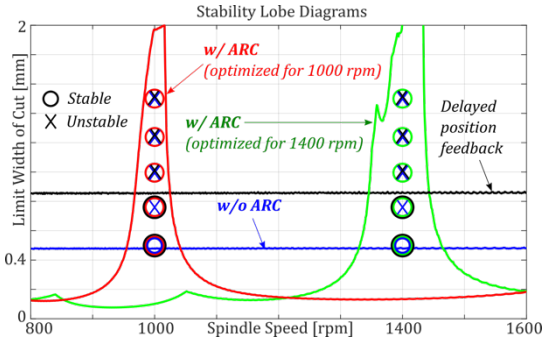

FIGURE 5: Validation of the proposed controller at 1000 and 1400 [rpm

REFERENCES

[1] Altintas Y, Weck M., 2004, Chatter stability in metal cutting and grinding. *Annals of the CIRP* 53(2):619-642.

[2] Munoa J, Beudaert X, Dombovari Z, Altintas Y, Budak E, Brecher C, Gtepan G., 2016, Chatter suppression techniques in metal cutting. *Annals of the CIRP* 65(1):785-808.

[3] Budak, E. and Tunc, L.T., 2010. Identification and modeling of process damping in turning and milling using a new approach. *Annals of the CIRP* 59(1):403-408.

[4] Shamoto, E., et. al., 2012. A novel tool path/posture optimization concept to avoid chatter vibration in machining–proposed concept and its verification in turning. *Annals of the CIRP* 61(1):331-334.

[5] Munoa J, Mancisidor I, Loix N, Uriarte LG, Barcena R, Zatarain M (2013) Chatter suppression in ram type traveling column milling machines using a biaxial inertial actuator. *Annals of the CIRP* 62(1):407-410.

[6] Lu X, Chen F, Altintas Y (2014) Magnetic actuator for active damping of boring bars. *Annals of the CIRP* 63(1):369-372.

[7] Chen F, Hanifzadegan M, Altintas Y, Lu X (2015) Active Damping of Boring Bar Vibration with a Magnetic Actuator. *IEEE ASME Trans Mechatronics*. 20(6):2783-2794.

[8] Zaeh MF, Kleinwort R, Fagerer P, Altintas Y., 2017, Automatic tuning of active vibration control systems using inertial actuators. *Annals of the CIRP* 66(1):365-368.

[9] Abele, E., Altintas, Y. and Brecher, C., 2010. Machine tool spindle units. *Annals of the CIRP 59*(2):781-802.

[10] Munoa, J., Beudaert, X., Erkorkmaz, K., Iglesias, A., Barrios, A. and Zatarain, M., 2015. Active suppression of structural chatter vibrations using machine drives and accelerometers. *Annals of the CIRP 64*(1):385-388.

[11] Van Dijk NJM, et. al. (2012) Robust Active Chatter Control in the High-Speed Milling Process. *IEEE Trans Control Syst Technol.,* 20(4):901-917.

[12] Mancisidor I, et. al. (2019) Delayed feedback control for chatter suppression in turning machines. *Mechatronics*. 63(1):102276.

[13] Altintas, Y. and Woronko, A., 2002. A piezo tool actuator for precision turning of hardened shafts. *Annals of the CIRP* 51(1), pp.303-306.

Single point diamond turning of CVC SiC using the Micro-LAM process

Hossein Shahinian[1], Yuxiang Zhong[1], Robert Turnbull[1], Charan Bodlapati[1], Jayesh Navare,Hossein Mohammadi[1]
[1]Micro-LAM , Inc
5960 S Sprinkle Rd
Portage, Michigan, USA

INTRODUCTION

Single point diamond turning (SPDT) has been an enabling technology, in that high precision optical components can be manufactured deterministically [1]. Conventional grinding and polishing, in contrast to SPDT, have several limitations such as low process determinism, difficulty with making complex geometries, and demand for high skilled workers. One key restraining factor of SPDT is the material of the workpiece [2]. Most of the optical materials are considered not “diamond turnable”. The ability to SPDT a certain material, or lack thereof, is determined by whether the process is capable of producing surfaces with low roughness values, as well as repeatable form of the optic produced. Producing optical quality surfaces is usually achieved when ductile material removal (DMR) can be realized.

The majority of the materials that are considered diamond turnable are soft metals such Cu, Al. etc., and a limited number of brittle crystals such as single crystalline Si, Ge, CaF2, or polycrystalline ZnS, ZnSe, etc. [3-6]. However, a key optical material that poses a great challenge in SPDT of its surface is SiC. SiC is a popular mirror or molding substrate for optical applications due to its superior mechanical and thermal properties [7].

An active area of research of SPDT of materials is the addition of assistive elements to conventional SPDT process with the goal of expanding the list of diamond turnable materials. A number of researchers have studied the effect of adding ultrasonic vibrations to the machining process. Bulla et al. [8] have reported machining of hardened steel to average roughness values below 5 nm Ra. Li et al. [9] studied the SPDT of WC molds using ultrasonic assisted machining (USM) technique. Gan et al. [10] have been able to produce surfaces with Ra values better than 100 nm on fused silica glass using USM.

Another common category of assistive machining techniques is generally referred to as laser assisted machining (LAM) [11]. In LAM the main idea is that the absorption of a laser beam by the workpiece material will raise the temperature of the surface, thereby altering the surface material properties in a favorable way for SPDT. The μ-LAM process is a form of LAM where the laser beam is directed through the tooling medium, see FIGURE 1. The advantage of this method is that the heat transfer is done in a very localized and targeted way in the neighborhood of the cutting edge.

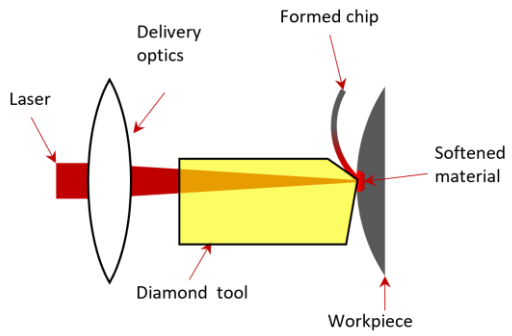

FIGURE 1. μ-LAM simplified concept

A commercialized solution using the μ-LAM process has been developed by Micro-LAM Inc. The Optimus T2, the tool holder, is made such that the optics responsible for the delivery of the laser beam are enclosed within an isolating volume, see FIGURE 2. In addition, fine adjusting stages are attached to the optical assembly for alignment of the laser beam relative to the cutting edge of the diamond tool.

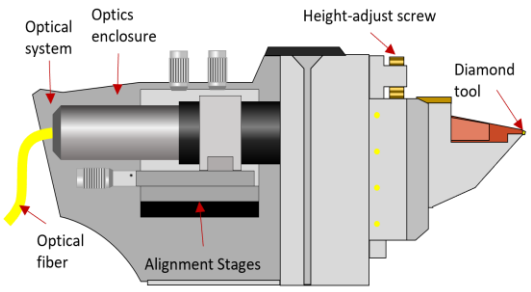

FIGURE 2. Optimus T2 tool holder

The application of the μ-LAM process for cutting difficult to machine materials such as optical silica glass and WC has been investigated in the past [12, 13]. In this paper we report on preliminary cutting data of chemical vapor composite (CVC) SiC using the μ-LAM process.

EQUIPMENT AND HARDWARE

Experimental test bed

The ultraprecision machining (UPM) center was a 4-axis Precitech NanoX. The machining was done, however, only using two axes, X and Z. FIGURE 3 depicts the UPM as well as the Optimus T2 tool holder mounted on the machine. The laser light with a wavelength of 1064 nm was delivered through an optical fiber in continuous wave (CW) mode. The coolant/lubricant used was odorless mineral spirits (OMS) and was spray misted on the cutting zone.

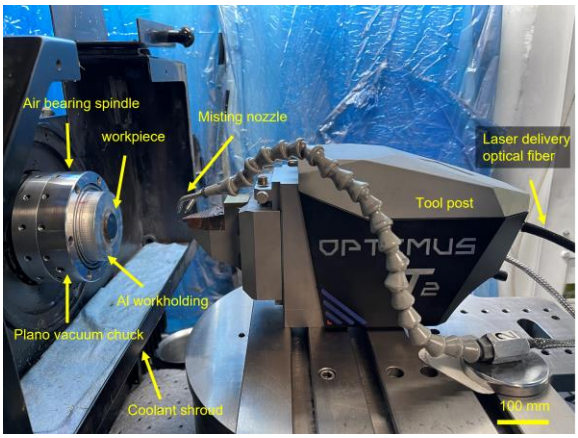

FIGURE 3. Experimental test bed

The part was a ∅25 mm planar CVC SiC. The part was blocked on a ∅64 mm planar Al using a UV cured glue. This was done to increase the surface area held by the planar vacuum chuck.

Surface Metrology

Surface roughness measurements were done using Zygo ZeGage HR, scanning white light interferometer (SWLI). A 50× Mirau objective was used, and the instrument had a 1024 × 1024 pixels size detector. A fourth order Chebyshev polynomial was removed from the raw data. The surface roughness was quantified by taking the root mean square (RMS) of the residual surface data. FIGURE 4(a), (b) show microscopic image and SWLI phasemap of the surface of the sample before the SPDT cuts.

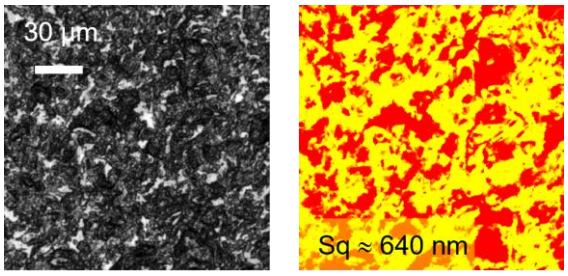

FIGURE 4. SiC sample surface before SPDT tests (a) 50× microscopic image (b) SWLI phase map

Diamond Cutting Tools

The tools were made of single crystalline diamond that were formed naturally. The diamond stone was oriented such that the top plane of the diamond was oriented in the <110> direction, while the cutting occurred in the {100} direction relative to the diamond crystal. The tool had a nose radius of 1.5 mm, rake angle of -25°, and a primary clearance of 10°. The tools were manufactured by Edge Technologies®.

Diamond turning conditions

Five tests were done. In all tests the spindle speed was kept at 375 RPM. The depth of cut (DoC) was also maintained at a constant 4 μm. The two variables were the tool linear feed, as well as the laser power transmitted through the diamond tool. For details regarding the laser alignment and power measurements see reference [14]. A summary of the cutting parameters can be found in Table 1.

Table 1. Process parameters

Test	Spindle speed (RPM)	Linear feed (mm/min)	Doc (μm)	Laser power (W)
1	375	1.25	4	6
2	375	0.6	4	6
3	375	0.3	4	6
4	375	0.3	4	12
5	375	0.15	4	12

RESULTS AND DISCUSSION

The first three tests in Table 1 were done in sequence with the same cutting tool. Due to considerable amount of tool wear after the third test the tool was resharpened for tests 4, and 5. After the tests, surface roughness measurements using the SWLI were acquired in

three different sections of the sample. Three measurement per section was taken. These sections are labeled "*center*" i.e., a zone within 1 mm radius of the center of the workpiece. "*middle*", i.e., a zone within an anulus enclosed at 5 mm and 7 mm radius from the center of the workpiece. And, "*edge*", i.e., a zone outside the radius of 12 mm from the center of the workpiece.

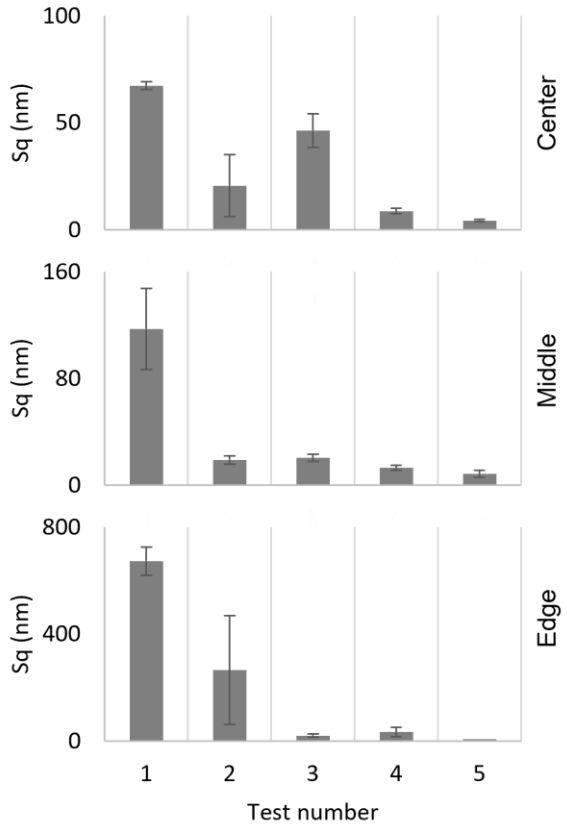

FIGURE 5. RMS surface roughness for "center", "middle", "edge" zones for tests 1 through 5

The RMS roughness of the three measurements per zone are calculated and averaged. FIGURE 5 depicts these average values for all the 5 tests. It appears that the roughness of the surface is inversely proportional to the linear feed (comparing tests 1, 2, and 3) for the "*middle"* and "*edge"* zones. The improvement of the surface quality with lower feeds should not be a surprise. The linear feed directly influences the chip thickness during material removal. Given the highly brittle nature of SiC, DMR is likely to happen for smaller chip thicknesses. It should also be noted that the improvement of the surface with reduction in feed is more gradual for the "*edge"* of the part. We speculate that this is due to the edge being the point of entry for the tool and therefore the surface will experience a larger variable force due to the onset of tool and part engagement. These variable forces will be an issue up to the point of full contact between the tool and the workpiece.

The surface roughness of the "*center"* of the part is not quite following the same trend as that of the "*middle"* and "*edge*". This could be due to the lower surface speeds near the center and thus making the brittle fracture less sensitive to the chip thickness. Further investigation of the relationship between surface speed and surface quality is underway.

Test 4 (laser power ≈ 12 W) has similar roughness to test 3 (laser power ≈ 6 W) at the "*edge"*. However, it can be seen that surface has improved on the "*middle"* and "*center"* by 35% and 83% respectively. It is suspected that the lower surface speeds in those zones allows a larger dwell time for the laser spot resulting in higher heating for the cutting zone. SiC is approximately 60% absorptive to the 1064 nm wavelength. The data appears to show that doubling the laser power (and therefore heating) has promoted DMR.

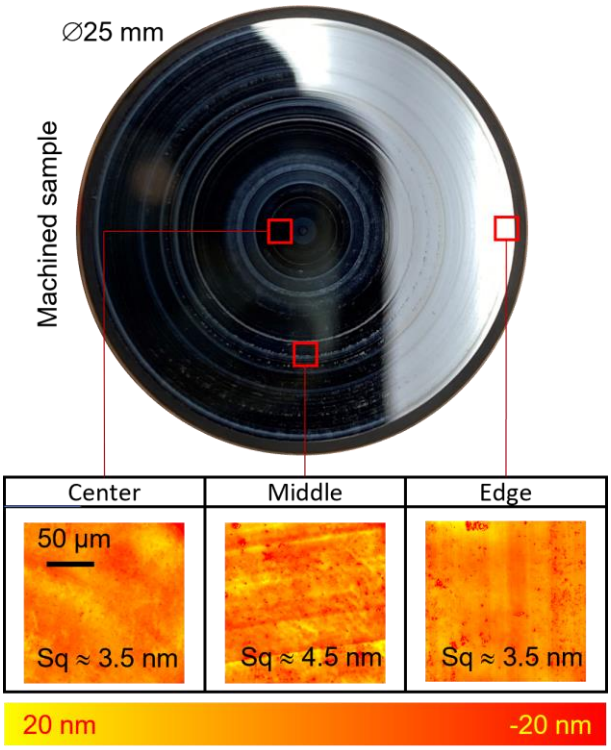

FIGURE 6. Machined SiC sample after test 5 and SWLI phasemaps of "center", "middle", and "edge"

As a final test, i.e. test 5, the tool feedrate was reduced even further to 0.15 mm/min, while maintaining the higher 12 W laser power. This test was done with the goal of producing the best possible surface. This is based on two conclusions from test 1 through 4; (1) reduced feedrate and consequently smaller chip thickness and (2) reduced linear speed and higher laser spot dwell times, appear to increase the probability of DMR. FIGURE 6 shows a photograph of the machined sample as well as SWLI phasemaps measured in the three "*center"*, "*middle"*, and "*edge"* zones. The surface in FIGURE 6 looks reasonably specular and uniform. Some zones can be observed that may indicate minute fractures on the surface. Reasons for such zoning is not quite understood at this point in time. With that being said, it appears that using the μ-LAM process and under certain machining parameters a specular surface on a planar geometry can be produced. The data may suggest that the heating effect of the laser can be beneficial in easing the material removal process and producing a smoother surface.

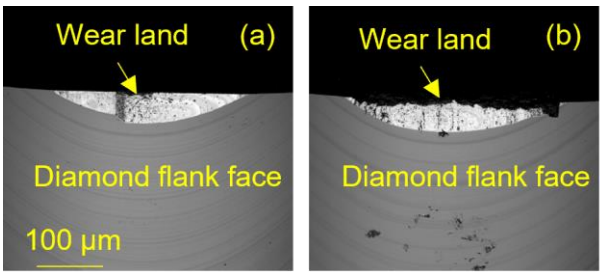

FIGURE 7. Microscopic images of diamond tools after (a) tests 1,2, and 3, (b) tests 4, and 5

Lastly, microscopic images of the diamond tool used in the tests 1, 2, and 3, and the tool used in tests 4 and 5 were taken, see FIGURE 7(a), (b). As evident in FIGURE 7 in both test the tool is worn significantly and the wear land at its maximum have approximately 50 μm width. The wear mechanisms were not investigated; however, this large amount of wear could be problematic for machining optics that require low form error control and will be studied for future efforts.

CONCLUSION AND FUTURE WORK

The studies presented in this paper are very preliminary and are the initial stages of exploring SPDT of CVC SiC. The work done showed that on this particular grade of SiC it is possible to generate surfaces that have roughness values below 10 nm RMS. In addition to the results above, while not reported here, we have studied the effect of different diamond crystals (e.g. cubic synthetic) and tool geometries with different rake angles. We have also explored the usage of water-based coolant during the cutting process. Neither of those studies produced promising results and therefore we made the decision to not to report them in this article.

While the results reported here can be an exciting prospect for the optics industry, a significant amount of time and research is warranted to realize a commercially viable solution. In doing so the future work for this research are as follows;

- Determination of the optimal laser power and other machining parameters such as spindle speed, feeds, and DoC.
- Studying the relationship between surface speed, as well as laser dwell times, and possible enhancement of DMR of SiC with the aforementioned variables.
- Better understanding the tool wear mechanism and efforts to develop tooling geometries that would experience less tool wear. It also should be noted that tool life is another matter of critical importance in this category.
- Investigation on the process efficiency in cutting nonplanar surfaces (spheres and aspheres). Specifically speaking, evaluating best possible surface form and roughness achievable.
- Studies on the effect of different coolants/lubricants in improving DMR of SiC.

In closing, it goes without saying that the opportunity of SPDT of SiC substrates is highly worth investigating, and this group will continue such efforts and publication of results in the near future.

REFERENCES

1. To, S.S., V.H. Wang, and W.B. Lee, *Single point diamond turning technology*, in *Materials Characterisation and Mechanism of Micro-Cutting in Ultra-Precision Diamond Turning*. 2018, Springer. p. 3-6.

2. Rhorer, R.L. and C.J. Evans, *Fabrication of optics by diamond turning.* Handbook of optics, 1995. **1**: p. 41.1-41.3.

3. Goel, B., S. Singh, R.V. Sarepaka, V. Mishra, N. Khatri, V. Aggarwal, K. Nand, and R. Kumar, *Diamond turning of optical materials: a review.* International Journal of Machining and Machinability of Materials, 2021. **23**(2): p. 160-190.

4. Turnbull, R., C. Bodlapati, Y. Zhong, D. Kang, J. Navare, and H. Shahinian. *The Manufacturing of a Zinc Selenide Toric Lens using Slow Slide Ultra-Precision Diamond Turning and Micro-LAM*. in *Optical Fabrication and Testing*. 2021. Optical Society of America.

5. Bodlapati, C., D. Kang, J. Navare, R. Turnbull, Y. Zhong, and H. Shahinian, *Cutting performance of laser assisted diamond turning of calcium fluoride with different crystal orientations.* Applied Optics, 2021. **60**(9): p. 2465-2470.

6. Navare, J., D. Kang, D. Zaytsev, C. Bodlapati, D. Ravindra, and H. Shahinian, *Experimental investigation on the effect of crystal orientation of diamond tooling on micro laser assisted diamond turning of zinc sulfide.* Procedia Manufacturing, 2020. **48**: p. 606-610.

7. Horvath, N., A. Honeycutt, and M.A. Davies, *Grinding of additively manufactured silicon carbide surfaces for optical applications.* CIRP Annals, 2020. **69**(1): p. 509-512.

8. Bulla, B., F. Klocke, O. Dambon, and M. Hünten. *Ultrasonic assisted diamond turning of hardened steel for mould manufacturing*. in *Key Engineering Materials*. 2012. Trans Tech Publ.

9. Li, Z., G. Jin, F. Fang, H. Gong, and H. Jia, *Ultrasonically assisted single point diamond turning of optical mold of tungsten carbide.* Micromachines, 2018. **9**(2): p. 77.

10. Gan, J., X. Wang, M. Zhou, B. Ngoi, and Z. Zhong, *Ultraprecision diamond turning of glass with ultrasonic vibration.* The International Journal of Advanced Manufacturing Technology, 2003. **21**(12): p. 952-955.

11. You, K., G. Yan, X. Luo, M.D. Gilchrist, and F. Fang, *Advances in laser assisted machining of hard and brittle materials.* Journal of Manufacturing Processes, 2020. **58**: p. 677-692.

12. Shahinian, H., C. Bodlapati, J. Navare, R. Turnbull, D. Kang, and Y. Zhong. *Laser assisted diamond turning of silica glasses*. in *Optical Fabrication and Testing*. 2021. Optical Society of America.

13. Kang, D., J. Navare, Y. Su, D. Zaytsev, D. Ravindra, and H. Shahinian. *Observations on ductile laser assisted diamond turning of tungsten carbide*. in *Optical Fabrication and Testing*. 2019. Optical Society of America.

14. Shahinian, H., J. Navare, D. Zaytsev, and D. Ravindra, *Microlaser assisted diamond turning of precision silicon optics.* Optical Engineering, 2019. **58**(9): p. 092607.

SIMULATION AND COMPARATIVE METROLOGY OF DIAMOND DIES, METAL MOLDS, AND REPLICATED MICROLENS ARRAYS FOR MASS FABRICATION

Parker Eaton[1], Dr. Stephen Furst[2], Dr. Nichole Cates[2], Lauren Micklow[2], Dr. Mark Pankow[1]
[1]Precision Engineering Consortium
North Carolina State University
Raleigh, NC, USA
[2]Smart Material Solutions, Inc.
Raleigh, NC, USA

MANUFACTURING OF MICROLENS ARRAYS

Motivation

Recent decades have seen the continued downsizing of electronic devices and computer chips, with the miniaturization of optical elements in cameras and displays following suit. Many smartphone and digital camera sensors comprise pixels with dimensions on the micrometer scale. These pixels are covered with a microlens array used primarily for guiding light to the pixel. To keep up with industry demands while remaining affordable to consumers, a method to manufacture microlens arrays of a tight tolerance rapidly and affordably must be employed. In this work, a closed-loop process is proposed to quantify, correct for, and minimize geometric form error associated with high-speed manufacturing of microlens array molds for optical applications. Nanocoining, a high-speed nanopatterning process, is the manufacturing method investigated in this work.

Traditional Methods

Microlens arrays, which are often made of plastics or polymers, may be manufactured via both direct and indirect methods. Direct methods include thermal reflow, microplastic embossing, and microdroplet jetting [1]. These approaches are typically associated with low accuracy and low cost, making them suitable for most industry applications where precision is not needed. Conversely, indirect methods such as photolithography, ultraprecision machining, injection molding, and compact molding are more accurate but significantly more expensive than direct methods [1]. Indirect methods rely on the fabrication of a negative, convex mold which is expensive and difficult to produce. These molds have traditionally been manufactured via ultra-high precision machining operations or photolithography which are costly and time consuming.

Nanocoining

Nanocoining is a technology developed at the Precision Engineering Consortium (PEC) at North Carolina State University and is being commercialized by Smart Material Solutions, Inc. Nanocoining improves on traditional practices by allowing the rapid manufacturing of seamless drum molds for the roll-to-roll (R2R) nanolithography of sub-wavelength topographical features [2]. Nanocoining significantly reduces the cost and time required to manufacture a metallic mold of a suitable size for a microlens array. Nanocoining can pattern a metallic mold several hundred times faster than electron beam lithography [3]**.** Forming operations that would take days using traditional methods can be reduced to hours with the use of nanocoining. Concave features are formed in the metallic mold using a diamond die with convex features focused ion beam (FIB) milled into the tip (see *FIGURE 1*). To create billions of features within a matter of hours, the die is mounted to an ultrasonic resonant actuator which indents the die into the metal mold at a rate of 45 kHz (*see FIGURE 2*) [4].

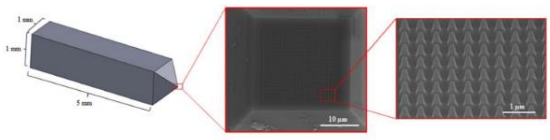

FIGURE 1. A typical nanocoining diamond die with nanostructures FIB milled into the tip [3].

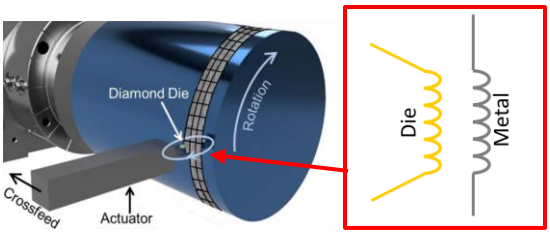

FIGURE 2. The nanocoining process featuring an ultrasonic resonant actuator (left) driving a diamond die into a cylindrical part (right) [3].

Smart Material Solutions, Inc., has used nanocoining primarily for the manufacturing of antireflective, light-absorbing, and dust-mitigating metasurfaces. The features integrated into these metasurfaces are typically sub-micrometer in pitch and height (see *FIGURE 5* for definition). Due to the nature of the application, the shape of the features is not as critical to their successful function as it would be for a microlens array, where the array's function is heavily dependent on the form of the lenses.

Challenges

Current nanocoining methods, while extremely fast, produce a mold composed of features with a degree of form error (*FIGURE 3*).

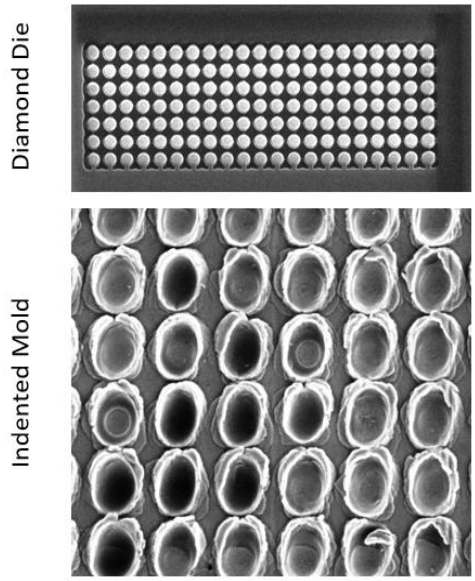

FIGURE 3. Geometric form errors are noticeable between the diamond die and the indented metal mold [3]. Note the pileup around features, inconsistent depth, and slight smearing of the features.

Due to the nature of current non-optical applications, this form error is tolerable as the feature geometry is adequate for the antireflective, light-absorbing, or dust-mitigating applications. Several factors may contribute to this form error including elastic rebound, plastic flow characteristics, surface preparation and treatment, and inaccuracies in diamond die alignment and positioning. Additional errors are exhibited when replicating the convex microlens array from the drum mold. Different materials and processes will result in an expansion or contraction of the material while molding. Depending on the lens material, these errors can be very large. Standard optics are innately subject to very tight tolerances and this fact does not change when scaled down to the micrometer and nanometer scale. As such, minimizing the error throughout the microlens array manufacturing process is critical for the array to operate as designed, bringing about the need for an error minimization process.

PROPOSED CLOSED-LOOP FORM ERROR MINIMIZATION METHODOLOGY

The proposed closed-loop form error minimization process is composed of four primary elements: a quasistatic finite element indenting simulation, a proprietary low-speed indenting system, a comprehensive atomic force microscopy (AFM)-based metrology and validation process, and a design modification step. The flowchart below in *FIGURE 4* illustrates the process undergone to create an error-minimized microlens array from a baseline lens design.

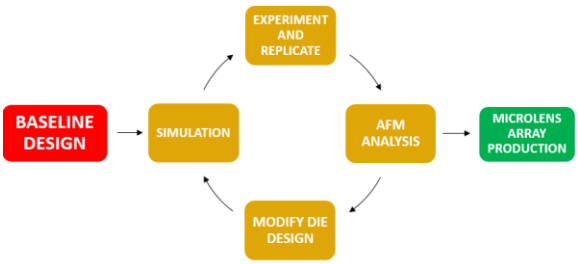

FIGURE 4. Proposed microlens form error minimization process.

To begin the process, a diamond die is designed virtually and then FIB milled to match the desired replicated microlens geometry. Indenting with the die is simulated in the quasistatic indenting finite element model (FEM) and baseline form errors are computed and noted. Following simulation,

the initial die is indented into a metallic mold and a microlens array of the desired lens material is replicated from the mold. The die, mold, and replicated microlenses are imaged via AFM. A MATLAB-based program processes the AFM and simulation data and presents aligned cross-sectional and topological plots. These figures allow for the analysis of form errors and the computation of transfer functions. Based on the AFM measurements, a transfer function is established between the replicated microlens array and the mold. Insights from simulation and this transfer function are used to model and manufacture a die designed to produce this ideal mold geometry. The cycle of simulation, experimentation and replication, and metrology continues until a microlens array within the desired tolerances is repeatedly produced.

Baseline Design

A microlens array geometry is established based on the desired lens performance, which may be, for example, collimating light rays. In practice, the collimating lens is defined by a parabolic shape with a lens height, pitch, and width. *FIGURE 5* illustrates this lens definition.

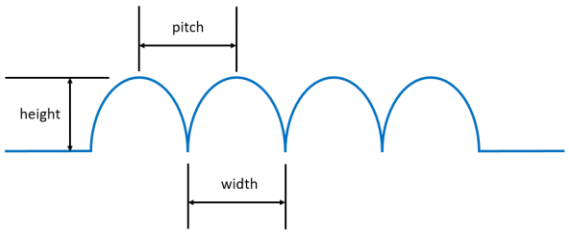

FIGURE 5. Illustration of microlens geometric parameters.

Smart Material Solutions, Inc. uses a proprietary FIB milling technique to manufacture a variety of feature profiles including the parabolic lens profile. FIB milling is completed on a FEI™ Quanta 3D DualBeam SEM/FIB at the Analytical Instrumentation Facility (AIF) at North Carolina State University in Raleigh, NC.

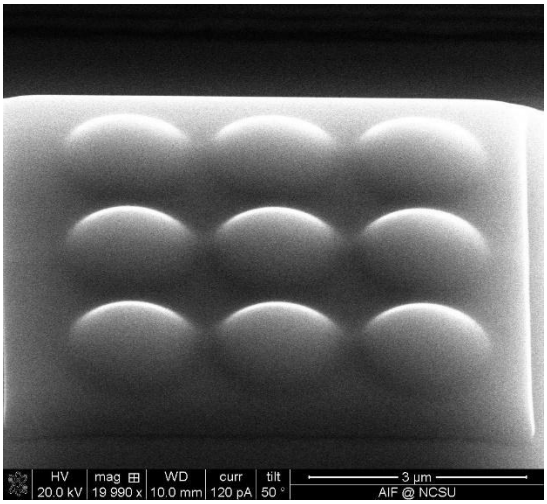

FIGURE 6. SEM image of a diamond die manufactured by Smart Material Solutions, Inc.

Manufacturing a die based solely on the desired lens geometry allows for the understanding of errors associated with each step of the manufacturing process. Quantifying these errors facilitates the derivation of transfer functions between each step of the manufacturing process for a given project which will reduce the number of innovation cycles needed to converge to a quality microlens array.

Quasistatic Indenting Simulation

A quasistatic finite element simulation is constructed in ABAQUS/Explicit™. The explicit solver offered by Simulia™ is used in simulations where large, nonlinear deformations are expected, such as in sheet metal forming or vehicle collision simulations. The FEM is used to estimate both initial form errors in the indented mold and the effect geometry changes will have when applied to the diamond die. The mold material is modeled using a Ramberg-Osgood material model which incorporates strain-hardening behavior. Strain-hardening is important to model in metal forming processes as material flow must be intelligently managed to prevent the material from becoming too hard, resulting in reduction of flow in the hardened region. The diamond die is imported as a STEP file created from an AFM image. The diamond die is modeled as a rigid body for the purpose of simplifying the model and reducing the run time.

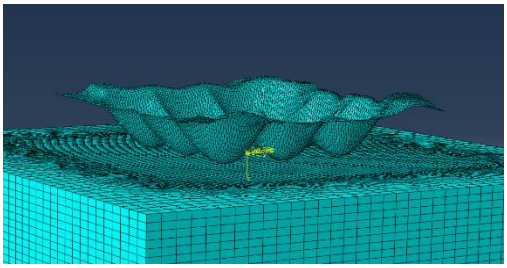

FIGURE 7. Meshed nine-feature diamond die and metallic mold in the FEM.

The simulation can model both a single indent or repeated indents into the mold material. This allows for the study of the effect different indenting techniques have on the indented mold geometry. After completion of the simulation, indenting force as a function of indenting depth plots may be created (*FIGURE 8*) and compared to those obtained from the actuator developed for low-frequency testing. Additionally, the indented mold surface may be output and used in comparative metrology in conjunction with AFM images of dies, molds, and replicas.

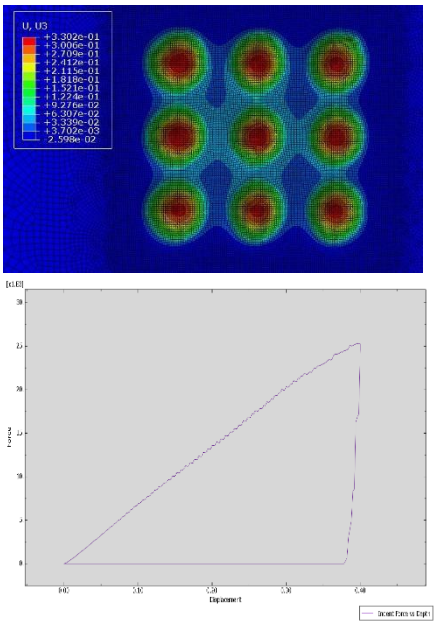

FIGURE 8. Deflection contour plot of simulated indents into a metallic mold (top) and a constructed indenting force (mN) vs indenting depth (μm) curve created from the FEM (bottom).

Low-frequency indenting and replication

Low-frequency (less than 100 Hz) indenting and microlens array manufacturing via replication is completed at Smart Material Solutions, Inc. The indenting system is controlled via Aerotech™ A3200 CNC software. Diamond-turned metallic molds are mounted to an air bearing spindle. The actuator repeatedly indents the mold with a predefined force to construct an array of concave microlenses (*FIGURE 9*). Low-frequency indenting is necessary due to the precise process control and data acquisition required to study the effects of die geometry and process parameters on the mold and replicated microlens geometries. A convex microlens array is then replicated from the mold (*FIGURE 10*)

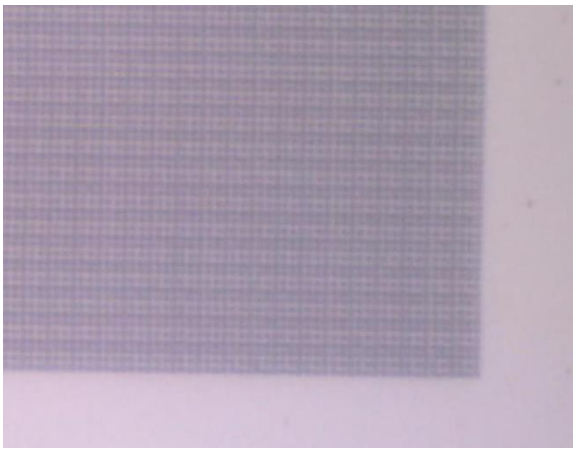

FIGURE 9. Microlens array indented on metallic mold.

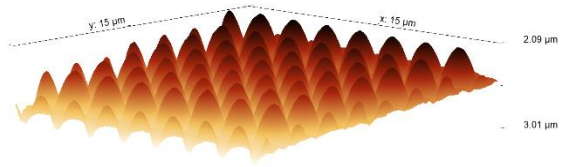

FIGURE 10. AFM image of a replicated microlens array.

AFM comparative metrology routine

An AFM-based comparative metrology routine is employed to quantify geometric form errors, analyze the root cause of these errors, and modify geometry to correct for error. AFM images are taken using an Asylum™ MFP-3D atomic force microscope located at the Analytical Instrumentation Facility (AIF) at North Carolina State University. The outputs of the MATLAB-based metrology program include cross-section plots (*FIGURE 14*), 3D surface plots of all surfaces of interest (*FIGURE 11*), and error surfaces (*FIGURE 15*). The error surfaces may be added or subtracted from certain imported

geometries such as the diamond die in the effort to compensate for form error. For any of the outputs to be of use, all data must be precisely aligned and overlayed. AFM data is imported to MATLAB in XYZ format.

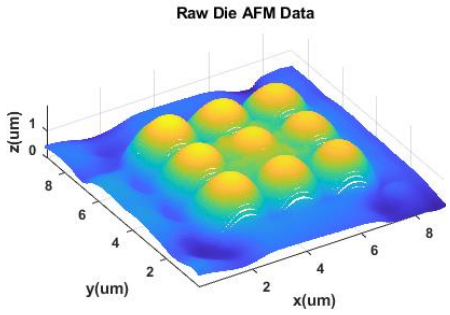

FIGURE 11. Raw, unaligned die AFM XYZ data.

Each image is sent through an iterative algorithm. The vertices of the indent/lens are detected and the data set is transformed iteratively until corner vertices lie in the same plane and align with the local coordinate system with the central vertex being coincident with the origin (*FIGURE 12*). Vertices are detected after each transformation. Additional transformations are conducted to align each local coordinate system with the global coordinate system. For example, an AFM image of the metallic mold might be taken 90 degrees relative to an image of an indent. This must be accounted for by rotating one data set 90 degrees relative to the other.

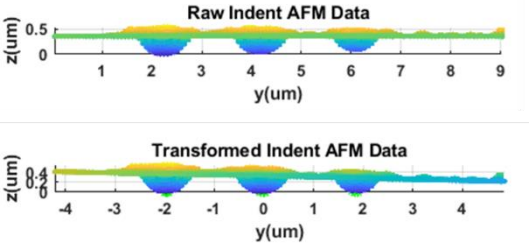

FIGURE 12. Alignment of an indent AFM data set to the x-y plane. Unaligned (top) and aligned (bottom). Note the green asterisks in the aligned image are the detected vertices.

Once aligned, a surface fit is conducted to ensure that all data points for each image lie directly on top of one another. Lastly, a compensation for error associated with the AFM probe tip radius is applied to the data. Now, the cross-section plots may be created. *FIGURE 13* illustrates the cross-sectional views. *FIGURE 14* presents example cross-section plots.

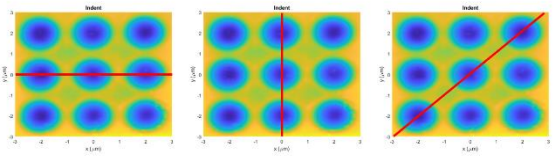

FIGURE 13. Cross-sectional view slices in red for the XZ (left), YZ (middle), and 45-degree (right) cross-sections.

With the data imported and aligned, analysis can be conducted to identify form error, potential sources of form error, and establish transfer functions between the steps of the microlens manufacturing process.

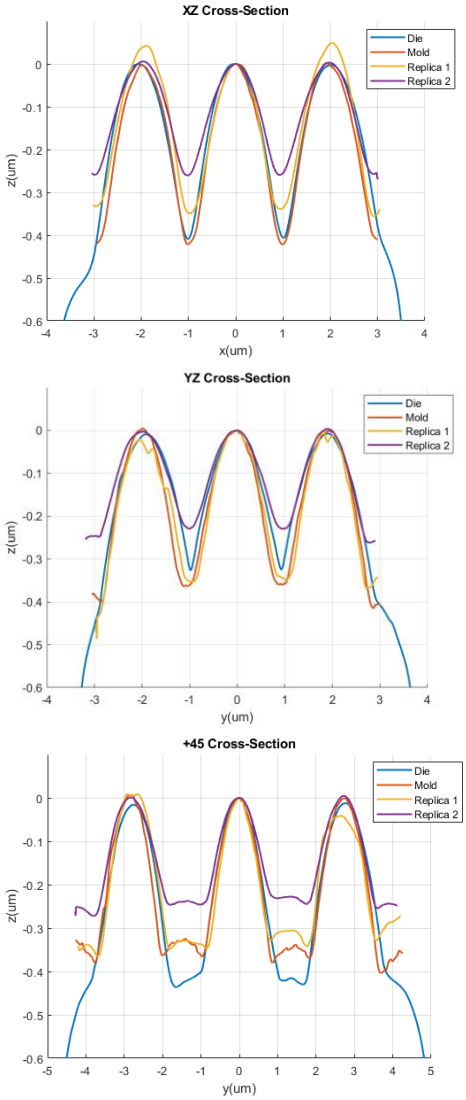

FIGURE 14. XZ, YZ, and 45-degree cross-sections of diamond die, metallic mold, and two replicated microlens arrays created using different methods and materials.

In addition to cross-sectional views, form error may be computed between any specific images. This is useful for identifying specific regions where large form error is present. An error surface may be computed. This surface can be added or subtracted to any image data set. For example, an error-compensated die may be exported as a STL file for importation and analysis in CAD software. During the initial stages of error minimization, an early error compensation can decrease the form error to a much more manageable level early on, decreasing the time spent within the error minimization loop.

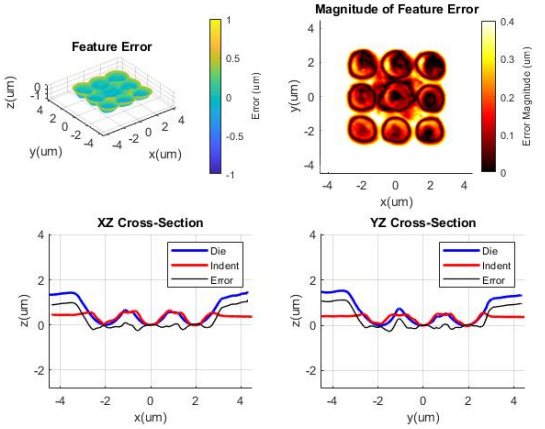

FIGURE 15. Geometric from error computation between the diamond die and the indented metal mold. The error surface is computed in the top left plot.

As iterations through the form error minimization loop continue, form error should steadily decrease until it is within an acceptable range. STL files of the microlenses may be output for use in optical simulations to verify their function and verify that the desired performance is achieved.

FUTURE WORK

In future work, a microlens array of a specified material will be prescribed and the entire process will be completed for that specific lens prescription. Completing the form error minimization process will highlight components needing improvement and offer insight into methods to speed up the process. The largest gains in cost reduction and time efficiency will be found in further improving the simulation abilities. Accurate insights gained through simulation are far more valuable than those same insights acquired through physical experimentation as the cost and time to manufacture diamond dies, indent with them, and perform metrology over many iterations is greater than a software license and a simulation's run time. The more analysis that can be done virtually, the faster and cheaper a process can be developed for manufacturing a microlens array. In addition to modeling the physical indenting process, a simulation of the microlens array molding process may be developed depending on the material and method used in forming the lenses. Having simulation capabilities to identify transfer functions virtually will allow for geometric form error to rapidly decrease before the first round of physical experimentation begins, thus again reducing the cost and time to develop the process.

REFERENCES

[1] W. Yuan, L. H. Li, W. B. Lee, and C. Y. Chan, "Fabrication of Microlens Array and Its Application: A Review," *Chinese J. Mech. Eng. (English Ed.*, vol. 31, no. 1, 2018, doi: 10.1186/s10033-018-0204-y.

[2] E. Zdanowicz, T. A. Dow, R. O. Scattergood, and K. Youssef, "Nanostructure fabrication on germanium and silicon by nanocoining imprint technique," *Precis. Eng.*, vol. 37, no. 4, pp. 871–879, 2013, doi: 10.1016/j.precisioneng.2013.05.004.

[3] N. Cates *et al.*, "Roll-to-roll nanoimprint lithography using a seamless cylindrical mold nanopatterned with a high-speed mastering process," *Nanotechnology*, vol. 32, no. 15, 2021, doi: 10.1088/1361-6528/abd9f1.

[4] T. A. Dow, J. Nowak, and J. R. Kessing, "Design of elliptically-vibrating ultrasonic actuator for nanocoining," *Precis. Eng.*, vol. 45, pp. 301–310, 2016, doi: 10.1016/j.precisioneng.2016.03.007.

METROLOGY OF ULTRA-HIGH PRECISION STAMPED METALLIC OPTICAL MIRRORS FOR PHOTONICS PACKAGING

Yang Chen[1], Rollin Johnstone, King-Fu Hii, and R. Ryan Vallance[1]
CudoForm, Inc., Camarillo, CA, USA, 93012

INTRODUCTION

Precision micro-optical components are common in photonic devices, optical interconnects, and illumination systems [1,2]. Conventional micro-optical benches are frequently fabricated in polymer or glass materials and then integrated into an optical bench with pick-and-place automation, passive alignment, active alignment, and joining process [3].

In recent years, CudoForm developed a manufacturing process to produce metallic optical benches with high precision stamping processes [4]. In the stamping process, microscale features are stamped into the metal surfaces with a proprietary stamping process. With stamping tools that meet stringent tolerance specifications on form, size, and location, it becomes possible to impart accurate tool geometry into stamped components. The features stamped with the tools are used to passively align optical components (e.g. optical fibers, lenses, filters, etc.) in optical sub-assemblies or optical connectors. A further recent innovation is the ability to stamp micro mirrors into aluminum surfaces of metallic optical benches (MOBs). These mirrors have finishes better than Sa 5 nm without any secondary processes. This ability expands the application of MOBs by enabling beam folding and beam shaping with aspherical mirrors or freeform mirrors at a low manufacturing cost. FIGURE 1 illustrates two examples of high precision, stamped metallic micro optical components: a stamped MOB that couples optical fibers to silicon photonics and a metallic optical reflector (MOR) that concentrates light emitted by an LED.

The metrology of stamped micro-optical components remains a challenge. It is difficult to accurately measure the metallic optical mirrors' form, size, tolerance, and surface characteristics due to the soft material, feature size, and steep slope of the mirrors. In this paper, we describe these challenges, our current metrology techniques, and then present some results for some stamped metallic optical components. Multiple metrology methods, including both contact and non-contact methods using coordinate metrology machine (CMM) and scanning white light interferometer (SWLI), are applied to measure both the roughness of mirrors, the form error of micro mirrors, and the form errors in the groove array. A metrology routine and post-processing algorithm to process the data from metrology is also described. Data from stamped prototype parts are summarized and presented.

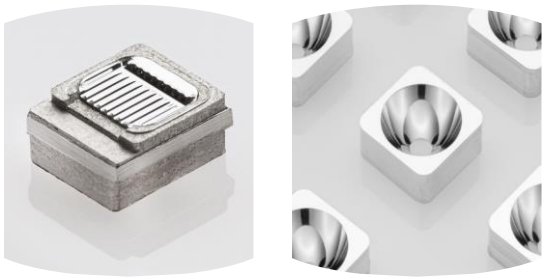

(a) (b)

FIGURE 1. CudoForm's high precision stamped micro-optics (a) metallic optical bench (MOB), and (b) metallic optical reflector (MOR).

METROLOGY OF STAMPING TOOLS

Microscale features are stamped into aluminum surfaces with CudoForm's patented stamping process. [5,6] The tools used in our stamping process contain the inverted geometry of the stamped features, and the tool's features meet tolerance specifications for form, size, and location for single-mode optical performance (generally better than 1μm). Since the stamping tool is made of a hard material, the accuracy of this tool can be measured with contact-based metrology techniques like a coordinate measuring machine (CMM). We use a Leitz Infinity CMM with a measurement uncertainty of about 300 nm. To measure the micro-features on the stamping tool, the radius of the CMM probe must be smaller than the radius of curvature of the micro-features. In our application, a 200 μm diameter ruby probe is used. With such a small probe, even a low probing force (~54 mN) generates sufficient contact pressure to yield the

tool surface. Therefore, ultra-low contact forces (~0.027 N) are necessary to prevent damage to the tool surface.

After contact measurement on the CMM, the point cloud is imported into commercial software and aligned to the reference 3D geometry using least squares alignment to datum features. Then, the deviations between each point and the CAD surface are calculated. FIGURE 2 shows a typical contour plot of deviations for critical features of a stamping tool. The deviations are generally within a tolerance band of +/- 200 nm, with only a few non-consequential exceptions outside the optical aperture or on non-critical surfaces.

The features that stamp micro grooves were also measured and compared to the reference CAD geometry using the same technique. Since the optical aperture and grooves were measured within same metrology setup, a single point cloud is used to evaluate the alignment between grooves and optical apertures within the mirror surfaces of the tool. As shown in FIGURE 2, the grooves are also generally within a tolerance band of +/- 200 nm over the region of the tool that forms the grooves, and the alignment between optical aperture and the grooves are better than +/- 200 nm.

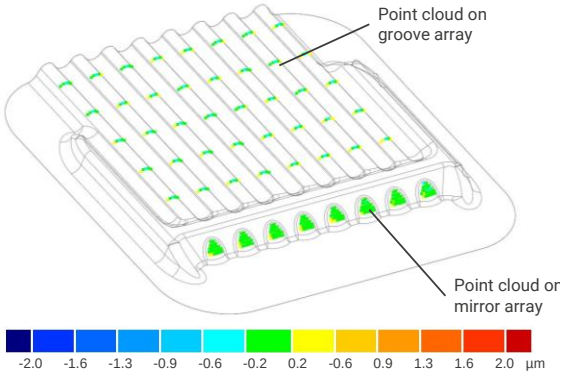

FIGURE 2. Metrology of the critical surfaces in a tool used to stamp MOBs. Color scale indicates deviations from the ideal geometry in features that form mirror array and groove array

The surface finish within the optical aperture of each mirror on the tool was also measured with a scanning white light interferometer (SWLI) using a high-pass filter with 17 µm cutoff to remove waviness and form. The average roughness was less than Sa = 3 nm.

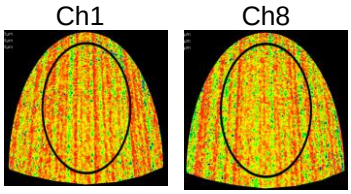

	Ch1	Ch8
Avg roughness (S_a)	3 nm	3 nm
RMS roughness (S_q)	4 nm	4 nm

FIGURE 3. Surface finish of two surfaces in a tool used to stamp aspherical mirrors into metallic optical benches (only showing the first and last channels as examples)

METROLOGY OF STAMPED METALLIC OPTICAL BENCHES

Contact-based metrology techniques cannot be used to measure the optical surfaces in stamped metallic optical benches since they are made of soft aluminum with a low yield strength. Even with lowest probing force, a ruby probe tip indents the stamped optical surface. Therefore, the accuracy of stamped metallic optical benches and the finish of their mirrors is evaluated with a scanning white light interferometer (SWLI) (Zygo, Nexview). A SWLI is a non-contact method to measure both the roughness of the mirrors, the form error in the array of micro mirrors, and the form error in the array of grooves without damaging the aluminum surface.

The fixturing arrangements on the SWLI, shown in FIGURE 4, are used in four metrology steps:

1. The finish of each mirror is measured and recorded. A measurement is performed with a 20X objective and 2X magnification so that the field of view is 211 µm X 211 µm, a little larger than a single mirror. Two roughness attributes are computed from the 3D data and recorded for each mirror: the 3D average roughness S_a and the 3D root mean square (*RMS*) roughness S_q. The raw data is filtered with a high-pass filter (cut-off wavelength of 17 µm) to remove waviness and form.

   FIGURE 5 illustrates the SWLI measurements for eight mirrors in a single stamped metallic optical bench. In the greyscale plots of the SWLI data, black corresponds to the deepest valley and white corresponds to the highest peak. The black ellipses superposed on the SWLI data identify the approximate optical aperture on the mirror surface.

2. The same data was used to evaluate the form error in each mirror, but a low-pass filter (17 μm cut-off wavelength) removed the surface roughness. After that, the point cloud was compared to the reference geometry using a least squares alignment method. The deviations from each point to the CAD surface were calculated, and the average deviation and RMS of all deviations was computed for each individual mirror and used for quality control. FIGURE 6 (a) shows a 3D contour plot of the deviations for an example mirror. The statistics of the deviations for each individual mirror (e.g., RMS deviation) provide a metric for evaluating the accuracy of the stamped mirrors. FIGURE 6(c) shows a box plot of statistics for the RMS deviation for a batch of 768 individual mirrors.

3. The 3D form of the entire array (1x8) of mirrors was evaluated using a 3D point cloud measured with the SWLI. The point cloud was measured with a 10X objective and 0.5X magnification, producing a field of view that was 1.66 mm X 1.66 mm. A sequence of 3 measurements (1X3) were stitched together in the SWLI software with an overlap of 45% to provide a composite point cloud with dimensions of 1.66 mm X 3.49 mm, which is just larger than the width of the MOB. The composite point cloud is compared with the reference CAD model by aligning the point cloud to the ideal CAD model with least-squares alignment and then computing the deviations from each point to the surface of the ideal model. FIGURE 6(b) shows a plot of the deviations which are essentially within a tolerance band of +/- 300 nm. A box plot illustrates the statistics for the RMS deviation for a batch of 90 stamped mirror arrays in FIGURE 6 (d).

4. The 3D form of the groove array was also evaluated using a 3D point cloud from the SWLI. The point cloud was measured with a 10X objective and 0.5X magnification so that the field of view was 1.66 mm X 1.66 mm. A sequence of 6 measurements (2X3) were stitched together with 45% overlap in the SWLI software to provide a composite point cloud with dimensions of 2.58 mm X 3.49 mm. The composite point cloud is evaluated against the reference geometry. However, the results presented in the next section show some potential errors in this SWLI stitching method.

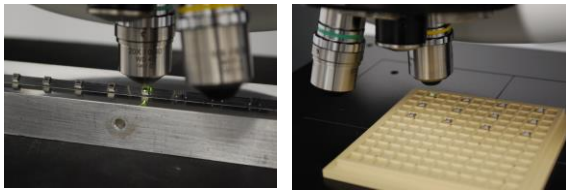

(a) (b)

FIGURE 4. Fixturing arrangement to measure finish and form of (a) stamped mirrors and (b) groove array in stamped MOBs

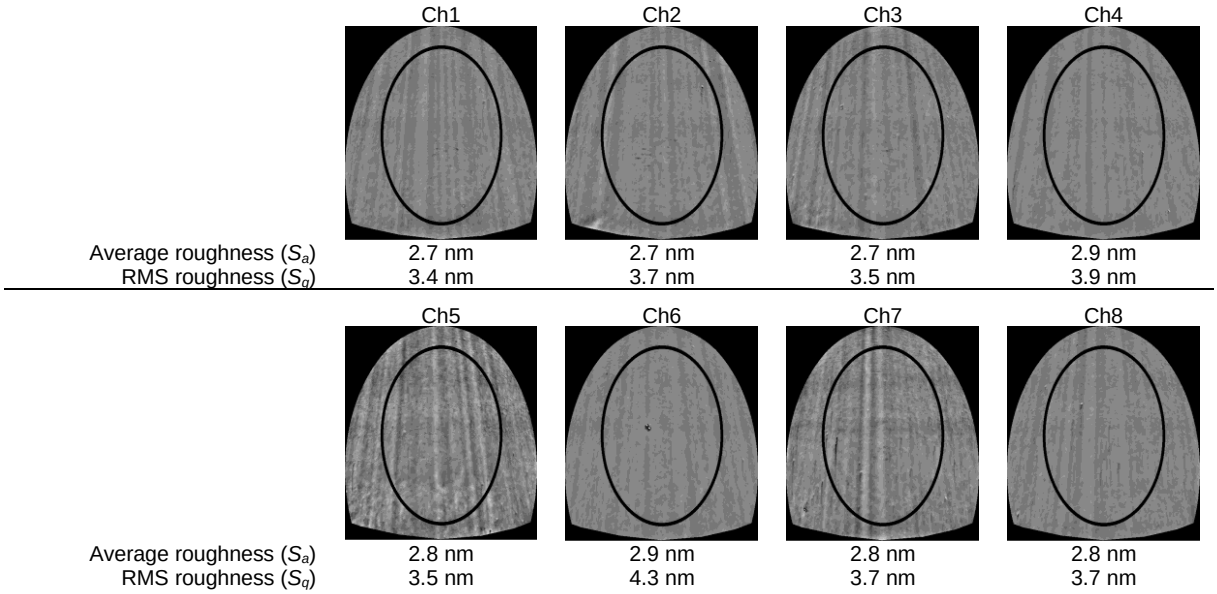

FIGURE 5. Typical surface finish for stamped mirrors in an 8X1 array, measured with a SWLI

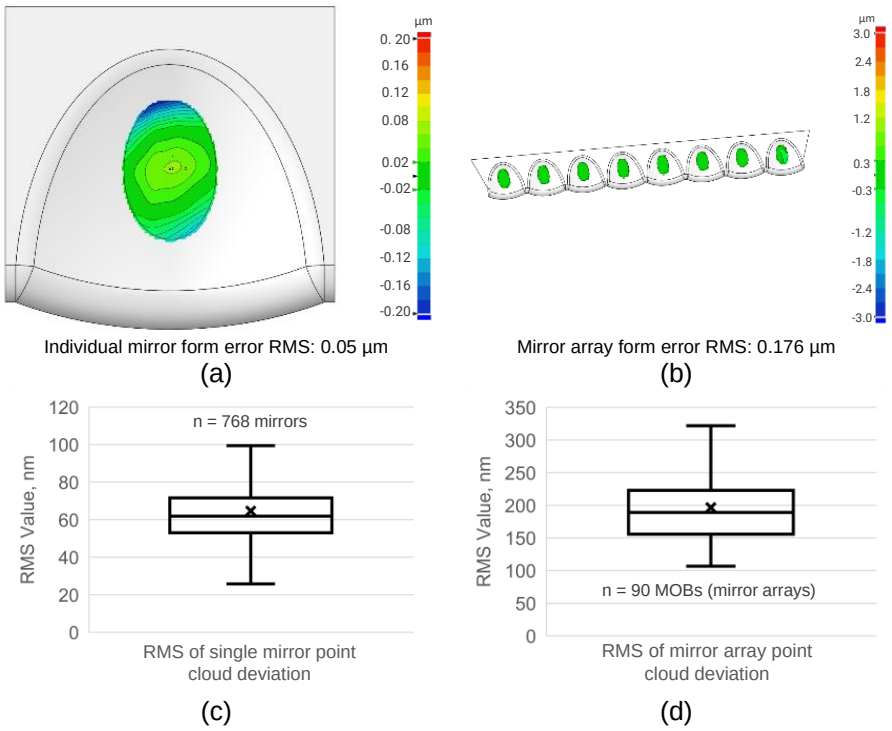

FIGURE 6. Form error measured with SWLI (a) Example of individual mirror form error defined as deviations from reference geometry in CAD model, (b) form error in apertures of mirror array, defined as deviations from reference geometry, (c) box plot of RMS of deviations for a batch of 768 individual mirrors stamped into metallic optical benches, (d) box plot of RMS of deviations for a batch of 90 mirror arrays stamped in metallic optical benches.

COMPARISON BETWEEN ALTERNATIVE METROLOGY METHODS

This section compares results that obtained using alternative techniques and instruments. The first study compares two different contact-based metrology methods for the measurement of hard stamping tools: CMM and stylus profilometer. FIGURE 7 shows metrology of a stamping tool using (a) contact probe and (b) stylus. The results of measurements with these two techniques are listed in TABLE 1. The two instruments show very good agreement. The difference between the two methods is less than 200 nm for the cumulative total pitch, which is within the instrument measurement uncertainty. Therefore, we use results from both instruments as a baseline for comparison to SWLI measurements.

Two different techniques were evaluated using the SWLI. The first process (referred to as SWLI Method 1 in TABLE 2) used a 2.5X objective lens and 1X magnification to produce a field of view that is 3.27 X 3.27mm, which covers the entire array of grooves. The second process (referred to as SWLI Method 2 in TABLE 2) is a stitching process (similar to the method described in the previous section) that used a 10X objective and 0.5X magnification to produce a field of view that was 1.66 mm X 1.66 mm. A sequence of 3 measurements (1X3) were stitched together in the SWLI software with adaptive overlap to provide a composite point cloud with dimensions of 3.8 mm X 1.5 mm. The same metallic fiber array was also measured by a profilometer with 2 µm conical diamond stylus tip, as shown in FIGURE 8. The results are listed in TABLE 2. The profilometer result agrees with nominal dimension with an average 20 nm deviation from the nominal pitch and 300 nm deviation on the cumulative total pitch. In contrast, the SWLI indicates +9 µm or -5 µm error on cumulative total pitch, respectively.

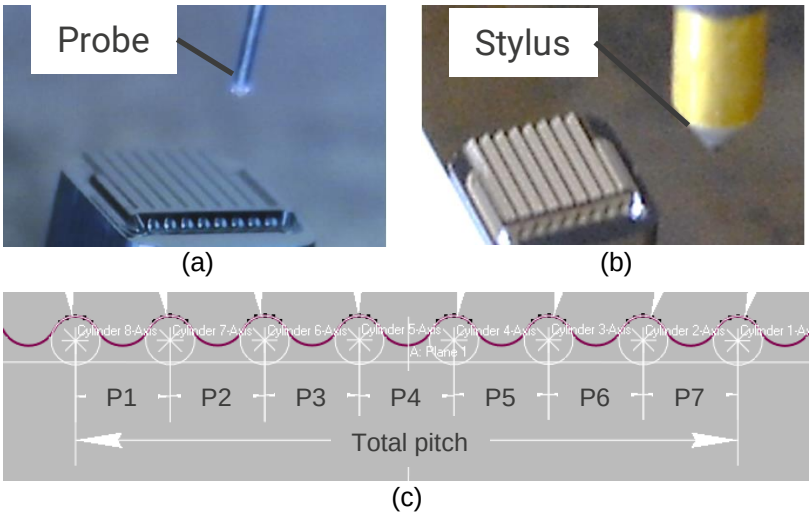

FIGURE 7. (a) Metrology of stamping tools' grooves with CMM contact probe and (b) stylus profilometer, and (c) dimensional results for groove-to-groove pitch

FIGURE 8. Measurements of a metallic fiber array with (a) profilometer and (b) SWLI

TABLE 1. The comparison of the measurement results from two different contact-based measuring tool CMM and Profilometer.

Metrology Instrument	(1) Groove-to-Groove Pitch, mm							(2) Total of Pitches
	P1	P2	P3	P4	P5	P6	P7	
CMM	0.2499	0.2502	0.2500	0.2500	0.2501	0.2500	0.2499	1.7501
Profilometer	0.2499	0.2500	0.2500	0.2500	0.2500	0.2500	0.2500	1.7499
Difference	0.0000	-0.0002	0.0000	0.0000	-0.0001	0.0000	0.0001	-0.0002

TABLE 2. The comparison of the measurement results between contact-based techniques and optical techniques using SWLI.

Measurement tool	Average groove to groove pitch, mm	Deviation from nominal 0.25, mm	Total pitch, mm	Deviation from nominal 2.75, mm
Profilometer	0.24998	0.00002	2.74970	-0.0003
SWLI Method 1	0.25082	0.00082	2.75897	0.0090
SWLI Method 2	0.24953	-0.00047	2.74480	-0.0052

CONCLUSIONS AND FUTURE WORK

This paper presented metrology process and data for high precision, stamped, metallic optical benches (MOBs) used for optical interconnects. Dimensional metrology performed with scanning white light interferometry demonstrated that the stamped mirror arrays typically have surface

finishes with average roughness in the range of 3 nm and RMS roughness in the range of 5 nm without any secondary processing. Furthermore, the accuracy of the mirror aperture across an 8X1 mirror array was adequate for single-mode applications as indicated by the RMS value of the individual deviations computed from SWLI point clouds, which typically ranged between 120 and 240 nm, and individual mirror RMS value less than 100 nm.

SWLI provides an efficient tool to evaluate the optical surface of stamped metallic optical bench, however further study revealed that it can introduce 4 to 5 µm of cumulative pitch error when used for measuring micro-groove features compared to contact-based metrology methods like CMM or profilometer. Unfortunately, the contact-based metrology methods cannot be used for stamped metallic optical bench optical surface measurements. Future study will be needed to develop an effective way to measure optical surface and groove information simultaneously on softer stamped MOBs.

REFERENCES

[1] L. P. Boivin, Thin-film laser-to-fiber coupler, **Applied Optics** 13(2), 391-395, 1974.

[2] Y. M. Sabry, B. Saadany, D. Khalil, and T. Bourouina, Silicon micromirrors with three-dimensional curvature enabling lensless efficient coupling of free-space light, **Light: Science and Applications** 2, Aug. 2013.

[3] T. Tekin, Review of packaging of optoelectronic, photonic, and MEMS components, **IEEE Journal of Selected Topics in Quantum Electronics** 17(3), 704-719, 2011

[4] Y. Chen, K-F. Hii, and R. R. Vallance, Metallic optical benches with stamped micro-mirrors for photonic assemblies and optical interconnects, **Proc. SPIE 11286**, Optical Interconnects XX, 112861C, Feb. 2020

[5] S. Li, R. R. Vallance, M. K. Barnoski, Y. Zhao, M. Gean, T. Mengesha, and R. D. Dannenberg, Stamping to form a composite structure of dissimilar materials having structured features, U.S. Patent 10,413, 953, September, 2019.

[6] M. K. Barnoski, D. Cohen, D. Harris, S. Kang, A. Levi, M. Pinilla, F. Prinz, and A. Tarasyuk, Stamping system for manufacturing high tolerance parts, U.S. Patent 7,343,770, March, 2008

PRECISION IN ROLL-2-ROLL PRINTED ELECTRONICS

Theresa M. Spaan-Burke, Rens van der Nolle, Jorrit de Vries, Behrooz Daneshkhah, Mario Felius, Peter Overschie, Stephan Hannot
IBS Precision Engineering, Eindhoven, Netherlands

1 INTRODUCTION

In the production of flexible electronics, such as organic LEDs or photo-voltaic foils, nanometer scale features critical to the device performance are often implemented. In-line 3D metrology of such profiles would revolutionize the production process by avoiding time consuming off-line measurements for process control. Achieving such measurements in a roll-2-roll environment is a precision challenge. In-line interferometry has been developed for this purpose delivering nanoscale accuracy on a moving flexible foil. Control techniques have been developed to track both in the travel and orthogonal direction. Stabilisation techniques have been developed for the vertical direction. Foil handling is optimized to reduce damage to sensitive foils. The system has been demonstrated on a pilot line, handling PV with ultra-low reflectivity, measuring nanometer features which is a world first.

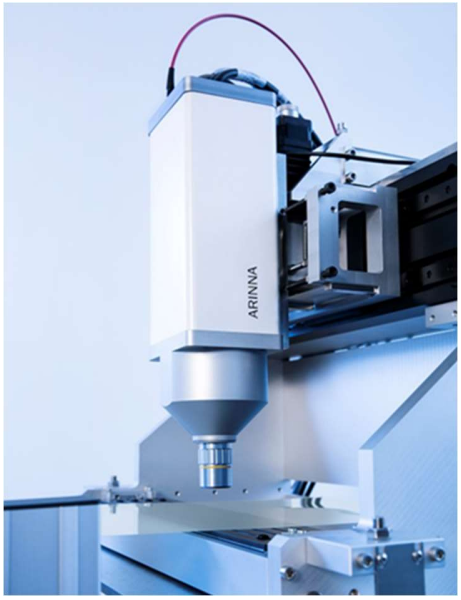

Figure 1 ARINNA interferometer

2 EXPERIMENTAL PROCEDURE

An areal interferometer has been developed based on wavelength selective interferometry. An acousto- optic tunable filter (AOTF) is used for wavelength scanning from a white light source. Interferograms of the surface are captured in under 1sec from a Linnik interferometer combined with a megapixel camera. The interferometer is able to measure discrete step heights and surface quality with a vertical resolution <2nm [1]. In-line measurement of printed electronic foils requires the ability to measure low reflective samples, “capture” of the moving foil, stabilization techniques and methodologies to overcome residual surface vibrations. An in-line system was developed to measure laser scribes in Organic printed Voltaic (OPVs). Scribe depths are of the order of 100nm and width 1μm.

Dancer development

Figure 2 Schematic of dancer. Dark blue - standard rollers, light blue- cylindricall porous media air bearings (airturns).

Nanometer features on foils moving at 1-5m/minute were targeted. Several potential strategies for capturing images from a moving web were explored, including mechanical (chasing the foil) or electronic (tracking in the camera). Given limited integration space in the final manufacturing line a dancer solution was chosen. A schematic is shown in Figure 2. At T0 the left airturn (cylindrical porous media air bearing) starts in the lower position while the right airturn starts in the higher position. When the buffer action is started the left airturn moves with half the speed of the web in the vertical direction towards position two. The right airturn follows the left airturn with the same speed in the opposite direction. At T1 the right airturn lies in the lowest position and the reverse process begins. Four

contact rollers and two air turns are used so that front contact is not made with the sensitive web. Buffering is triggered by a marker on the foil. Alternatively is can be set of user chosen intervals. In Figure 3 the dancer is shown as built.

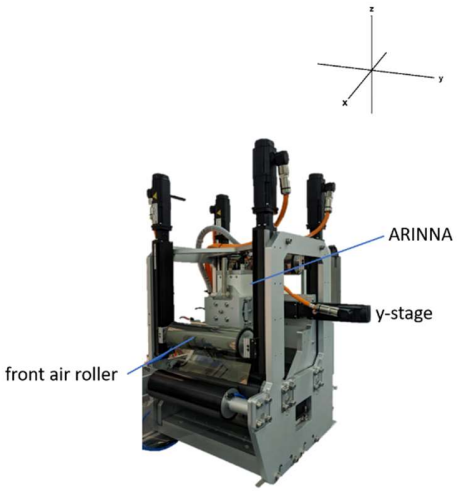

Figure 3 Dancer

During laser scribe measurements, ideally the web should be stationary. Most critical is the movement perpendicular to the travel direction, which should be smaller than the width of the laser scribe, hence of the order of 1 µm.

To evaluate the dancer performance new object tracking software was implemented. This software can track an arbitrary object for the duration of the interferometer image capture, by analysing the movement of the object during the wavelength sweep used to measure the surface. So not only the marker on the edge of the web can be analysed but any position on the web. This software is used to detect the x/y accuracy the dancer achieves.

In, Figure 4 left, the encoder measured web speed at the entrance to the dancer is shown in the IBS line. In Figure 4 right, object detection on a laser scribe is shown. In Figure 5 the measured displacement of the web with the improved speed monitoring is shown. The data left shows the x-direction performance which was measured as stable with an 0.8µm RMS. From the data right, an RMS value of 0.3µm has been achieved in the y-direction.

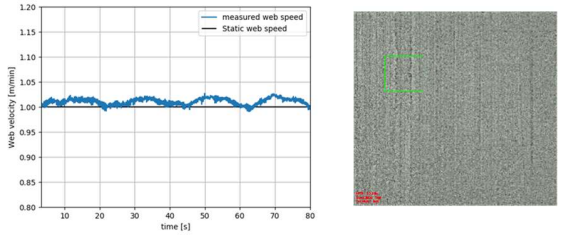

Figure 4 Left - encoder measured web speed. Right - marker detected, position used to verify dancer velocity accuracy.

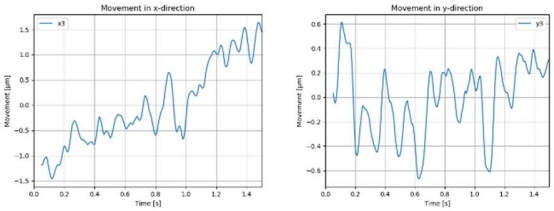

Figure 5 Left: x-position of laser scribe on web during dancing (std. dev. 0.8µm. Right: y-position (std dev. of 0.3µm).

Web stabilisation

Laser scribe depths can be measured by the interferometer to an accuracy of nanometers. It is critical that the web is stable in the vertical z-direction during measurement to achieve these accuracies. Typical motion of webs in the z-direction during production is of the order of more than 300 µm (previously measured by IBS). To stabilise the web below the ARINNA in the vertical direction, an air table has been placed under the web.The air table utilizes both vacuum and air pressure to set pretension on the web and cancel any vibrations from the roll to roll line. To cancel any vibration induced by the dancer motors, the metrology frame is decoupled from the dancer frame. Figure 6 shows the z-stability during dancing to be of the order of +/- 0.25µm.

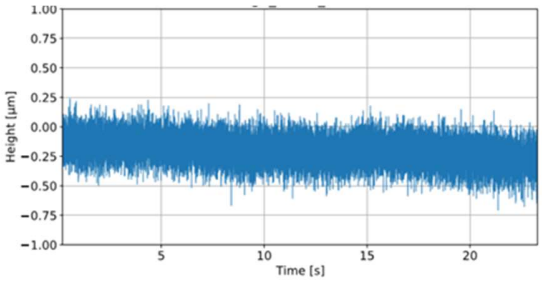

Figure 6 z-stability of web during dancing and stabilisation with air table.

Vibration compensation
With the foil stabilised in x, y and z the surface topology can be measured. Within the interferometer, compensation is applied for residual vertical motion of the foil during data capture. Advanced modelling identified a number of improvement opportunities, including enhanced hardware filtering and optimised microprocessor speeds, to increase the bandwidth of this vibration compensation. Applying these improvements enhanced the bandwidth of the vibration compensation from 280Hz to 650Hz. This in turn has enabled stable measurement of webs floating on the air table.

2 In-Line Measurement

The OPV samples to be measured are shown in Figure 7. Laser scribes are made at four stages in the processing of these devices. Scribe depths vary from 100nm for the P1A type to 1.5μm for the P3. Scribe widths are of the order of 1μm.

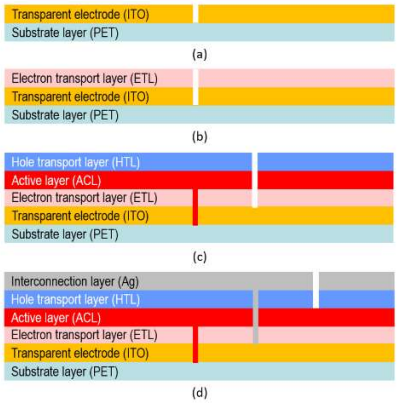

Figure 7 Schematic representation of the organic electronics stack, with (a) the P1A type, (b) the P1B type, (c) the P2 type, and (d) the P3 type laser scribes.

OPV samples are by definition low reflective. Thus ARINNA was optimised to enable measurement at low return light levels. This included both hardware updates to increase the incident light and software updates to accommodate potentially higher noise levels. To our knowledge the measurements presented here are the first ever topological surface measurements for such materials.

When manufacturing such devices SEM measurements have typically been used to assess laser scribes. A small piece of the print run is removed and sent for analysis, which typically takes more than a week. Measurements provide 2D data only, indicating a scribe width. Quantitative interpretation of the images is used to confirm the form of the scribe (wall edges, debris etc.) First measurements from the interferometer were compared to SEM.

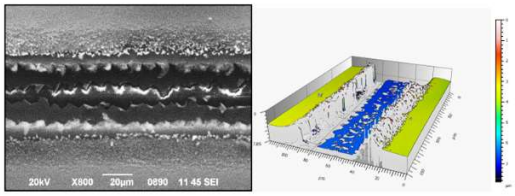

Figure 8 Comparison between SEM image (left) and ARINNA interferometer measurement (right) for P3 scribe.

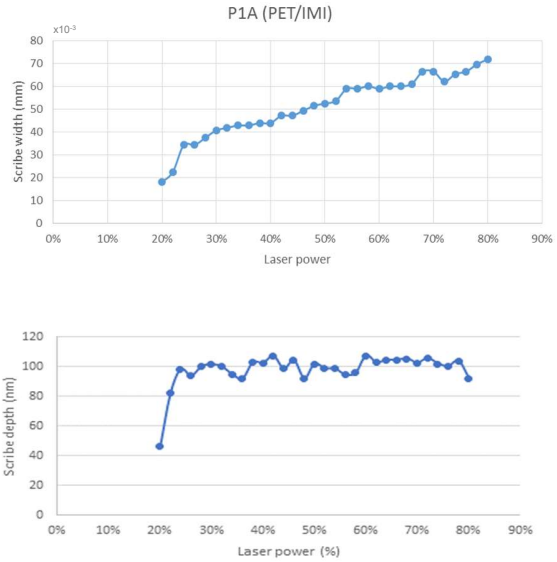

Figure 9 Measured P1A scribe width (upper graph) and depth (lower graph) as a function of laser power.

In Figure 8 an example is shown, where features apparent at the base of the scribe are also present in the surface topology measurement of the interferometer. In Figure 9 measurements are shown for P1A scribes in PET/IMI where the laser power has been varied from 20 to 80%. The scribe width is seen to increase continuously from 20μm to 70μm. At the same time, the scribe depth

is seen to increase between power of 20 to 24% and thereafter plateau at the nominal depth of 100nm, as the scribe has cut through to the PET.

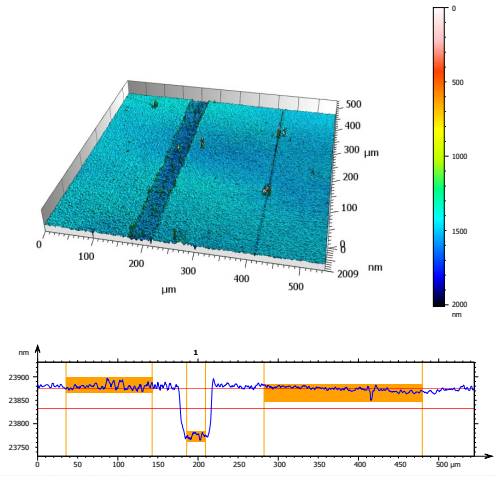

Figure 10 P1A scribe in PET/ITO on foil moving at 1m/min

In Figure 10 measurement of a P1A scribe on PET/ITO is shown, measured in-line with a foil speed of 1m/min. Cross-section shows a scribe depth of 100nm in line with the expected ITO layer thickness.

The system has been developed to provide automated measurement at a pre-defined time interval. Automatic feature extraction is performed for surface features, in this instance the scribe width and depth. A validity check is made against pre-set tolerance values. TCP/IP communication of the depth and width is sent to a client to allow for laser power adjustment. A typical trend graph is shown in Figure 11.

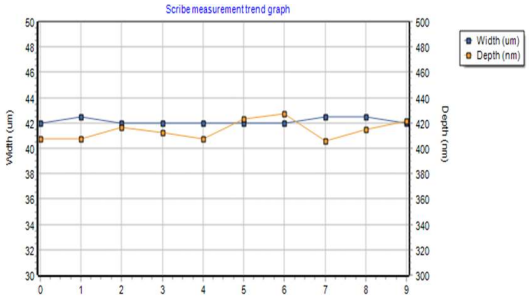

Figure 11 Trend graph of laser scribe and width taken in-line.

Statistical analysis of 100s of sampled data measurements was used to identify the impact of factors including light intensity, exposure time and interferometer optical settings. From these, optimum conditions were identified. A dataset with the preferred settings comprised 367 measurements. The mean depth obtained from this set for a laser scribe of nominal depth 100 nm was (104.7 ± 1.0) nm. The standard deviation of the measurements was 9.5 nm, the standard error of the mean 0.497 nm.

A further 100 measurements were taken of the same foil moving at 1/min as shown in Figure 12. The tolerance range was set between 50 and 150nm. Nine out of the 100 measurements were seen to fall out of the tolerance range. The mean depth obtained from the remaining data set was 96.96nm. The standard deviation of the measurements was 15.3 nm, the standard error of the mean was 1.92nm.

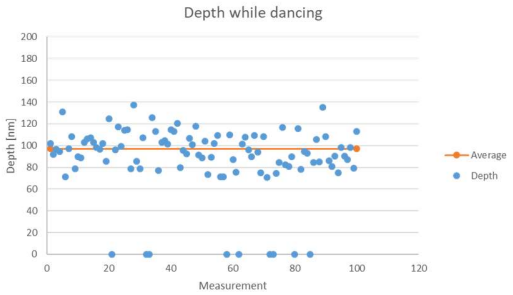

Figure 12 100 scribe measurements measured in-line at 1m/min.

3. CONCLUSIONS

First the first time, laser scribes have been measured interferometrically for OPV samples. Measurements have been successfully made in-line across the full width of the web using a dancer combined with autofocus capability and feature extraction.

[1] Robuste Oberflächenmessung mit Interferometrie Mikroproduction,65 04/15.

.

Single-Point Diamond Turning of Features with Large Azimuthal Slope

Alex Sohn, Neil Naples
Facebook Reality Labs
Redmond, WA, USA

INTORDUCTION

Molded plastic optics, specifically anamorphic and freeform components, have become almost exclusively reliant on single-point diamond turning of molds and masters. Since diamond turning is a deterministic process, it can integrate mechanical and optomechanical features into the same machining operation and guarantee alignment with optical surfaces. With the advent of XZC turning and fast tool servo (FTS) machining processes, it became possible to diamond turn non-rotationally symmetric optical surfaces and other features. However, XZC and FTS are both limited by tool clearance when surfaces become steep in the azimuthal (rotational) direction. Large primary clearance tools are one way to address this, but those tools are costly, can be time consuming to manufacture, and have fragile edges susceptible to wear and damage. Diamond milling is another possibility for dealing with large azimuthal slopes, but this usually comes at the price of diminished surface roughness and surface figure error related to long cycle times. We present here a process for diamond turning steep azimuthal slopes using conventional diamond turning tools by taking advantage of multi-axis motions available on diamond turning machines with a vertical Y-axis.

METHOD

As illustrated by the example cylindrical lens schematically being turned in Fig. 1, as the azimuthal slope is large near the periphery of the part, the front clearance angle of the diamond tool is insufficient for a conventional XZC or FTS operation. However, as illustrated in Fig. 2, additional front clearance in the azimuthal direction can be gained if the tool is rotated about its axis (parallel to the turning axis). Essentially, this results in trading some radial clearance for azimuthal clearance.

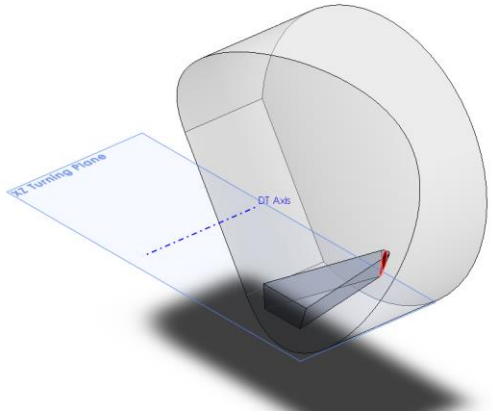

FIGURE 1. Example of a steep cylindrical lens surface (50° edge slope) being conventionally diamond turned via XZC or FTS turning. Using a 12° clearance tool, the clearance face of the tool interferes with the lens surface.

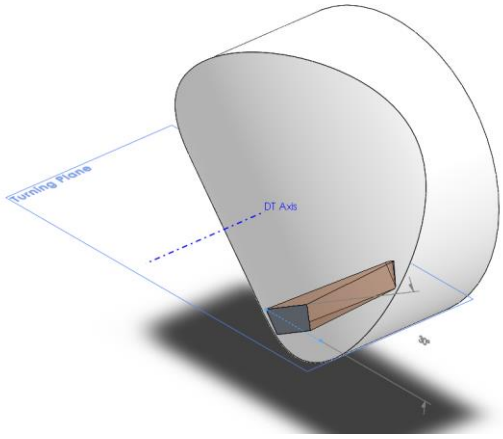

FIGURE 2. For the same part and tool as in Fig. 1, the primary clearance issue is resolved when the tool is rotated about its shank axis by 30°.

While rotating the tool about its axis can solve the interference problem between its front clearance face and surface, it would require an additional axis generally not available on diamond turning machines (DTM's). In contrast, many DTM's do,

nowadays, have a (vertical) Y-axis in addition to the traditional X- and Z- lathe axes. Leveraging this additional motion axis, one can achieve the effect of rotating the tool about its axis by the addition of Y-axis motion. By rotating the interpolation or turning plane of the toolpath (a plane intersecting both the rotation axis of the workpiece and the contact point of the tool) about the turning axis, as seen in Fig. 3, additional freedom in manipulating tool clearances can be gained. This rotation angle, or skew angle, thus increases the range of available surface slopes to be machined with a given diamond tool.

To visualize how skew angle affects tool clearance, it is useful to project the tool onto the radial and azimuthal cutting planes. Figure 4 illustrates how the azimuthal clearance is limited by the front tool clearance angle for negative cutting slopes and the rake face for positive slopes. In contrast and shown in Fig. 5, radial clearance is governed entirely by the tool's window or radius included angle.

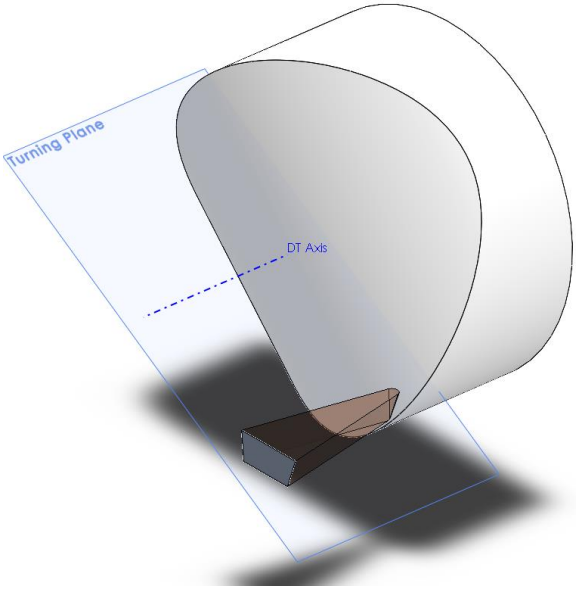

FIGURE 3. Since the tool cannot be easily rotated about its axis by 30°, the identical effect can be obtained by moving the tool out of the usual XZ turning plane by moving the Y-axis. This effectively tilts the turning path plane.

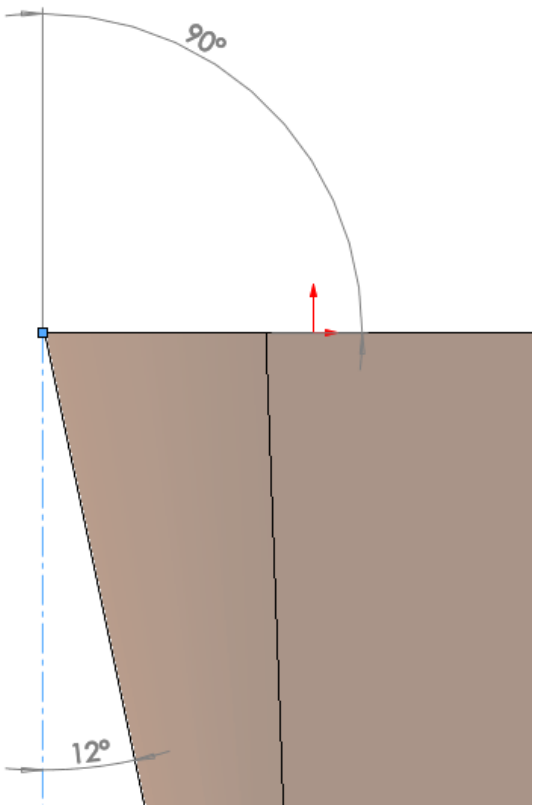

FIGURE 4. Example tool shown perpendicular to the rake face and parallel to the cutting direction for standard cutting with no skew.

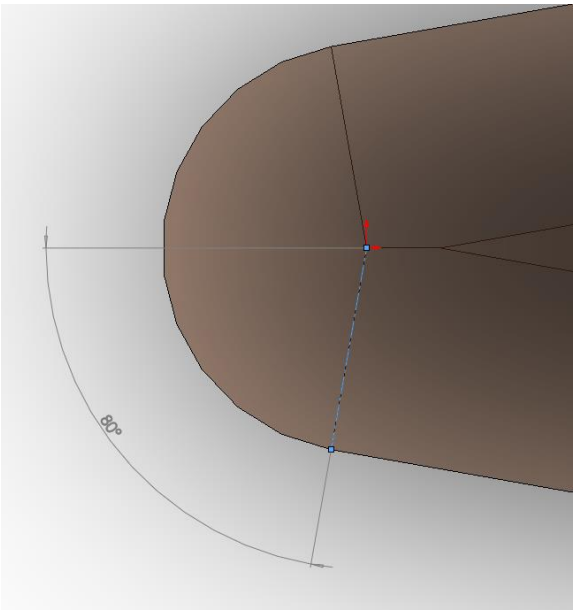

FIGURE 5. Example tool shown parallel to rake face in the radial clearance plane. In normal cutting (no skew), the radial clearance is ±80°

When adding a skew angle to the tool, its clearances change significantly after projecting the rotated tool onto the radial and azimuthal cutting planes, as shown in figures 6 and 7.

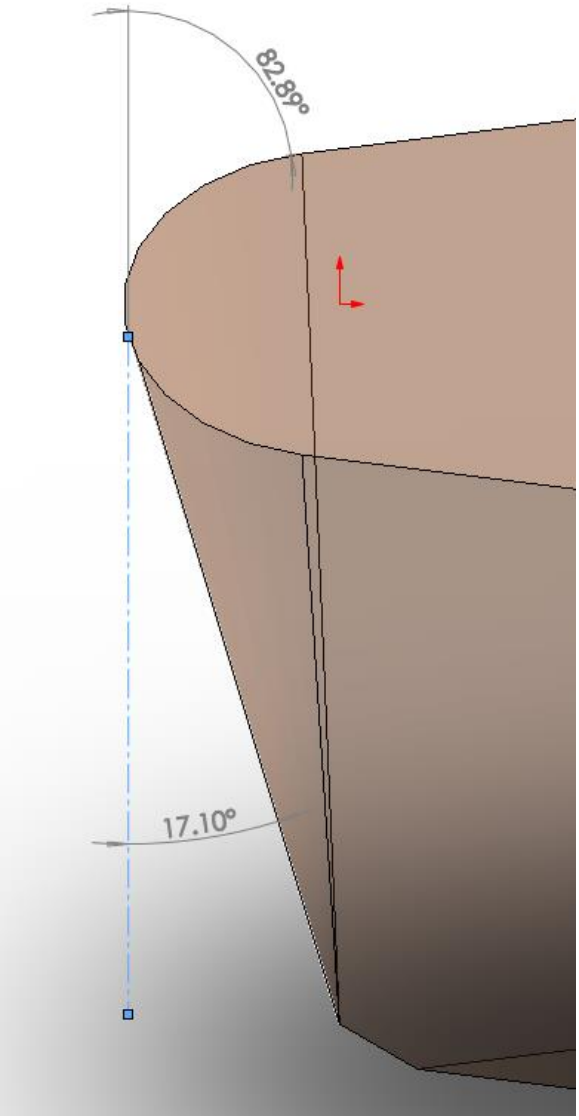

FIGURE 6. Example tool shown rotated to a skew angle of 45°. Note that the negative slope clearance angle has increased to about 17° and the positive clearance has decreased to about 83°.

Of particular interest when turning surfaces with large azimuthal slopes is the most limiting tool clearance, which is the negative azimuthal clearance angle. The relationship between this angle, α_{A-}, the primary conical clearance, α, and the skew angle, θ_s, is described by

$$sin(\alpha_{A-}) = \frac{\sin(\alpha)}{\cos(\theta_s)}. \quad (1)$$

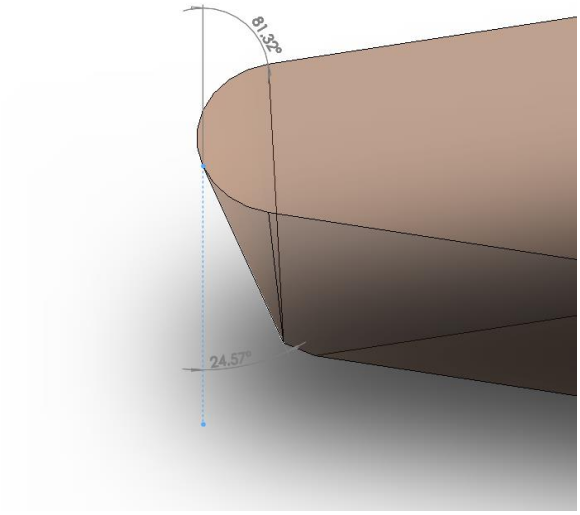

FIGURE 7. A 60° skew angle (the maximum practical) doubles the negative slope clearance angle and nominally decreases the positive clearance angle.

CUTTING MECHANICS

With the introduction of a programmed skew angle, diamond turning cutting mechanics can change significantly. Skew angles are, in principle, not unprecedented in machining. Wood planes, as pictured in Fig. 8, have been employing skew cutting to aid in shearing fibers on end-grain for centuries. While the variation of rake angle [1] on a cutting tool influence forces and surfaces in diamond turning of free-forms, relatively little data is available on skew angle impact to date.

Figure 8. Wood cutting hand plane showing a skewed blade to aid in cutting wood fibers.

Large variations in rake and skew angle change geometry, friction and chip area. In the first order, the geometrical relationship between tool and workpiece is changing so that the local nose radius of the diamond tool effectively changes, impacting the theoretical surface finish of the surface. The geometry impact can be approximated by projecting the actual nose radius of the tool onto the turning plane. This produces either an oblate or prolate ellipse for increased rake or skew angle magnitude, respectively. The major and minor axes of this ellipse, *a* and *b*, respectively can then be given by

$$a = r_t \cdot \cos|\alpha| \qquad (2)$$
$$b = r_t \cdot \cos|\theta_s|$$

where r_t is the tool nose radius in the rake plane, α is the rake angle and θ_s is the skew angle. Determining the projected nose radius then becomes a matter of calculating the localized radius at the contact point of the tool. For a flat, this effective nose radius is

$$r_{eff} = \frac{b^2}{a}. \qquad (3)$$

This effective tool radius can then be used to calculate a theoretical rms surface roughness

$$R_q \cong \frac{f^2}{24 r_{eff}} \qquad (4)$$

Generally, this means that increased rake angle magnitude increases the nose radius for decreased theoretical roughness and increased skew angle decreases the local nose radius for increased theoretical roughness. Additionally, since the cutting tool is potentially tilted about multiple axes, the preferred method of tool radius compensation for XZC and FTS turning is only along the Z-axis, ensuring there are no oscillations in the toolpath along the vertical or radial axes. To compute compensated toolpath coordinates along the Z-axis only, it is necessary to raise the tilted tool along the positive Z-axis by the amount of overcut that would otherwise occur if no tool radius compensation were performed at all [2].

EXPERIMENTAL RESULTS

In practice, feeds and speeds can be adjusted so that tool geometry is not ultimately the driver of surface roughness. Since rake angles due to azimuthal slope changes and added skew angles have a significant impact on material shearing and removal, their interaction with the material tends to drive the surface finish. To determine some of these limits, experiments with varying rake and skew angles were performed by diamond turning high-phosphorous nickel using a conventional 20° conical clearance single-crystal diamond tool with a nose radius of 0.25 mm, as shown in Fig. 9. The tool was set up in a YZ turning configuration with the tip coincident with the machine B-axis. This allowed the skew angle to be controlled via X-axis offset and the rake angle via B-axis rotation. A mist of mineral spirits was used as coolant. Feedrate and depth of cut on the finish pass were 1 µm/rev and 1 µm, respectively.

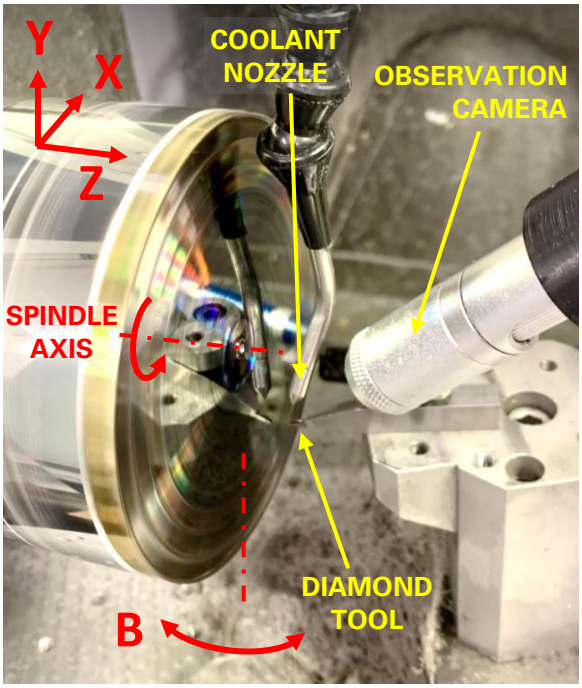

Figure 9. Diamond turning of high-phosphorous nickel with varying skew and rake angles.

Roughness data was collected using an optical profilometer and are shown as a function of skew and rake in Fig. 10. The results show that at the extremes of both rake and skew angle, the surface finish degrades significantly. Not shown are cutting results for ±80° of skew angle, which resulted in poor surface finish over most of the rake angle range. The key takeaway from the data, though, is that the technique produces good surface finishes over a wide range of rake and skew angles, showing that this diamond turning technique is useable in a wide range of applications.

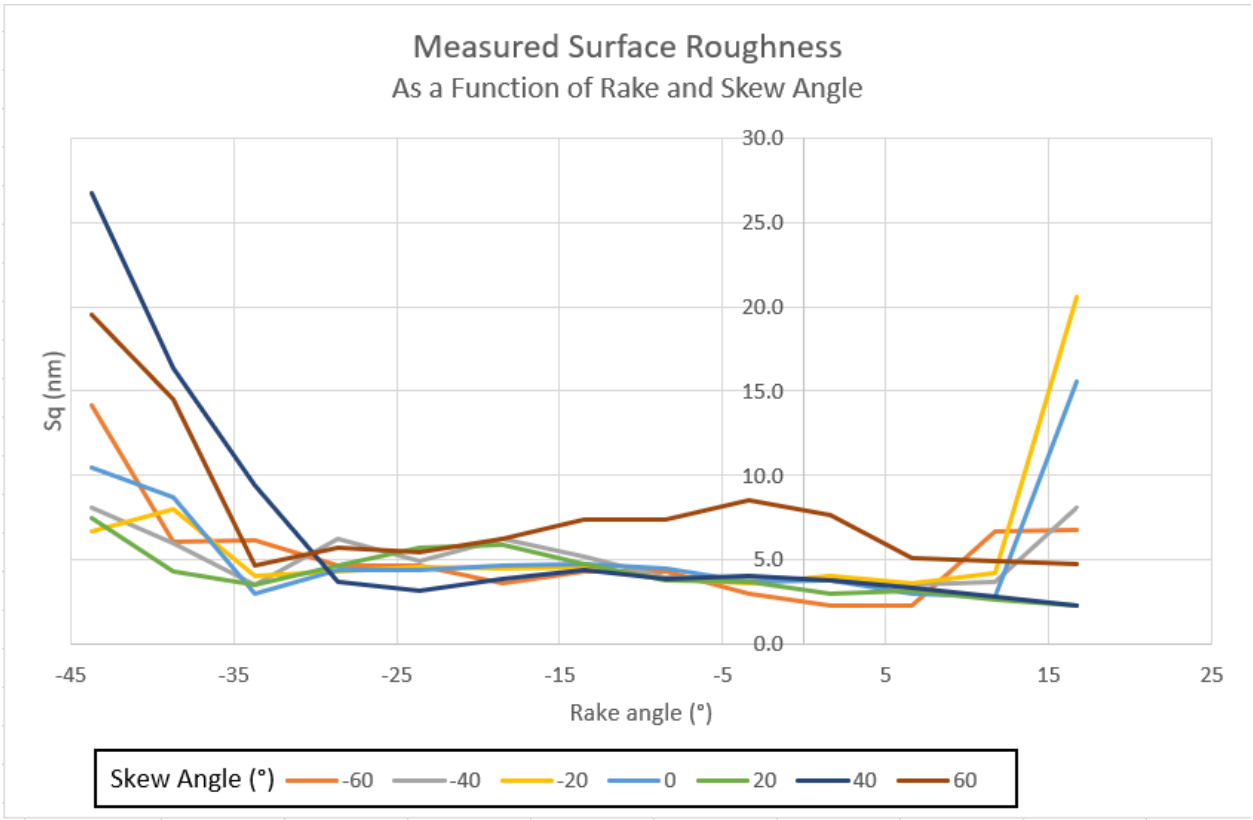

Figure 10. Experimental surface roughness results for rake angles between -45° and 18° and skew angles between -60° and 60°.

The two chief drivers of surface finish degradation at extreme rake and skew angles appear to be accumulation of a built up edge and vibration from high thrust force. As shown in Figure 12, discontinuous lines of material build-up on the material are an indicator of built-up edge (BUE) on the tool rake face [3]. BUE is not only problematic in directly driving significant increases in surface roughness, but may also drive a dramatic increase in tool wear. The other mechanism driving surface finish at high negative rake and skew is vibration. As shown in Fig. 13, high-frequency synchronous vibration has all the hallmarks of being cutting force driven tool vibration given the consistent vibration frequency of 68 kHz. Stiffenting the tool may produce better behaivior at these extremes.

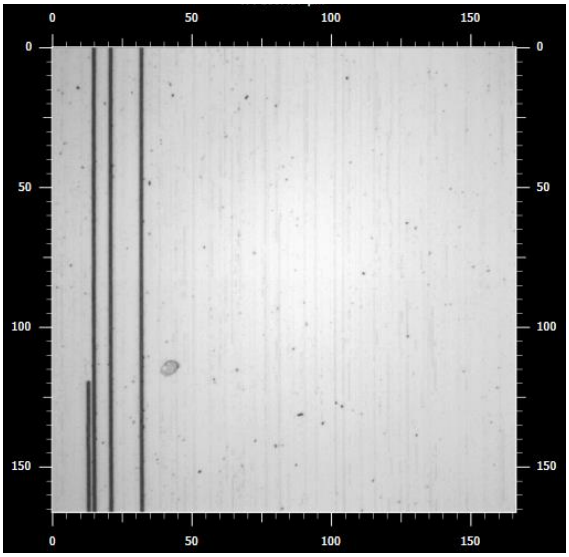

Figure 12. At steep rake angles, the surface finish is driven by drag buildup in the material. The sudden stopping and starting of buildup lines indicates that this is likely to be from a built-up edge on the tool. Data from at -60° skew, 2° rake.

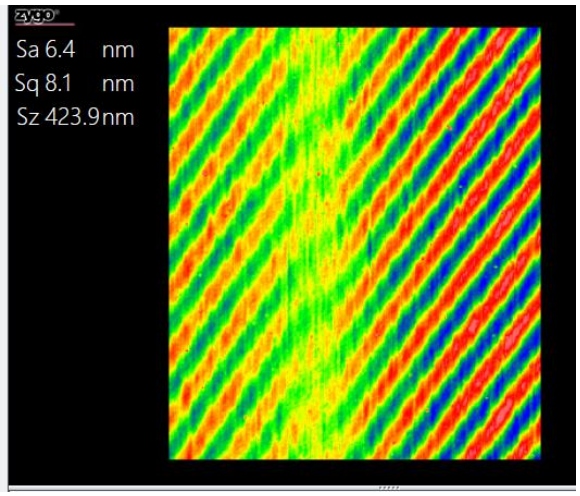

Figure 13. When skew angle and rake are strongly negative, high machining forces drive high-frequency vibrations in the tool leading to degraded surface finish. Data from at -40° skew, -44° rake.

CONCLUSIONS

By introducing a programmable skew angle that takes advantage of Y-axis motion now available on modern diamond turning machines, it has been shown that substantial gains can be made in the types of non-rotationally symmetric surfaces that can be diamond turned using XZC and fast-tool servo turning. Not only is it possible, but it is practical to take advantage of this newfound freedom in diamond tool motion as evidenced by the fact that good surface finishes are possible even when skew and rake angles are relatively large. At least for high-phosphorous nickel, a significant material for diamond turned molds used in injection molded optics, the work envelope is usefully and significantly expanded. Other materials will certainly show variations and will have to be explored.

REFERENCES

[1] A. Sohn, "Rake angle variation in diamond turning," in 22nd ASPE Annual Meeting, Dallas, TX, 2007.

[2] D. P. Yu, S. W. Gan, Y. S. Wong, G. S. Hong, M. Rahman and J. Yao, "Optimized tool path generation for fast tool servo diamond turning of micro-sctructured surfaces," The International Journal of Advanced Manufacturing Technology, vol. 63, no. 9-12, p. 1137–1152, 2012.

[3] Suit, Brandon Michael. "Analysis of Accelerated Tool Wear and Built Up Edge when Diamond Turning Ferrous Materials." (2016).

Qualitative Edge Topology Inspection and Interpretation by Enhanced Knife-Edge Interferometry

Zhikun Wang[1], and ChaBum Lee[*,1]
[1]J. Mike Walker '66 Department of Mechanical Engineering
Texas A&M University
College Station, TX, USA

INTRODUCTION

Edge topography measurement technology is vital in many engineering applications such as cutting tool inspection, photomask inspection, or corrosive wear inspection. Although those applications require high-level sharpness or smoothness of the edges to achieve their needs, there is little measurement and inspection technology available. Most of the current surface metrology and inspection technology is primarily focused on planar surface characterization [1-3], and sometimes indirect methods such as measuring the cutting force or acceleration to interpret tool wear propagation during the machining process are used [4]. This paper presents the enhanced knife-edge interferometry (KEI) that measures optical scattering behaviors that originated from the edge. KEI utilizes the optical interference of incident light and scattered light at the edge and produces the fringe patterns proportional to edge quality [5-7]. Analysis of such fringe patterns enables monitoring edge quality. We recently improved KEI performance by shaping the beam with the objective lens (4×, 10×). The incident plane wave was turned into a spherical wave by the objective lens, and the spherical wave and the diffracted wave at the edge interfered. As a result, the strong interference effect was observed, and over 3 times fringe patterns were obtained compared to the interference results of no objective case. The enhanced KEI was employed for edge quality inspection of sharp edges (razor blade), cutting tools, and photomask.

MEASUREMENT PRINCIPLE

The principle of enhanced KEI can be easily explained in geometrical optics. When we are using the objective lens in the system, the output plane wave will first focus on the focal point of the objective lens and then disperse. Now the light source can be viewed as a point source and the diffraction can simplify as a Fresnel number modal. In this modal, the number means the half-period zones in the plane. Each zone implies the constructive/destructive light intensity effect to our on-axis observation point. The equation for Fresnel number is listed as follows:

$$F = \frac{a^2}{\lambda \times Z_{eff}} \tag{1}$$

In this equation, a means the radius of the light beam at the plane, λ means the wavelength of the laser, Z_{eff} is the effective distance, which equals to:

$$\frac{1}{Z_{eff}} = \frac{1}{Z_o} + \frac{1}{Z_{src}} \tag{2}$$

Where Z_o is the distance between the edge plane and the sensor and Z_{src} is the distance between the edge plane and the focal plane. The experiment principle can be seen in Figure 1. Another adventure for the enhanced KEI system is its high sensitivity. Ideally, the simulation result is just the output intensity of the on-axis point, but in a conventional KEI system, the output plane wave from the laser will be fully emitted to the sensor, which normally has its size in units of ~100 μm. Unfortunately, those off-axis points on the sensor will also receive the light intensity and will be recorded in data collection. The intensity from those off-axis points will decrease the sensitivity of recorded data and generate the attenuated fringe pattern from a diverse beam. But in the enhanced KEI system, the light will diverge after the focal point and only a small amount of light will be recorded since the light was scattered.

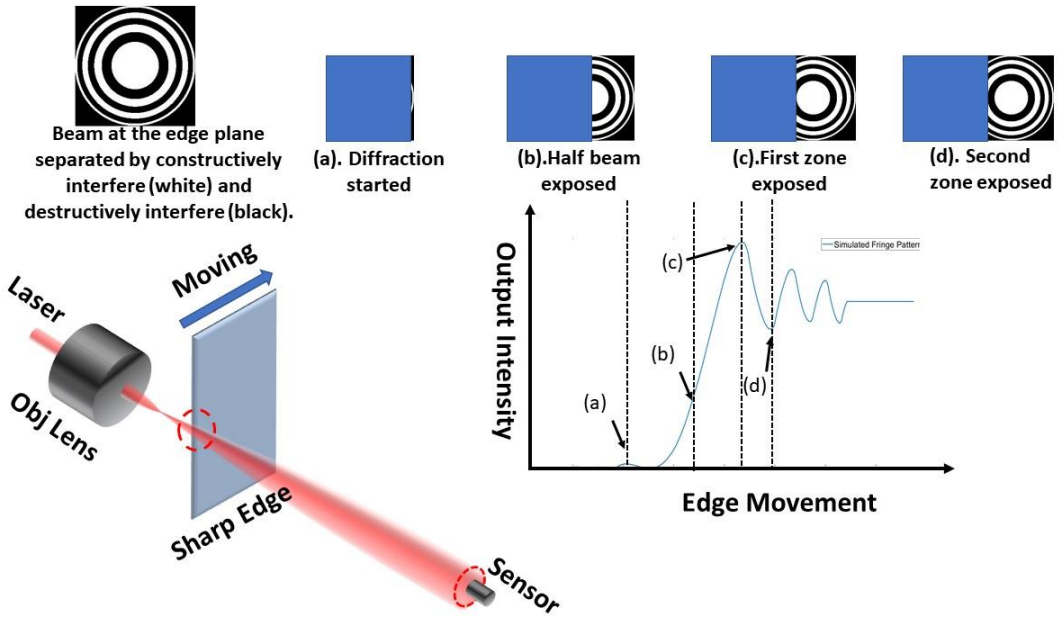

FIGURE 1. Principle of experiment

EXPERIMENTAL RESULTS

Experiment Setup

As shown in Figure 2, a 10× objective lens was mounted at the front of the edges to shape the beam, and an avalanche photodiode (APD) recorded the output fringe pattern by scanning the razor blade. The four different edge conditions were prepared by using the grinding tools to wear out the edge sequentially. After each worn-out process, the edge will be scanned by the laser and the edge profile will be captured by the microscope for verification.

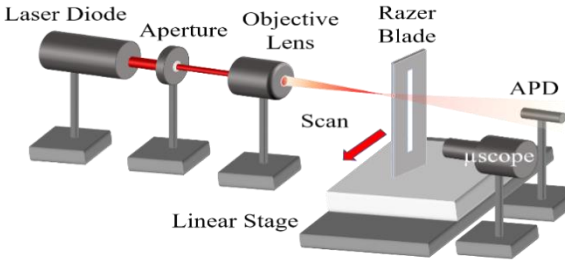

FIGURE 2. Experimental setup.

The measurement fringe pattern result for each stage can be seen in Figure 3. The data were analyzed by using cross-correlation. After that, we will get two parameters: the lag and the similarity. While the similarity illustrates the edge defect in microscale (less than 10 micron), the lag shows the edge damage in macro scale (over 10 micron).

Experiment Results

Compared with the conventional knife-edge diffraction method, the similarity of the experiment results with 10× objective lens decreases from 1 to 0.98 while the conventional knife-edge diffraction system gives us less than 0.01 changes in the value of similarity. The photomask patterns (width, line-edge roughness) were also tested. By adding the defect to the photomask pattern, the width of the transparent area decreases from 0.995 mm to 0.668 mm, and the similarity changes from 0.987 to 0.907 after adding the defect. The fringe pattern for the experiment group and the control group can be seen in Figure 4. This study has the potential to be used in high-resolution optical metrology systems for edge topography characterization, such as photomask inspection or micro-machining verification. Its improved resolution and highly sensitive features may bring another low-cost, in situ, direct testing method into the industry of precision engineering.

ACKNOWLEDGEMENTS

This research has been supported by National Science Foundation (CMMI #1855473).

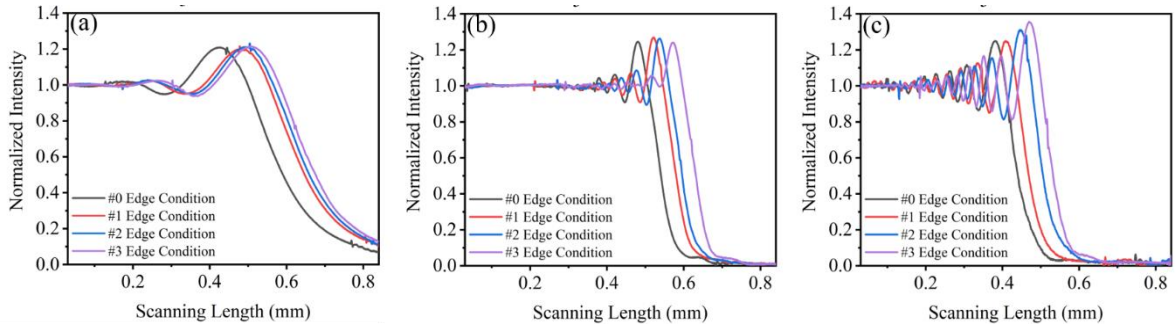

FIGURE 3. Knife-edge interferograms for (a) no objective lens case, (b) 4× objective lens case, and (c) 10× objective lens case.

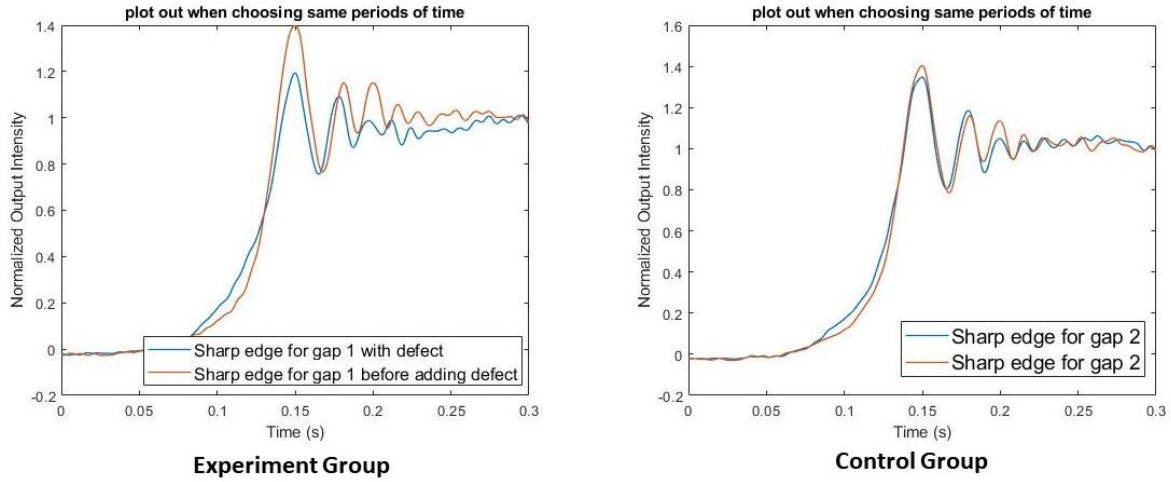
plot out when choosing same periods of time
Normalized Output Intensity
Time (s)
Sharp edge for gap 1 with defect
Sharp edge for gap 1 before adding defect
Experiment Group
plot out when choosing same periods of time
Normalized Output Intensity
Time (s)
Sharp edge for gap 2
Sharp edge for gap 2
Control Group

FIGURE 4. Knife-edge interferograms for (a) clear edge and defected edge on the photomask, (b) clear edge scanning twice for the control group.

Reference:

[1] Herminso Villarraga Gomez, ChaBum Lee, and Stuart T. Smith, "Dimensional metrology with X-ray CT: a comparison with CMM measurements on internal features and compliant structures," Precision Engineering, 51, pp. 291-307 (2018).

[2] Seongkyul Jeon, Christopher K. Stepanick, Abolfazl A. Zolfaghari, ChaBum Lee, "Knife-edge interferometry for cutting tool wear monitoring," Precision Engineering, Vol. 50, pp. 354-360 (2017).

[3] SungHan Kim, Andreas A. Polycarpou, and Hong Liang, "Active control of surface forces via nanopore structures," APL Materials, Vol. 1, 032118 (2013).

[4] Seongkyul Jeon, Abolfazl Zolfaghari, ChaBum Lee, "Dicing wheel wear monitoring technique utilizing edge diffraction effect," Measurement, 121, pp. 139-143 (2018).

[5] Zhikun Wang and ChaBum Lee, Knife-edge interferogram analysis for corrosive wear propagation at sharp edges, Applied Optics, Vol. 60, Iss. 5, pp. 1373-1379 (2021).

[6] ChaBum Lee, Sun-Kyu Lee and Joshua A. Tarbutton, Novel design and sensitivity analysis of displacement measurement system utilizing knife edge diffraction for nanopositioning stages, Review of Scientific Instruments. Vol. 85, 095113, 2014.

[7] ChaBum Lee, Sun-Kyu Lee and Joshua A Tarbutton, Positioning control effectiveness of optical knife edge displacement sensor-embedded monolithic precision stage, Sensors and Actuators A: Physical, Vol. 233, pp. 390-396 (2015).

THE EFFECT OF MOTION BLUR ON PHOTOGRAMMETRIC MEASUREMENTS OF A ROBOTIC MOVING TARGET

Mohammed A. Isa[1], Richard Leach[1,2], David Branson[1], and Samanta Piano[1]
[1]Manufacturing Metrology Team
Faculty of Engineering, University of Nottingham, Nottingham, UK
[2]Taraz Metrology, Nottingham, UK

MOTION BLUR

Photogrammetric measurement of a moving optical target can be prone to image distortion and blurring during acquisition. In high-precision optical tracking, where there is a relative motion between camera and target, image blur presents challenges to measurement accuracy because it can influence feature detection algorithms [1], which in turn, can alter three-dimensional (3D) coordinate measurements. In conventional photogrammetric systems, stable and sharp images are ensured by fixing the relative position between the camera and the measured target [2]. However, maintaining a static camera-target position during image acquisition is not possible in some applications, such as robotic tracking and unmanned air vehicle surveillance. In these situations, images should ideally be captured instantaneously. However, current technologies require the sensors to be exposed to light for some time to accumulate sufficient charge to build a high-intensity signal [3]. Furthermore, non-static photogrammetry applications require high-resolution, compact hardware and potentially multiple sensors, making the use of costly high-speed imaging disadvantageous and impractical. Motion blur effects occur when the shutter mechanism of a camera exposes its sensor to a moving scene, where the projected scene alters by more than the size of the sensor pixel during the exposure time. When the scene projection changes by tens of pixels, the blur effect is aggravated and localisation of features can become problematic. Consequently, blurred images can lead to erroneous photogrammetry results and the level of confidence in the measurement results is difficult to ascertain.

Most previous research on motion blur focuses on image restoration and camera stabilisation, where qualitative image improvement is emphasised, with less regard to how the 3D coordinate measurements obtained from the images are influenced [4]. Commonly, research on motion blur aims at improving image quality by estimating the image motion parameters and restoring the image quality using estimated point spread functions (PSFs) simplified as convolution kernels [5,6]. Imaging systems are fitted with motion sensors to better estimate movements, such as human hand jitters [7]. Even for a non-blind system, where the motion blur kernel is known, image deblurring can be complex and computationally expensive [5]. For metrological purposes, measurement precision and accuracy are fundamental and factors that influence blurring, such as the relative camera-target trajectory, need to be accurately measured.

By accurately measuring the displacement of a target with a laser interferometer, we investigate the effect of motion blur in a photogrammetry system. The idea is to use the controlled experimental environment to identify and characterise the image blurring phenomenon on a moving target before mounting the target on a robot. From the experiment, the performances of generated blur kernels are evaluated by comparing the acquired blurred images to their artificial counterparts derived from the static images of the targets. The measurement accuracy of the target is also evaluated for various camera-target displacements to obtain a basis for both a blur correction scheme and camera parameter selection. A significant reduction in measurement precision can be expected when motion blur increases in the images of measured targets [4]. Sieberth et al. [8] showed that an observed feature size increases exponentially as the scene-camera relative displacement increases during exposure. For photogrammetric systems that depend on the dimensions of features on an artefact, such as the robotic target in this paper, high displacements during exposure can easily render images unusable.

It is important for robotic target artefacts to allow six-dimensional (6D) pose tracking, which can be achieved by using target that has features with premeditated dimensions. [9]. As a result, when the target artefact is calibrated, it can serve as a

reliable reference for photogrammetric measurements. Successful tracking of these 6D targets depends on the ability to distinguish the dimensions of its features. Since blurring can distort sizes and dimensions of target features, it becomes necessary to investigate how 3D coordinate measurements of the target features are affected by motion blur.

EXPERIMENT

Displacements of a 6D robotic target were measured using both laser interferometry and photogrammetry. As an accurate and traceable benchmark for measuring displacements [10], the interferometry readings were used as reference for evaluating the performance of the photogrammetric measurements. Images of the target in motion were used to investigate motion blur and its effects on photogrammetric measurement.

Setup specifications

Three 20 mega-pixel Basler machine vision cameras were used to take images of the target. The parameters of the cameras were pre-calibrated using Zhang's method [11] and images were captured at 90 ms exposure time through 16 mm focal length lenses. In addition to individual cameras, multi-camera parameters defining image-based correspondences within the camera pairs were obtained. These parameters were used for the match selection and triangulation of identified features in obtained images.

The robotic target consists of eleven Polyoxymethylene spherical balls attached to dark contrasting plates (FIGURE 1). The size and spacing of the spheres were designed to reinforce identification at all possible poses. Dimensions of the target, such as sphere diameters and spacings, have been traceably measured using a mechanical coordinate measuring machine. For this study, the target was fixed to a linear actuator stage that moves in a single direction as shown in FIGURE 1. Kinematic errors in the two linear and three angular constrained degrees of freedoms were neglected. As justification for the simplification, the magnitude of the corresponding errors from the constrained motion have been shown to be less 10 μm for a linear actuator of similar build [12].

A Renishaw XL-80 laser interferometer was used to determine the displacements of the linear actuator. As illustrated in FIGURE 1, a retroreflector was placed on the moving actuator stage while the interferometer optical components were rigidly fixed to the optical table. Displacement measurement accuracy of 0.2 μm is given by the manufacturer for the measurement range of 300 mm. The linear actuator is open-loop controlled and its movement is synchronised with data collection from both the laser interferometer and the photogrammetric system.

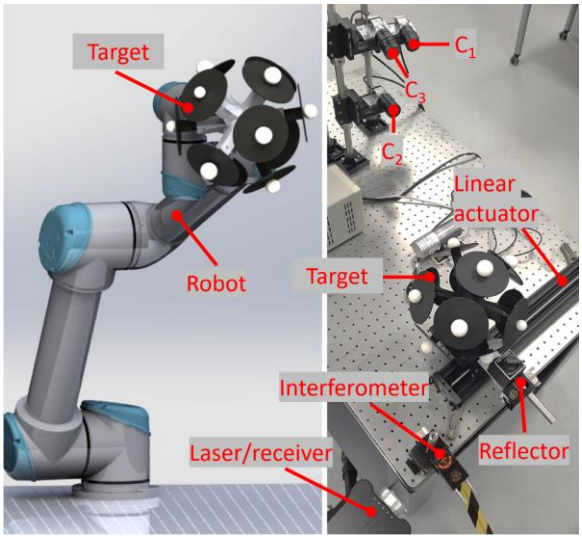

FIGURE 1. A photogrammetric target designed for use on a collaborative robot is placed on a linear actuator where displacement is measured with a linear interferometer. Three cameras C_1, C_2 and C_3 are used to capture images of the target.

Motion speed test

It is important to ensure that the motion of the target artefact is well characterised when the cameras are triggered to acquire images. To ensure that a desired speed is attained, the maximum speed setting of the actuator was varied from 500 mm min^{-1} to 6000 mm min^{-1} and displacements were recorded at 0.1 s time intervals. FIGURE 2 shows that the desired speed settings were attained in each case at around 0.2 s. The maximum speed of 6000 mm min^{-1} was reached when the total displacement was around 30 mm. Based on this finding, the cameras were set to be triggered at 0.25 s after the linear actuator starts moving and a displacement interval of 30 mm or more was used for the speed settings above. Images acquired in the motion blur experiments given in this paper were taken in the exposure time window shown in FIGURE 2.

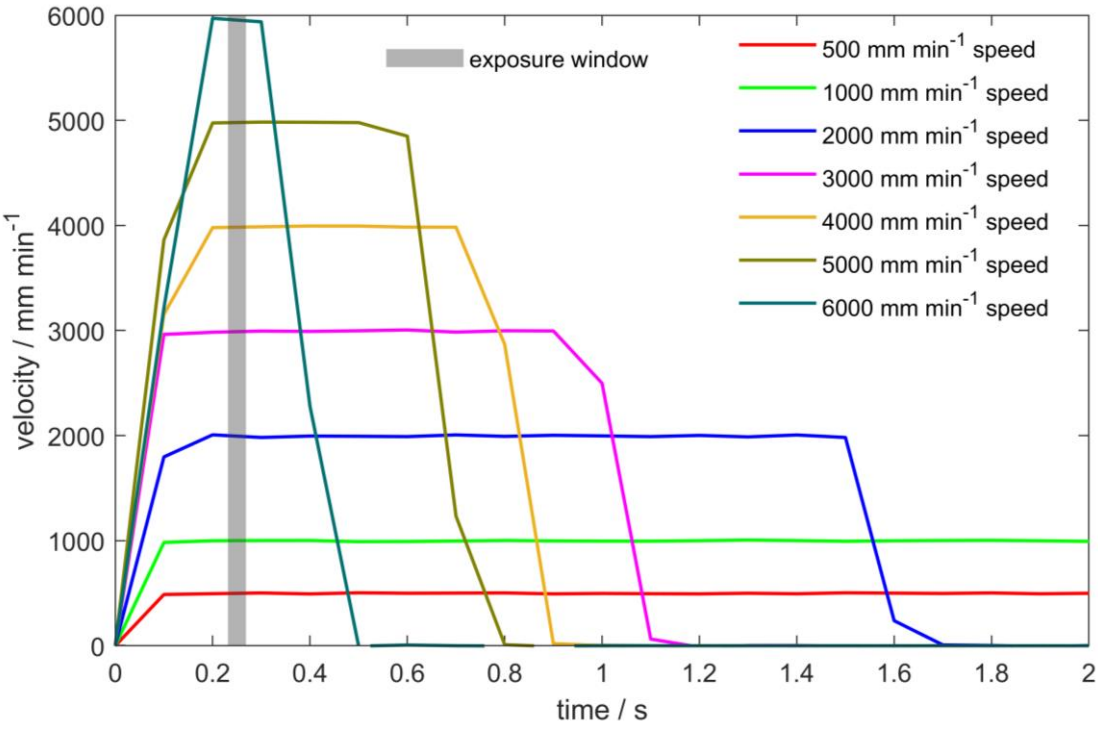

FIGURE 2. Measured velocity profiles at various maximum speed settings. The velocities are derived from measured displacements at 0.1 s intervals from the laser interferometer.

Motion blur experiment

Two sets of images were obtained for the motion blur experiment at camera measurement depths of around 600 mm to 800 mm. The first set contains images of the moving target captured at 500 mm min^{-1} to the maximum speed of 6000 mm min^{-1}. Immediately after the three cameras were triggered, before the image frames were fully formed, displacement readings from the laser interferometer were taken. The target was then brought to rest after a 30 mm displacement and the process was repeated, until the total travel distance of 300 mm was reached. For the second set of images, another run was initiated, but this time, the linear actuator was displaced to the exact locations recorded during the first run. The target was allowed to rest at this location before the images were taken. Hence, the second set of images represent the static counterparts of the first set of images. The average time it took to trigger the three cameras was 8.4 ms and the time elapsed to request a reading from the laser interferometer was 3.5 ms.

PHOTOGRAMMETRY

Photogrammetric measurement provides the overall configuration and 3D location of the experimental setup. Knowing the speed of the moving target is not sufficient to determine the form of image blur. Objects moving at different orientations or positions will be blurred differently. It is, therefore, necessary to determine the 3D location and motion direction of the desired features relative to the cameras.

Multi-view stereo correspondence

The network of three stereo-camera pairs (C_{12}, C_{13}, C_{23}) is formed and the correspondence between the image points from each stereo pair is determined by a fundamental matrix. For a camera pair where the first camera C_i and second camera C_j are characterised by the fundamental matrix $\boldsymbol{F}_{ij}$, two matching image points $\boldsymbol{x}_i$ and $\boldsymbol{x}_j$ from the first and the second camera respectively should reduce the epipolar relationship $\epsilon_{ij} = \boldsymbol{x}_j^T \cdot \boldsymbol{F}_{ij} \cdot \boldsymbol{x}_i$ to zero. Here, the two image points are expressed in homogenous coordinates [13]. Due to digital noise and other sources of error, it is normally difficult to obtain $\epsilon_{ij} = 0$ exactly from a set of candidate image points [14]. A practical approach is to choose a threshold ϵ_m such that matches are accepted only if $\epsilon_{ij} < \epsilon_m$. In this paper, ϵ_m is determined from a maximum allowable image pixel deviation. The pixel

deviations can be obtained by normalising ϵ_{ij} based on each epipolar line in $\boldsymbol{F}_{ij} \cdot \boldsymbol{x}_i$.

Once the image points are matched, triangulation of the matches reconstructs the 3D points. The measured 3D points correspond to the centres of the target spheres. Beside the centre points, diameters of the spheres are estimated from the stereo images. The collection of distances and diameters reconstructed from each frame of the three cameras are cross-referenced with the CMM-measured dimensions of the target.

Evaluation of image blur length and orientation

3D locations of identified target artefact spheres are used to determine the motion direction of the stage. The motion direction $\boldsymbol{v}_m$ expressed as a unit vector, can be used to determine the change in the image centre points of the target spheres. For a measured 3D centre of a sphere $\boldsymbol{p}$ moving with speed s, the image projection of its centre after the exposure time t_e is given by

$$\boldsymbol{x_b} = \boldsymbol{K} \cdot [\boldsymbol{R}|\boldsymbol{t}] \cdot (\boldsymbol{p} + st_e\boldsymbol{v}_m), \quad (1)$$

where $\boldsymbol{K}$ is camera intrinsic matrix, and $\boldsymbol{R}$ and $\boldsymbol{t}$ are the respective rotation and translation of the origin of $\boldsymbol{p}$ with respect to the camera origin. The change in image projection of a point moving in a straight line can be obtained from Equation (1) as $\Delta\boldsymbol{x_b} = \boldsymbol{K} \cdot [\boldsymbol{R}|\boldsymbol{t}] \cdot st_e\boldsymbol{v}_m$. The magnitude and direction of $\Delta\boldsymbol{x_b}$ determines the motion blur kernel used in this study. The motion blur kernel, generated using the MATLAB image processing toolbox, serves as the shift-invariant PSF of the motion blur.

RESULTS

Reconstructed points are used to determine the displacement error of the photogrammetry system. Generated blurred images of the target spheres are also analysed.

Displacement error

Step displacements at the image acquisition intervals of the motion blur experiment were evaluated from the 3D reconstructed points of matched sphere centres. Displacement errors were obtained by subtracting the reference laser interferometer displacement from the photogrammetric displacement in each step. The displacements of spheres that match both the multi-view stereo criteria and the internal spatial conditions of the target are computed. Ensuring both matches are satisfied reduces the likelihood of error in matching.

FIGURE 3 gives the mean displacement error for the three camera pairs with error bars indicating the maximum and minimum error at the linear actuator positions given as the abscissa of the graphs. Due to reliance of the identification algorithm on the internal spatial matching of the target spheres, the number of successful sphere centre reconstructions began to drop below three at the speed of 1000 mm min^{-1}. In FIGURE 3a), for the speed of 1000 mm min^{-1}, there were no 3D points reconstructed at the linear actuator position of 240 mm and above. A similar case was observed for speeds of 2000 mm min^{-1} to 6000 mm min^{-1}. At these high speeds, the image acquired was too degraded for the detection and identification algorithm using similar thresholding parameters with the static images. Future work will investigate integrating colour invariants and background modelling [15] to isolate a target so that some of the detection parameters can be relaxed.

The mean error from the static images shown in FIGURE 3 are less than 80 µm throughout the experiment. The maximum mean error increases to around 100 µm for images captured at 500 mm min^{-1} with the error range observed to increase significantly too. At the speed of 1000 mm min^{-1}, some mean errors approach 600 µm, and in some cases, the measured displacement error exceeds 1 mm.

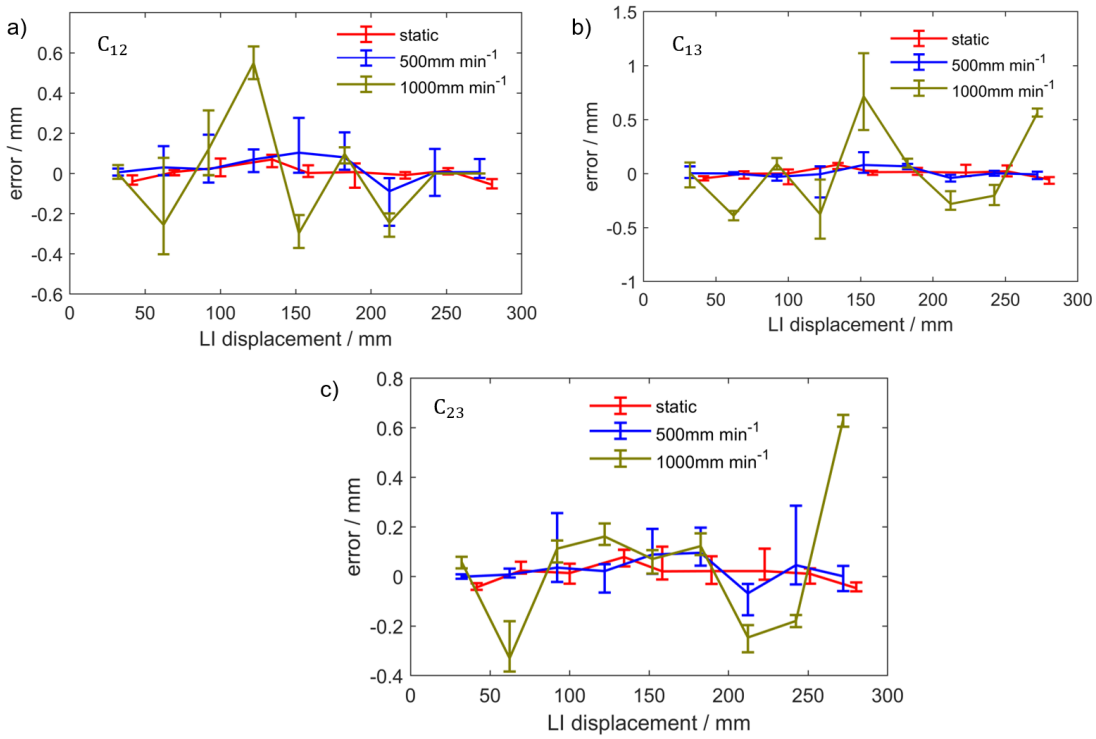

FIGURE 3. Displacement errors for subsequent image acquisition intervals of the photogrammetry system are given. Errors from stereo-camera pairs C_{12}, C_{13} and C_{23} are given in 3(a), 3(b) and 3(c) respectively. Reference displacements are obtained from the laser interferometer (LI).

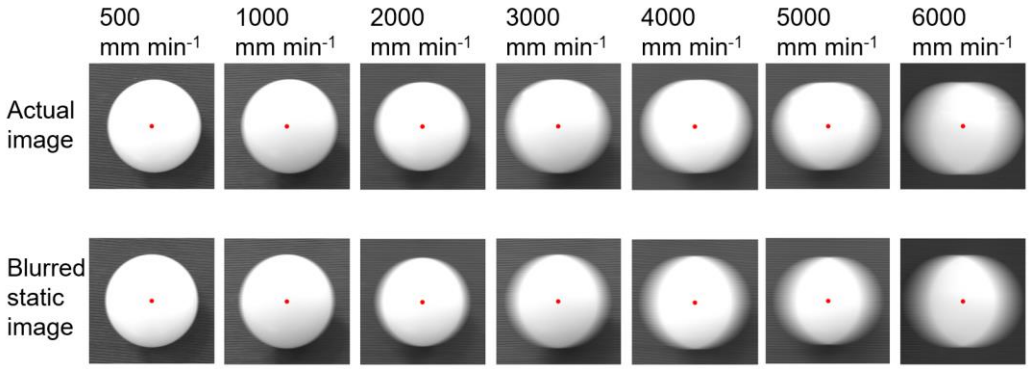

FIGURE 4. Generated blurred images at detected target spheres are compared with the actual images captured from the camera at different speed settings.

Generation of motion blur

Blurring reduces the sharpness of images, therefore, reducing high gradient and frequency features in the spatial and frequency domains of images respectively. Most detection algorithms, such as edge detection-based methods, rely on these high gradient (and high spatial frequency) features and are, therefore, affected when an image is blurred. Specific to this study, sphere edges in severely blurred images do not meet some criteria, such as, having a minimum radial gradient value and are, therefore, undetected. FIGURE 4 compares the blurring effect on the actual images captured in motion with the generated blur on static images.

A quantitative analysis of the image regions of the matched spheres is given in FIGURE 5 as mean-squared errors (MSEs) of the blurred static images. The MSE is the measure of the difference between the pixel intensities of the generated blurred images and the actual moving

images captured. Both images are 8-bit quantised and padded on each side of the detected sphere by 60 pixels. The MSE is mostly below 1000, except for images obtained at 6000 mm min^{-1}. At the maximum speed, sphere centre positions in the two images compared vary significantly.

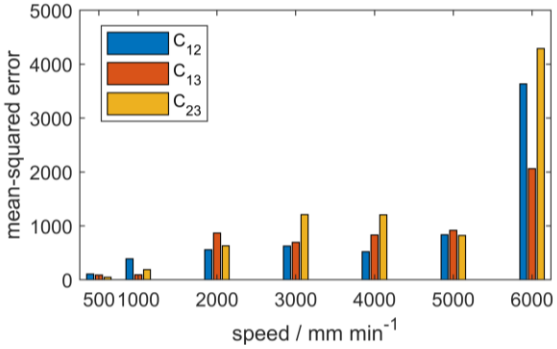

FIGURE 5. Mean-squared error of generated blurred spheres evaluated from the actual images captured in motion.

CONCLUSION

This paper investigates the effect of motion blur on the photogrammetric measurement of a 6D robotic target. 3D coordinate measurement of the moving target is investigated using reference laser interferometer measurements. It is observed that photogrammetric 3D measurement is possible when the target moves at speeds below 1000 mm min^{-1}. In addition, accurately measured displacements of the target are used to simulate blurred images that are comparable with the actual moving images. Further research will investigate more complex motion and devise computationally efficient strategies that can reduce the error caused by image blurring.

Acknowledgments: This work is funded by the Engineering and Physical Sciences Research Council (EPSRC) under grant number: EP/T023805/1—High-accuracy robotic system for precise object manipulation (HARISOM).

REFERENCES

[1] Mei C, Reid I. Modeling and generating complex motion blur for real-time tracking. 2008 IEEE Conf. Comput. Vis. Pattern Recognit., IEEE; 2008.

[2] Sims-Waterhouse D, Leach R K, Piano S. Close-range photogrammetry. Advanced Optical Form and Coordinate Metrology, IOP Publishing; 2020, p. 4–18.

[3] Luo Y, Ho D, Mirabbasi S. Exposure-programmable CMOS pixel with selective charge storage and code memory for computational imaging. IEEE Trans. Circuits Syst. I Regul. Pap. 2018;65:1555–66.

[4] Yang H, Yi Y, Liu G, Shi X. CS-BS-EF: An integrated method for tracking flying ping-pong with motion blur. Proc. 2013 Int. Conf. Mechatron. Sci. Electr. Eng. Comput., 2013, p. 1220–3.

[5] Rajagopalan A N, Chellappa R, editors. Motion Deblurring: Algorithms and Systems. Cambridge University Press; 2014.

[6] Zhao H, Shang H, Jia G. Simulation of remote sensing imaging motion blur based on image motion vector field. J. Appl. Remote Sens. 2014;8:083539.

[7] Yang C, Feng H, Xu Z, Chen Y, Li Q. Image deblurring utilizing inertial sensors and a short-long-short exposure strategy. IEEE Trans. Image Process. 2020;29:4614–26.

[8] Sieberth T, Wackrow R, Chandler J. Influence of blur on feature matching and a geometric approach for photogrammetric deblurring. Int. Arch. Photogramm. Remote Sens. Spat. Inf. Sci. 2014;XL–3:321–6.

[9] Pintaric T, Kaufmann H. A rigid-body target design methodology for optical pose-tracking systems. Proc. 2008 ACM Symp. Virtual Real. Softw. Technol.; 2008.

[10] Isa M A, Sims-Waterhouse D, Piano S, Leach R K. Volumetric error modelling of a stereo vision system for error correction in photogrammetric three-dimensional coordinate metrology. Precis. Eng. 2020;64:188–99.

[11] Zhang Z. A Flexible New Technique for Camera Calibration. IEEE Trans. Pattern Anal. Mach. Intell. 2000;22:1330–4.

[12] Isa M A, Sims-waterhouse D, Piano S, Leach R K. Kinematic error analysis of stage tracking using stereo vision. Proc. ASPE, 2019.

[13] Guan B, Yu Y, Su A, Shang Y, Yu Q. Self-calibration approach to stereo cameras with radial distortion based on epipolar constraint. Appl. Opt. 2019;58:8511–21.

[14] Zhou H, Chen Y, Feng R. A novel background subtraction method based on color invariants. Comput. Vis. Image Underst. 2013;117:1589–97.

Preliminary Study on Fluorescence Strobo-Stereoscopy for 3D Surface Imaging

Xiangyu Guo[1] and ChaBum Lee[1]
[1]J. Mike Walker' 66 Department of Mechanical Engineering
Texas A & M University
College Station, Texas, USA

INTRODUCTION

Stereo vision is the most popular vision technology for 3D measurement based on 2D stereoscopic images, based on the triangulation principle, this technique can achieve vertical resolution up to 1 μm. Apart from uncertainty sources like the calibration error, low image resolution, and surface interaction [1], it is widely recognized that the quality and appropriateness of lighting are critical components of developing high-quality, robust, and timely vision inspection for stereoscopy systems [2].

Commonly, the stereoscopy is applied to diffused reflection surface. Due to the directionality of the surface specular reflection, the quality of reconstructed 3D surface imaging can be significantly degraded, and the information about the surface beneath the specular reflection area can be lost. For the well-machined surface measurement, like cylinders, under the stereoscopy system, because of such effect, the 3D surface image quality can be decreased extensively, and the surface information under the specular reflection area can be lost. The smoother the machined surface is, the more crucial the specular reflection is. Additionally, for surface without irregular structures, another challenging difficulty in stereo vision is locating corresponding feature image points, as there are fewer reference points with high-quality surfaces.

With the characteristics of eliminating specular reflection and a high speckle contrast that can be used to highlight defects or changes in the surface texture that can be used as reference points [3], fluorescent fluids or dyes can be used in conjunction with reflective surface 3D stereoscopic metrology.

In this paper, to demonstrate the advantage of fluorescent fluid in removing specular reflections during stereoscopy 3D reconstruction, we present a comparative experiment reconstructing a cylinder and square patterned structure. Additionally, to implement the previously designed strobo-stereoscopy system, this fluorescent fluid-based implementation is included.

BACKGROUND STUDY

Fluorescence Effect

One property of the fluorescent dye is explained by Stokes shift, which occurs when the dye is activated by a certain ultraviolet (UV) light and its emission wavelength is shifted as a result of the energy received and released. The emission and excitation wavelengths do not overlap [4]. Thus, specular reflection from the exciting wavelength can be separated by providing the vision system with bandpass filters.

Meanwhile, fluorescent liquid is well-known for increasing speckle contrast and enabling simultaneous observation of surface textures, which can improve reconstruction accuracy for the presence of more reference matching points in the pair of images, as well as the higher contrast surface information. The Stoke shift effect of PAG 150 UV dye is depicted in Figure 1.

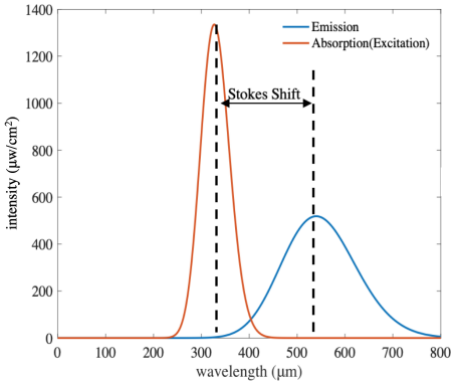

FIGURE 1. The Stoke Shift effect for under 365 nm excitation wavelength.

Strobo-stereoscopy System

The strobo-stereoscopy is a whole-view 3D reconstruction method [5]. The binary stereoscopic vision system is chosen for its rapid ability to provide three-dimensional information, ease of composition, and low vibration requirements for the surrounding environment. While other optical systems, such as microscopy and machine vision, such as 2D image feature extraction and intensity analysis, can only provide local information or be performed offline, due to the complexity of metrology systems, the requirement for operational stability, and the inadequacy of metrology software, not to mention online measurement at high working speeds.

We introduce the stroboscopy into the system, which is used to scan the target sample in full view using a phase-shifting technique. It is implemented as a light illumination control that is synchronized with the machine tool's operating speed, making it suitable for high-speed online measurement while tracking the machine tool's performance at various locations, allowing for the avoidance of defective parts and optimization of machine maintenance schedules. Additionally, pulsed stroboscopic illumination can eliminate the contribution of ambient light. This primary strobo-stereoscopy technique addresses the requirement for in-situ high-speed, high-resolution imaging of large-area objects at a resolution of 1 μm. Figure 2 shows the working principle.

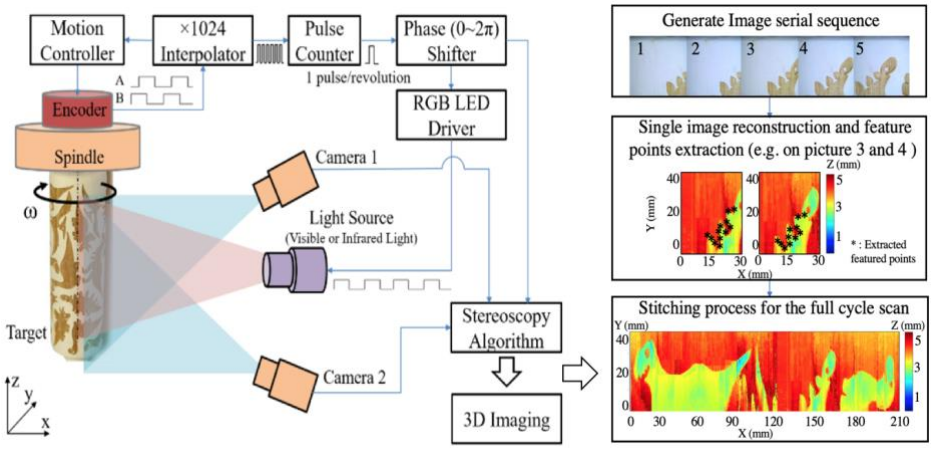

FIGURE 2. Strobo-Stereoscopy methodology.

EXPERIMENT SETUP

In this fluorescence strobe-stereoscopy method, a pair of CCD cameras are included for the images capturing, a 365 nm (λ_{ex}) UV light is prepared for the exciting light source, a pair of highpass filters (BPF >370 nm) are chosen from the emission wavelength 520 nm (λ_{em}) of the fluorescent fluid, and an air spindle is used for the target rotation. This method can remove the system's sensitivity to the illumination system and highlight the defects information and tool wear information, which can provide the opportunity to characterize the defects types.

In order to show the advantage of the fluorescent fluid in eliminating specular reflections, a comparative experiment of reconstructing a 3D surface was conducted with the machined aluminum rod (ø 25.4 mm). Figure 3 (a) offers the methodology schematic, figure 3(b) shows the specular reflection effects on stereoscopy reconstruction, and figure 3(c) presents the result when the fluorescent dye fluid was applied, from which we can conclude that the fluorescent liquid can improve the optical quality-surface map reconstruction ability.

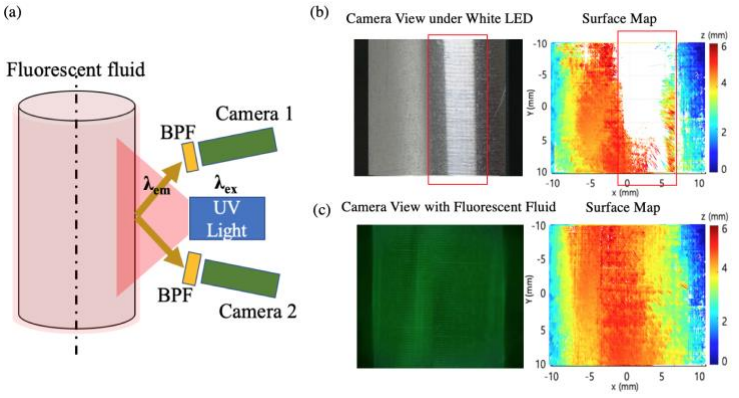

FIGURE 3. Methodology schematic of fluorescence strobo-stereoscopy (a), the comparison results for with (b) and without (c) fluorescent fluid applied, the red framed area is the specular reflection area.

COMPARATIVE EXPERIMENTS

Reflecting patterned surface comparison

Figure 3 demonstrates the fluorescent liquid's advantages in compensating for the loss of information due to specular reflection. For further detailed discussion, we conducted a comparative experiment employing a flat reflecting target surface with square patterning information.

The overall size of the pattern, including the groves, is 4.2 4.2 mm in total. The effects of surface reconstruction under white light LED, UV light along with fluorescent liquid are depicted in Figure 4. It is self-evident that fluorescent liquid applied cases have a greater level of quality and accuracy than the other case.

In addition, a linear scan across the square pattern is performed on the 2D average mean removed filtered surface. The reconstructed pattern sizes for the white light LED and fluorescent cases are 5.2 and 5mm, respectively, while the grove depths are 0.25 and 0.21 mm, respectively. This validates the benefit of using fluorescent liquids in the 3D reconstruction process.

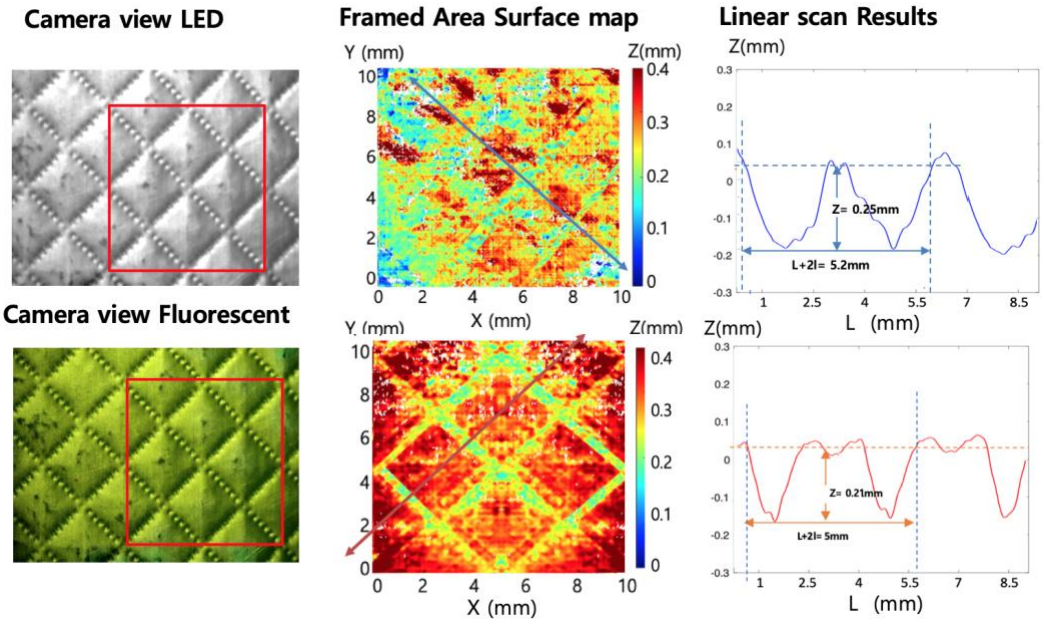

FIGURE 4. Patterned surface reconstruction comparison between white light LED and fluorescent liquid applied stereoscopy method.

FSS whole view reconstruction

We then performed fluorescent strobe-stereoscopy metrology on a patterned 2" diameter target surface based on the results of the flat patterned surface and cylinder surface comparisons. The procedure and results of reconstructing the entire picture are shown in Figure 5. The target sample was photographed every 45 degrees throughout the rotation, totaling eight photographs for the stitching procedure.

The stereoscopic algorithm is used to build the center surface. Prior to recovering the depth map, pre-processing is required to center the target, remove distortion, and adjust the brightness. To eliminate system noise, a 2D average removal filter is used. After expanding the rebuilt surface to the tilted surface using the known rotational angle, the stitching position may be matched, and the phase unwrapping procedure can continue. Following the balance process, the panorama surface is gathered, and the 3D full view can eventually be reconstructed.

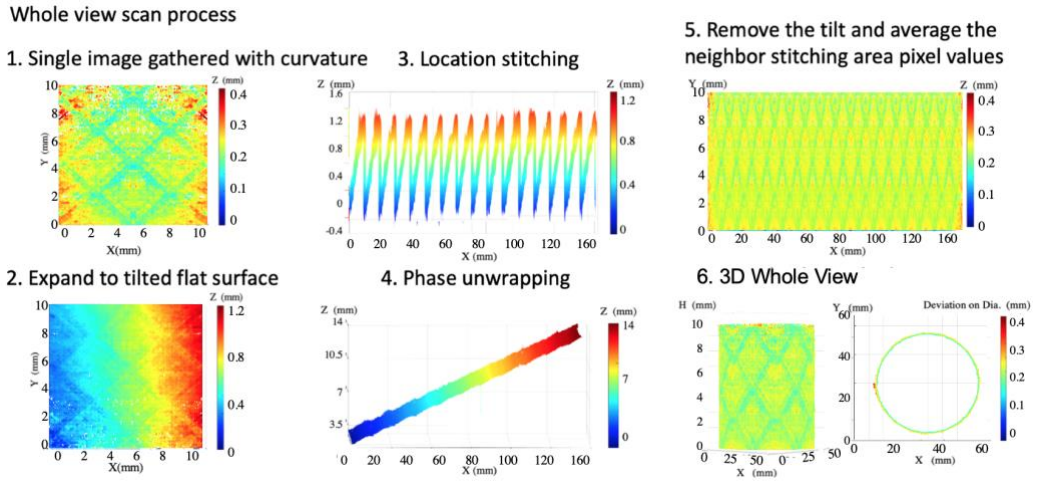
Whole view scan process
1. Single image gathered with curvature
3. Location stitching
5. Remove the tilt and average the neighbor stitching area pixel values
2. Expand to tilted flat surface
4. Phase unwrapping
6. 3D Whole View

FIGURE 5. FSS Whole view reconstruction process and results.

FURTHER DISCUSSION AND CONCLUSION

This paper describes the fluorescent strobe-stereoscopy methodology, as well as the principle of fluorescent liquid implementation and the previously presented strobe-stereoscopy strategy. The preliminary investigations on the flat reflective pattern-surface proved the fluorescent liquid's ability to enhance the quality of the reflecting surface's 3D reconstruction, since the Stokes shift effect suppresses specular reflection. Furthermore, when combined with primary fluorescence stereoscopy (FSS), whole-view 3D reconstruction can provide comprehensible geometric information. As the fluorescent dye is immersed in the cutting fluid, this technology can be employed as an on-machine or even in-process metrology for ongoing development regardless of the on-machine goal measurement setting.

ACKNOWLEDGEMENTS

This work is funded by the Department of Energy's Kansas City National Security Campus operated by Honeywell Federal Manufacturing & Technologies, LLC under contact number DE-NA0002839.

REFERENCES

[1] Gao W, Haitjema H, Fang FZ, Leach RK, Cheung CF, Savio E, Linares JM. On-machine and in-process surface metrology for precision manufacturing. CIRP Annals. 2019 Jan 1;68(2):843-66.

[2] Martin D. A practical guide to machine vision lighting. Midwest Sales and Support Manager, Adv Illum2007. 2007 Oct:1-3.

[3] Dong B, Li C, Pan B. Fluorescent digital image correlation applied for macroscale deformation measurement. Applied Physics Letters. 2020 Jul 27;117(4):044101.

[4] Lakowicz JR, editor. Principles of fluorescence spectroscopy. Springer science & business media; 2013 Apr 17.

[5] Guo X, Lee C. Preliminary study of phase-shifting strobo-stereoscopy for cutting tool monitoring. Journal of Manufacturing Processes. 2021 Apr 1;64:1214-22.

Ultra-High-Speed Micromachining Spindle Metrology under Radial Loading Conditions

Sudhanshu Nahata*[,1], and O. Burak Ozdoganlar[1,2]
[1]Department of Mechanical Engineering
Carnegie Mellon University
Pittsburgh, PA, USA
[2]Department of Biomedical and Material Science and Engineering
Carnegie Mellon University
Pittsburgh, PA, USA

INTRODUCTION

Although methodologies have been developed for characterizing the error motions of ultra-high-speed (UHS) micromachining spindles [1-3], to date, these methodologies have not involved applying loads to the spindles. These loads arise during micro-cutting operations, resulting in micromachining forces. The ISO standard (for axes of rotation metrology [4]) does not explicitly describe a procedure for measurement of error motions of an externally loaded spindle. However, as shown in the case of macro-scale spindles [5], radial (static) loading has a significant effect on the spindle error motions. Correspondingly, we hypothesize that external radial loading will have a substantial effect on the error motions of an UHS spindle. Because spindle speed has a significant impact on error motions [6], an analysis of UHS spindle error motions requires measurements at various spindle speeds. Such error motions have a direct impact on the geometric accuracy and surface finish of the micromachined parts [7].

For macro-scale spindles, use of master axis for characterization of spindle error motions under load has been prescribed by Marsh *et al.* [8]. ASME standards [9] also require that dynamic compliance be measured using the master axis method by applying load to the master axis stator. However, this method is unsuitable to UHS spindles because their dynamic radial stiffness values are extremely low and, in many cases, ambiguous. Even a minor misalignment with the master axis would result in permanent damage to the (fragile) spindle.

In this paper, we present a non-contact magnet-based method for applying radial (static) loads to a spindle via an artifact. Subsequently, we measure the radial motions from the surface of the artifact along two mutually perpendicular directions and use multi-probe error separation method [10] to remove the form error of the artifact, yielding the radial throw of the tool axis. The radial motion in each measurement direction is further decomposed into fundamental (or one-per-rev) component and residual synchronous error motions, which are then compared at different load levels to make observations.

EXPERIMENTAL SETUP

Figure 1 depicts the experimental setup used in this study. It is made up of an UHS spindle that is mounted on a vibration isolation table via a polymer granite block. The spindle has a maximum speed of 140,000 rpm and consists of a pair of hybrid ceramic bearings (IBAG HT 45 S 140). The spindle is water cooled, where the temperature of the water kept within 2 degrees Celsius of the set point of 27 degrees Celsius by an external chiller unit. The spindle's rotation axis is defined as the z-axis (also known as the axial direction), while the x- and y-axes denote radial directions. The x, y and z axes are a set of mutually orthogonal axes.

A non-contact loading setup is designed to apply a pull type loading along the *-y* direction, that loads the spindle in the radial direction. The loading setup consists of a precision 3-axis stage and a load cell (Omega LCM105-10) to which a permanent magnet is attached. The magnet attracts a ferromagnetic test artifact in the form of a Class XX gage pin, resulting in radial loads. The

* Corresponding author; currently at Kulicke and Soffa Industries, Inc.

permanent magnet (NdFeB Grade N50) has a pyramid-shaped geometry with a 25.4 mm square base, a 25.4 mm height, and a 3.1 mm square top. This magnet is housed within a 3D printed (material: VeroWhite) enclosure. Radial loads can be precisely controlled by varying the airgap (g) between the magnet and the artifact using the precision stages.

The present configuration can apply a maximum load of 6 N at a ~1 mm airgap. Higher loading can be achieved by reducing the airgap further, but for the sake of the spindle's safety, it was decided to limit the airgap to 1 mm. Based on the average forces encountered during mechanical micromachining processes such as micro-milling [11], a radial load of 6 N is deemed sufficient.

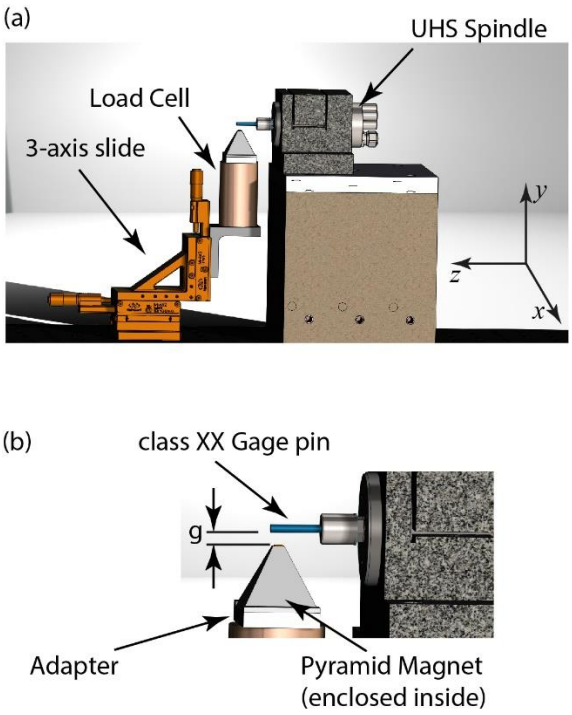

FIGURE 1. Experimental setup used to radially load an UHS spindle: (a) overall setup, (b) test artifact, permanent magnet and the airgap, g, between them.

Since the artifact form is expected to be of similar order of magnitude as the spindle error motions, error separation is required. In this work, a multi-probe error separation is implemented with three displacement probes (LDVs *M1*, *M2* and *M3*) as shown in Figure 2. It is well known that multi-probe method suffers from harmonic suppression [10]. Therefore, to avoid harmonic suppression within first 25 harmonics, the angles between the probes α and β are carefully optimized [12] keeping in mind the physical constraint of the existing metrology setup. A favorable set of angles is determined at α = 90+/-2 degree and β = 175+/-2 degree.

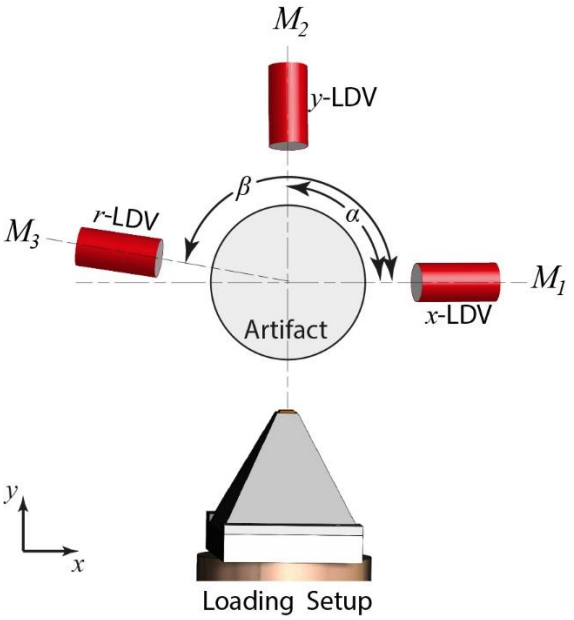

FIGURE 2. Schematic showing the relative angular placement of the three LDV probes in the x-y plane for the multi-probe error separation. A portion of the loading setup is also shown.

Revolution markers (i.e., indicating the start of each revolution) are obtained by sensing a reference mark on the collet-nut with an infrared (IR) sensor [13]. The thermal state of the spindle is monitored by a temperature sensor connected to the coolant outlet line. A custom LabVIEW environment is built to collect four different quantities at once: x- and y- (or r-) displacements, revolution markers, spindle temperature, and static forces from the load cell.

The experiments are carried out at radial loading levels of 0, 3 and 6 N. The artifact overhang length was set at 20 mm and the radial load was applied at 16.5 mm away from the spindle nose (see Figure 3). The displacement measurements are taken at a 5 mm axial distance from the spindle nose.

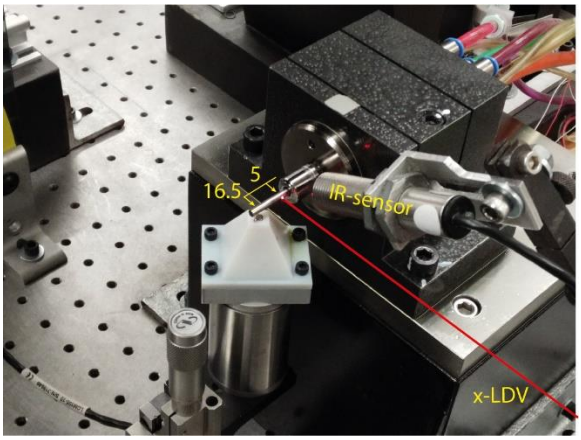

FIGURE 3. Physical experimental setup indicating the load application and measurement location from the spindle nose (z=0). The dimensions are in mm. Note: only x-LDV is shown.

DATA PROCESSING

For conducting multi-probe error separation, pairwise LDV measurements consisting of (x, y) and (x, r) motions from the surface of the artifact, pulse signal from IR sensor, and temperature measurements from coolant outlet line are simultaneously acquired. For each speed, the data is collected for a time duration of 1 second, corresponding to at least 600 revolutions. This procedure is repeated for all the speed under consideration. Data is collected at five different temperatures covering the coolant thermal cycle at each speed.

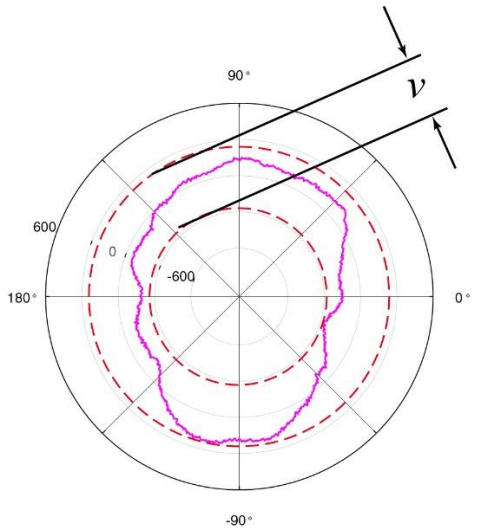

FIGURE 4. Residual synchronous error motion value, v, derived from the polar plots of the residual synchronous error motions [1].

The measured radial motions are decomposed into various components using the data processing scheme presented in [14] and subsequently, the artifact form error is removed at each spindle speed. At each speed, both the fundamental amplitude and the residual synchronous error motions are presented along the x and y axes. In the results section, the average value is shown, with the error bars representing the standard deviation calculated from five different runs during the coolant thermal cycle. A commonly used metric, residual synchronous error motion value, v, is also calculated and discussed in the results (see Figure 4 for a sample calculation).

VALIDATION OF ERROR SEPARATION

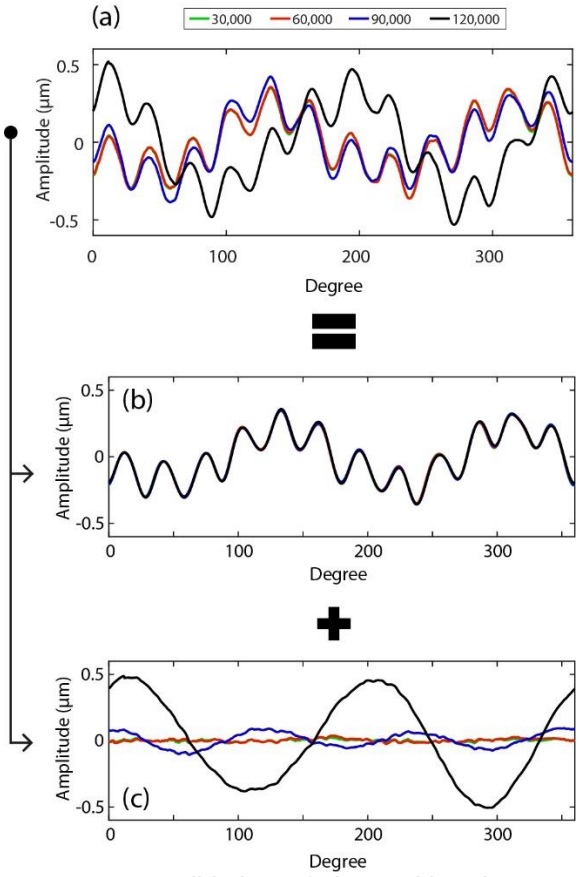

FIGURE 5. Validation of the multi-probe error separation technique by separating artifact form and spindle error motions at four different spindle speeds (rpm): (a) residual synchronous error motions including the artifact form, (b) artifact form at all the tested speeds (overlapped), and (c) true residual synchronous error motions, after removal of artifact form errors.

The multi-probe error separation method is validated by comparing form errors of the artifact at four different spindle speeds at a fixed axial measurement location. Figure 5 present artifact form error and spindle error motions at various spindle speeds. Since the (axial) measurement location is kept fixed, the artifact form is expected to be constant at all speeds. The maximum difference in the artifact form error between speeds is less than 30 nm. There are two possible explanations for this discrepancy: (1) uncertainty of a few nm due to the synchronous components of structural error motions, and (2) gradual axial growth of the shaft by a total of 10 um as the spindle speeds is increased from 60k to 120k rpm (figure not shown), which changes the measurement location on the artifact by the same amount. As a result, for the results shown below, the artifact form was obtained at each spindle speed of interest.

RESULTS AND DISCUSSION

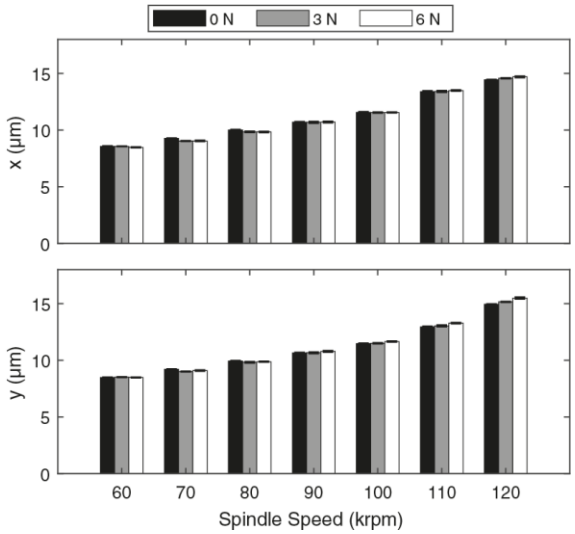

FIGURE 6. Fundamental component at different radial loads as a function of spindle speed.

Figure 6 presents the x- and y- amplitude of fundamental component (of radial throw) at various radial loads for a range of spindle speeds. The standard deviation is <1% of the measured motions (error bars are hardly visible) which demonstrate that the data highly repeatable. The maximum change in average fundamental component along the x-axis is 254 nm (~2.5 %) at 80 krpm. At 120 krpm (~3.5 %), a maximum change of 550 nm in average fundamental component is observed along the y-axis. For majority of cases, the change in fundamental component is less than 1% which can be considered negligible. This result could be expected because a static load likely caused a static shift in the location of axis average line due to the finite radial and bending stiffness of the spindle. As a result, during pure static loading, the eccentricity or the dynamic response is not expected to change provided the spindle's stiffness-load relationship is sufficiently linear.

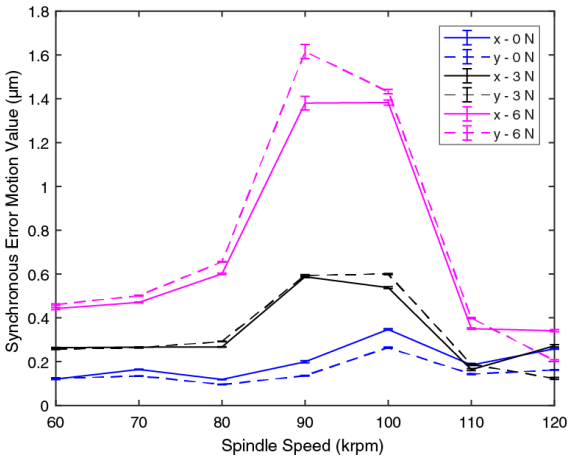

FIGURE 7. Residual synchronous error motion value at different radial loads for both x and y directions of measurement.

Figure 7 shows the residual synchronous radial error motion values along x- and y-directions for a range of spindle speeds (after removing the artifact form). At speeds of 90-100 krpm, the residual synchronous radial error motion values are greater than all other speeds by about 50% or more. On an increase in radial loading, the residual synchronous radial error motion values are found to increase for all speeds, except for 3 N load at 110 krpm. The increase in the residual synchronous radial error motion values is disproportionally higher for 90-100 krpm spindle speeds when a radial load of 6 N is applied. Both x- and y-directions follow similar trends. This could be due to contact stiffness and/or contact angle changes at certain rotational speeds leading to softness in bearings.

Figure 8 shows polar plots of residual synchronous radial error motions at selected spindle speeds of 60, 90 and 120 krpm. Significant differences in residual synchronous radial error motions are observed at different speeds and at different loading levels. At 60 krpm, the predominant motion along the

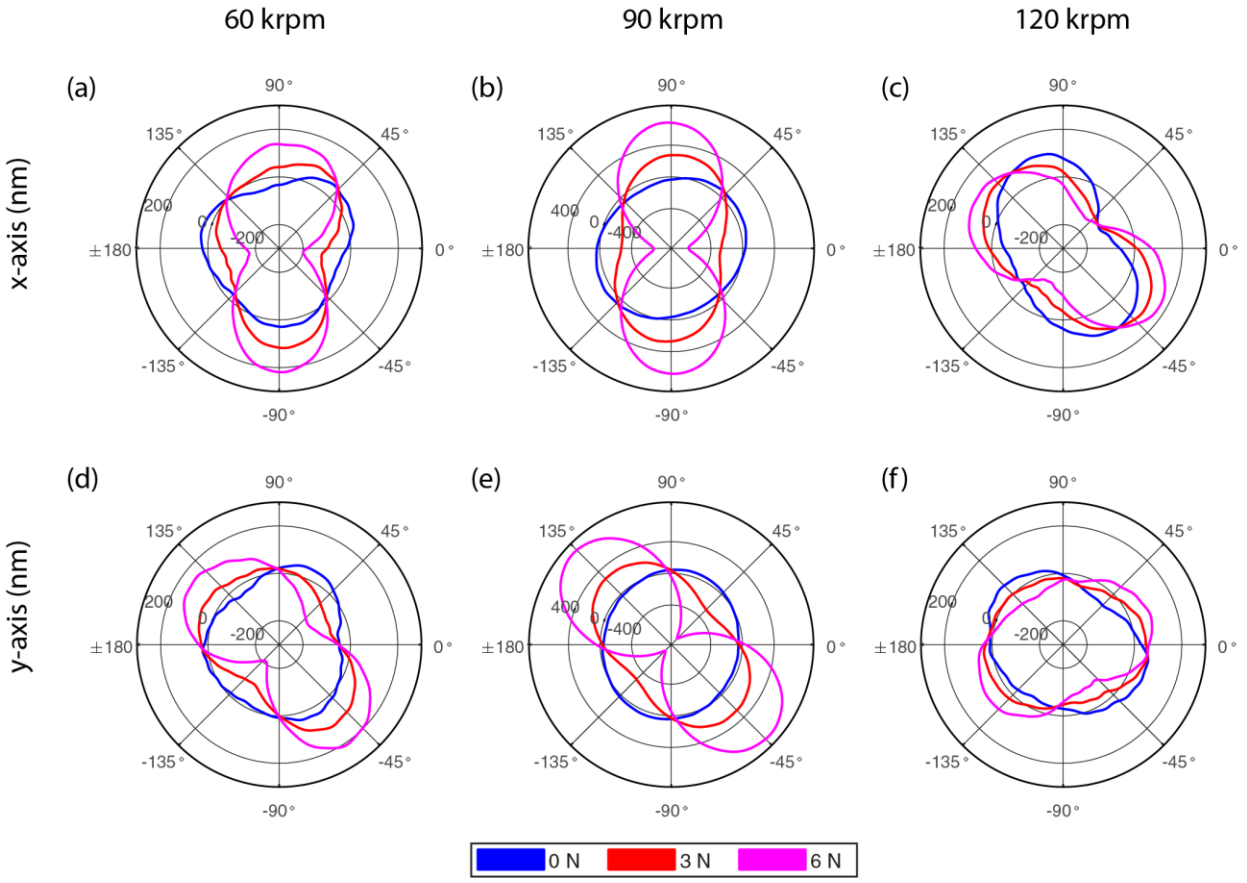

FIGURE 8. Polar plots showing the residual synchronous radial error motions for two mutually perpendicular fixed-sensitive directions.

x-direction changes from a 3-lobe at 0 N to a 2-lobe at 6 N force. The effect of radial loading is clearly identified as a significant jump in 2 cpr (cycles per revolution) values for both 60 and 90 krpm when a radial load is applied. For 120 krpm, the synchronous radial error motions do not show a significant change in amplitude on application of radial loading. The trends and the magnitudes are similar for motions along both the x- and the y-directions on application of radial loading.

CONCLUSION

The use of permanent magnets for applying static radial loads to UHS spindles has been investigated in this work. The multi-probe method of error separation was successfully implemented on an UHS spindle. The implementation is validated by comparing the artifact form extracted at four different spindle speeds where the artifact form error was found to be similar at all spindle speeds. Depending on the axial growth of the spindle under test, error separation at each speed could be required.

On varying radial loads, the fundamental component of radial throw remains within 1% for the majority of spindle speeds, whereas the residual synchronous spindle error motions are found to increase by more than 200%. The residual synchronous spindle error motions depend strongly on the magnitude of force. An increase in 2 cpr was observed for both the x- and y- directions.

It is noted that these results are applicable for the tested spindle only and cannot be generalized. However, the presented method of load application and subsequent evaluation procedure could be adopted to any micromachining spindle for performance assessment.

ACKNOWLEDGEMENTS

This work was supported by the NIST award #70NANB12H208 (Ozdoganlar). The authors wish to thank Drs. Alkan Donmez and Shawn Moylan for their inputs and guidance during this work.

REFERENCES

[1] Fujimaki K, Mitsui K. Radial error measuring device based on auto-collimation for miniature ultra-high-speed spindles. International Journal of Machine Tools and Manufacture. 2007 Sep 1;47(11):1677-85.

[2] Nahata S, Anandan KP, Ozdoganlar OB. LDV-based spindle metrology for ultra-high-speed micromachining spindles. Proceedings of NAMRI/SME. 2013; 41:2-7.

[3] Anandan KP, Ozdoganlar OB. A multi-orientation error separation technique for spindle metrology of miniature ultra-high-speed spindles. Precision Engineering. 2016 Jan 1; 43:119-31.

[4] ISO 230-7:2006 Test Code for Machine Tools. Part 7: Geometric Accuracy of Axes of Rotation. 2006.

[5] Sharma AK, Patterson SR. Investigations into Spindle Error Motions using a Modified Loading Device. In ASPE Annual Meeting Annual Meeting 1999 (pp. 1-4).

[6] K.P. Anandan, O.B. Ozdoganlar, Analysis of error motions of ultra-high-speed (UHS) micromachining spindles, Int. J. Mach. Tools Manuf. 70 (2013) 1–14.

[7] Nahata S, Onler R, Ozdoganlar OB. Radial throw in micromilling: a simulation-based study to analyze the effects on surface quality and uncut chip thickness. Journal of Micro and Nano-Manufacturing. 2019 Mar 1;7(1).

[8] Marsh E, Gredja R D. Experiences with Master Axis Method for Measuring Spindle Error Motions. Precision Engineering. 2000; 24: 50-57.

[9] ANSI/ASME B89.3.4M. Axes of Rotation: Methods of Specifying and Testing. 2010.

[10] Whitehouse DJ. Some theoretical aspects of error separation techniques in surface metrology. Journal of Physics E: Scientific Instruments. 1976 Jul 1;9(7):531.

[11] Dow TA, Miller EL, Garrard K. Tool force and deflection compensation for small milling tools. Precision engineering. 2004 Jan 1;28(1):31-45.

[12] Cappa S, Reynaerts D, Al-Bender F. A sub-nanometre spindle error motion separation technique. Precision Engineering. 2014 Jul 1;38(3):458-71.

[13] Nahata S, Onler R, Shekhar S, Korkmaz E, Ozdoganlar OB. Radial throw in micromachining: Measurement and analysis. Precision Engineering. 2018 Oct 1; 54:21-32.

[14] Anandan K P, Ozdoganlar O B. An LDV-based Methodology for Measuring Axial and Radial Motions when using Miniature Ultra-High-Speed (UHS) Micromachining Spindles. Precision Engineering. 2013; 37: 172-186.

LATERAL SHIFT MAPPING FOR ABSOLUTE METROLOGY OF ACYLINDRICAL X-RAY TELESCOPE MIRRORS

Hayden J. Wisniewski[1], Mallory M. Whalen[2], Ralf K. Heilmann[2], Mark L. Shattenburg[2], and Brandon D. Chalifoux[1]
[1]James C. Wyant College of Optical Sciences
The University of Arizona
Tucson, Arizona, USA
[2]MIT Kavli Institute for Astrophysics and Space Research
Massachusetts Institute of Technology
Cambridge, Massachusetts, USA

INTRODUCTION

Currently, acylindrical X-ray telescope mirror segments for systems such as the Lynx X-ray Observatory concept can be measured through a variety of methods: X-ray pencil beam metrology [1], Hartmann testing [2], Fizeau interferometry with a refractive or diffractive cylindrical null [3-5], long trace profilometry [6,7], Shack-Hartmann wavefront sensing [8,9], and deflectometery [10]. Fizeau interferometry is particularly useful for making rapid full-surface measurements. However, the cylindrical wavefront produced by the refractive or diffractive cylindrical null is difficult to characterize due to the lack of point symmetry. To meet the Lynx X-ray Observatory performance goal of 0.5 arcsec half-power diameter on axis [11], this wavefront must be characterized to a 5 nm uncertainty (k = 1) [12]. If the reference surface in a Fizeau interferometer can only be characterized to this uncertainty or worse, then it is impossible to extract whether artifacts in the interferogram are due to the reference surface or the surface under test (SUT). For systems with point symmetry (optical flats and spherical surfaces), this problem is solved with absolute metrology methods, which allow both surface error maps to be separated through a series of measurements.

A well-known absolute metrology method for optical flats is the three flat test [13]. Three flats are put through a specific sequence of measurements, after which each surface can be known with very low uncertainty. During this sequence a flat is moved from the reference position to the test position of a Fizeau interferometer setup, and is flipped in the process. This repositioning of the flat creates an invariant line across all the measurements taken. The original method of the three flat test extracts the surface line of all three flats along this invariant line with very low uncertainty. It has since been expanded to full surface extraction [14]. The shift-rotation method is an absolute metrology technique for spherical surface that extracts the rotationally symmetric surface terms with a lateral angular shift and extracts the rotationally asymmetric terms through a surface rotation [15,16]. Unfortunately, neither technique can be expanded to X-ray telescope mirrors, which are acylindrical surfaces with a small cone angle (~1º) and a curved axial profile.

The difficult to characterize surface profiles of X-ray telescope mirrors (off-axis hyperboloids and paraboloids) implies that a new absolute metrology technique must be created that is viable for curved surfaces without point symmetry [17,18]. Here we present lateral shift mapping, an interferometric absolute surface measurement for X-ray telescope mirrors. This method was studied in 2010 for flat surfaces [19]. We recreate and confirm this method for flat surfaces and present plans to expand this method to X-ray telescope mirrors. Due to the ray direction in an X-ray telescope, the axial profile (curve along the optical axis) and its relation to the optical axis (cone angle) are crucial for system performance [11]. For this method to be viable for X-ray telescope mirrors, lateral shift mapping must measure the axial profile and cone angle variation, with particular attention to the quadratic term in the axial profile. Lateral shift mapping as presented here aims to accurately measure the quadratic and higher order terms of an optical flat, with the goal of extending this method to X-ray telescope mirrors with similar accuracy.

METHOD

Lateral shift mapping involves holding one of the surfaces in a Fizeau interferometer set up stationary while the other surface is shifted perpendicular to the optical axis of the interferometer [18]. The surface profile can only be extracted along the direction of shifting, but both the stationary and shifted surface can be extracted with low uncertainty. In this experiment involving two optical flats, the reference flat was held stationary while the SUT was shifted laterally using a roller bearing stage.

Matrix extraction method

If the reference is not assumed to be perfect, a measurement by the interferometer will contain the surface height information of the reference and the test added together as

$$h_{i,j} = S_i + R_i \tag{1}$$

where h is the surface height at index i, during shift j, S is the actual height of the SUT, and R is the actual height of the reference. We then shift the SUT laterally by a distance equal to an integer multiplied by the projected pixels size of the interferometer CCD (100 μm for our experiment) [20]. We now measure

$$h_{i,j+1} = S_{i+1} + R_i \tag{2}$$

where the surface index i is in reference to the interferometer. As the SUT shifts, contributions to the interferogram due to the reference will remain stationary with respect to the interferometer, whereas contributions dues to the SUT will move by an integer number of pixels. We can extract both surfaces because of the invariance of the reference surface in each interferogram.

Equations (1) and (2) create a linear system of equations that can be rewritten as

$$K \bullet \vec{z} = \vec{m} \tag{3}$$

where K is a matrix that relates the actual surface heights at each pixel of the two surfaces in the z-vector to the measured surface at each pixel in the m-vector. This system of equations can be solved using the well-known least mean squares method of the Moore-Penrose inverse. Equation (3) is then solved as

$$\vec{z} = (K^T K)^{-1} K^T \vec{m} = K^+ \vec{m} \tag{4}$$

where both surfaces are extracted in one step. Shifting multiple times over-determines the system of equations, leading to lower uncertainty in the final extracted surface due to averaging.

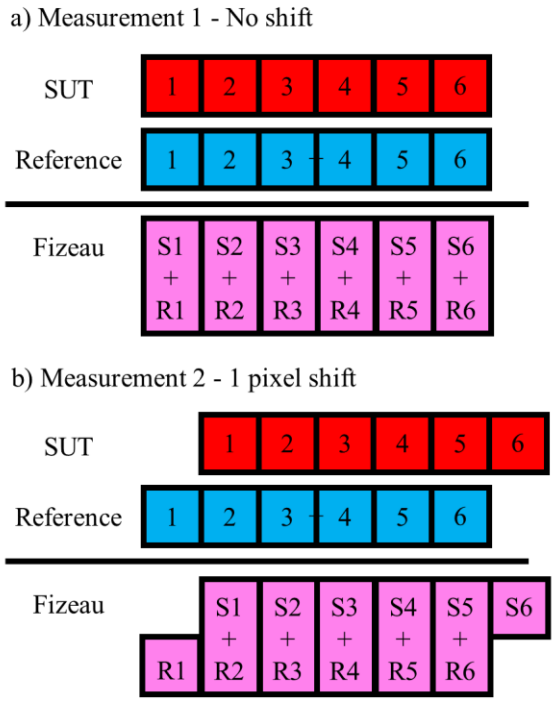

FIGURE 1. Each surface is a pixel-by-pixel addition of the reference and SUT. Contributions due to the reference being invariant across every measurement allows the two surfaces to be extracted from each other. Surfaces can be shifted by an integer number of pixels.

Removal of quadratic error

This extraction method can be thought of as an integration of slopes across the surface. Because of this pseudo-integration, the quadratic term must be handled with great care as linear tilt errors introduced by the stage during shifting become quadratic errors in the final extracted surface [21]. A quadratic term in the final surface can either be a real quadratic term or an artifact of this tilt error and they cannot be differentiated with just Fizeau interferograms. To measure the quadratic surface errors, angular SUT motions must be measured between shifts. An autocollimator sits perpendicular to the interferometer optical axis and monitors the tilt of the SUT as it shifts. This is then used to remove relative tilts between interferograms being

compared, which eliminates the quadratic error. This blindness to the quadratic term is specific to lateral shift mapping. Other metrology techniques, such as long-trace profilometry, are not blind to this term because of a tilt measurement [7].

We present the data with the quadratic term dealt with in two ways. Because the autocollimator is a potential noise source, the data is presented with the quadratic term artificially removed and with the quadratic term processed using the autocollimator. To artificially remove this term, a quadratic model is fit to the data and then subtracted out. We can see if lateral shift mapping accurately extracts the higher order terms of the surface by removing the quadratic term artificially. We can then better determine how accurately the surface with a quadratic was extracted using the autocollimator.

EXPERIMENTAL SETUP

A Zygo Verifire Fizeau interferometer was used to obtain the surface profiles of the optical flats. Two Zygo optical transmission flats rated at λ/20 P-V (λ = 633 nm) were used as the reference and SUT. One optical flat was inserted into the head of the interferometer while the other was inserted into a 5-axis mount. This mount was then connected to an Aerotech XY130 stage, which was capable of translating the SUT perpendicular to the optical axis (x-axis in FIGURE 2).

To measure the relative tilts between measurements, an Elcomat 3000 autocollimator was placed with its optical axis along the translation direction. A mirror in a low drift mount was attached to the 5-axis stage to reflect the autocollimator beam. We attached this mirror in a way to minimize hardware between the mirror and the SUT, mitigating drift in the system.

We found that air currents and vibrations were limiting sources of noise. To mitigate air currents, an airbox was constructed around the system. To minimize vibrations, the system was moved to a quieter environment and onto a vibration isolation optical table. A diagram of the experimental setup can be seen in FIGURE 2 and a picture of the setup can be seen in FIGURE 3.

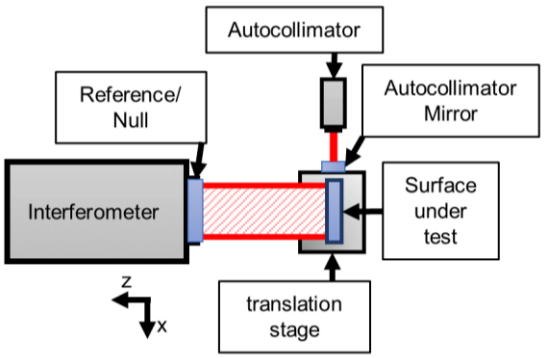

FIGURE 2. Plan view of experimental setup. SUT translates in the x-direction. Tilts during shifting are measured by the autocollimator measuring a mirror connected and perpendicular to the SUT.

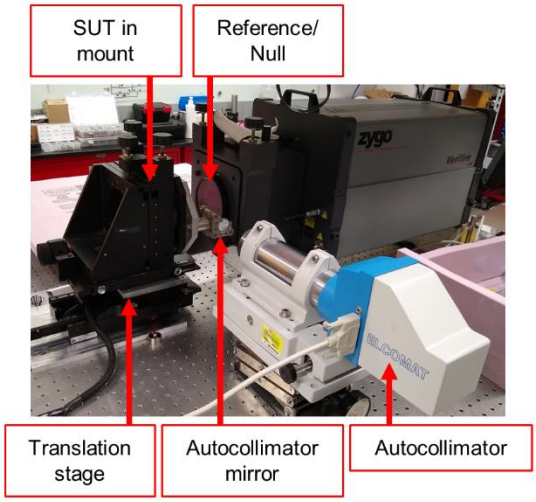

FIGURE 3. Picture of current setup with airbox removed. The autocollimator mirror can be seen attached to the 5-axis mount that holds the SUT. Translation stage moves toward the autocollimator during measurements.

RESULTS

The experimental results are shown with the quadratic term artificially removed and with the quadratic term removed through use of the autocollimator. The results shown are using the same set of data taken with the Fizeau interferometer. The final surfaces are the result of averaging 25 sets of measurements, and each set was comprised of 40 shifts with a shifting distance of 2 pixels each (100 μm per pixel). To minimize noise from vibrations and air currents, the interferogram was averaged 100 times per measurement and the autocollimator collected 1000 data points per measurement. With these

high number of averages per measurement, the full 25 sets of measurements took 36 hours in total. These measurements were not designed to be fast, rather were aimed at eliminating some environmental noise. Time scales on future measurement sets will be much smaller. A three flat test was also performed on the same day using a third optical flat. This was to ensure that the comparison three flat test data was taken under the same environmental conditions. Three separate three flat tests were performed and averaged together to avoid any environmental effects, such as vibrations. A low pass spatial frequency filter was applied to filter all signals with a spatial wavelength smaller than 1 mm to eliminate effects due to scattering.

Artificial removal of quadratic terms

The artificial quadratic term extraction involves fitting a quadratic model to the data and then subtracting this model from the data. This artificial quadratic extraction was done to both the lateral shift mapping surface and the three-flat test surface to ensure that any post processing done was done equally to both surfaces. Therefore, the power term is missing in the three flat test profile as well. This is to test whether the lateral shift mapping method is accurate for higher-order terms.

A comparison between the three-flat test measurement and the lateral shift mapping method can be seen in FIGURE 4. The rms difference between the two measurements is 0.53 nm for the SUT and 0.68 nm for the reference. This great agreement between the two surfaces demonstrates that lateral shift mapping is a valid absolute measurement technique when the quadratic term is left out. This also means that with the power term left in the extraction, it is possible to extract the surface of the two flats as long as the method for dealing with the quadratic error is precise enough.

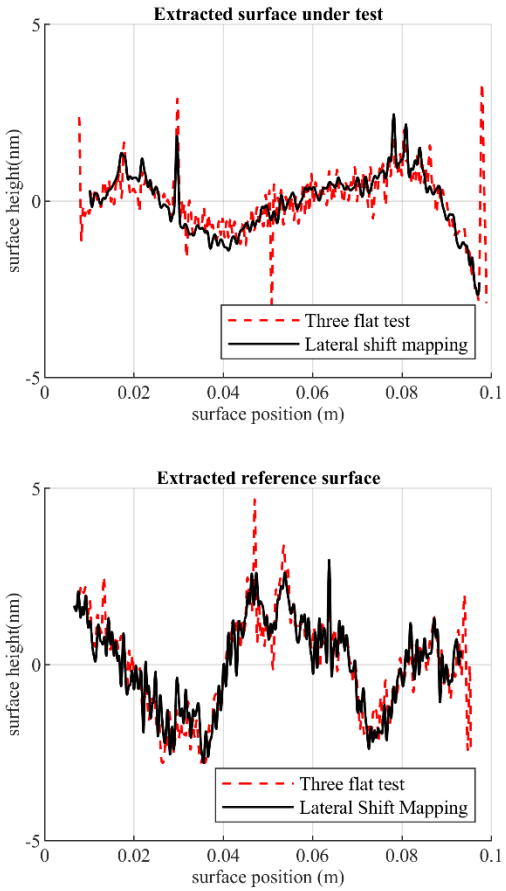

*FIGURE 4. SUT (*top*) and reference surface (*bottom*) when extracted by the three-flat test and by lateral shift mapping with the quadratic term artificially removed. The rms difference between the three-flat test method and lateral shift mapping method for the SUT was 0.53 nm and for the reference surface was 0.68 nm.*

Autocollimator removal of quadratic terms

Using autocollimator measurements, we remove the relative tilts of the reference surface and SUT before processing the data. For each surface measurement, the autocollimator gathered and averaged 1000 points of data to minimize random error. In a set of 40 shifts, the autocollimator measurement was used to remove any relative tilt by subtracting a best fit line of angle times surface length. If there was no error in the autocollimator, all surfaces would then have the same linear trend as the first line, with different surface values because of the shifts.

The extracted surfaces are shown in FIGURE 5 and a clear quadratic trend can be seen. Since the underlying data set is the same as in FIGURE

4, the surface information is present but hidden by the quadratic term. This quadratic term is due to either angle measurement errors or unmeasured relative tilts between the reference and SUT. The surfaces have an rms difference of 18.90 nm for the reference surface and 20.07 nm for the SUT when compared to the Three flat test. The source of the noise must be found and reduced for this method to prove viable for X-ray telescope mirrors.

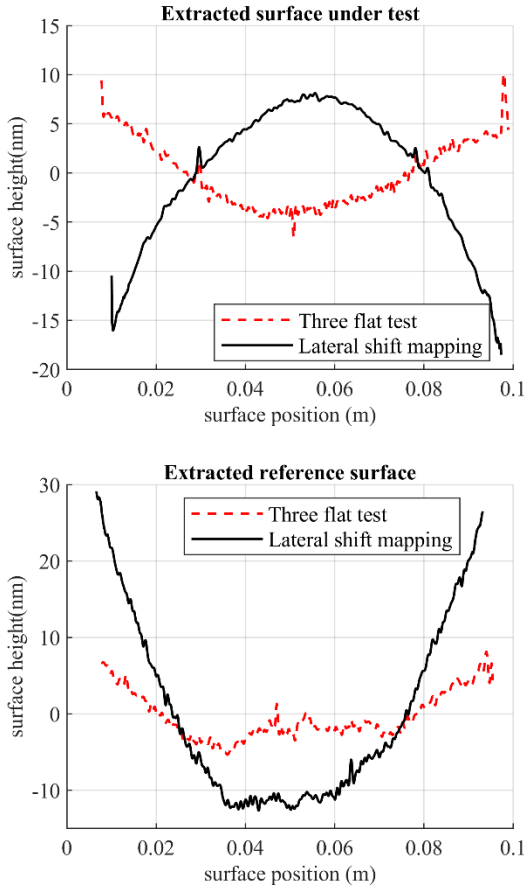

*FIGURE 5. SUT (*top*) and reference surface (*bottom*) when extracted by the three-flat test and by lateral shift mapping when the tilt in the mirror is measured and removed with an autocollimator. The rms difference between the three-flat test method and lateral shift mapping method for the SUT was 20.07 nm and for the reference surface was 18.90 nm, which is a large error compared to removing the quadratic artificially (FIGURE 4)*

ERRORS

The largest source of error is in the measurement of relative tilts between the reference and the SUT, as evidenced by the large quadratic error seen in FIGURE 5. The autocollimator random noise was 260 nrad rms over about 78 seconds. We simulated measurements with this error included, and the resulting quadratic error was about 1 nm, suggesting this is not a cause of the observed quadratic error. The error is likely a product of unmeasured drift somewhere in the system. Unmeasured tilt error could have been introduced by the reference surface (not monitored during this experiment) drifting in the tip-tilt mount of the interferometer, or the autocollimator mirror mounted to the SUT drifting in reference to the SUT. It was discovered that in the direction that we were measuring (rotations about the y-axis) the autocollimator measured a linear drift of ~150 nrad/hr. Simulating measurements with 150 nrad/hr tilt produced quadratic errors of about 90 nm rms. This is much larger than the error that we measure. An autocollimator drift of 35 nrad/hr produces an error of 20 nm rms, which suggests angular drift on this scale as a plausible cause of the quadratic error. It is possible that there is an unobserved drift on the order of 35 nrad/hr (for example, the unmonitored reference surface could be drifting in its mount) which is masked by the larger 150 nrad/hr drift we did measure and account for in our analysis.

FUTURE WORK

Before this method can be extended to cylindrical surfaces, the drift in the system must be addressed. Experiments conducted after the presented data showed that the autocollimator does not have a natural linear drift, rather there is drift due to temperature variation. On small enough time scales this drift is linear and can be accounted for in post processing. This is most likely not our source of unmonitored drift.

As we continue to look for the source, we have developed a new shifting scheme that we expect to mitigate quadratic error due to drifting. The current shifting scheme scans the SUT from left to right in pixel sized steps. In the new scheme, the first measurement will be taken in the right most position, the second measurement in the left most position, the third measurement in the second right most position, continuing on to the middle positions of the field. This outside-in approach will balance the tilt error due to drift and should minimize its effect on the surface extraction. A plot of quadratic error using the different shifting schemes versus drift amount can be seen in FIGURE 6. A random position shifting

scheme was also included for comparison. It can be seen that the outside-in approach leads to nearly an order of magnitude improvement in error when compared to the straight across method.

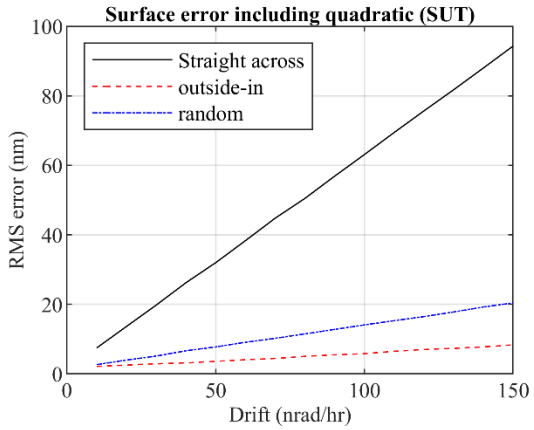

FIGURE 6. Surface error when considering the quadratic term vs drift. Multiple shifting schemes are presented. The straight across is the current method. Error due to drifting over time may be drastically reduced by using the outside-in shifting method. Each data point was generated assuming a linear drift over the whole measurement set with 2 min between each measurement.

Once drift in the system is mitigated, we plan to expand lateral shift mapping to axial shift mapping, where we can measure cylindrical surfaces. We will use a refractive or diffractive (computer generated hologram) null to generate a reference cylindrical wavefront. A z-theta stage must also be designed to extend this method. A theta-stage at the center of curvature will provide the theta motion, while a z-stage connected to the theta-stage by a radial arm will provide the z-motion. Because the quadratic term along the z-direction will determine the effectiveness of this mirror, this stage must also be able to accommodate the autocollimator measuring tilts along the z-axis. With the null and z-theta stage we aim to measure X-ray telescope mirror segments with an rms uncertainty of less than 5 nm.

CONCLUSION

We presented results demonstrating the ability to absolutely measure a surface profile of an optical flat using lateral shift mapping if the power term is artificially removed. We confirmed this by comparing results for lateral shift mapping against the results for a three flat test, a well-known absolute metrology technique. We also showed results for extracting the surface, but eliminating the power term by removing relative tilts with autocollimator measurements. These results contained large quadratic errors. It was found that the large difference in the two methods is likely due to slow angular drifts in the system. This error source will be addressed before continuing on to curved optics.

We finished by presenting a concept for a z-theta stage that will allow lateral shift mapping to be extended to curved optics, specifically acylindrical optics. This will allow cylindrical nulls, which are historically difficult to measure, to be characterized to the 5 nm rms domain. Well characterized cylindrical nulls will aid in the characterization of X-ray telescope mirrors, with the overall impact of aiding the effort to create a high resolution X-ray telescope like the Lynx X-ray Observatory concept.

ACKNOWLEDGEMENTS

We would like to thank Will Zhang at NASA Goddard Space Flight Center and David Windt at RXO for engaging conversations while developing this method. We want to thank Heng Zuo at MIT for giving us access to the translation stage used. This work was funded by NASA grant 80NSSC20K0907.

REFERENCES

[1] G. Vacanti, N. M. Barrière, M. J. Collon, E. Hauser, L. Babić, A. Bayerle, D. Girou, R. Günther, L. Keek, B. Landgraf, B. Okma, S. Verhoeckx, M. Vervest, L. Voruz, M. Bavdaz, E. Wille, M. Krumrey, P. Müller, and E. Handick, "X-ray testing of silicon pore optics," in Proc. SPIE 11119, p. 111190I. (2019).

[2] T. T. Saha, K.-W. Chan, J. R. Mazzarella, R. S. McClelland, P. M. Solly, W. W. Zhang, V. Burwitz, G. Hartner, M.-M. L. Caria, and C. Pelliciari, "Analysis of the NGXO telescope x-ray Hartmann data," in Proc. SPIE 10699, p. 1069952 (2018).

[3] J. P. Lehan, T. Hadjimichael, and C. Skocik, "Testing of the mirrors for the Constellation-X spectroscopy x-ray telescope with a refractive null," in Proc. SPIE, Vol. 6688, pp. 668819-668819–8 (2007).

[4] J. P. Lehan, M. Atanossova, K.-W. Chan, T. Hadjimichael, T. T. Saha, M. Hong, W. W.

Zhang, and P. Blake, "Progress toward a complete metrology set for the International X-ray Observatory (IXO) soft x-ray mirrors," in Proc. SPIE, Vol. 7437, pp. 74370R(2009).
[5] Y. Soong, T. Okajima, P. J. Serlemitsos, S. L. Odell, B. D. Ramsey, M. V. Gubarev, M. Ishida, Y. Maeda, R. Iizuka, T. Hayashi, Y. Tawara, A. Furuzawa, H. Mori, T. Miyazawa, H. Kunieda, H. Awaki, S. Sugita, K. Tamura, K. Ishibashi, T. Izumiya, S. Minami, T. Sato, K. Tomikawa, N. Kikuchi, and T. Iwase, "ASTRO-H Soft X-ray Telescope (SXT)," in Proc. SPIE, Vol. 9144, p. 914428 (2014).
[6] H. Li, P. Z. Takacs, and T. Oversluizen, "Vertical scanning long trace profiler: a tool for metrology of x-ray mirrors," in Materials, Manufacturing, and Measurement for Synchrotron Radiation Mirrors (International Society for Optics and Photonics, Vol. 3152, pp. 180–188 (1997).
[7] M. V. Gubarev, T. Kester, and P. Z. Takacs, "Calibration of a vertical-scan long trace profiler at MSFC," in Proc. SPIE, Vol. 4451, pp. 333–340 (2001).
[8] R. Allured et al., “Measuring the performance of adjustable x-ray optics with wavefront sensing,” Proc. SPIE 9144, 91441D (2014).
[9] C. R. Forest, C. R. Canizares, D. R. Neal, M. McGuirk, and M. L. Schattenburg, "Metrology of thin transparent optics using Shack-Hartmann wavefront sensing," Opt. Eng 43(3), 742–753 (2004).
[10] K. Kilaru, B. D. Ramsey, W. H. Baumgartner, S. D. Bongiorno, D. M. Broadway, P. R. Champey, J. M. Davis, S. L. O’Dell, R. F. Elsner, J. A. Gaskin, S. Johnson, J. K. Kolodziejczak, O. J. Roberts, D. A. Swartz, and M. C. Weisskopf, "Full-shell x-ray optics development at NASA Marshall Space Flight Center," J. Astron. Telesc. Instrum. Syst. 5(2), (2019).
[11] Gaskin, J. A. et al., “Lynx X-Ray Observatory: an overview,” J. of Astronomical Telescopes, Instruments, and Systems. 5(2), (2019).
[12] W. W. Zhang, K. D. Allgood, M. Biskach, K.-W. Chan, M. Hlinka, J. D. Kearney, J. R. Mazzarella, R. S. McClelland, A. Numata, R. E. Riveros, T. T. Saha, and P. M. Solly, "High-resolution, lightweight, and low-cost x-ray optics for the Lynx observatory," J. Astron. Telesc. Instrum. Syst. 5(2), 021012 (2019).
[13] G. Schulz and J. Schwider, “IV Interferometric Testing of Smooth Surfaces,” Progress in Optics 13, 118-140 (1976)
[14] U. Griesmann, “Three-flat test solutions based on simple mirror symmetry,” Appl. Opt. 45(23), 5856-5865 (2006)
[15] D. Su, E. Miao, Y. Sui, and H. Yang, "Absolute surface figure testing by shift-rotation method using Zernike polynomials," Opt. Lett. 37, 3198-3200 (2012)
[16] W. Song, F. Wu, X. Hou et al. “Absolute calibration of a spherical reference surface for a Fizeau interferometer with the shift-rotation method of iterative algorithm,” Opt. Eng. 52(3), (2013).
[17] L. P. VanSpeybroeck, and R. C. Chase, "Design Parameters of Paraboloid-Hyperboloid Telescopes for X-ray Astronomy," Appl. Opt. 11, 440-445 (1972).
[18] Y. Huang, J. Ma, C. Yuan, C. Pruss, W. Sun, M. Liu, R. Zhu, Z. Gao, and W. Osten, "Absolute test for cylindrical surfaces using the conjugate differential method," OE 55, 114104 (2016).
[19] E. E. Bloemhof, “Absolute surface metrology by differencing spatially shifted maps from a phase-shifting interferometer,” Opt. Lett. 35(14), 2346-2348 (2010).
[20] E. E. Bloemhof, “Absolute surface metrology with a phase-shifting interferometer for incommensurate transverse spatial shifts,” Opt. Lett. 53(5), 792-797 (2014).
[21] C. Elster, I. Weingärtner, and M. Schulz, "Coupled distance sensor systems for high-accuracy topography measurement: Accounting for scanning stage and systematic sensor errors," Precision Engineering 30, 32–38 (2006).

A PILOT STUDY ON UNCERTAINTY ANALYSIS FOR STEREO-VISION PHOTOGRAMMETRY

Ren Lifei[1,3], Cheung Chi Fai[1], Cao Yanlong[2,3], Li Da[1], Yang Jiangxin[2,3], Cao Yanpeng[2,3]

[1] State Key Laboratory of Ultra-precision Machining Technology, Department of Industrial and Systems Engineering, The Hong Kong Polytechnic University, Hung Hom, Kowloon, Hong Kong, China

[2] State Key Laboratory of Fluid Power and Mechatronic Systems, School of Mechanical Engineering, Zhejiang University, Hangzhou, China

[3] Key Laboratory of Advanced Manufacturing Technology of Zhejiang Province, School of Mechanical Engineering, Zhejiang University, Hangzhou, China

INTRODUCTION

Stereo-vision photogrammetry is a passive 3D measuring technology using triangulation of corresponding feature points in binocular images, which is widely used in manufacturing [1], robotics [2] and biological engineering [3] because of its advantage of high efficiency, simple structure and low cost. In addition, fringe projection profilometry [4] can also be regarded as a modification of stereo-vision photogrammetry in which the projector can be seen as an inverse camera. However, the complex and nonlinear process of stereo-vision photogrammetry and the triangulation of common feature points in binocular images make it difficult to determine the propagation of errors through the system.

This paper presents an evaluation method based on Monte Carlo method to estimate the discrete spatial errors of target points measured by stereo vision. The influence on the measurement uncertainty induced by the spatial resolution limits of two cameras are investigated. The distribution in 3D measuring volume and the influence of base length and focal length is also analyzed for stereo vision.

The remaining of the paper is organized as follows. Section 2 describe the process of uncertainty evaluation methods based on Monte Carlo method for computing the error propagation in the triangulation of corresponding feature points in binocular images. In Section 3, some simulation tests are conducted, proving the availability of the uncertainty evaluation method. Moreover, the distribution of the uncertainty induced by baseline length and focal length is analyzed.

METHODS

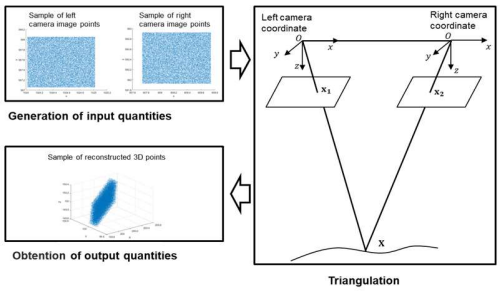
Sample of left camera image points
Sample of right camera image points
Generation of input quantities
Sample of reconstructed 3D points
Obtention of output quantities
Left camera coordinate
Right camera coordinate
Triangulation

Figure 1 Framework of measurement uncertainty evaluation

Figure 1 shows the framework of the measurement uncertainty evaluation. Firstly, the samples of two camera image points are generated according to distribution induced by different types of error sources, then the 3D reconstructed points are computed with triangulation method. The uncertainty of the measured points can be estimated through the statistical parameter of the reconstructed 3D points.

1). Triangulation in stereo-vision photogrammetry

In stereo-vision photogrammetry, a 3D point denoted by $\mathbf{X} = [X \quad Y \quad Z]^T$ is captured by two cameras on 2D point denoted by $\mathbf{x_1} = [u_1 \quad v_1]^T$ and $\mathbf{x_2} = [u_2 \quad v_2]^T$ respectively. $\tilde{\mathbf{x}}$ is used to represents the augmented vector by adding 1 as the last element: $\tilde{\mathbf{X}} = [X \quad Y \quad Z \quad 1]^T$, $\tilde{\mathbf{x_1}} = [u_1 \quad v_1 \quad 1]^T$ and $\tilde{\mathbf{x_2}} = [u_2 \quad v_2 \quad 1]^T$. The relationship between the 3D point $\mathbf{X}$ and its image projection on two cameras $\mathbf{x_1}$ and $\mathbf{x_2}$ is given by

$$s_1\tilde{\mathbf{x_1}} = \boldsymbol{A_1}[\boldsymbol{R_1} \quad \boldsymbol{t_1}]\tilde{\boldsymbol{X}} \tag{1}$$

$$s_2\tilde{\mathbf{x_2}} = \boldsymbol{A_2}[\boldsymbol{R_2} \quad \boldsymbol{t_2}]\tilde{\boldsymbol{X}} \tag{2}$$

where s_1 and s_2 are arbitrary scale factors, $(\mathbf{R_1}, \mathbf{t_1})$ and $(\mathbf{R_2}, \mathbf{t_2})$ are extrinsic parameters, which indicate the rotation and translation from the world coordinate system to the two camera coordinate systems, respectively. Specially, when one of the camera coordinates systems is assigned to be coincided with the world coordinate system, $\mathbf{R_1}$ is 3×3 identity matrix, $\mathbf{t_1}$ is zero vector and $(\mathbf{R_2}, \mathbf{t_2})$ is the rotation and translation between the two camera coordinate systems. $\mathbf{A_1}$ and $\mathbf{A_2}$ are given by

$$\mathbf{A_1} = \begin{bmatrix} \alpha_1 & \gamma_1 & u_{01} \\ 0 & \beta_1 & v_{01} \\ 0 & 0 & 1 \end{bmatrix} \tag{3}$$

$$\mathbf{A_2} = \begin{bmatrix} \alpha_2 & \gamma_2 & u_{02} \\ 0 & \beta_2 & v_{02} \\ 0 & 0 & 1 \end{bmatrix} \tag{4}$$

where u_{01} and u_{02} is the coordinates of the principal points. α_1, α_2 and β_1, β_2 are the scale factors in image u and v axes. γ_1 and γ_2 is the skewness of the two image axes.

Let

$$\mathbf{P_1} = \boldsymbol{A_1}[\boldsymbol{R_1} \quad \boldsymbol{t_1}] \tag{5}$$

$$\mathbf{P_2} = \boldsymbol{A_2}[\boldsymbol{R_2} \quad \boldsymbol{t_2}] \tag{6}$$

$\mathbf{P_1}$ and $\mathbf{P_2}$ are called camera matrix.

$$\mathbf{P_1} = [\mathbf{p_{11}} \quad \mathbf{p_{12}} \quad \mathbf{p_{13}}]^T \tag{7}$$

$$\mathbf{P_2} = [\mathbf{p_{21}} \quad \mathbf{p_{22}} \quad \mathbf{p_{23}}]^T \tag{8}$$

Then

$$s_1\begin{bmatrix} u_1 \\ v_1 \\ 1 \end{bmatrix} = \begin{bmatrix} \mathbf{p_{11}} \\ \mathbf{p_{12}} \\ \mathbf{p_{13}} \end{bmatrix}\begin{bmatrix} X \\ Y \\ Z \\ 1 \end{bmatrix} \tag{9}$$

$$s_2\begin{bmatrix} u_2 \\ v_2 \\ 1 \end{bmatrix} = \begin{bmatrix} \mathbf{p_{21}} \\ \mathbf{p_{22}} \\ \mathbf{p_{23}} \end{bmatrix}\begin{bmatrix} X \\ Y \\ Z \\ 1 \end{bmatrix} \tag{10}$$

Then the following equation can be obtained.

$$\begin{bmatrix} \mathbf{p_{11}} - u_1\mathbf{p_{13}} \\ \mathbf{p_{12}} - v_1\mathbf{p_{13}} \\ \mathbf{p_{21}} - u_2\mathbf{p_{23}} \\ \mathbf{p_{22}} - v_2\mathbf{p_{23}} \end{bmatrix}\begin{bmatrix} X \\ Y \\ Z \\ 1 \end{bmatrix} = \begin{bmatrix} 0 \\ 0 \\ 0 \\ 0 \end{bmatrix} \tag{11}$$

The homogeneous coordinate of the 3D point can be computed as the least square solution using singular value decomposition [5].

2) Consideration of lens distortion

Due to the optical effects of the lenses and misalignment of the optical components [6], the radial and tangential distortion can change the direction of incoming light. The projection of a point in camera coordinate $\mathbf{X}_c = (x_c, y_c, z_c)^T$ at the normalized plane is

$$\begin{pmatrix} x_n \\ y_n \end{pmatrix} = \begin{pmatrix} x_c/z_c \\ y_c/z_c \end{pmatrix} \tag{12}$$

The radical distortion $\boldsymbol{\delta}_\mathbf{r}$ can be written as

$$\boldsymbol{\delta}_\mathbf{r} = \begin{pmatrix} k_1 r_n^2 + k_2 r_n^4 + k_3 r_n^6 \\ k_1 r_n^2 + k_2 r_n^4 + k_3 r_n^6 \end{pmatrix}\begin{pmatrix} x_n \\ y_n \end{pmatrix} \tag{13}$$

where $r_n = \sqrt{x_n^2 + y_n^2}$.

The tangential distortion $\boldsymbol{\delta}_\mathbf{t}$ can be written as

$$\boldsymbol{\delta}_\mathbf{t} = \begin{pmatrix} 2k_4 x_n y_n + k_5(2x_n^2 + r_n^2) \\ k_4(2y_n^2 + r_n^2) + 2k_5 x_n y_n \end{pmatrix} \tag{14}$$

Then the normalized point can be represented as

$$\mathbf{x}_{dn} = \begin{pmatrix} x_{dn} \\ y_{dn} \end{pmatrix} = \begin{pmatrix} x_n \\ y_n \end{pmatrix} + \boldsymbol{\delta}_\mathbf{r} + \boldsymbol{\delta}_\mathbf{t} \tag{15}$$

When two corresponding 2D points of two cameras are obtained. Firstly, the images of the two cameras

are needed to be undistorted according to Eq.(12)-Eq.(15) and then the 3D points are reconstructed according to Eq.(1)-Eq.(11).

3) *Uncertainty evaluation based on Monte Carlo method*

The reconstructed 3D points are determined by the 2D points on two cameras, the intrinsic parameters of two cameras, the distortion of two camera lens and the rotation and translation matrix between two cameras. Any error of these factors can induce the error of the reconstructed 3D points. In this case, to analyse the reconstructed error of the quantization error of the pixel coordinate, the camera intrinsic parameters, distortion of the camera lens and the rotation and translation matrix between two camera coordinates are assumed to be ideal and then the 2D points of two cameras $\mathbf{x_1} = (u_1 \quad v_1)$ and $\mathbf{x_2} = (u_2 \quad v_2)$ can be regarded to be random variables uniformly distributed in a certain interval.

$$\begin{aligned} u_1 &\sim U(a_1, a_1 + \delta) \\ v_1 &\sim U(b_1, b_1 + \delta) \\ u_2 &\sim U(a_2, a_2 + \delta) \\ v_2 &\sim U(b_2, b_2 + \delta) \end{aligned} \tag{16}$$

Then the reconstructed 3D points $\mathbf{X}$ can be regarded as random variable determined by the distribution of $\mathbf{x_1}$ and $\mathbf{x_2}$.

$$\mathbf{X} = \mathbf{f}(\mathbf{x_1}, \mathbf{x_2}) \tag{17}$$

The distribution of $\mathbf{X}$ can be computed by Monte-Carlo simulation: A large amount of the samples of 2D points on two cameras $\mathbf{x_1}$ and $\mathbf{x_2}$ are generated according to the assigned random distribution and then the corresponding samples of reconstructed 3D point $\mathbf{X}$ can be obtained and then the distribution of the reconstructed 3D points can be obtained. The samples of reconstructed 3D points are noted as $\{\mathbf{X}_i | i = 1,2, \dots, N\}$. Then the mean and covariance matrix of reconstructed 3D points can be determined by the following equation.

$$\overline{\mathbf{X}} = \frac{1}{N}\sum_{i=1}^{N} \mathbf{X}_i \tag{18}$$

$$cov(\mathbf{X}) = \frac{1}{N}\sum_{i=1}^{N} (\mathbf{X_i} - \overline{\mathbf{X}})(\mathbf{X_i} - \overline{\mathbf{X}})^T \tag{19}$$

The standard uncertainty of the reconstructed points can be expressed by the standard deviation and the end points that covers a chosen probability p.

TESTS AND RESULTS

TABLE 1. The parameters of the configuration of stereo-vision photogrammetry

Category	Primitive parameter	Value
Left Camera	f_x / (pixel)	530.3463
	f_y / (pixel)	528.7529
	u_0 / (pixel)	316.8934
	v_0 / (pixel)	234.5535
Right Camera	f_x / (pixel)	529.4051
	f_y / (pixel)	527.0524
	u_0 / (pixel)	325.7300
	v_0 / (pixel)	237.7642
Rotation	x / (rad)	-0.0045
	y / (rad)	-0.0069
	z / (rad)	-0.0027
Translation	x / (mm)	-121.5110
	y / (mm)	0.0939
	z / (mm)	-0.3216
Resolution of cameras		1280×720

In this test, the parameters of the stereovision photogrammetry are listed in Table 1. The average and covariance of the reconstructed 3D points are estimated by Monte Carlo method. Figure 2 shows the means and covariances of the reconstructed 3D point against different number of samples computed by Monte Carlo methods. As shown in Figure 2, when the number of samples is small, the range of the estimated value shows a large fluctuation. However, the estimated means and

covariance of the reconstructed 3D point tend to reach a stable value when the number of samples is large. This implies that the number of iterations is sufficient to accurately represent the measurement uncertainty for Monte Carlo method. Based on the analysis above, the iteration number is set to 3×10^4 in the following test.

Figure 3(a), Figure 3(b) and Figure 3(c) show the distribution of the uncertainty of measured points along X, Y and Z axis respectively (The chosen probability is 95% and the coverage factor is 2). As shown in Figure 3(a) the uncertainty of x coordinate of reconstructed 3D points along X axis is a V-curve while the uncertainty of y, z coordinate of reconstructed 3D points along X axis is almost the same. The uncertainty distribution along Y axis is similar with the above analysis according to Figure 3(b). As shown in Figure 3(c), the uncertainty of x, y coordinate of reconstructed 3D points increase approximately linearly with the z coordinate and the uncertainty of z coordinate of reconstructed 3D points increases sharply as the z coordinate increases

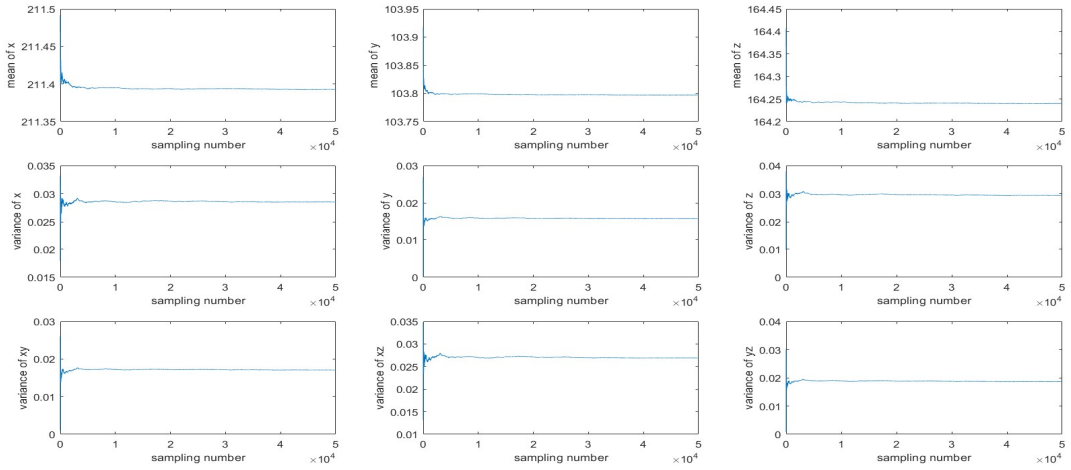

FIGURE 2. Estimated covariance of the coordinate of the reconstructed 3D point

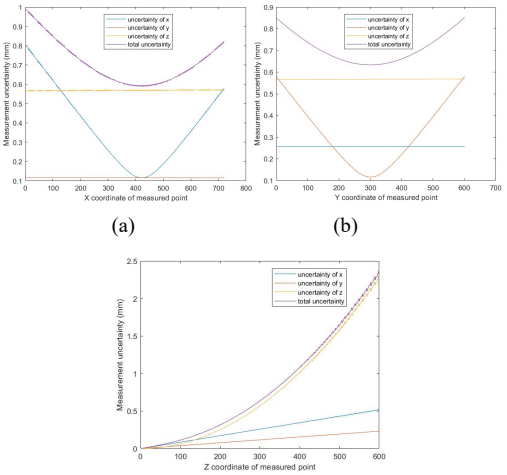

(a) (b)

(c)

FIGURE 3 (a) The distribution of uncertainty along x axis (b) The distribution of uncertainty along y axis (c) The distribution of uncertainty along z axis

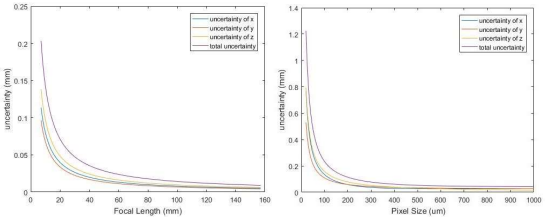

(a) (b)

FIGURE 4 The uncertainty against different of base length and focal length

As shown in Figure 4, the reconstruction error of the 3D point is inversely proportional to the length of base line and focal length.

CONCLUSION

In this paper, the measurement uncertainty of reconstructed 3D points in stereovision photogrammetry is analyzed based on Monte Carlo method. The distribution of uncertainty along X, Y and Z axis is investigated. Additionally, the sensitivity to the length of base line and focal length is also analyzed. In future, a more efficient methods can be explored to evaluate the uncertainty of reconstructed 3D points and measurement strategy can be optimized based on the uncertainty analysis method.

ACKNOWLEDGEMENT

The work described in this paper was supported by a PhD studentship (project account code: RK2W) from The Hong Kong Polytechnic University.

REFRENCES

[1]. Yin ZQ, Xiong J. Stereovision measurement of layer geometry in wire and arc additive manufacturing with various stereo matching algorithms. J Manuf Process. 2020;56:428-38.

[2]. Wang JS, Tao B, Gong ZY, Yu SP, Yin ZP. A Mobile Robotic Measurement System for Large-scale Complex Components Based on Optical Scanning and Visual Tracking. Robotics and Computer-Integrated Manufacturing. 2021;67:9.

[3]. Chiari Y, Wang B, Rushmeier H, Caccone A. Using digital images to reconstruct three-dimensional biological forms: a new tool for morphological studies. Biol J Linn Soc. 2008;95(2):425-36.

[4]. Xu J, Zhang S. Status, challenges, and future perspectives of fringe projection profilometry. Optics and Lasers in Engineering. 2020;135:14.

[5]. Golub GH, Reinsch C. SINGULAR VALUE DECOMPOSITION AND LEAST SQUARES SOLUTIONS. Numer Math. 1970;14(5):403-&.

[6]. Ricolfe-Viala C, Sanchez-Salmeron AJ. Robust metric calibration of non-linear camera lens distortion. Pattern Recognition. 2010;43(4):1688-99.

SINGLE POINT DIAMOND CUTTING OF HIGH-ASPECT RATIO V-GROOVES: ALTERNATIVE FLANK CUTTING STRATEGY AND PRELIMINARY BURR FORMATION ANALYSIS

Otoniel F. Rangel[1], O. Remus Tutunea-Fatan[1], and Evgueni V. Bordatchev[2]
[1]Department of Mechanical and Material Engineering
Western University
London, Ontario, Canada
[2]Automotive and Surface Transportation Research Center
National Research Council of Canada
London, Ontario, Canada

INTRODUCTION

During recent years, micromachining became more and more used in surface functionalization, a process through which surfaces can obtain an augmented functional role [1]. Among the numerous microstructures that can be used for functional enhancements of the surface, V-grooves represent one of the common geometries, primarily due to their versatility. Mechanical, electronic, photonic, biomechanical and optical components [2] could all benefit from the addition of V-grooves on their outer surfaces.

Owed to their practical potential, V-grooves have to be fabricated with an elevated accuracy. This is typically performed by means of rotational or non-rotational cutting tools. Among the rotational methods, fly cutting, milling, and several others are usually regarded as good candidates for V-groove fabrication. Various non-rotational methods were also used for V-groove generation. Nonetheless, this study will focus only on single point cutting (SPC) of V-grooves. Previous studies involving rotational tools suggested that although this manufacturing approach works relatively well for shape accuracy and surface quality, certain issues related to process characteristics might have a significant effect on the geometry of the microstructures to be produced [3]. For instance, although micro-fly cutting, can be used to generate grooves as narrow as 1µm, fabrication of curvilinear V-grooves could be challenging [4]. By contrast, non-rotational cutting methods can be more versatile. For example, SPC enables the generation of microgrooves with broad curvatures [5]. Nevertheless, irrespective of the differences between rotational and non-rotational methods, they can both produce V-groove microstructures with submicron dimensional accuracy as well as surface roughness [5].

On the other hand, although SPC is an effective method for V-groove generation, certain challenges still have to be overcome.

SPC FABRICATION CHALLENGES

Some of the most common V-groove fabrication challenges are related to: presence of burrs, bending/twisting of the riblet solid body, or breakage of the riblet tip. Burrs are a common occurrence in SPC-based operations. Burrs are typically caused by a combination of mechanisms involving the plastic flow of the material that is being removed from the core of the groove. Different manufacturing methods generate burrs of different shapes and geometries while V-grooves are typically characterized by top side burrs, also known as Poisson burrs (Figure 1).

Furthermore, machining parameters such as cutting speed, depth of cut, and cutting area greatly influence the amount of force developed in the cutting process [6]. As such, if cutting forces are not controlled, their excessive magnitude could lead to the bending of the microstructures [7], particularly when fabricating arrays or matrices of V-grooves (Figure 2).

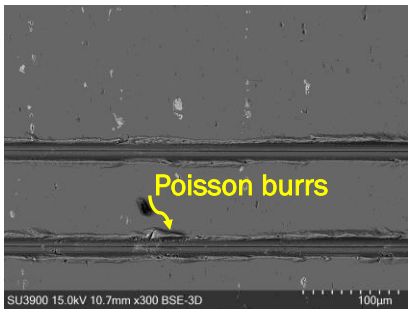

FIGURE 1. Example of Poisson burrs associated with V-groove fabrication.

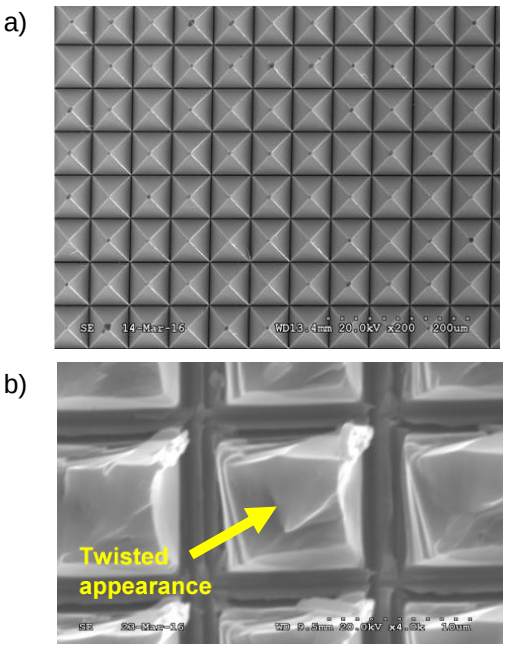

FIGURE 2. V-groove-fabrication: a) array of pyramidal structures, b) V-groove tip bending caused by excessive cutting forces.

Despite the benefits associated with the use of SPC for manufacturing of V-grooves, the associated tool path planning is often limited to strategies that generate the groove from the center of the profile [8-10]. Along these lines, the conventional technique involving V-groove cutting in a single pass enhances the possibility for burrs to form [8]. Single flank V-groove cutting approaches were also demonstrated [11], but their effect on burr formation was not investigated.

To better understand how machining parameters affect burr formation, a novel non-rotational flank cutting strategy will be outlined further. In this new approach, left and right facets of the V-groove will be alternatively and sequentially generated while maintaining a constant uncut chip thickness. Owed to the cutting strategy chosen, the top burr will develop only during the very first pass (and not the subsequent ones) and its quantification will be performed by means of the average burr cross sectional height and burr volume.

ALTERNATING FLANK CUTTING STRATEGY WITH CONSTANT CHIP THICKNESS

Same as in the prior studies, the term "alternating flank cutting" is determined by inherent nature of cutting kinematics [11]. In the current approach, the tool moves not only in the *YZ* plane, but also along the *X*-axis (Figure 3a) when transitioning to a new cut. As such, both cutting edges of the tool are being used alternatively. In all cutting passes, the tool follows a repeated sequence going down-across-up in the *YZ* plane before moving to the next cutting pass. In this strategy, material removal happens when tool travels from P_a to P_b in the negative *Y*-direction (Figure 3b). This is followed by an upward motion that prepares the tool to transition to the next pass, going from P_b' to P_a' (Figure 3a).

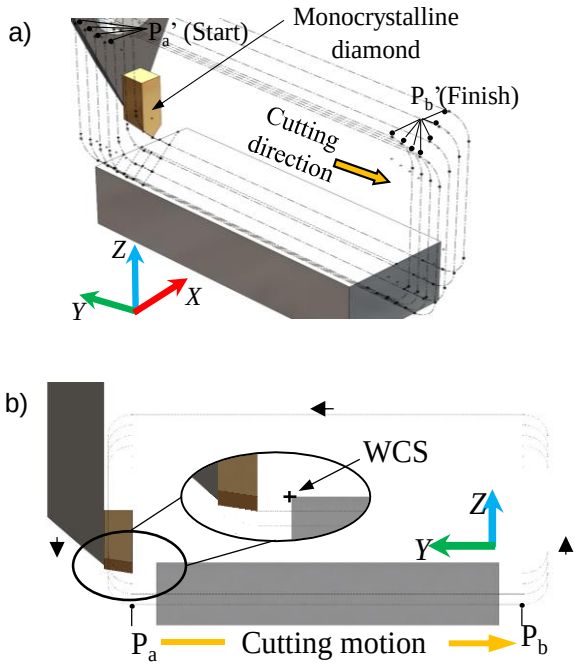

FIGURE 3. Cutting kinematics: a) Isometric view; b) side view along the +X direction.

Furthermore, the tool steps down further at the beginning of the new "across" motion and is always positioned at the bottom of the groove that will be cut (Figure 5), similar to the previously published cutting strategies [6, 11]. As shown in Figure 4, the distance between points P_1 and P_7 is kept constant due the constant uncut chip thickness (δ_{th}) that is in effect for the current cutting strategy. The only exception, however, is the distance from the top of the workpiece to point P_1 that could happen at a thickness that is smaller than δ_{th}. This is typically a consequence of the difficulty to accurately determine the *Z*-height of the tool tip combined with the fact that the development of the cutting kinematics model started from the bottom (and not the top) of the V-groove.

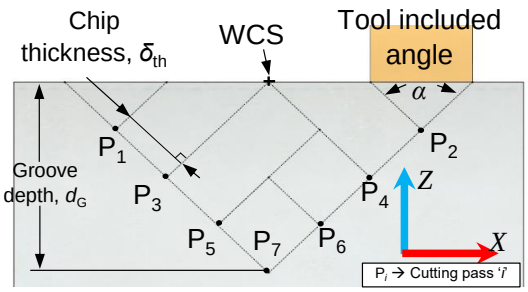

FIGURE 4. Alternating flank cutting: front view along +Y direction.

The first aforementioned factor causes an inherent error on the first pass (P_1 or d_1) across the workpiece and it translates into a small chip thickness. The calculation of this error can be done by first assuming that it is within the range of the constant depth of cut, Δd , then the first cutting pass is $d_1 = \Delta d^{+0.0}_{-\Delta d}$. After the first cutting pass, the cutting depth for subsequent passes becomes $d_n = (d_{n-1} + \Delta d)^{+0.0}_{-\Delta d}$. Based on the error in setting the d_1 value and by assuming that a negligible manufacturing error is associated with the included angle of the tool (α), the error in determination of the cutting area can be assessed as $e_A = A^{+0.0}_{-\Delta d^2}$. The typical geometry of the V-groove for the current cutting strategy is characterized by the total cutting depth (d_G) and the included angle (α) (Figure 5).

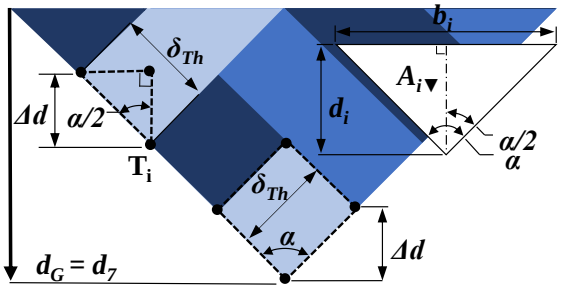

FIGURE 5. Geometric parameters of the V-groove.

Determination of the cutting area (A_i) for each pass across the workpiece is divided in two parts: triangular and rectangular area calculations. Equations 1-4 are formulated based on the characteristic parameters of the V-groove geometry:

$$d_i = \delta_{th} \cos(\alpha / 2) \quad (1)$$

$$b_i = 2 d_i \tan(\alpha / 2) \quad (2)$$

$$A_{i\blacktriangledown} = b_i d_i / 2 = d_i^2 \tan(\alpha / 2) \quad (3)$$

$$A_i = A_{i\blacktriangledown} - A_{(i-1)\blacktriangledown} \quad (4)$$

The combination between the depth of cut (d_i in Eq. 1) and base of the triangle (b_i in Eq. 2) enables determination of the first cutting area (Eq. 3). For the subsequent cuts – depicted by the alternating, blue-toned colours in Figure 6a – the cutting area results from the subtraction of the previous triangles from the current triangles (Eq. 4).

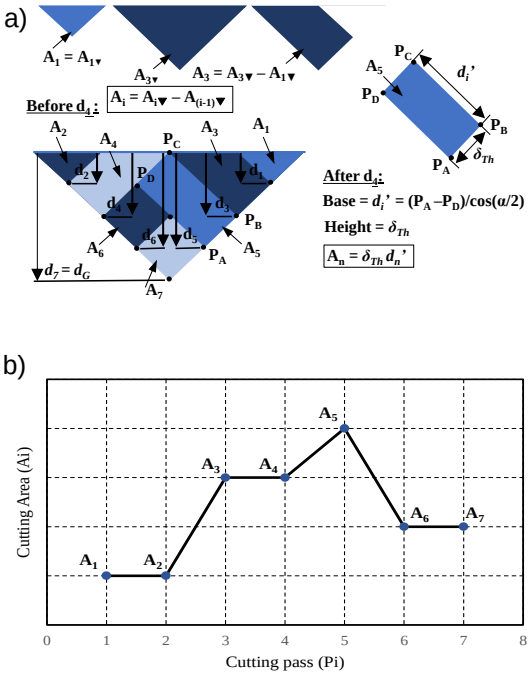

FIGURE 6. Dependence between cutting area and cutting pass: a) geometric representation; b) graphical representation

Point T_i in Figure 6 marks the transition from triangular to rectangular geometrical calculations to proceed as follows:

$$d'_i = (P_A - P_D) / \cos(\alpha / 2) \quad (5)$$

$$A'_n = d'_n \delta_{Th} \quad (6)$$

To simplify the calculation of the rectangular areas, all 4 points of each rectangle are first calculated by means of trigonometry (P_A, P_B, P_C, and P_D in Figure 6a) and after that, the base and height of each rectangle are determined. In these relations, d'_i corresponds to the length of each rectangle (Eq. 5). Since the base of the rectangle is represented by the uncut chip thickness, the corresponding area can be found by means of Eq. 6. The trend shown in Figure 6b can be explained through the fact that triangular cutting areas are perfectly duplicated until they transition into the rectangular ones. Of note, the cutting pass after the transition usually represents the largest cutting area in the process.

DETERMINATION OF THE BURR VOLUME

As previously mentioned, burrs represent an important challenge in SPC. Poisson burrs are usually a consequence of the plastic deformation that occurs during chip formation and separation. As such, it is important to limit burr formation rather than to perform deburring in subsequent time-consuming operations. Various past studies [12-14] have analyzed different geometric parameters (burr height, burr root thickness, projection area, etc.) in order to be able to quantify the process of burr formation. Nonetheless, although burr height measurement has been a common practice in the past, the evaluation of the burr volume would provide a more comprehensive characterization of the burr geometry. Figure 7 shows a schematic diagram of the 3D geometry of a Poisson burr generated during SPC. According to this approach, the volume of the burr can be obtained via a double integration first over the projected area of the burr onto the *XZ* plane (A_i cross section), followed by another one with respect to the height (*YZ* plane). Moreover, since the burrs form at the top of the V-groove channel, the volume is calculated above the Z-zero level.

EXPERIMENTAL RESULTS

To demonstrate the viability of the proposed V-groove strategy, preliminary experiments were performed to analyze burr height and volume. For this purpose, V-grooves with an included angle of 52.8 degrees were cut on a flat brass sample while cutting speed was varied from 100 to 1700 mm/min and depth of cut ranged from 2 to 25 µm. The cutting tool consists of a monocrystalline diamond insert and triangular holder, similar to the experimental setup presented in [11].

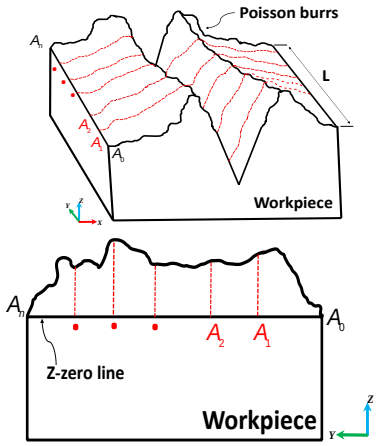

FIGURE 7. Schematic diagram of the 3D configuration of a Poisson burr.

The surface quality of the grooves was then measured with an optical profilometer (WYKO NT1100) with a vertical resolution of 0.1 nm. Following this, the average burr cross-section, height, and volume were determined by means of a custom-written Matlab code. Furthermore, SEM (Hitachi SU3900) images of top burr were also acquired for visual comparison and qualitative analysis.

The method used to assess burr height and volume consists of several sequential steps. More specifically, after raw data was acquired, a tilt removal plane technique was used to level the data (i.e., make it parallel to the horizontal plane). The plane used as a reference for the tilt removal operation was created by linearly interpolating data points from the extreme left and right sides of the overall profile followed by its subtraction from the raw data. Since the Poisson burrs are regarded as top burrs, all points lower than the *Z* zero value were set to zero. Therefore, the mean height of the burr can be calculated by obtaining the mean of all cross-sectional planes A_i in the *XZ* plane (Figure 8). Standard deviation was also calculated along with average surface roughness (R_a) and root mean surface roughness (R_q). A method similar to the one outlined above was used to assess the burr volume. In brief, after raw data was detrended and the negative *Z* height values were disregarded, a numerical double integration was used to determine the burr volume. The integration procedure started by first integrating all points in the *XZ* plane in order to obtain the areas of each planar cross-section. Next, these planar areas were integrated along the length of the V-groove (*YZ* plane).

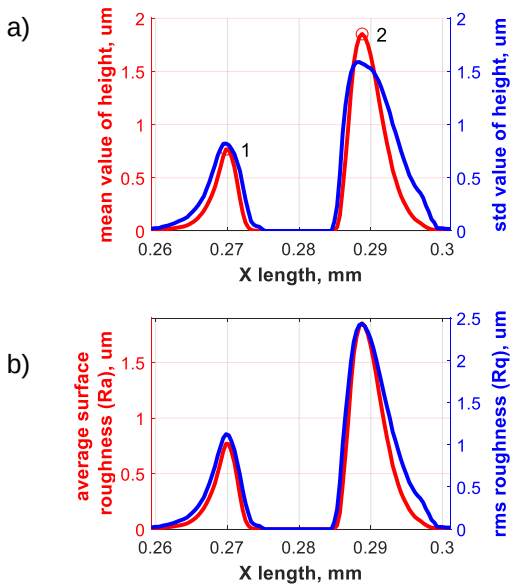

FIGURE 8. Burr characteristics for a depth of cut of 10 µm: a) mean profile height, b) roughness values.

Figure 9 shows preliminary results for burr height and volume. As previously mentioned, depths of cut ranging from 2 to 25 µm were employed in this experiment. Nonetheless, only 2 and 25 µm depths will be presented herein. Evidently, as the depth of cut increases, burr volume also increases. However, the dependence of burr volume on feed rate is not as strong as compared to the depth of cut. Burr heights (left and right) show a similar trend.

The left burr height plot exhibits a pattern of variation similar to the volume. However, this does not seem to be the case for the right burr that seems to have a looser correlation with the volume. While the actual reason for this discrepancy is unknown at this time, it could be speculated that it might be related to different tool edge conditions and/or material properties. Furthermore, the right burr seems to be consistently of a larger height and volume with respect to its left counterpart. It is very possible that this is a consequence of a tool that was misaligned with respect to the actual feed direction. This misalignment will inevitably lead to unequal burr volumes on the two sides of the tool. Consequently, it becomes apparent that the quantification of the burr volume is capable to provide insight on the cutting process that is superior to the one derived from burr height solely.

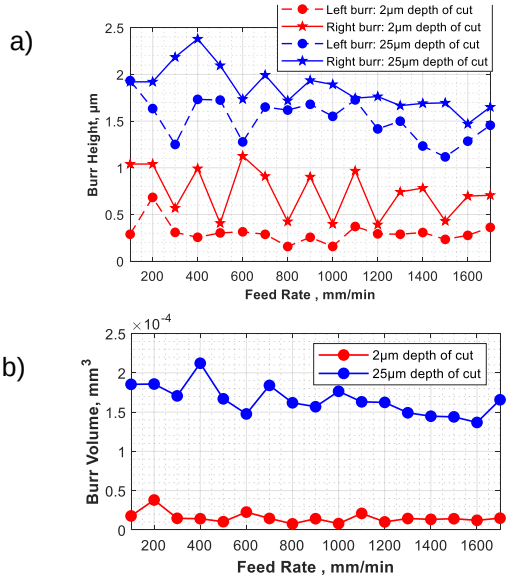
a)
Left burr: 2µm depth of cut
Right burr: 2µm depth of cut
Left burr: 25µm depth of cut
Right burr: 25µm depth of cut
Burr Height, µm
Feed Rate , mm/min
b)
Burr Volume, mm3
2µm depth of cut
25µm depth of cut
Feed Rate , mm/min

FIGURE 9. Burr characteristics: a) height measurements, b) volume measurements.

For further qualitative comparisons of the burrs, SEM was used (Figure 10).

From the SEM pictures, it is evident that as the feed rate increases, not much change happens regarding the configuration of the burr. For the case of 2µm, for example, the amount of burrs formed on the side of the V-grooves is virtually similar. Furthermore, the same happens with the other depths of cut. Thus, supporting the fact that the influence of the feed rate on the formation of burrs is not as strong. On the contrary, as the pictures are analyzed from left to right and the depth of cut increases, the volume of burrs deposited to the side of the grooves is much larger.

SUMMARY AND CONCLUSION

The preliminary analysis of the top burr demonstrates that the material being removed from the groove during double flank cutting moves concurrently both in longitudinal and transversal directions. This material movement leads to the formation of the chip and side bulge/Poisson burrs, respectively. Moreover, the analysis performed suggests that the depth of cut has a more significant effect on the burr formation than the cutting speed. It is expected that that these results will enable a more in-depth analysis of the mechanics and dynamics associated with single point cutting of high-aspect/high-precision trilateral structures to eventually advance their use in surface functionalization applications.

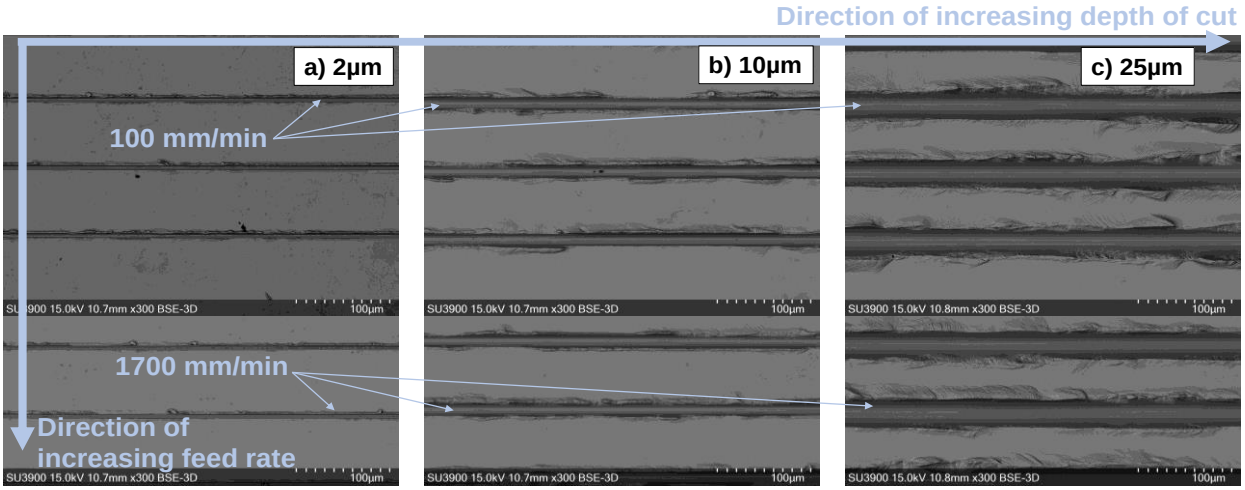

FIGURE 10. SEM pictures of the burrs for different depths of cut: a) 2 µm, b) 10 µm, c) 25 µm.

ACKNOWLEDGEMENTS

The work presented in this study is the result of the collaboration between Western University (London, Ontario) and National Research Council of Canada (London, Ontario). Partial financial support was also provided by Natural Sciences and Engineering Research Council (NSERC) of Canada.

REFERENCES

[1] Byun, D. and H.C. Park. Drag reduction on micro-structured super-hydrophobic surface. in 2006 IEEE International Conference on Robotics and Biomimetics. 2006. IEEE.

[2] Fang, F., et al. Fabrication of micro grooves. in Proceedings for ASPE 18th Annual Meeting, Portland, USA. 2003. Citeseer.

[3] Moriya, T., et al., Creation of V-shaped microgrooves with flat-ends by 6-axis control ultraprecision machining. CIRP annals, 2010. 59(1): p. 61-66.

[4] Bourne, K.A., Development of a high-speed high-precision micro-groove cutting process. 2010: University of Illinois at Urbana-Champaign.

[5] Wang, S., et al., Development of a precision grinding machine system for the fabrication of micro V-grooves array. The International Journal of Advanced Manufacturing Technology, 2018. 97(5-8): p. 2141-2150.

[6] Joao, D., et al., Axial strategy for ultraprecise single point cutting of V-grooves Case 1: constant chip thickness. Procedia Manufacturing, 2019. 34: p. 440-445.

[7] Li, P., et al., Micromilling of thin ribs with high aspect ratios. Journal of Micromechanics and Microengineering, 2010. 20(11): p. 115013.

[8] Peng, Y., T. Jiang, and K. Ehmann, Research on single-point diamond fly-grooving of brittle materials. The International Journal of Advanced Manufacturing Technology, 2014. 75(9-12): p. 1577-1586.

[9] Wang, S., et al., A study of the fabrication of v-groove structure in ultra-precision milling. International Journal of Computer Integrated Manufacturing, 2014. 27(11): p. 986-996.

[10] Yan, J., et al., Fabricating microgrooves with varied cross-sections by electrodischarge machining. The International Journal of Advanced Manufacturing Technology, 2010. 50(9-12): p. 991-1002.

[11] Joao, D., et al., One-Side Cutting Strategy for Ultraprecise Single Point Cutting of V-grooves Case 1: Constant Chip Thickness. IFAC-PapersOnLine, 2019. 52(10): p. 306-310.

[12] Deng, W.J., et al., Study on Burr Formation at the Top Edge in Rectangular Groove Cutting. Advances in Materials Science and Engineering, 2012. 2012: p. 956208.

[13] Medeossi, F., et al., Novel method for burrs quantitative evaluation in micro-milling. Precision Engineering, 2018. 54: p. 379-387.

[14] Qiao, Z., et al., Experimental investigation of the influence of chip interference on burr height in machining micro V-grooves on electroplated copper roll die. 2018. 232(8): p. 1491-1497.

TOOL WEAR EVALUATION USING A CONSTRAINED-MOTION DYNAMOMETER

Michael Gomez[1*] and Tony Schmitz[1,2]
[1]Manufacturing Science Division
Oak Ridge National Laboratory
Oak Ridge, TN, 37830, USA
[2]Department of Mechanical, Aerospace, and Biomedical Engineering
University of Tennessee, Knoxville
Knoxville, TN, 37996, USA

ABSTRACT
This paper describes in-process tool wear evaluation using a constrained-motion cutting force dynamometer (CMD). Tool condition monitoring is traditionally categorized by two approaches: direct and indirect. Direct approaches provide a quantitative wear measurement. Examples of direct measurements include the use of microscopes for visual inspection, laser beams in optical tool setting systems, and electrical resistance in contact tool setting stations. Practical limitations, such as line-of-sight obstruction, coolant interference, and access problems during machining, limit the wide-spread use of these techniques. Alternatively, indirect measurement approaches allow the tool condition to be quantified through auxiliary signals. Examples include acoustic emission, temperature, motor power and current, and cutting force. The benefit of indirect techniques is that they are more suitable for shop-floor implementation because the machining processes can be continuously monitored via sensing devices which quantify the process performance or provide information for process optimization [1].

The focus of this work is force measurement. Initial results are presented which examine the variation in wear features and cutting force as the tool wear progresses from a new tool condition to a significantly worn state.

KEYWORDS
Milling, force, milling, tool wear

INTRODUCTION

The CMD combines a flexure-based constrained-motion mechanism with a low-cost optical displacement sensor, where displacement is inferred from an optical interrupter. In this approach, a knife edge is attached to the movable platform and partially blocks the optical beam during motion caused by the milling force. The displacement is used to calculate force from the known CMD structural dynamics. The result is low-cost, high accuracy dynamic force measurement. This sensor has the added benefit of a compact footprint and fast response time (10 µs) without the need for a supplementary amplifier [2-3]. A primary use of this low-cost technology is to evaluate tool wear during machining operations. The proposed solution is to: 1) select a standard witness sample (such as 6061-T6 aluminum) and mount it to the dynamometer; 2) determine the expected cutting force level for pre-defined axial and radial depths of cut for this sample; 3) periodically perform test cuts on the sample as the tool wears in the work material; and 4) alert the machinist that a tool change is required when the force grows above a pre-selected level.

TOOL WEAR VALIDATION

To demonstrate this concept, preliminary cutting tests were performed on a Haas TM-1 CNC vertical milling machine. An Inconel® 718 AMS 5596 workpiece was mounted in a vise and a CMD was mounted to the table with an Al 6061-T6 witness sample mounted to the moving platform. A single flute, 19.05 mm diameter, endmill was used to perform machining passes at a 1.9 mm radial depth of cut (10% radial

[1] Notice: This manuscript has been authored by UT-Battelle, LLC, under contract DE-AC05-00OR22725 with the US Department of Energy (DOE). The US government retains and the publisher, by accepting the article for publication, acknowledges that the US government retains a nonexclusive, paid-up, irrevocable, worldwide license to publish or reproduce the published form of this manuscript, or allow others to do so, for US government purposes. DOE will provide public access to these results of federally sponsored research in accordance with the DOE Public Access Plan (http://energy.gov/downloads/doe-public-access-plan).

immersion) and 3 mm axial depth of cut at a cutting speed of 50 m/min. The insert was uncoated carbide (Sandvik 390R-070204E-NL H13A). The cutting test cases for the Inconel ® 718 work material is presented in Table 1. In-situ vibration signals were collected using the knife-edge sensor on the CMD and converted to force using the structural deconvolution procedure [2-3]. A pair of optical microscopes (DinoLite Pro-AM4137) were used to record wear features on the rake and flank face of the cutting insert during tool wear testing. The experimental setup is depicted in Fig. 1. An inductive power sensor (Powertek UPC 120V) was used to monitor spindle power consumption during the tool wear tests.

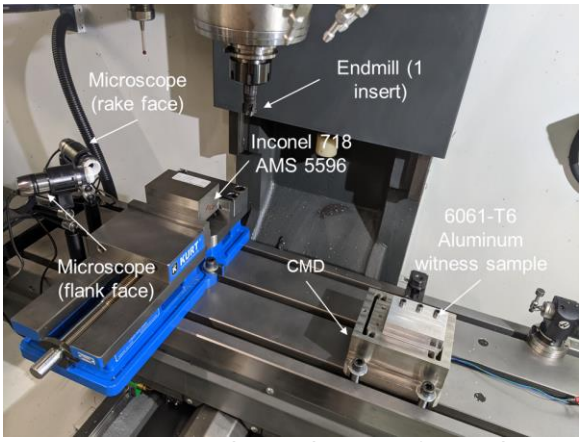

FIGURE 1. Experimental setup for tool wear measurement.

INITIAL RESULTS

To begin, a reference cutting force signal was recorded using the cutting parameters listed in Table 1. In situ vibration signals were collected using the knife-edge sensor on the CMD and subsequently converted to force using a structural deconvolution procedure [2-3]. The corresponding force is plotted in Fig. 2. For this research, the measured milling forces were parsed to capture the steady-state behavior and were then separated into 70 individual tooth impacts and averaged. This provides a compact representation of the cutting force signal over a brief time period.

Table 1. Tool description and cutting parameters for tool wear trials.

Diameter	Teeth	Insert material
19.05 mm	1	Uncoated carbide (Sandvik 390R-070204E-NL H13A)

Cutting parameters for down milling tests	
Spindle speed	835 rpm
Feed per tooth	0.1 mm
Axial depth	3.0 mm
Radial depth	1.9 mm (10% radial immersion)

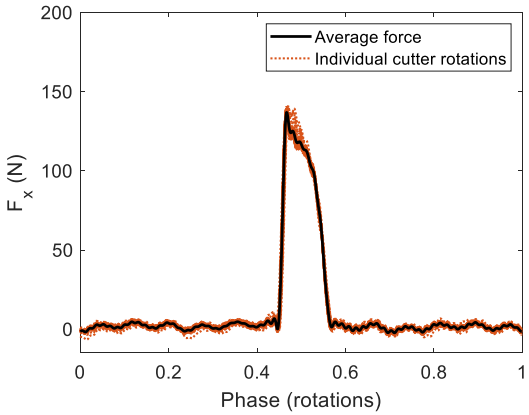

FIGURE 2. Measured cutting forces over 70 revolutions of the cutting tool (dotted red line) and their average (solid black line) for a milling operation using a new cutting insert.

The aluminum witness sample force measurement was followed by a 100 mm test cut on the Inconel® 718 work material. The normalized spindle power consumption for these tests is shown in Fig. 3. Note that there is a significant increase in power consumption between Trials 1 and 2 which is confirmed by the wear transition between the 'New insert' and the 'State 1' wear condition.

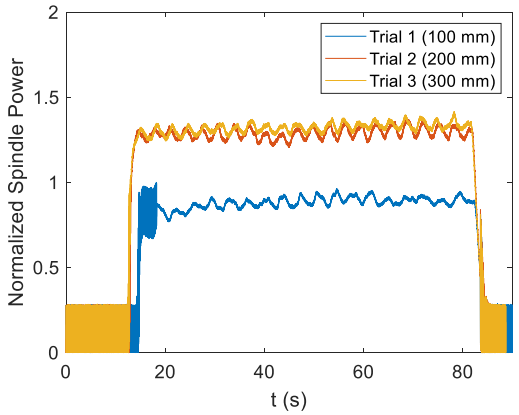

FIGURE 3. Normalized power consumption for the cutting tests in the Inconel ® 718 AMS 5596 work material.

In this research, ‘Trials’ indicate tests performed in the Inconel® 718 work material while ‘States’ indicate the reference tests performed in Al 6061-T6 on the CMD. Following each cutting trial, the tool wear condition was recorded using a pair of optical microscopes. These results are shown in Fig. 4. The maximum flank wear width (FWW) was recorded and as expected, the FWW increased with cutting time.

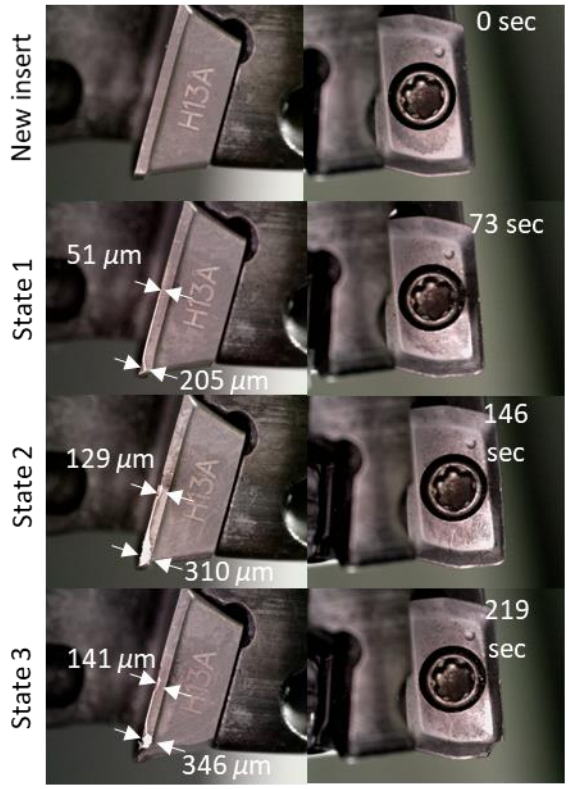

FIGURE 4. Tool wear progression. In the images, the flank face is shown by the left column and the rake face is shown by the right column.

Once the tool wear condition was measured, a cutting test was performed on the Al 6061-T6 witness sample affixed to the CMD. The purpose of these trials was to monitor the growth in cutting force levels as the tool progresses from a new to significantly, and in some cases, catastrophic wear levels. The normalized spindle power for the Al 6061-T6 witness sample is shown in Fig. 5. Traditionally, spindle power measurements are used to classify the tool wear condition. In this case, there is not a clear difference between the nominal reference force measurement (New insert) and subsequent wear states (States 1-3). This is expected since the power consumption required for Al 6061-T6 material removal considerably smaller than for the same cutting parameters in the Inconel® work material.

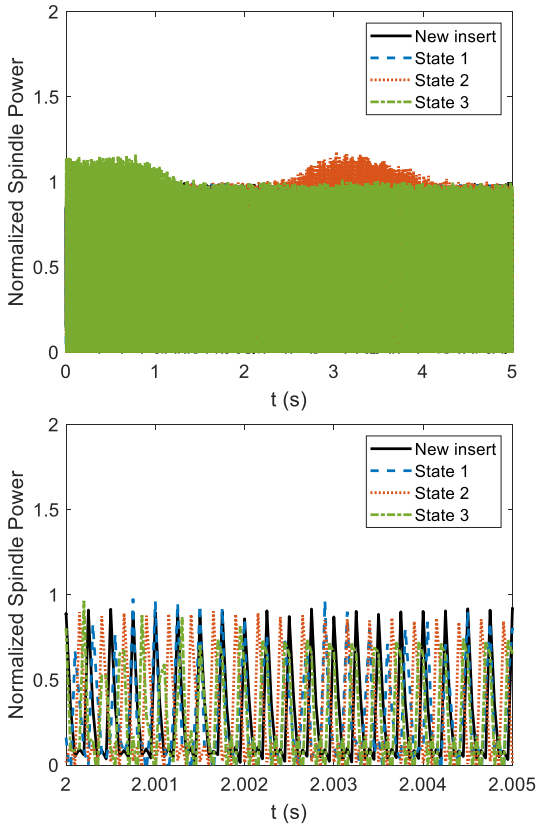

FIGURE 5. Normalized power consumption for the cutting tests on the Al 6061-T6 witness sample work material. These are indicative of the wear states in Fig. 4.

Finally, the averaged CMD cutting forces for unidirectional trials are presented for the various levels of tool wear progression, Fig. 6. Note that the cutting force signature varies depending on the tool wear condition, Fig. 4. In this case, the cutting force signature is slightly increasing with increased tool wear. In many instances, a tool is considered worn once a FWW of 300 μm is achieved. As shown by Figs. 4 and 6. The various ‘States’ demonstrate the subtle variability in cutting forces which are not detectable in the respective spindle power measurements; see Fig. 5.

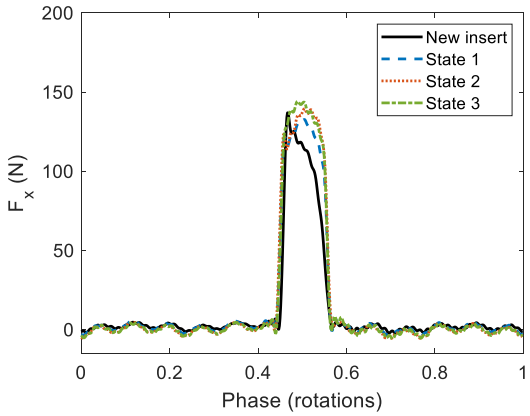

FIGURE 6. Variation in cutting force with tool wear progression in the Al 6061-T6 witness sample work material. The state levels are described by the images in Fig. 4.

FUTURE WORK

Follow-on efforts will focus on performing additional tool wear trials in various work materials including low-carbon steel alloys, titanium alloys, and Inconel® alloys. As noted previously, the research methodology is to: 1) select a standard material sample (such as 6061-T6 aluminum) and mount it to the dynamometer; 2) determine the expected cutting force level for pre-defined axial and radial depths of cut for this sample; 3) periodically perform test cuts on the sample as the tool wears; and 4) alert the machinist that a tool change is required when the force grows above a pre-selected level. The resulting cutting force signals are considered digital signatures which can identify wear features and expected cutting forces in real-time which can reduce the risk of scrapped parts, cyber-intrusion, and operator/programmer error.

ACKNOWLEDGEMENTS

This manuscript has been authored by UT-Battelle, LLC, under contract DE-AC05-00OR22725 with the US Department of Energy (DOE). The US government retains and the publisher, by accepting the article for publication, acknowledges that the US government retains a nonexclusive, paid-up, irrevocable, worldwide license to publish or reproduce the published form of this manuscript, or allow others to do so, for US government purposes. DOE will provide public access to these results of federally sponsored research in accordance with the DOE Public Access Plan (http://energy.gov/downloads/doe-public-access-plan).

REFERENCES

[1] Byrne, G., Dornfeld, D., Inasaki, I., Ketteler, G., König, W., Teti, R., 1995, Tool condition monitoring (TCM) – The status of research and industrial application, CIRP Annals, Vol. 44. Iss. 2: 541-567

[2] Gomez, M. and Schmitz, T., 2020, Low-cost, constrained-motion dynamometer for milling force measurement, Manufacturing Letters, 25: 34-39.

[3] Gomez, M., Honeycutt, A., Schmitz, T., 2021, Hybrid manufactured dynamometer for cutting force measurement, Manufacturing Letters, 29: 65-69.

INTEGRAL BLADE ROTOR MILLING IMPROVEMENT BY PHYSICS-GUIDED MACHINE LEARNING

Gregory Corson[1], Jaydeep Karandikar[2] and Tony Schmitz[1,2]
[1]Mechanical, Aerospace, and Biomedical Engineering
University of Tennessee, Knoxville
Knoxville, TN 37996, USA
[2]Manufacturing Science Division
Oak Ridge National Laboratory
Oak Ridge, TN 37830, USA

INTRODUCTION

In this paper, an integral blade rotor (IBR), or blisk, is used as the test case for the development and implementation of a physics-guided machine learning (PGML) framework for milling performance improvement. The project is motivated by the importance and inherent challenges of the computer-numerically controlled (CNC) machining industry. There is significant cost embedded in the starting material, capital resources, and hourly rates, making it essential that parts are not scrapped and the machine/tooling is not damaged. Part production that conform to design drawing specifications in a first-part-correct, high-profit scenario requires that the machining parameters, including depths of cut, spindle speed, and feed rate, as well as the material removal strategy embedded in the computer-aided manufacturing (CAM) toolpath, are optimized.

PGML

The first step of the PGML approach is the selection of: 1) cutting tools applicable to the design geometry; and 2) initial machining parameters provided by tool manufacturer recommendations and common industry handbooks; the latter provides a baseline to benchmark performance improvement. Second, a digital twin of the machining process is defined by physics-based models. This includes measurement of the tool tip frequency response function (FRF) using tap testing, where an instrumented hammer is used to excite the tool tip and the response is measured using a low-mass accelerometer. The cutting force model is selected using the workpiece material and prior experience/literature review. The cutting force model and tool tip dynamics are then used to define stable spindle speed-axial depth of cut combinations that avoid self-excited vibration, or chatter, which results in large cutting forces and poor surface finish [1]. Third, the machining parameters are used to generate toolpaths in HyperMill™, a CAM software. Finally, the Production Module™ software from Third Wave Systems is used to update the feed rates, optimize tool paths, and predict cycle times [2].

Within the PGML framework, the machining stability predictions from the physics-based models are used as training data for a Bayesian machine learning model [3]. The prior (initial beliefs about milling stability) is defined using two approaches: 1) uninformed, where the only information used is the tendency for stability to decrease with increasing axial depth; and 2) informed, where the physics-based models are incorporated in a Monte Carlo simulation to include input uncertainties and define the spindle speed and axial depth-dependent probability of stability.

Given the prior, milling tests are completed to update the probability of stability as a function of spindle speed and axial depth of cut. The frequency content of sound data collected during the milling process is analyzed to label a test as stable (content only at the tooth passing frequency and its multiples), or unstable/chatter (content also present at other frequencies) [1]. The tests are used to update the probability of stability using the Bayesian machine learning method [3]. The updated probability of stability

[2] Notice: This manuscript has been authored by UT-Battelle, LLC, under contract DE-AC05-00OR22725 with the US Department of Energy (DOE). The US government retains and the publisher, by accepting the article for publication, acknowledges that the US government retains a nonexclusive, paid-up, irrevocable, worldwide license to publish or reproduce the published form of this manuscript, or allow others to do so, for US government purposes. DOE will provide public access to these results of federally sponsored research in accordance with the DOE Public Access Plan (http://energy.gov/downloads/doe-public-access-plan).

(which represents new beliefs about stability after several tests) is finally used to select optimal material removal conditions.

EXPERIMENTAL SETUP

For an initial machining trial, a mock IBR geometry was designed with straight blades. This design consisted of three blades that were 2 mm thick and 25.4 mm tall. The material was 6061-T6 aluminum. See Fig. 1.

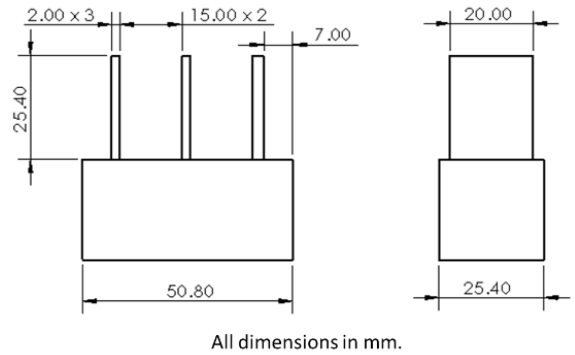

FIGURE 1. Straight blade IBR design.

An endmill was selected and the spindle speed and feed rates for partial radial immersion and slotting conditions were recorded from the tool manufacturer. The recommended feeds and speeds were used as input parameters for part programming. The tool dimensions and recommended machining parameters are provided in Table 1.

TABLE 1. Tool geometry and machining conditions.

Teeth	Corner style	Diameter (mm)	Max axial depth (mm)	Material
3	Square	12.7	25.4	PVD coated carbide
Recommended down milling for 6061-T6 Al				
Condition	Spindle speed (rpm)	Axial depth (mm)	Feed per tooth (mm)	
Slotting	6264 - 24828	6.35	0.102	
Side milling (10% radial immersion)		25.4		

The machining strategy was as follows:

- face the workpiece top;
- profile the width of the blades;
- rough the blades at maximum stable slotting depth;
- finish blades;
- repeat roughing and finishing operations in axial steps (equal to maximum stable slotting depth) down the blade height.

This machining strategy was chosen to retain the blade stiffness. Finishing passes only took place at the current bottom of the blades (stiffest location) as the cycle progressed. Alternatively, roughing the entire height of the blades would have significantly increased the compliance of the blades and, subsequently, the time required for the finishing process. This strategy enabled the stability analysis to consider only the tool dynamics.

Machining trials were completed on a Haas VF-4 three-axis computer numerically controlled (CNC) milling machine. A low-mass accelerometer and instrumented hammer were used to measure the tool tip FRF in both the *x* and *y* machine axes; see Fig. 2. The measured FRF and cutting force model were used to construct a stability map for the selected tool-holder-spindle-machine assembly [1]. This map was used to establish the prior (initial beliefs) for the PGML updating. This was done by assigning uncertainties in the cutting force coefficients and propagating them through the stability model using a Monte Carlo simulation [4].

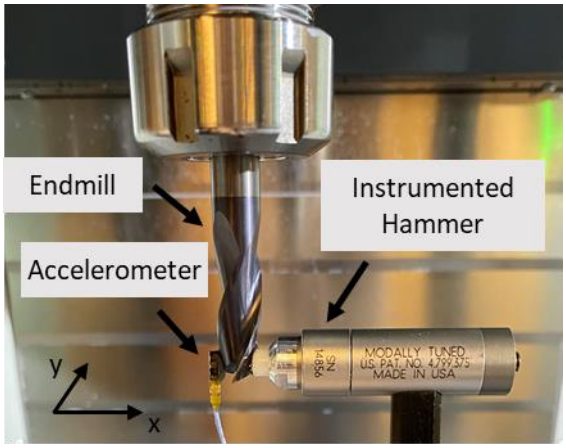

FIGURE 2. Endmill modal tap test.

To update the PGML model, audio content from test cuts was recorded using a Shure SM94 instrument microphone. Best results were

obtained with the microphone located inside the enclosure.

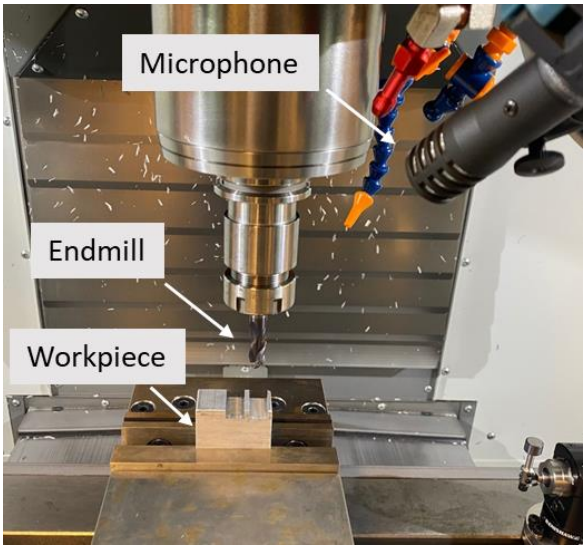

FIGURE 3. Machining audio sampling.

The time domain audio content was converted to the frequency domain using the fast Fourier transform (FFT). Test cuts were performed for slotting and 50% radial immersion (6.35 mm radial depth). The audio signal frequency content and visual inspection of the surface finish were used to determine if the spindle speed-axial depth combination was stable or unstable. For a stable combination, the frequency content occurs at the tooth passing and its multiples. FIGURE 4 shows a comparison of the frequency content for stable, 2.3 mm, and unstable, 3.0 mm, axial depths for slotting passes with a spindle speed of 7310 rpm (365.5 Hz tooth passing frequency).

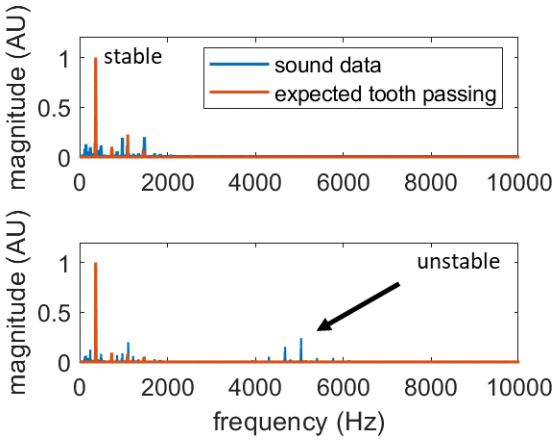

FIGURE 4. Stable (top) and unstable (bottom) frequency domain content for slotting tests.

The results from the trials were used to update the probability of stability using the Bayesian machine learning method. The test parameters were determined using an expected improvement in material removal rate criterion [3]. The tests were terminated when the expected improvement in material removal rate was less than 5%. The details of the Bayesian learning algorithm and test parameter selection are described in [3].

The straight bladed IBR design was used as the initial test case for the PGML framework. The geometry was then updated to include more realistic curved blades; see Fig. 5.

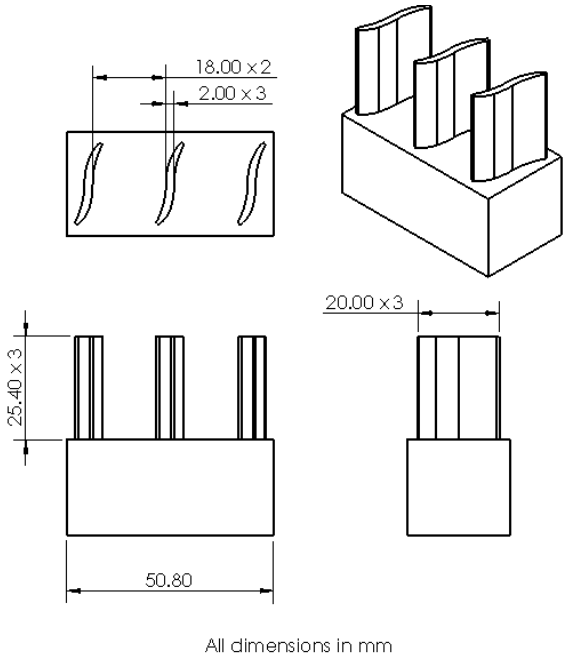

FIGURE 5. Curved blade IBR design.

The fixed-level roughing and finishing strategy previously detailed was adapted for the curved blade design. Videos were recorded for all machining cycles to document time savings seen at the machine and compare to software predictions.

PRODUCTION MODULE

Production Module™ (PM) is a toolpath level analysis and optimization software offered by Third Wave Systems [2]. PM has configurable machine kinematics that refine cycle time predictions as compared to CAM software by including acceleration/deceleration rates for rapid and feed motions. For cycle time reduction and program optimization, gain multipliers were set to increase the calculated mean tangential force on the tool while limiting the maximum in-cut feed

rate and load per unit length (average tangential force divided by tool-workpiece interference length). PM's optimization process overwrites the commanded feed rate in the toolpath program to achieve the scaled tangential force. The optimization values used for both toolpath programs in this study are described in Table 2.

TABLE 2. Production Module optimization multipliers.

Tangential force	1.2
Load per unit length	1.3
Max in-cut feed rate	1.5

The roughing and finishing cycles were separated in PM to accurately scale the mean tangential force for each respective machining operation.

RESULTS AND DISCUSSION

Modal tap testing provided the vibrational response for the tool-holder-spindle-machine assembly used in this study. A stability map was constructed for slotting conditions; see FIGURE 6. Any spindle speed and axial depth combination contained under the solid boundary (in the unshaded region), was expected to be stable. Meanwhile, combinations greater than the boundary were expected to be unstable.

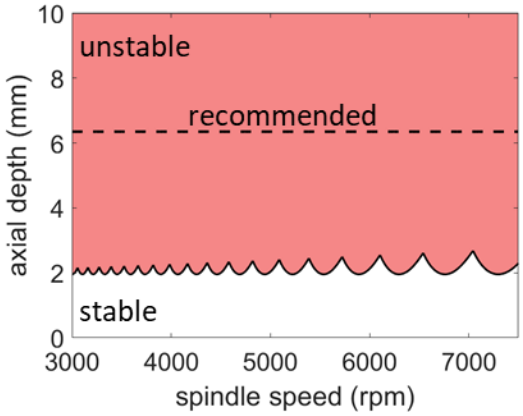

FIGURE 6. Slotting stability map.

The dotted line in Fig. 6 shows the recommended axial depth for slotting provided by the tool manufacturer. The recommended depth was significantly greater than the measured stability limit for the machine's entire spindle speed range. Results for machining tests using the recommended cutting conditions are displayed in Fig. 7.

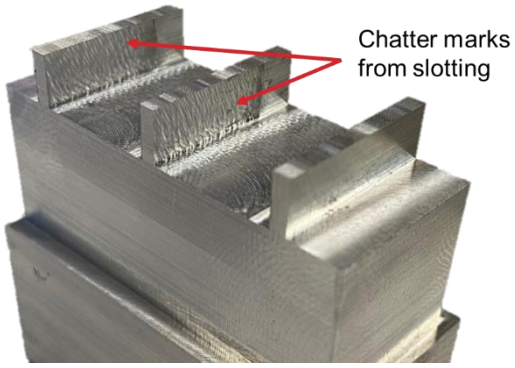

FIGURE 7. *Machining results using manufacturer-recommended parameters.*

FIGURE displays the probabilistic stability diagram for slotting that the PGML framework produced with an uninformed prior. In this case, the tap test and force model data were not used to determine the prior probabilities. The prior probability was assumed to reduce linearly with increasing axial dept. The color gradient represents the probability of stability, with 1.0 (gray) indicating stable and 0.0 (white) indicating unstable parameters. The results of 18 test cuts are included. The predicted stability limit for slotting was identified to be 2.3 mm at 7130 rpm.

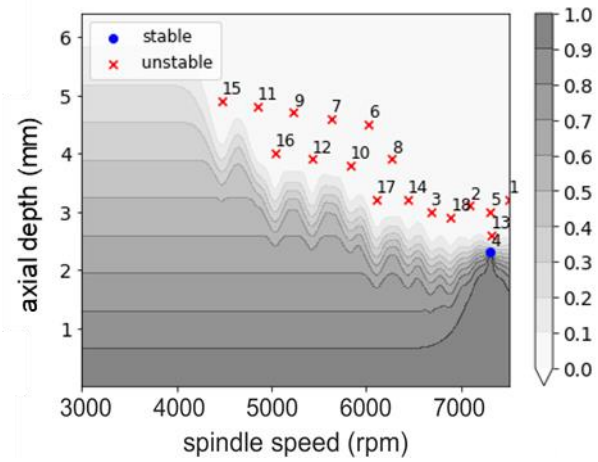

FIGURE 8. Probabilistic stability lobe diagram with uninformed prior.

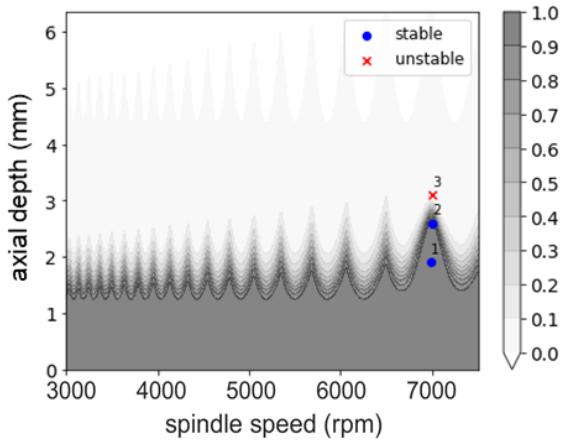

FIGURE 9. Probabilistic stability lobe diagram with informed prior.

FIGURE shows the probabilistic stability limit where an informed prior was implemented. In this case, the tap test FRFs, cutting force model, and corresponding uncertainties were included in a Monte Carlo simulation to establish the probability of stability. For this prior, only three test cuts were required. The maximum stability limit was 2.6 mm at 7000 rpm. The informed prior stability limit was used to program the toolpaths for both the straight and curved blade geometries.

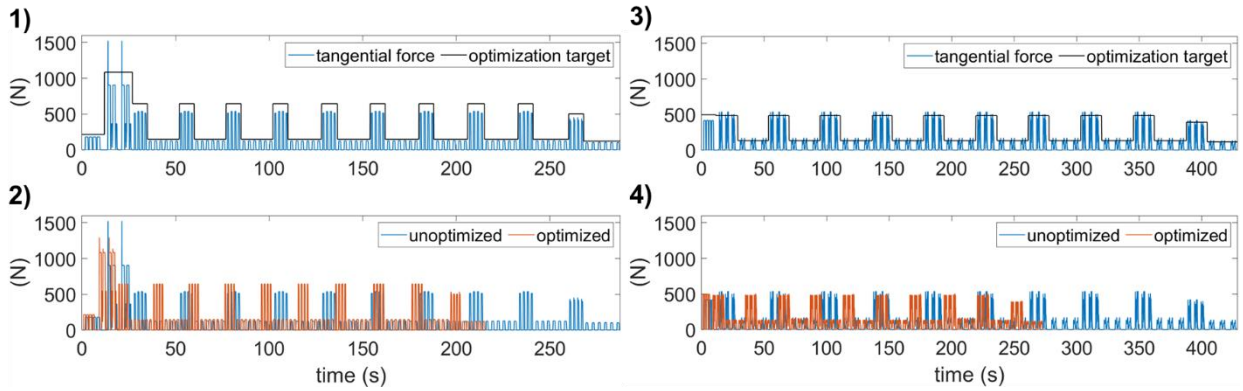

FIGURE 10. Production Module results: 1) force analysis and optimization targets for straight blade program; 2) optimized and unoptimized comparison for straight blade program; 3) force analysis and optimization targets for curved blade program; and 4) optimized and unoptimized comparison for curved blade program.

TABLE 3. Cycle time predictions and recorded improvements for PM toolpath optimization.

Program	Unoptimized		Optimized		Improvement	
	source	time (s)	source	time (s)	(%)	time (s)
Straight blade	hyperMILL	159	hyperMILL	-	-	-
	Production Module	287	Production Module	216	24.7	-71
	actual	304	actual	240	21.1	-64
Curved blade	hyperMILL	350	hyperMILL	-	-	-
	Production Module	429	Production Module	273	36.4	-156
	actual	441	actual	286	35.1	-155

FIGURE 1010 shows the PM force analysis and optimization effort for the straight and curved blade programs. The cycle times for both programs were reduced significantly within PM and as recorded on the machine. The mean tangential force in the straight blade program was nearly constant for the roughing and finishing operations. The optimization process resulted in a consistent increase of the feed rate, and subsequent force, that resulted in the cycle time

reductions listed in TABLE 3TABLE 3. Cycle time predictions and recorded improvements for PM toolpath optimization.

The tangential force in the curved blade program fluctuated much more due to the changing radial engagement and curvature of the design geometry. The feed rate adjustments resulted in a more continuous force profile with maximum values that were less than the peak forces observed in the original toolpath. For both programs, the out-of-cut time was decreased considerably. The in- and out-of-cut optimization of the straight and curved blade programs resulted in cycle time reductions of 21.1% and 35.1%, respectively. The recommended parameters from the tool manufacturer did not provide suitable machining conditions (i.e., chatter occurred) and, therefore, no comparative improvement through the PGML process was available. This shows that accurate recommendations for CAM programming requires knowledge of the tool tip dynamics.

CONCLUSIONS

This paper demonstrated a physics-guided machine learning (PGML) framework for milling performance improvement. The application was integral blade rotor (IBR), or blisk, machining.

The PGML framework provided optimized machining conditions using two scenarios: 1) an uninformed prior, where the only information used was the tendency for stability to decrease with increasing axial depth; and 2) an informed prior, where a physics-based stability model was implemented that used the tool tip FRF and force model together with a Monte Carlo simulation to include input uncertainties and define the spindle speed and axial depth-dependent probability of stability.

Given the prior, milling tests were completed to update the probability of stability as a function of spindle speed and axial depth of cut. The frequency content of sound data was collected during the milling process and analyzed to label a test as stable or unstable/chatter. The tests were used to update the probability of stability using Bayesian machine learning approach. The updated probability of stability (which represents new beliefs about stability after several tests) was finally used to select optimal material removal conditions. It was shown that the machining parameters recommended by the manufacturer did not produce acceptable IBRs (chatter occurred), while the optimized parameters were stable and provided the required surface finish.

Additionally, the toolpaths were optimized using Production Module™ (PM), a toolpath level analysis and optimization software offered by Third Wave Systems. Cycle time reductions of 21.1% and 35.1% were obtained for the two IBR designs (straight and curved blades).

ACKNOWLEDGEMENTS

This research was supported by MxD project number 20-11-04 Physics-Guided Machine Learning (PGML) for CNC Milling. This material is based on research sponsored by Office of the Under Secretary of Defense for Research and Engineering, Strategic Technology Protection and Exploitation, Defense Manufacturing Science and Technology Program under agreement number W15QKN-19-3-0003 between MxD and the Government. The U.S. Government is authorized to reproduce and distribute reprints for Governmental purposes.

REFERENCES

[1] Schmitz, T. and Smith, K.S., 2019, Machining Dynamics: Frequency Response to Improved Productivity, Second Edition, Springer, New York, NY.

[2] https://thirdwavesys.com/machining-modeling/productionmodule/

[3] Karandikar, J., Honeycutt, A., Schmitz, T. and Smith, S., 2020. Stability boundary and optimal operating parameter identification in milling using Bayesian learning. *Journal of Manufacturing Processes*, *56*, pp.1252-1262.

[4] Duncan, G., Schmitz, T.L. and Kurdi, M.H., 2000. Uncertainty propagation for selected analytical milling stability limit analyses. Society of Manufacturing Engineers.

A NEW DIAMOND TURNING MODEL FOR GENERATING SCRATCH-FREE SURFACE WITH AL6061 EMBEDDED WITH HARD PARTICLES

J. Roblee[1] and X. Ding[1]
[1]AMETEK Precitech Inc.
44 Black Brook Rd, Keene, NH 03431

ABSTRACT
In single point diamond turning of Al 6061 T6, cracked particles and scratches were observed on the finished surface as the result of the diamond tool encountering hard and brittle particles embedded in its matrix. A series of machining tests were conducted to study the mechanism of crack generation and propagation within the hard particles and their effects on the finished surface. A new model is developed to explain the effects of critical chip thickness, its location on the chip and scratches on the finished surface of Al 6061 T6. Along the tool-material interface, cracks are initiated and generated within hard particles when the chip thickness approaches a critical value $T_{C,C}$. The debris of the fractured particle can propagate down to the finished surface when the location $D_{T.C}$ of $T_{C,C}$ is reduced to its critical value $D_{T.CS}$. Machining strategies are proposed to control the position of $D_{T.CS}$ and/or its relative position to the depth of cut, *DOC,* to ensure the finished surface is free from scratches. A mathematical model is created to calculate $T_{C,C}$, $D_{T.C}$, for different tool radii, *DOCs* and feeds. The model highlights the role of particle size in the machinability of aluminum.

INTRODUCTION AND OBJECTIVE
Al 6061 T6 is widely used to fabricate high precision optics that require excellent mechanical and thermal stability and optical properties. However, it is a precipitation-hardened alloy with hard and brittle particles embedded in its matrix [1, 2, 3, 4, 5, 6]. The compound of the hard particles has been identified as Fe_3SiAl_{12}, which is hard and brittle [6]. The particles can crack, and the resulting debris can scratch lines into the finished surface during single point diamond turning (SPDT) when the particles are machined in the brittle regime.

Ding et al. [6, 7] and Yan et al. [8] concluded that it was possible to avoid or minimize crack generation within particles embedded in the matrix of Al 6061 T6 [6, 7], or SiC grains in reaction-bonded silicon carbide [8], when the particles/grains along the tool-material interface fall below a critical chip thickness. Below this thickness, the particles are machined in the ductile regime.

In this study, a new machining model is firstly proposed as a hypothesis and then proved by a series of quantitative experiments. Research work was conducted to understand the mechanism of crack generation and propagation within hosting particles and their effects on the finished surface in SPDT Al 6061. This model leads to machining strategies for the diamond turning of Al 6061 so that a scratch-free, finished surface is generated. On the flip side, this work also defines the material properties that will enhance the machinability of new aluminum alloys.

HYPOTHESIS OF A NEW MACHINING MODEL

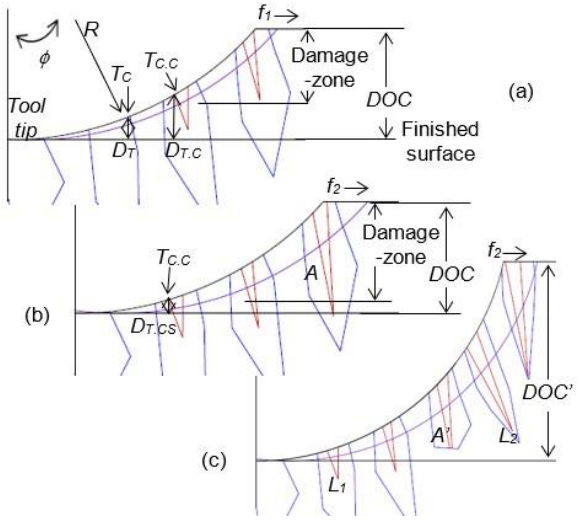

FIGURE 1. Finished surface affected by cracks propagating within embedded particles along the tool-material interface during SPDT. $f_2 > f_1$, $D_{T.C} > D_{T.CS}$, $DOC' > DOC$, $L_2 > L_1$.

A new model is proposed to explain the effects of a critical thickness of the chip $T_{C,C}$ and its location $D_{T.C}$ on the finished surface of Al 6061 by extending the model developed by Blackley and Scattergood [9]. This new model illustrates the basic mechanism of machining a material embedded with hard particles, aids the analysis

of experimental data, and it points to machining strategies for a damage-free diamond turned surface.

Fig. 1 shows the projection of the theoretical chip cross-section in the machining direction during SPDT of a material embedded by hard and brittle particles using a round nose tool. In a real piece of 6061 there is a distribution of particle sizes, but for clarity, we are only showing the larger particles in this figure, and we are showing a higher density of them than reality. The tool nose radius is *R*. The cross feed is *f*, and the depth of cut is *DOC* which can be very large. The maximum value for ϕ is 90°, but with larger radius tools it is usually much smaller than 10°. The chip thickness T_C varies from zero near the tool tip to its maximum at the uncut shoulder. The height at T_C is D_T. Cracks will be initiated within hard particles when T_C approaches its critical value $T_{C.C}$. There will be no, or minor, cracks within the hard particles located at $T_C < T_{C.C}$, and extensive cracks generated and propagated within the hard particles located at $T_C > T_{C.C}$.

The location of $T_{C.C}$ is determined by its height $D_{T.C}$. For a fixed value of $T_{C.C}$, $D_{T.C}$ shifts along the tool-edge as a function of both *f* and *R*. When using a very fine *f*, $T_{C,C}$ and $D_{T.C}$ are close to the uncut shoulder far away from the finished surface. A finished surface free from damage will be generated because any cracked particles will be removed with the chip and have no chance to propagate to the finished surface, as shown in Fig. 1(a). A damage-zone can be found near the uncut shoulder. When increasing *f*, $T_{C,C}$ and $D_{T.C}$ shift down towards the finished surface resulting in a larger damage-zone as shown in Fig. 1(b). When *f* increases to its critical value f_C, scratches are found on the finished surface because the cracks propagate to the finished surface, as denoted by $D_{T.C} = D_{T.CS.}$

Effects of particles size (such as particles hosting cracks A and A') and location (such as particles hosting cracks L_1 *and* L_2) are displayed in Fig. 1(b) and (c). Crack A' cannot propagate to the finished surface because it is limited by the size of its hosting particle. Crack L_2 cannot propagate to the finish surface because of the location of its hosting particle ($L_1<L_2$). The material properties including particle compositions and sizes and precipitate density play an important influence on $D_{T.CS}$. Reduction in the particle size, or increase in the ductility of particles, will reduce the crack propagation length, leading to a larger $D_{T.CS}$.

Several methodologies were employed to prove this Hypothesis:

- To ensure the existence of f_C, scratches were observed on the finished surface when $f \geq f_C$
- To identify $T_{C,C}$, cracks were observed at $T_C \geq T_{C.C}$ when they propagated to the finished surface, $D_{T.C} \geq D_{T.CS}$.
- The new model was used to generate machining strategies that were tried successfully.

Equations 1 and 2 were developed to calculate T_C and D_T from *f, R* and ϕ in Fig. 1.

$$T_C = R + f\ sin\,\phi - \sqrt{R^2 - f^2\ cos^2\,\phi} \quad (\phi \geq 0) \qquad [1]$$

$$D_T = R - (R - T_c)\ cos\ \phi \qquad [2]$$

$T_{C.C}$ can be estimated from experimental data from two pairs of *R* and *f* tests and the application of these equations.

EXPERIMENTAL SETUP AND EXPERIMENTS

SPDT Al 6061 T6 was carried out on a Precitech NanoForm X. SCD tools with nose radii *R* of 3, 500 and 1500 µm were used in the turning tests. All tools had 0° rake angles and 10° clearance angles. All workpieces used in this study were prepared from a single block of material which presented relative even particle distribution and smaller precipitate density and size as compared with many other 6061 alloys on the market.

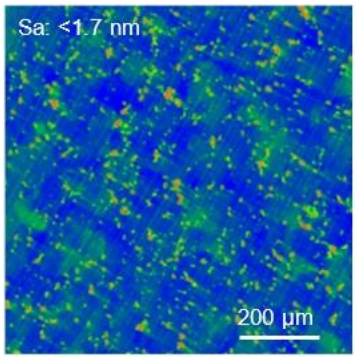

FIGURE 2. Scratch-free diamond shaped surface.

To ensure consistent and accurate results, before each turning test, the sample surface was "shaped" to a surface quality of Sa < 2.5 nm by a carefully diamond turning a flat surface 15 mm in diameter. No scratches were observed by means of a ZYGO optical profiler (ZeGage PROHR). Diamond turned surfaces were also observed with a Field Emission Scanning Electron Microscope (FESEM), and a Keyence VHX digital

Microscope. The precipitate density with particle sizes larger than 0.45 µm was 40~55 particles randomly distributed over a square area of 100 × 100 µm^2, as observed with an FESEM. The largest particle found was around 10 µm in size.

Tests to identify f_C and $T_{C,C}$

TABLE 1. Machining parameters with R = 500 µm and 1500 µm.

Test #	*R* µm	*f* µm/rev	*DOC* µm
T500.1-T500.4	500	4, 7, 9, 11	20
T500.5		12(f_C),	
T500.6		15	
T1500.1-1500.4	1500	9, 10, 11, 12	
1500.5		14(f_C)	
1500.6		20	

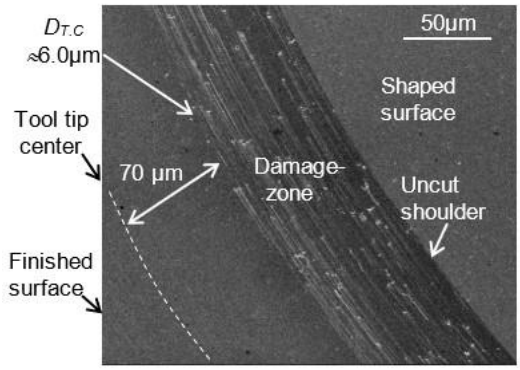

(a). T500.1: f = 4 µm/rev.

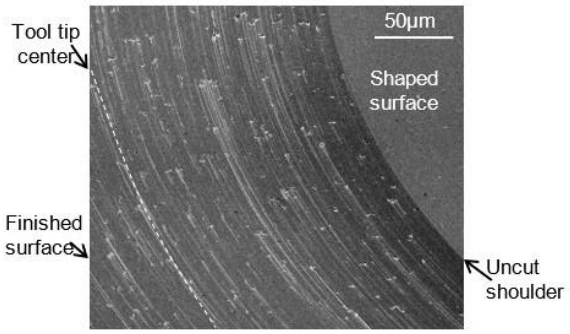

(b). T500.5: f_C = 12 µm/rev.

FIGURE 3. The machined surface near the uncut shoulder at different f. R= 500 µm; DOC= 20 µm.

Table 1 lists machining parameters with tool *R* =500 µm and 1500 µm at *DOC* = 20 µm. With a fine cross feed, such as *f* ≤11 µm/rev with *R* =500 µm and *f* ≤12 µm/rev with *R* =1500 µm, the damage-zone containing cracks and heavy scratches are observed as a narrow zone near the uncut shoulder, as shown in Fig. 3(a) at *f* = 4 µm/rev and *R* = 500 µm. The lower boundary of the damage-zone is about 70 µm away the tool tip. No, or only minor, cracks were observed on the finished surface with *Sa* 1.7 nm, as shown in Fig. 4(a).

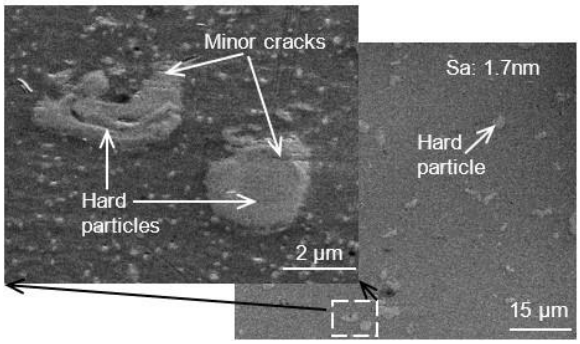

(a). T500.1: f = 4 µm/rev.

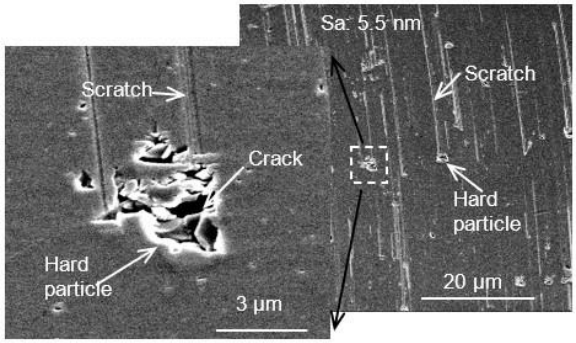

(b). T500.5: f_C = 12 µm/rev.

FIGURE 4. Magnified details of the finished surfaces from FIGURE 3.

When the cross-feed approached and exceeded its critical value, such as *f* ≥ 12 µm/rev with *R* = 500 µm, and *f* ≥ 14 µm/rev with *R* =1500 µm, damage containing cracks and heavy scratches covers the entire machined surface below the uncut shoulder. This is shown in Fig. 3(b). It leads to a rough finished surface with *Sa* 5.5 nm as shown in Fig. 4(b). The damage-zone extended all the way to the finished surface near the tool tip. A larger *R* increases the critical feed, f_C.

The existence of f_C is confirmed as:

- f_C ≈12 µm/rev for *R* =500 µm.
- f_C ≈14 µm/rev for *R* =1500 µm.

When these two pairs of data are used in Eqn.1, the critical chip thickness is determined to be $T_{C,C}$ ≈0.60 µm for the Al 6061 used in this study.

Tests to confirm $T_{C,C}$

As previously described for a given *R*, when $f \geq f_C$, cracks will propagate to the finished surface.

For a *DOC* of 1 µm, the crack propagation lengths will be controlled to ≈1 µm, and $D_{T.CS}$ ≈1 µm. Table 2 shows tests that are designed to determine $D_{T,CS}$ using a tool with R =3 µm and *DOC* =1 µm. Machining results are displayed in Table 2 and Fig. 5. When f ≤0.5 µm, no scratches were found on the finished surface as shown in Fig. 5(a). However, when f approaches 1 µm/rev ≈ f_C, heavy scratches were found on the finished surface as shown in Fig. 5(b). The crack propagation length L ≈$D_{T.CS}$ is ≈1 µm when R =3 µm.

Consequently, $T_{C.C}$ is ≈0.65 µm when Eqns. 1 and 2 are applied. This is very close to the $T_{C.C}$ ≈0.6 µm value obtained in the previous section.

TABLE 2. Tests with R =3 µm.

Test #	R µm	f µm/rev	*DOC* µm	Finished surface	$D_{T.C}$ /$D_{T.CS}$ µm
T3.1	3	0.25	1	No Scratches	>1
T3.2		0.5		No Scratches	>1
T3.3		1 (f_C)		Scratches	1 ($D_{T.CS}$)

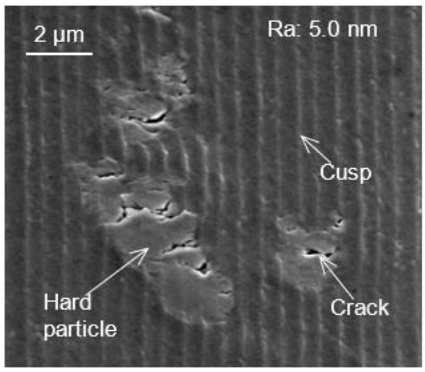

(a) T3.2: f = 0.5 µm/rev.

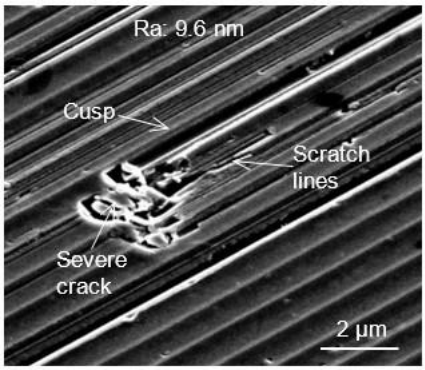

(b) T3.3: f_C = 1 µm/rev.

FIGURE 5. Finished surfaces with R =3 µm and DOC =1 µm.

Confirmation tests of the new model

Referring to Fig. 1(a) and (b) with a fixed R, when *DOC* > $D_{T.CS}$ cracks will extend to the finished surface if $f \geq f_C$, as shown by tests #T500.5, #T500.6, #T1500.5 and #T1500.6. However, when *DOC* < $D_{T.CS}$, at any feed f, no scratches can be observed on the finished surface because cracks within their hosting particles were always at $T_C < T_{C,C}$. Turning tests were carried out to prove this by generating a finished surface free from scratches at $f \geq f_C$ with *DOC* < $D_{T.CS}$. The machining parameters are listed in Table 4. DIFFSYS was used to generate the NC program with a variable f across a distance of 3 mm.

TABLE 4. Tests with R = 500 µm at variable f.

Test #	f µm/rev	*DOC* µm
T500.7	6 - 16	20
T500.8	6 - 16	0.8

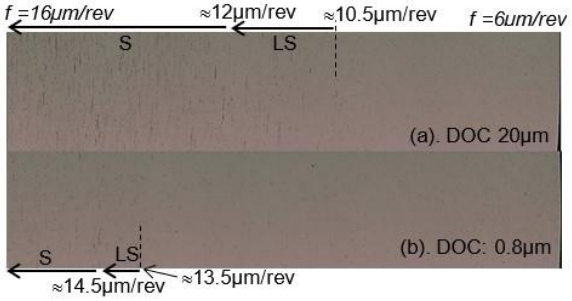

FIGURE 6. Finished surfaces with R = 500 µm at 6 µm/rev ≤ f ≤16 µm/rev. (a). T500.7: DOC = 20 µm and (b). T500.8: DOC = 0.8 µm. LS: Light scratches. S: Massive scratches.

TABLE 5. $D_{T.C}$ when R = 500 µm, DOC = 20 µm.

f µm/rev	6	10.5	12 (f_C)	13.5	14.5	16
$D_{T.C}$ µm*	2.8	1.15	0.97 ($D_{T.CS}$)	0.84	0.79	0.72

*By $T_{C.C}$ = 0.6 µm

Fig. 6 shows the finished surfaces from T500.7 and T500.8 using R = 500 µm and *6 µm/rev ≤ f ≤16 µm/rev* at *DOC* = 20µm (Fig. 6(a)) and *DOC* = 0.8 µm (Fig. 6(b)). Three zones were identified as no-scratch, light scratches, and massive scratches. These results further confirm the proposed new model because:

- No scratches occurred at f < 10.5 µm/rev for both *DOCs* when $f < f_C$.
- Light scratches occurred at 10.5 µm/rev < f < 12 µm/rev when *DOC = 20 µm and w*hen f is near f_C and *DOC* > $D_{T.CS.}$

- Massive scratches at f >12 µm/rev and DOC =*20 µm* when $f > f_C$ at $DOC > D_{T.CS.}$
- No scratches were found at 13.5 µm/rev > f > 10.5 µm/rev at DOC = 0.8 µm when $f > f_C$ and $DOC < D_{T.CS}$ values shown in Table 5.
- Light scratches were observed at 14.5 µm/rev > f >13.5 µm/rev at DOC =0.8 µm and $f > f_C$ because the DOC is near to the $D_{T.CS}$ values shown in Table 5.
- Massive scratches at f ≥ 14.5µm/rev and DOC =*0.8 µm* when $f > f_C$ and $DOC > D_{T.CS}$.

APPLICATION OF THE NEW MODEL

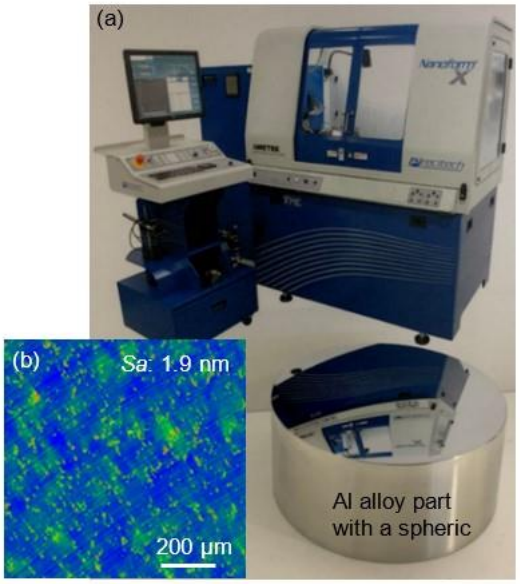

FIGURE 7. Diamond turned Al 6061 T6 part with a spherical profile. (a). Diamond turned optical part with Precitech Nanoform X. (b). Finished surface.

Based on the new machining model, new machining strategies for Al 6061 are proposed:

- A scratch-free, finished surface can be achieved when the $DOC < D_{T.CS}$, at any feed f.
- When the $DOC \geq D_{T.CS}$, no cracks will extend to the finished surface when $D_{T.C}$ can be shifted to the uncut shoulder by $f < f_C$ or increasing radius R.
- The machinability of Al 6061 is increased by reducing the size and brittleness of the embedded particles.

This machining strategy was applied to SPDT of a spherical optical mirror with R = 700 µm, f = 2.5 µm and DOC = 2 µm, as shown in Fig. 7. The part diameter is 76.2 mm with a radius of curvature of 254 mm. No scratches, diffractive color or tool marks could be observed on the diamond turned surface. A form error of 61 nm PV and a surface finish Sa < 2 nm were achieved.

ADDTIONAL DISCUSSION

Fresh cutting edge effects on f_C

Using either R =*500 µm* or R =*1500 µm* and DOC = 20*µm,* scratches could be found over the entire finished surface at any f when the total cutting length was less than 200 m. However, values of f_C≈12 µm/rev with R =*500 µm* and f_C ≈14 µm/rev with R=*1500 µm* were obtained when the total cutting length exceeded 600 m. These results imply that a few rough cuts on a fresh diamond can modify the condition of the cutting edge for a better machining performance. Further studies are being carried out at Precitech to better understand this effect, but we surmise that a very sharp diamond can more readily crack the embedded particles. In this study, all tests were done with total cutting distances between 600 m and 1600 m.

Large particle size effects on f_C and damage-zone width

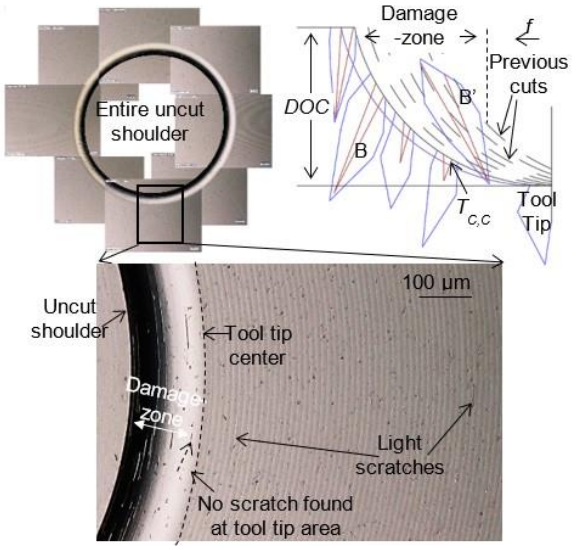

FIGURE 8. The uncut shoulder region at a 2 mm diameter of T500.4, with R =500 µm, DOC =20 µm and f =11 µm/rev. The dashed arrow shows the nearest scratch to the tool tip. Note the multiple encounters that one particle can have with large radii tools.

Very light scratches were randomly found on the whole finished surface when f = 11 µm/rev, R =*500 µm* and DOC =20 µm in Fig. 8. However, no scratch was found near the last location of the tool tip. It is different from results shown in Figs. 3(b) and 5(b) in which the damage-zone

extended to the tool tip. The calculated damage-zone width is around 107 µm by $T_{C.C}$ =0.60 µm and $D_{T.C}$ =1.1 µm. The calculated distance between the lower boundary of damage-zone and the tool tip is around 33 µm. The dashed arrow points to one single scratch located 20 µm away the tool tip which is the shortest distance found on the entire uncut shoulder. It caused a wider damage-zone of 120 µm than the calculated 107 µm. Large particles allow cracks to be generated at $T_C > T_{C.C}$ and propagate to the finished surface ahead of damage-zone, as shown by B in Fig. 8. This will cause light scratches on the finished surface. Light scratches can also occur at $T_C < T_{C.C}$, such as B', causing a larger damage-zone. The value of f_C needs to be more carefully defined to take more effects into consideration, such as fresh edge effects, tool radius, particle size and orientation and measurement methodology to better account for more machining scenarios.

CONCLUSIONS

A machining mechanism was investigated as a basis for a new model that defines machining strategies for the generation of scratch-free, finished surfaces in SPDT Al 6061 T6 that is embedded with hard particles.

- Along the tool-material interface there is a critical chip thickness $T_{C.C}$ beyond which extensive cracks are generated and propagated within hard particles. Its location from the finished surface is $D_{T.C}$.
- As the cross-feed f is increased, $T_{C.C}$ and $D_{T.C}$ shift down towards the finished surface. Cracks at locations where $T_C \geq T_{C.C}$ can propagate to the finished surface when $f \geq f_C$. $D_{T.C} \geq D_{T.CS}$.
- Scratch-free, finished surfaces can be achieved by using a machining depth $DOC < D_{T.CS}$ at any f, and/or locating the critical chip thickness T_C close to the uncut shoulder by $f << f_C$ or increasing the tool radius R.
- A mathematical model was developed to calculate the T_C and D_T for different tool radii, *DOCs* and feeds.
- Large particle sizes allow cracks to be generated at $T_C > T_{C.C}$ and then propagate to the finished surface ahead of the theoretical damage-zone.
- This work provides strategic ideas for the development of new aluminums by modifying material properties such as particle size and density and changing particle shape, orientation and ductility to get better machining performance.
- More work is needed to study the effects of the cutting edge on hard particles, especially for larger radius tools. A more complex definition of f_C and $T_{C.C}$ will likely be necessary to better represent the machining mechanisms over a wider range of machining parameters.

REFERENCES

[1] R. G. Jasinevicius, J. G. Duduch and A. J. V. Porto, Critical Aspects on the behavior of Material from the Mechanical Tool–Workpiece Interaction in Single Point Diamond Turning. In Journal of the Brazilian Society of Mechanical Sciences. 21(3), 509-18, 1999.

[2] M. R. Shankar, S. Chandrasekare, W. D. Compton and A. H. King, Characteristics of aluminum 6061-T6 deformed to large plastic strains by machining. In Materials Science and Engineering A. 410-411, 2005.

[3] S. Ferrasse, V. M. Segal, K. T. Hartwig, and R. E. Goforth, Development of a submicrometer-grained microstructure in Aluminum 6061 using equal channel angular extrusion. In Journal of Materials Research. 12(5), 1253-61, 1997.

[4] X. Liu, R. E. DeVor, S. G. Kapoor, K. F. Ehman, The mechanics of machining at the micro scale: assessment of the current state of the science. In Journal of Manufacturing Science and Engineering. 126, 666-7, 2004.

[5] H. Agarwal, A. M. Gokhale, S. Graham, M. F. Horstemeyer, Void Growth in 6061-aluminum alloy under triaxial Stress State. In Material Science and Engineering A. 341, 35-42, 2003.

[6] X. Ding, L. C. Lee, D. L. Butler and C. K. Cheng, The effects of hard particles on the surface quality when micro-cutting aluminum 6061 T6. In Journal of Micromechanics and Microengineering. 19, 115013-20, 2009.

[7] X. Ding, M. Rahman, A study of the performance of cutting polycrystalline Al 6061 T6 with single crystalline diamond micro-tools. In Precision Engineering. 36(4), 593-603, 2012.

[8] J. W. Yan, Z. Y. Zhang, T. Kuriyagawa, Mechanism for Material Removal in Diamond Turning of Reaction-bonded Silicon Carbide. In International Journal of Machine Tools and Manufacture. 49, 366-374, 2009.

[9] W.S. Blackley and R.O. Scattergood, Ductile-regime machining model for diamond turning of brittle materials, Precision Engineering. 13(2), 95-103, 1991.

DUCTILE CUTTING REGIME IN DIAMOND MILLING OF MONOCRYSTALLINE SILICON

Marvin Groeb[1,2], Matthias Fritz[1], Johann Groeb[3], Wolfgang Ensinger[2]
[1]Kern Microtechnik GmbH
Eschenlohe, Germany
[2]Department of Materials Science
Technical University of Darmstadt
Darmstadt, Germany
[3]Independent Researcher
Darmstadt, Germany

INTRODUCTION

The market for optical elements has been valued at $ 3.6 billion in 2012, and has been forecast to reach $ 12.3 billion by 2019 [1]. Rising requirements to the finished surface inevitable lead to higher part cost, as the required machine tool, tooling and process time increase the overall cost dramatically. Because of the low density, low thermal expansion and relatively low cost, monocrystalline silicon is chosen as a lens material in IR and X-ray applications [2]. Moreover, silicon is one of the building blocks of the current semiconductor technology [3]. The quality control of packaged chips via ultrasonic microscopy requires high quality surface finishes [4], [5]. Currently, high quality finishes are achieved via either chemical-mechanical polishing [6], [7], lapping [8], [9] or diamond turning [10], [2]. Since the late 80s, single point diamond turning (SPDT) uses the phenomena of a brittle to ductile transition [11], [12] to achieve high quality finishes in brittle materials. Unfortunately, SPDT is characterized with low productivity and high part cost, [13] as well as limited shape freedom due to the accessability from the diamond tool. Mirror finish milling with monocrystalline diamond tools has been possible in a number of brittle materials such as Germanium [14], glass [15], but also softer non-ferrous material, for instance aluminium [16]. This paper explores the side as well as face milling in polish quality of monocrystalline silicon with a monocrystalline diamond tool.

METHODOLOGY

The milling experiments were performed on a Kern Micro HD precision CNC machining center. It features microgap hydrostatic guideways, linear motors and glass scales with nanometric resolution, enabling a positional accuracy well below 1 µm. The machine was equipped with an HSK 40 spindle manufactured by Fischer, having a maximum rotational speed of 42000 min^{-1} and a rated power of 15.6 kW. The sample specimen was fixtured by superglueing it to a piece of aluminium (EN AW 5081). The material used is an industry standard semiconductor grade monocrystalline silicon. Roughing and semi finishing was undertaken with PCD endmill (diameter 8 mm) manufactured by Dixi Polytool. The used NC code was written in Heidenhain plain text on the TNC 640 control. A contour smoothing cycle of 0.0005 mm was active during the operation. The coolant used is a GTL oil (Oelheld SintoGrind TC-X 1500). The monocrystalline flat end mill (6 mm diameter) was produced by Contour Fine Diamonds. The tools were held in a Regofix PowRgrip toolholder. Tests were performed in a temperature controlled environment. Before taking a cut, a spindle warm-up period of 2 minutes was completed, to reduce thermal influences. The work piece temperature was further stabilized by application of the tempered flood coolant for 10 minutes before the experiment. Measurements were taken after the sample was cleaned with isopropyl alcohol in an ultrasonic cleaner. The accoustic emission (AE) signal (Marposs AE6000) is recorded via a Picoscope 5244D digital oscilloscope. All quantitative measurements were recorded with a Confovis CLSM, whereas qualitative analysis was done with a Phenom XL scanning electron microscope.

EXPERIMENTS

In order to achieve a stable testing environment, the semiconductor grade silicon sample specimen are prepared identically. For this, the aluminium fixture is machined flat with a generic DLC coated endmill. A level surface with a roughness of R_a 0.1 µm was achieved. After milling, the surface is cleaned with isopropyl alcohol and the sample specimen superglued (Ergo 5210) to the

fixture. During glue hardening, a weight of 100 g was placed on the specimen to ensure contact. The sample specimen is then located via the built-in touch probe (Blum TC52 LF). The MCD flat endmill is measured after chemical cleaning with the equipped BLUM LC50 laser. Runout is verified via the laser to better than 1 µm. To account for unwanted thermal expansion of the spindle, the spindle is warmed up for 5 minutes before measuring.

Design of Experiments

In order to achieve a stable ductile cutting regime, a number of trials were undertaken to better understand and identify the influencing factors. By using a Taguchi-based Design of Experiment, a variety of parameters were analysed in two different experiment series. First, the parameters cutting speed, depth of cut and median chip thickness were varied in a side milling experiment. To further explore this, a second experiment series was undertaken, where face milling parameters (depth of cut, median chip thickness and feedrate direction) derived from the first experiment series were further analysed. Table 1 lists the analysed experimental parameters.

TABLE 1. The experiment series with the examined process parameters

Parameter	Experiment 1	Experiment 2
Parameter 1	Cutting speed	Chip thickness
Parameter 2	Depth of cut	depth of cut
Parameter 3	Median chip thickness	Feedrate direction

Because the endmill is kept in a low radial engagement, the median chip thickness is a lot lower than the calculated feed per tooth. The median chip thickness is calculated via equation 1 [17]. Here, φ_s is the radial engagement angle, a_e the radial engagement, ι the angulation and D the endmill diameter.

$$H_m = \frac{360}{\pi \cdot \varphi_s} \cdot \frac{a_e}{D} \cdot F_z \cdot sin(\iota) \qquad (1)$$

Figure 1 shows the geometric dependence of the chip thickness through chip thinning.

Experiment Series 1

From a plethora of possible influencing parameters, the cutting speed, depth of cut and median

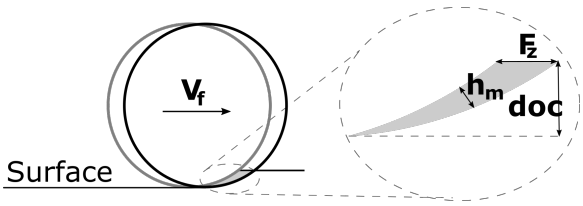

FIGURE 1. Hm as the result of chip thinning with low radial engagement.

chip thickness have the most significant impact on achieving a ductile cutting regime. [18] For this reason, a scoping experiment is undertaken. Table 2 lists the parameters and their corresponding levels, which were analysed in a Taguchi T16 orthogonal array. The cutting speed was chosen so that both the lower end (6631 RPM) of the achievable rotational speed, as well as a high, but very smooth running speed (39789 RPM) are well represented.

TABLE 2. Parameters and Levels used

Parameter	Level 1	Level 2	Level 3	Level 4
Vc in m/min	125	250	500	750
DOC in µm	0.5	1	1.5	2
Hm in nm	5	10	50	100

Research has shown, that the ductile cutting regime requires a very thin median chip thickness [18], which unlike in single point diamond turning can be achieved with varying depths of cut in milling operations. The depths of cut were chosen for their reliable achievement on the utilized machining centre, whereas the median chip thickness was chosen to cover a broad possible spectrum.

All experiments are undertaken in a sequence, during which the accoustic emission spektrum is recorded for a period of one second. Afterwards, the samples are cleaned with isopropyl alcohol, and dried in a low vacuum desiccator to prohibit the formation of condensation induced blemishes. The samples are then analysed for their qualitative appearance in the scanning electron microscope, and afterwards in a CLSM for their quantitative results such as roughness and material ratio.

The achieved roughness, as well as the inverse areal material ratio Smc (10%) is shown in figure

2. The texture aspect ratio Str was calculated, but did not differ significantly from 1 (isotropic) in this study and was thus not further included.

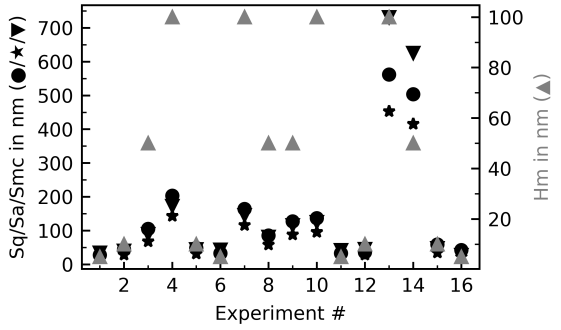

FIGURE 2. Overview of the resulting ISO 25178 parameters from the first experiment series.

It can be seen, that a series of parameters achieve a very low surface roughness (between 10 and 20 nm Sa/Sq), whereas some parameters have a high surface roughness (approaching 600 nm). The correlation between Sa, Sq, but also Smc is strong, pointing towards a smooth and isotropic surface.

A subsequent ANOVA analysis (table 3, qualitity parameter Sq) shows a significant influence (Pr (>F) 0.0036) of the median chip thickness and a less significant influence of the cutting speed (Pr (>F) 0.0209). Fitting a linear model to the data, shows that with decreasing chip thickness, the surface roughness improves.

TABLE 3. Results of the ANOVA analysis.

Parameter	Sum Sq 1	F Sq	Pr(>F)
Vc	81162	7.049	0.0209
DOC	30067	2.611	0.132066
Hm	149843	13.014	0.0036

This correlation is well visible in the recorded data. Figure 3 shows a detailed listing of the root mean square roughness in relation to the median chip thickness.

The recorded accoustic emission signals are transformed via a FFT (method: Welch, window: 2048) to a power spectral density (PSD). Figure 4 shows two different AE signals, whereas figure 5 shows two representative PSD.

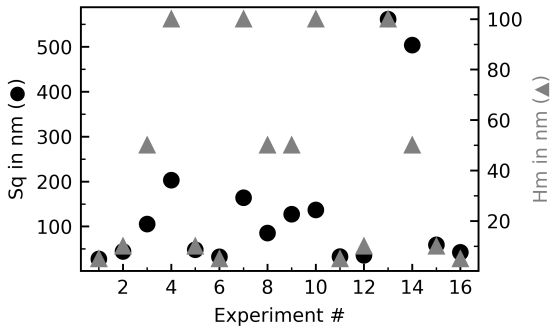

FIGURE 3. The RMS areal roughness Sq in relation to the median chip thickness.

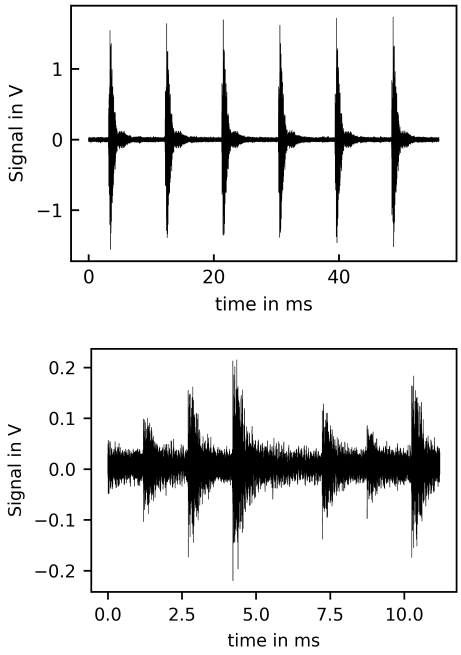

FIGURE 4. The recorded AE signal for two exemplary parameter sets. Upper: low surface roughness, likely ductile cutting regime. Lower: High surface roughness, likely brittle material removal mode. Note the random height of the signal peaks in the second signal.

The PSD shows the expected larger vibrations near the lower frequencies, stemming from machine aggregates, milling tool tooth entry frequency and the used flood coolant. Around 200 kHz, a significant increase of the signal is visible if the material removal mode is dominated by brittle material removal.

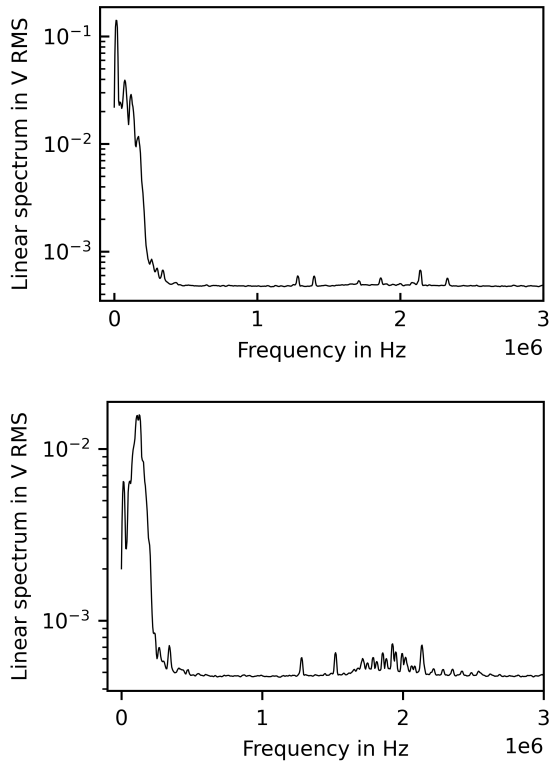

FIGURE 5. The linearized PSD for two exemplary parameter sets. Upper: low surface roughness, likely ductile cutting regime. Lower: High surface roughness, likely brittle material removal mode.

Experiment Series 2

In order to further explore the limiting factors, but also see whether the conclusions from the first experiment series are transferable towards a different milling application, a face milling experiment is undertaken. Table 4 lists the analysed parameters.

TABLE 4. Parameters and Levels used in the second experiment series.

Parameter	Level 1	Level 2	Level 3
DOC in µm	2.5	5	-
Hm in nm	5	10	20
Feed direction	Climb	Conventional	

Because the first experiment series already explored a wide range of possible parameters, the spindle speed was fixed at a cutting speed of 750 m/min. The milled samples are cleaned and measured in an identical fashion to the first experiment series. Directly visible to the naked eye are small, circular breakout areas in the conventional feed milled area.

Figure 6 shows the resulting ISO 25178 parameters, whereas table 5 shows the conducted ANOVA analysis, based on the quality parameter Sq.

TABLE 5. Results of the ANOVA analysis.

Parameter	Sum Sq 1	F Sq	Pr(>F)
Dir	2010	1.900	0.2054
DOC	700	0.662	0.4393
Hm	6	0.006	0.9412

No significant influence factor can be detected. It can be seen, that a sub 20 nm roughness can be achieved with very little variance between different parameters. A larger variance is visible in the experiments 7 to 12, which are milled with a conventional feed direction.

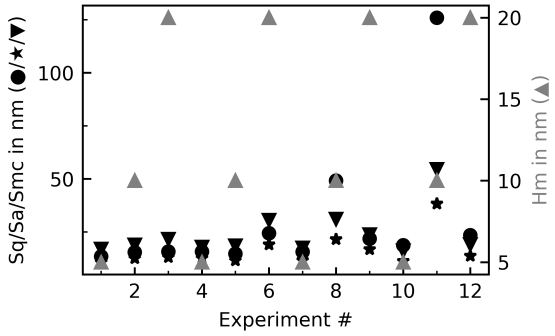

FIGURE 6. Overview of the resulting ISO 25178 parameters from the second experiment series.

RESULTS AND DISCUSSION

The milled surfaces in the first and second experiment series show a range of surface finishes ranging from very rough (Sq ~ 500 nm) to polish quality (Sq ~ 10 nm). Besides the surface roughness values, the surface was analysed in a scanning electron microscope for the surface structure.

The surface exhibits a very regular, smooth appearance. At 5000x magnification (see figure 7), a shallow feed of the tool cutting edge is visible in the form of curved tracks along the surface.

The conventional milled surface, which exhibits easily visible breakouts, show brittle failure at random points along the surface (see figure 7, lower). Because the chip generation in conventional milling starts at the very thinnest point, the

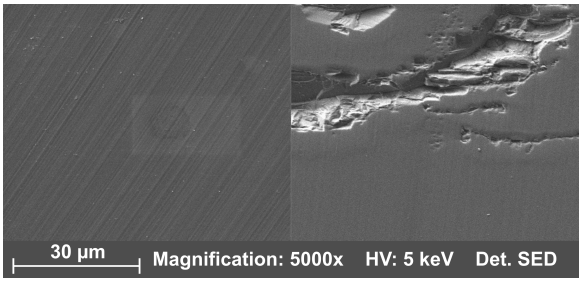

FIGURE 7. SEM micrograph of a climb (upper) and conventional (lower) feed direction surface.

cutting edge relief is rubbing along the material before the critical cutting depth is reached and a chip can form. This results in a large stress on the material, leading to breakouts. In climb milling, the chip formation starts at the maximum thickness, and progressively grows smaller. The cutting edge is therefore able to start in a brittle material removal process, reducing the stress on the material. Figure 8 shows the different feed directions and their influence on the creation of micro cracks in the material.

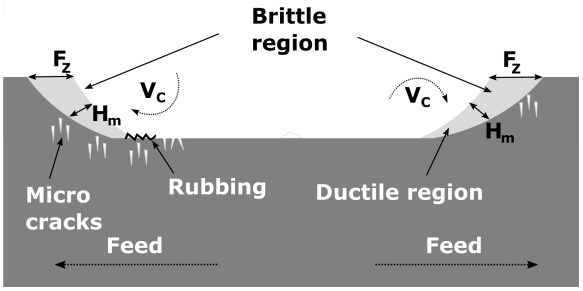

FIGURE 8. Schematic depiction of the creation of sub surface damages in conventional (left side) and climb feed rate direction.

Once a critical chip thickness is reached, a transition towards ductile material removal sets in, prohibiting further sub-surface damages in the material. Because the depth of cut is larger than the depth at which sub-surface damage is induced, an unblemished surface is created.

Chips collected from two exemplary cutting parameter sets (corresponding to the PSD spectra shown in the experimental chapter) show broken debris (figure 9) in the brittle material removal mode as well as thin, ductile chips once the median chip thickness is below 20 nm (figure 10). Larger SEM surveys of the chips show a remarkably homogeneous creation of both the debris in brittle mode, as well as the flowing chips in the ductile mode.

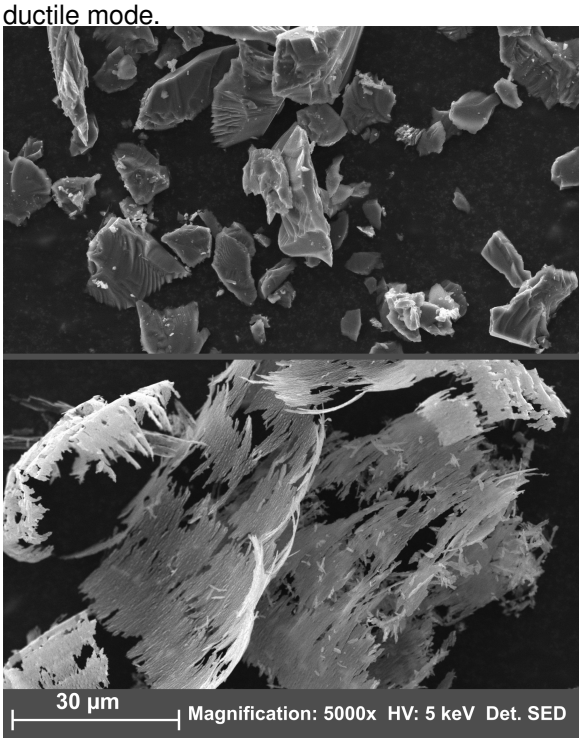

FIGURE 9. SEM micrograph of brittle material removal debris (upper) and ductile mode (lower) chips.

To further look into the random amplitude distribution in the AE signal during brittle material removal, high speed videos (10500 frames per second) of the milling process were taken with a Chronos 2.1HD camera. By tracking the debris flying away from the endmill, it can be seen that the material removal is randomly distributed and some rotations pass without material removal. Figure 10 shows 4 consecutive revolutions. The debris is highlighted with a white circle, only appearing every few rotations.

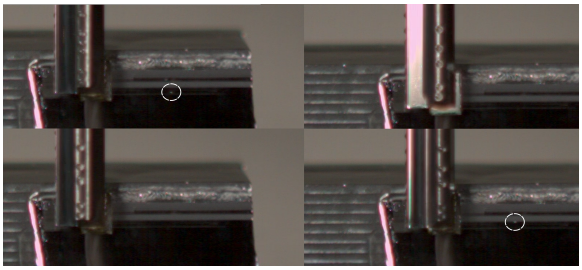

FIGURE 10. Still images taken from a high speed video, showing 4 consecutive full revolutions (CCW from top left).

This can explain the random appearance of larger

peaks in the AE signal. It is likely that the tool is in some rotations not cutting but rubbing along the material, leading to smaller amplitude peaks, followed by a rotation with a cut. After the cut, the absence of material leads to a much reduced rubbing and therefore the absence of a peak in the AE signal (compare figure 4).

CONCLUSION

A plethora of experiments were conducted to explore the conditions in reaching a ductile cutting regime in monocrystalline silicon. The defining influence on the achievement of a ductile cutting regime is the median chip thickness. By thinning the chip below 20 nm a smooth, unblemished surface can be created, achieving a RMS areal surface roughness Sq of 10 nm (see figure 11). The cutting speed has no large impact on the achievable surface roughness, and thus a comparatively productive process at high rotational speeds can be conducted. The depth of cut, within the tested parameters, has no influence on the surface generation. SEM micrographs show clear ductile cutting below 20 nm median chip thickness, and the ejection of brittle debris above 50 nm. Through accoustic emission spectroscopy and high speed video analysis, a mixture between cutting and rubbing was identified in the brittle material removal mode. Moreover, the accoustic emission signal can differentiate between the two cutting modes, which could lead towards a process supervision in industrial applications. The authors see promise in expanding the application towards freeform surface milling as well as extending the tool lifetime through different cooling solutions.

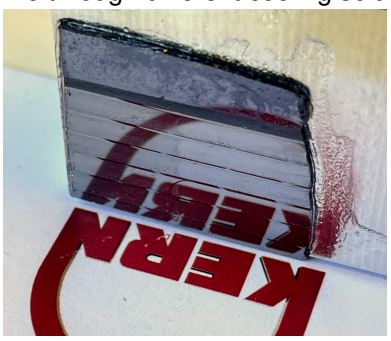

FIGURE 11. Several different parameter sets on a sample, showing mirror polish finish in monocrystalline Silicon.

References

[1] Study:, Optical Components: Market shares, strategies, and Forecasts, Worldwide, 2013 - 2019, Technical Report, Winter Green Research, Lexington, Massachusetts, 2013.

[2] S. Goel, X. Luo, R. L. Reuben, Wear mechanism of diamond tools against single crystal silicon in single point diamond turning process, Tribology International 57 (2013) 272–281. doi:10.1016/j.triboint.2012.06.027.

[3] S. Zhang, Review of modern field effect transistor technologies for scaling, Journal of Physics: Conference Series 1617 (2020) 012054. doi:10.1088/1742-6596/1617/1/012054.

[4] A. Phommahaxay, I. D. Wolf, T. Djuric, P. Hoffrogge, S. Brand, P. Czurratis, H. Philipsen, G. Beyer, H. Struyf, E. Beyne, Defect detection in through silicon vias by GHz scanning acoustic microscopy: Key ultrasonic characteristics, in: 2014 IEEE 64th Electronic Components and Technology Conference (ECTC), IEEE, 2014. doi:10.1109/ectc.2014.6897385.

[5] W. Dallas, O. Polupan, S. Ostapenko, Resonance ultrasonic vibrations for crack detection in photovoltaic silicon wafers, Measurement Science and Technology 18 (2007) 852–858. doi:10.1088/0957-0233/18/3/038.

[6] Y. Zhao, L. Chang, A micro-contact and wear model for chemical–mechanical polishing of silicon wafers, Wear 252 (2002) 220–226. doi:10.1016/s0043-1648(01)00871-7.

[7] C. Teichert, J. F. MacKay, D. E. Savage, M. G. Lagally, M. Brohl, P. Wagner, Comparison of surface roughness of polished silicon wafers measured by light scattering topography, soft-x-ray scattering, and atomic-force microscopy, Applied Physics Letters 66 (1995) 2346–2348. doi:10.1063/1.113978.

[8] H. Young, H. Liao, H. Huang, Surface integrity of silicon wafers in ultra precision machining, The International Journal of Advanced Manufacturing Technology 29 (2006) 372–378. doi:10.1007/s00170-005-2508-1.

[9] S. Ozturk, L. Aydin, N. Kucukdogan, E. Celik, Optimization of lapping processes of silicon wafer for photovoltaic applications, Solar Energy 164 (2018) 1–11. doi:10.1016/j.solener.2018.02.039.

[10] T. Leung, W. Lee, X. Lu, Diamond turning of silicon substrates in ductile-regime, Journal of Materials Processing Technology 73 (1998) 42–48. doi:10.1016/s0924-0136(97)00210-0.

[11] P. N. Blake, R. O. Scattergood, Ductile-regime machining of germanium and silicon, Journal of the American Ceramic Society 73 (1990) 949–957. doi:10.1111/j.1151-2916.1990.tb05142.x.

[12] T. Shibata, S. Fujii, E. Makino, M. Ikeda, Ductile-regime turning mechanism of single-crystal silicon, Precision Engineering 18 (1996) 129–137. doi:10.1016/0141-6359(95)00054-2.

[13] Z. Zhang, J. Yan, T. Kuriyagawa, Manufacturing technologies toward extreme precision, Journal of extreme Manufacturing 1 (2019) 022001. doi:10.1088/2631-7990/ab1ff1.

[14] B. S. Dutterer, J. L. Lineberger, P. J. Smilie, D. S. Hildebrand, T. A. Harriman, M. A. Davies, T. J. Suleski, D. A. Lucca, Diamond milling of an alvarez lens in germanium, Precision Engineering 38 (2014) 398–408. doi:10.1016/j.precisioneng.2013.12.006.

[15] Y. Takeuchi, K. Sawada, T. Sata, Ultraprecision 3d micromachining of glass, CIRP Annals 45 (1996) 401–404. doi:10.1016/s0007-8506(07)63090-x.

[16] S. Wang, S. To, X. Chen, X. Chen, An investigation on surface finishing in ultra-precision raster milling of aluminum alloy 6061, Proceedings of the Institution of Mechanical Engineers, Part B: Journal of Engineering Manufacture 229 (2014) 1289–1301. doi:10.1177/0954405414535588.

[17] J. Dietrich, Praxis der Zerspantechnik, Springer Fachmedien Wiesbaden, 2016. doi:10.1007/978-3-658-14053-3.

[18] S. Goel, The current understanding on the diamond machining of silicon carbide, Journal of Physics D: Applied Physics 47 (2014) 243001. doi:10.1088/0022-3727/47/24/243001.

ULTRAFAST LASER STRESS FIGURING OF FUSED SILICA MIRRORS

Kevin A. Laverty, Ian J. Arnold, and Brandon D. Chalifoux
James C. Wyant College of Optical Sciences, University of Arizona, 1630 E. University Boulevard, Tucson, AZ

INTRODUCTION

We present a method of figuring thin fused silica optical components, after coatings have been applied, by utilizing stress generated by means of an ultrashort pulsed (USP) laser. Many methods exist to alter the surface profile of glass, such as conventional polishing, magnetorheological finishing (MRF), and ion beam figuring (IBF). When dealing with thin optical components, such as wearable optics for virtual/augmented reality hardware or large-area space telescopes, conventional polishing can deform the substrate leading to low-spatial frequency error. Deterministic finishing techniques like IBF and MRF can achieve extremely precise surface profiles but have much lower material removal rate and must be performed prior to applying any coatings, which exhibit stress that can significantly deform thin substrates.

In contrast to material removal figuring techniques, stress figuring relies on the controllable generation of stress within a substrate to induce the required bending moments needed to adjust the surface profile of the substrate. Focused ultrashort laser pulses can generate localized structural modifications in fused silica that generate stress within the body of the substrate [1,2]. Unlike conventional figuring techniques, ultrafast laser pulse stress figuring can work with thin optical components, be performed after coating to counteract thin film induced stresses and has a much higher equivalent material removal rate than existing deterministic finishing techniques.

To perform full surface figure correction, it is in general necessary to control all three components of plane stress, with both positive and negative magnitudes [3]. The laser-generated stress components are highly dependent on the laser's operating parameters including power, polarization, raster speed, pulse duration and repetition rate. To explore this very large parameter space efficiently, we have designed and built an in-situ surface metrology system that quickly characterizes the modifications produced from a specific laser parameter set.

In this paper, we show that only a relatively small area (1.8%) of the total sample needs to be modified in order to generate substrate deformations on the order of 10s of microns. This will allow us to potentially recorrect any remaining surface figure errors by performing additional modification runs. Additionally, we will demonstrate USP laser flattening of mirror coated fused silica wafers and quantify the equivalent material removal rate and accuracy.

EQUIPMENT

The laser used in this work is a Trumpf Trumicro 2030 Laser. 1030nm wavelength pulses from 400 femtoseconds to 20 picoseconds long can be generated, with pulse energies up to 20uJ, at a maximum repetition rate of 1000KHz.

The output beam from the laser is passed through a Glan-Taylor Prism to produce a highly polarized beam with a well-defined orientation. Following the prism is a half wave plate on a rotatable stage, which allows us to rotate the polarization of the beam. Previous work by Li et. al. [4] has shown a clear dependance on laser polarization and writing direction, which is why the polarization of the beam is controlled during the modification process. The beam is then focused into the sample using a 0.4 NA lens.

The samples themselves are spring-mounted onto a machined aluminum holder which is translated underneath the focused beam by a 3-axis motorized stage (Aerotech PlanarDL/AVSI100). Stage translations upwards of 500mm/s can readily be achieved. Additionally, this stage allows for 0.4 um positioning accuracy.

To determine where the front surface of the sample is with respect to the focal point of the

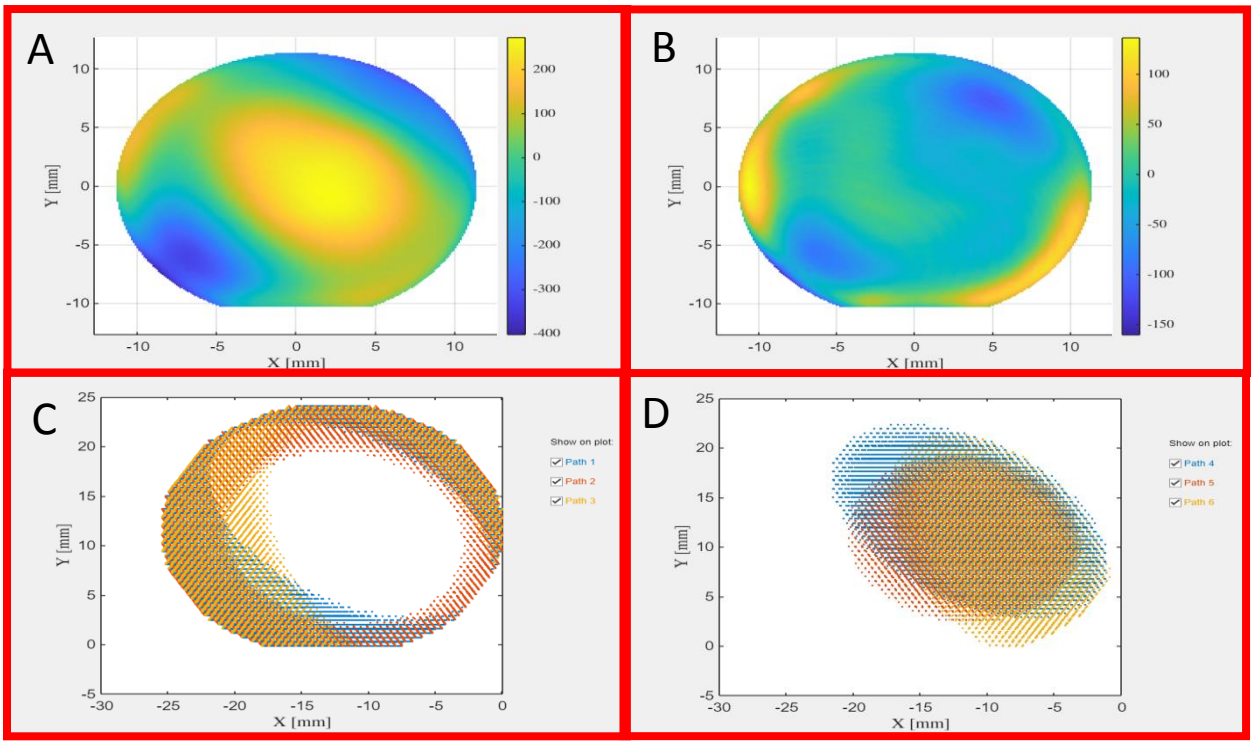

FIGURE 1. – A) Initial surface profile of the fused silica sample (P-V: 677nm, RMS: 153nm). B) Post-modification profile (P-V: 297nm, RMS: 46nm). C) Deep modification paths. D) Shallow modification paths.

lens, a back reflection monitor (BRM) camera was set up. An illumination IR laser diode and camera were coupled to the optical system via a beam splitter cube. To prevent the high energy laser pulses from reflecting into the camera, the optical path of the reflection was isolated using a short-wave-pass filter that blocks the laser light but passes the illumination diode light. When the surface of the sample is near the focal point of the focusing lens, a well-defined airy pattern is displayed on the BRM camera. With this BRM in place, it is possible for us to precisely determine where the front surface of the sample is located. This information, along with knowledge of the substrate thickness and refractive index, allow us to accurately modify different depths within the sample.

In order to improve the data collection flow, a Thorlabs WFS40-14AR Shack-Hartmann Wavefront Sensor (SHWFS) was incorporated into the system. A SHWFS sensor consists of an array of small lenses placed in front of a CCD camera. The aperture of each lens samples a small section of the incoming light. The average slope of the sampled wavefront will determine the location of the focal spots of each lenslet on the CCD. By determining the location of the spots before and after modification of the sample, it is possible to determine how much the surface has changed due to the modifications made. Due to poor wavefront control within the SHWFS setup, the SHWFS was only used to measure relative surface changes. In order to perform accurate surface figure correction, a high-quality measurement of the starting surface profile must be done. For actual stress-figuring runs, the initial surface profile of the samples were measured on a Zygo Verifire Fizeau Interferometer.

RESULTS

Using 350 fs pulses with 650 nJ of energy at a repetition rate of 1 MHz, 6 sets of lines were written into the uncoated glass side of a fused silica aluminum mirror. Lines oriented at 0, 120, and 240 degrees with respect to a reference flat on the sample were written across the sample at depths of 50um and 890um below the surface. After each modification, the surface figure of the mirror was measured. From the change in surface shape after each modification, it is possible for us to determine the magnitude and

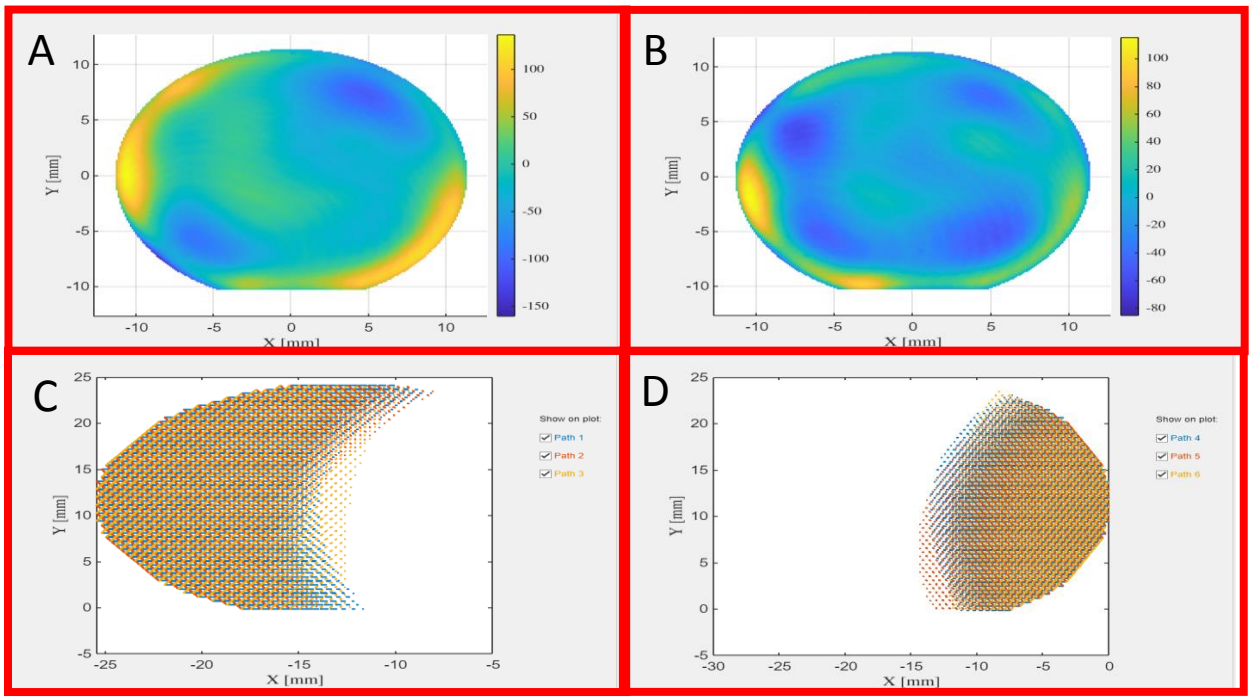

Figure 2. – A) Initial surface profile of the already modified fused silica sample. B) Post Modification Profile. C) Deep modification paths. D) Shallow modification paths.

orientation of the stress components produced by each set of lines.

After measuring the initial surface of a dielectric mirror coated fused silica substrate, we were able to calculate the stress required to correct the surface of the wafer. Using the data collected from the previous calibration runs, it was possible for us to determine a grid of desired laser-modified spots that can produce the desired corrective stress distribution in the substrate. For this particular sample, the initial surface profile and the calculated modification distribution is shown in Figure 1.

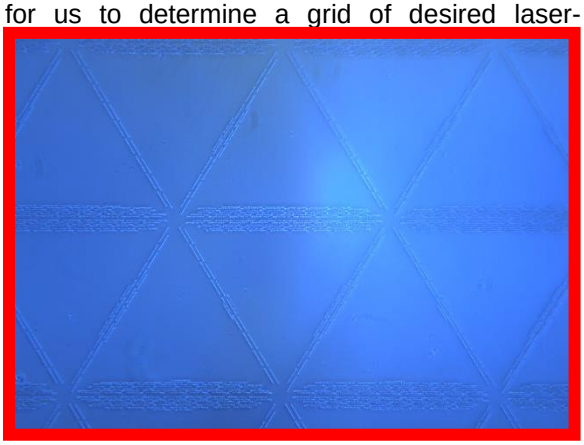

Figure 3 – A typical triangular writing pattern used for our figure correction viewed through a polarization microscope. Each line segment is 45um x 2um (L x W). A majority of the sample area is left unaltered and is therefore available for further corrections.

After running this modification recipe, the surface went from 677nm P-V with 153nm RMS to 297nm P-V with 46nm RMS – showing a 2x improvement in P-V and a 3x improvement in RMS. From start to finish, these modifications only took ~15 minutes to complete.

Inspecting the modification pattern in Figure 3, we can see that a vast majority of the sample area is left un-altered. The modification pattern works out to being ~1.8% of the sample surface and should allow us to easily modify the sample again. Since we know where the previous modification run altered the substrate, we can exclude these areas from any further modification recipe calculation.

A new stress profile was calculated for this same wafer, and a new modification recipe was compiled and ran overtop the existing modifications – see Figure 2. After running this second modification recipe, the sample's surface went from 297nm P-V with 46nm RMS, to 200nm P-V with 28nm RMS; showcasing that this

method can be performed in an iterative manner to achieve desired surface figures.

CONCLUSIONS

We have demonstrated arbitrary stress generation and control by using ultrafast laser pulses. We were able to characterize laser generated stress in fused silica and use it to manipulate the surface figure of a fused silica mirror. We have also demonstrated that this process can be performed iteratively to achieve improved results.

REFERENCES

[1] Y. Bellouard, A. Champion, B. McMillen, S. Mukherjee, R. R. Thomson, C. Pepin, et. al., *Stress-state manipulation in fused silica via femtosecond laser irradiation.* In Optica 3, 1285-1293, 2016.

[2] H. E. Zuo, B. D. Chalifoux, R. K. Heilman, and M. L. Schattenburg, *Ultrafast laser micro-stressing for correction of thin fused silica optics for the Lynx X-ray Telescope Mission*. In Volume 10699 of SPIE Proceedings, 1069954, 2018.

[3] B.D. Chalifoux, R. K. Heilmann, and M. L. Schattenburg, *Correcting flat mirrors with surface stress: analytical stress fields.* In J. Opt. Soc. Am. A 35, 1705, 2018.

[4] X. Li, J. Xu, Z. Lin, J. Qi, P. Wang, W. Chu, et. al., *Polarization-insensitive space-selective etching in fused silica induced by picosecond laser irradiation.* In Applied Surface Science 485, 188-193, 2019.

FUNDAMENTAL PRECISION LIMIT OF FREQUENCY MEASUREMENT OF LINEAR HARMONIC OSCILLATORS

Mingkang Wang[1,2], Rui Zhang[3], Robert Ilic[1], Yuxiang Liu[3], and Vladimir A. Aksyuk[1]
[1]Microsystems and Nanotechnology Division
National Institute of Standards and Technology
Gaithersburg, MD 20899 USA
[2]Institute for Research in Electronics and Applied Physics
University of Maryland
College Park, MD 20742, USA
[3]Department of Mechanical Engineering
Worcester Polytechnic Institute
Worcester, MA 011609 USA

INTRODUCTION

Resonance-based measurements are widely used in scientific research and high-precision metrology, where an unknown physics quantity is coupled to the resonance frequency of a linear harmonic oscillator. For example, in the micro/nano mechanical domain researchers are both actively advancing the understanding of fundamentals and device-related metrological limits [1-3], and discovering unprecedented performance gains and unexpected measurement regimes for resonators, in synergy with advances in cavity optomechanics [4-5]. Yet, surprisingly, quantitative, unified, and a general understanding of the eigenfrequency measurement precision limits for linear harmonic oscillators is currently absent. Instead, there is a plethora of separate and often conflicting analyses considering particular ways of estimating resonance frequency [6-10].

Breaking with this traditional paradigm of analyzing specific estimator performance, we use Cramer Rao Low Bound (CRLB) [11-13], valid for any possible estimation procedure, to derive frequency measurement limits for a linear harmonic oscillator subject to thermodynamic fluctuations, quantum uncertainty/backaction as well as detection noise. The exact analysis seamlessly covers quantum as well as classical regimes. Furthermore, we propose and implement a practical and general maximum-likelihood frequency estimator that is optimal for nearly all of the conditions discussed in previous works. We validate the derived frequency estimator and frequency measurement uncertainty limit on a strain-engineered SiN tuning fork resonator with an effective mode mass $m \approx 1$ pg. By using the statistically optimal frequency estimator, we find that the frequency bias stability of the undriven tuning fork reaches 0.4 ppm at 1 s averaging, which is better than the state-of-the-art nanomechanical resonators in such mass range and under strong drive [14]. More importantly, the great agreement between the measured frequency uncertainty and the derived frequency uncertainty limit verifies the method.

METHOD

Experimental setup

To verify the proposed general frequency estimator and theoretical thermodynamic limit (CRLB), we experimentally test them on a high-quality factor nanomechanical resonator with integrated cavity-optomechanical readout in the classical regime. Figure 1(a) shows the false-colored scanning electron microscopy micrograph of the strain-engineered tuning fork. The tuning fork stretching by a tension bar on the right-hand side (light blue bar) has a high fQ product of $\approx 10^{12}$. The nanomechanical resonator is driven by thermal noise and an external harmonic electrostatic drive. A microdisk optical resonator is evanescently coupled to the tuning fork, providing a readout of the mechanical motion of the tuning fork. Figure 1(b) shows the measured transmission intensity spectrum of an optical fiber coupled to the optical microdisk. When the working wavelength is fixed at λ_0 on the shoulder of the optical mode, the mechanical motion of the tuning fork modulates the optical resonance frequency of the integrated optical resonator, generating a time-varying transmission signal. The optical transmission is proportional to the mechanical displacement of

the tuning fork. Figure 1(c) presents the mechanical noise power spectral density of the tuning fork at room temperature.

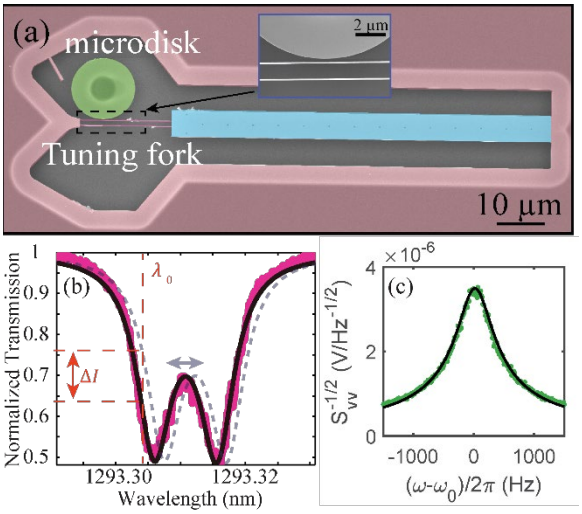

FIGURE 1: System introduction. (a) False-colored SEM image of the nanomechanical resonator (tuning fork). Inset shows the coupling part between the optical cavity (microdisk) and the tuning fork. (b) Operating principle. Transmission intensity at the working wavelength is modulated by optomechanical coupling with the fork. (c) Mechanical noise power spectral density. ω_0 =27.8 MHz. The black line indicates the Lorentzian fit

The mechanical displacement of the tuning fork is measured by a lock-in amplifier with a reference frequency $\omega \approx \omega_0$ and a bandwidth $BW \gg \Gamma$ where $\frac{\omega_0}{2\pi} \approx 27.8$ MHz and $\frac{\Gamma}{2\pi} \approx 620$ Hz are the eigenfrequency and damping coefficient of the tuning fork. Figure 2(a) shows the measured in-phase and quadrature components under different driving strengths. From low to high amplitude, they correspond to driving strength equals 0 V, 0.5 V, 1 V, and 1.5 V. The inset shows the distribution of sampled positions along the *y*-axis. The peaks have Gaussian profiles with mean values proportional to the driving strength and variance of $\sigma_V^2 \approx 2.3 \times 10^{-8}\ \mathrm{V}^2$. Based on the equipartition theorem, $\sigma_X^2 = \frac{k_b T}{m{\omega_0}^2}$ where k_b is the Boltzmann constant, $T = 293\ \mathrm{K}$ is the effective temperature and $m \approx 1$ pg is the effective mass of the tuning fork, we get the calibration constant $\kappa = 2.43$ nm/V.

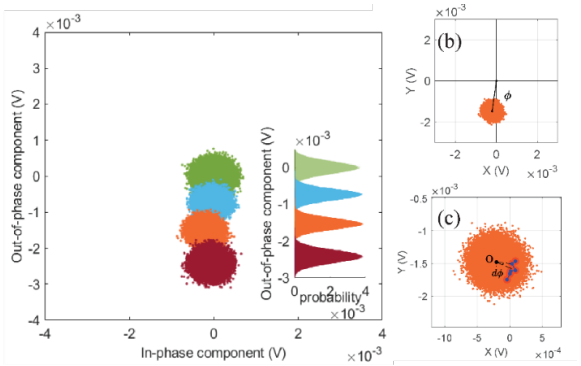

FIGURE 2: Experimentally measured mechanical response in the phase diagram. (a) Thermal fluctuations of the nanomechanical resonator. Different colors correspond to different driving strengths. The driving frequency is set at the resonance frequency. The inset shows the distribution density of the out-of-phase component. The phase and phase gradient contributions to the estimated frequency are shown as (b) and (c), respectively.

Frequency detection uncertainty limit derived from Cramer-Rao lower bound

The equation of motion of a linear harmonic oscillator subject to dissipation, harmonic drive, stochastic fluctuations is written as:

$$\ddot{x} + \Gamma\dot{x} + {\omega_0}^2 x = \frac{F(t) + f}{m} \qquad (1)$$

where x is the displacement, $F(t)$ is the harmonic drive, and f is the fluctuating force following $\langle f(t)f(t')\rangle = f_{rms}^2\delta(t-t')$ with a constant f_{rms}^2. For Langevin force (thermal flucuations) $f_{rms}^2 = 2\Gamma k_b T m$, while for quantum backaction-induced fluctuations, $f_{rms}^2 = 2k\hbar^2$ with position measurement strength k [15]. In a rotating frame (such as for the lock-in amplifier), x is refined by a slow variable u as $x = \frac{1}{2}(ue^{i\omega t} + u^* e^{-i\omega t})$. Eq. (1) in the rotating frame is rewritten as:

$$\dot{u} + \frac{\Gamma}{2}u + i\Delta\omega u = \frac{F_0}{2i\omega m} + \frac{f_1 - if_2}{i\omega m} \qquad (2)$$

where $\langle f_i(t)f_j(t')\rangle = \frac{1}{2}f_{rms}^2\delta(t-t')\delta_{ij}$ are the in-phase and quadrature components of the fluctuation forces near resonance.

As shown in Fig. 2(c), slow variable u evolves in the phase diagram around the steady states $O(\Delta\omega) = \langle u\rangle = \frac{A\Gamma}{2\Delta\omega + i\Gamma}$ following Eq. (2), where $A = \frac{F_0}{m\omega_0\Gamma}$, $\Delta\omega = (\omega_0 - \omega) \ll \omega_0$. By considering the dynamics of the tuning fork and the white

detection noise of variance $\sigma_{\mathrm{n}}^2 \propto 1/\mathrm{d}t$ ($\mathrm{d}t$ is the sampling time interval), we derive a recursive formula that distinguishes the mechanical motion u from the detection noise with the theoretically highest certainty [15]. In other words, the formula provides the best estimation of the position u_k based on *k* times continuous measurement $U_m^k = \{u_m^1 \dots u_m^k\}$:

$$u_k = \frac{\left[\frac{1}{(1-\Gamma \mathrm{d}t)\sigma_{k-1}^2 + \sigma_{dt}^2} u_{k-1} e^{\left(i\Delta\omega - \frac{\Gamma}{2}\right)\mathrm{d}t} + \frac{1}{\sigma_{\mathrm{n}}^2} u_m^k\right]}{\left(\frac{1}{(1-\Gamma \mathrm{d}t)\sigma_{k-1}^2 + \sigma_{dt}^2} + \frac{1}{\sigma_{\mathrm{n}}^2}\right)} \quad (3)$$

$$\frac{1}{\sigma_k^2} = \frac{1}{(1-\Gamma \mathrm{d}t)\sigma_{k-1}^2 + \sigma_{dt}^2} + \frac{1}{\sigma_{\mathrm{n}}^2} \quad (4)$$

where the superscript *m* represent the value is a measured value containing detection noise, u_k is the best estimation of the position u after *k* times measurement (i.e. maximum removal of detection noise), u_m^k is the measured position at the *k*th time and it contains detection noise, σ_k^2 is the uncertainty of the estimated u_k.

This update can be intuitively understood in two steps. First, the prior position is evolved in time $\mathrm{d}t$ as a harmonic oscillator, $u_{k-1} \to e^{\left(i\Delta\omega - \frac{\Gamma}{2}\right)\mathrm{d}t} u_{k-1}$, while the variance undergoes decay and diffusion $\sigma_{k-1}^2 \to (1-\Gamma \mathrm{d}t)\sigma_{k-1}^2 + \sigma_{dt}^2$. Second, information from the new measurement u_m^k is incorporated via an inverse-variance weighted average of the evolved prior position and u_m^k with variance of σ_{n}^2.

Cramer-Rao lower bound is a powerful mathematic tool that gives the variance of a parameter in unbiased estimators [11-13]. The frequency detuning $\Delta\omega$ is a parameter of the unbiased estimator, therefore, its variance can be calculated by its Cramer-Rao lower bound as:

$$\mathrm{Var}(\Delta\omega) \geq -\left[\mathrm{E}\left(\frac{\partial^2}{\partial \Delta\omega^2} \ln \mathrm{P}(U, \Delta\omega)\right)\right]^{-1} \quad (5)$$

where $\mathrm{P}(U_{\mathrm{m}}^N, \Delta\omega)$ is the probability of obtaining a specific series of $U_m^N = \{u_m^1 \dots u_m^N\}$ from N times continuous measurement [15]:

$$\mathrm{P}(U_{\mathrm{m}}^N, \Delta\omega) = \mathrm{P}(u_{\mathrm{m}}^1) \prod_{k=2}^{N} \mathrm{P}(u_{\mathrm{m}}^k | U_{\mathrm{m}}^{k-1})$$

$$= P(u_m^1) \prod_{k=2}^{N} \frac{1}{2\pi\sigma_n^2} e^{-\frac{\left|u_m^k - e^{\left(i\Delta\omega - \frac{\Gamma}{2}\right)dt} u_{k-1}\right|^2}{2\sigma_n^2}} \quad (6)$$

Combining Eq. (3-6), we get the variance of $\Delta\omega$ as:

$$\mathrm{I}(\Delta\omega) = I_{DRV} + I_{FL} \quad (7)$$

where

$$I_{DRV} = \frac{1}{\Gamma}\frac{|O|^2}{\sigma^2}\frac{4}{\left(\frac{2\Delta\omega}{\Gamma}\eta\right)^2 + \eta^2 + 4} \times \left(\tau + \frac{1 - \mathrm{e}^{-\Gamma\left(1+2\frac{D}{\eta}\right)\tau}}{\Gamma\left(1+2\frac{D}{\eta}\right)} - \left[\frac{\mathrm{e}^{\left(i\Delta\omega - \frac{\Gamma}{2}\left(1+2\frac{D}{\eta}\right)\right)\tau} - 1}{i\Delta\omega - \frac{\Gamma}{2}\left(1+2\frac{D}{\eta}\right)} + c.c.\right]\right) \quad (8)$$

$$I_{FL} = \frac{4}{\Gamma}\frac{D^2}{(\eta+2D)(\eta+D)} \times \left(\tau + \frac{(\eta+D)}{D}\frac{1 - \mathrm{e}^{-\Gamma\left(1+2\frac{D}{\eta}\right)\tau}}{\Gamma\left(1+2\frac{D}{\eta}\right)} - \frac{(\eta+2D)}{D}\frac{1 - \mathrm{e}^{-\Gamma\left(1+\frac{D}{\eta}\right)\tau}}{\Gamma\left(1+\frac{D}{\eta}\right)}\right) \quad (9)$$

$I_{DRV} \propto |O|^2$ and $I_{FL} \propto D^2$ are the Fisher information contained in the driven signal and the stochastic fluctuations, respectively, and $\eta = \sqrt{\frac{\sigma_{\mathrm{n}}^2 \Gamma \mathrm{d}t}{\sigma^2}}$ is the ratio of the detection noise within the linewidth Γ and $D = \frac{\sqrt{\eta^2+4} - \eta}{2}$. These two components correspond to the frequency information contained in the phase and phase gradient of the oscillator in the phase diagram as shown in Fig. 2(b) and (c). For the undriven case, $|O|^2 = 0$, the Fisher information is only from the fluctuation term I_{FL}.

Frequency estimator

For a harmonic resonator, its frequency is typically estimated by either phase estimator [10] or Kay's estimator (phase gradient estimator) [16] in different averaging time scales (detection bandwidth). However, the estimation does not guarantee that the estimated frequency has the lowest possible uncertainty.

Here we provide a general estimator that works on any averaging time scales and has the lowest possible uncertainty. Frequency estimator for a measurement U_{m}^N returns the most likely $\Delta\omega$ when $\partial \mathrm{P}(U_{\mathrm{m}}^N, \Delta\omega)/\partial\Delta\omega = 0$. From Eq. (6), we obtain:

$$\delta\omega = \frac{\hat{I}(\tau)}{\hat{J}(\tau)} = \frac{\int_0^\tau [(u_m(\mathrm{t}) - u)u'^* + c.c.]dt}{\int_0^\tau [2u'u'^* - \{(u_m(\mathrm{t}) - u)u''^* + c.c.\}]dt} \quad (10)$$

where $\delta\omega$ is the estimated frequency after measurement from t = 0 to τ, $u_m(\mathrm{t})$ is the measured position at time t, and u is the estimated u_k at $t = kdt$ from Eq. (3)

With the estimated frequency from continuous measurement, we can obtain their Allan variance as:

$$\sigma_f^2(\tau) = \frac{1}{2}\left\langle\left(\frac{\hat{J}_n}{\langle \hat{J}_n \rangle_{\mathrm{T}_0}}\right)^2 \left[\delta\omega_{(n+1)\tau}/2\pi - \delta\omega_{n\tau}/2\pi\right]^2\right\rangle_{T_0} \quad (11)$$

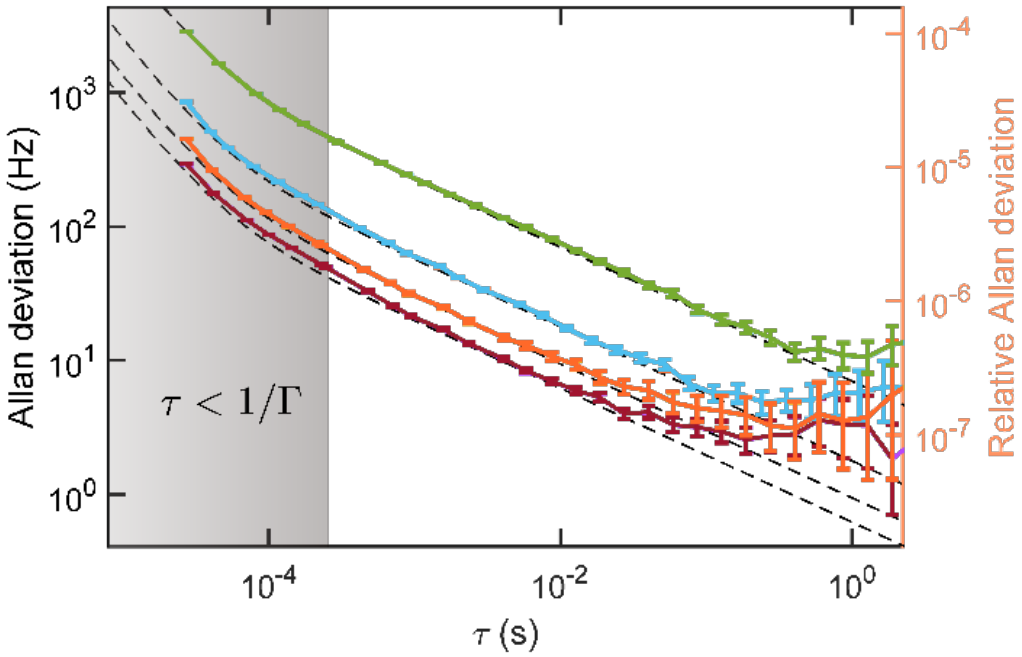

FIGURE 3. Allan deviation calculated from the measured four groups data using the optimal frequency estimator. The dashed lines show the corresponding derived general CRLB of frequency precision.

RESULTS AND CONCLUSION

We applied the derived frequency estimator, Eq. (10), on the four group data shown in Figure 2(a). Their Allan deviation is calculated by Eq. (11). Remarkably, their Allan deviation agrees exactly, without adjustable parameters, with the derived fundamental limits (CRLB) across 4 decades of measurement bandwidth as shown in Figure 3.

At small τ, the frequency uncertainty follows $\tau^{-3/2}$ due to detection noise. The thermodynamic limit proportional to $\tau^{-1/2}$ is reached by all four groups of data at $\tau \approx 0.1\ \mathrm{ms} < 1/\Gamma$. Importantly, the relative frequency bias stability of the undriven case (green line) reaches ≈ 0.4 ppm at $\tau \approx 1$ s. This performance is better than the average performance of the state-of-the-art driven MEMs of similar mass [14]. The great performance is attributed to its ultra-high fQ product and the low detection noise optomechanical detection scheme. It paves the way to passive frequency-based sensing only using thermal fluctuations. With increasing the driving strength, the relative frequency bias stability is reduced to ≈ 0.09 ppm. Further reduction is limited by the nonlinearity of the tuning fork.

We thank Dr. Michael Zwolak, Dr. Daniel Lopez, Dr. Linhai Huang, Dr. Christopher Wallin, Dr. J. Alexander Liddle and Dr. Marcelo Davanco for reviewing this paper and giving meaningful suggestions. M.W. is supported by the Cooperative Research Agreement between the University of Maryland and the National Institute of Standards and Technology Center for Nanoscale Science and Technology, Award 70NANB10H193, through the University of Maryland;

REFERENCES

[1] T. R. Albrecht, P. Grütter, D. Horne, D. Rugar, Frequency modulation detection using high-Q cantilevers for enhanced force microscope sensitivity. Journal of Applied Physics. 69, 668–673 1991.

[2] A. N. Cleland, M. L. Roukes, Noise processes in nanomechanical resonators. Journal of Applied Physics. 92, 2758–2769 2002.

[3] K. L. Ekinci, Y. T. Yang, M. L. Roukes, Ultimate limits to inertial mass sensing based upon nanoelectromechanical systems. Journal of Applied Physics. 95, 2682–2689 2004.

[4] V. T. K. Sauer, Z. Diao, J. N. Westwood-Bachman, M. R. Freeman, W. K. Hiebert, Single laser modulated drive and detection of

a nano-optomechanical cantilever. AIP Advances. 7, 015115 2017.
[5] Y. Liu, H. Miao, V. Aksyuk, K. Srinivasan, Wide cantilever stiffness range cavity optomechanical sensors for atomic force microscopy. Opt. Express, OE. 20, 18268–18280 2012.
[6] A. N. Cleland, M. L. Roukes, Noise processes in nanomechanical resonators. Journal of Applied Physics. 92, 2758–2769 2002.
[7] K. L. Ekinci, Y. T. Yang, M. L. Roukes, Ultimate limits to inertial mass sensing based upon nanoelectromechanical systems. Journal of Applied Physics. 95, 2682–2689 2004.
[8] E. Gavartin, P. Verlot, T. J. Kippenberg, Stabilization of a linear nanomechanical oscillator to its thermodynamic limit. Nat Commun. 4, 2860 2013.
[9] M. Sansa, E. Sage, E. C. Bullard, M. Gély, T. Alava, E. Colinet, A. K. Naik, L. G. Villanueva, L. Duraffourg, M. L. Roukes, G. Jourdan, S. Hentz, Frequency fluctuations in silicon nanoresonators. Nature Nanotech. 11, 552–558 2016.
[10] S. K. Roy, V. T. K. Sauer, J. N. Westwood-Bachman, A. Venkatasubramanian, W. K. Hiebert, Improving mechanical sensor performance through larger damping. Science. 360, eaar5220 2018.
[11] A. D. Campos, An extension of the Cramér-Rao inequality for the sequential case. Trabajos de Estadistica y de Investigacion Operativa. 30, 65–70 1979.
[12] 18. G. Malécot, Statistical methods and the subjective basis of scientific knowledge. Genetics Selection Evolution. 31, 269 1999.
[13] 19. C. W. Gardiner, Handbook of stochastic methods (springer Berlin, 1985), vol. 3.
[14] M. Sansa, E. Sage, E. C. Bullard, M. Gély, T. Alava, E. Colinet, A. K. Naik, L. G. Villanueva, L. Duraffourg, M. L. Roukes, G. Jourdan, S. Hentz, Frequency fluctuations in silicon nanoresonators. Nature Nanotech. 11, 552–558 2016.
[15] Mingkang Wang, Rui Zhang, Robert Ilic, Yuxiang Liu, Vladimir A Aksyuk, Fundamental limits and optimal estimation of the resonance frequency of a linear harmonic oscillator. Communications Physics, 4.1: 1-11 2021.
[16] S. Kay, A fast and accurate single frequency estimator. IEEE Trans. Acoustics, Speech, and Signal Processing. 37, 1987–1990 1989.

CNC MACHINING AND METROLOGY TRAINING: ACE PROGRAM UPDATE

Tony Schmitz[1,2], Aaron Cornelius[1], Jake Dvorak[1], Jose Nazario[1], Emma Betters[1,2], Scott Smith[2], Craig Blue[2], Joannie Harmon[3], Mark Morrison[3], Tyler Blevins[3], and John Hopkins[3]

[1]Department of Mechanical, Aerospace, and Biomedical Engineering
University of Tennessee, Knoxville, Knoxville, TN 37996, USA
[2]Manufacturing Science Division
Oak Ridge National Laboratory, Oak Ridge, TN, 37830, USA
[3]IACMI – The Composites Institute, Knoxville, TN 37932, USA

ABSTRACT
This paper provides an update on the workforce development activities supported by America's Cutting Edge (ACE), a national initiative for machine tool technology development and advancement. ACE is supported by the Department of Defense Industrial Base Analysis and Sustainment program from the Office of Industrial Policy. Both the online and in-person components of the computer numerically controlled machining and metrology training programs are summarized and participation information is provided.

KEYWORDS
Education, training, workforce, machining, metrology

INTRODUCTION
The existing shortfall in the US manufacturing workforce has been well-documented and broadly discussed. For example, a 2018 Deloitte report predicts up to 2.4M manufacturing jobs may go unfilled by 2028 and that these workforce limitations could place $454B in production at risk in the US [1].

Due to the increasing connectivity between systems and widespread automation, including computer control of nearly all manufacturing equipment, the required skills are evolving with the new digital manufacturing paradigm. This places new demands on efforts to prepare the next generation workforce. Not only must the education and training efforts evolve, but the target audience is broad. The existing workers must be up-skilled to keep pace with new technology. Community college and trade school curricula must be expanded to provide not only a fundamental understanding of manufacturing processes, but must also provide exposure to digital communication and cybersecurity. Universities must prepare machine designers and entrepreneurs, for example, to energize the US machine tool industry.

To address workforce challenges in the machining industry, the America's Cutting Edge (ACE) training program was developed at the University of Tennessee, Knoxville and launched in December 2020 in collaboration with Oak Ridge National Laboratory and IACMI – The Composites Institute through support from DoD's Industrial Base Analysis and Sustainment (IBAS) program. There are currently two modules; both are offered at no cost.

The online computer numerically controlled (CNC) machining training curriculum is composed of:

- a machining tutorial, which covers topics including chip formation, tool wear, machining processes, machining equipment, CNC machining, computer aided manufacturing (CAM), and work holding
- CAM instruction through multiple lessons using an example part
- a machining dynamics tutorial, which describes the importance of considering machining vibration when selecting machining parameters in CAM software
- CAM lessons that leverage CAM+, a stand-alone app that simulates machining performance
- an introduction to machining cost
- multiple choice quizzes to assess learning and track progress.

The online metrology training curriculum is composed of:

OPTICAL KNIFE-EDGE DISPLACEMENT SENSOR MODELING

Ross Zameroski[1], Michael Gomez[2], and Tony Schmitz[1,2]
[1]Department of Mechanical, Aerospace, and Biomedical Engineering
University of Tennessee, Knoxville
Knoxville, TN 37996, USA
[2]Manufacturing Science Division
Oak Ridge National Laboratory
Oak Ridge, TN, 37830, USA

ABSTRACT
This paper describes an analytical model for the well-known optical knife-edge displacement sensor that predicts the relationship between the knife-edge displacement and photointerrupter output. The model includes: 1) the geometry of a rectangular knife-edge profile penetrating a circular laser beam perpendicular to the beam axis; and 2) the (assumed) Gaussian intensity profile for the beam cross-section. A comparison between the model predictions and measured photointerrupter for a linear range of knife-edge displacements is provided. It is shown that good agreement is obtained without model calibration.

KEYWORDS
Displacement, optical, knife-edge

INTRODUCTION
Optical beam profiling and dynamic displacement measurement are common applications of the knife-edge technique. In this approach, the knife-edge partially blocks the beam of interest and the unblocked portion is incident on a photodetector that generates an electrical signal proportional to intensity [1-17]. The photodetector voltage output varies from a maximum value (fully unblocked) to zero (fully blocked) as the knife-edge is displaced transversely across the beam's cross-section. The knife-edge position vs. photodetector voltage is nonlinear but may be linearized by selecting a region where is the beam is approximately 50% blocked. This is the typical approach so that the displacement may be calculated from voltage using only a calibration constant (e.g., µm/V).

The purpose of this paper is to consider both the geometry of a rectangular knife edge passing through a laser beam perpendicular to the beam axis and the (assumed) Gaussian beam profile to analytically predict the displacement-photodetector output relationship. This model may then be used to pre-select the linear range for the optical knife-edge displacement sensor because the linear range has design implications when integrating the sensor in an electromechanical system for measurement and/or control.

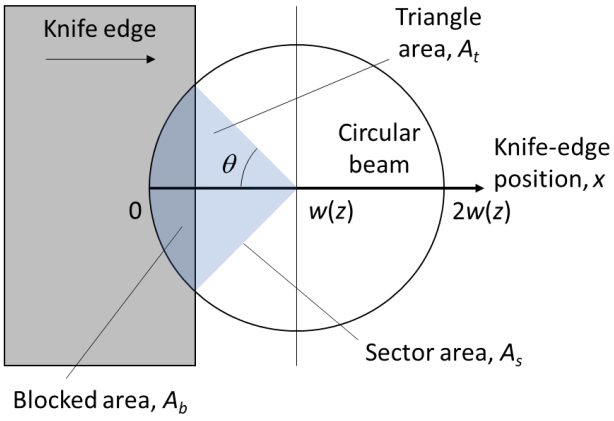

FIGURE 1. Blocked area geometry as the knife-edge covers the circular laser beam. The x = 0 knife-edge position represents fully unblocked and x = 2w(z) represents fully blocked.

OPTICAL KNIFE-EDGE DISPLACEMENT SENSOR MODELING
The model incorporates the basic geometry of the rectangular knife-edge penetrating a circular beam, while also considering the radially-

[2]Notice: This manuscript has been authored by UT-Battelle, LLC, under contract DE-AC05-00OR22725 with the US Department of Energy (DOE). The US government retains and the publisher, by accepting the article for publication, acknowledges that the US government retains a nonexclusive, paid-up, irrevocable, worldwide license to publish or reproduce the published form of this manuscript, or allow others to do so, for US government purposes. DOE will provide public access to these results of federally sponsored research in accordance with the DOE Public Access Plan (http://energy.gov/downloads/doe-public-access-plan).

symmetric Gaussian intensity distribution for the beam's cross-section. The model geometry is displayed in Fig. 1, where the knife-edge moves from left to right to sequentially block the laser beam. At any position, x, the blocked area, A_b, depends on x and the beam radius, $w(z)$. As shown in Fig. 2, the beam radius is a function of the location along the beam's propagation direction, z, and is minimum at the beam waist.

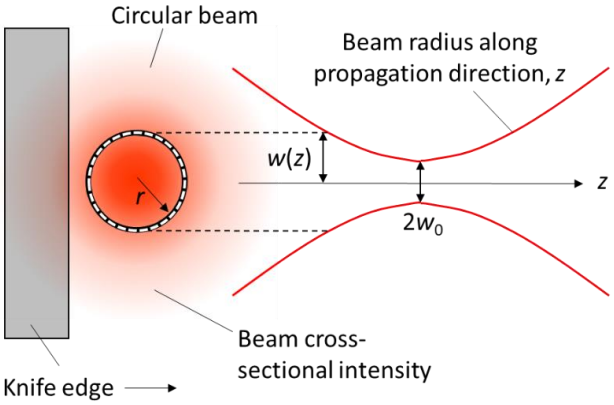

FIGURE 2. Beam intensity variation in the radial direction, r. The beam radius, w(z), is a function of the location along the beam propagation direction, z, and is minimum at the beam waist where the beam radius is w_0 and z = 0.

The blocked area can be calculated by recognizing that the shaded sector area, A_s, in Fig. 1 is composed of the blocked area (represented by the darker shading) and two right triangles. The sector area is:

$$A_s = w(z)^2\theta, \tag{2}$$

where the half-angle, θ, for the sector is:

$$\theta = \operatorname{acos}\left(\frac{w(z)-x}{w(z)}\right). \tag{3}$$

The area, A_t, for both the upper and lower right triangles in Fig. 1 (top panel) is:

$$A_t = \frac{1}{2}(w(z)-x)\sqrt{w(z)^2-(w(z)-x)^2}. \tag{4}$$

The blocked area is calculated using Eq. 5. The nonlinear variation in blocked area with knife-edge position is plotted in Fig. 3. The blocked area is normalized to the beam cross-sectional area, $A = \pi w(z)^2$, for generality.

$$A_b = A_s - 2A_t = w(z)^2\operatorname{acos}\left(\frac{w(z)-x}{w(z)}\right) - (w(z)-x)\sqrt{w(z)-(w(z)-x)^2} \tag{5}$$

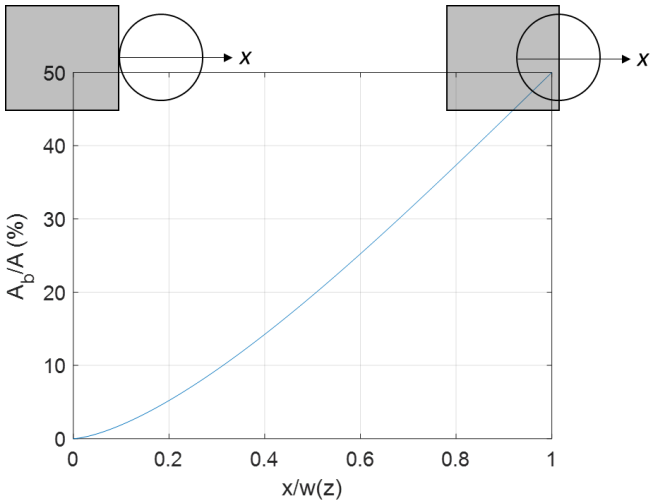

FIGURE 3. Variation of blocked area with knife-edge position.

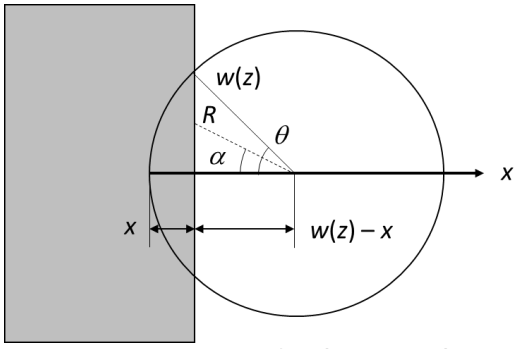

FIGURE 4. Geometry for incorporating radial intensity variation for beam cross-section.

The purely geometric model presented in Eq. 5 is not sufficient, however, because the beam intensity is not uniform across its cross-section, in general. Rather, it is often Gaussian and varies with the radial distance, r, from the beam axis, as described by Fig. 2 and Eq. 6, where I_0 is the maximum intensity at r = 0. If the knife-edge penetrates the beam at its waist (where z = 0), Eq. 6 simplifies to Eq. 7.

$$I(r,z) = I_0\left(\frac{w_0}{w(z)}\right)^2\exp\left(\frac{-2r^2}{w(z)^2}\right) \tag{6}$$

$$I(r) = I_0\exp\left(\frac{-2r^2}{{w_0}^2}\right) \tag{7}$$

To improve the geometric model, the cross-sectional intensity variation was incorporated.

Specifically, blocking the beam near its center (small r values) has a stronger effect on the photodetector output than blocking the beam far from its center. As shown in Fig. 4, however, the knife-edge does not block the beam at a single radius value. Rather, there is a continuous range of radii from ($w(z) - x$) along the x axis up to $w(z)$ as the angle θ is increased.

To proceed with the analysis, a mean radius value, R, may be calculated by integrating over the full θ range for each x value. The integration variable, α, is defined by Eq. 8. The mean radius is then calculated by rearranging Eq. 8 and writing the integral; see Eq. 9.

$$\alpha = \operatorname{acos}\left(\frac{w(z)-x}{R}\right) \tag{8}$$

$$R = \frac{1}{\theta}\int_0^{\theta} \frac{w(z)-x}{\cos\alpha}\, d\alpha = \frac{w(z)-x}{\theta}\int_0^{\theta} \sec\alpha\, d\alpha \tag{9}$$

Solving the Eq. 9 integral and evaluating over the integration limits gives Eq. 10, where θ is defined by Eq. 3, and the mean radius, R, depends on the knife-edge position, x. Both variables are normalized to the beam radius for plotting purposes.

$$R = \frac{w(z)-x}{\theta}\left(\ln|\sec\theta + \tan\theta| - \ln|\sec 0 + \tan 0|\right) \tag{10}$$

The next step is to substitute R for r in Eq. 6 to describe the intensity at the mean radius as a function of the knife-edge position. The final step is to multiply the Eq. 6 intensity factor by A_b from Eq. 5, where the effect is to "weight" the geometric solution by the exponential Gaussian intensity function. Example results for $w(z) = w_0$ are displayed in Fig. 5. For comparison purposes, the normalized blocked area curve from Fig. 4 is also included. It is observed that the slope is significantly affected. It is reduced near the beam edge, where the lower intensity portion of the beam cross-section is blocked, and increased near the center, where more of the higher intensity portion of the beam is blocked.

To complete the analysis, the Fig. 5 $(A_b/A)(I/I_0)$ result is scaled from 0 to 0.5 (i.e., the percent scaling is removed), mirrored about the vertical axis where $x/w(z) = 1$, and inverted to give the full available range of $x/w(z) = 0$ to 2 for the knife-edge position. Finally, this result is subtracted from 1 to mimic the normalized photodetector output, which is typically 1 when the beam is fully unblocked and 0 when the beam is fully blocked. See Fig. 6.

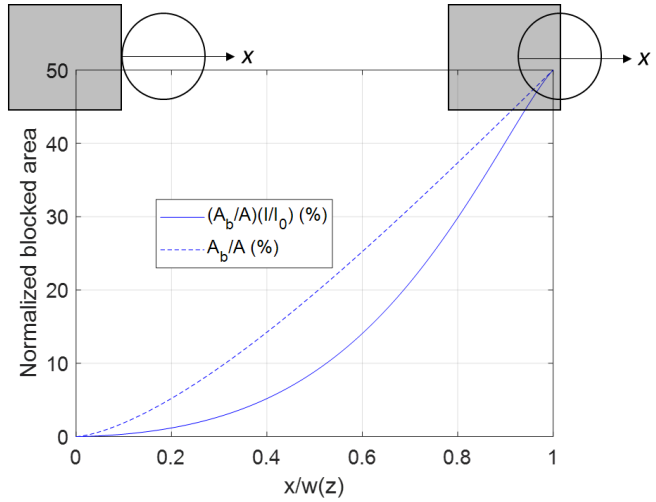

FIGURE 5. Normalized blocked area versus knife-edge position with (solid line) and without (dashed line) weighting by the normalized intensity at the mean beam radius for the knife-edge position.

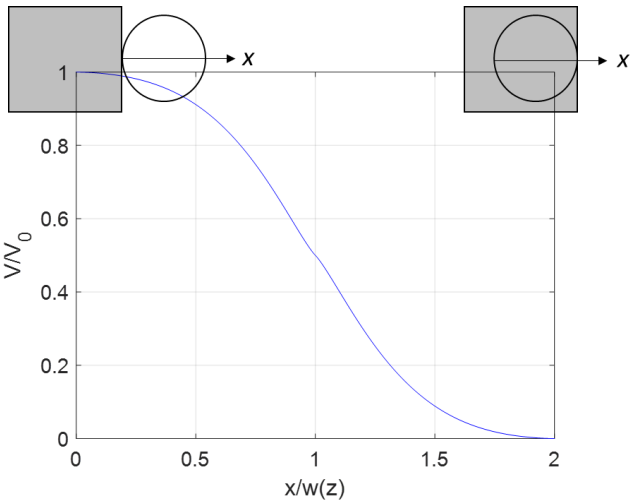

FIGURE 6. Modeled photodetector output displayed as normalized voltage versus normalized knife-edge position.

EXPERIMENTAL SETUP

To verify the model prediction, a photointerrupter (OMRON EE-SG3) was selected and a knife-edge (X-ACTO™ #17) was positioned within the beam using a linear air bearing stage (Aerotech ABL 10100-LT). The stage position was commanded and the photointerrupter output was measured, where the photointerrupter location was fixed and the knife-edge moved with the stage. The stage had a manufacturer-specified

positioning uncertainty of +/-0.2 µm and resolution of 0.5 nm. For the test sequence, the knife-edge was positioned outside the photointerrupter emitter-detector range and moved towards the sensor in 5 µm increments, with a 1 second dwell time, until the full range was exceeded (i.e., the beam was fully blocked).

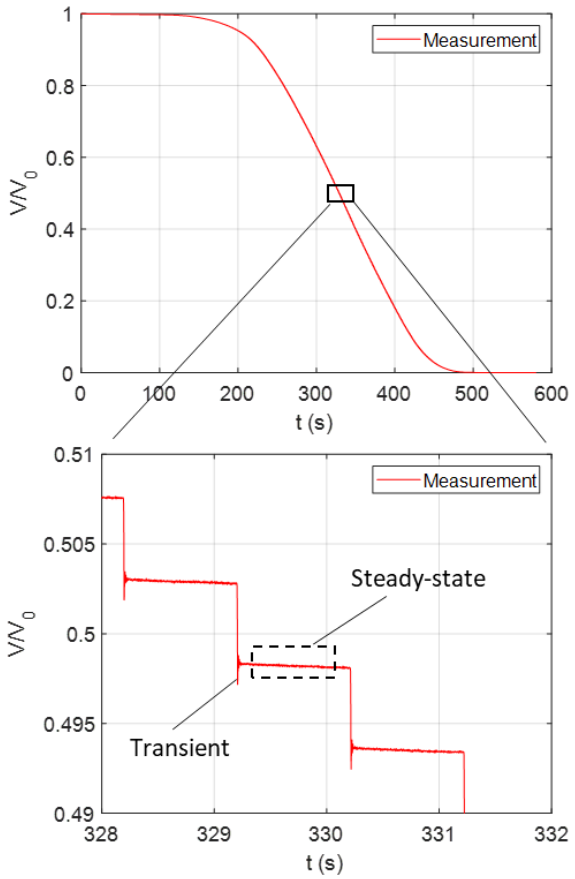

FIGURE 7. Time-domain normalized output voltage from the test sequence.

The total range of travel was approximately 2 mm and the corresponding working voltage was 2 V. The displacement-dependent output voltage was measured with a sampling frequency of 1000 Hz (Data Translation 9837B). A linear scaling technique was applied to the measured output voltage to normalize the voltage response. See Eq. 11, where V is the voltage for any knife-edge position, V_{min} is the fully blocked voltage and V_{max} is the fully unblocked voltage. The stepwise response for the test sequence is displayed in Fig. 7.

$$\frac{V}{V_0} = \frac{V - V_{min}}{V_{max} - V_{min}} \quad (11)$$

Next, the mean and standard deviation values for the steady-state portion of the stepwise response were determined. The steady-state response was selected to exclude the motion transient after each step; it was confirmed with a separate capacitance gage measurement that these transients were due to the stage control system and not the optical knife-edge displacement sensor. The result is presented in Fig. 8 with mean values and error bars that represent the type A measurement uncertainty (coverage factor of k = 2 on the calculated standard deviation) for the steady-state portion of each step.

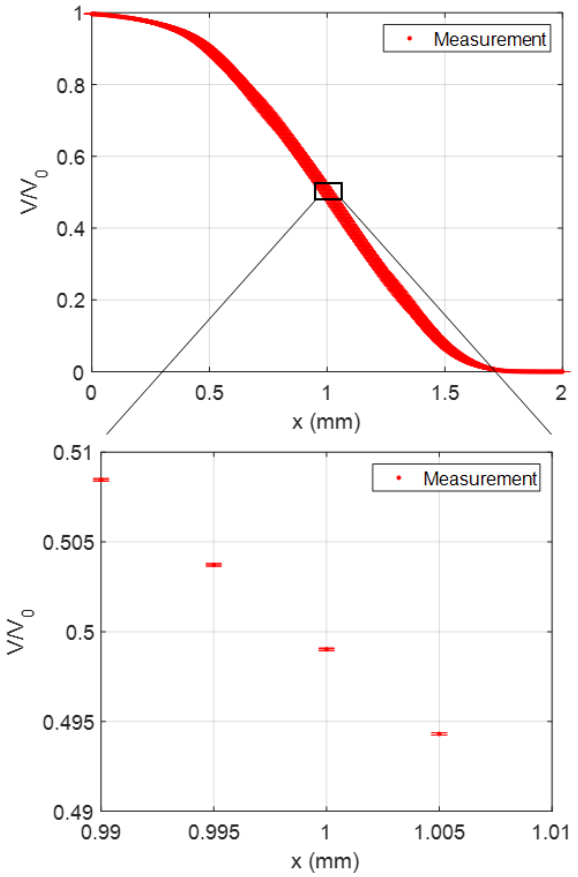

FIGURE 8. Stepwise optical knife-edge displacement sensor response with mean values and error bars, which identify standard deviations with a coverage factor of k = 2, for the normalized photointerrupter voltage.

RESULTS

The photodetector voltage output is compared to the model prediction in this section. Figure 9 displays the normalized voltage and model vs. knife-edge displacement, where it was assumed that the knife-edge penetrated the beam at its waist with a radius of 1 mm for the model. As

noted, no information was provided by the photointerrupter manufacturer regarding the waist location or beam radius, a 2 mm diameter hole was identified on the photointerrupter schematic as the laser source location. A 1 mm radius was therefore assumed with the waist located at the geometric center between the emitter and detector.

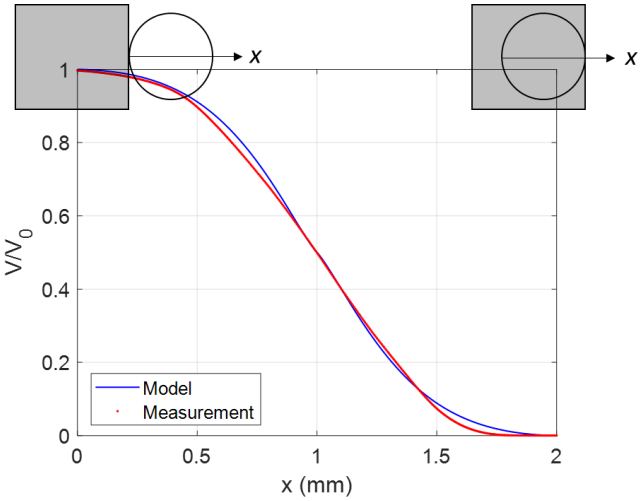

FIGURE 9. Comparison of measurement and model. The model assumed $w(z) = w_0 = 1$ mm in the absence of additional information from the photointerrupter manufacturer.

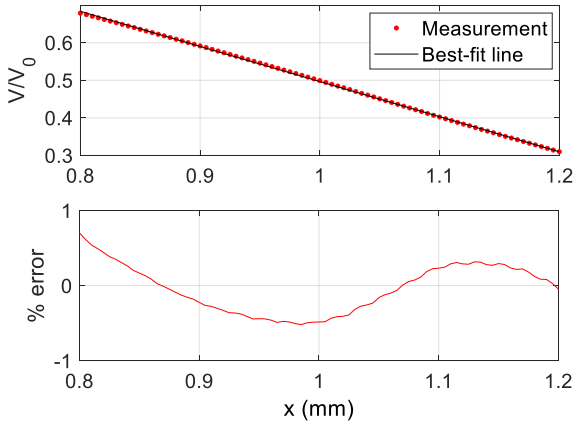

FIGURE 10. (Top) Linear section of measurement data with best-fit line. (Bottom) Percent error between the measurement data (normalized photointerrupter voltage) and best-fit line.

As noted, while the knife-edge position vs. photodetector voltage is nonlinear, it may be linearized by selecting the region where is the beam is approximately 50% blocked. For the model in Fig. 9, a range from 0.8 mm to 1.2 mm was chosen for analysis. The percent error between the normalized photodetector voltage and best-fit line is displayed in Fig. 10, where the slope of the best-fit line is -0. 9344 mm^{-1} with an R^2 value of 0.9998. It is observed that the error is less than 1% over the full range with some remaining structure. The corresponding percent error between the model and best-fit line over the same range is shown in Fig. 11, where the best-fit line slope is -0. 9991 mm^{-1} with an R^2 value of 0.9994. Again, the error is less than 1% with similar, but not identical, structure. The percent error between the modeled and measured slopes is 6.9%.

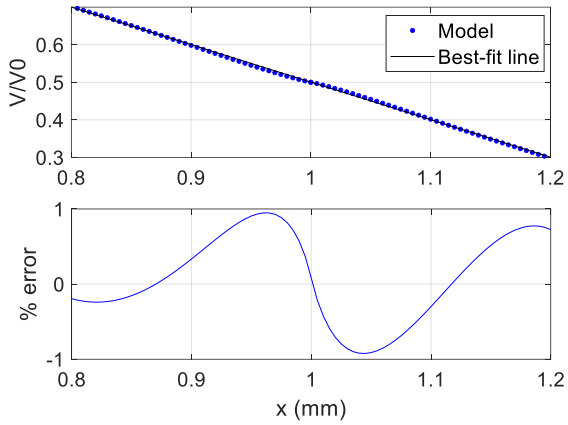

FIGURE 11. (Top) Linear section of model with best-fit line. (Bottom) Percent error between model and best-fit line.

CONCLUSIONS

This paper described the derivation and validation of an analytical model to predict the relationship between the knife-edge displacement and photointerrupter output for the well-known optical knife-edge displacement sensor. The model simultaneously considers the geometry of a rectangular knife-edge profile penetrating a circular laser beam perpendicular to the beam axis and the radially-symmetric Gaussian intensity profile for the beam cross-section.

Experiments were completed to compare the model to measured performance for a selected knife-edge and photodetector pair by prescribing known displacements using a linear air bearing stage. A stepwise pause-repeat positioning sequence was performed to compare the measured photointerrupter voltage to the model

prediction. It was found that the error between the predicted and measured slopes was 6.9% with errors less than 1% between the model/measurement and corresponding best-fit lines. Note that this agreement was obtained without calibration. The only input was the beam radius. The conclusion is that the model can be effectively applied as a design tool when implementing the optical knife-edge displacement sensor for measurement and control applications.

ACKNOWLEDGEMENTS

This manuscript has been authored by UT-Battelle, LLC, under contract DE-AC05-00OR22725 with the US Department of Energy (DOE). The US government retains and the publisher, by accepting the article for publication, acknowledges that the US government retains a nonexclusive, paid-up, irrevocable, worldwide license to publish or reproduce the published form of this manuscript, or allow others to do so, for US government purposes. DOE will provide public access to these results of federally sponsored research in accordance with the DOE Public Access Plan (http://energy.gov/downloads/doe-public-access-plan).

REFERENCES

1. Firester, A.H., Heller, M.E. and Sheng, P., 1977. Knife-edge scanning measurements of subwavelength focused light beams. Applied Optics, 16(7), pp.1971-1974.
2. de Araújo, M.A., Silva, R., de Lima, E., Pereira, D.P. and de Oliveira, P.C., 2009. Measurement of Gaussian laser beam radius using the knife-edge technique: Improvement on data analysis. Applied optics, 48(2), pp.393-396.
3. Karabacak, D., Kouh, T., Huang, C.C. and Ekinci, K.L., 2006. Optical knife-edge technique for nanomechanical displacement detection. Applied Physics Letters, 88(19), p.193122.
4. Chiu, Y. and Pan, J.H., 2007. Micro knife-edge optical measurement device in a silicon-on-insulator substrate. Optics Express, 15(10), pp.6367-6373.
5. Gu, G.M., Shin, Y.K., Son, J. and Kim, J., 2012. Design and characterization of a photo-sensor based force measurement unit (FMU). Sensors and Actuators A: Physical, 182, pp.49-56.
6. Gomez, M. and Schmitz, T., 2020. Low-cost, constrained-motion dynamometer for milling force measurement. Manufacturing Letters, 25, pp.34-39.
7. Gomez, M.F. and Schmitz, T.L., 2019. Displacement-based dynamometer for milling force measurement. Procedia Manufacturing, 34, pp.867-875.
8. Braunsmann, C., Prucker, V. and Schäffer, T.E., 2014. Optical knife-edge displacement sensor for high-speed atomic force microscopy. Applied Physics Letters, 104(10), p.103101.
9. Lee, C., Lee, S.K. and Tarbutton, J.A., 2014. Novel design and sensitivity analysis of displacement measurement system utilizing knife edge diffraction for nanopositioning stages. Review of Scientific Instruments, 85(9), p.095113.
10. Lee, C., Lee, S.K. and Tarbutton, J.A., 2015. Positioning control effectiveness of optical knife edge displacement sensor-embedded monolithic precision stage. Sensors and Actuators A: Physical, 233, pp.390-396.
11. Lee, C., Jeon, S., Stepanick, C.K., Zolfaghari, A. and Tarbutton, J.A., 2017. Investigation of optical knife edge sensor for low-cost, large-range and dual-axis nanopositioning stages. Measurement, 103, pp.157-164.
12. Zolfaghari, A., Jeon, S., Stepanick, C.K. and Lee, C., 2017. A novel sensor for two-degree-of-freedom motion measurement of linear nanopositioning stage using knife edge displacement sensing technique. Review of Scientific Instruments, 88(6), p.065110.
13. Kim, J.C., Kim, K.S. and Kim, S., 2013. Note: A compact three-axis optical force/torque sensor using photo-interrupters. Review of Scientific Instruments, 84(12), p.126109.
14. Lee, C., Mahajan, S.M., Zhao, R. and Jeon, S., 2016. A curved edge diffraction-utilized displacement sensor for spindle metrology. Review of Scientific Instruments, 87(7), p.075113.
15. Wang, C., Zhong, F. and Ellis, J.D., 2017. Two-dimensional straightness measurement based on optical knife-edge sensing. Review of Scientific Instruments, 88(9), p.095109.
16. Jeong, S., Chitalia, Y. and Desai, J.P., 2020. Miniature force sensor based on dual-photointerrupter with high linearity and disturbance compensation. IEEE Sensors Journal, 20(11), pp.5855-5864.
17. Lee, C., 2019. A first review of optical edge-diffraction technology for precision dimensional metrology. The International Journal of Advanced Manufacturing Technology, 102(5), pp.2465-2480.

- an introduction to manufacturing measurements, which covers measurement transducers for displacement, velocity, acceleration, strain, temperature, part dimensions, surface finish, and internal geometry
- an introduction to measurement uncertainty, which includes a definition of terms, a description of measurement uncertainty evaluation, and a case study for density measurement
- multiple choice quizzes to assess learning and track progress.

The intent of the ACE program is to educate and train the next-generation machine tool workforce, including future manufacturing engineers, machine tool designers, entrepreneurs, machinists, metrologists, and others.

FIGURE 1. Locations for 1588 CNC machining participants from 46 states.

FIGURE 2. Locations for 580 industry participants for CNC machining.

ACE PARTICIPATION

CNC machining

Since its December 7, 2020 launch, the program has grown rapidly. As of August 26, 2021, there were 1588 online participants from 46 states. These participants include 508 from industry (37%) and 1008 students from four-year colleges and universities, two-year community colleges, and high schools (63%). The US locations for the participants are displayed in Fig. 1. The industry locations are shown in Fig. 2. The student breakdown includes: 836 from colleges and universities, 56 from community colleges, and 116 from high schools; see Fig. 3. Among the 1588 participants who have started the online training, 507 (32%) have completed all training modules and had certificates awarded from IACMI.

FIGURE 3. Locations for 1008 students in CNC machining. Black symbols are for colleges and universities, blue symbols for community colleges, and orange symbols for high schools.

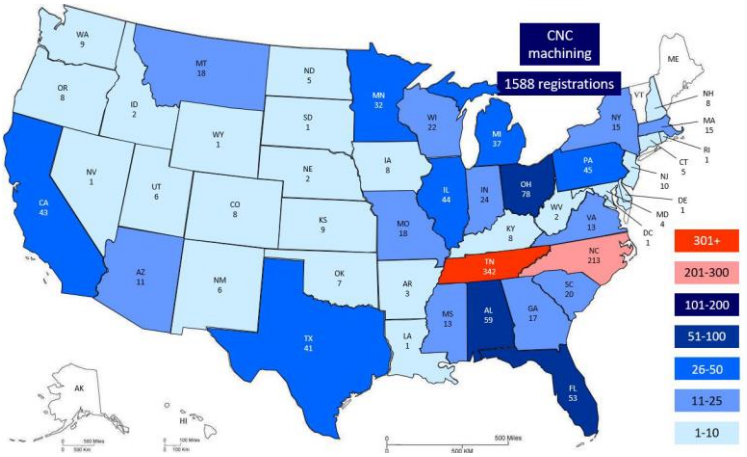

FIGURE 4. CNC machining participants by state.

Figure 1 shows that the registrations have the highest density in the Eastern US, although the upper Midwest, Texas, and West coast are also well-represented. The states with the highest numbers of online participants are listed. Figure 4 presents all registrations by state.

1. Tennessee, 342
2. North Carolina, 213
3. Ohio, 78
4. Alabama, 59
5. Florida, 53
6. Pennsylvania, 45

7. Illinois, 44
8. California, 43
9. Texas, 41
10. Michigan, 37

Eight one-week, in-person CNC machining training sessions were also completed from May to August, 2021 at three locations in Knoxville, TN. Those participants that completed the online training were eligible.

- May 10-14, 7 participants, University of Tennessee, Knoxville
- May 24-28, 10 participants, University of Tennessee, Knoxville
- June 7-11, 9 participants, University of Tennessee, Knoxville
- July 19-23, 11 participants, University of Tennessee, Knoxville
- June 7-11, 5 participants, Pellissippi State Community College
- June 14-18, 6 participants, Pellissippi State Community College
- July 19-23, 9 participants, Oak Ridge National Laboratory's Manufacturing Demonstration Facility
- August 9-13, 10 participants, Oak Ridge National Laboratory's Manufacturing Demonstration Facility

The 67 in-person participants represented nine states and included: 45 students (six high school), three educators (university, community college, NIST MEP), five engineers, six machinists, and eight veterans. The gender breakdown was 58 males and nine females (13%).

FIGURE 5. Toolpath programming using CAM software.

FIGURE 6. CNC machining by participant.

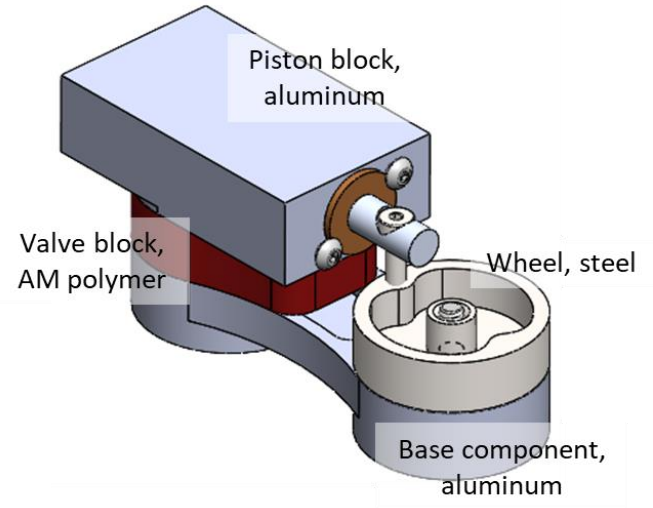

FIGURE 7. Oscillating piston air engine produced during in-person CNC machining training.

The five-day (8:30 am to 4:30 pm) in-person training included the use of CAM software to program toolpaths for four parts; see Fig. 5. These toolpaths were then used by the participants to machine the parts; see Fig. 6. Finally, the participants assembled the parts to produce an oscillating piston air engine; see Fig. 7.

The topics for each day of the five-day schedule are summarized. These activities include both classroom and laboratory sessions.

1. Monday – machining review, M/G code introduction, machine air engine base component
2. Tuesday – machining dynamics review, workholding, datums, machine piston block
3. Wednesday – machining cost review, machine valve block

4. Thursday – metrology review, machine wheel, assemble air engines; see Fig. 8
5. Friday – CAM+ review, on-machine tap test and chatter example, air engine part swap/assembly, logo machining, program evaluation

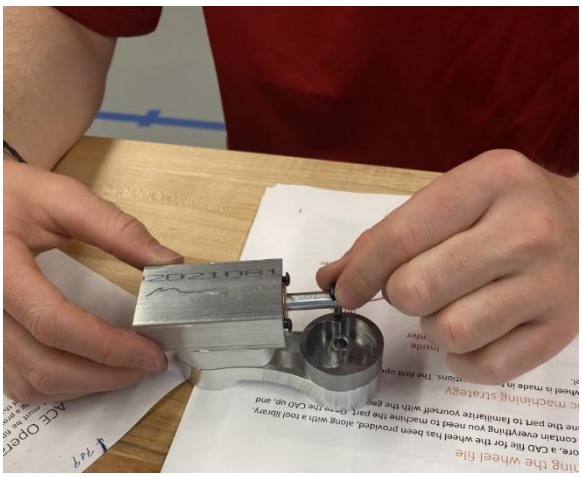

FIGURE 8. Assembly of oscillating piston air engine by CNC machining training participant.

Metrology

Since its March 16, 2021 launch, the program has grown to more than 300 participants. As of August 26, 2021, there were 303 online participants from 35 states. These participants include 136 from industry (45%) and 167 students from four-year colleges and universities, two-year community colleges, and high schools (55%). The US locations for the participants are displayed in Fig. 9. The student breakdown includes: 148 from colleges and universities, 12 from community colleges, and 7 from high schools. Among the 303 participants who have started the online training, 94 (31%) have completed all training modules and had certificates awarded from IACMI.

FIGURE 9. Locations for 303 metrology participants from 35 states.

Figure 9 shows that the registrations have the highest density in the Eastern US. The states with the highest numbers of online participants are listed. Figure 10 presents all registrations by state.

1. Tennessee, 64
2. North Carolina, 21
3. California, 15
4. Florida, 10
5. Ohio, 9
6. Illinois, 7
7. New Mexico, 7
8. Alabama, 6
9. Indiana, 6
10. Pennsylvania, 6

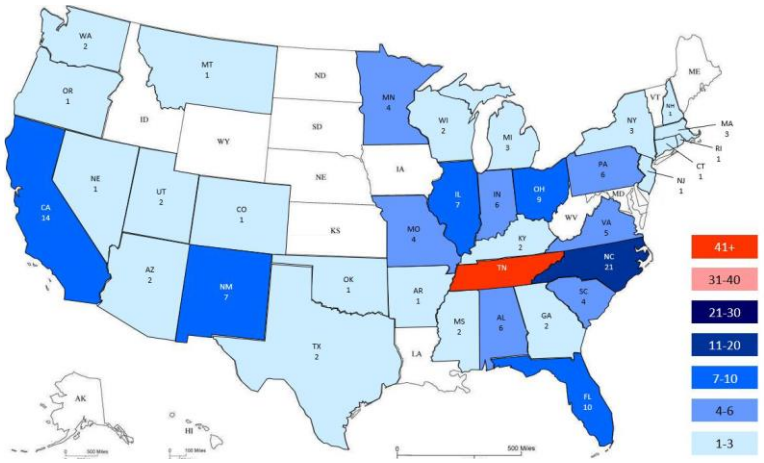

FIGURE 10. Metrology participants by state.

CONCLUSIONS

This paper provided an update on the workforce development activities supported by America's Cutting Edge (ACE), a national initiative for machine tool technology development and advancement. Both the online and in-person components of the CNC machining and metrology training modules were summarized and participation information was provided.

Details were given about the eight in-person CNC machining training sessions held at the University of Tennessee, Knoxville, Pellissippi State Community College, and Oak Ridge National Laboratory during Summer 2021. The 67 participants received training in both the classroom and laboratory; see Figs. 11 and 12.

Each of the participants rated the training either 4/5 or 5/5 during the post-training assessment. All stated that they found both the classroom and

laboratory sessions to be helpful. Selected quotes are included in the following paragraphs.

FIGURE 11. Classroom instruction was provided during the in-person training events.

"As a mechanical engineer, this ACE bootcamp is helping me to have a practical mindset in terms of designing something with the latest machining equipment and technology that can be manufactured efficiently in the US." – Air Force active duty, graduate student

"The online portion of ACE has been beneficial because I have no prior experience with CNC machining and getting the foot in the door with the online learning and now seeing it first hand and physically be able to do it is a great advantage to me as a hands-on physical learner. Being able to do it myself has given me a lot more confidence in my abilities to continue." – Aerospace engineering student, Air Force veteran

"Unmatched machining development program. Before ACE, I must confess I was quite concerned for the machining industry. It seems the suppliers and in-house providers I work with base their entire machining experience on tribal knowledge and arbitrary experimentation. To find the online curriculum and hands-on training that ACE provided…was a godsend." – Practicing engineer in the forging and machining industry

"The tap test demonstration is for real. The industry has battled chatter for years but learning the science behind chatter and how to avoid chatter conditions is transformational." – Third-generation machinist in family-owned company

"ACE on-line and hands-on CNC training has given me insight into a future career. ACE has shown me the importance of time and efficiency when producing a product and how energy and cost efficiency in CNC machining relates to environmental engineering." – High school student from underserved community

"ACE has reassured me that women are made for machining! We have acute attention to detail, our ability to hear higher pitches will help diagnose issues sooner, and there is actually room to move up within the industry." – Graduate student in materials science

"ACE hands-on experience with the CNC machines which will directly help me as a start a summer machining internship and pursue a career in manufacturing." – High school student

"Our country has great value in untapped human resources and ACE training, at no cost, has immense potential to extract diamonds in the rough." – Senior fitter

"Patriotism, that's one reason I became interested in ACE. The US cannot progress without building back its domestic manufacturing. ACE has taught me improved methods of finding machining stability without requiring years of experience." – Graduate student and Army veteran

FIGURE 12. Laboratory instruction included CNC machining, tooling setup, fixturing, work offsets and probing, and part measurement.

Moving forward, additional partners to host the in-person events will be identified and training materials will be provided in the form of comprehensive “instructor kits”. This is part of an agenda that includes a national roll-out of the ACE program.

To learn more about ACE or to register for the training modules, visit the following web sites.

CNC machining
https://mtrc.utk.edu/ace/

Metrology
https://mtrc.utk.edu/ace/ace-metrology/

ACKNOWLEDGEMENTS
The authors acknowledge funding from the Industrial Base Analysis and Sustainment program. This manuscript has been authored by UT-Battelle, LLC, under contract DE-AC05-00OR22725 with the US Department of Energy (DOE). The US government retains and the publisher, by accepting the article for publication, acknowledges that the US government retains a nonexclusive, paid-up, irrevocable, worldwide license to publish or reproduce the published form of this manuscript, or allow others to do so, for US government purposes. DOE will provide public access to these results of federally sponsored research in accordance with the DOE Public Access Plan (http://energy.gov/downloads/doe-public-access-plan).

REFERENCES
1. https://www.forbes.com/sites/willemsundbladeurope/2020/04/23/the-labor-shortage-is-still-coming-stay-prepared/#2d31ef453892.

STABILITY ANALYSIS OF A CONSTRAINED-MOTION DYNAMOMETER

Michael Gomez[1] and Tony Schmitz[1,2]
[1]Manufacturing Science Division
Oak Ridge National Laboratory
Oak Ridge, TN, 37830, USA
[2]Department of Mechanical, Aerospace, and Biomedical Engineering
University of Tennessee, Knoxville
Knoxville, TN, 37996, USA

ABSTRACT
This paper describes the stability analysis of a constrained-motion dynamometer (CMD) for milling force measurement. Multi-axis piezoelectric dynamometers are a popular choice for cutting force measurement. These dynamometers rely on specific piezoelectric transducer arrangements and the structural dynamics of the system, while stiff, are not rigid. Although these systems offer a large measuring range, high sensitivity, and fast response time, the systematic errors caused by their complex structural dynamics must generally be compensated using advanced post-processing techniques. Here, the system structural dynamics are a principal element in the design space which are easily altered with material selection, flexure element geometry and arrangement. In milling applications, a limitation on the allowable axial depth of cut is regenerative chatter. With the ability to modify the dynamic response of a cutting force dynamometer, the stability limit and bandwidth can be modified either through an increase in stiffness or damping. In this paper, a passive damping approach was selected to modify the viscous damping ratio to increase the critical stability limit of a CMD compared to the undamped design.

KEYWORDS
Force, measurement, milling, chatter

INTRODUCTION
There are many types of passive damping approaches, including: shear film damping, constrained layer damping (CLD), damping by addition of energy absorbing foams and viscoelastic materials, and dynamic absorbers [1]. For this application, a viscoelastic material was deposited between the CMD flexure elements and the mechanism frame. When milling force is applied to the CMD, energy is dissipated through the viscoelastic medium due to the relative motion between the movable platform and mechanism frame. The advantage of this approach is the ability to obtain a relatively high amount of energy dissipation in a flexure mechanism without compromising the stiffness or mass of the dynamometer. Additionally, it provides a general strategy for reducing the vibration amplitude at low cost. For this study, a widely available silicone rubber sealant was used to demonstrate its benefits as a passive damping medium for the CMD.

MILLING STABILITY VALIDATION

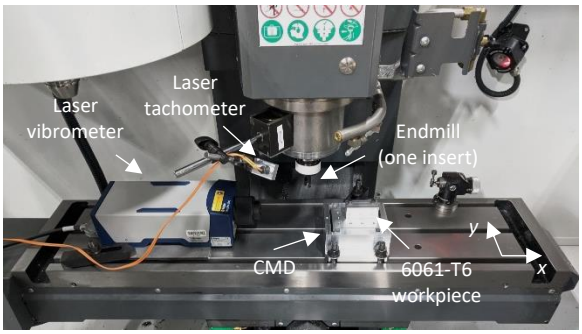

FIGURE 1. Experimental setup for stability testing.

[1] Notice: This manuscript has been authored by UT-Battelle, LLC, under contract DE-AC05-00OR22725 with the US Department of Energy (DOE). The US government retains and the publisher, by accepting the article for publication, acknowledges that the US government retains a nonexclusive, paid-up, irrevocable, worldwide license to publish or reproduce the published form of this manuscript, or allow others to do so, for US government purposes. DOE will provide public access to these results of federally sponsored research in accordance with the DOE Public Access Plan (http://energy.gov/downloads/doe-public-access-plan).

Cutting tests were performed on a Haas TM-1 CNC vertical milling machine; see Fig. 1. A 6061-T6 aluminum workpiece was mounted to the CMD. A single flute, 15.88 mm diameter endmill (Kennametal M1D062E1401W075L150) was used to perform up-milling machining passes at a 3 mm radial depth of cut and a variable axial depth of cut. Once-per-tooth sampling was achieved using a laser tachometer, where a reflective target was attached to the rotating tool holder. In situ vibration signals were collected using the laser Doppler vibrometer. The tool and workpiece FRFs were measured by impact testing, where an instrumented hammer is used to excite the structure and the response is measured using a linear low-mass accelerometer. The FRFs are displayed in Figs. 2 and 3 for an Al 6061-T6 CMD and a damped Al 6061-T6 CMD, respectively. The modal parameters for the CMD x-direction are presented in Table 1. The addition of the silicone medium resulted in a 130% increase in damping with negligible change to the modal mass and stiffness parameters.

Table 1. X-direction modal parameters for the SDOF CMDs.

Modal Parameters	Al 6061-T6 CMD	AL 6061-T6 CMD (damped)
Direction	*x*	*x*
m (kg)	0.689	0.701
k (N/m)	2.08×10^7	2.07×10^7
c (N-s/m)	43	99

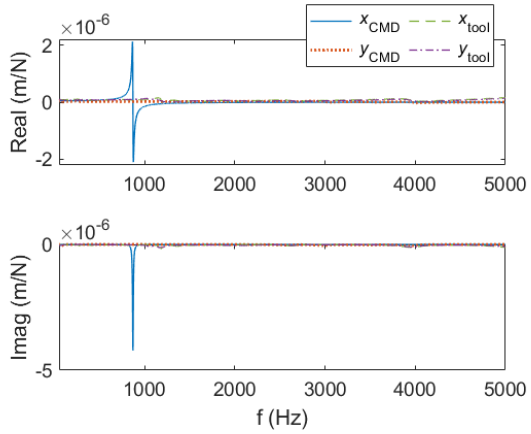

FIGURE 2. Modal fit FRFs of the tool and CMD (no added damping) for the stability validation setup.

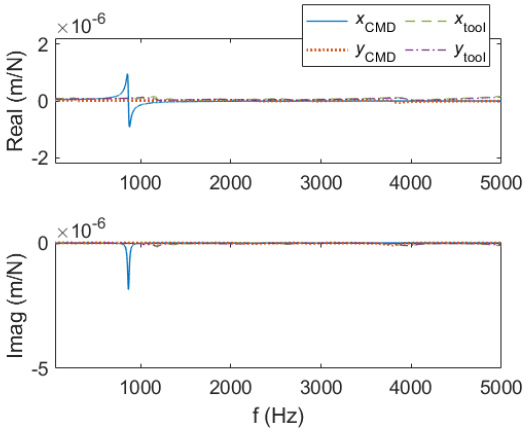

FIGURE 3. Modal fit FRFs of the tool and CMD (damped) for the stability validation setup.

The tool description and cutting conditions for the stability validation is presented in Table 2. The dominant system dynamics are provided in Table 1 for the Al 6061-T6 CMDs. The natural frequency for the CMD's x-direction changed slightly after each cut because the material was removed from the workpiece; therefore, the workpiece was replaced after every test cut. The Al 6061-T6 workpiece dimensions were nominally 30 mm x 70 mm x 30 mm with a mass of 164 ± 1 g.

Table 2. Tool description and cutting parameters for stability trials.

Diameter (mm)	Teeth	Insert material
15.88	1	Coated carbide (Kennametal EC 1402FLDJ)
Cutting parameters for up milling tests		
Spindle speed (rpm)	4900	
Feed per tooth (mm)	0.1	
Axial depth (mm)	Various	
Radial depth (mm)	2 (19% radial immersion)	

To explore the stability behavior in detail, a grid of time-domain simulations was completed at spindle speeds of 4000 rpm to 5000 rpm (10 rpm steps) and axial depth from 0.1 mm to 20 mm (0.1 mm steps). The stability behavior was automatically determined by a synchronous sampling strategy. The results of this strategy are represented by the stability maps in Figs. 4 and 5. Stable cutting behavior can be identified from periodically sampled points. If the points repeat

with each revolution, then only forced vibration is present and the cut is stable. If the points do not repeat with each revolution, then either secondary Hopf or period-n bifurcations are present. The stability metric is defined by Eq. 1:

$$M = \sum_{i=2}^{N} \frac{|x_s(i) - x_s(i-1)|}{N} \quad (1)$$

where, x_s is a vector of sampled x direction displacements and N is the number of samples. For a stable cut, the absolute value of the difference between subsequent points is ideally zero; as a result, their normalized sum is also ideally zero [2, 3].

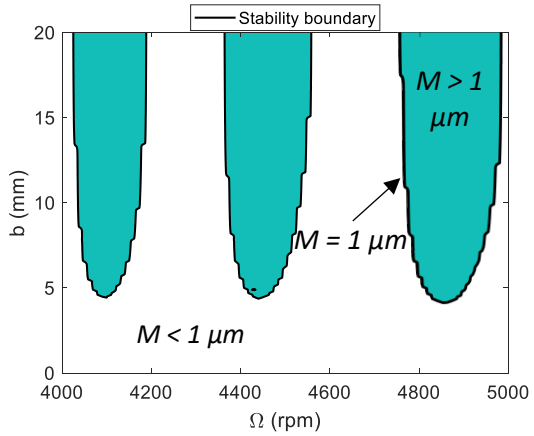

FIGURE 4. Time-domain stability limit (TDS), solid black line with teal infill, expressed as a function of spindle speed, Ω, for the Al 6061-T6 CMD (no added damping).

For an unstable cut, the difference between subsequent points is nonzero and their normalized sum is greater than zero [2, 3]. For this research, the limiting value of the metric, M, was selected to be 1 µm. To interpret the stability map, stable zones are represented by the white area bounded by the stability contour, where M < 1 µm; the stability boundary is represented by the dark stability contour, where M = 1 µm; and unstable zones are represented by the dark green region bounded by the stability contour, where M > 1 µm.

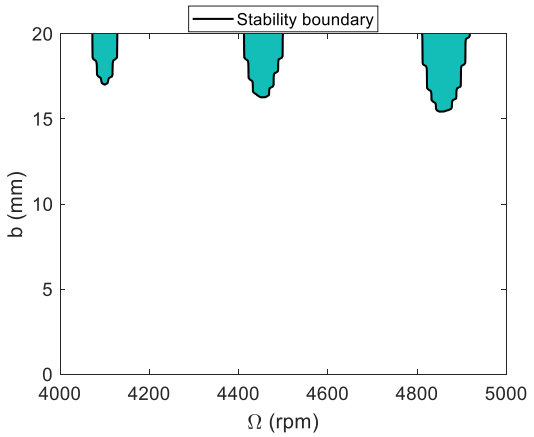

FIGURE 5. Time--domain stability limit (TDS), solid black line with teal infill, expressed as a function of spindle speed, Ω, for the Al 6061-T6 CMD (damped).

RESULTS

The milling stability validation proceeded by completing tests cuts on the Al 6061-T6 CMD until the critical depth of cut was reached. Afterwards, the same procedure was performed for the damped Al 6061-T6 CMD to demonstrate the increase in the stability limit due to the modification of the viscous damping coefficient by the addition of the passive damping medium.

To establish stability, the CMD x-direction displacement and velocity signals were sampled once per revolution at the spindle rotating frequency. This periodic sampling approach was used to determine if the milling response was synchronous with the spindle rotation or not by constructing Poincaré maps (the periodically sampled displacement versus the periodically sampled velocity) for both experiment and prediction. To interpret these Poincaré maps, if the cut is stable (i.e., it exhibits forced vibration only), the data repeats with each spindle revolution and the sampled points appear at one location. If self-excited vibration (chatter or secondary Hopf bifurcation) occurs, however, an elliptical distribution of sampled points is observed due to the presence of both the chatter frequency and the tooth passing frequency and its harmonics. The cutting test cases for the Al 6061-T6 CMDs are presented in Tables 3 and 4, respectively. The displacement and velocity profiles for the first table entry in Table 3 {4900 rpm, 1 mm} is presented in Fig. 6 to demonstrate the good agreement between the simulated (top plot) and experimental (bottom plot) results. Note that the entry and exit transients were removed before plotting.

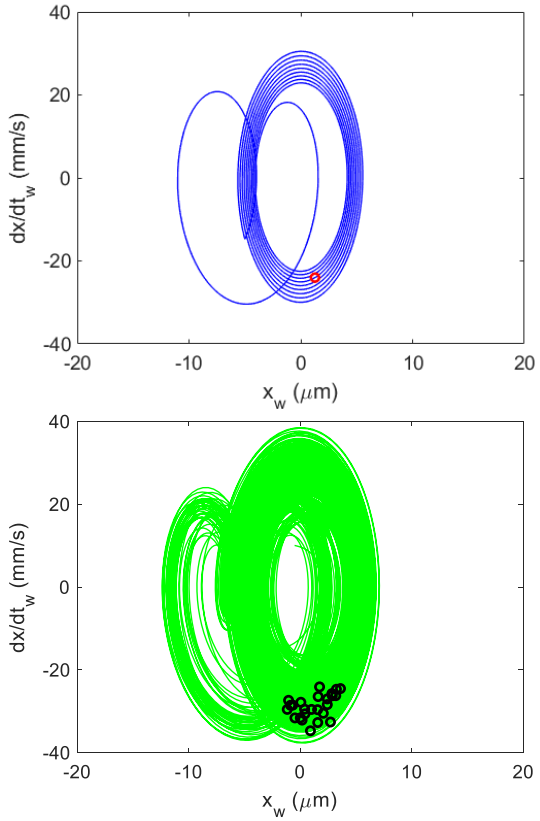

FIGURE 6. Al 6061-T6 (no added damping) Poincaré maps for stable cutting at {4900 rpm, 1 mm}. Predicted (top) and measured (bottom).

Good agreement is observed in each case. It was found that the Al 6061-T6 CMD had a critical stability limit of approximately 4.3 mm. For cases of regenerative chatter (see Fig. 7), the displacement amplitude approaches, and in some cases exceeds, the permissible displacement before exceeding the yield strength for the flexure leaf elements. Therefore, the CMD's critical stability limit is directly dependent on the flexure element design parameters.

Next, the stability results are presented for the damped AL 6061-T6 CMD, see Figs. 8 and 9. Again, good agreement between prediction and measurement was observed at all test locations. There was a significant increase in the stability limit with respect to its undamped counterpart. The maximum allowable depth of cut for the cutting tool was reached without an unstable result. The critical depth of cut for the damped Al 6061-T6 CMD was predicted to be 15.4 mm. The ability to modify the dynamic response of the dynamometer is unique to the proposed CMD and can be leveraged in future dynamometer designs.

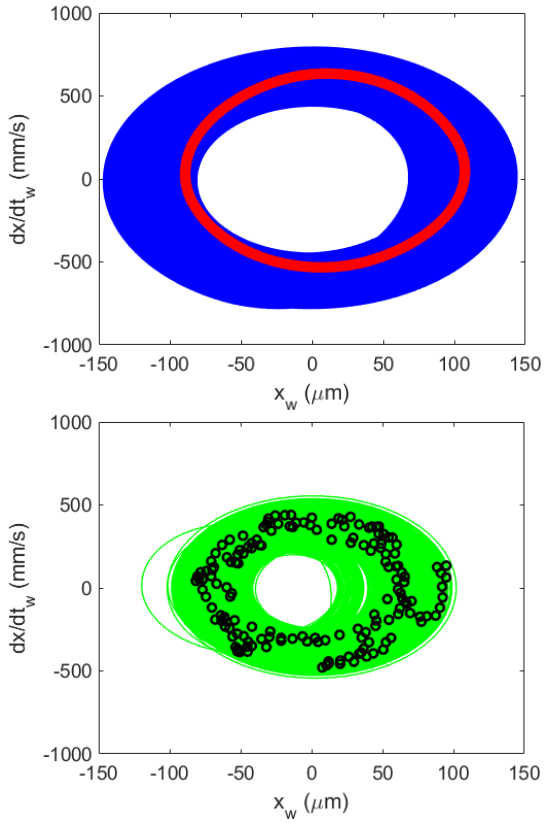

FIGURE 7. Al 6061-T6 (no added damping) Poincaré maps for stable cutting at {4900 rpm, 6 mm}. Predicted (top) and measured (bottom).

Table 3. Cutting conditions and stability metrics for the Al 6061-T6 CMD (no added damping).

Spindle speed (rpm)	Axial depth (mm)	Radial depth (mm)	Metric, M (μm)
4900	1	3	0.32
4900	2	3	0.57
4900	3	3	0.51
4900	4	3	1.16
4900	5	3	58.80
4900	6	3	49.35

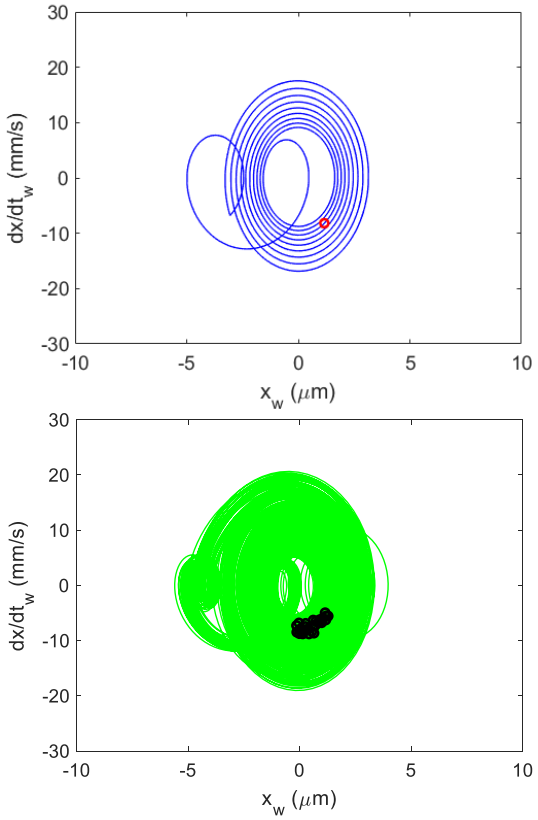

FIGURE 8. Al 6061-T6 (damped) Poincaré maps for stable cutting at {4900 rpm, 1 mm}. Predicted (top) and measured (bottom).

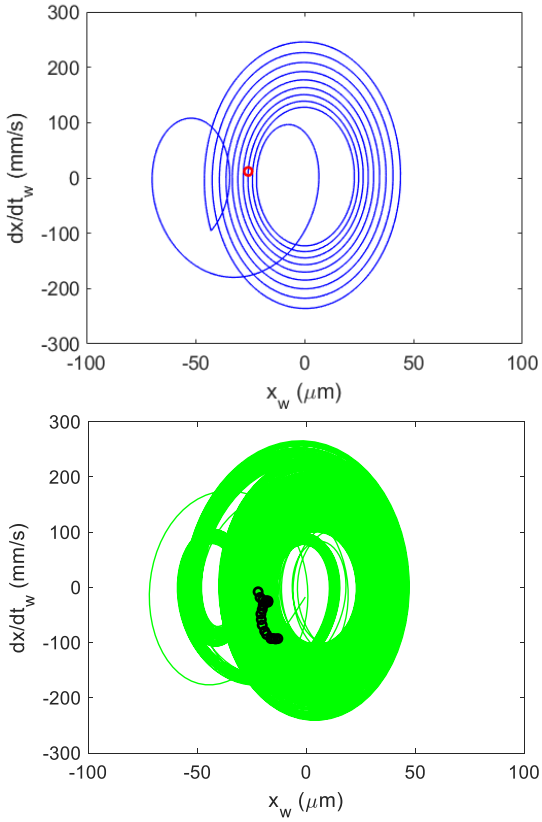

FIGURE 9. Al 6061-T6 (damped) Poincaré maps for stable cutting at {4900 rpm, 14 mm}. Predicted (top) and measured (bottom).

Table 4. Cutting conditions and stability metrics for the Al 6061-T6 CMD (damped).

Spindle speed (rpm)	Axial depth (mm)	Radial depth (mm)	Metric, M (µm)
4900	1	3	0.10
4900	2	3	0.20
4900	3	3	0.18
4900	4	3	0.24
4900	5	3	0.24
4900	6	3	0.32
4900	7	3	0.33
4900	8	3	0.30
4900	9	3	0.88
4900	10	3	0.31
4900	11	3	0.73
4900	12	3	0.36
4900	13	3	0.34
4900	14	3	0.83

CONCLUSIONS

In all machining applications, a limitation on the allowable axial depth of cut is regenerative chatter. Available dynamic force measurement (dynamometer) systems often rely on specific piezoelectric transducer arrangements and the structural dynamics of the system are often assumed to be rigid. Here, the system structural dynamics are a principal element in the design space which are altered by material selection, flexure element geometry, and flexure element arrangement [4].

With the ability to modify the dynamic response of a cutting force dynamometer, the stability limit and bandwidth can be modified through an increase in stiffness or damping. A passive damping approach was used to increase the critical stability limit for an Al 6061-T6 CMD compared to its original counterpart. It was shown that the viscous damping coefficient increased by 130%. As a result, the milling process model simulation revealed that the critical stability limit increased from 4.3 mm to 15.4 mm at a selected

spindle speed. The simulation results were validated using measured displacement and velocity signals to construct Poincaré maps. Good agreement was observed for all test cases. The milling stability tests are summarized in Fig. 10 and Fig. 11 for the undamped and damped Al 6061-T6 CMDs, respectively [4].

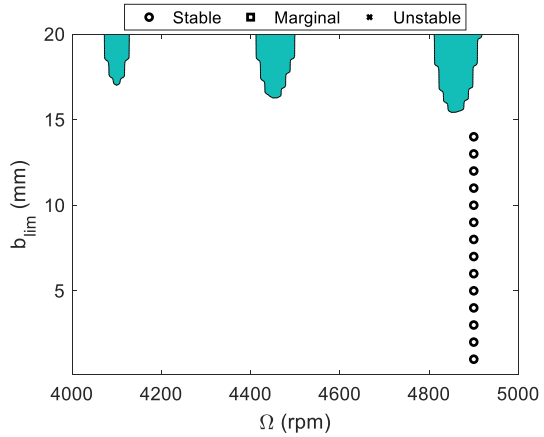

FIGURE 10. Milling stability validation for the Al 6061-T6 CMD (no added damping).

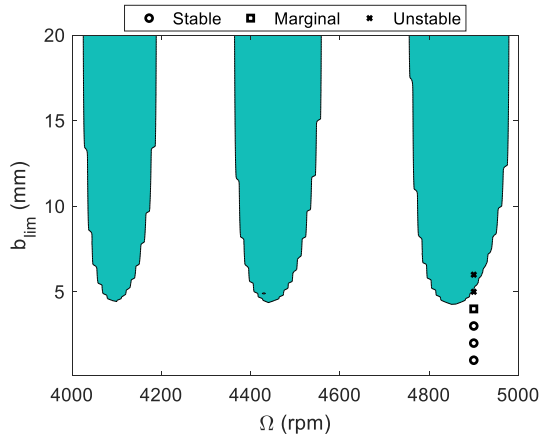

FIGURE 11. Milling stability validation for the Al 6061-T6 CMD (damped).

ACKNOWLEDGEMENTS

This manuscript has been authored by UT-Battelle, LLC, under contract DE-AC05-00OR22725 with the US Department of Energy (DOE). The US government retains and the publisher, by accepting the article for publication, acknowledges that the US government retains a nonexclusive, paid-up, irrevocable, worldwide license to publish or reproduce the published form of this manuscript, or allow others to do so, for US government purposes. DOE will provide public access to these results of federally sponsored research in accordance with the DOE Public Access Plan (http://energy.gov/downloads/doe-public-access-plan).

REFERENCES

[1] Smith, S.T., 2000, Flexures: Elements of Elastic Mechanisms, CRC Press, Boca Raton, FL.

[2] Honeycutt, A., and Schmitz, T., 2016, A numerical and experimental investigation of period-n bifurcations in milling, Journal of Manufacutring Science and Engineering, 139/1: 011003.

[3] Gomez, M., Betters, E., Eichenberger, J., Delio, T.S., Schmitz, T.L., 2019, Laser Doppler vibrometry for machining dynamics analysis, Proceedings of the 34th American Society for Prec. Engineering Annual Meeting.

[4] Gomez, M. and Schmitz, T., 2020, Low-cost constrained-motion dynamometer for milling force measurement, Manufacturing Letters, 25: 34-39.

TOOL WEAR EVALUATION USING A CONSTRAINED-MOTION DYNAMOMETER

Michael Gomez[1*] and Tony Schmitz[1,2]
[1]Manufacturing Science Division
Oak Ridge National Laboratory
Oak Ridge, TN, 37830, USA
[2]Department of Mechanical, Aerospace, and Biomedical Engineering
University of Tennessee, Knoxville
Knoxville, TN, 37996, USA

ABSTRACT
This paper describes in-process tool wear evaluation using a constrained-motion cutting force dynamometer (CMD). Tool condition monitoring is traditionally categorized by two approaches: direct and indirect. Direct approaches provide a quantitative wear measurement. Examples of direct measurements include the use of microscopes for visual inspection, laser beams in optical tool setting systems, and electrical resistance in contact tool setting stations. Practical limitations, such as line-of-sight obstruction, coolant interference, and access problems during machining, limit the wide-spread use of these techniques. Alternatively, indirect measurement approaches allow the tool condition to be quantified through auxiliary signals. Examples include acoustic emission, temperature, motor power and current, and cutting force. The benefit of indirect techniques is that they are more suitable for shop-floor implementation because the machining processes can be continuously monitored via sensing devices which quantify the process performance or provide information for process optimization [1].

The focus of this work is force measurement. Initial results are presented which examine the variation in wear features and cutting force as the tool wear progresses from a new tool condition to a significantly worn state.

KEYWORDS
Milling, force, milling, tool wear

INTRODUCTION

The CMD combines a flexure-based constrained-motion mechanism with a low-cost optical displacement sensor, where displacement is inferred from an optical interrupter. In this approach, a knife edge is attached to the movable platform and partially blocks the optical beam during motion caused by the milling force. The displacement is used to calculate force from the known CMD structural dynamics. The result is low-cost, high accuracy dynamic force measurement. This sensor has the added benefit of a compact footprint and fast response time (10 µs) without the need for a supplementary amplifier [2-3]. A primary use of this low-cost technology is to evaluate tool wear during machining operations. The proposed solution is to: 1) select a standard witness sample (such as 6061-T6 aluminum) and mount it to the dynamometer; 2) determine the expected cutting force level for pre-defined axial and radial depths of cut for this sample; 3) periodically perform test cuts on the sample as the tool wears in the work material; and 4) alert the machinist that a tool change is required when the force grows above a pre-selected level.

TOOL WEAR VALIDATION

To demonstrate this concept, preliminary cutting tests were performed on a Haas TM-1 CNC vertical milling machine. An Inconel® 718 AMS 5596 workpiece was mounted in a vise and a CMD was mounted to the table with an Al 6061-T6 witness sample mounted to the moving platform. A single flute, 19.05 mm diameter, endmill was used to perform machining passes at a 1.9 mm radial depth of cut (10% radial

[1] Notice: This manuscript has been authored by UT-Battelle, LLC, under contract DE-AC05-00OR22725 with the US Department of Energy (DOE). The US government retains and the publisher, by accepting the article for publication, acknowledges that the US government retains a nonexclusive, paid-up, irrevocable, worldwide license to publish or reproduce the published form of this manuscript, or allow others to do so, for US government purposes. DOE will provide public access to these results of federally sponsored research in accordance with the DOE Public Access Plan (http://energy.gov/downloads/doe-public-access-plan).

immersion) and 3 mm axial depth of cut at a cutting speed of 50 m/min. The insert was uncoated carbide (Sandvik 390R-070204E-NL H13A). The cutting test cases for the Inconel ® 718 work material is presented in Table 1. In-situ vibration signals were collected using the knife-edge sensor on the CMD and converted to force using the structural deconvolution procedure [2-3]. A pair of optical microscopes (DinoLite Pro-AM4137) were used to record wear features on the rake and flank face of the cutting insert during tool wear testing. The experimental setup is depicted in Fig. 1. An inductive power sensor (Powertek UPC 120V) was used to monitor spindle power consumption during the tool wear tests.

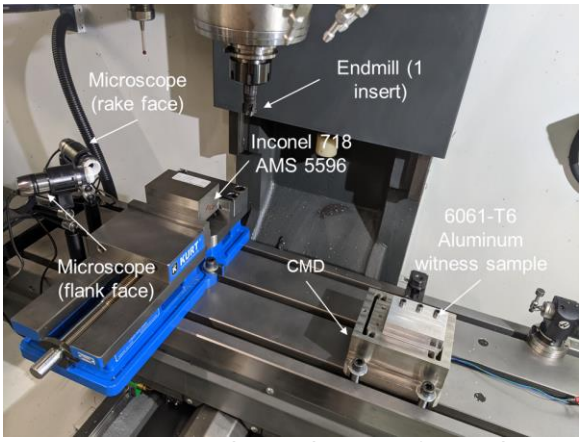

FIGURE 1. Experimental setup for tool wear measurement.

INITIAL RESULTS

To begin, a reference cutting force signal was recorded using the cutting parameters listed in Table 1. In situ vibration signals were collected using the knife-edge sensor on the CMD and subsequently converted to force using a structural deconvolution procedure [2-3]. The corresponding force is plotted in Fig. 2. For this research, the measured milling forces were parsed to capture the steady-state behavior and were then separated into 70 individual tooth impacts and averaged. This provides a compact representation of the cutting force signal over a brief time period.

Table 1. Tool description and cutting parameters for tool wear trials.

Diameter	Teeth	Insert material
19.05 mm	1	Uncoated carbide (Sandvik 390R-070204E-NL H13A)

Cutting parameters for down milling tests	
Spindle speed	835 rpm
Feed per tooth	0.1 mm
Axial depth	3.0 mm
Radial depth	1.9 mm (10% radial immersion)

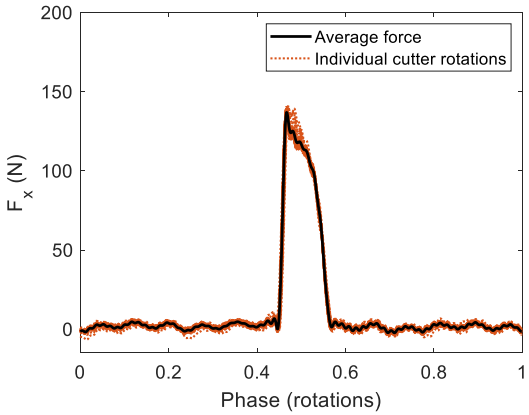

FIGURE 2. Measured cutting forces over 70 revolutions of the cutting tool (dotted red line) and their average (solid black line) for a milling operation using a new cutting insert.

The aluminum witness sample force measurement was followed by a 100 mm test cut on the Inconel® 718 work material. The normalized spindle power consumption for these tests is shown in Fig. 3. Note that there is a significant increase in power consumption between Trials 1 and 2 which is confirmed by the wear transition between the 'New insert' and the 'State 1' wear condition.

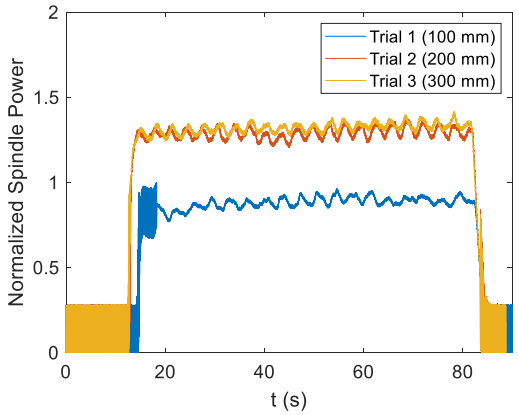

FIGURE 3. Normalized power consumption for the cutting tests in the Inconel ® 718 AMS 5596 work material.

In this research, ‘Trials’ indicate tests performed in the Inconel® 718 work material while ‘States’ indicate the reference tests performed in Al 6061-T6 on the CMD. Following each cutting trial, the tool wear condition was recorded using a pair of optical microscopes. These results are shown in Fig. 4. The maximum flank wear width (FWW) was recorded and as expected, the FWW increased with cutting time.

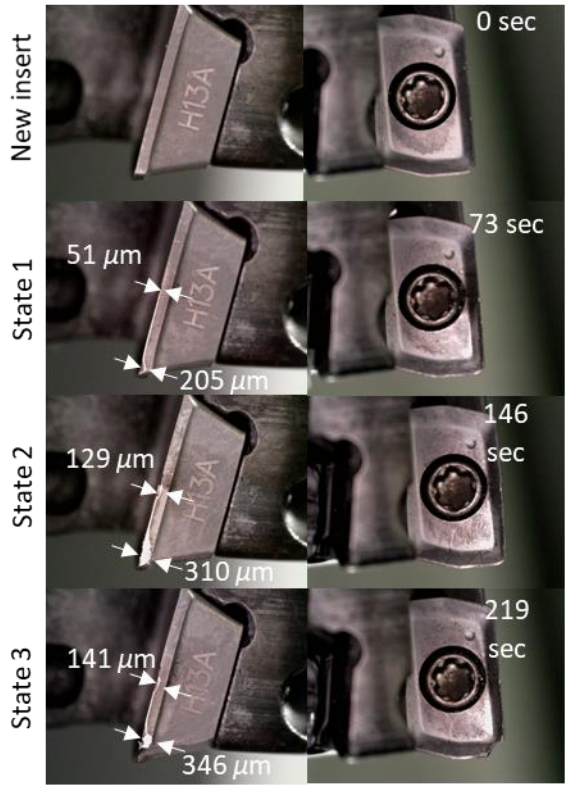

FIGURE 4. Tool wear progression. In the images, the flank face is shown by the left column and the rake face is shown by the right column.

Once the tool wear condition was measured, a cutting test was performed on the Al 6061-T6 witness sample affixed to the CMD. The purpose of these trials was to monitor the growth in cutting force levels as the tool progresses from a new to significantly, and in some cases, catastrophic wear levels. The normalized spindle power for the Al 6061-T6 witness sample is shown in Fig. 5. Traditionally, spindle power measurements are used to classify the tool wear condition. In this case, there is not a clear difference between the nominal reference force measurement (New insert) and subsequent wear states (States 1-3). This is expected since the power consumption required for Al 6061-T6 material removal considerably smaller than for the same cutting parameters in the Inconel® work material.

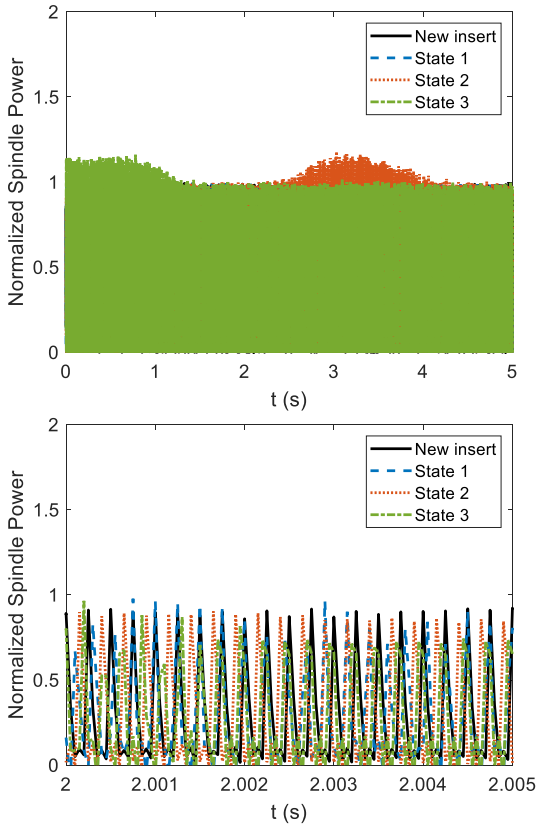

FIGURE 5. Normalized power consumption for the cutting tests on the Al 6061-T6 witness sample work material. These are indicative of the wear states in Fig. 4.

Finally, the averaged CMD cutting forces for unidirectional trials are presented for the various levels of tool wear progression, Fig. 6. Note that the cutting force signature varies depending on the tool wear condition, Fig. 4. In this case, the cutting force signature is slightly increasing with increased tool wear. In many instances, a tool is considered worn once a FWW of 300 μm is achieved. As shown by Figs. 4 and 6. The various ‘States’ demonstrate the subtle variability in cutting forces which are not detectable in the respective spindle power measurements; see Fig. 5.

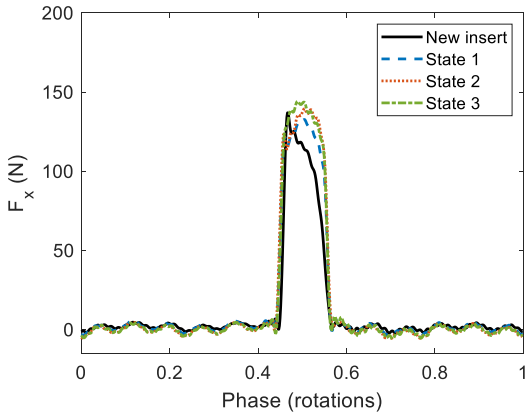

FIGURE 6. Variation in cutting force with tool wear progression in the Al 6061-T6 witness sample work material. The state levels are described by the images in Fig. 4.

FUTURE WORK

Follow-on efforts will focus on performing additional tool wear trials in various work materials including low-carbon steel alloys, titanium alloys, and Inconel® alloys. As noted previously, the research methodology is to: 1) select a standard material sample (such as 6061-T6 aluminum) and mount it to the dynamometer; 2) determine the expected cutting force level for pre-defined axial and radial depths of cut for this sample; 3) periodically perform test cuts on the sample as the tool wears; and 4) alert the machinist that a tool change is required when the force grows above a pre-selected level. The resulting cutting force signals are considered digital signatures which can identify wear features and expected cutting forces in real-time which can reduce the risk of scrapped parts, cyber-intrusion, and operator/programmer error.

ACKNOWLEDGEMENTS

This manuscript has been authored by UT-Battelle, LLC, under contract DE-AC05-00OR22725 with the US Department of Energy (DOE). The US government retains and the publisher, by accepting the article for publication, acknowledges that the US government retains a nonexclusive, paid-up, irrevocable, worldwide license to publish or reproduce the published form of this manuscript, or allow others to do so, for US government purposes. DOE will provide public access to these results of federally sponsored research in accordance with the DOE Public Access Plan (http://energy.gov/downloads/doe-public-access-plan).

REFERENCES

[1] Byrne, G., Dornfeld, D., Inasaki, I., Ketteler, G., König, W., Teti, R., 1995, Tool condition monitoring (TCM) – The status of research and industrial application, CIRP Annals, Vol. 44. Iss. 2: 541-567

[2] Gomez, M. and Schmitz, T., 2020, Low-cost, constrained-motion dynamometer for milling force measurement, Manufacturing Letters, 25: 34-39.

[3] Gomez, M., Honeycutt, A., Schmitz, T., 2021, Hybrid manufactured dynamometer for cutting force measurement, Manufacturing Letters, 29: 65-69.

MACHINING CONSIDERATIONS FOR WAAM PREFORMS

Jake Dvorak[1], Aaron Cornelius[1], Greg Corson[1], Ross Zameroski[1], Leah Jacobs[1], Joshua Penney[1], and Tony Schmitz[1,2]
[1]Department of Mechanical, Aerospace, and Biomedical Engineering
University of Tennessee, Knoxville
Knoxville, TN 37996, USA
[2]Manufacturing Science Division
Oak Ridge National Laboratory
Oak Ridge, TN, 37830, USA

ABSTRACT
Hybrid manufacturing consisting of metal additively manufactured preforms and computer numerical control (CNC) machining has been established to be an effective method for higher material use rates than traditional manufacturing methods. However, hybrid manufacturing introduces unique challenges. Near-net shape designs are typically selected, which results in a smaller margin for part placement within the stock. Consequently, when moving the workpiece between deposition and machining systems, the work coordinate system must be maintained to ensure part placement. Additionally, less stock material reduces the preform stiffness, which limits the material removal rates during machining. To date, a comprehensive digital twin methodology to accurately predict the machining outcome has not been presented.

KEYWORDS
Wire-arc additive, milling, hybrid manufacturing, fiducial, structured light scanning, machining dynamics

INTRODUCTION
The key topics of this research effort are hybrid manufacturing and the associated digital twin. While many digital twin descriptions are available [2-5], for the purposes of this study the working definition is: the digital counterpart, or twin, of a physical process that uses models and real-time data to predict the behavior of the physical process. Hybrid manufacturing encompasses a sequence of activities that integrate additive manufacturing (AM) with other processes. Here, AM + metrology + machining activities are used to produce the final part with geometry and surface finish that meet the designer's intent. The digital twin for this particular application of hybrid manufacturing includes:

- the AM material, parameters, and path used to fabricate the preform
- the preform geometry
- the preform structural dynamics
- the machining parameters and tool path
- the tool-holder-spindle-machine assembly structural dynamics
- a physics-based model to relate the preform material's cutting force model, preform and tool-holder-spindle-machine assembly structural dynamics, and milling stability [1]
- the final part geometry and surface finish.

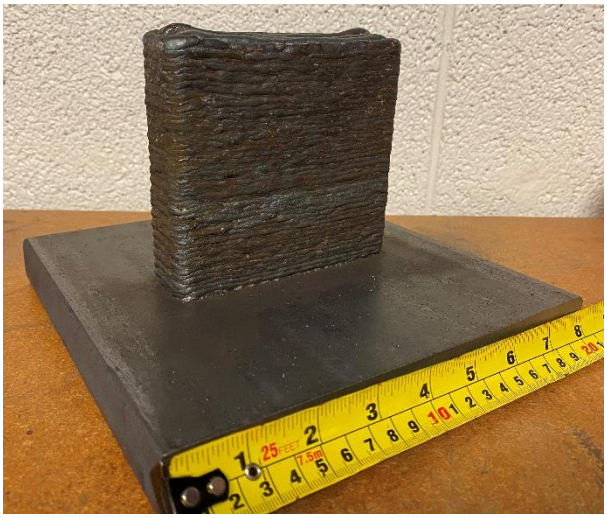

FIGURE 1. Wall preform as printed on a baseplate.

In this research, the focus is the digital twin information associated with the machining steps. This includes: 1) a structured light scan of the AM preform with temporary fiducials used to identify a local coordinate system; 2) selection of the cutting tool used to machine the preform; 3) measurements of the tool-holder-spindle-machine and preform frequency response functions, or FRFs, which describe their vibration

behavior; 4) the milling parameters, which include the axial and radial depths of cut, spindle speed, and feed per tooth values; 5) the tool paths generated by the CAM software; and 6) the machined part geometry and surface finish. For the purposes of demonstrating these steps a WAAM wall-shaped preform was printed on a steel baseplate with dimensions as shown in Fig. 1.

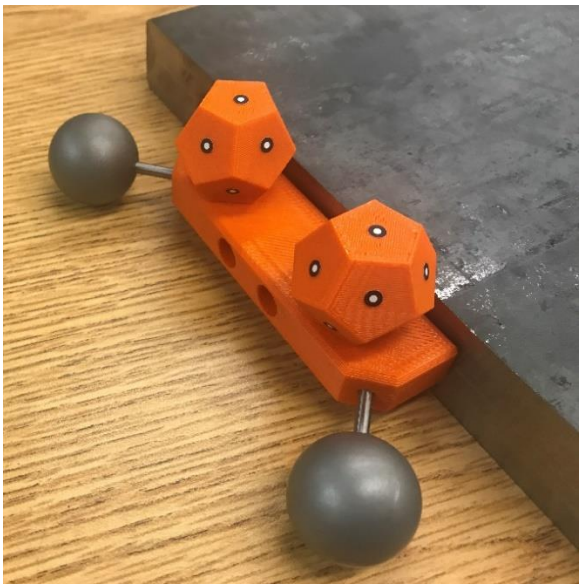

FIGURE 2. External fiducial apparatus that supports the fiducials (25.4 mm diameter, satin-finish spheres) and dodecahedron scan targets.

EXTERNAL FIDUCIAL APPARATUS

An external fiducial apparatus was designed and fabricated using fused filament fabrication (FFF) with ABS material. The apparatus volume is small to limit material use and avoid obscuring the preform during scanning, while remaining generic for use with various preform geometries. The fiducial apparatus serves two major purposes. First, it supports fiducials (tooling spheres in this case) that can be located in both the scan and in the milling machine. Second, it supports targets that the scanning software requires to maintain tracking across scans. Therefore, targets are not needed on the baseplate or part itself. The fiducial apparatus was attached via two threaded fasteners on both the left and right side of the baseplate; see Fig. 2. The left fiducial apparatus contained two spheres while the right contained only one sphere (not shown).

The fiducials were 25.4 mm diameter satin-finish spheres designed for optical scanning calibration (Bal-tec SAT-B100). The spheres were attached to the apparatus using press-fit dowel pins. Because it is necessary for the spheres to be accessible to both the structured light scanner (line-of-sight imaging) and the spindle-mounted probe on the milling machine, the fiducial apparatus was designed to hold the fiducials at a 45 degree angle to maximize probe access. It was not necessary to specifically locate the spheres since their positions are measured using the structured light scanner.

The scanning targets were placed on the faces of two dodecahedrons per fiducial apparatus (four total). The dodecahedron was chosen to provide multiple faces/targets at any viewing angle. The structured light scanning system used in this research (GOM ATOS Q) requires at least three targets to be in view from one scan to the next.

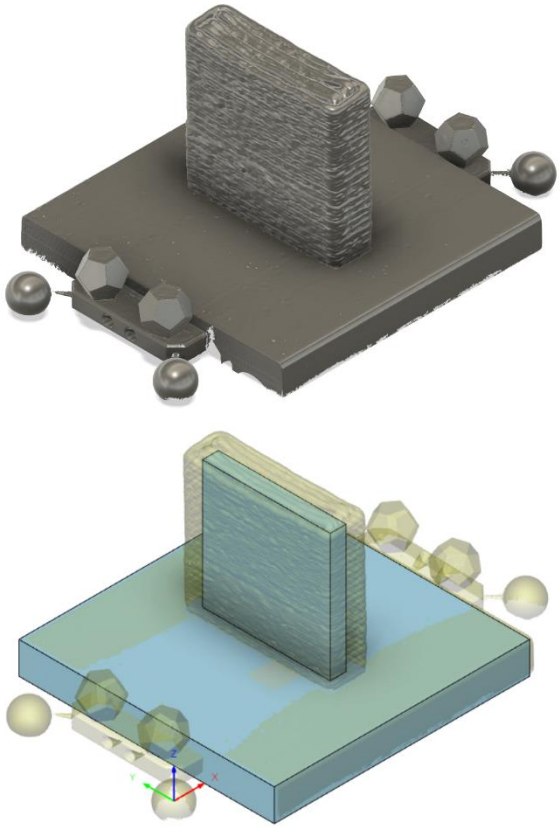

FIGURE 3. Scan of wall with attached fiducials (top). Alignment of wall geometry inside the preform (bottom).

SCAN TO CAM

An initial scan of the preform with fiducials is displayed in Fig. 3. The computer-aided design (CAD) digital preform model was aligned to the scan using the three planes of the base plate. The

final alignment of the scan to preform model is also shown in Fig. 3. This alignment was used to visually ensure that the preform model was fully contained within the scan (as-printed preform).

After the preform scan and model were aligned, the shared coordinate system was established. The coordinate system was defined kinematically based on a series of best-fit primitives [6]. The center of the first sphere was selected as the part origin, fixing three translational degrees of freedom. The bottom of the build plate was defined the Z axis, fixing two rotational degrees of freedom. The line between the centers of the first and second spheres (left and right front spheres in Fig. 3) defined the X axis, fixing the final rotational degree of freedom. The third sphere was redundant due to the build plate geometric constraint and was not used to define the coordinate system. The coordinate system is displayed in Fig. 3.

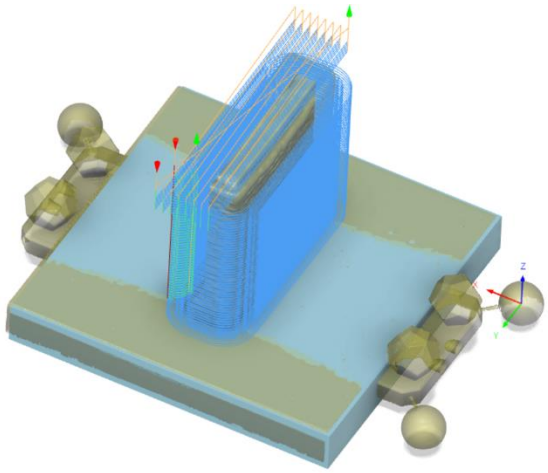

FIGURE 4. CAM toolpaths for wall machining.

Toolpaths were then defined relative to the established coordinate system within the CAM software (Fig. 4). The scan was imported directly as a stock model to enable full digital simulation. A snapshot of the simulation is shown in Fig. 5. This simulation, again, provided verification that the model was fully contained within the preform. Other benefits enabled by an accurate stock model include collision detection and the actual surface location for setting the initial radial depth of cut to engage the cutter the desired amount into the rough WAAM surface.

The preform was then loaded into a Haas VF-4 CNC milling machine and clamped to the table using a vise; this aligned the bottom of the baseplate to the machine table and defined the same Z axis direction for each. To fully relate the preform and machine coordinate systems, two tooling spheres (left and right front spheres in Fig. 3) were probed using the on-machine touch trigger probe and built-in routines to find the sphere centers. The line between these centers described the preform's X axis. A coordinate rotation about the Z axis was then performed to align the machining X direction with the preform X direction. No specific probing of the preform was required since the tooling spheres were already related to the preform location in the scan and, therefore, the CAM stock model used to generate the toolpaths.

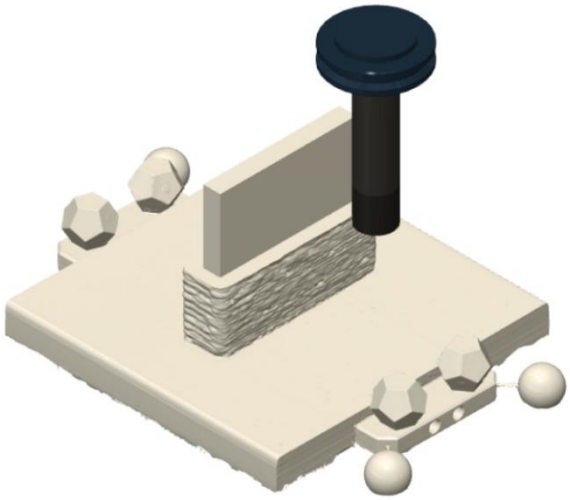

FIGURE 5. CAM simulation of wall machining.

MILLING PARAMETER SELECTION

A four flute, 25.4 mm diameter end mill with a 25.4 mm flute length (YG1 model UGMF73912) was used to machine the preform. The endmill had a 103 mm extension length from the tool holder and had a reduced shank diameter to enable machining of the full wall height. To determine optimum milling parameters a tap test was performed both at the tool's free end and the preform's top corner to measure the frequency response functions, or FRFs. Figure 6 shows that the tool was much less stiff (i.e., larger amplitudes in the real and imaginary parts of the complex-valued FRFs) than the preform and therefore dominated the selection of stable milling parameters. The tool and preform FRFs were then used to generate the corresponding stability maps (Fig. 7), where the specific cutting force for the steel preform was 1985 N/mm^2. An initial axial depth of cut of 2 mm and spindle speed of 5300

rpm were selected to obtain stable (chatter-free) cutting conditions. The corresponding surface speed was 422.9 m/min and the feed per tooth was 0.026 mm

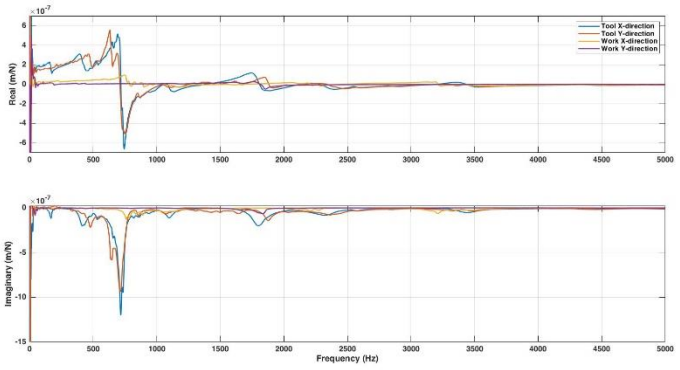

FIGURE 6. Real and imaginary parts of the tool and preform FRFs in the X and Y directions.

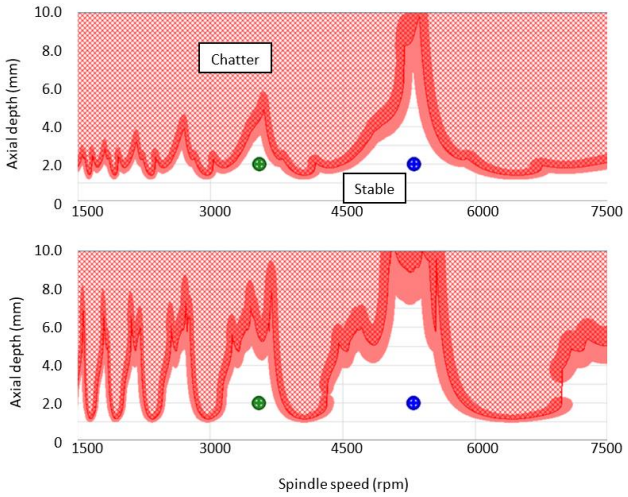

FIGURE 7. Stability map for X direction milling (top). Stability map for Y direction milling (bottom). The blue marker designates the parameters for the initial 10 mm of material removal (near the perform top). The green marker designates the parameters for the remaining preform height.

The machining process consisted of two primary operations completed in a single setup. First, the perform top was faced. Second, the perform sides were machined. The top facing nominally consisted of four axial steps down; however, an extra step was added due to the discovery of internal voids created by the WAAM process. This reduced the wall's final height by 2 mm. The side milling operations included three radial steps: 3.05 mm radial depth to clean up the preform's initial rough surface; 5.08 mm to remove the bulk of the material; and 2.54 mm for the final pass. A photograph of the preform after facing the top and completing a few axial steps down the perform sides is provided in Fig. 8.

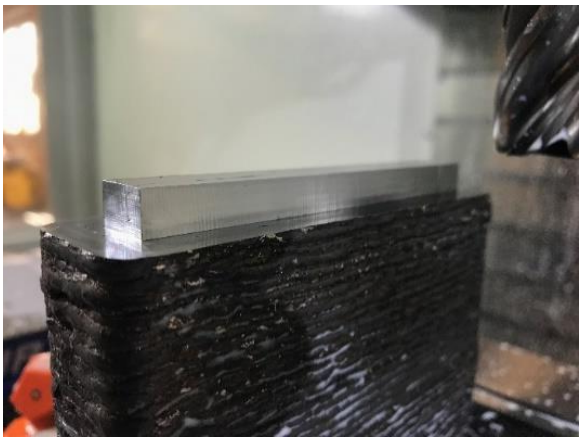

FIGURE 8. Photograph during preform milling.

At a height of 10 mm from the preform top, the spindle speed was reduced to 3550 rpm since initial wear was observed on the endmill. The reduced cutting speed (283.3 m/min) decreased the wear rate and enabled the wall to the finished, while retaining stable cutting conditions. This second selected point is also identified in the Fig. 7 stability maps.

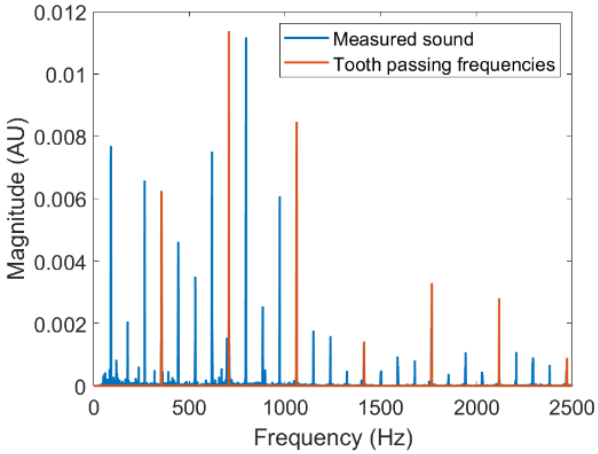

FIGURE 9. Frequency content of sound signal measured during milling at the preform top (5300 rpm).

To verify that the machining conditions were stable, audio data was recorded during machining and the frequency content was evaluated; see Fig. 9. It is observed that the measured sound occurs at the tooth passing

frequency (spindle speed multiplied by the number of teeth), integer multiples of the tooth passing frequency, or runout frequencies (spindle speed and integer multiples). A photograph of the wall after machining is displayed in Figure 10.

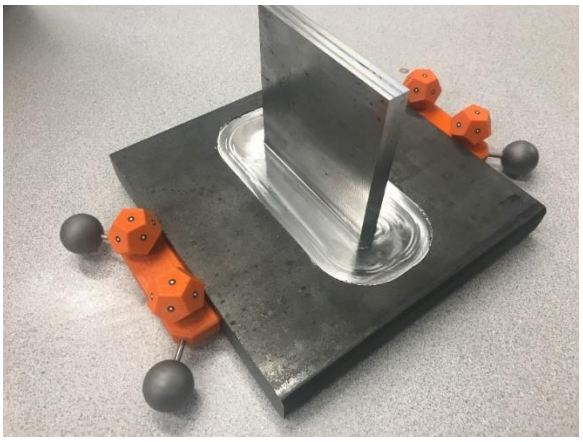

FIGURE 10. Wall geometry after milling. The fiducials are still attached to baseplate.

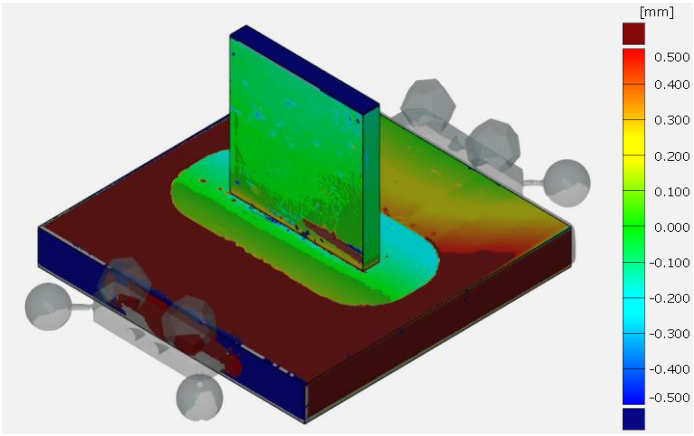

FIGURE 11. Surface deviation between the as-machined scan and the CAD model.

POST-MACHINING MEASUREMENTS

Further measurements were completed after machining to verify the size, shape, and surface finish of the wall. First, a scan was completed of the wall with the fiducials still attached. A surface deviation plot was created in comparison to the intended CAD model; see Fig. 11. Note that the top of the wall shows an error of over 0.5 mm due to the additional facing step completed at the wall top (not originally modeled in CAD). Other significantly negative values are due to voids left by the WAAM process. Positive readings are attributed to tool wear, which exceeded 0.6 mm flank wear width at the end of the cut; see Fig. 12.

FIGURE 12. Tool wear on the most worn relief face after machining.

A stylus profilometer was used to further examine the machined surface. Average roughness (Ra) measurements were performed in the feed direction (Y) at various Z heights in the YZ plane; see Figure 13. These Ra values agree with the expected surface roughness for the selected feed per tooth.

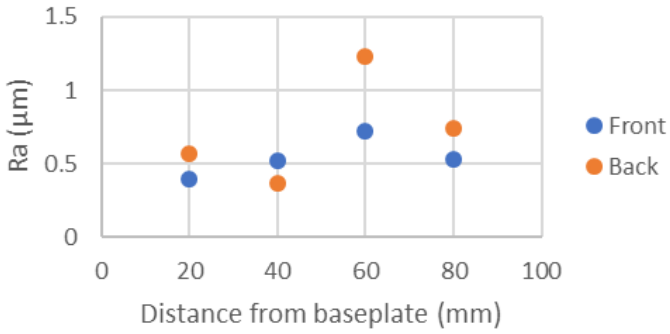

FIGURE 13. Average roughness for selected locations on wall sides.

DISCUSSION

This work demonstrates the value of a digital twin for machining operations in hybrid manufacturing. The combination of the fiducial apparatus and structured light scanning provide not only an accurate stock model, but also a connection between the preform and machine coordinate systems. This reduces setup time on the CNC machining center, confirms that the desired part geometry is contained within the as-printed preform for the machining orientation, and enables accurate CAM simulation of the toolpaths.

Measurement of the preform and tool tip FRFs enables selection of machining parameters that provide stable cutting conditions which respect

the limitations imposed by the process dynamics, while obtaining the highest possible metal removal rate and, therefore, highest process efficiency. Similarly, by considering the preform dynamics, the initial preform design can be informed (or modified) to ensure that the preform does not significantly reduce metal removal rates due to low dynamic stiffness. This can be a natural outcome of "too near-net" shape designs.

While measuring the preform and tool tip dynamics enables the pre-process selection of stable cutting parameters with high productivity, tool wear and measurement uncertainties can lead to uncertainty in the stability map. Therefore, in-process signals, such as the audio signal during machining, can serve to augment the predictions and identify unwanted outcomes, such as chatter.

Post-machining part measurements are used to confirm that the intended geometry, surface finish, and dynamics are achieved. In this case, a stylus profilometer was used, although optical methods are also available. Tap testing may also be used to identify natural frequencies, modal stiffness and damping ratio values, and mode shapes of the machined part. FEA comparisons may be completed for comparison.

Collectively, these components form the machining digital twin for hybrid manufacturing. Further work to test this digital twin methodology will include increasingly complex preform and CAD model geometries. This will test the robustness of the methodology while providing further detail on the "manual" step of aligning the stock model and CAD model.

CONCLUSIONS

In this paper, multiple aspects of a machining digital twin for hybrid manufacturing were shown. Temporary fiducials were attached to a WAAM preform and scanned via structured light to define a local coordinate system and CAM stock model. The WAAM preform and tool were tap tested to generate a stability map for the machining process, allowing for tool and milling parameter selection, including axial and radial depths of cut, spindle speed, and feed per tooth. Audio was recorded during machining and surface profilometry was completed post-machining to validate the absence of chatter and expected surface finish. A structured light scan of the final part was taken to compare to the CAD model. The proposed machining digital twin provided an accurate model for the machining process as demonstrated by validation experiments.

ACKNOWLEDGEMENTS

This work relates to Department of Navy award (ONR Award No. N00014-20-1-2836) issued by the Office of Naval Research. The United States Government has a royalty-free license throughout the world in all copyrightable material contained herein.

This manuscript has been authored by UT-Battelle, LLC, under contract DE-AC05-00OR22725 with the US Department of Energy (DOE). The US government retains and the publisher, by accepting the article for publication, acknowledges that the US government retains a nonexclusive, paid-up, irrevocable, worldwide license to publish or reproduce the published form of this manuscript, or allow others to do so, for US government purposes. DOE will provide public access to these results of federally sponsored research in accordance with the DOE Public Access Plan (http://energy.gov/downloads/doe-public-access-plan).

REFERENCES

1. Schmitz, T. and Smith, K.S., 2019, Machining Dynamics: Frequency Response to Improved Productivity, Second Edition, Springer, New York, NY.
2. Tuegel, E.J., Ingraffea, A.R., Eason, T.G. and Spottswood, S.M., 2011. Reengineering aircraft structural life prediction using a digital twin. International Journal of Aerospace Engineering, 2011.
3. Shafto, M., Conroy, M., Doyle, R., Glaessgen, E., Kemp, C., LeMoigne, J. and Wang, L., 2012. Modeling, simulation, information technology & processing roadmap. National Aeronautics and Space Administration, 32, pp.1-38.
4. Grieves, M., 2014. Digital twin: manufacturing excellence through virtual factory replication. White paper, 1, pp.1-7.
5. Boschert, S. and Rosen, R., 2016. Digital twin—the simulation aspect. In Mechatronic futures (pp. 59-74). Springer, Cham.
6. Smith, S.T., Chetwynd, DG., 1992. Foundations of Ultraprecision Mechanism Design. Gordon and Breach Science Publishers, Belgium.

EFFECTS OF SURFACE TREATMENTS ON ABS MECHANICAL PROPERTIES FROM FUSED FILAMENT FABRICATION

Jing-Jing Shen[1], Matthew Robert Patterson[1], Erin Marshall[1], Jake Dvorak[1], Stian Romberg[1], Brett Compton[1], Tony Schmitz[1,2]
[1]Department of Mechanical, Aerospace, and Biomedical Engineering
University of Tennessee, Knoxville
Knoxville, TN 37996, USA
[2]Manufacturing Science Division
Oak Ridge National Laboratory
Oak Ridge, TN, 37830, USA

ABSTRACT
This paper investigates the effect of surface treatments on the material properties of acrylonitrile-butadiene-styrene (ABS) samples printed by fused filament fabrication (FFF). The surface treatments are epoxy coating, abrasive media blasting, and acetone immersion. The measured properties are elastic modulus, tensile strength, yield strength, and fracture strain for ASTM D638 Type-I samples printed on a Stratasys Fortus 250mc printer. Moisture absorption was also studied.

KEYWORDS
Additive manufacturing (AM), fused filament fabrication (FFF), surface treatment, epoxy coating, abrasive media blasting, acetone immersion

INTRODUCTION
Although FFF enables the rapid and low-cost development of new designs, parts produced via FFF typically have reduced mechanical properties compared to those made via traditional methods, such as injection or compression molding. Specifically, insufficient bonding at bead-to-bead interfaces can weaken interlayer adhesion [1]. Moreover, the oblong cylindrical geometry of the extruded beads produces voids that serve as stress concentration sites [2]. The layer-by-layer FFF process can give rise to poor surface finish as a consequence of the staircase effect, necessitating post-treatments for as-printed materials [3-4]. Applying surface treatments that reduce this porosity may also enhance the properties of FFF materials.

Prior efforts have applied solvent treatments in order to improve the mechanical properties of FFF components [3,6-7]. While acetone treatment and water sealants have been studied, epoxy coatings have received less attention in literature. Epoxy coatings can fill resin pores and provide improved mechanical properties over neat ABS [8]. By reducing or creating surface irregularities of parts fabricated through FFF, surface treatments can influence the surface roughness and uniformity of printed parts, impacting their tensile strength and ductility [3]. Mechanical abrasion or acetone treatment may also improve surface finish.

FIGURE 1. Tensile test experimental setup. The ABS specimen is clamped in the universal testing machine.

EXPERIMENTAL SETUP
To examine the surface treatment effects, the following procedure was used.

1. ASTM D638-14 Type-I "dogbone" test specimens were fabricated using a Stratasys Fortus 250mc printer with a $\pm 45°$ raster pattern, 0.18 mm layer height, Blue Stratasys P430 ABS*plus* material from new stock, and a solid infill.

2. Samples were subject to: brush coating with epoxy; media blasting; immersion in an acetone solution; or no treatment.
3. Measurements were made of each sample, and surface morphology was observed using optical microscopy and a surface profilometer.
4. Select samples were submerged in water and weighed every hour for 8 hours to measure mass changes due to water absorption.
5. The surface finish was re-observed and surface roughness values were calculated post treatment.
6. Samples were tested using an MTS Criterion Model 45 universal testing machine at a strain rate of 5 mm/min. (Samples used in water immersion tests were not tested.) See Fig. 1.
7. Surface fracture morphology was observed using optical microscopy.
8. From the tensile test data, elastic modulus, yield strength, tensile strength, and fracture strain for all sample types were calculated; see Fig. 2 for all stress-strain data.

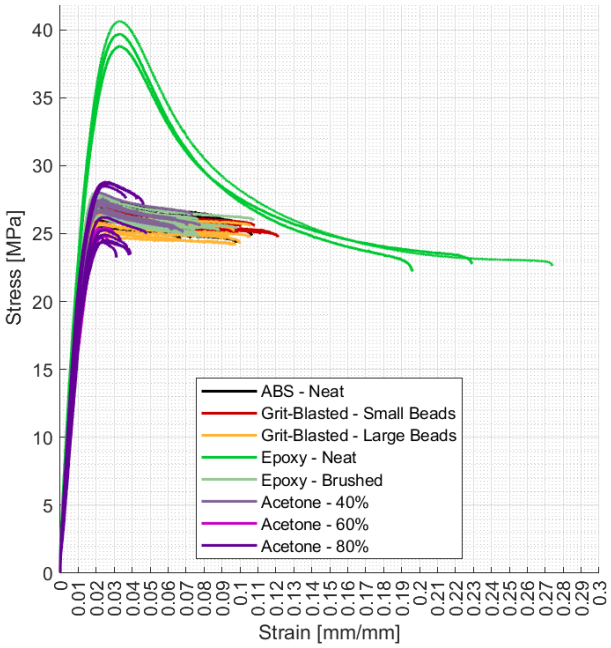

FIGURE 2. Stress-strain curves for all sample types.

MATERIALS AND METHODS

According to the manufacturer specifications (Stratasys) for the ABS filament, the tensile strength of the material is 33 MPa, the elastic modulus is 2.2 GPa, and the fracture strain is 6% [8]. In total, 20 untreated test specimens were printed and tested to use as a baseline for the treated specimens. A Mitutoyo Surftest SJ-210 stylus profilometer [9] was used to measure the surface roughness. For each dogbone test specimen, four regions over the test surfaces were analyzed to determine average roughness (R_a) values, where the ISO 1997 standard was used in conjunction with Gaussian filtering with a 0.25 mm cutoff and λ_s value of 2.5 µm and cutoff number of 9. Optical microscopy was also employed to inspect the topography of both the sample surface and the fracture site (VHX 5000 Keyence digital microscope).

Mechanical Media Blasting

Mechanical media blasting, also known as grit blasting (GB) or sandblasting, entails the use of an abrasive material to roughen, smooth, or shape a given surface using high pressure, localized impacts. The surfaces of printed specimens were subjected to media blasting with either large glass beads (40 to 60 grit, 254 to 365 µm diameter) or small glass beads (200 grit, 84 µm diameter). A total of six passes per side were completed in a manual sandblasting glove box. The media were propelled by compressed air at a pressure of 80 psi (0.55 MPa) with the nozzle approximately 10 cm from the sample surface.

Epoxy Coating

As a surface treatment, epoxy can impart numerous benefits to coated surfaces, including improved mechanical properties such as tensile strength and modulus, as well as thermal and chemical resistance [10]. Smooth-On XTC-3D High-Performance epoxy coating was chosen given its commercial availability and intended application for FFF components. The epoxy resin and hardener were combined in a 2:1 volumetric ratio and mixed for one minute. For each of 18 printed dogbone samples, 0.3 mL of the epoxy mixture was loaded into a syringe and deposited on one side and smoothed using a silicone-tipped doctor blade. After two hours of curing at room temperature, samples were flipped over, and the coating procedure was repeated for the other side.

To determine the performance of the epoxy alone, five additional samples were created by pouring neat epoxy into a silicone mold and cutting dogbone samples using a water-jet system. The only material property provided by the epoxy manufacturer was a Shore Hardness of 80D [11].

Acetone Immersion

Acetone is commonly used for postprocessing AM parts, specifically for polylactic acid (PLA) and ABS. However, prolonged exposure to high concentrations of acetone can affect the part geometry and make parts unsuitable for use [12].

Test specimens were immersed in varying concentrations of liquid acetone. The specimens were fully submerged in either a 40%, 60%, or 80% by volume acetone solution; the balance of the solutions was water. In total, 15 samples were treated for each concentration. In each of three batches, five samples were immersed in the solution for a duration of 10 minutes and the same solution was used for all three batches.

After immersion, the 40% and 60% acetone samples were removed from the solution, patted dry with paper towels, and placed upright along their long edge to dry overnight and evaporate any remaining acetone or water. To prevent the 80% acetone samples from deforming, they were laid horizontally on a silicone mat to dry.

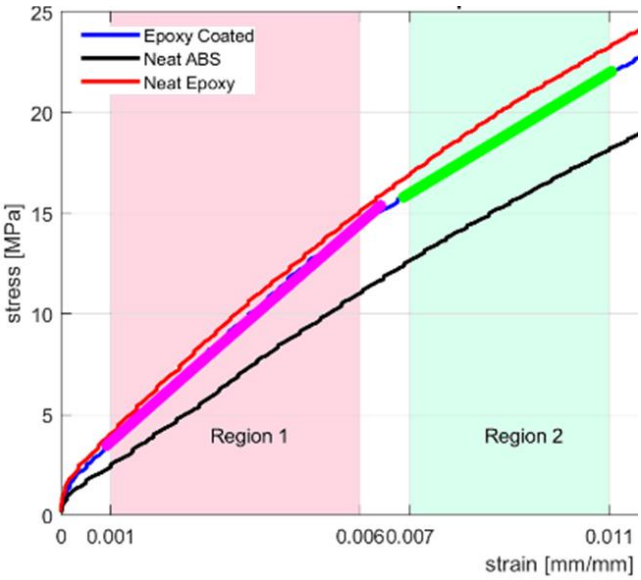

FIGURE 3. Stress-strain curves for neat ABS, neat epoxy, and epoxy-coated samples. Two distinct linear regions are identified for the epoxy-coated samples (magenta and green zones).

Tensile Testing

To complete the tensile testing of the neat and treated ABS samples, an MTS Criterion Model 45 universal testing machine with a 100 kN load cell was used. Each test specimen was clamped at both ends and pulled at a strain rate of 5 mm/min until failure. Two pieces of reflective tape were placed at the boundary of the 50 mm gauge length for each specimen, and an MTS laser extensometer [13] was used to record the displacement.

TABLE 1. Values for the mechanical properties of all sample types. Blue highlight indicates a statistically significance difference from neat ABS.

Treatment (% change from neat ABS)	Elastic modulus (MPa)	Tensile strength (MPa)	Fracture strain (%)
Neat ABS (value ± std. dev.	2183 ± 83	26.6 ± 0.7	8.34 ± 0.01
GB – Small Beads	2232 (2.2% increase)	26.5 (0.4% decrease)	10.2 (22% increase)
GB Large Beads	2188 (0.2% decrease)	25.9 (2.6% decrease)	8.8 (6.0% increase)
Neat Epoxy	2843 (30.2% increase)	39.7 (49.2% increase)	23.3 (180.7% increase)
Brushed Epoxy	2426 (11.1% increase	26.9 (1.2% increase)	8.1 (2.4% decrease)
40% Acetone	2224 (1.9% increase)	27.1 (1.9% increase	6.4 (23.2% decrease)
60% Acetone	2011 (7.9% decrease)	25.3 (4.9% decrease)	2.7 (67.6% decrease)
80% Acetone	2020 (7.5% decrease	26.1 (1.9% decrease)	3.8% (54.4% decrease)

Water Absorption and Mass Change

The FFF process can make parts prone to water absorption from the environment and affect both the quality of the surface finish and the dimensional accuracy [4]. The material itself can also become degraded, contributing to a decrease in tensile strength. ABS possesses hygroscopic tendencies, where the polymer can absorb or adsorb water present in the surrounding environment [14].

To assess the hygroscopic tendencies of the treated versus untreated ABS, water absorption tests were conducted. From each treatment group, three samples were immersed in a graduated cylinder filled with water for eight hours. Specimens were removed from the water, their mass was measured, and they were then replaced in the water each hour.

Data Analysis Methodology

Engineering stress-strain curves were generated using the force data from the MTS crosshead and displacement data from the laser extensometer. In order to calculate elastic moduli for the samples, points from the initial linear portion of the stress-strain curve were fit using a first-degree polynomial with a zero intercept. The slope was used as the elastic modulus.

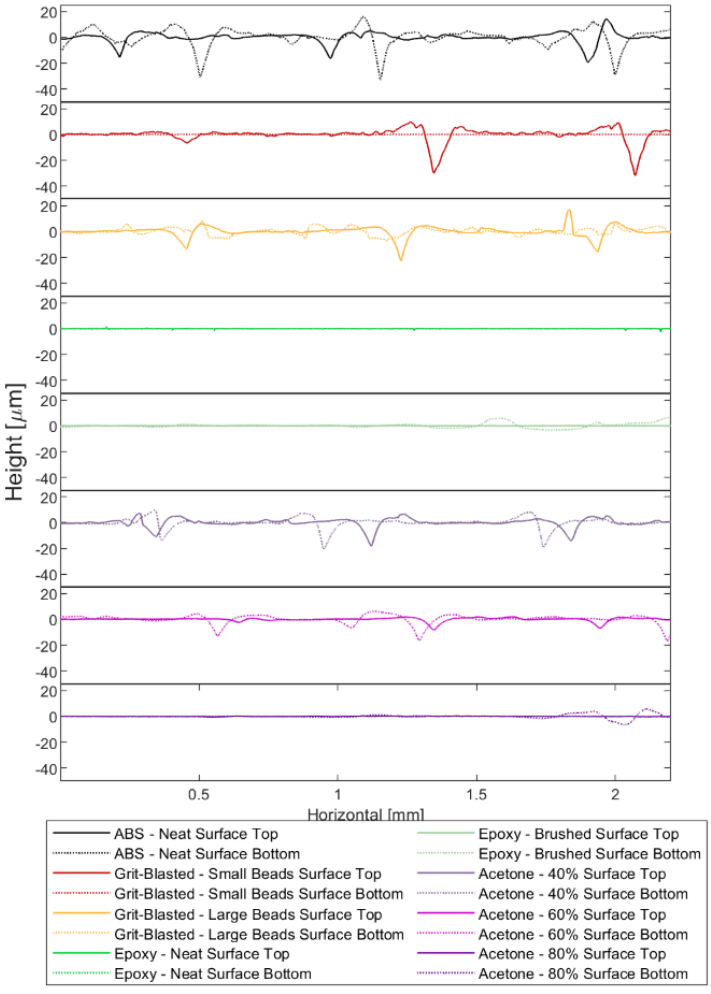
Height [μm]
Horizontal [mm]
ABS - Neat Surface Top
ABS - Neat Surface Bottom
Grit-Blasted - Small Beads Surface Top
Grit-Blasted - Small Beads Surface Bottom
Grit-Blasted - Large Beads Surface Top
Grit-Blasted - Large Beads Surface Bottom
Epoxy - Neat Surface Top
Epoxy - Neat Surface Bottom
Epoxy - Brushed Surface Top
Epoxy - Brushed Surface Bottom
Acetone - 40% Surface Top
Acetone - 40% Surface Bottom
Acetone - 60% Surface Top
Acetone - 60% Surface Bottom
Acetone - 80% Surface Top
Acetone - 80% Surface Bottom

FIGURE 4. Surface profiles for all sample types.

For the epoxy-coated samples, two linear regions were identified; these are visible in Fig. 3. The yield strength was calculated using the 0.2% offset method. Pooled t-tests and t*-tests (α = 0.05) were used to determine if each treatment type was statistically different from the control group for each material property. The results are displayed in Table 1.

RESULTS

Surface profiles for samples from every treatment group are shown in Fig. 4. All R_a values obtained from stylus profilometry data are provided in Table 2.

TABLE 2. Pre- and post-treatment R_a values for all sample types.

Treatment	Top R_a [um]		Bottom R_a [um]	
	Pre	Post	Pre	Post
Neat ABS	2.4	-	4.8	-
GB Small	2.6	2.8	5.0	0.03
GB Large	2.2	1.2	5.0	2.1
Neat Epoxy	0.04	-	0.21	-
Brushed Epoxy	2.2	0.04	6.3	1.2
40% Acetone	2.1	2.1	4.0	3.8
60% Acetone	3.6	0.76	5.0	2.2
80% Acetone	3.2	0.01	5.0	0.08

Mechanical Media Blasting

Overall, grit blasting the ABS samples with either small or large beads led to the surface textures of both sides of the sample becoming more similar to each other. Media blasting with small beads did not have any significant effect on modulus, although a significant increase in fracture strain was noted. Small beads were visibly embedded in the voids of the sample surface. Meanwhile, media blasting with large beads also did not lead to any significant impacts on modulus or fracture strain; rather, slight decreases in tensile strength were observed. Larger beads did not embed in sample voids but instead tended to discolor the ABS surface with pockmarks.

Epoxy Coating

Neat epoxy demonstrated a significantly higher modulus (30.2% increase), tensile strength (39.7% increase), fracture strain (180.7% increase), and a smoother surface morphology

compared to neat ABS. The modulus of the epoxy-coated samples, which consisted of ABS coated with epoxy resin, was between that of neat epoxy and neat ABS, confirming expectations for the composite material. Additionally, epoxy-coated samples yielded a higher modulus compared to neat ABS (11.1% increase), together with a smoother surface texture than neat ABS. The superior modulus of the epoxy-coated samples may be a consequence of epoxy infiltration, which has been reported to strengthen interlayer bonding [15]. The epoxy penetration was uneven across the samples.

Even though the brushed epoxy samples had a higher modulus, tensile strength was not significantly different. It is likely that the epoxy began to delaminate from the ABS at a relatively low strain, leading the samples to behave more like neat ABS samples in terms of yield strength and tensile strength. Figure 3 shows a visible change in modulus (slope) for region 2 (relative to region 1) that is within 0.05% of the neat ABS modulus at approximately 0.6% strain, suggesting the epoxy and ABS delaminated.

Acetone Immersion

The change in materials properties of the acetone-treated samples depended on the acetone concentration. Treatment with 40% acetone did not have any significant effect on modulus, yield strength, or surface morphology, but a decrease in fracture strain was observed. On the other hand, immersion in 60% acetone contributed to a smoother surface texture, decrease in modulus, and a significant reduction in fracture strain. Finally, submersion in 80% acetone led to the most prominent smoothing of the sample surface, a decreased fracture strain (brittle fracture), as well as a warping of the sample into a curved geometry; see Fig. 5. This latter observation may be a result of the permeation of the strongly concentrated acetone into the pores of the sample.

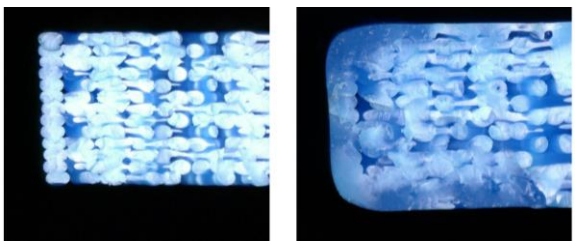

FIGURE 5. Optical fractographs of an untreated sample (left) and a sample treated with 80% acetone solution (right).

Moisture Absorption

The average percent mass change for water-immersed samples from each treatment group is conveyed in Fig. 6, which includes standard error bars showing 95% confidence intervals and red stars denoting which treatments held statistical significance in comparison to neat ABS. In general, all surface treatments, except for grit blasting with small beads, were able to significantly ($\alpha = 0.05$) reduce percent mass change due to hygroscopic absorption, relative to neat ABS.

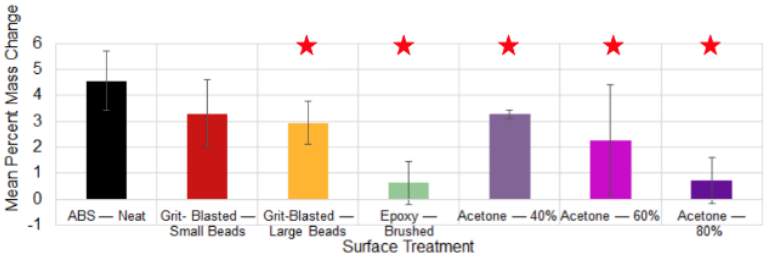

FIGURE 6. Mean percent mass change due to surface treatment and water absorption. The 95% confidence intervals are included.

CONCLUSIONS

Currently, additive manufacturing, and fused filament fabrication in particular, have led to a diverse array of applications spanning mechanical, biomedical, and aerospace engineering, in addition to products in electrical sensing and renewable energy. The continued exploration of surface treatments has the potential to advance the understanding of 3D printed materials and their applications in engineering, medicine, and beyond.

The surface treatments examined in this study, excluding grit blasting with large beads and immersion in 60% acetone, did not exhibit significant effects on the tensile strength of ABS. However, grit blasting with small beads was observed to increase fracture strain compared to neat ABS; acetone immersion in either 40%, 60%, or 80% solution, however, led to more brittle fracture modes. Importantly, epoxy brush coating contributed to notable increases in elastic modulus, together with reduced moisture uptake by the ABS. Overall, considering the insignificant impacts of most of the surface treatments studied on the tensile strength of ABS, this study concludes that these surface modifications can be customized to tune the desired properties.

ACKNOWLEDGEMENTS

The authors acknowledge funding from the 2021 Student Mentoring and Research Training (SMaRT) program supported by the US Department of Energy's Office of Energy Efficiency and Renewable Energy (EERE) through award number DE-EE0009177 provided to the University of Tennessee-Oak Ridge Innovation Institute (UT-ORII) and the UT Science Alliance program.

REFERENCES

1. Papon EA, Haque A, Spear SK. Effects of functionalization and annealing in enhancing the interfacial bonding and mechanical properties of 3D printed fiber-reinforced composites. Materials Today Communications. 2020 Dec 1;25:101365.
2. van de Werken N, Tekinalp H, Khanbolouki P, Ozcan S, Williams A, Tehrani M. Additively manufactured carbon fiber-reinforced composites: State of the art and perspective. Additive Manufacturing. 2020 Jan;31:100962.
3. Hambali RH, Cheong KM, Azizan N. Analysis of the influence of chemical treatment to the strength and surface roughness of FDM. IOP Conf Ser: Mater Sci Eng. 2017 Jun;210:012063.
4. Lavecchia F, Percoco G, Pei E, Galantucci LM. Computer Numerical Controlled Grinding and Physical Vapor Deposition for Fused Deposition Modelled Workpieces. Advances in Materials Science and Engineering. 2018 Nov 1;2018:1-7.
5. Gao H, Kaweesa D, Moore J, Meisel N. Investigating the Impact of Acetone Vapor Smoothing on the Strength and Elongation of Printed ABS Parts. JOM. 2016 Dec 12;69.
6. Leite M, Varanda A, Ribeiro AR, Silva A, Vaz MF. Mechanical properties and water absorption of surface modified ABS 3D printed by fused deposition modelling. Rapid Prototyping Journal. 2018 Jan 1;24(1):195-203.
7. Belter JT, Dollar AM. Strengthening of 3D Printed Fused Deposition Manufactured Parts Using the Fill Compositing Technique. PLOS ONE. 2015 Apr 16;10(4):e0122915.
8. ABSplusTM-P430 [Internet]. Eden Prairie, MN: Stratasys; 2014. [cited 2021, August 17th]. 2 p. Available from: https://support.stratasys.com/sitecore/api/downloadazurefile?id={B26724DB-1684-4E3B-9E4A-3B1345AFF721
9. Portable Surface Roughness Tester Surftest SJ-210/310 Series [Internet]. Aurora, IL: Mitutoyo America Corporation; March, 2021 [cited 2021, Aug. 17]. 20 p. Bulletin No. 2307. Available from: https://www.mitutoyo.com/wp-content/uploads/2021/03/Surftest_SJ-210_310.pdf
10. Saliu HR, Ishiaku US, Yakubu MK, Kolawole EG, Adefila SS, Bakar MBA, et al. The Effect of Epoxy Concentration and Fibre Loading on the Mechanical Properties of ABS/Epoxy-Coated Kenaf Fibre Composites. OJCM. 2015;05(02):41-8
11. XTC-3D™ High Performance 3D Print Coating [Internet]. Macungie, PA: Smooth-On [cited 2021, August 17th]. 3 p. Available from: https://www.smooth-on.com/tb/files/XTC3D_TB.pdf
12. Kozior T, Mamun A, Trabelsi M, Sabantina L, Ehrmann A. Quality of the Surface Texture and Mechanical Properties of FDM Printed Samples after Thermal and Chemical Treatment. Strojniski Vestnik. 2020 Feb 13;66:105-13.
13. The LX Laser Extensometer Series [Internet]. Eden Prairie, Minnesota: MTS; 2009 [cited 2021, August 17th]. 2 p. Available from: https://corp.mts.com/cs/groups/public/documents/library/dev_003699.pdf
14. Ferrell WH, Arndt CM, TerMaath S. Tensile strength dependence of FFF fiber reinforced ABS on environmental conditioning. Mechanics of Advanced Materials and Structures. 2020 Feb 18;1-14.
15. Zaldivar R J, McLouth T D, Patel D N, Severino J V. Strengthening of plasma treated 3D printed ABS through epoxy infiltration. Progress in Additive Manufacturing. 2017;(2):193-200.

A PROTOTYPE CONTAMINATION INSPECTION SYSTEM FOR DUV/EUV RETICLES

Iosif Papadakis Ktistakis, Michal E. Pawlowski, James Walsh, Corey Loke, Aage Bendiksen, Ryan Munden, Steve Roux

ASML
Wilton, CT, USA 06897

ABSTRACT
The objective of this work is to describe the development of a functional prototype system able to inspect EUV and DUV reticles. Reticles are inspected before or after exposure to ensure the quality of the lithographic process. Each reticle has two sides, the pellicle side and the back side, and both are normally inspected. Reticle diffractive pattern from the perspective of reticle inspection system can redirect light in arbitrary direction, which may lead to generation of stray light and consequently potential false positive detections.

To tackle that problem we tested functional prototype of an inspection system, based on structural illumination, capable of automatic rejection of a stray light signal. In our approach a sinusoidal frequency modulated signal is obliquely projected onto surface under test. The illumination pattern frequency changes with object spatial coordinates. Because camera and projector optical axes are not parallel to each other, algorithms known from close range photogrammetry can be leveraged to distinguish between light scattered by particles located on the test surface from a light diffracted by the reticle pattern

In our manuscript we will describe the opto-mechanical layout of the prototype system together with its principle of operation. In order to be able to image and measure contamination particles at the μm level, our prototype needed to conform to certain parameters that will be described. Experimental data illustrating system capabilities will be provided and directions of system development will be delineated

INTRODUCTION
Photolithographic masks or more commonly known as reticles, are glass plates with a pattern deposited on one side. The reticle pattern is subsequently photolithographically reproduced on wafers to create electronic circuitry. The patterns that are contained on the reticle during exposure are being printed on the wafer. The reticles has two surfaces, the front or pellicle side and the back side, that are inspected before exposure to ensure the cleanliness requirements. Extreme Ultraviolet (EUV) and Deep Ultraviolet (DUV) reticles are inspected to allow correct placement and intensity of the aerial image. For EUV systems the back side of the reticle is inspected to ensure overlay performance while for DUV systems it is inspected for obstruction free illumination of the pattern. The inspection's purpose is to detect the presence of contaminants on the surface of the reticle, which during exposure may distort the image of the projected pattern on the wafer.

Imaging systems are good candidates for inspection of a reticle as they have the resolution and the field of view that can be optimized based on the wanted minimum size of particles and the throughput. Imaging systems are used to identify particles in the order of tens of nanometers [1 ,2, 3], while microscopes and confocal are used [4, 5, 6] for particles that are hundreds of micrometers in diameter. A reticle inspection system in principle needs to reject the stray light induced by the pattern and because the properties of the reticle pattern are not known to, it is very difficult to predict the size and location of the stray light.

There is a range of commercially available systems that assess the cleanliness of the reticle [7, 8, 9] but not all adhere to the demands of size precision and throughput. Scanning electron microscopes (SEM) and atomic force microscopes (AFM) for example have high resolution and small field of view but they result in low throughput, thus are not viable solutions to reticle inspection. However, scatterometers [1, 2, 3] are fast enough to be accepted for reticle inspection. Even though scatterometers have an acceptable throughput, they may suffer from errors that are related to unpredictable particle

scattering properties and reticle pattern induced stray light.

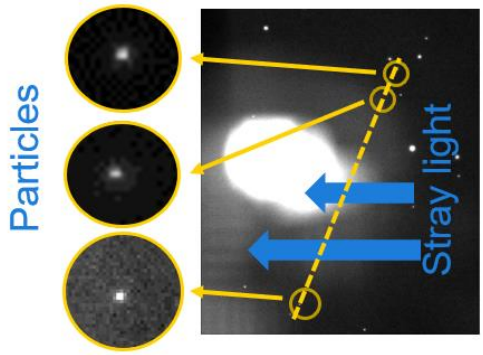

FIGURE 1. Particles shown on the back side of a DUV reticle after light reflection. Contrast has been enhanced for visualization purposes on the 2D image only.

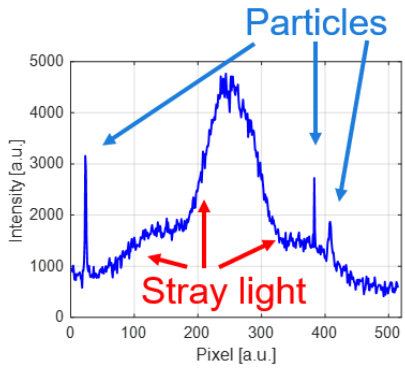

FIGURE 2. Intensity cross-section of the particles from Fig 1.

In the figures 1 and 2, an example is provided to show particles on a reticle (Figure 1) and an intensity cross-section through those particles (Figure 2). As can be observed the 2 particles show a non-uniform background and it is difficult to identify because of their shape, size and intensity that could lead to false positives or false negatives. The difference in the intensities shows that a global threshold will not work as some particles will not get classified as true positive. Stray light does not have to be smooth like shown in Figure 2 and in general it is possible for sharp changes in intensity to be noticed. This means that not only a global threshold will not work but also a local threshold may not be the best option either.

OVERVIEW OF THE DESIGN

In this paper we present a reticle inspection imaging system utilizing dark field frequency encoding structural illumination. The illumination system is used to automatically delineate between particles and the stray light.

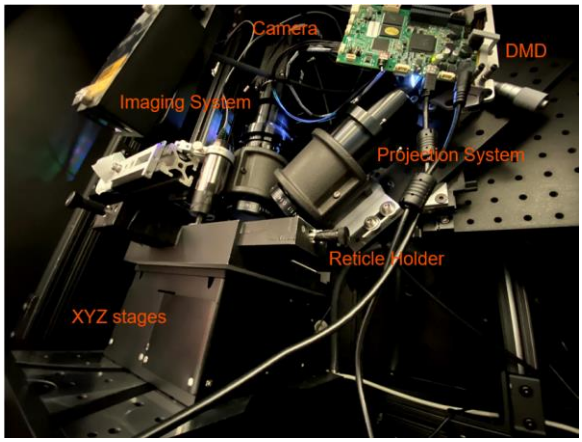

FIGURE 3. Prototype Inspection System image utilizing frequency encoded structural illumination.

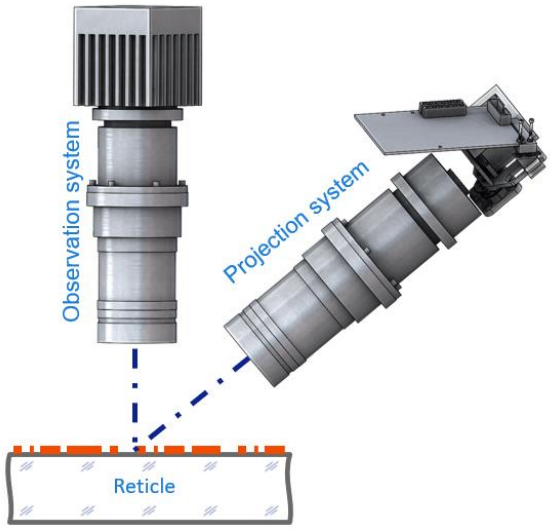

Figure 4. Representation of the projection system in angle over the object at test (Reticle) and the observation system at normal.

An oblique angle of illumination is used for the reticle surface with a spatial and temporal pattern projected on it. A detector (camera) is placed normal to the inspected surface to record the light scattered by the particles on that surface. The

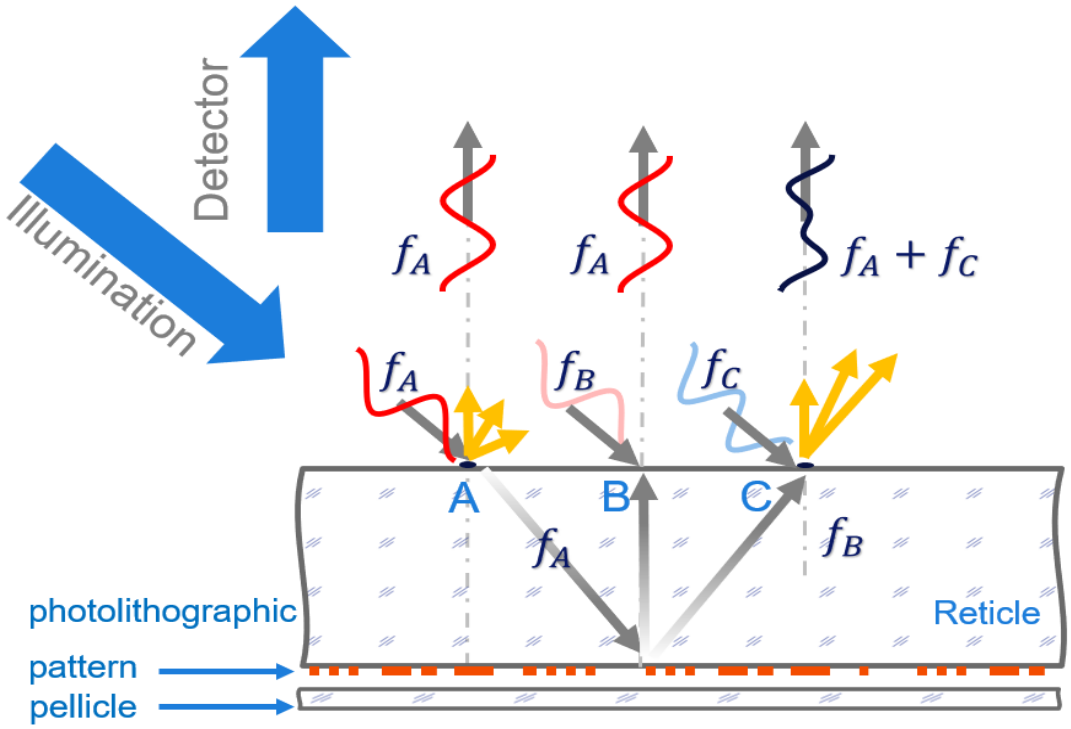

FIGURE 5. Schematic that illustrates the principle of operation of the structural illumination on our prototype inspection system.

illumination is a time varying sinusoidal signal and its temporal frequency changes according to the spatial coordinates. Meaning that depending on the location on the inspection surface of the reticle a different frequency will be projected ending up in a frequency encoding.

From the detector's perspective the specific frequency signal is bound to the projection angle and a location on the reticle. This is used to distinguish and identify the spatial position of the signal source, since the particles are so small compared to the distance between front and back side of the reticle. In our system the acquired data (images) are analyzed pixel by pixel using Fourier transformation [10].

A prototype was built to verify the performance of a system utilizing frequency encoding to inspect the side of a reticle. The illumination system utilized a digital micromirror device (DMD) that enables the generation of spatial and temporal variable signals. The detector is an off the shelf monochromatic complementary metal oxide semiconductor (CMOS) camera that utilizes a double telecentric lens. For the change of location a set of X-Y-Z motion stages was utilized with a reticle mount on top of them to enable access to all parts of the reticle. Other sensors such as a laser triangulation distance sensor was used in the process of our experiments to automate depth and focus of the reticle towards the camera.

FREQUENCY ENCODING STRUCTURAL ILLUMINATION SYSTEM

The reticle is clamped in the reticle holder that is mounted on top of the XYZ stages, the optics normal to the reticle surface and the projected pattern is given by illuminating at an oblique angle, we can calculate the signal acquired by the camera with the following equation:

$$I(x, y; t) = I_{DC}(x, y) + I_A(x, y)\cos[2\pi f(x, y)t + \delta(x, y)] \quad (1)$$

Where: $I(x, y; t)$ is the intensity observed by the detector at coordinates (x,y), $IDC\ (x, y)$ is the intensity offset, $IA(x, y)$ is the amplitude of signal at pixel (x,y), $f(x, y)$ is the temporal signal frequency, t is the time and $\delta(x, y)$ is the phase offset.

Whether the reticle is an EUV or a DUV type we can divide the detected signal in the detector pixel into the following categories:

i. Background/stray light
ii. Particles
iii. Mixed stray light with particle signal

Particles that are illuminated directly will generate a signal that will have an equal temporal frequency to the illumination's beam frequency, so it is best to compare the frequency of illumination at (x,y) knowing the Z position of the inspected surface with the frequency observed. The shift in Z will be reflected in (x,y) dependent frequency shift. In Figure 6 we can see the frequency shift map, where a single particle can be seen, a point that shows the stray light and finally a point that shows the mixed particle with stray light signal.

RESULTS

We analyze the acquired data pixel by pixel, therefore there is no need to utilize 2D morphological functions to distinguish the particle light from the stray light. We acquire data by projecting 64 patterns and each one is acquired as an image. Using equation (1) with the frequency change taking place in the X direction only and a phase offset set to zero for every point we generate the patterns. The intensity offset and the amplitude of signal are set to 128 in order to maximize the dynamic range of the projector. Every pattern was generated using all the projector's diodes on (red, green and blue), creating a polychromatic range. No efforts were made at this point to white balance the projector in order to optimize the camera – projector system but in general it is possible to adjust the projector output spectra to the camera sensitivity curve.

In Figure 7 an example of the different signals can be observed. The red point presents the mixed signal of the particle and the stray light. The green point shows the particle only signal. We can identify the particle signal by comparing the frequency of the point with the expected one. Respectively, the following Figure 8 present the cross section intensities of the two points.

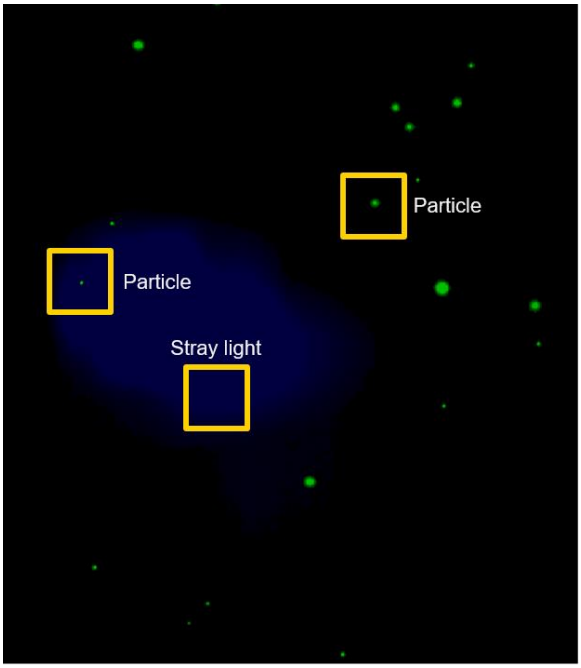

FIGURE 6. Frequency Shift Map

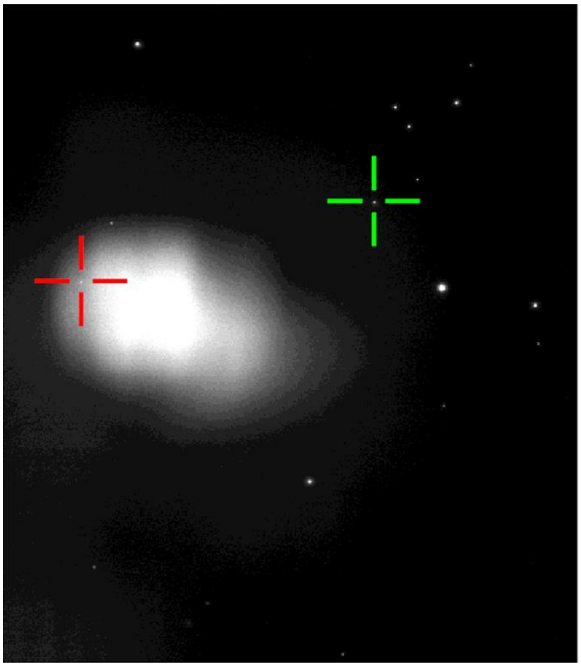

FIGURE 7. Example of a raw image of a reticle acquired during inspection. Two points marked with red and green are located on the image to show the cross section intensities.

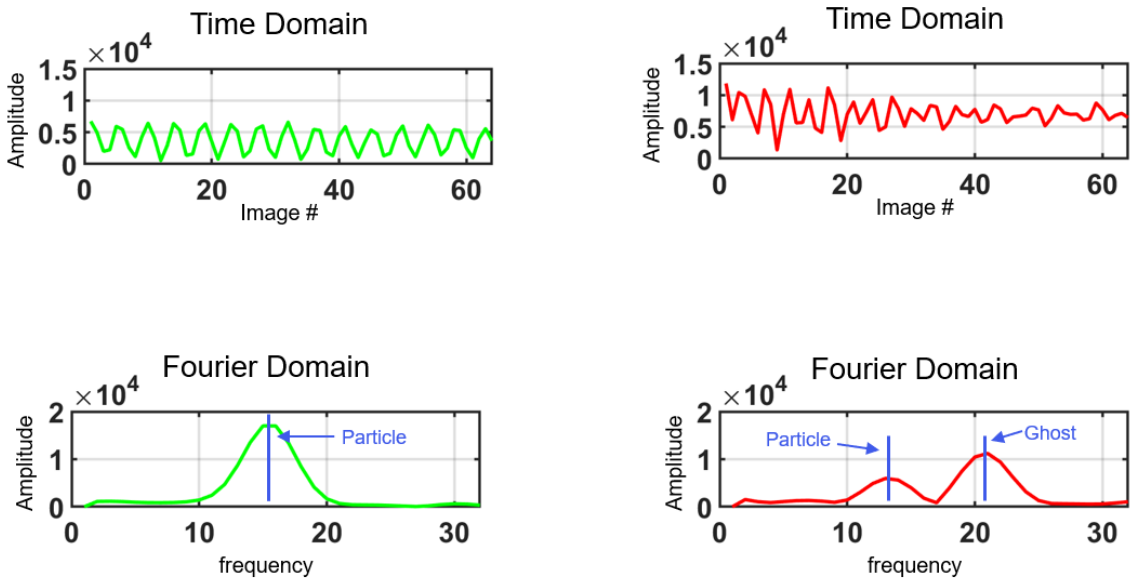

FIGURE 9. Top Left: Intensity cross section of Green particle in Time Domain. Top Right: Intensity cross section of Red particle in Time Domain. Bottom Left: Intensity cross section of Green particle in Fourier Domain. Bottom Right: Intensity cross section of Red particle and Stray light in Fourier Domain.

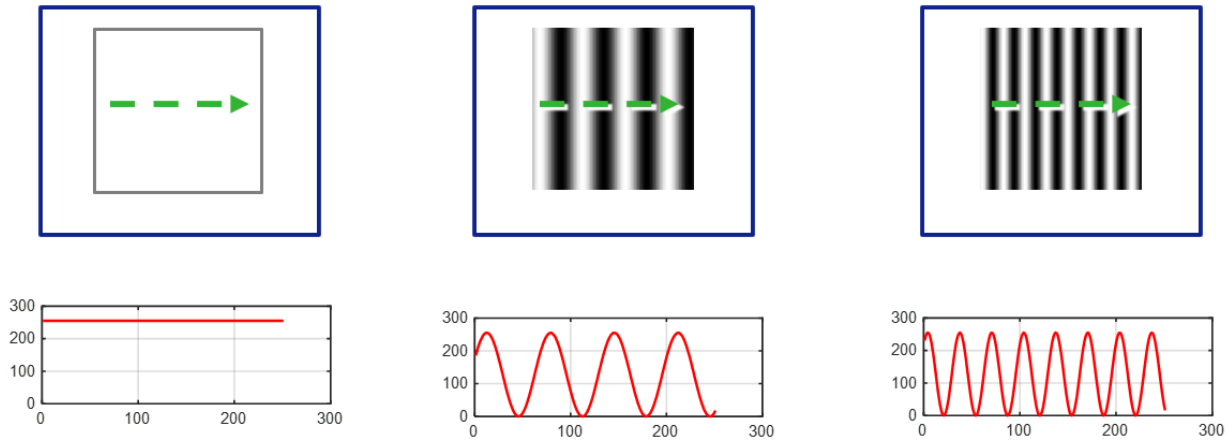

FIGURE 8. Example of different Illumination Patterns projected with their respective intensity cross sections. 250x250 pixels portion of the projected pattern with the cross section intensities taken in the direction of the arrow.

As an example we also provide images of the 64 patterns, and more specifically patterns 0, 31 and 63 as well as their intensity cross sections to showcase the proposed methodology in Figure 5. We operate in the visible range and we are limited in experimental system to spectral range of the projector LEDs.

CONCLUSIONS

A prototype particle detection system was presented that utilizes structural illumination and is able to automatically delineate between real particles and false positives. We used a time varying pattern with a different temporal frequency according to the spatial coordinates on the surface of the reticle. We analyzed the acquired data (images) pixel by pixel using Fourier transformation that helped us in differentiating the unwanted stray light, that is occurring by a diffractive pattern on the reticle, from the particle signal. The signal coming from

real particles is analyzed and compared to the measured frequency with the expected one and this way we can classify them as real particles over false positives.

Experimental results were provided to validate the concept and the prototype. With those data we were able to reconstruct the 3D geometry of the particle. In principle the prototype was built in a way that another type of pattern source could be projected on the inspected surface. Particles size can be identified with scatterometry and also in imaging mode. Due to the opto-mechanical layout and the illumination our prototype system is a viable alternative to scatterometers, interferometers and confocal microscopes.

ACKNOWDLEDGEMENTS

In accomplishing this work, we would like to thank Hao Zheng, Bixing Yan, Earl Ebert, Perry Goodman, Phani Kottapalli and Sreelakshmi Talluri for their work on designing and building this prototype particle detection system on its early stages. We would also like to thank Lilliana Delmonico, Ronald Chasse and John Moriarty for their work on testing early prototype of a particle detection system based on Frequency Encoding scheme.

REFERENCES

[1] Diebold, Alain C., ed. [Handbook of silicon semiconductor metrology] CRC Press (2001).

[2] Kolenov, D., and S. F. Pereira. "Machine learning techniques applied for the detection of nanoparticles on surfaces using coherent Fourier scatterometry." Optics Express 28.13, 19163-19186 (2020).

[3] Raymond, Christopher. "Overview of scatterometry applications in high volume silicon manufacturing." AIP Conference Proceedings. Vol. 788. No. 1. American Institute of Physics (2005).

[4] Pluta, Maksymilian, ed. [Advanced Light Microscopy, Vol.3: Measuring Techniques], Elsevier Science & Technology, (1993).

[5] Takeo Tanaami, Shinya Otsuki, Nobuhiro Tomosada, Yasuhito Kosugi, Mizuho Shimizu, and Hideyuki Ishida, "Highspeed 1-frame/ms scanning confocal microscope with a microlens and Nipkow disks," Appl. Opt. 41, 4704-4708 (2002)

[6] Nektarios Koukourakis, Markus Finkeldey, Moritz Stürmer, Christoph Leithold, Nils C. Gerhardt, Martin R. Hofmann, Ulrike Wallrabe, Jürgen W. Czarske, and Andreas Fischer, "Axial scanning in confocal microscopy employing adaptive lenses (CAL)," Opt. Express 22, 6025-6039 (2014)

[7] https://www.lasertec.co.jp/en/products/semiconductor/mask_semicon/X810.html (23 August, 2021).

[8] https://www.kla-tencor.com/products/reticle-manufacturing (23 August, 2021).

[9] https://www.drschenk.com/products/customized-solutions/photomask-inspection.html (23 August, 2021).

[10] Yamaguchi, Shinji, et al. "Performance of EBeyeM for EUV mask inspection." Photomask Technology 2011. Vol. 8166. International Society for Optics and Photonics (2011).

A TORSION PENDULUM FOR CHIP-SCALE RELATIVE GRAVIMETRY

Jon R Pratt[1], Stephan Schlamminger[1], Aman R. Agrawal[2], and Dalziel J. Wilson[2]
[1]National Institute of Standards and Technology, Gaithersburg, MD,
[2] College of Optical Sciences, University of Arizona, Tucson, AZ

ABSTRACT
Pendulums were the original tool of gravimetry. Here, we introduce a new microscale platform aimed at this task that takes the form of a chip-scale torsion resonator. We derive a lumped parameter model for the physics of the device, illustrating that the torsional stiffness depends on gravity along with the material and internal stress of its thin-film nanoribbon torsion fiber. Dissipation dilution is introduced within the context of fundamental noise limits of detection, and its influence on design choices discussed. We provide proof of concept data from an "accidental" prototype, resolving a 20 % shift in the device frequency that occurs when inverted in the earth's gravity to within a few parts in 10^6. Our result suggests that a chip-scale gravimeter is achieved using nothing more sophisticated than an optical lever to read out the frequency of this resonator.

INTRODUCTION
The length of a simple pendulum with a period of 2 seconds, the so-called seconds pendulum, is given by g/π^2, a value very close to 1 m. It gained an essential role in early geodesy after Jean Richer measured in 1671 that the seconds pendulum near the equator is 2.6 mm shorter than in Paris [1], providing the first experimental evidence that the Earth is an oblate spheroid and not a sphere. In the next 300 years following Richer and still today, more sophisticated pendula were used for gravimetric surveys, most notable the horizontal pendulum that employs a zero-length spring invented in 1936 by Lucien LaCoste and Arnold Romberg [2].

Since the period of a pendulum depends only on the square root of the ratio of gravity to its length, a pendulum with suitable frequency stability (parts in 10^8) and quality factor (Q > 10^5) makes an excellent gravimeter. With an eye towards optomechanical seismometers [3], relative gravimeters for the National Institute of Standards and Technology (NIST) Kibble Balance [4], quantum limited optomechanics [5], measurements of universal gravitation [6], tests of the equivalence principle [7], and dark matter detection [8,9], we have recently fabricated an extraordinarily high Q chip-scale torsion pendulum. The remainder of this paper offers an overview of this versatile device concept, describes its unique features and basic design strategies, and offers preliminary performance data and evidence of gravity detection.

A LUMPED MODEL
Relative gravimeters are compact weak force sensors that monitor for changes or probe gradients in the earth's local gravitational field. While new approaches have emerged, the most common and robust sensors are still variations of a mass on a spring. As gravity changes, so does the length of the spring, and the deflection of the suspended mass is detected as the readout parameter. By far the most successful implementation is a torsion spring device [2] where a rigid balance beam pivots about an axis horizontal to the earth's local gravity, like a child's seesaw. The beam is deliberately imbalanced in these systems (one side of the seesaw is heavier), so that a gravity torque deflects the beam from equilibrium. The highest sensitivity is achieved using the weakest spring, so that to maintain stability the deflections are usually nulled, an action accomplished to first order using a zero-length spring, but ultimately by detecting the tilt angle and applying a feedback force. In contrast, here we consider a beam that is balanced, omit the zero-length spring and feedback, and explore the dynamic behavior of a torsion oscillator where the center of gravity is offset directly below the axis of torsion, as illustrated in Figure 1.

The local acceleration of gravity *g* in Figure 1 acts on a rigid balance beam with moment of inertia *I*. The center of gravity is offset from the pivot by a fixed distance *r*, producing a gravitational torque $\tau_g = -mgr\ \sin\theta$, where *m* is the total mass of the beam. The pivot is a mechanical spring with complex torsional spring constant κ, and the entire device is assumed to be in vacuum so that we can neglect viscous damping. The simple harmonic motion for small deflection angles is described by

$$(I + mr^2)\ddot{\theta} + \kappa\theta + mgr\theta = 0 \qquad (1)$$

From which we see that the mechanics is a hybrid of a torsion spring and pendulum oscillator where the square of the radial frequency of oscillation ω depends on gravity according to

$$\omega^2 = \frac{\kappa}{I+mr^2} + \frac{mgr}{I+mr^2} \qquad (2)$$

Letting the torsion beam inertia be negligible for the moment, we have

$$\omega^2 = \frac{\kappa}{mr^2} + \frac{g}{r} = \omega_0^2 + \frac{g}{r} \quad (3)$$

so that our gravity signal rides on an offset ω_0^2 due to the torsion spring κ, while the absolute sensitivity of the frequency to gravity is

$$\Delta\omega^2 \approx \frac{1}{r}\Delta g \quad (4)$$

Which yields two familiar counterintuitive results: the mass is inconsequential, and the sensitivity improves as the pendulum length shrinks.

As ever, there is nothing for free, and the price of a vanishingly short pendulum will be that the frequency change will occur between two very high frequencies, unless the torsion spring constant can be made exceedingly small. It may be that a more useful performance goal is to push the ratio

$$\frac{\kappa_g}{\kappa} = \frac{mgr}{\kappa} \geq 1 \quad (5)$$

So that the pendulum character of the device dominates over the torsion spring.

THE STIFFNESS OF A RIBBON

A ribbon is a beam with a thickness so much smaller than its length that bending moments are negligible. It can be thought of as a collection of parallel strings and makes an excellent low stiffness hinge (leaf spring) or pivot (torsion fiber). In either case, one's intuition about such hinges and pivots can be developed by considering a ribbon as a pair of parallel strings, a bifilar suspension [10], as in Figure 2.

A rigid body suspended from a pair of parallel strings can hinge out of the plane, like a trapeze or swing, creating the pendulum of Figure 2 (a). Note that the suspended beam can also twist about the longitudinal axis, creating a torsion pendulum, as illustrated. Seeking a short pendulum with a weak pivot, we focus on this latter possibility, but rotate the orientation as in Figure 2 (b), where we fully constrain the mass and introduce a tensile load. Such a tensioned suspension can in principle be made arbitrarily long (and therefore quite weak) without compromising the length of the pendulum, which is now just the distance to the center of mass hanging below the "ribbon".

We employ a pair of doubly clamped nanoribbons for our concept where the length to thickness ratio l/t exceeds 10^4, and each nanoribbon is under tensile stress σ. Ribbon suspensions and their torsional stiffness κ have been considered for gravity detection [11], and it was discovered [10] that

$$\kappa = \kappa_E + \kappa_\sigma \quad (6)$$

where the first term is attributed to elastic deformation and the second to the tensile load. Applying this model to doubly clamped ribbons of width w and modulus of rigidity G we find

$$\kappa_E = \frac{2wt^3}{3l} G(1 + i\delta) \text{ and } \kappa_\sigma = \frac{tw^3}{6l}\sigma \quad (7)$$

where δ is the loss angle intrinsic to the material.

Typically, an axial load arises in a torsion pendulum from hanging a massive torsion beam from the ribbon, just as illustrated in Figure 2 (a). When the ribbon is twisted it lifts the mass, doing work against the gravitational field. The beauty of this restoring torque is that it is lossless since it is gravitational in origin. We hypothesize that a large constant residual stress might be employed as a surrogate for gravity, as illustrated in Figure 2 (b), at least in the limit of small deflections. The reasoning is as follows. Assume an infinitely thin doubly clamped ribbon can be approximated as a collection of parallel strings, as in [10]. The prestress means that each string is under tension, like the string of a guitar. Pairs of strings symmetric about the center line create a force couple when the ribbon is twisted about its longitudinal axis at the midpoint (the bifilar effect). The resulting torque acting on the torsion beam is approximately lossless under these assumptions, since the change in tension due to stretching is a nonlinear term that vanishes in the small deflection limit.

THERMAL NOISE AND DISSIPATION DILUTION

The spectral amplitude density of the thermal noise force (or torque, in this case) driving an oscillator in thermal equilibrium is given by

$$F = \sqrt{4k_B T \,\mathrm{Im}(\kappa)} \quad (8)$$

where $\mathrm{Im}(\kappa)$ is the imaginary part of the combined torsional stiffness. For a given temperature, thermal noise can be made smaller by decreasing the imaginary part of the spring constant, $\mathrm{Im}(\kappa)=\delta\kappa_E$. Consistent with our goal of a vanishingly small pivot stiffness, that means lowering κ_E since the loss angle δ is fixed for a given material system.

We cannot remove all the material from the torsion ribbon, or it will no longer constrain the balance beam to rotate, nor support the beam's weight under gravitational load. Given that there will be a pivot with a finite restoring torque, we pick a material and geometry to minimize the intrinsic loss of our torsion ribbon.

Single crystal materials are perhaps ideal, but thin films of silicon nitride are also an excellent and

popular choice for nanomechanical systems and have the advantage of being well studied. Furthermore, it has been shown for transverse modes of silicon nitride nanoribbons that the effect of the remaining intrinsic loss can be greatly diluted by maximizing the contribution of stress induced restoring forces to the overall stiffness. By analogy, we assume dissipation in torsion can be diluted by the ratio of stress induced to elastic effects, and predict the amount of dissipation dilution for torsion is approximately

$$\frac{\kappa_\sigma}{\kappa_E} \approx \frac{1}{4}\left(\frac{w}{t}\right)^2 \frac{\sigma}{G} \qquad (8)$$

Realistically, the residual stress must be considerably less than the elastic limit to avoid device mechanical failure. A tensile stress of approximately 1 GPa is typical for high stress silicon nitride, so the ratio of σ/G (G ≈ 135 GPa) is on the order of 10^{-2}. This would seem to move in the wrong direction, but silicon nitride nanoribbons with w/t as large as 10^4 have been made, indicating that dilution factors of 10^6 might be possible.

AN ACCIDENTAL PROTOTYPE

Our first device, shown in Figure 3, consists of a nominally 0.1 mg (approx. 100 μm thick x 600 μm x 600 μm of silicon) mass suspended from a silicon nitride nanoribbon (σ=1GPa, G= E/2 =135 GPa, l=3 mm, t=80 nm, w=24 μm), forming a *chip-scale* torsional resonator. The prismatic mass, composed of silicon substrate material remaining under the center pad after etching, hangs below the resonator so that its center of gravity is offset from the pivot axis by half the thickness. We estimate r on the order of 50 μm.

Typically, a trampoline resonator [5] has a paddle that is constrained by 4 “ribbons” at its corners. By removing 2 ribbons from diagonally opposite corners, you end up with a torsion resonator. The sensor of Figure 3 was created by accident when 2 ribbons failed in just such a fashion during fabrication of resonators like those in [5].

Although the sensor was not specifically designed for gravity sensing, we find a favorable hierarchy of stiffnesses $\kappa_E \approx 3 \times 10^{-13}$ Nm/rad, $\kappa_\sigma \approx 5 \times 10^{-11}$ Nm/rad and $\kappa_g \approx 4 \times 10^{-11}$ Nm/rad applying the models discussed above. The predicted ratio of gravitational to pivot stiffness is nominally 0.8, and the predicted dilution factor is 170. Based on these calculations, we expect the total stiffness of an inverted sensor---shifting the suspended mass from below to above the nanoribbon, i.e., an inverted pendulum--- to be 10 % of its noninverted value, since the sign of κ_g reverses for this orientation. Furthermore, the resonance should have a quality factor Q ≈ 10^6 based on the computed dilution factor and surface loss models developed for transverse modes of silicon nitride beams [13].

The device was placed in a high-vacuum chamber to minimize gas damping, and ringdown measurements were performed using an optical lever (laser light was bounced off the paddle) in conjunction with radiation pressure driving (light from an intensity modulated source). Frequencies were determined from Fourier spectrums (Figure 3d) and Q factors were inferred from fitting of the ringdown measurements (energy inferred from the variance of displacement near resonance, Figure 3c). The relative imprecision of frequency measurements is estimated to be on the order of 10^{-5} Hz.

The stress-induced quality factor $Q \approx 2.5\,x\,10^6$ is higher than expected. On the other hand, the drop in frequency from 35 Hz to 25 Hz is less than expected, but consistent with pendulum like behavior, and indicative of sensitivity to relative changes in g on the order of 10^{-6}. Note also that a gravitational torque acting on a suspended mass would be lossless, so that the dissipation dilution factor for the sensor (not just the ribbon) should take κ_g into account. Thus, the reduction of Q on inversion is further evidence of pendulum like behavior.

CONCLUSIONS

A new torsion resonator has been modeled, fabricated, measured, and shown capable of detecting gravity to within a few parts in 10^6 using an optical lever to monitor the motion of the suspended torsion beam. The qualitative agreement between lumped model predictions and device behaviors is very encouraging. Quantitative discrepancies may be due to inaccuracies of the estimated physical geometries, or inadequacies of the simple model. For example, the suspension undoubtedly sags under the mass load. Nevertheless, both gravitational and stress induced dissipation dilution of nanomechanical torsion were demonstrated, both of which are new to nanomechanical studies. The frequency of the device displayed a very promising sensitivity to gravity, but the stability is an open question for further research. We anticipate the techniques outlined here, combined with this simple, easily fabricated device geometry, can be varied in multiple ways to create high Q pendulums and torsion oscillators for all manner of applications.

REFERENCES

[1] J. Richer "Observations Astronomiques et Physiques faites en L'isle de Caïenne″

Mémoires de l'Académie Royale des Sciences. **7** 231–326 (1729).
[2] L. LaCoste and A. Romberg "Force measuring device" US Patent Office, Patent, 1945, No. 2293437
[3] J.R. Pratt *et al*, "Verification of an in-situ calibrated optomechanical accelerometer for use as a strong ground motion seismic reference", *Metrologia* (2021).
[4] E. J. Leaman *et al.*, "A Determination of the Local Acceleration of Gravity for the NIST-4 Watt Balance" *IEEE Trans. Instum. Meas.* **64**, 1663 (2015).
[5] C. Pluchar *et al.*, "Towards cavity-free ground-state cooling of an acoustic-frequency silicon nitride membrane" *Appl. Opt.* **59**, G107 (2020).
[6] T. Quinn *et al.*, "The BIPM measurements of the Newtonian constant of gravitation, G" *Phil. Trans. R. Soc. A* **372**, 20140032, 2014.
[7] S. Schlamminger *et al.*, Test of the Equivalence Principle using a Rotation Torsion Balance, *Phys. Rev. Lett.* **100**, 041101 (2008).
[8] J. Manley *et al.*, "Searching for Vector Dark Matter with an Optomechanical Accelerometer" *Phys. Rev. Lett.* **126**, 061301 (2021).
[9] D. Carney *et al*, "Mechanical quantum sensing in the search for dark matter", *Quantum Sci. Technol.* **6** 024002 (2021).
[10] J.C. Buckley M.Sc. Lxxxiv. "The bifilar property of twisted strips". *The London, Edinburgh, and Dublin Philosophical Magazine and Journal of Science* **28,** 778 (1914).
[11] C.C. Speake *et al*, "Experiment and theory in anelasticity" *Meas. Sci. Technol.* **10,** 430 (1999).
[13] L.G. Villanueva and S. Schmid, "Evidence of Surface Loss as Ubiquitous Limiting Damping Mechanism in SiN Micro- and Nanomechanical Resonators", Phys. Rev. Lett., 113(22), 227201, 2014.

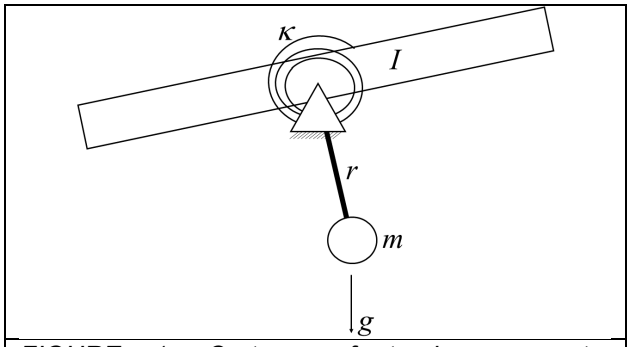

FIGURE 1. Cartoon of torsion resonator highlighting the lumped spring, mass, and pendulum features

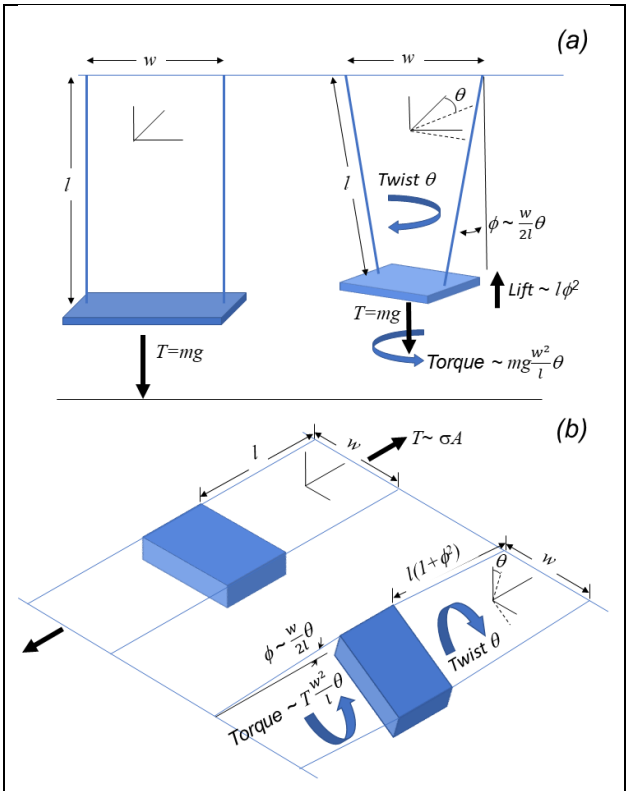

FIGURE 2. Geometry of torsion ribbons illustrated using bifilar suspensions

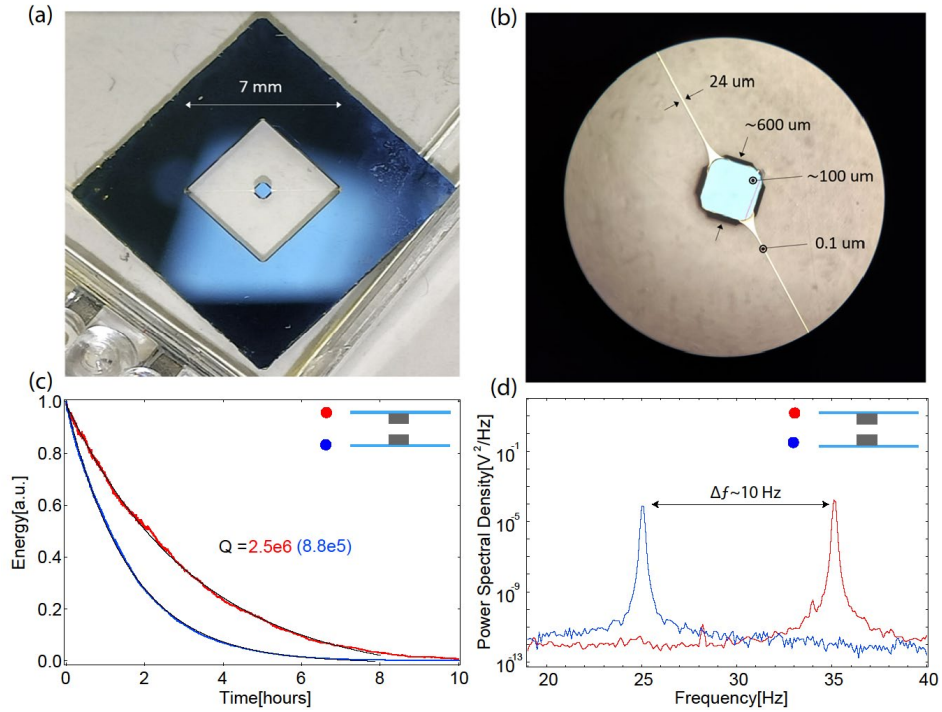

Figure 3. A micromechanical torsion balance based on high-stress silicon nitride thin film technology. (a-b) Photographs of the device at two magnifications. (c) Ringdown of a representative device in high vacuum for two orientations with respect to gravity. (d) Natural frequency observed for the two orientations.

REMOTE BAYESIAN UPDATING FOR MILLING STABILITY

Jaydeep Karandikar[1], Christoph Ramsauer[2], David Leitner[2], Tony Schmitz[1,3]
Friedrich Bleicher[2]
[1]Manufacturing Science Division
Oak Ridge National Laboratory
Oak Ridge, TN 37830, USA
[2]TU Wien, Vienna, Austria
[3]Mechanical, Aerospace, and Biomedical Engineering
University of Tennessee, Knoxville
Knoxville, TN 37996, USA

INTRODUCTION

Machining stability is an important limitation in high-speed machining. The physical mechanism for unstable machining, or chatter, is the regeneration of surface waviness during material removal [1]. Stable operating parameters in milling may be selected using the stability boundary, which separates stable spindle speed-axial depth of cut combinations from unstable (or chatter) combinations [1]. While analytical models exist to predict machining stability, their cost-efficient implementation can be hampered by the need for information on the tool point frequency response function (FRF) and the cutting force coefficients. Without knowledge of the tool point FRF and the cutting force coefficients for the tool-material combination, machining parameters are typically selected using tool supplier and handbook recommendations, or previous experience. If unstable behavior (chatter) is observed, the parameters are often adjusted by trial and error until stable behavior is obtained. Typically, this means reducing the spindle speed and axial depth of the cut. In this work, remote identification of optimal stable milling parameters with Bayesian learning using test results is presented. The test cuts were monitored with a wireless sensory tool holder instrumented with an accelerometer. The test results were analyzed for stability remotely, used to learn the stability boundary, and recommend parameters for the next test using a Bayesian learning approach. The iterative process was repeated until convergence to a stable optimal process parameter set was achieved. The described approach can be automated to enable optimizing machining processes in production environments through data sharing with a central location where the analysis is completed.

REMOTE BAYESIAN UPDATING FOR MILLING STABILITY

The procedure for remote Bayesian updating for milling stability is as follows. Milling tests were performed on a milling machine at the TU Wien, Vienna, Austria. The milling tests were monitored using a wireless sensory tool holder instrumented with an accelerometer [2, 3]. The accelerometer data was shared through the cloud with Oak Ridge National Laboratory, Oak Ridge, Tennessee, USA, and the University of Tennessee, Knoxville, Tennessee, USA. The recorded data from a milling test cut was used to classify the cut as stable or unstable based on the frequency content [1]. The test cut result was given as input to a Bayesian learning algorithm for milling stability. The algorithm updated the probability of stability as a function of axial depth of cut and spindle speed based on the test results [4]. The probability of stability was subsequently used to recommend the axial depth and spindle speed for the next test cut based on a maximum expected improvement in the material removal rate criterion. The optimal test parameters were then communicated back to TU Wien in real-time for subsequent testing. The iterative process between two transatlantic locations was repeated until convergence to a stable optimal process parameter set was achieved.

TEST SETUP AND MONITORING

The milling tests were performed on a DMG MORI DMU 75 monoBLOCK milling machine at TU Wien, Vienna, Austria. The workpiece material was Aluminum 6060-T6. Figure 1 shows the test setup. The tool was a 10 mm diameter four flute solid carbide end mill. The axial depth of cut and spindle speed range for the testing was 0 mm – 8 mm and 5000 rpm – 9000 rpm. The radial depth of cut was

2 mm and feed per tooth was 0.1 mm/tooth. The cuts were down-milling. The workpiece was saved after each test cut to enable inspection of the machined surface. To ensure tight and repeatable clamping of the workpiece, specific vice jaws were used.

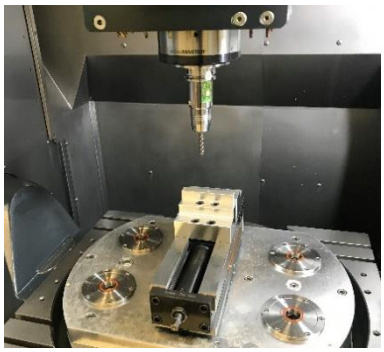

Figure 1. Setup for the cutting tests.

The test cuts were monitored with a wireless sensory tool holder instrumented with an accelerometer [2, 3]. The sensory tool holder can be used for process monitoring and process control and is depicted in detail in Figure 2. Without changing the outer contour of the tool holder, a battery, telemetry system, and an accelerometer mounted on a circuit board have been integrated into the holder. The accelerometer measures the radial acceleration of the tool holder vibration and has a range of up to +-100 g. The vibration data is transmitted out of the rotational system to the receiver unit via a wireless digital communication link, based on Bluetooth low energy [3]. The receiver unit forwards the time-stamped data to a processing unit. A laptop can be used for saving the data as a .csv file to the cloud. The sensor and radio transmission system was installed directly into an HSK-A 63 tool holder as shown in Figure 2.

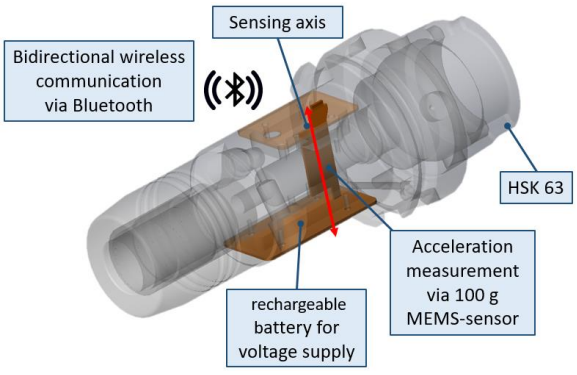
Sensing axis
Bidirectional wireless communication via Bluetooth
HSK 63
Acceleration measurement via 100 g MEMS-sensor
rechargeable battery for voltage supply

Figure 2. Sensory tool holder [3].

STABILITY CLASSIFICATION

The accelerometer data was shared through the cloud with the analysis framework implemented at the Oak Ridge National Laboratory, Oak Ridge, Tennessee, USA, and the University of Tennessee, Knoxville, Tennessee, USA. The first step of the analysis framework was to classify the test cut as stable or unstable based on the accelerometer data. The stability classification was performed using frequency analysis. For stable cutting conditions, there is frequency content only at the tooth passing frequencies and its harmonics. For unstable test cuts, there is content at chatter frequencies in addition to the tooth passing frequencies. Note that since the accelerometer in the sensory tool holder is not stationary, the frequencies are split by the spindle rotational frequencies [3]. To illustrate, Figure 3 shows the frequency spectrum of the accelerometer data from the sensory tool holder for the test at {9000 rpm, 4 mm} using. The tooth passing frequency is 600 Hz and the spindle rotational frequency is 150 Hz. Due to the nonstationary nature of the accelerometer, the tool passing frequency is split by the spindle rotational frequency at 450 Hz and 750 Hz. To compare, Figure 4 shows the FFT from a sound measurement of the same test cut measured with a microphone. The FFT from the sound signal is at the tooth passing frequency and its harmonics.

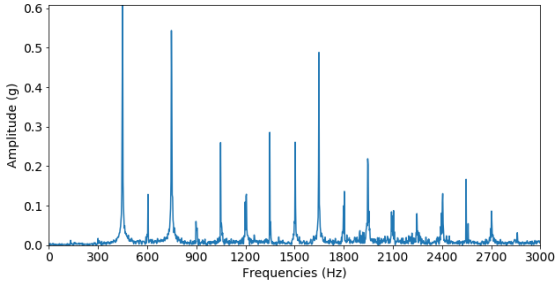

Figure 3. Frequency spectrum for the test at {9000 rpm, 4 mm} using accelerometer data from the sensory tool holder.

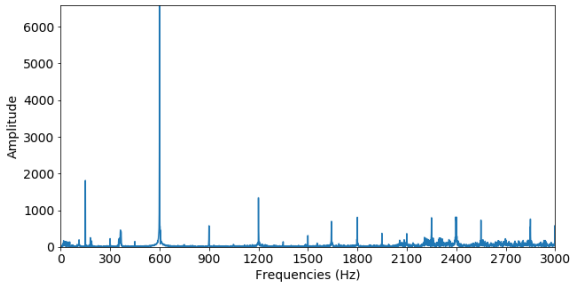

Figure 4. Frequency spectrum for the test at {9000 rpm, 4 mm} using a microphone.

BAYESIAN LEARNING AND TEST PARAMETER SELECTION

The second step of the analysis framework is the Bayesian learning and the test parameter selection algorithms. The Bayesian learning approach updates the probability of stability using test results. Before any tests are performed, a probability of stability map is generated in the spindle speed - axial depth of cut range. This is done by discretizing the spindle speed and axial depth range into grid points and assigning a probability of stability to each point. If the information on the frequency response function is not available, the probability of stability is decided from the knowledge that it is more likely to observe an unstable result at higher axial depths of cut. In this case, the probability of stability is taken to decrease linearly from one at the minimum axial depth of cut to 0.01 at the maximum axial depth of cut. After an experimental result is made available, the probability of stability at each grid point is updated using Bayes' rule as shown in Eq. 1 [4]:

$$p(s_g|r_t) = \frac{p(r_t|s_g)p(s_g)}{p(r_t)} \quad (1)$$

In Eq. 1, *g* is an arbitrary grid point in the spindle speed and axial depth domain and *t* is the test grid point. The test result at *t*, denoted by *r*, can either be stable or unstable. $p(s_g)$ is the prior probability of stability at grid point *g*, $p(r_t | s_g)$ is the likelihood probability of the result *r* at grid point *t* given grid point *g* is stable, $p(r_t)$ is the probability of the test result at grid point t, and $p(s_g | r_t)$ is the posterior probability of stability at grid point *g* given test result *r*, at grid point *t.* The Bayes' learning algorithm considers the physics of the stability boundary for updating the probability of stability. For brevity, the mathematical details of the Bayesian learning algorithm are not included in the paper; the reader is referred to [4] for details. After a test is completed, the result is used to update the probability of stability using Eq. 1. The posterior probability of stability becomes the prior for the next update and so on.

Using the probability of stability, the optimal test parameter is decided based on an expected improvement in material removal rate, MRR, criterion [4]. The expected improvement in MRR at a grid point is given by Eq. 2.

$$E[I(MRR)]_g = p(s_g) \times \frac{(MRR_g - MRR_{prior})}{MRR_{prior}} \quad (2)$$

In Eq. 2, the optimal MRR before a test is completed, denoted as MRR_{prior}, is determined as the optimal material removal rate among parameters that are stable with certainty. The expected improvement in the MRR criterion balances the trade-off between the prior probability of stability and the improvement in MRR if the parameter is stable. To illustrate the Bayes' learning procedure, Figure 5 shows the prior probability of stability. Recall that the axial depth of cut and spindle speed range for the testing was 0 mm – 8 mm and 5000 rpm – 9000 rpm. For the prior probability of stability, it is assumed that the information of the tool frequency response function is not known. The probability of stability decreases linearly from one at 0.01 mm to 0.01 at 8 mm. Note that classical stability analytical models consider stationary dynamics of the tool point FRF in a fixed coordinate frame. The structural dynamics of the instrumented tool holder change as the spindle rotates. It is shown that the stability diagram for a rotating asymmetric dynamic system changes [5]. This further presents the motivation for using an uninformed prior shown in Fig. 5 for the instrumented tool holder with asymmetric rotating dynamics.

The optimal parameter before any test is {9000 rpm, 0.01 mm}. The spindle speed and the axial depth of cut range are discretized in intervals of 10 rpm and 0.01 mm, respectively. The expected improvement in percentage material removal rate at each grid point is calculated using Eq. 2. Figure 6 shows the results. The optimal parameters for the first test are {9000 rpm, 4 mm}; this is shown as a yellow half-circle in Figure 6.

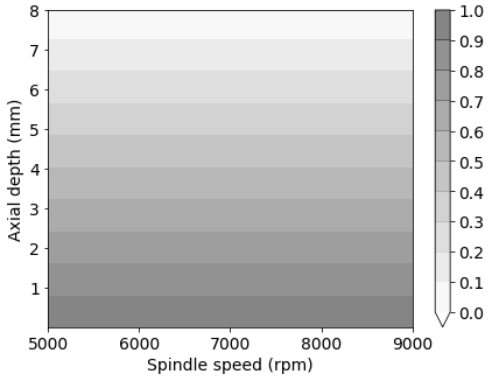

Figure 5. Prior probability of stability.

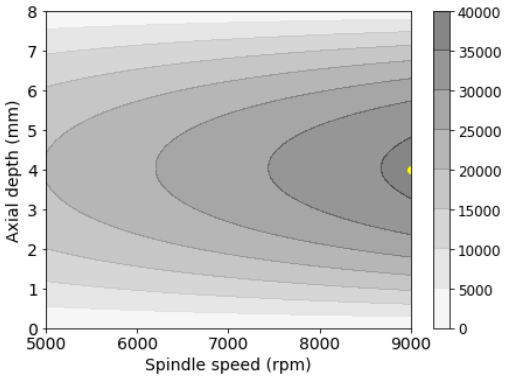

Figure 6. Expected improvement in percentage material removal rate for the first test.

RESULTS

As noted, the optimal test parameters are communicated to the TU Wien, Vienna, Austria. The test parameters were manually entered on the CNC machine and the test was completed. Future work will focus on automating the procedure by communication with the machine controller. The first test at {9000 rpm, 4 mm} was stable (see Figure 3). Figure 7 shows the updated probability of stability using the first test result and Figure 8 shows the expected percentage improvement in MRR for the second test. The optimal parameters for the second test were {9000 rpm, 5.2 mm}. The iterative testing procedure was repeated till the expected improvement in percentage MRR was less than 1%. Figure 9 shows the final results. The optimal parameters were {8700 rpm, 6.7 mm} after 11 tests. The maximum expected improvement in MRR after the 11th test is 0.2%, indicating convergence to the optimal parameters.

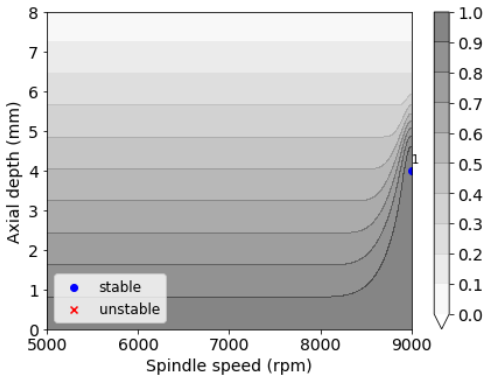

Figure 7. Updated probability of stability after a stable result at {9000 rpm, 4 mm}.

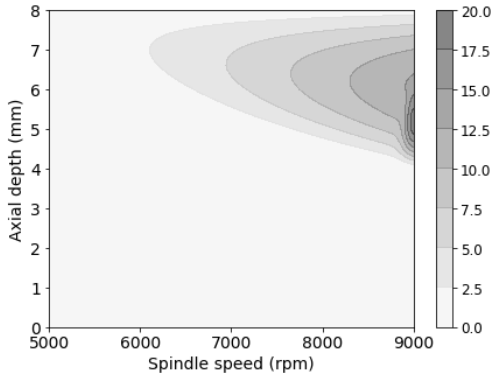

Figure 8. Expected improvement in percentage material removal rate for the second test.

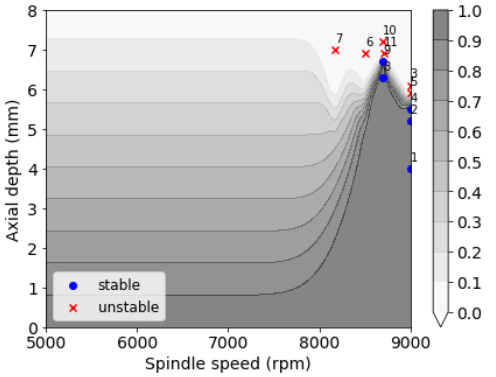

Figure 9. Updated probability of stability after 11 tests; the optimal stable parameters were {8700, 6.7 mm}.

CONCLUSIONS

This paper demonstrated a remote Bayesian learning approach for optimal stable parameter selection in milling. The test cuts were completed at the TU Wien, Vienna, Austria, and monitored with a sensory tool holder instrumented with an accelerometer. The data was shared through the cloud with Oak Ridge National Laboratory, Oak Ridge, Tennessee, USA, and the University of Tennessee, Knoxville, Tennessee, USA. The accelerometer data was used to classify the test cut as stable and unstable. The test result was used to update the probability of stability using a Bayesian learning method and select optimal test parameters, which were communicated back to the TU Wien for subsequent testing. The iterative process between two transatlantic locations was repeated and converged within 11 test cuts, achieving an optimal process parameter set.

The described approach can be automated to enable optimizing machining processes in production environments through data sharing

with a central location where the analysis is completed. The sensory tool holder enables continuous monitoring of the milling process. The combination of sensory tool holder and Bayesian stability map updating enables optimizing milling operations across different machines and tools. Future work will focus on monitoring production parts with the sensory tool holder and enabling a self-optimizing milling operation, where process parameters are updated in each successive run to converge to the optimal stable parameters.

ACKNOWLEDGEMENTS

This research was supported by the DOE Office of Energy Efficiency and Renewable Energy (EERE), Energy and Transportation Science Division, and used resources at the Manufacturing Demonstration Facility, a DOE-EERE User Facility at Oak Ridge National Laboratory. The authors also want to express appreciation and thanks to the Austrian Marshall Plan Foundation for supporting the research work and strengthening the academic exchange between TU Wien and U.S. universities.

REFERENCES

[1] Schmitz, T., and Smith, K.S., 2019, Machining Dynamics: Frequency Response to Improved Productivity, Second Edition, Springer, New York, NY.

[2] Bleicher, F., Schörghofer, P. and Habersohn, C., 2018. In-process control with a sensory tool holder to avoid chatter. Journal of Machine Engineering, 18.

[3] Bleicher, F., Ramsauer, C.M., Oswald, R., Leder, N. and Schoerghofer, P., 2020. Method for determining edge chipping in milling based on tool holder vibration measurements. CIRP Annals, 69(1), pp.101-104.

[4] Karandikar, J., Honeycutt, A., Schmitz, T. and Smith, S., 2020. Stability boundary and optimal operating parameter identification in milling using Bayesian learning. Journal of Manufacturing Processes, 56, pp.1252-1262.

[5] Comak, A., Ozsahin, O. and Altintas, Y., 2016. Stability of milling operations with asymmetric cutter dynamics in rotating coordinates. Journal of Manufacturing Science and Engineering, 138(8).

ACCOUNTING FOR SHRINKAGE IN FUNCTIONAL CERAMIC STRUCTURES PRINTED THROUGH TWO-PHOTON POLYMERIZATION

John Cortes[1], Magi Mettry[1], Matthew Worthington[1], Swetha Chandrasekaran[1], Robert Panas[1]
[1]Lawrence Livermore National Laboratory
Livermore, California, USA

INTRODUCTION

Advances in additive manufacturing during the last decade or two have revolutionized the way highly complex devices are both designed and manufactured at all scales. Geometries that were previously considered impossible to manufacture are now commonly printed through several methods and materials. Additive manufacturing creates the opportunity to manufacture highly intricate 3-dimensional structures using a single, highly repetitive process, one layer at a time.

Although most of that work has focused on macro-scale printing processes with plastics (and more recently, metals and composites), a significant scientific push has been made to also develop processes in the micron and sub-micron scale [1, 2, 3]. These advances have been advantageous for fields such as MEMS/NEMS, microfluidics and micro-scale optical systems.

Two-photon Polymerization (2PP) is one of the technologies that has allowed for development of 3D-printed microstructures. Two-photon Polymerization utilizes femtosecond laser pulses with two-photon absorption to generate features using a wide variety of photon-activated photoresists and resins with a resolution as high as 100 nm [4]. The print resolution of 2PP processes is determined by the exposure dose to the smallest polymerized volume. This dose can be finely tuned by both the pulse energy and the scanning speed [5] used during the writing step. Other parameters such as layer distance, hatching distance and number of scans per layer can also be implemented to tune the dose and material response more precisely.

Most of these resins result in polymer structures which are limited in their application due to their poor mechanical properties. However, the use of ceramic resins has recently been developed for 2PP processes [6, 7]. They generally come in the form of polymer-derived ceramics (PDC) and are highly tuneable based on their molecular compositions. While these resins feature much more favourable mechanical properties, they tend to shrink anywhere from 30-55% during post-processing [8, 9]. This may not be desirable and difficult to design for in precise MEMS/NEMS applications, therefore it is crucial that this shrinkage be fully understood and accounted for in structures that may require assembly and precise placement.

In this work, we study the shrinkage of 2PP-printed silicon oxycarbide (SiOC) disk microstructures that feature strain relief structures. These are meant to keep these micro-disks centered and aligned for assembly purposes. This type of procedure could be useful in the assembly process of many MEMS devices, such as micromirrors, which require precise positioning between capacitance-driven paddles and the mirrors [10].

METHODS

The two-photon printing process was carried out in a commercially available NanoScribe GmbH Photonic Professional GT laser lithography system at LLNL's Advanced Manufacturing Laboratory (AML). This device features a TOPTICA laser with a wavelength of 780 nm and a pulse duration of approximately 100 fs. The lens used was a Zeiss 63x1.4NA oil DIC M27. A single-side polished silicon chip measuring approximately 1 cm by 1 cm was treated by 3-(Trimethoxysilyl)propyl methacrylate (Silane) for 5 minutes at 90 °C to aid with print adhesion.

After the treatment, the silicon chip was cleaned with IPA. A drop of the custom polymer-derived ceramic (PDC) resin was applied to the polished side of the silane-treated silicon chip. The structures were printed up-side-down using "dip-in laser lithography." The printed structure was then developed by submerging it in a beaker of propylene glycol monomethyl ether acetate (PGMEA) overnight.

After full development, the sample was dried using a Microscopy Sciences 3100 critical point

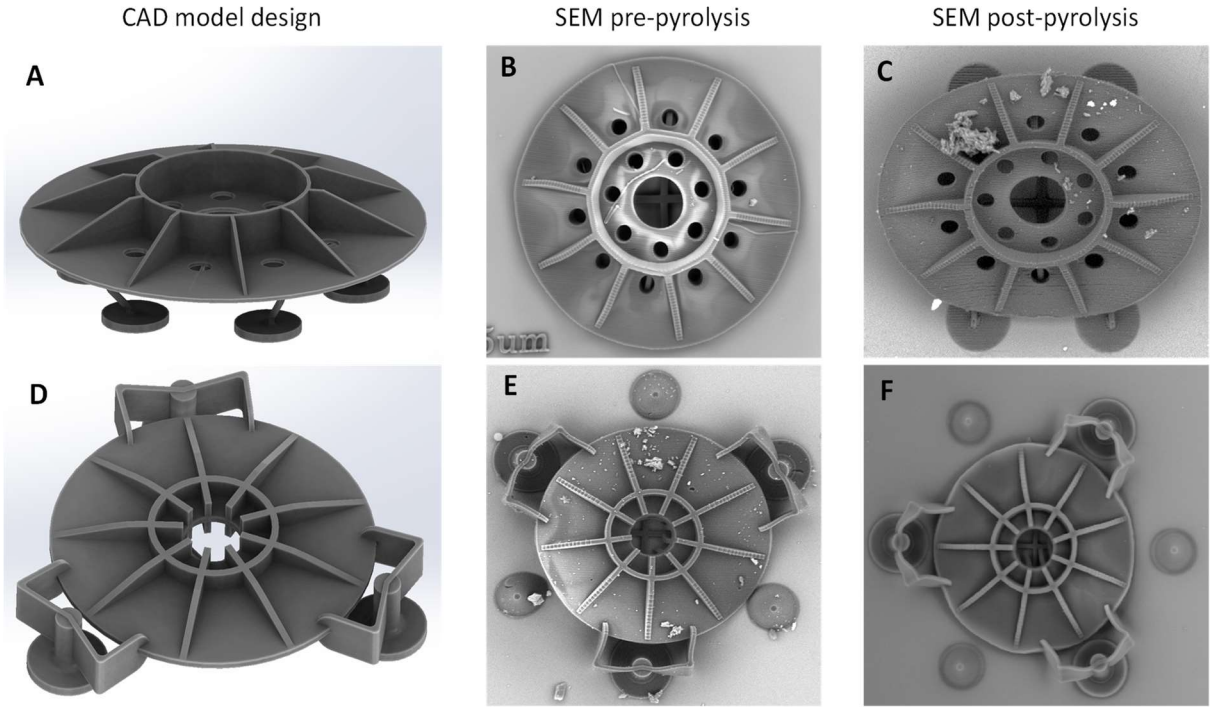

FIGURE 1. A) CAD model of a 120 µm diameter disk with six self-centering stress relief legs. B) SEM image of the disk before the pyrolysis step. C) SEM image of the disk after pyrolysis after 35% isotropic shrinkage. D) CAD model of a 120 µm diameter disk with three self-centering stress relief blades. E) SEM image of the disk before the pyrolysis step. F) SEM image of the disk after pyrolysis after 38% isotropic shrinkage.

drying system. After critical-point-drying, the samples were pyrolyzed in an oven in a nitrogen atmosphere at temperatures of 250° C, 400° C, 600° C and 1000° C, each step for an hour. The sample was then allowed to cool down to room temperature at a rate of 5° C per min. The samples were then characterized using a Phenom XL benchtop scanning electron microscope (SEM).

RESULTS

We have designed and fabricated 120.0 µm wide, 2.5 µm thick suspended disks that feature two different types of self-centering strain relief legs that are designed to account for the shrinkage that is characteristic of 2PP-printed ceramic materials. These types of strain-relief structures are necessary for ceramic prints because the shrinkage generally causes the print to delaminate from the surface as it contracts.

The two different designs are shown in figure 1. The first design (panels A, B, C) features legs that accommodate the shrinkage by rotating underneath the disk about the anchor base and act as a pin joint. Each individual leg features two "pinch points" that flatten the otherwise circular legs to promote bending towards the center axis of the disk.

The legs themselves are 3.0 µm in diameter but are reduced to a width of 1.5 µm at the pinch points. This design is effective in guiding the disk's outer edge towards the center axis as it shrinks. Though the shrinkage of these pre-ceramic resins is known to be mostly isotropic in nature, variations in thickness and feature type could cause misalignment during shrinkage. Adding these engineered strain-relief legs accounts for those potential variations.

The second design (panels D, E, F) features a set of three, 2.0 µm thick, 10.0 µm tall vertical blades that bend inward as the main disk structure shrinks. The blades are anchored by a 6.0 µm thick post which is designed to be rigid, with minimal bending. Both of these designs are able to accommodate shrinkages as high as 50% before mechanical failure.

More importantly, these strain relief structures have been shown to not only accommodate for

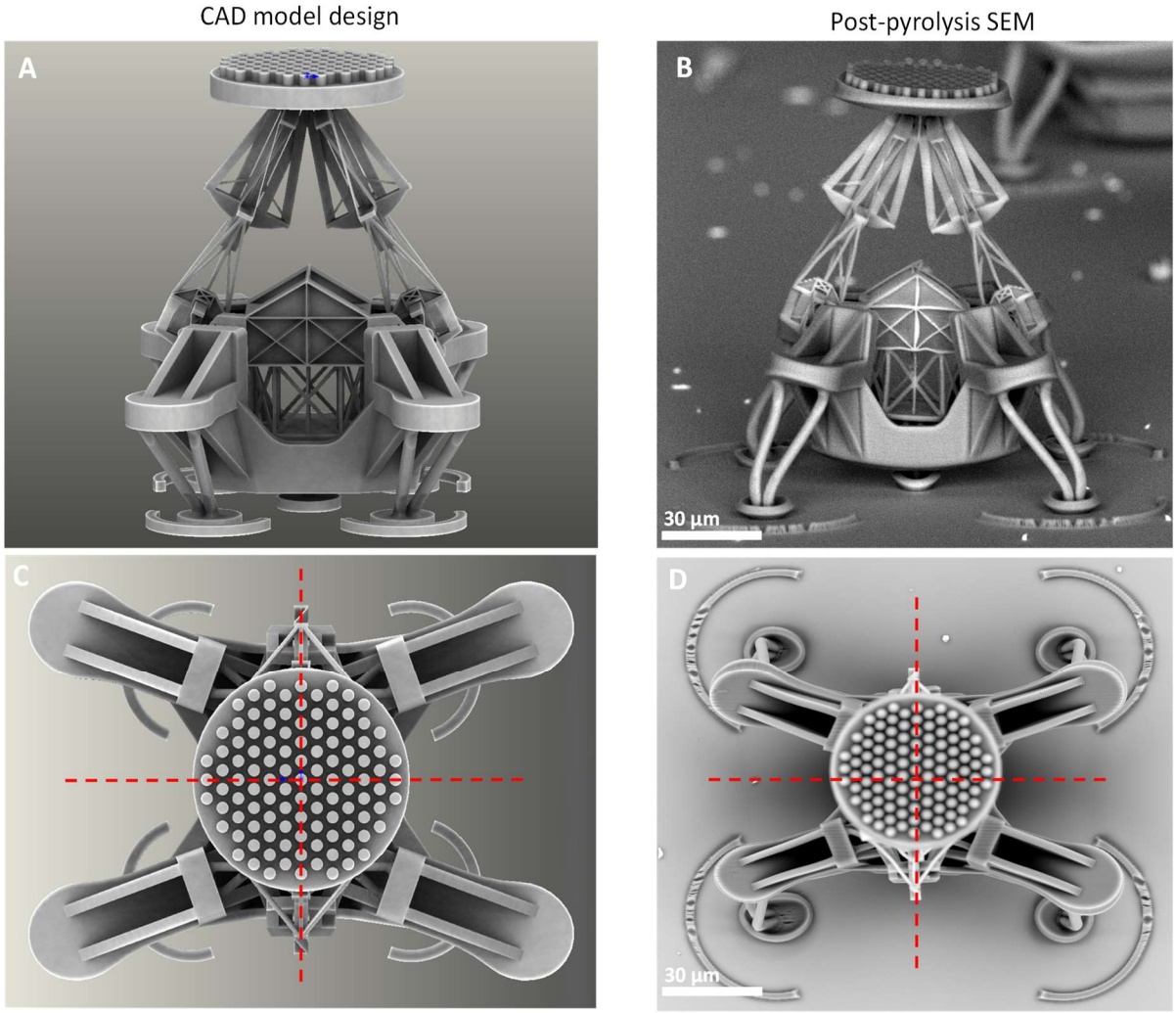

FIGURE 2. A) Side view of the CAD model of a functional MEMS component within a self-centering structure with four stress relief legs. B) Side view SEM image of the structure after shrinking during the pyrolysis step. C) Top view of the CAD model of a functional MEMS component within a self-centering structure with four stress relief legs. D) Top view SEM image of the structure after shrinking showing the centered alignment.

the shrinkage in the ceramic material, but they also keep the centerline of the disk within an acceptable range for precision assembly. Each ceramic print features a crosshair at the base in the center, so that the shift from the center axis can be fully characterized. We found that even though the disks themselves shrink as much as 40%, the centerline of the disks remain within approximately 3 µm of their starting position when measured from above through SEM imaging. Out of the 20 total disks that were printed (10 of each strain relief structure type), the maximum deviation was 3.5 µm. seven out of the twenty disks shifted less than 1 µm from their centerline, though they displayed shrinkage of about 35%-40%.

These structures were printed with optimized parameters to minimize the amount of shrinkage. The power input to each voxel ranged from 35% to 45% (of the maximum 150 mW produced by the Nanoscribe laser) with scan speeds ranging from 6,000 µm/s to 8,000 µm/s. In addition to these parameters, each individual voxel was printed with a multi-pass approach which energized each layer after a brief pause. The layer-to-layer distance was kept at a constant 100 nm. Similarly, the lateral hatching distance was maintained at a constant 300 nm.

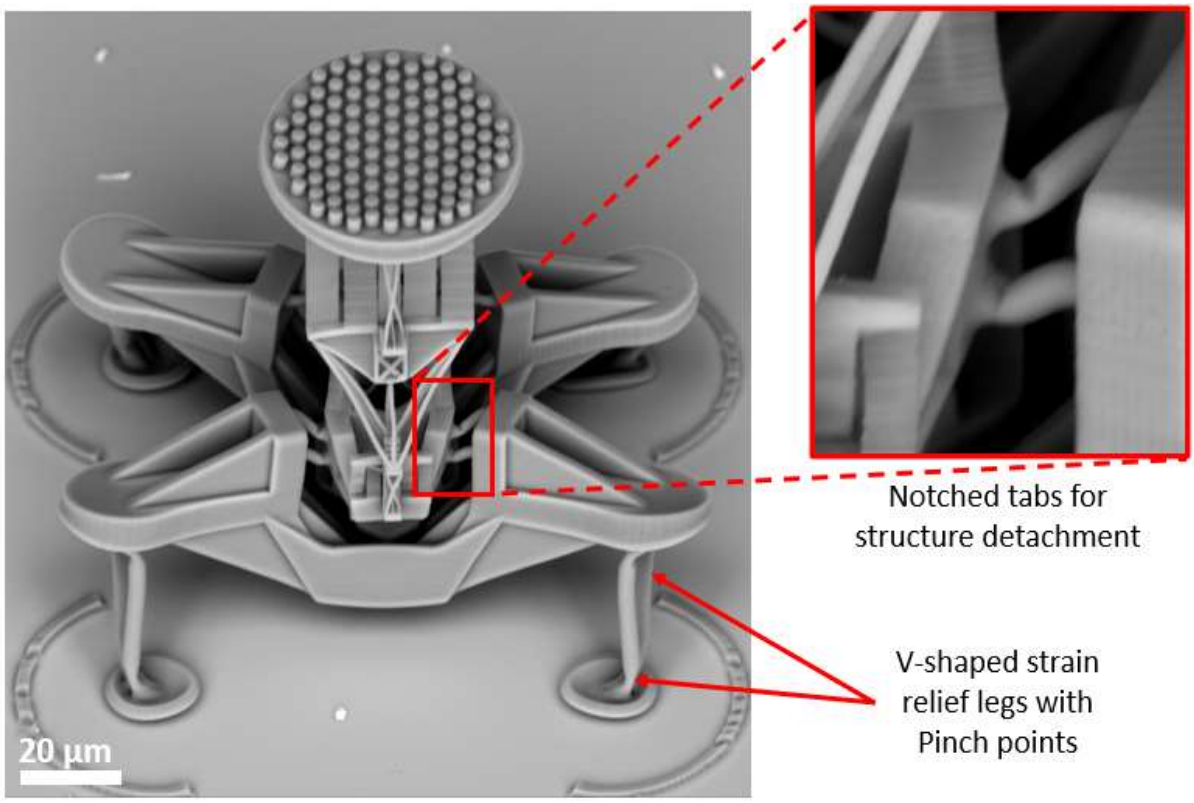

FIGURE 3. SEM image of a complex MEMS micromirror leg printed on a strain-relief structure. The structure features four sets of flexible legs that guide the central structure during shrinkage and ensure that it remains aligned with its center axis during the process. The leg and strain relief structure are connected by 8 notched linkages, which are designed to mechanically fail when the MEMS leg is pulled in the upward direction.

The multi-pass approach resulted in the maximum amount of cross-linking in the material before the critical point drying and pyrolysis steps, which contribute to the overall shrinkage of the structure. Testing found that doing two passes per voxel produced the least amount of shrinkage while producing accurate prints.

Adding more passes slightly decreased shrinkage by about 5%, but there is a significant sacrifice in print quality and accuracy to the designed model. Phantom features can be created as the laser's focal point changes due to the voxels being crosslinked from previous passes. This can be more problematic on functional prints that have small, sub-micrometer features whose performance depends on model to print accuracy.

CASE STUDY: MEMS MICROMIRRORS

We turned our focus on testing one the strain-relief approaches for functional devices as well, not just static disks. Figure 2 shows the strain-relief approach being applied to a set of legs meant for a functional MEMS micro-mirror device. In this application, four sets of V-shaped "pinched" legs are implemented to not only keep the functional structured centered, but also to minimize potential rotation during shrinkage. The legs themselves are 2 µm in diameter and are reduced to 1 µm at the pinch point. There is also an additional attachment point at the bottom of the structure in the center in the structure

These highly complex devices were printed and processed using the same approach as for the disks. The design shows that even highly complex structures can remain centered during shrinkage with this approach. We take advantage of the fact the shrinkage is both linear and isotropic. Specifically, we were able to

consistently produce structures that are aligned within 2 μm of their designed center axis. Being able to maintain this level of alignment is very important for this specific set of legs, since they will eventually be integrated into a large micromirror array that will feature hundreds of legs that must be aligned to micrometer scale for the whole device to work properly.

The leg itself is detachable through a set of pop-out tabs that have small notches on them, as shown in Figure 3. This allows the central support structure (which is maintained centered by the strain relief legs) to remain in place while the stamp procedure is performed. A similar process is outlined in [10] for an array featuring seven mirrors with 2PP-printed polymer legs. These ceramic legs would allow these types of MEMS micro-mirrors to have an increased range of motion at even higher frequencies.

CONCLUSION AND FUTURE WORK

This work shows a path towards integrating ceramic-based, 2PP-printed structures with functional devices that would benefit from the improved mechanical properties. One of the current barriers to this integration and wider implementation is the amount of shrinkage that the preceramic resins display. We propose to account for that shrinkage with the use of engineered strain relief support structures, which contain the functional structure within them and maintain it centered within an acceptable range for assembly.

The next step of this project is to test the detachable structures for stamping and assembly. We will then move to test multiple structures at one time and perform single and double-stamp procedures to assemble functional structures into pre-determined positions. Future research will also explore the possibility of developing new resin recipes to produce ceramic prints that do not shrink as much during pyrolysis.

ACKNOWLEDGEMENTS

This work was performed under the auspices of the U.S. Department of Energy by Lawrence Livermore National Laboratory under Contract DE-AC52-07NA27344 (LLNL-CONF-826753) and supported by LDRD 19-ERD-018.

REFERENCES

[1] Saha, et al. “Scalable Submicrometer Additive Manufacturing.” Science, vol. 366, no. 6461, 2019, pp. 105–109.

[2] Chu, et al. “Centimeter Height 3D-Printing with Femtosecond Laser Two-Photon Polymerization.” Advanced Materials Technologies, vol. 3, no. 5, 2018, p. 1700396.

[3] Ngo, Kashani, Imbalzano, Nguyen and Hui. “Additive manufacturing (3D printing): A review of materials, methods, applications and challenges.” Composites Part B: Engineering, vol. 143 (2018).

[4] Zheng, Kurselis, El-Tamer, Hinze, Reinhardt, Overmeyer and Chichkov. “Nanofabrication of High-Resolution Periodic Structures with a Gap Size Below 100 nm by Two-Photon Polymerization.” Nanoscale Res Lett., vol. 14, 134 (2019).

[5] Ovsianikov et al. “Two Photon Polymerization of Polymer–Ceramic Hybrid Materials for Transdermal Drug Delivery.” Int. J. Appl. Ceram. Technol. 2007, vol. 4, issue 1, p. 22–29.

[6] Cui, et al. “Additive Manufacturing and Size-Dependent Mechanical Properties of Three-Dimensional Microarchitected, High-Temperature Ceramic Metamaterials.” Journal of Materials Research, vol. 33, no. 3, 2018, pp. 360–371.

[7] Eckel, et al. “Additive Manufacturing of Polymer-Derived Ceramics.” Science, vol. 351, no. 6268, 2015, pp. 58–62.
Polymerization.” Nanoscale Res Letters, vol. 14, 134 (2019).

[8] Brigo, Schmidt, Gandin, Michieli, Colombo and Brusatin. “3D Nanofabrication of SiOC Ceramic Structures.” Adv. Sci. 2018, vol. 5, 1800937.

[9] Bauer et al. “Additive Manufacturing of Ductile, Ultrastrong Polymer-Derived Nanoceramics.” Matter, vol. 1, no. 6, 2019, p. 1547-1556.

[10] Hopkins, et al. "A High-Speed Large-Range Tip-Tilt-Piston Micromirror Array." Journal of Microelectromechanical Systems, vol. 26, no. 1, pp. 196-205, Feb. 2017.

PRECISION STAMP-BASED 2D MATERIAL TRANSFER SYSTEM USING SOFT-ROBOTIC MANIPULATION

Seong-Hyo Ahn and Lei Zhou
Walker Department of Mechanical Engineering
University of Texas at Austin, TX, USA

INTRODUCTION

Monolayer 2D materials, such as graphene, hBN, and MoS_2, can be assembled into vertical-layered heterostructures (VLH) to realize a new class of ultra-thin opto-electronic devices [1, 2], which have excellent potential for various applications including transparent displays and optical sensor arrays. The recent advances in material synthesis techniques, such as chemical vapor deposition, have enabled the fabrication of large-area 2D materials, and lithographic technology can produce patterned arrays of 2D materials. However, to date, the assembly of VLH from monolayer material building blocks is primarily through manual operation under visual alignment inspection using an optical microscope and is typically limited to the fabrication of a single device or a small-area device array. Such a manual assembly approach is not feasible for VLH array manufacturing over a large area, and the lack of a reliable and automated monolayer assembly approach has been limiting the application of 2D-material-based electronics. Therefore, the long-term objective of our work is to create a precise, scalable, and defect-free assembly approach for patterned 2D monolayers into wafer-scale VLH-based devices and even integrated circuits.

Among various 2D material transfer approaches [3], dry stamp transfer is having the best potential in scaling up for automatic monolayer assembly to have high throughput, precision alignment, and a clean interface between layers. Figure 1 shows a schematic for the envisioned process of stamp-based 2D material pickup and transfer for VLH manufacturing. Here, a soft stamp made of a transparent, viscoelastic polymer (typically PDMS) with precision position and force control is used to manipulate the monolayer materials using the interfacial adhesion properties. The adhesion strength between the stamp and substrate can be controlled via external stimuli such as temperature or peeling speed. This approach has been used for micro-contact printing and imprint lithography [4–6].

As a first step towards our long-term vision, this paper presents the design, building, and testing of a soft-robotic elastomer stamp head unit for thin-film material manipulation, and specifically to achieve step (b) in Figure 1, i.e. making bubble-free contact between the stamp and a silicon wafer substrate over a large area. The main contribution of this paper include: (a) created a simple approach to achieve bubble-free contact between the stamp and the target over a large area (Diameter $\sim$50 mm) through automatic operation, and (b) experimentally validated the performance of the proposed approach.

HARDWARE OVERVIEW

Fig. 2a shows a CAD model for the proposed soft-robotic stamp prototype, and Fig. 2b shows a diagram of the pneumatic actuation of the stamp's bowing motion. The soft-robotic stamp's main features include: (1) The PDMS stamp is clamped down to a solid transparent stamp chuck by a ring-shaped vacuum clamp; (2) The stamp's out-of-plane motion is controlled pneumatically in order to make stamp-substrate contact without air bubbles; (3) Flexure mechanism is used to allow the stamp chuck's vertical-, tip-, and tilt-directional motion; (4) Four inductive sensors are used to measure the vertical-, tip-, and tilt-directional relative position between the stamp chuck and the substrate, and four voice coil actuators are used to control the stamp's motion in these degrees of freedom when making contact and applying pressing force.

We have designed and constructed a prototype for the proposed soft-robotic stamp head unit as shown in Fig. 3, which mainly consists of a voice-coil-driven flexure system to actuate the rigid body motion at the stamp chuck, a pneumatic actuation system for the PDMS stamp for the bowing motion, and an instrumentation and control system. The rest of this section discusses the design and prototyping of these subsystems.

Pneumatic Actuation of Stamp

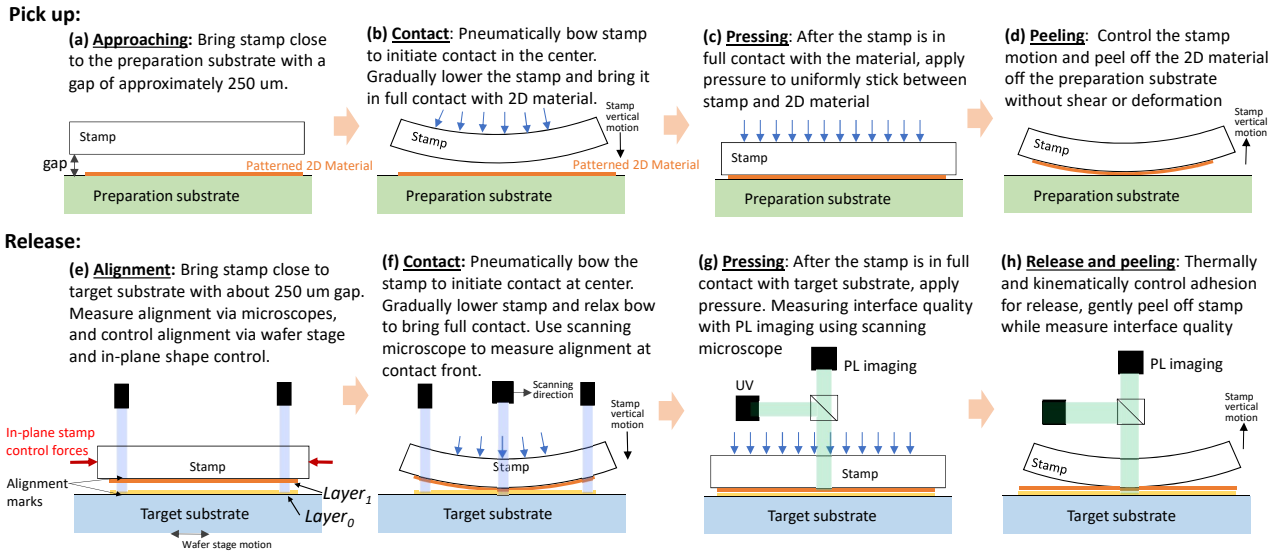
Pick up:
(a) Approaching: Bring stamp close to the preparation substrate with a gap of approximately 250 um.
(b) Contact: Pneumatically bow stamp to initiate contact in the center. Gradually lower the stamp and bring it in full contact with 2D material.
(c) Pressing: After the stamp is in full contact with the material, apply pressure to uniformly stick between stamp and 2D material
(d) Peeling: Control the stamp motion and peel off the 2D material off the preparation substrate without shear or deformation
Stamp
gap
Patterned 2D Material
Preparation substrate
Stamp vertical motion
Release:
(e) Alignment: Bring stamp close to target substrate with about 250 um gap. Measure alignment via microscopes, and control alignment via wafer stage and in-plane shape control.
(f) Contact: Pneumatically bow the stamp to initiate contact at center. Gradually lower stamp and relax bow to bring full contact. Use scanning microscope to measure alignment at contact front.
(g) Pressing: After the stamp is in full contact with target substrate, apply pressure. Measuring interface quality with PL imaging using scanning microscope
(h) Release and peeling: Thermally and kinematically control adhesion for release, gently peel off stamp while measure interface quality
In-plane stamp control forces
Alignment marks
Target substrate
Wafer stage motion
Scanning direction
UV
PL imaging

FIGURE 1. Diagram for stamp-based pick-up and release manufacturing process.

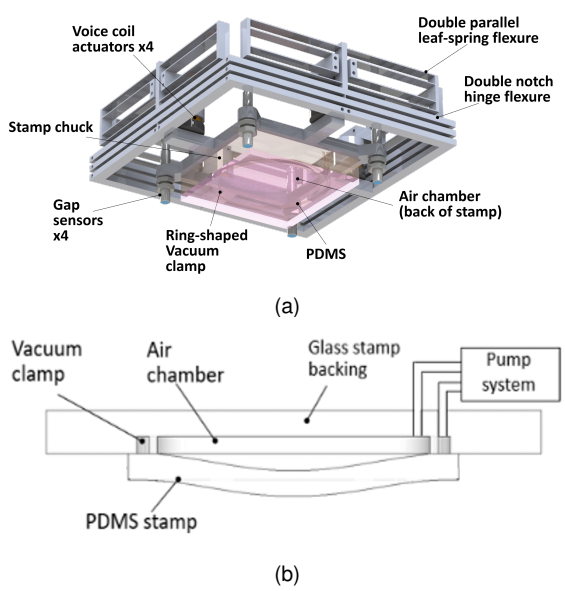

FIGURE 2. (a) CAD model of a flexure-supported stamp. (b) Diagram of pneumatic actuation of the stamp.

Fig. 2b shows the design of the pneumatic actuation system for the PDMS stamp. The 100x100x5 mm PDMS(Sylgard 184, 10:1 mix ratio) is clamped onto an optically transparent acrylic stamp chuck via vacuum clamping. Pneumatic pressure is applied in the air chamber at the center of the stamp chuck, which is controlled by a syringe pump driven by a stepper motor supported via a lead screw (Fig. 3). The pressure is measured by a pressure sensor

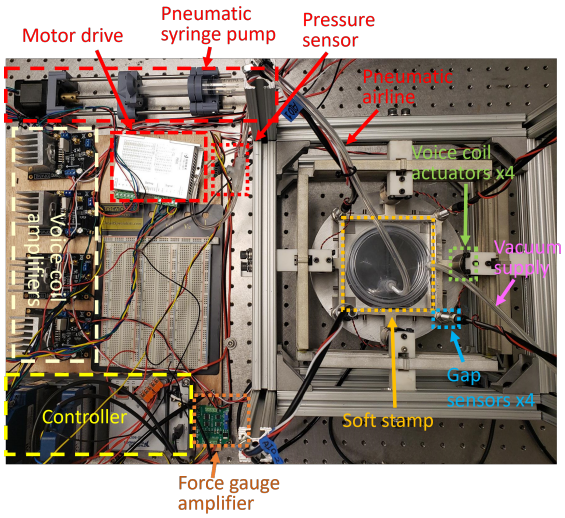

FIGURE 3. Photograph of the soft-robotic stamp head unit prototype

(ADP51B62, Panasonic). Fig. 4 shows the deflection of the PDMS stamp, where Fig. 4a shows the finite-element-simulated out-of-plane motion of the PDMS stamp under 1.5 kPa pneumatic pressure, and Fig. 4b shows the experimentally measured maximum out-of-plane displacement of the stamp at the center under varying pneumatic pressure measured by a pressure sensor. It can be observed, within a small deflection range (stamp out-of-plane displacement within 5 mm), the stamp's deformation is largely linear with respect to the pneumatic pressure applied.

Voice-Coil-Driven Flexure Stage

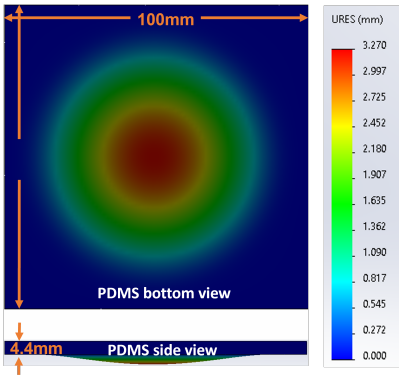

(a)

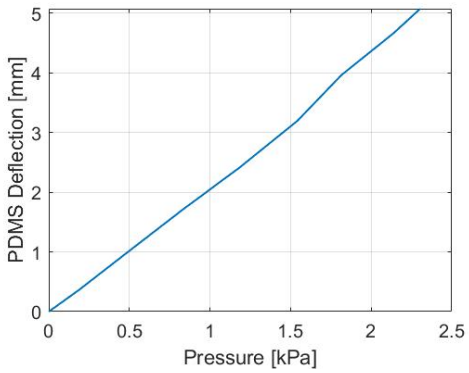

(b)

FIGURE 4. (a) Finite element simulated out-of-plane deflection of the PDMS stamp under 1.5 kPa pneumatic pressure. PDMS mechanical properties: E(Young's modulus)=1.39 MPa, ν(Poisson's ratio)=0.499 [7]. (b) Experimentally measured out-of-plane motion of PDMS stamp under varying pneumatic pressure.

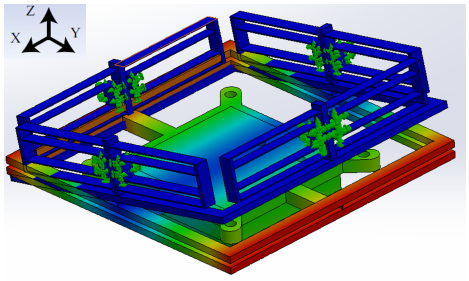

(a)

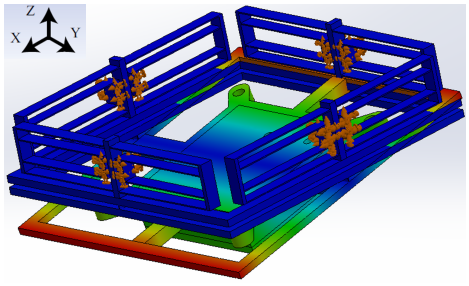

(b)

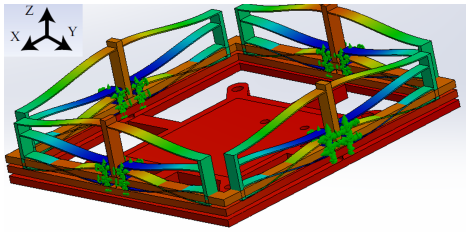

(c)

FIGURE 5. First three vibration modes of the flexure for stamp chuck. (a) Tip mode, resonance frequency 8.27 Hz. (b) Tilt mode, resonance frequency 10.31 Hz. (c) Vertical translation mode, resonance frequency 12.93 Hz.

To achieve controlled contact and pealing of thin-film material from flat substrates, the stamp needs to allow motion in tip, tilt, and vertical degrees of freedom. To accomplish this desired stamp motion, we designed and fabricated a flexure system which constrains the stamp's lateral- and yaw-directional motions, and is compliant with the desired motion DOFs. Fig. 2a shows the CAD model for the flexure system design, and Fig. 5 shows its first three vibration modes. The proposed flexure system consists of a double notch hinge flexure mechanism and a double parallel leaf-spring flexure mechanism connected in series [8]. The double notch hinge flexure (Fig. 5a and b) enables compliance in the tip- and tilt-DOFs, and the double parallel leaf-spring flexure (Fig. 5c) enables long-stroke translational motion along the vertical axis. The flexure system is designed surrounding the stamp chuck to avoid blocking the optical path from the top, which is critical to allow optical inspection for precision alignment between layers. Four voice coil actuators (LVCM-025-022-01, Monticont) are used to actuate the stamp chuck's motion in the vertical-, tip-, and tilt-directions, and four inductive sensors (DW-AX-509-M8-390, Contrinex) are arranged at the four corners of the stamp chuck to measure the displacement of the stamp chuck. Fig. 6 shows the flexure system actuation performance: maximum possible bending angle(0.62°) and maximum possible vertical translation travel length(7.20 mm).

Instrumentation and Control

The real-time control for the soft-robotic stamp head unit uses a CompactRIO with the control loop operating at a sampling rate of 1 kHz. The real-time controller measures the output from the inductive sensors and pressure sensors, and out-

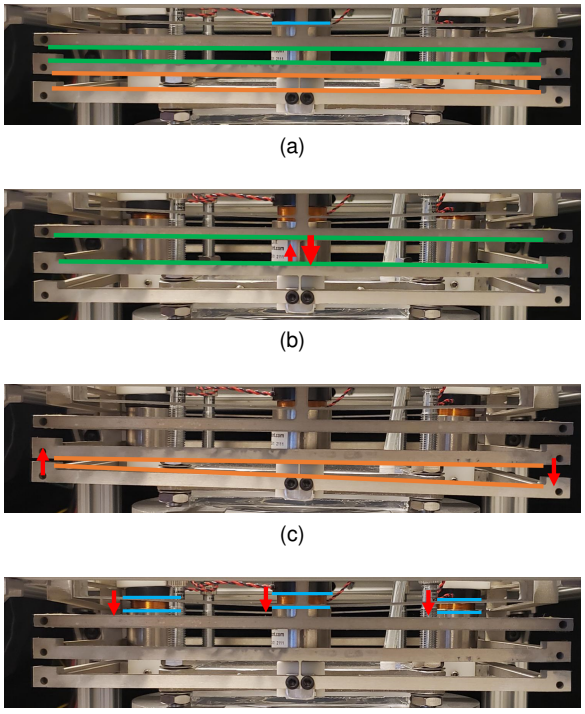

(a)

(b)

(c)

(d)

FIGURE 6. Maximum flexure displacements in tip, tilt, and vertical translation mode. (a) Initial position. (b) Tip mode(0.62°). (c) Tilt mode(0.62°). (d) Vertical translation mode(7.20 mm).

puts the signals to control the pneumatic pressure as well as the voltage command to the voice coil actuators. Four linear power amplifiers (OPA541, Texas Instruments) are used to generate the current to energize the voice coil actuators. In addition, As shown in Figure 7, an S-shape load cell (DY, DYLY, measurement range: 0-5 kg) is fixed underneath the target substrate in order to measure the force pressing and peeling force between the stamp and the substrate. An optical microscope (3134-A62509, Plugable, 50x magnification) is used to inspect the stamp-substrate contact quality.

EXPERIMENTAL EVALUATIONS

Experiments of automatic gentle contact between the soft-robotic PDMS stamp and a flat substrate are conducted to evaluate the performance of the system, with a target of generating bubble-free contact of an area over 50 mm diameter. Here, a 4-inch silicon wafer is used as the substrate, which is held by an aluminum wafer holder. The stamp-wafer contact process is as follows: (1) Bring the stamp chuck close to the substrate with a gap of 3 mm with the PDMS stamp flat and not pressurized; (2) Pressurize the air chamber in the

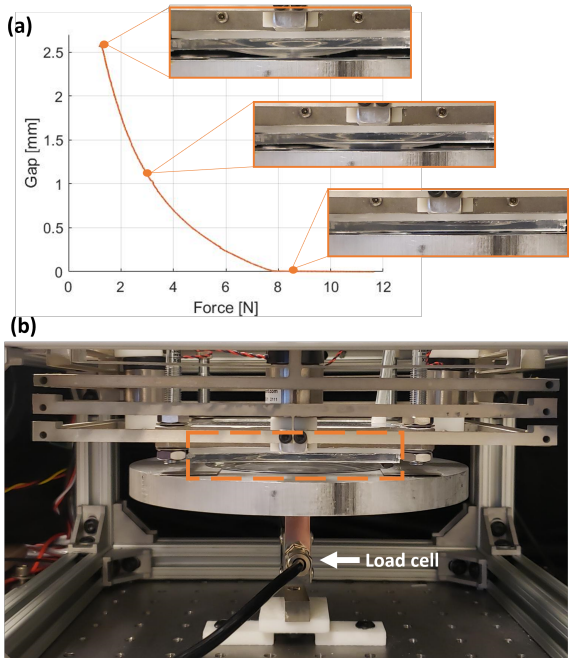

FIGURE 7. (a) Experimentally measured stamp-substrate gap under varying pressing force. (b) Side view photograph of the experimental setup.

stamp chuck and bow out the PDMS stamp until the stamp touches the wafer substrate at its center; (3) Slowly lowers the stamp chuck by the voice coil actuators to increase the stamp-wafer contact area while reducing the air pressure, until the contact area is sufficiently large. In the experiment process, stamp-wafer pressing forces and gap between the wafer and stamp chuck are measured in real-time, and the optical microscope is used to visually inspect the contact quality.

Fig. 7 shows the experimentally measured pressing force and the gap length between the stamp chuck and the substrate. It can be observed that as the gap reduces, the required force to further bring the stamp chuck close to the substrate is increasing. This is because the pressurized PDMS behaves like a spring with increasing stiffness in this process. The PDMS stamp is in full contact with the wafer when the gap measurement reaches 0 mm, which takes 8 N from the voice coil actuators. The system can then further increases the pressing force between the stamp and the substrate 11.7 N, and this force can be used to further facilitate sticking between the stamp and target material to be transferred in our future tests for material transfer.

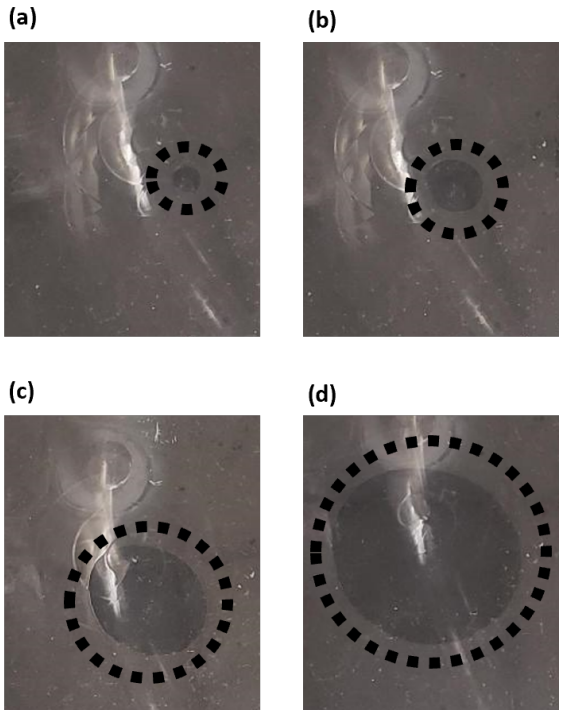

FIGURE 8. Microscope images of the stamp-wafer contact process under 50x magnification. (a)–(d) Contact area grows from 2mm to 25mm diameter.

Fig. 8 shows the snapshots of the contact front between the PDMS stamp and the wafer taken by the microscope during the contact process. It can be observed that the contact surface area is gradually increased from the apex of the dome-shaped PDMS stamp, and the contact front expands radially. Note that these contact experiments were conducted without contamination control, and thus dust particles were inevitably collected in the stamp-wafer interface. In future, we will repeat the tests with clean and freshly-cured PDMS stamps in a clean-room environment to minimize contamination.

Fig. 9 shows a comparison between the stamp and wafer contact quality with and without the stamp bowing out. Fig. 9a and b are images of the contact interface without the PDMS bow-out motion, which show that air bubbles are trapped in the stamp-wafer interface. When using the stamp for material transfer, such air bubbles create missing flake errors in the contact which is detrimental to the device array quality. In contrast, Fig. 9c shows a microscope view of a stamp-wafer contact interface created by the stamp first bowed

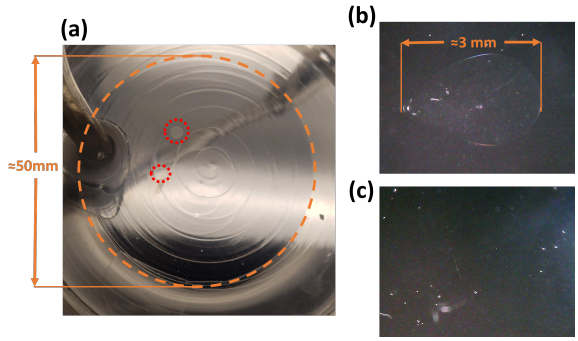

FIGURE 9. Comparison between the stamp-substrate contact quality without and with stamp bowing out. . (a) without bowing out (b) Microscopic view of an air bubble trapped in the PDMS-wafer interface. (c) Microscopic view of a bubble-free contact interface.

out pneumatically, where no air bubble is generated as the contact area increases. This comparison shows the effectiveness of the proposed soft-robotic stamp for bubble-free contact, which is critical to avoid bubble-type defects in the material transfer.

CONCLUSION AND FUTURE WORK

In this work, we have designed and built a soft-robotic stamp head unit for a PDMS stamp targeting a thin-film material transfer application. We showed that the proposed system can effectively create high-quality bubble-free contact of a large area of 50 mm diameter through automatic operation, which shows promise for the effective manipulation of thin-film materials. Our future works include: (1) experimentally test the pick-up and transfer of thin-film materials using the soft robotic stamp, and (2) identify the key parameters that determine the material handling and release quality through inline and offline optical microscope-based inspections.

REFERENCES

[1] Geim AK, Grigorieva IV. Van der Waals heterostructures. Nature. 2013;499(7459):419–425.

[2] Hou L, Zhang Q, Shautsova V, Warner JH. Operational Limits and Failure Mechanisms in All-2D van der Waals Vertical Heterostructure Devices with Long-Lived Persistent Electroluminescence. ACS nano. 2020;14(11):15533–15543.

[3] Fan S, Vu QA, Tran MD, Adhikari S, Lee YH. Transfer assembly for two-dimensional van

der Waals heterostructures. 2D Materials. 2020;7(2):022005.

[4] Carlson A, Bowen AM, Huang Y, Nuzzo RG, Rogers JA. Transfer printing techniques for materials assembly and micro/nanodevice fabrication. Advanced Materials. 2012;24(39):5284–5318.

[5] Meitl MA, Zhu ZT, Kumar V, Lee KJ, Feng X, Huang YY, et al. Transfer printing by kinetic control of adhesion to an elastomeric stamp. Nature materials. 2006;5(1):33–38.

[6] Bender M, Plachetka U, Ran J, Fuchs A, Vratzov B, Kurz H, et al. High resolution lithography with PDMS molds. Journal of Vacuum Science & Technology B: Microelectronics and Nanometer Structures Processing, Measurement, and Phenomena. 2004;22(6):3229–3232.

[7] Johnston I, McCluskey D, Tan C, Tracey M. Mechanical characterization of bulk Sylgard 184 for microfluidics and microengineering. Journal of Micromechanics and Microengineering. 2014;24(3):035017.

[8] Hopkins JB, Culpepper ML. Synthesis of precision serial flexure systems using freedom and constraint topologies (FACT). Precision Engineering. 2011;35(4):638–649.

DUCTILE CUTTING REGIME IN DIAMOND MILLING OF MONOCRYSTALLINE SILICON

Marvin Groeb[1,2], Matthias Fritz[1], Johann Groeb[3], Wolfgang Ensinger[2]
[1]Kern Microtechnik GmbH
Eschenlohe, Germany
[2]Department of Materials Science
Technical University of Darmstadt
Darmstadt, Germany
[3]Independent Researcher
Darmstadt, Germany

INTRODUCTION

The market for optical elements has been valued at $ 3.6 billion in 2012, and has been forecast to reach $ 12.3 billion by 2019 [1]. Rising requirements to the finished surface inevitable lead to higher part cost, as the required machine tool, tooling and process time increase the overall cost dramatically. Because of the low density, low thermal expansion and relatively low cost, monocrystalline silicon is chosen as a lens material in IR and X-ray applications [2]. Moreover, silicon is one of the building blocks of the current semiconductor technology [3]. The quality control of packaged chips via ultrasonic microscopy requires high quality surface finishes [4], [5]. Currently, high quality finishes are achieved via either chemical-mechanical polishing [6], [7], lapping [8], [9] or diamond turning [10], [2]. Since the late 80s, single point diamond turning (SPDT) uses the phenomena of a brittle to ductile transition [11], [12] to achieve high quality finishes in brittle materials. Unfortunately, SPDT is characterized with low productivity and high part cost, [13] as well as limited shape freedom due to the accessability from the diamond tool. Mirror finish milling with monocrystalline diamond tools has been possible in a number of brittle materials such as Germanium [14], glass [15], but also softer non-ferrous material, for instance aluminium [16]. This paper explores the side as well as face milling in polish quality of monocrystalline silicon with a monocrystalline diamond tool.

METHODOLOGY

The milling experiments were performed on a Kern Micro HD precision CNC machining center. It features microgap hydrostatic guideways, linear motors and glass scales with nanometric resolution, enabling a positional accuracy well below 1 µm. The machine was equipped with an HSK 40 spindle manufactured by Fischer, having a maximum rotational speed of 42000 min^{-1} and a rated power of 15.6 kW. The sample specimen was fixtured by superglueing it to a piece of aluminium (EN AW 5081). The material used is an industry standard semiconductor grade monocrystalline silicon. Roughing and semi finishing was undertaken with PCD endmill (diameter 8 mm) manufactured by Dixi Polytool. The used NC code was written in Heidenhain plain text on the TNC 640 control. A contour smoothing cycle of 0.0005 mm was active during the operation. The coolant used is a GTL oil (Oelheld SintoGrind TC-X 1500). The monocrystalline flat end mill (6 mm diameter) was produced by Contour Fine Diamonds. The tools were held in a Regofix PowRgrip toolholder. Tests were performed in a temperature controlled environment. Before taking a cut, a spindle warm-up period of 2 minutes was completed, to reduce thermal influences. The work piece temperature was further stabilized by application of the tempered flood coolant for 10 minutes before the experiment. Measurements were taken after the sample was cleaned with isopropyl alcohol in an ultrasonic cleaner. The accoustic emission (AE) signal (Marposs AE6000) is recorded via a Picoscope 5244D digital oscilloscope. All quantitative measurements were recorded with a Confovis CLSM, whereas qualitative analysis was done with a Phenom XL scanning electron microscope.

EXPERIMENTS

In order to achieve a stable testing environment, the semiconductor grade silicon sample specimen are prepared identically. For this, the aluminium fixture is machined flat with a generic DLC coated endmill. A level surface with a roughness of R_a 0.1 µm was achieved. After milling, the surface is cleaned with isopropyl alcohol and the sample specimen superglued (Ergo 5210) to the

fixture. During glue hardening, a weight of 100 g was placed on the specimen to ensure contact. The sample specimen is then located via the built-in touch probe (Blum TC52 LF). The MCD flat endmill is measured after chemical cleaning with the equipped BLUM LC50 laser. Runout is verified via the laser to better than 1 µm. To account for unwanted thermal expansion of the spindle, the spindle is warmed up for 5 minutes before measuring.

Design of Experiments

In order to achieve a stable ductile cutting regime, a number of trials were undertaken to better understand and identify the influencing factors. By using a Taguchi-based Design of Experiment, a variety of parameters were analysed in two different experiment series. First, the parameters cutting speed, depth of cut and median chip thickness were varied in a side milling experiment. To further explore this, a second experiment series was undertaken, where face milling parameters (depth of cut, median chip thickness and feedrate direction) derived from the first experiment series were further analysed. Table 1 lists the analysed experimental parameters.

TABLE 1. The experiment series with the examined process parameters

Parameter	Experiment 1	Experiment 2
Parameter 1	Cutting speed	Chip thickness
Parameter 2	Depth of cut	depth of cut
Parameter 3	Median chip thickness	Feedrate direction

Because the endmill is kept in a low radial engagement, the median chip thickness is a lot lower than the calculated feed per tooth. The median chip thickness is calculated via equation 1 [17]. Here, φ_s is the radial engagement angle, a_e the radial engagement, ι the angulation and D the endmill diameter.

$$H_m = \frac{360}{\pi \cdot \varphi_s} \cdot \frac{a_e}{D} \cdot F_z \cdot sin(\iota) \qquad (1)$$

Figure 1 shows the geometric dependence of the chip thickness through chip thinning.

Experiment Series 1

From a plethora of possible influencing parameters, the cutting speed, depth of cut and median

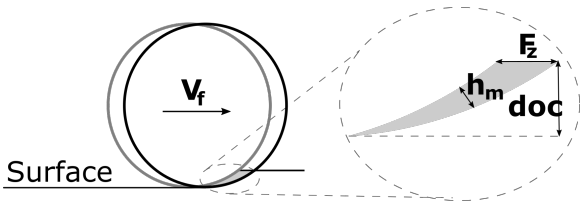

FIGURE 1. Hm as the result of chip thinning with low radial engagement.

chip thickness have the most significant impact on achieving a ductile cutting regime. [18] For this reason, a scoping experiment is undertaken. Table 2 lists the parameters and their corresponding levels, which were analysed in a Taguchi T16 orthogonal array. The cutting speed was chosen so that both the lower end (6631 RPM) of the achievable rotational speed, as well as a high, but very smooth running speed (39789 RPM) are well represented.

TABLE 2. Parameters and Levels used

Parameter	Level 1	Level 2	Level 3	Level 4
Vc in m/min	125	250	500	750
DOC in µm	0.5	1	1.5	2
Hm in nm	5	10	50	100

Research has shown, that the ductile cutting regime requires a very thin median chip thickness [18], which unlike in single point diamond turning can be achieved with varying depths of cut in milling operations. The depths of cut were chosen for their reliable achievement on the utilized machining centre, whereas the median chip thickness was chosen to cover a broad possible spectrum.

All experiments are undertaken in a sequence, during which the accoustic emission spektrum is recorded for a period of one second. Afterwards, the samples are cleaned with isopropyl alcohol, and dried in a low vacuum desiccator to prohibit the formation of condensation induced blemishes. The samples are then analysed for their qualitative appearance in the scanning electron microscope, and afterwards in a CLSM for their quantitative results such as roughness and material ratio.

The achieved roughness, as well as the inverse areal material ratio Smc (10%) is shown in figure

2. The texture aspect ratio Str was calculated, but did not differ significantly from 1 (isotropic) in this study and was thus not further included.

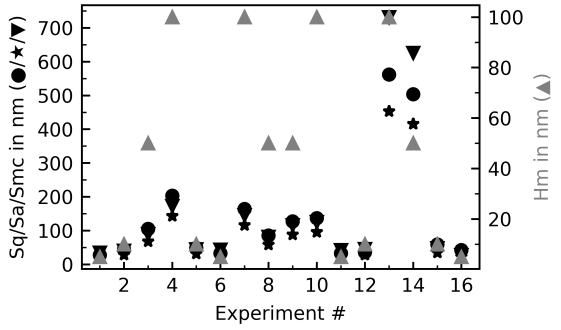

FIGURE 2. Overview of the resulting ISO 25178 parameters from the first experiment series.

It can be seen, that a series of parameters achieve a very low surface roughness (between 10 and 20 nm Sa/Sq), whereas some parameters have a high surface roughness (approaching 600 nm). The correlation between Sa, Sq, but also Smc is strong, pointing towards a smooth and isotropic surface.

A subsequent ANOVA analysis (table 3, qualitity parameter Sq) shows a significant influence (Pr (>F) 0.0036) of the median chip thickness and a less significant influence of the cutting speed (Pr (>F) 0.0209). Fitting a linear model to the data, shows that with decreasing chip thickness, the surface roughness improves.

TABLE 3. Results of the ANOVA analysis.

Parameter	Sum Sq 1	F Sq	Pr(>F)
Vc	81162	7.049	0.0209
DOC	30067	2.611	0.132066
Hm	149843	13.014	0.0036

This correlation is well visible in the recorded data. Figure 3 shows a detailed listing of the root mean square roughness in relation to the median chip thickness.

The recorded accoustic emission signals are transformed via a FFT (method: Welch, window: 2048) to a power spectral density (PSD). Figure 4 shows two different AE signals, whereas figure 5 shows two representative PSD.

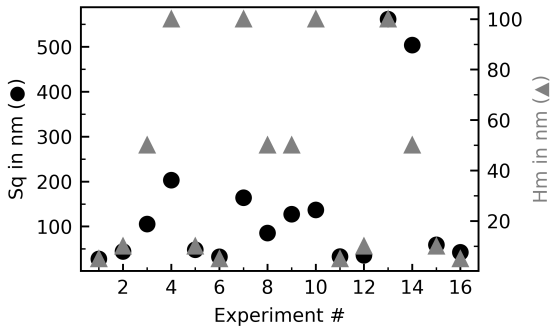

FIGURE 3. The RMS areal roughness Sq in relation to the median chip thickness.

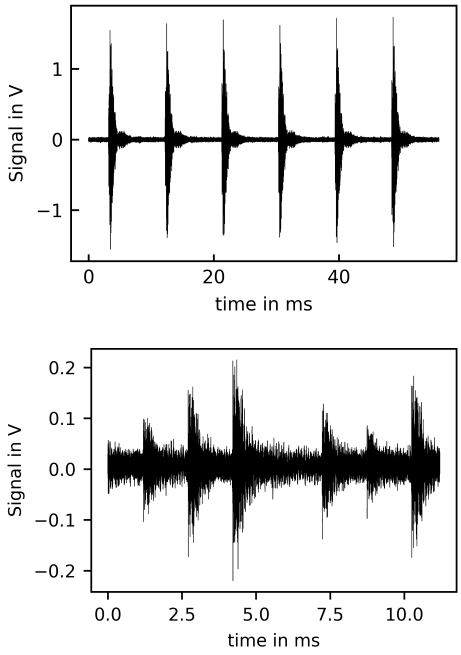

FIGURE 4. The recorded AE signal for two exemplary parameter sets. Upper: low surface roughness, likely ductile cutting regime. Lower: High surface roughness, likely brittle material removal mode. Note the random height of the signal peaks in the second signal.

The PSD shows the expected larger vibrations near the lower frequencies, stemming from machine aggregates, milling tool tooth entry frequency and the used flood coolant. Around 200 kHz, a significant increase of the signal is visible if the material removal mode is dominated by brittle material removal.

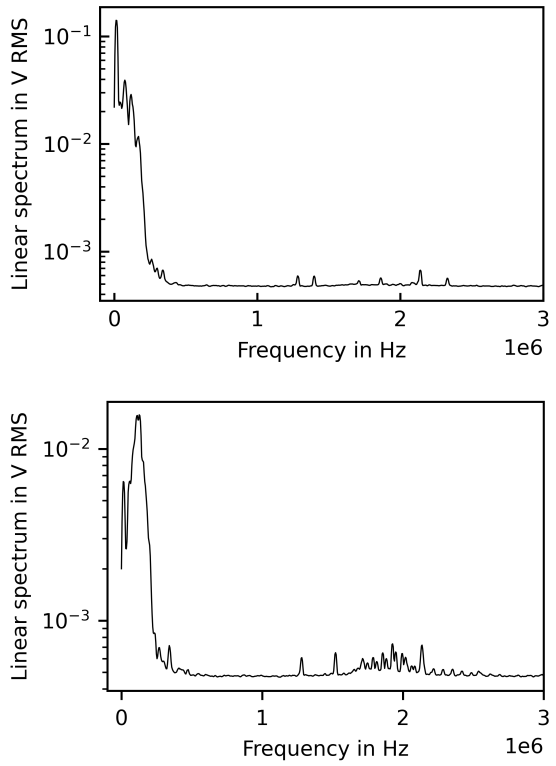

FIGURE 5. The linearized PSD for two exemplary parameter sets. Upper: low surface roughness, likely ductile cutting regime. Lower: High surface roughness, likely brittle material removal mode.

Experiment Series 2

In order to further explore the limiting factors, but also see whether the conclusions from the first experiment series are transferable towards a different milling application, a face milling experiment is undertaken. Table 4 lists the analysed parameters.

TABLE 4. Parameters and Levels used in the second experiment series.

Parameter	Level 1	Level 2	Level 3
DOC in µm	2.5	5	-
Hm in nm	5	10	20
Feed direction	Climb	Conventional	

Because the first experiment series already explored a wide range of possible parameters, the spindle speed was fixed at a cutting speed of 750 m/min. The milled samples are cleaned and measured in an identical fashion to the first experiment series. Directly visible to the naked eye are small, circular breakout areas in the conventional feed milled area.

Figure 6 shows the resulting ISO 25178 parameters, whereas table 5 shows the conducted ANOVA analysis, based on the quality parameter Sq.

TABLE 5. Results of the ANOVA analysis.

Parameter	Sum Sq 1	F Sq	Pr(>F)
Dir	2010	1.900	0.2054
DOC	700	0.662	0.4393
Hm	6	0.006	0.9412

No significant influence factor can be detected. It can be seen, that a sub 20 nm roughness can be achieved with very little variance between different parameters. A larger variance is visible in the experiments 7 to 12, which are milled with a conventional feed direction.

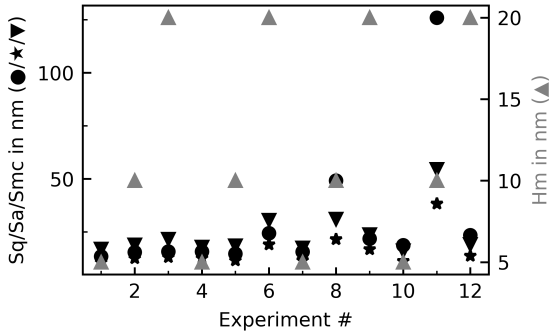

FIGURE 6. Overview of the resulting ISO 25178 parameters from the second experiment series.

RESULTS AND DISCUSSION

The milled surfaces in the first and second experiment series show a range of surface finishes ranging from very rough (Sq ~ 500 nm) to polish quality (Sq ~ 10 nm). Besides the surface roughness values, the surface was analysed in a scanning electron microscope for the surface structure.

The surface exhibits a very regular, smooth appearance. At 5000x magnification (see figure 7), a shallow feed of the tool cutting edge is visible in the form of curved tracks along the surface.

The conventional milled surface, which exhibits easily visible breakouts, show brittle failure at random points along the surface (see figure 7, lower). Because the chip generation in conventional milling starts at the very thinnest point, the

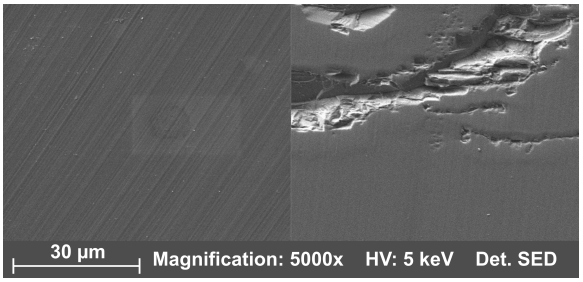

FIGURE 7. SEM micrograph of a climb (upper) and conventional (lower) feed direction surface.

cutting edge relief is rubbing along the material before the critical cutting depth is reached and a chip can form. This results in a large stress on the material, leading to breakouts. In climb milling, the chip formation starts at the maximum thickness, and progressively grows smaller. The cutting edge is therefore able to start in a brittle material removal process, reducing the stress on the material. Figure 8 shows the different feed directions and their influence on the creation of micro cracks in the material.

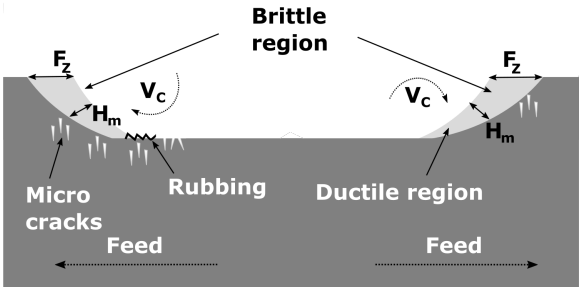

FIGURE 8. Schematic depiction of the creation of sub surface damages in conventional (left side) and climb feed rate direction.

Once a critical chip thickness is reached, a transition towards ductile material removal sets in, prohibiting further sub-surface damages in the material. Because the depth of cut is larger than the depth at which sub-surface damage is induced, an unblemished surface is created.

Chips collected from two exemplary cutting parameter sets (corresponding to the PSD spectra shown in the experimental chapter) show broken debris (figure 9) in the brittle material removal mode as well as thin, ductile chips once the median chip thickness is below 20 nm (figure 10). Larger SEM surveys of the chips show a remarkably homogeneous creation of both the debris in brittle mode, as well as the flowing chips in the ductile mode.

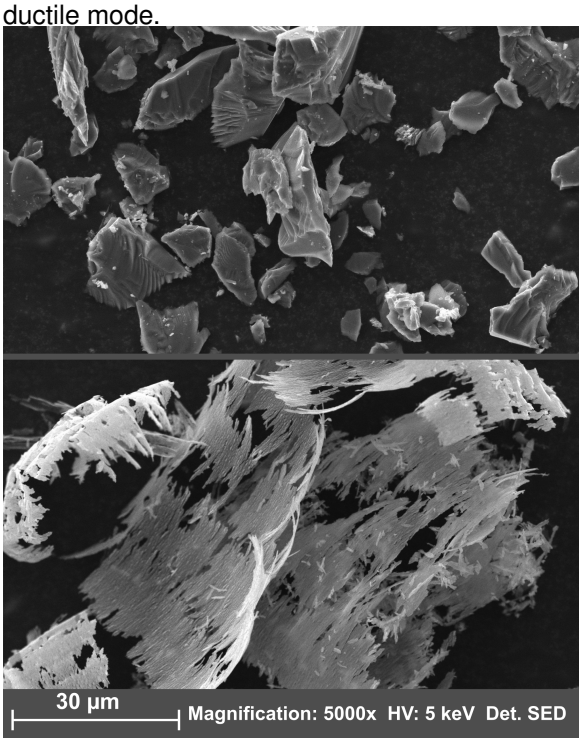

FIGURE 9. SEM micrograph of brittle material removal debris (upper) and ductile mode (lower) chips.

To further look into the random amplitude distribution in the AE signal during brittle material removal, high speed videos (10500 frames per second) of the milling process were taken with a Chronos 2.1HD camera. By tracking the debris flying away from the endmill, it can be seen that the material removal is randomly distributed and some rotations pass without material removal. Figure 10 shows 4 consecutive revolutions. The debris is highlighted with a white circle, only appearing every few rotations.

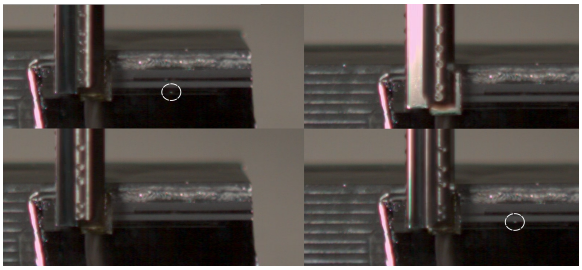

FIGURE 10. Still images taken from a high speed video, showing 4 consecutive full revolutions (CCW from top left).

This can explain the random appearance of larger

peaks in the AE signal. It is likely that the tool is in some rotations not cutting but rubbing along the material, leading to smaller amplitude peaks, followed by a rotation with a cut. After the cut, the absence of material leads to a much reduced rubbing and therefore the absence of a peak in the AE signal (compare figure 4).

CONCLUSION

A plethora of experiments were conducted to explore the conditions in reaching a ductile cutting regime in monocrystalline silicon. The defining influence on the achievement of a ductile cutting regime is the median chip thickness. By thinning the chip below 20 nm a smooth, unblemished surface can be created, achieving a RMS areal surface roughness Sq of 10 nm (see figure 11). The cutting speed has no large impact on the achievable surface roughness, and thus a comparatively productive process at high rotational speeds can be conducted. The depth of cut, within the tested parameters, has no influence on the surface generation. SEM micrographs show clear ductile cutting below 20 nm median chip thickness, and the ejection of brittle debris above 50 nm. Through accoustic emission spectroscopy and high speed video analysis, a mixture between cutting and rubbing was identified in the brittle material removal mode. Moreover, the accoustic emission signal can differentiate between the two cutting modes, which could lead towards a process supervision in industrial applications. The authors see promise in expanding the application towards freeform surface milling as well as extending the tool lifetime through different cooling solutions.

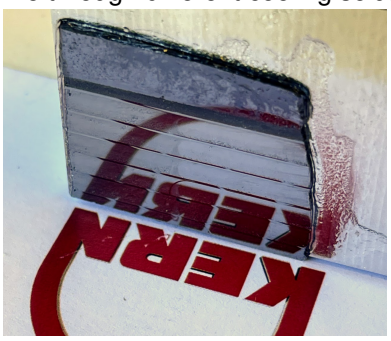

FIGURE 11. Several different parameter sets on a sample, showing mirror polish finish in monocrystalline Silicon.

References

[1] Study:, Optical Components: Market shares, strategies, and Forecasts, Worldwide, 2013 - 2019, Technical Report, Winter Green Research, Lexington, Massachusetts, 2013.

[2] S. Goel, X. Luo, R. L. Reuben, Wear mechanism of diamond tools against single crystal silicon in single point diamond turning process, Tribology International 57 (2013) 272–281. doi:10.1016/j.triboint.2012.06.027.

[3] S. Zhang, Review of modern field effect transistor technologies for scaling, Journal of Physics: Conference Series 1617 (2020) 012054. doi:10.1088/1742-6596/1617/1/012054.

[4] A. Phommahaxay, I. D. Wolf, T. Djuric, P. Hoffrogge, S. Brand, P. Czurratis, H. Philipsen, G. Beyer, H. Struyf, E. Beyne, Defect detection in through silicon vias by GHz scanning acoustic microscopy: Key ultrasonic characteristics, in: 2014 IEEE 64th Electronic Components and Technology Conference (ECTC), IEEE, 2014. doi:10.1109/ectc.2014.6897385.

[5] W. Dallas, O. Polupan, S. Ostapenko, Resonance ultrasonic vibrations for crack detection in photovoltaic silicon wafers, Measurement Science and Technology 18 (2007) 852–858. doi:10.1088/0957-0233/18/3/038.

[6] Y. Zhao, L. Chang, A micro-contact and wear model for chemical–mechanical polishing of silicon wafers, Wear 252 (2002) 220–226. doi:10.1016/s0043-1648(01)00871-7.

[7] C. Teichert, J. F. MacKay, D. E. Savage, M. G. Lagally, M. Brohl, P. Wagner, Comparison of surface roughness of polished silicon wafers measured by light scattering topography, soft-x-ray scattering, and atomic-force microscopy, Applied Physics Letters 66 (1995) 2346–2348. doi:10.1063/1.113978.

[8] H. Young, H. Liao, H. Huang, Surface integrity of silicon wafers in ultra precision machining, The International Journal of Advanced Manufacturing Technology 29 (2006) 372–378. doi:10.1007/s00170-005-2508-1.

[9] S. Ozturk, L. Aydin, N. Kucukdogan, E. Celik, Optimization of lapping processes of silicon wafer for photovoltaic applications, Solar Energy 164 (2018) 1–11. doi:10.1016/j.solener.2018.02.039.

[10] T. Leung, W. Lee, X. Lu, Diamond turning of silicon substrates in ductile-regime, Journal of Materials Processing Technology 73 (1998) 42–48. doi:10.1016/s0924-0136(97)00210-0.

[11] P. N. Blake, R. O. Scattergood, Ductile-regime machining of germanium and silicon, Journal of the American Ceramic Society 73 (1990) 949–957. doi:10.1111/j.1151-2916.1990.tb05142.x.

[12] T. Shibata, S. Fujii, E. Makino, M. Ikeda, Ductile-regime turning mechanism of single-crystal silicon, Precision Engineering 18 (1996) 129–137. doi:10.1016/0141-6359(95)00054-2.

[13] Z. Zhang, J. Yan, T. Kuriyagawa, Manufacturing technologies toward extreme precision, Journal of extreme Manufacturing 1 (2019) 022001. doi:10.1088/2631-7990/ab1ff1.

[14] B. S. Dutterer, J. L. Lineberger, P. J. Smilie, D. S. Hildebrand, T. A. Harriman, M. A. Davies, T. J. Suleski, D. A. Lucca, Diamond milling of an alvarez lens in germanium, Precision Engineering 38 (2014) 398–408. doi:10.1016/j.precisioneng.2013.12.006.

[15] Y. Takeuchi, K. Sawada, T. Sata, Ultraprecision 3d micromachining of glass, CIRP Annals 45 (1996) 401–404. doi:10.1016/s0007-8506(07)63090-x.

[16] S. Wang, S. To, X. Chen, X. Chen, An investigation on surface finishing in ultra-precision raster milling of aluminum alloy 6061, Proceedings of the Institution of Mechanical Engineers, Part B: Journal of Engineering Manufacture 229 (2014) 1289–1301. doi:10.1177/0954405414535588.

[17] J. Dietrich, Praxis der Zerspantechnik, Springer Fachmedien Wiesbaden, 2016. doi:10.1007/978-3-658-14053-3.

[18] S. Goel, The current understanding on the diamond machining of silicon carbide, Journal of Physics D: Applied Physics 47 (2014) 243001. doi:10.1088/0022-3727/47/24/243001.

Milling force prediction case study for non-standard geometry endmill using structured light scanning

Timothy No[1], Michael Gomez[2], and Tony Schmitz[1,2]
[1]Department of Mechanical, Aerospace, and Biomedical Engineering
University of Tennessee, Knoxville
Knoxville, TN, 37996, USA
[2]Manufacturing Science Division
Oak Ridge National Laboratory
Oak Ridge, TN, 37830, USA

INTRODUCTION

The ability to model and predict milling forces enables the selection of optimal machining parameters. While feasible for endmills with standard cutting edge geometries, non-standard geometry endmills prove more difficult to accurately model. The main limitation is not knowing the location and radii of the cutting edges along the cutting edge length. This issue has been addressed using a structured light scanner to generate a 3D model of the endmill. From the model, the tool-specific cutting edge geometry is identified and used to predict milling behavior by time domain simulation.

Examples of non-standard geometries include serrated cutting edges, variable pitch, variable helix, and inserted/indexable endmills. The tool selected for this case study was a 12.7 mm diameter, four flute, solid carbide, square endmill, with two smooth and two serrated helical cutting edges arranged in an alternating pattern (Iscar FINISHRED™, part number 5622230). The tool design specifications were determined from the reverse engineering capabilities of the structured light scanner.

Two methods were applied to determine the force model. First, experimental cutting forces were measured with a cutting force dynamometer at prescribed machining parameters and the force model coefficients were extracted by performing a linear regression of the mean cutting forces. Second, finite element cutting simulations were performed, which incorporated the rake and relief profile of the cutting edge, to predict the orthogonal cutting force components and determine the force model coefficients. The cross-sectional profile was obtained from the tool scan.

The time domain simulation incorporates the cutting edge measurements from the scan, the force model coefficients derived from experimental cutting tests and finite element cutting simulations, and the tool point structural dynamics in order to predict the cutting forces. The milling force predictions were validated with measured cutting forces.

This paper builds on prior efforts utilizing structured light scanning to determine tool specific geometries in a digital modeling approach to predict milling forces [1-9].

SCANNING METROLOGY

A structured light scanner was used to generate a 3D model of the endmill. The scanning proceeded by first preparing the solid carbide endmill surface using a removable anti-glare coating. Reference targets were placed onto the surface of the rotary table to enable multiple scans to be stitched together and to generate the solid 3D model. The endmill and 3D model are displayed in Fig. 1. The coordinate system was established by fitting a cylinder to the tool shank and defining a plane at the fluted end's extreme point. The intersection of the cylinder's axis and the plane was set as the origin of the coordinate system. The edge coordinates and scale of the

[2] Notice: This manuscript has been authored by UT-Battelle, LLC, under contract DE-AC05-00OR22725 with the US Department of Energy (DOE). The US government retains and the publisher, by accepting the article for publication, acknowledges that the US government retains a nonexclusive, paid-up, irrevocable, worldwide license to publish or reproduce the published form of this manuscript, or allow others to do so, for US government purposes. DOE will provide public access to these results of federally sponsored research in accordance with the DOE Public Access Plan (http://energy.gov/downloads/doe-public-access-plan).

tool scan are shown in Fig. 2. The GOM ATOS Q system was used for this research.

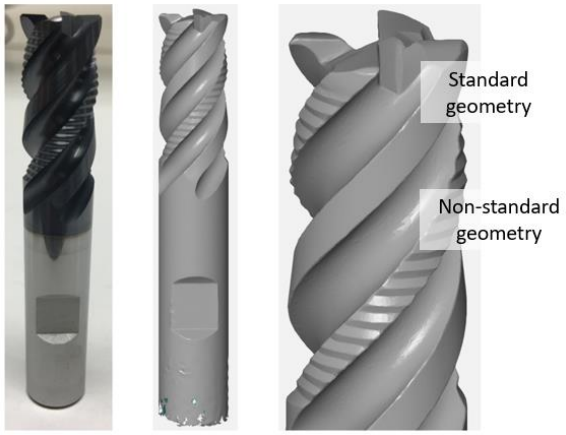

FIGURE 1. Iscar endmill and 3D model.

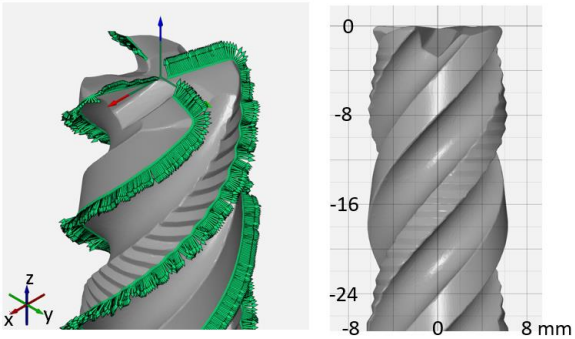

FIGURE 2. (Left) Edge coordinates and (Right) scale of scanned tool.

The edge radius values as a function of the z (axial) location are displayed in Fig. 3. The different radial profiles for the two different teeth geometries are observed (standard and serrated cutting edges). It can be seen that the serration profile of tooth 2 and tooth 4 are offset by 180 degrees. The angle values are shown in Fig. 4. The tooth spacing is 90 deg.

Planar cross-sections were created along the tool's axis (z direction). Each cross-section contained the rake and relief profiles of each tooth at the corresponding axial location; an example cross-section is displayed in Fig. 5.

TIME DOMAIN SIMULATION DESCRIPTION

Time domain simulation enables numerical solution of the coupled, second-order, time-delay differential equations of motion for milling in small time steps [10]. It is well suited to incorporating the inherent complexities of milling dynamics,

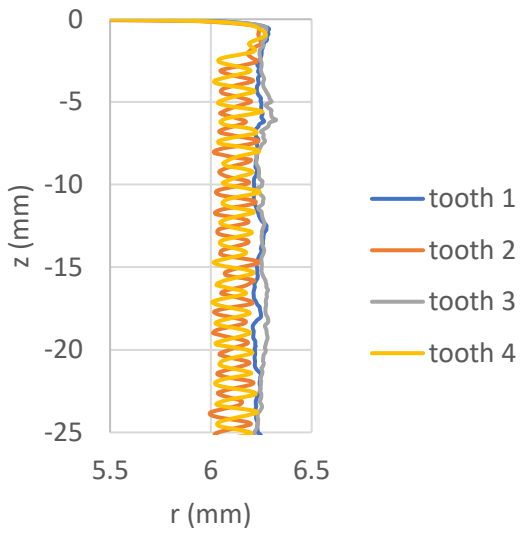

FIGURE 3. Iscar endmill radius values for the four teeth as a function of the z location along the tool axis.

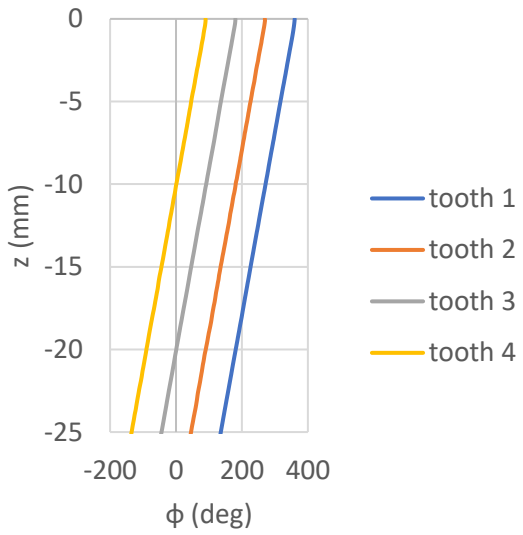

FIGURE 4. Iscar endmill angle values for the four teeth as a function of the z location along the tool axis.

including complicated tool geometries (runout of the cutter teeth, non-uniform teeth spacing, variable helix, and indexable geometries) and the nonlinearity that occurs if the tooth leaves the cut due to large magnitude vibrations. As opposed to analytical or semi-analytical stability maps that provide a global picture of the stability behavior, time domain simulation provides information regarding the local cutting force and vibration behavior for the selected cutting conditions.

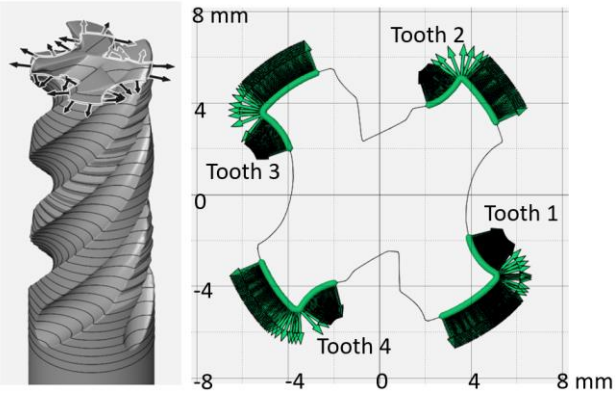

FIGURE 5. (Left) Planar cross-section for 3D model. (Right) Cross-section showing rake and relief faces for all four teeth.

The time domain simulation directly incorporates the measured tooth angles and radius variation from the tool scan. The radius variation for each tooth is included as runout, RO. Given this information, the simulation proceeds as follows:

1. The instantaneous chip thickness, *h(t)*, is determined using the commanded chip thickness, runout, and vibration of the current and previous teeth at the selected tooth angle for the current axial slice.
2. The cutting force components in the tangential, *t*, and normal, *n*, directions are calculated at each axial slice using the cutting force coefficients obtained from finite element analysis:

$$F_t(t) = k_{tc} b h(t) + k_{te} b \quad (1)$$
$$F_n(t) = k_{nc} b h(t) + k_{ne} b \quad (2)$$

   where *b* is the axial slice width and the cutting force coefficients are identified by the subscripts *t* or *n* for direction and *c* or *e* for cutting or edge. These forces are then summed over all axial slices engaged in the cut.
3. The summed force components are used to find the new displacements by numerical integration of the second-order differential equations of motion in the *x* (feed) and *y* directions:

$$m_x \ddot{x} + c_x \dot{x} + k_x x = F_t(t)\cos\phi + F_n(t)\sin\phi \quad (3)$$
$$m_y \ddot{y} + c_y \dot{y} + k_y y = F_t(t)\sin\phi - F_n(t)\cos\phi \quad (4)$$

   where *m* is the modal mass, *c* is the modal viscous damping coefficient, and *k* is the modal stiffness. The subscripts (*x* or *y*) identify the direction. While these equations include only a single degree of freedom in each direction, multiple degrees-of-freedom in each direction can be accommodated by summing the modal contributions.
4. The tool rotation angle is incremented, and the process is repeated.

FORCE MODELING

For this case study, the four cutting force coefficients from Eqs. 1 and 2 were identified using two methods: 1) experimentally using the average force, linear regression approach [10]; and 2) using AdvantEdge™ finite element software and the proprietary 6061-T6 aluminum flow stress model.

For the first method, down milling tests were completed for: 3.18 mm radial depth, 5 mm axial depth, 5000 rpm spindle speed, and six feed per tooth values with the 6061-T6 workpiece mounted on a cutting force dynamometer. The mean force in the *x* (feed) and *y* directions was plotted against the commanded feed per tooth and linear regressions were completed. The slope and intercept values were then used to determine the cutting force coefficients. Three trials of these variable feed cutting tests were completed.

For the second method, the following procedure was followed to calculate the cutting force coefficients:

1. The proprietary 6061-T6 material model was selected. The tool material was set as carbide.
2. The cutting edge cross-sectional geometry was imported as a series of points that defined the rake and relief profiles.
3. The orthogonal cutting parameters were specified including the cutting speed, chip width, and chip thickness.
4. The simulation was completed and the mean feed direction, F_t, and surface normal direction, F_n, force values were recorded (initial transients at cut entry and final transients at cut exit were excluded).
5. The force coefficients were calculated by dividing the mean force components by the uncut chip area (i.e., the product of the chip width and chip thickness).
6. The chip thickness was modified and steps 4 and 5 were repeated.

A comparison between the experimental (average force, linear regression, AFLR) and AdvantEdge™ (finite element, FE) coefficients is

provided in Figs. 6 and 7. The error bars on the AFLR values represent ± three standard deviations obtained from three repeated trials where all six cutting tests were completed (at each feed per tooth value). There are no uncertainty intervals for the FE values because the proprietary flow stress model was applied in the finite element calculations and the model type and coefficients were unknown.

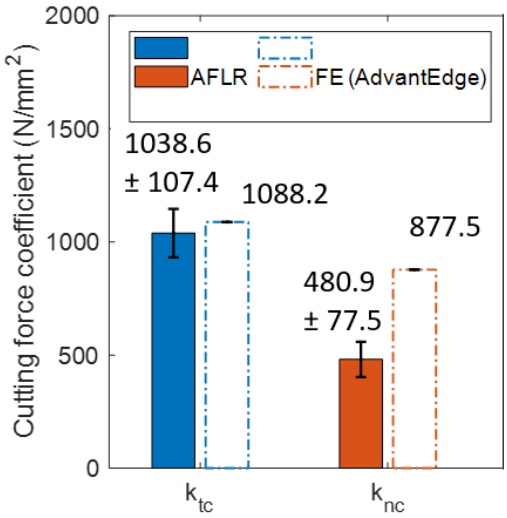

FIGURE 6. Cutting coefficients from Eqs. 1 and 2 obtained by average force linear regressions (AFLR) and finite element (FE) analysis.

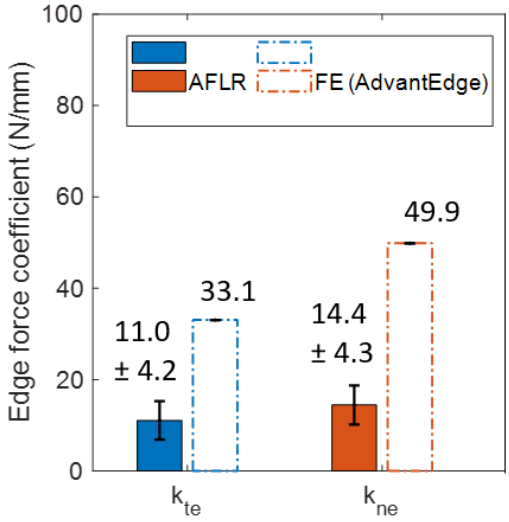

FIGURE 7. Edge coefficients from Eqs. 1 and 2 obtained by average force linear regressions (AFLR) and finite element (FE) analysis.

CUTTING FORCE COMPARISON

Cutting tests were completed on the Haas VF-4 CNC milling machine. The 6061-T6 aluminum workpiece was mounted on a Kistler 9257B cutting force dynamometer; the endmill was clamped in the collet holder and inserted in the CAT-40 spindle interface; see Fig. 8.

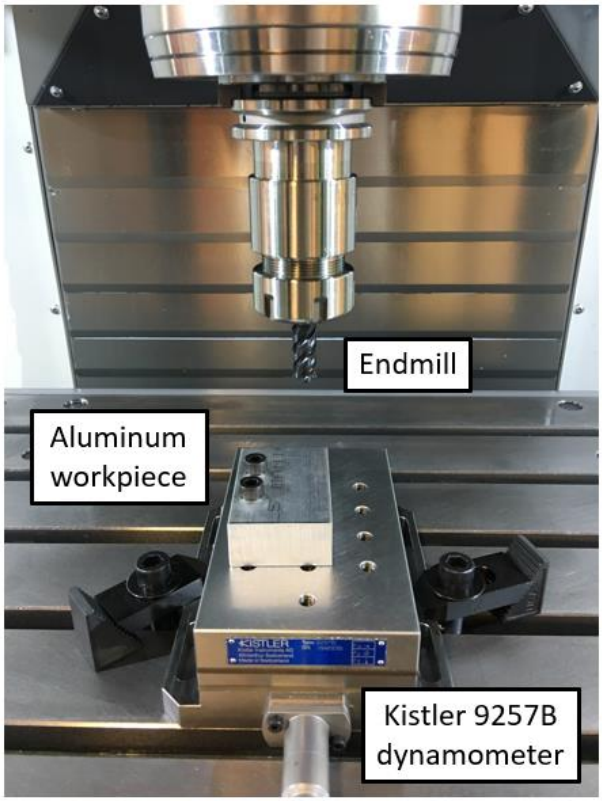

Figure 8. Experimental setup for Iscar endmill cutting force measurement.

The tool tip and workpiece FRFs were measured by impact testing. The FRFs are displayed in Fig. 9. No significant vibration modes were identified for the workpiece. The tool tip FRFs were fit and the modal parameters were used in the time domain simulation.

Down milling tests were performed at a radial depth of 6.35 mm (50% radial immersion), feed per tooth value of 0.075 mm/tooth, 5000 rpm spindle speed, and the axial depth was varied from 2 mm to 8 mm in steps of 2 mm. The predicted and measured *x* and *y* direction forces are displayed in Fig. 10 through 13. Results for both force models are included: 1) the average force, linear regression results are represented by ± three standard deviation error bounds (green filled range); and 2) the finite element-based force model predictions are represented by the dotted blue line. The experimental results are identified by the red dash-dot line.

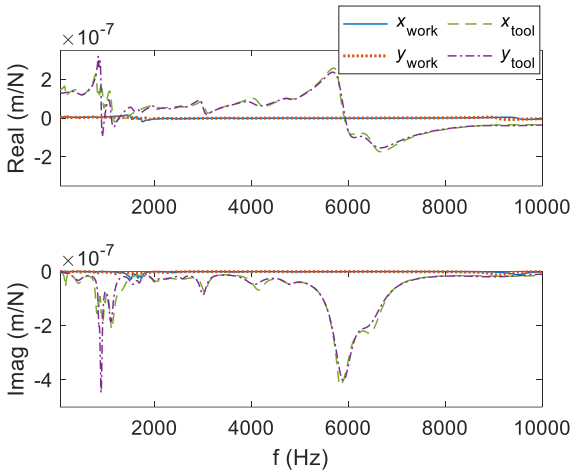

FIGURE 9. Tool tip and workpiece FRFs for the x and y directions. The (top) real and (bottom) imaginary parts of the complex-valued FRFs are presented.

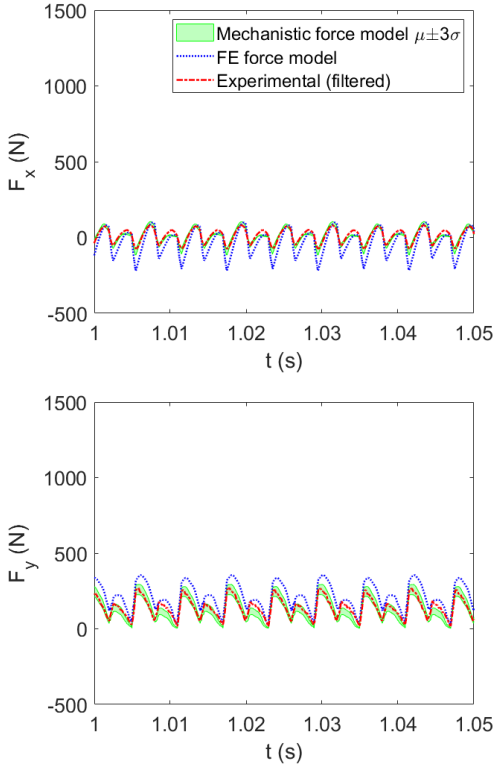

FIGURE 10. 6.35 mm radial depth (50% radial immersion), 0.075 mm/tooth, 2 mm axial depth.

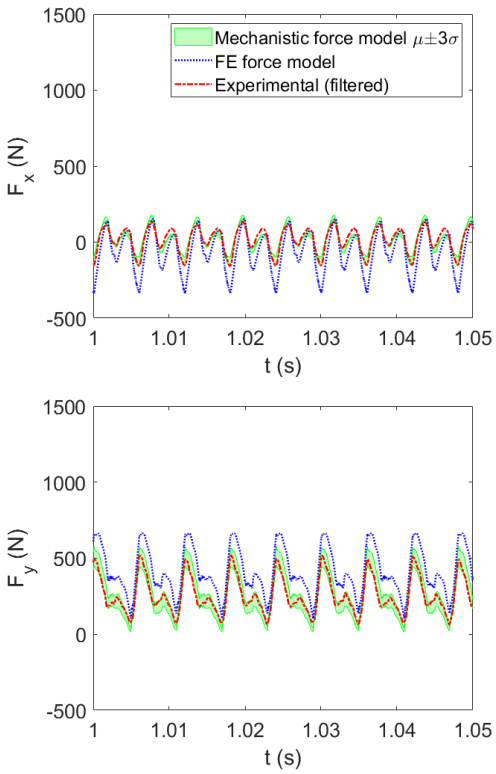

FIGURE 11. 6.35 mm radial depth (50% radial immersion), 0.075 mm/tooth, 4 mm axial depth.

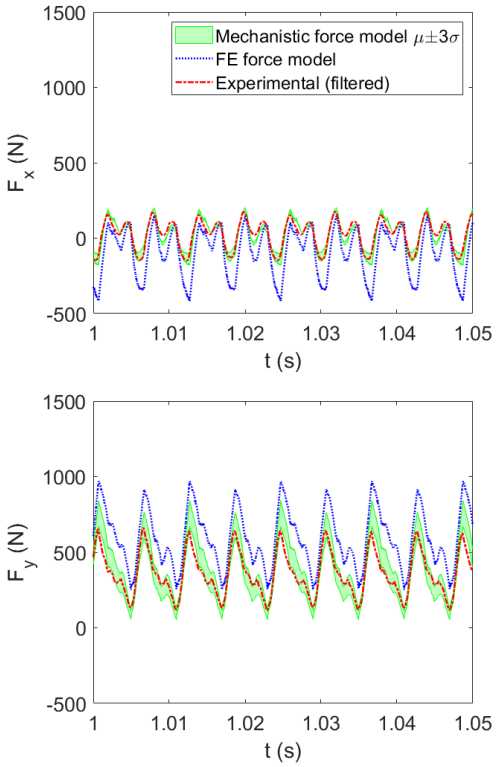

FIGURE 12. 6.35 mm radial depth (50% radial immersion), 0.075 mm/tooth, 6 mm axial depth.

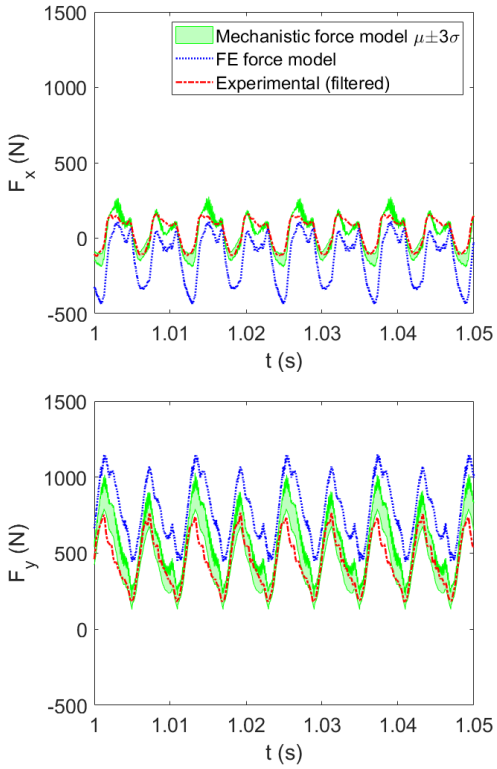

FIGURE 13. 6.35 mm radial depth (50% radial immersion), 0.075 mm/tooth, 8 mm axial depth.

For the results displayed in Figs. 10 through 13, it is seen that the measured force profiles are contained within the ± three standard deviation error bounds from the linear regression identification of the cutting force coefficients. The finite element-based predictions overpredict the force levels in both the *x* and *y* directions

CONCLUSIONS

This paper describes a case study for using structured light scanning to predict cutting forces for a non-standard geometry endmill. The measured cutting edge geometry was incorporated into a time domain simulation used to predict the milling forces. Two methods were used to derive the force models: 1) experimental cutting tests; and 2) orthogonal finite-element cutting simulations. The predicted forces were validated with cutting tests performed at varying axial depths of cut. Good agreement between predicted and measured cutting forces for both force models (experimental and finite element-based) was obtained. This digital force modeling approach can be used for any endmill geometry and peripheral milling process.

REFERENCES

1. No, T., Gomez, M., Copenhaver, R., Uribe Perez, J., Tyler, C., and Schmitz, T., 2019, Force and Stability Modeling for Non-standard Edge Geometry Endmills, Journal of Manufacturing Science and Engineering, 141(12): 121002.
2. No, T., Gomez, M., Copenhaver, R., Uribe Perez, J., Tyler, C., and Schmitz, T., 2019, Scanning and Modeling for Non-standard Edge Geometry Endmills, Procedia Manufacturing, 34: 305–315.
3. No, T., Gomez, M., Copenhaver, R., and Schmitz, T., 2019, Structured light scanning for endmill modeling, American Society for Precision Engineering Annual Meeting, October 28-November 1, Pittsburgh, PA.
4. Gomez, M., No, T., Smith, S., and Schmitz, T., 2020, Cutting Force and Stability Prediction for Inserted Cutters, Procedia Manufacturing, 48: 443-451.
5. Gomez, M., No, T., and Schmitz, T., 2020, Digital Force Prediction for Milling, Procedia Manufacturing, 48: 873-881.
6. No, T., Gomez, M., Smith, S., and Schmitz, T., 2020, Cutting Force and Stability for Inserted Cutters using Structured Light Metrology, Procedia CIRP, 53rd CIRP Conference on Manufacturing Systems, July 1-3, 2020, Chicago, IL.
7. No, T., Gomez, M., Karandikar, J., Heigel, J., Copenhaver, R., and Schmitz, T., 2021, Contributions of Scanning Metrology Uncertainty to Milling Force Prediction, Procedia Manufacturing, 53: 213-222.
8. No, T., Gomez, M., and Schmitz, T., 2021, Propagation of Johnson-Cook Flow Stress Model Uncertainty to Milling Force Uncertainty using Finite Element Analysis and Time Domain Simulation, Procedia Manufacturing, 53: 223-235.
9. Titu, N.A., Baucum, M., No, T., Trotsky, M., Karandikar, J., Schmitz, T.L. and Khojandi, A., 2021, Estimating Johnson-Cook Material Parameters using Neural Networks, Procedia Manufacturing, 53: 680-689.
10. Schmitz, T. and Smith, K.S., Machining Dynamics: Frequency Response to Improved Productivity, Second Edition, Springer, New York, NY, 2019.

.

FORCE-CONTROLLED ELECTRODE HOLDER FOR LATHE-TYPE ELECTROCHEMICAL DISCHARGE MACHINE

Katsushi Furutani[1], and Takahiro Tsuchiya[1]
[1]Department of Advanced Science and Technology
Toyota Technological Institute
Nagoya, Aichi 468-8511 Japan

INTRODUCTION

Electrochemical discharge machining (ECDM) is a micromachining method for insulated materials such as glass and piezoelectric ceramics. In ECDM, a workpiece is immersed in electrolyte and discharge occurs in the bubbles at a high applied voltage. Since only the discharge around the tip of the tool electrode contributes the removal, the tool electrode preferably contacts onto the workpiece. The authors have developed a lathe-type ECDM machine [1] and measured the principal force and thrust with a strain gauge type force sensor during ECDM [2]. A passive force sensor for a small load is too flexible to machine thin rod with precision. Consequently, the authors have machined one with a rigid electrode holder at a constant feed rate after predicting a removal rate [3]. The thrust applied to the electrode is generally less than 0.1 N by the gravity to prevent the breakage of the workpiece or by compensating for a weight of the electrode with a balance mechanism [4]. The inertia of the electrode holder often slows the electrode motion. A servo-type force sensor accomplishes a high response and minute measurable range by estimating the force from the driving current or voltage of embedded actuators [5]. A force sensor with a voice coil actuator has been proposed to measure the thrust in the *z*-direction during hole-ECDM [6].

This paper describes an electrode holder for controlling the thrust of a tool electrode onto a glass rod in the lathe-type ECD machine.

ELECTRODE HOLDER WITH SERVO-TYPE FORCE SENSOR

Figure 1 shows a configuration of the lathe-type electrochemical discharge machine. It consists of a force-controlled tool electrode holder driven with a motorized XZ-stage, spindle, DC power supply and working tank. The coordinate system is the same as general lathes. The structure was mainly made of PEEK resin. The machine is controlled with a digital signal processor (DSP).

Figure 2 shows a structure of the electrode holder with servo-type force sensor. The both ends of a plunger attaching a tool electrode at the lower end were suspended with coil springs. The plunger was driven by electromagnetic attractive force generated with a solenoid. The displacement of the plunger was measured with a Hall device. The applied voltage was controlled by a proportional–integral-derivative (PID) compensator. The whole unit of the electrode holder was roughly moved in the *x*- and *z*-directions with a motor-driven stage to follow the eccentricity of the workpiece. When the plunger moves for Δx from a balanced position and a solenoid current varies Δi, a motion equation can be linearized as:

$$\frac{d^2\Delta x}{dt^2} = \left\{\frac{2KI_0^2}{mX_0^3} - \frac{4k(3X_0^3 - 2LX_0)}{ml^2}\right\}\Delta x - \frac{2K}{m}\frac{l_0}{X_0^2}\Delta i \qquad (1)$$

where m is the mass of the plunger, l is the equivalent natural length of springs in the x-direction, k is the spring constant, K is the electromagnet constant, I_0 is the solenoid current at a balanced position, X_0 is the initial distance from the solenoid and electrode and L is the initial length.

Figure 3 shows a block diagram of the electrode holder. The plunger position was regulated to a reference one by PID control using the DSP with an A/D and D/A converters. The sampling time was 12 μs. The thrust at the reference position was estimated by the driving current of the

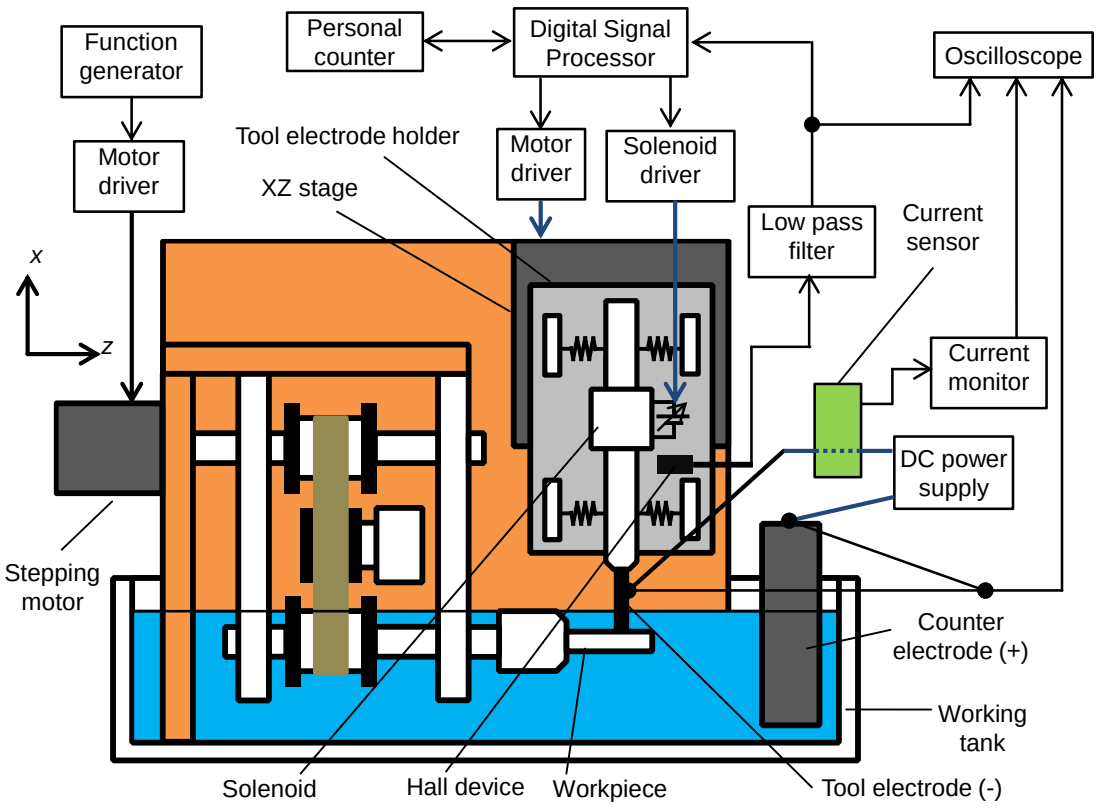

FIGURE 1. Configuration of lathe-type electrochemical discharge machine.

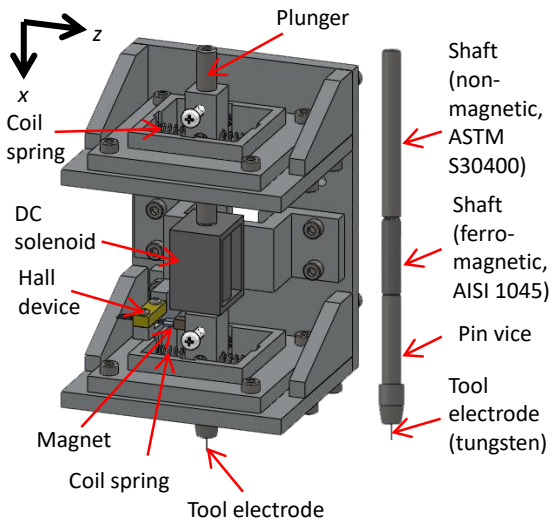

FIGURE 2. Structure of electrode holder with servo-type force sensor (left: overview, right: plunger).

solenoid and approximated as the second-order function as shown in Figure 4. The solenoid current was decreased in the used range with an

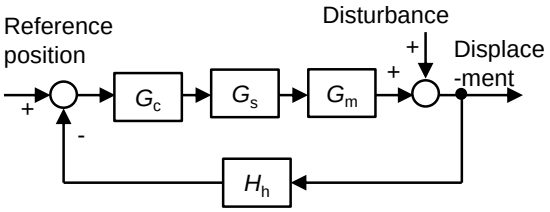

FIGURE 3. Block diagram of system (G_c: DSP controller, G_s: servo-amplifier, G_m: attractive mechanism, H_h: Hall device).

increase of the thrust because the thrust is decreased by the attractive force with the solenoid.

EXPERIMENTS

This device was used in the lathe-type machine for peripheral turning of a glass rod. Table 1 shows the machining conditions. The average thrust was controlled between 0.06-0.08 N. Because the thrust varies also by the eccentricity of the workpiece, the feeding step of the stage was 0.25 μm to enhance the tracking performance.

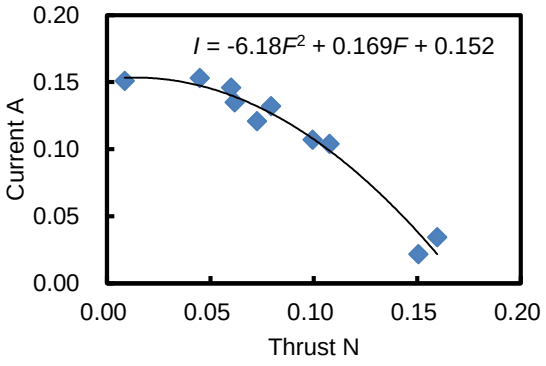

FIGURE 4. Relationship between current and thrust.

TABLE 1. Machining conditions.

Tool electrode	Tungsten, 2 mm in diameter
Auxiliary electrode	Graphite
Workpiece	Soda lime glass
Applied voltage	40 V
Electrolyte	NaCl solution, 20 wt%
Depth of electrolyte	2 mm
Revolution of workpiece	2 min^{-1}
Machining time	60 min
Feeding step in *x*-direction	0.25 μm

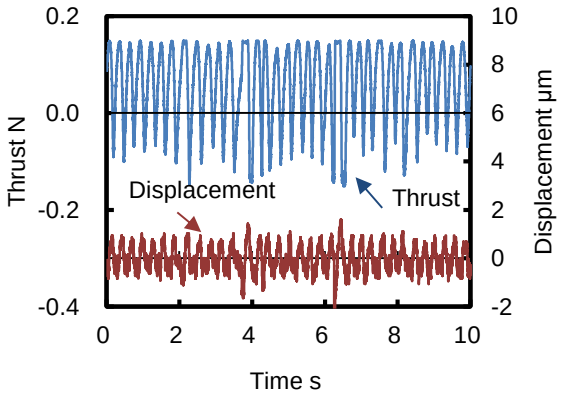

(a) Estimated thrust and displacement.

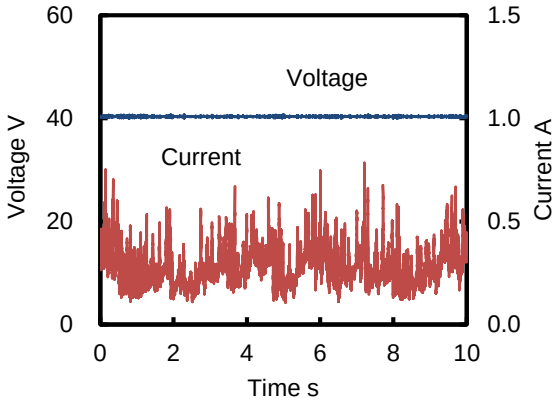

(b) Applied voltage and machining current.
FIGURE 5. Thrust, displacement of tool electrode, voltage and machining current during ECDM.

Figure 5 (a) shows examples of estimated thrust and displacement of the electrode during ECDM. Because the workpiece was rigid, the displacement was oscillational due to the integral component in PID control so that the thrust was also oscillational. This oscillation did not affect the machining current fluctuating sharply by the discharge as shown in Figure 5 (b).

Figure 6 shows an example of machined groove. The center depth and width were 410 μm and 408 μm, respectively for 60-min machining. The side walls sloped due to a long-time machining, especially the upper edges. The thrust was disturbed by a rough bottom of the groove with a progress of machining. The workpiece is hardly removed just under the tool electrode in hole ECDM because the electrolyte cannot dragged into the narrow gap between the tool electrode and workpiece. However, the electrolyte is easy dragged by the workpiece rotation in the lathe-type ECDM machine and the center of the groove was removed most. The intervals of bumps of 160 μm coincided with the electrode oscillation cycle.

CONCLUSIONS

The electrode holder for controlling the thrust of a tool electrode was developed and a glass rod was machined in the lathe-type ECDM machine.

For a future work, the thrust will be made more stable by a synchronous motion of the solenoid and the motorized stage.

This study was financially supported by JSPS KAKENHI Grant-in-Aid for Scientific Research (C) (JP18K03885).

REFERENCES

[1] Lindeke R, Schoenig F Jr, Khan A, Haddad J. Machining of α,β-Titanium with Ultra-High Pressure Through the Insert Lubrication/Cooling. Transactions of the

North American Manufacturing Research Institution of SME. 1991; 19: 154-161.
[2] Trigger K, Chao B. An Analytical Evaluation of Metal Cutting Temperatures. ASME Transactions, Journal of Engineering for Industry. 1951; 73: 57-68.
[3] Ulsoy A, DeVries W. Microcomputer Applications in Manufacturing. John Wiley and Sons, Inc. New York: 1989.
[1] Furutani K, Maeda H. Machining glass rod with lathe type electro-chemical discharge machine. Journal of Micromechechanics and Microengineering. 2008; 18: 065006.
[2] Furutani K, Arai K. Removal Mechanism of Glass Using Lathe-Type Electrochemical Discharge Machine. International Journal of Electrical Machining. 2018; 23: 1-8.
[3] Furutani K, Kojima S. Prototyping of Acceleration Sensor by Using Lathe-type Electro-chemical Discharge Machine. Procedia CIRP. 2016; 42: 772-777.
[4] Kurafuji H, Suda K. Electrical Discharge Drilling of Glass. Annals of CIRP. 1968; 16: 415-419.
[5] Chino S, Kato Y, Ishino Y, Takasaki M, Mizuno T. Actuation Force Characteristics of Non-contact Ultrasonics Suspension Mechanism for Minute Object -1st Report Fabrication of Actuation Force Measurement Mechanism and Obtain of Actuation Force Characteristics. Journal of Japan Society for Precision Engineering. 2012; 78: 332-337.
[6] Ziki J D A, Wüthrich R. Forces exerted on the tool-electrode during constant-feed glass micro-drilling by spark assisted chemical engraving. International Journal of Machine Tools and Manufacture. 2013; 73: 47-54.

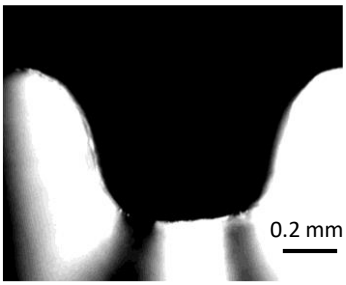

(a) Side view.

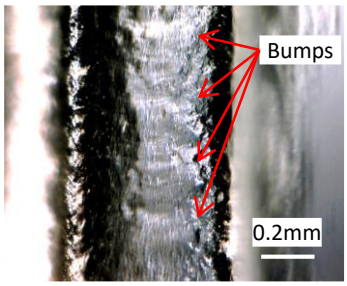

(b) Top view.

FIGURE 6. Machined groove (contrast was adjusted).

IN-PROCESS CUTTING TEMPERATURE MONITORING METHOD BASED ON IMPEDANCE MODEL OF DIELECTRIC COATING LAYER AT TOOL-CHIP INTERFACE

Heebum Chun[1], Jungsub Kim[1], and ChaBum Lee[1]
[1]J. Mike Walker '66 Department of Mechanical Engineering
Texas A&M University
College station, TX 77843, USA

ABSTRACT

This paper introduces a novel approach that enables the in-process cutting temperature monitoring at the tool-chip interface (TCI) by utilizing the impedance model of the dielectric coating layer of the cutting tool. The impedance of the dielectric layer coated on the surface of the cutting tool was characterized through the Nyquist diagram that was obtained by using an impedance analyzer for validating the changes in the relative permittivity of the dielectric layer under various temperature conditions. As a result, the impedance of the dielectric layer was subject to change according to temperature, and with its temperature-dependent impedance characteristics, the true cutting temperature at the localized TCI could be in-situ predicted during the machining. The impedance of TCI was monitored through a simple RC equivalent circuit model under the milling process, and the test results showed remarkable changes in its impedance response under different machining conditions. The preliminary study showed the feasibility of using an electrical impedance model of the dielectric coating layer for an in-process machining process monitoring method to measure and analyze the machining process at the local hot spot region. The outcomes of this study will potentially provide utilization in advanced manufacturing for improving final part quality and productivity.

INTRODUCTION

Monitoring the cutting process that includes cutting temperature, vibration, cutting force, tool wear, and so on is significant, and those cutting mechanics should be adequately diagnosed and controlled to achieve high-performance machining [1]. A considerable amount of heat is generated when the workpiece is shearing during the machining process. Controlling and monitoring the generated heat is important because it may expedite the aging of tools with an increasing abrasive, adhesive, and diffusive wear. Moreover, the build-up edge can be more formed on the cutting surface. These factors are not negligible since it directly related to the final part quality [2-4]. Additionally, the cutting temperature is also a crucial indicator of the machining performance, relating to the cutting force [5-7]. However, controlling and monitoring the cutting mechanics in the region of TCI is challenging due to its physical inaccessibility by mechanical interference. Up to now, various cutting temperature measurement techniques such as tool-workpiece thermocouple, embedded thermocouple, and tool-insert thermocouple [8-11] have been well-introduced. However, there is still room for improvements in current techniques because such techniques measure distributed temperature over the workpiece, which is not the true cutting temperature at the local hot spot. Also, sometimes, it requires electric isolation from the machining system. Furthermore, the junction size of the thermocouple needs to be small for obtaining higher resolution.

In this study, the proposed impedance model-based in-process cutting temperature monitoring method uses the dielectric coating layer of cutting tools to directly probe and monitor the cutting temperature at the localized TCI during the machining. Sub- and up to tens of microns of coating layers are formed on cutting tools for improving the tool life, hardness, toughness while preventing wear, oxidation, diffusion, and thermal shock. Cutting tools used in high-speed machining for difficult-to-cut materials are coated with dielectric materials such as diamond, cubic boron nitride (CBN), and ceramics that are electrically insulated [12-13]. Due to their high breakdown voltage, these dielectric materials with high impedance characteristics are often used in capacitors and high-power batteries [14]. When cutting is in process, the dielectric material-coated cutting tool contacts a workpiece, forming a dielectric capacitor. The principal characteristic utilized for the in-process machining process monitoring method is the impedance of dielectric materials that is related

to the relative permittivity, and the relative permittivity of the dielectric layer changes with the temperature. Hence, measuring a cutting temperature at the localized TCI is achievable by using the impedance characteristics of a dielectric layer. The proposed impedance-based in-process monitoring method enables in-situ monitoring of the cutting mechanics precisely at the local hot spot region.

METHODOLOGY

The dielectric coating layer formed on the surface of the tool becomes sandwiched structure when cutting is in process and electrically functions as a dielectric capacitor, as schematically illustrated in Figure 1. Chips and base material of tools that conduct electricity behave as electrodes, while the coating layer works as the dielectric capacitance under the electric field. The equivalent electric circuit model can be established containing the parallel capacitance C and leakage resistance R_L. The capacitance depends not only on the contact area and the thickness of the coating layer but also on the relative permittivity of the coating layer, and the relative permittivity is subject to change as temperature changes. The proposed method is operated when the sandwiched structure is formed while machining is in the process. Thus, by characterizing the electrical impedance response of the dielectric material throughout the Nyquist diagram, Bode plot, and with a simple RC circuit, the cutting temperature at the local hot spot region can be in-situ monitored.

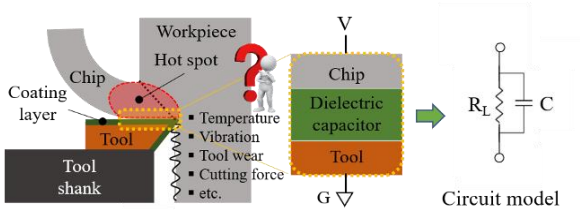

FIGURE 1. Schematic of tool-chip impedance-based in-process machining monitoring method with an equivalent circuit.

IMPEDANCE SPECTROSCOPIC

The impedance of the diamond-coated insert tool (Manufacturer Sandvik) was experimentally characterized using an impedance analyzer (CHI-604D). In this experiment, the thermal experiment of dielectric material was primarily focused on validating whether the impedance of the 10 µm thick diamond-coated layer is sensitive to temperature variations. Three temperature conditions, room temperature, 100 °C, and 200 °C, were considered for the study. The temperature was monitored by using a thermocouple attached near the chip (electrode) on the top surface of the cutting tool. The Nyquist diagrams under varying temperatures were simultaneously drawn while increasing the temperature. The Nyquist diagram was obtained from 0.1 Hz to 100 kHz due to the limitation of the impedance analyzer. As a result, shown in Figure 2, the Nyquist diagram showed 1st order response with no inductance and no parasitic resistance at room temperature. The leakage resistance R_L (described in Figure 1) estimated approximately 54 MΩ at the room temperature dropped to 0.29 MΩ and 0.1 MΩ at 100 °C and 200 °C as the temperature raised. The parasitic resistance at higher temperatures could not be monitored due to the limited range of the impedance analyzer. Additionally, the natural frequency of dielectric material predicted at 45-degree phase shifts from a phase diagram increased at least two orders as temperature raised. Therefore, with the temperature-dependent impedance characteristics of dielectric material validated throughout the experiment, the impedance model-based machining monitoring method could be used for the in-process monitor of the cutting temperature at the local TCI region.

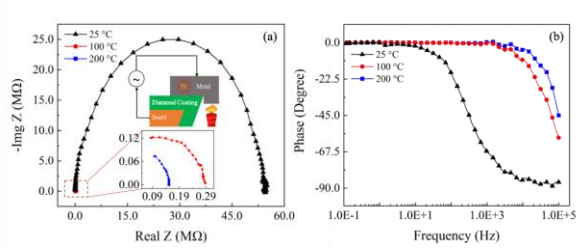

Figure 2. Impedance spectroscopy results of the dielectric coating layer under varying temperatures.

EXPERIMENT SETUP

An experimental setup for machining was made to test the feasibility of capturing the localized cutting temperature while machining is in process. Due to the limitation with the current machining system, slot machining was considered for an experiment to reduce uncertain parameters, and 10 µm thick diamond-coated milling tool with a cutting diameter of ½ inch was used for the machining. To observe the variations in the impedance response of the dielectric coating layer as cutting temperature rise at the hot spot region during the machining, a simple RC circuit was made with the current machining system as described in Figure 3. The

diamond coating layer was excited with a sinusoidal wave at 1 kHz, and the variations in $V_o(t)$ across the RC circuit due to temperature-dependent impedance characteristic of the coated tool could be monitored by demodulating the $V_o(t)$ using a lock-in amplifier. 30 mm long aluminum block was used for the machining experiment.

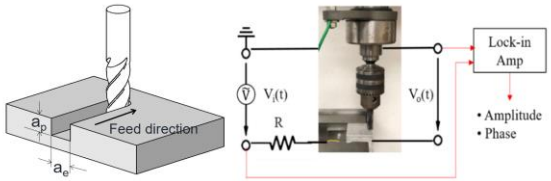

Figure 3. Experimental setup for impedance measurement using the diamond-coated cutting tool while machining is in process.

RESULTS

A preliminary experiment was conducted by comparing two different cutting speed conditions (1 mm/s and 2 mm/s) while the axial and radial depth of cut (a_p and a_e, respectively, illustrated in Figure 3) was fixed at 1.0 mm and 12.7 mm, respectively. The ratio of $V_i(t)$, excited input of RC circuit, and $V_o(t)$, the output of RC circuit could be obtained using a lock-in amplifier as impedance changes. Subsequently, similar to the results shown in the previous thermal experiment with an impedance analyzer, both cases showed the voltage drops after a few seconds of machining started, implying the impedance decreasing as temperature increasing, and the dropped voltage saturated at some point, as shown in Figure 4. Additionally, the relatively slower feed rate at 1 mm/s showed more voltage drop than the 2 mm/s case, which might be caused by the slower feed rate generated more heat due to the ductility of the aluminum workpiece.

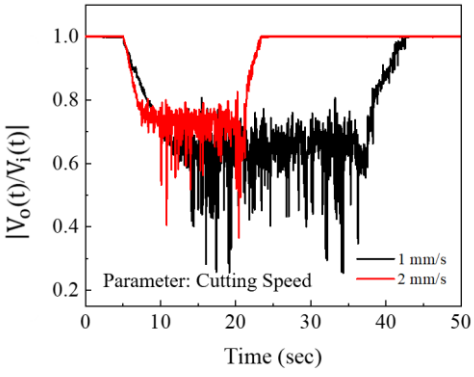

Figure 4. Machining experiment results under the different cutting speed conditions: 1 mm/s and 2 mm/s.

Another machining experiment was tested by giving the control parameter with the axial depth of cut but fixing the radial depth of cut (12.7 mm) and the cutting speed (1 mm/s). In the case of depth of cut controlled experiment, lower the depth of cut showed the higher voltage drop, which tells the greater the cutting temperature at the lower depth of cut as shown in Figure 5. However, it is early to conclude because the optimal cutting parameters are unknown for the current machining system. Nevertheless, the preliminary study showed that the temperature-dependent impedance model showed the feasibility of implementing into in-process monitoring the cutting mechanics. It can monitor the machining phenomenon at the localized hot spot that was not physically accessible and monitor the cutting mechanics in an accurate and precise manner.

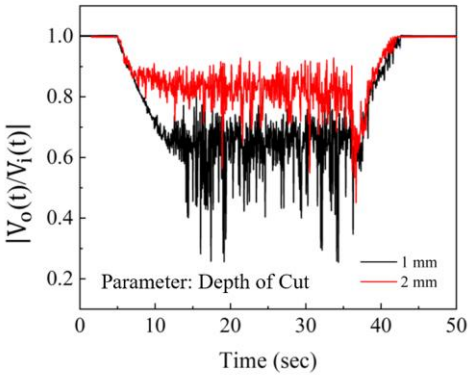

Figure 5. Machining experiment results under the different axial depth of cut conditions: 1 mm and 2 mm.

FUTURE WORKS

For future works, the current source will be implemented to measure the impedance of the dielectric coating layer, and the temperature-dependent impedance model will be identified throughout the calibration process. Since the impedance response of the dielectric coating layer is also depends on the contact area and coating thickness, it is expected to monitor the vibration phenomenon of the machining process that occurred at the TCI. Furthermore, the wear of the tool and cutting force will also be characterized during the machining process. Therefore, various cutting mechanics and machining processes will be assessed and monitored using a proper impedance model with the proposed method.

CONCLUSION

The preliminary study of the impedance model-based in-process cutting temperature monitoring method was first introduced. The impedance of the coating layer, the dielectric material, was experimentally characterized under varying temperature conditions, and the impedance is dependent on the temperature. Machining experiment was also conducted under different cutting speeds and depth of cut, and the results showed the feasibility of implementing into the machining system for monitoring the temperature. The proposed method is not confined to the cutting temperature measurement. This method can also be used to measure the vibration while machining is in process since the impedance will change as the contact area changes. Chip formations can be predicted, and the wear of the tool can also be monitored as the thickness of the coating layer is worn out. In addition, the cutting force is expected to be measured. This proposed technique, with its versatility, can be utilized for various machining processes and cutting mechanics monitoring methods. In sum, the impedance-based in-process monitoring method could be implemented in dynamic systems that monitor the cutting mechanics at the local hot spot region to improve the control of cutting mechanics for advanced manufacturing.

ACKNOWLEDGEMENT

In the study, this work was supported by the Texas A&M University (MEEN Seed Grants) and partially the Korea Institute of Industrial Technology (Development of robotic machining state monitoring and process technology for improving product quality).

REFERENCES

[1] Anand J. Patel and Gülenay A. Kilic, “A Review on Advanced Manufacturing Techniques and Their Applications”, IntechOpen (2021).

[2] Geoffrey Boothroyd and Winston A Knight, Fundamentals of Machining and Machine Tools Third Edition, CRC Press, 2005.

[3] Wit Grzesik, Advanced Machining Processes of Metallic Materials, Elsevier, 2008.

[4] Frederick Winslow Taylor, On the Art of Cutting Metals, American Society of Mechanical Engineers, 1907.

[5] E.M. Trent, P.K. Wright, Metal Cutting, 4th ed., Butterworth–Heinemann, Boston, USA, 2000, 446p.

[6] S.R. Carvalho, S.M.M. Lima e Silva, A.R. Machado, G. Guimaraes, Temperature determination at the chip–tool interface using an inverse thermal model considering the tool and tool holder, Journal of Materials Processing Technology Vol. 179, pp. 97–104 (2006).

[7] J. M. Rodríguez, P. Jonsén, A. Svoboda, Simulation of metal cutting using the particle finite-element method and a physically based plasticity model, Computational Particle Mechanics, Vol. 4, Iss. 1 (2017).

[8] Ismail Lazoglu, Yusuf Altintas, Prediction of tool and chip temperature in continuous and interrupted machining, International Journal of Machine Tools and Manufacture, Vol. 42, Iss. 9, pp. 1011-1022 (2002).

[9] Kesriklioglu, S., Arthur, C., Morrow, J. D., and Pfefferkorn, F. E., Characterization of Tool–Chip Interface Temperature Measurement With Thermocouple Fabricated Directly on the Rake Face. ASME. *J. Manuf. Sci. Eng*. Vol. 141, Iss. 9, 091008 (2019).

[10] Sutter, G., L. Fauré, A. Molinari, N. Ranc and V. Pina. An experimental technique for the measurement of temperature fields for the orthogonal cutting in high speed machining. *International Journal of Machine Tools & Manufacture, Vol.* 43, pp. 671-678 (2003).

[11] Kesriklioglu, S., Morrow, J. D., and Pfefferkorn, F. E., Tool–Chip Interface Temperature Measurement in Interrupted and Continuous Oblique Cutting. ASME. *J. Manuf. Sci. Eng*. Vol. 140, No. 5, 051013 (2018).

[12] Akbar F., Mativenga P.T., Sheikh M.A. (2007) An Investigation of the Tool-Chip Interface Temperature and Heat Partition in High-speed Machining of AISI/SAE 4140 Steel with TiN-coated Tool. In: Hinduja S., Fan KC. (eds) Proceedings of the 35th International MATADOR Conference. Springer, London. https://doi.org/10.1007/978-1-84628-988-0_48

[13] J. Karner, M. Pedrazzini, I. Reineck, M. E. Sjostrand, and E. Bergmann, CVD diamond coated cemented carbide cutting tools, Materials Science and Engineering: A, Vol. 209, Iss. 1-2, pp. 405-413 (1996).

[14] W. Ebert, M. Adamschik, P. Gluche, A. Flöter, and E. Kohn, High-temperature diamond capacitor, Diamond and Related Materials, Vol. 8, pp. 1875-1877 (1999).

MICROFABRICATION AND EXPERIMENTAL INVESTIGATION OF DRAG REDUCTION AND FOULING RESISTANCE POTENTIAL OF ASYMMETRIC TRIANGULAR RIBLETS

Benjamin W. Hamilton[1], O. Remus Tutunea-Fatan[1], and Evgueni V. Bordatchev[2]
[1]Department of Mechanical and Material Engineering
Western University
London, Ontario, Canada
[2]Automotive and Surface Transportation
National Research Council of Canada
London, Ontario, Canada

INTRODUCTION

Surface fouling is the unwanted accumulation of environmental contaminants leading to a loss of its intended function. These contaminants are typically categorized as either organic (living matter) or inorganic (non-living matter).The underwater surfaces of ship hulls are susceptible to organic fouling in the form of barnacles and algae [1]. This accumulation is associated with multifaceted challenges: the attached organisms roughen the surface thus leading to increased drag and fuel consumption. As such, the service life of the ship is decreased due to the corrosion caused by fouling. It is estimated that the global cost associated with this type of challenges is $150 billion (USD) annually [2].

To combat fouling, ship hulls have been coated with tin-based biocide paints. These paints are prone to leach out compounds into the environment, thereby poisoning nearby organisms. While being effective at hull fouling prevention, the impact of biocide paints on the environment could not be overlooked. In 2008, the International Maritime Organization issued a global ban on all tin-based biocide paints [3]. Nonetheless, the alternate biocide-free fouling resistant coatings are not as effective at preventing the settlement of organic foulants. This aspect has prompted emerging but still ongoing research toward the development of a new generation of fouling resistant coatings [4].

Over the past 30 years, scientists have discovered that many plants and animals have natural defense mechanisms against organic and inorganic fouling. These can include one or a combination of surface topography, mucous secretion, flexion, sloughing, and surface energy accumulation [5]. Of these, the most widely applicable for engineering applications remains surface topography.

Shark skin is typically considered the “state-of-the-art” model for fouling resistance [6] because the skin of many shark species is covered by small denticles (similar to scales) that are covered with micro-riblets aligned parallel with the swimming direction. This hierarchical topography gained research interest owed to its ability to reduce fluid drag compared to a flat surface. The riblets have a decisive effect on the otherwise chaotic motion of the water layer near the surface. This decreases the momentum transfer, ultimately reducing friction and thereby allowing the shark to swim faster and/or more efficiently.

Subsequent studies found that shark skin inspired micro-riblets are capable of reducing organic fouling by as much as 86% [7]. It is believed that drag reduction is positively correlated with fouling resistance. While the exact mechanism responsible for this correlation is still insufficiently understood, one of the common assumptions/hypotheses is that a drag reducing surface allows the water layer near the surface to travel more quickly, thus carrying away foulant particles that would otherwise settle and adhere to the surface.

More recently, fish-scales have demonstrated lower Reynolds drag reduction of up to 3% owing to their ability to delay the onset of turbulent flow and the increased drag associated with it [8]. Further investigations into the drag reducing mechanisms of bioinspired fish-scales along with their ability to resist fouling is expected to further substantiate the anticipated connection between drag reduction and fouling resistance.

GEOMETRY AND HYDRODYNAMIC PERFORMANCE OF ATR

Asymmetric triangular riblets (ATR) were introduced in a previous study as a potential simplification of fish-scales as well as a novel fouling resistant surface topography [9]. Low Reynolds drag reduction up to 3% was demonstrated thus showing good agreement with the more complex topography of natural fish-scales.

The two-dimensional simplification of the rather complex semicircular layering of fish-scales is a repeating pattern of right triangular V-grooves oriented such that the 90° corner forms the trough of the groove, while the grooves are oriented perpendicular to the nominal flow direction (FIGURE 1). There are two facets whose nomenclature follows the exposure to the flow: the primary facet being the windward side, and the secondary facet being the leeward side.

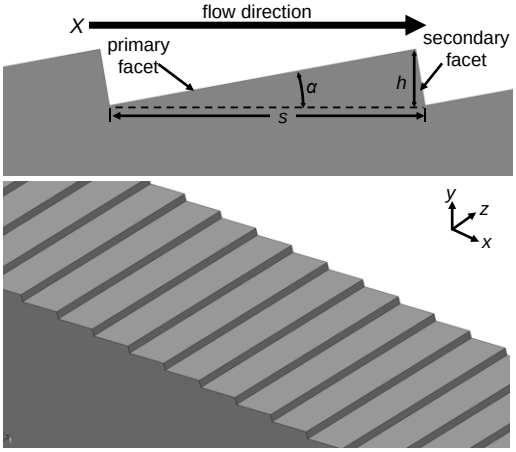

FIGURE 1. Details of ATR geometry.

The geometry is fully defined by two dimensions, the angle of the primary facet, α, with respect to the horizontal plane, and *s*, the spacing, or period between adjacent grooves. The height of each groove, *h*, is measured normal to the surface between the root and peak of each groove and is a function of *s* and *α,*

$$h = \frac{s}{2}\sin 2\alpha \qquad (1)$$

NUMERICAL SIMULATION OF ATR PERFORMANCE

The previous study was carried out across a range of dimensions for the two parameters. The baseline geometry had α = 10°, and *s* = 585 µm in order to achieve a 100 µm height. From this baseline geometry, the angle was varied between 2° and 14°, and the spacing was varied from 351 to 877.5 µm by increasing the number of ribs in the computational domain.

Numerical simulations were conducted using Ansys Fluent and the large eddy simulation (LES) model along with the Smagorinsky-Lilly subgrid model. This model has been employed in similar studies in order to evaluate the drag reduction potential of surface topography [10]. The *x*, *y*, and *z* axes of the computational domain denote the streamwise, wall-normal, and spanwise directions, respectively. *U* denotes the mean streamwise velocity. The inlet and outlet, along with the left and right surface, were prescribed as periodic boundary conditions. These boundary conditions behave in a manner that allows flow to pass through one surface and be reintroduced on the matching surface, therefore allowing the domain to behave in a semi-infinite manner. The ATR geometry was applied to the bottom surface, while the top, smooth surface was used as a reference to calculate drag reduction. As such, a no-slip boundary was applied. The inlet conditions were prescribed such that the peak centreline velocity was approximately 0.75 m/s.

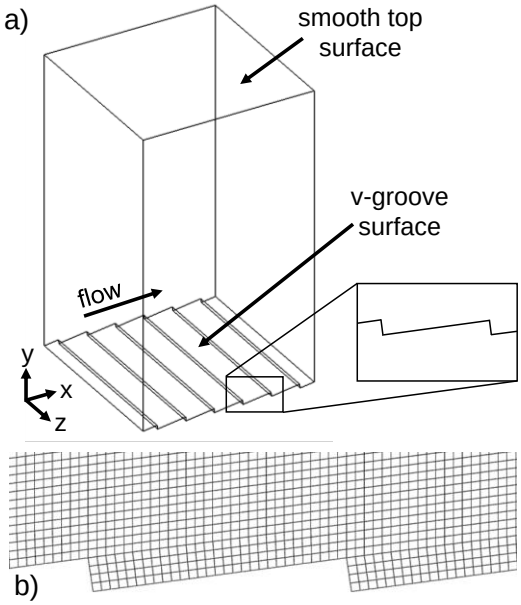

FIGURE 2. a) Computational domain for 8° case, and b) mesh detail near ATR topography.

For most cases, the computational domain was discretized in the X, Y, and Z directions with 170, 84, and 170 cells, respectively. Cell sizes near the top and bottom surfaces were decreased similar to the study [10] in order to capture the

flow field in these regions more accurately. The result is a computational domain comprised of approximately 2.5 million tetrahedral cells.

Drag reduction performance is traditionally reported as:

$$DR = (\tau - \tau_0) / \tau_0 \quad (2)$$

where τ is the shear stress on the surface topography, and τ_0 is the shear stress on a flat surface under identical flow conditions. Negative values correspond to a drag reduction, and positive values to drag increases. The objective of the present study was to explore a range of smaller spacings and angles that were not considered in the previous study (TABLE 1).

TABLE 1. Analyzed geometric parameters.

Case ID	*α* (°)	*s* (μm)	*h* (μm)
3.1	0.2	583.3	2.0
3.2	0.5	583.3	5.1
3.3	0.8	583.3	8.1
3.4	1.2	583.3	12.2
3.5	1.6	583.3	16.3
3.6	4	583.3	40.6
3.7	8	583.3	80.4
3.8	12	583.3	118.6
4.1	10	291.7	49.9
4.2	10	250.0	42.8
4.3	10	194.4	33.3
4.4	10	159.1	27.2
4.5	10	125.0	21.4
4.6	10	116.7	20.0
4.7	10	87.5	15.0

The computational domain remained unchanged from the previous study, with X, Y, and Z dimensions of 3.5, 6.0, and 3.5 mm, respectively. The Reynolds number for a channel of this nature is calculated as,

$$Re = \frac{U_l L}{\nu} \quad (3)$$

where U_l is the centreline velocity, ν is the kinematic viscosity of the the working fluid, and L is half height of the channel (3.0 mm). The transition from laminar to turbulent flow is considered to occur at $2000 < Re < 4000$. The previous study used $Re = 2250$, while the present study relied on $Re = 3000$ (owed to an increased velocity) in order to increase the drag reduction.

Transient simulations were run while monitoring the drag reduction performance in order to determine when the solution has reached the steady state. The results demonstrate the anticipated breakdown in drag reduction as *s* and *α* decrease (*i.e. h* as shown in equation 1). However, the optimal performance for the present, higher *Re* study was not captured (FIGURE 3). Instead, the optimal performance appears to be at larger spacings and angles. This behaviour is likely caused by the increased Reynolds values used in the present study.

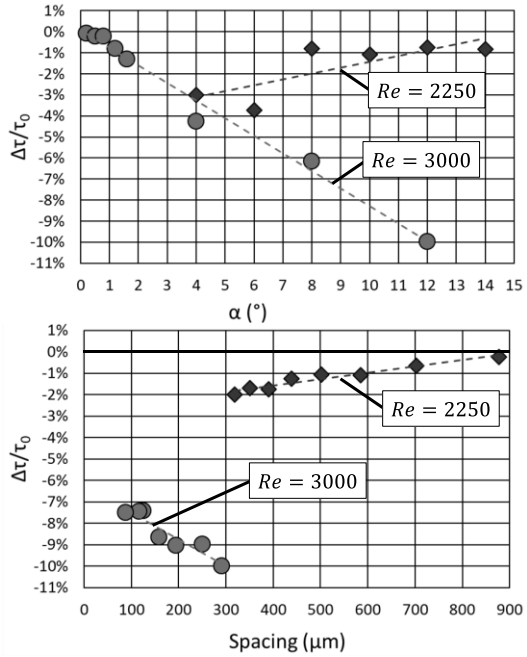

FIGURE 3. Change in drag for varied a) angles with s = 585 μm, and b) spacing with α = 10°.

Similar to the findings of previous studies on fish-scale topography, the ATR geometry delays the onset of turbulence by trapping and recirculating flow in the groove valleys [11].

MICROFABRICATION OF ASYMMETRIC TRIANGULAR RIBLETS

Several samples were fabricated on acrylic using a Kugler Microgantry Nano 5x ultraprecise five-axis CNC machine tool and single-point diamond tooling. The machine tool has three linear axes (*X*, *Y*, and *Z*), two rotary axes (*A* and *C*), and a spindle aligned with the *Z*-axis. According to convention, the rotary axes are labeled corresponding to the linear axes they are aligned with. In this case, the machine tool's rotary axes, *A* and *C*, are aligned with the *X* and *Z* axes, respectively (FIGURE 4a).

The monocrystalline diamond end mill used was characterized by a 1.0 mm diameter and had a sharp corner to facilitate simultaneous machining

of the primary and secondary facets of the geometry (FIGURE 4b). Furthermore, this particular tool geometry was chosen to optimize surface finish without compromising material removal rates. The workpiece was rotated in such a way that grooves were aligned with the X-axis, and the primary facet was oriented parallel to the XY plane of the machine coordinate system, thus requiring A-axis rotation.

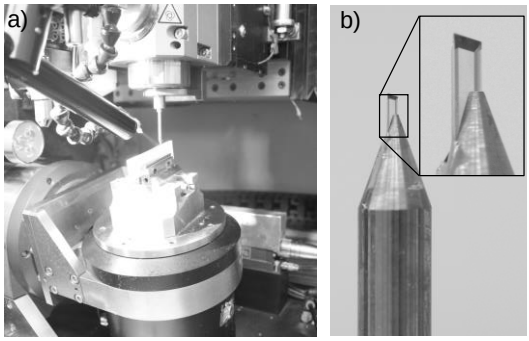

FIGURE 4. a) Ultraprecise machine tool, and b) single-point monocrystalline diamond tool.

As a result of this kinematics, groove geometry was fabricated by a rotating tool with X-axis cutting motions alone and each groove was generated in a single cutting motion. (FIGURE 5)

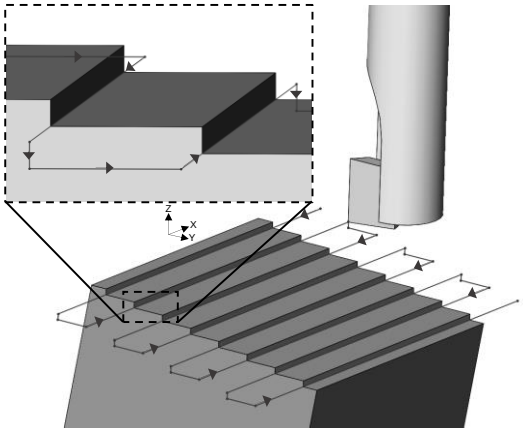

FIGURE 5. Cutting kinematics for ATR.

The tool was rotated at 42,000 rpm and travelled across the workpiece at 420 mm/min in order to ensure the desired 10 µm/tooth. At the end of each groove cut, the tool continued to move in the X-direction until it cleared the groove surface. This was necessary for the subsequent positioning motions that align the tool with the next groove to be cut. Since the primary facet of the V-groove is aligned with the *XY* plane, the *Y* positioning motion is equal to the length of the primary facet and the *Z* positioning motion equal to the secondary facet length. In machine coordinate system, these motions are calculated as a function of *s* and *α*:

$$\begin{aligned} Y_{pos} &= s\cos\alpha \\ Z_{pos} &= s\sin\alpha \end{aligned} \tag{4}$$

The "zig-zag" cutting strategy illustrated in FIGURE 5 results in alternating climb and conventional milling for each groove. Clearly, this approach favors cutting efficiency over surface finish.

Three samples were fabricated with a two-fold purpose: a comprehensive analysis of the geometry, followed by a fouling resistance study. Since drag reduction was present for all angles and spacings considered in the numerical studies, it is also of importance to analyze any of its possible implications on fouling resistance. The geometry chosen for this study was suggested by the anticipated interaction between fouling particles and feature height. The three heights chosen for this study were 8, 16, and 32 µm, corresponding to periods of 46.8. 93.6, and 187.1 µm (α = 10°). Samples were fabricated on the narrow edge of 2.9 x 75 x 20 mm acrylic workpieces.

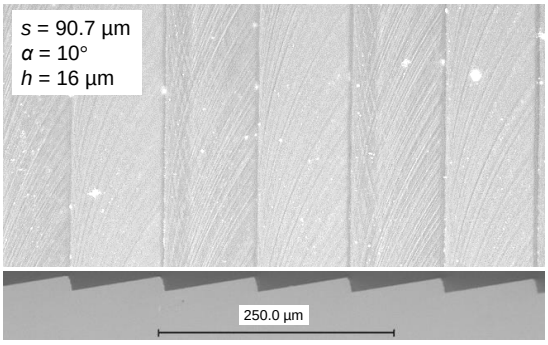

FIGURE 6. Microscope images of 16 µm ATR.

The resulting surfaces were analyzed with an optical microscope and CCD camera, and an optical profilometer. The images seen in **Error! Reference source not found.** illustrate the machined topography. The alternating climb and conventional milling strategy resulted in variations of the surface finish between adjacent grooves, qualitatively seen as small differences of the grooves left by the rotating end mill.

An optical profilometer was used to further assess the samples for geometric accuracy and surface finish. The 2D plot shown in FIGURE 7a,

represents data captured along the horizontal line at 500 µm. The average feature height for the 16 µm sample was 16.49 ± 0.29 µm, while the average period was 93.87 ± 1.69 µm, approximately 0.33% larger than the target period of 93.56 µm. The deviations associated with both these values may be attributed to the 384 nm resolution of the optical profilometer used for analysis. However, the average angle of the primary facet was 10.16°. This corresponds to a feature height of 16.25 µm for the 93.56 µm period (Eq. 1).

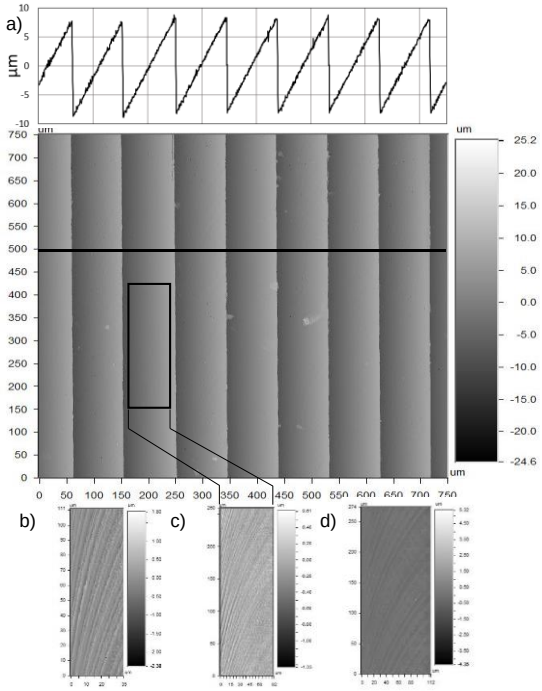

FIGURE 7. ATR form of: a) 750 x 750 µm area of 16 µm sample, b), c), and d) surface topography of 8, 16, and 32 µm samples.

Areal surface roughness (*Sa*) was measured on several locations of the primary facets (FIGURE 7). The discrepancy between climb and conventional milling was 28.0 nm while mean surface roughness for all measured regions was 167 nm. While this is above optical quality, the achieved roughness came out better than in typical conventional micromilling operations and around the same range as grinding [12].

FEASIBILITY ANALYSIS OF FOULING RESISTANCE

Fouling resistance studies were conducted by exposing the fabricated samples to a contaminated flow of water at 1 mL/s for 100 seconds. The samples were inclined at 45° to facilitate gravity-driven flow across the microtopography. In order to direct the flow of water over the narrow 2.9 mm surface of the fabricated topography, a channel was created by placing the sample between two glass plates, the plates forming the channel walls, and the ATR topography forming the bottom surface of the channel. The specified flow rate and channel dimensions resulted in a peak velocity of approximately 0.45 m/s as verified by a high speed camera.

Similar to studies conducted by Bixler *et al.,* silicon carbide (SiC) particles were used to contaminate the water because their size, shape, and hydrophilicity mimic those of natural dirt [5]. Particles with an average size of 15 µm were added to the water at a mass concentration of 0.50% SiC. Following exposure to the contaminated flow, samples were air-dried at room temperature for 30 minutes before particle analysis. Using an optical microscope and CCD camera, several 1000 x 750 µm images were captured and the total fouled area was calculated with a purpose-built program developed using Matlab's image analysis package. For each sample, a total of eight images were utilized to establish a mean representative percentage of fouling coverage. Few depictions of the fouled 16 µm sample are presented in FIGURE 8.

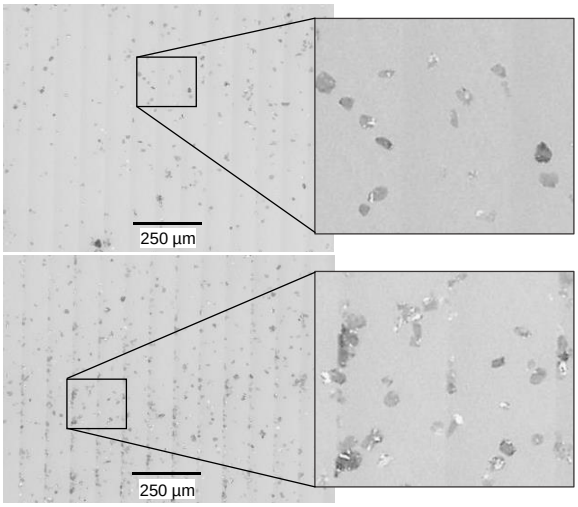

FIGURE 8. Images of 16 µm ATR following exposure to contaminated flow.

Fouling resistance efficacy was quantified as the area covered by SiC particles represented as a percentage of the total area. The 8 µm sample was anticipated to demonstrate a distinct advantage over the larger samples, owing to the feature height being less than average size of the

SiC particles, preventing their settlement. However, it was observed that the baseline flat geometry outperformed all three cases of the asymmetric triangular riblets with a mean particle coverage of just 0.18%. The 8, 16, and 32 µm samples respectively had 2.47, 2.71, and 0.99% mean coverage. Contrary to the anticipated findings, the 32 µm geometry had the lowest fouling coverage of the three.

As mentioned previously, simulations were conducted such that the Reynolds number was within the transition to turbulence regime. The calculated Reynolds number within the flow channel was 1200, within the laminar flow regime. It may be argued that different flow regimes contribute to the contradictory results; however, previous studies have concluded that drag reduction mechanism of fish scales is owed to their ability to maintain laminar flow at large Reynolds numbers. Therefore, even at small Reynolds numbers, fouling resistance should be present. These findings suggest fish may rely on alternate mechanisms for fouling resistance, or that the biomimetic geometry of asymmetric triangular riblets does not perform the dual function of drag reduction and fouling resistance. Future studies will address fouling resistance and self-cleaning capabilities at larger Reynolds numbers within the transition and fully turbulent regimes.

SUMMARY AND CONCLUSIONS

Asymmetric triangular riblets represent a novel topography for drag reduction and fouling resistance. Numerical simulations were performed to determine the optimal dimensions for drag reduction in an aqueous environment. A maximum drag reduction of nearly 10% was achieved, essentially matching the previously reported performance of sharkskin-inspired riblets.

For experimental purposes, three samples were fabricated in acrylic. However, the results obtained suggested that the analyzed surface microstructures are suitable for fouling resistant purpose. Nonetheless, this study cannot be considered conclusive and future studies will be conducted at higher Reynolds numbers.

ACKNOWLEDGEMENTS

The work presented in this study is the result of the collaboration between Western University (London, Ontario) and National Research Council of Canada (London, Ontario). Partial financial support was also provided by Natural Sciences and Engineering Research Council of Canada.

REFERENCES

[1] Bixler G., Bhushan G., Biofouling: Lessons from Nature. Phil. Trans. R. Soc. A. 2012, 370:2381-2417.

[2] Schultz M., Bendick J., Holm E., Hertel W. Economic Impact of Biofouling on a Naval Surface Ship. Biofouling. 2011; 27: 87-98.

[3] Champ M., Economic and Environmental Impacts on Port and Harbors from the Convention to Ban Harmful Marine Anti-fouling Systems. Mar Pollut Bull. 2003, 46:935-940.

[4] Scardino A., Hudleston D., Peng Z., Paul N., de Nys R., Biomimetic Characterisation of Key Surface Parameters for the Development of Fouling Resistant Materials. Biofouling. 2009, 25:1, 83-93.

[5] Bixler G., Bhushan B., Fluid Drag Reduction and Efficient Self-Cleaning with Rice Leaf and Butterfly Wing Bioinspired Surfaces. Nanoscale. 2013, 5:7685-7710.

[6] Bechert D., Bruse M., Hage W., Van Der Hoeven J., Hoppe G., Experiments on Drag-Reducing Surfaces and Their Optimization with an Adjustable Geometry. J. Fluid Mech. 1997, 338:59-87.

[7] Carman M., Estes T., Feinberg A., Schumacher J., Wilkerson W., Wilson L., Callow M., Callow J., Brennan A., Engineered Antifouling Microtopographies – Correlating Wettability with Cell Attachment. Biofouling. 2006, 22:1 11-21.

[8] Muthuramalingam M., Villemin L., Bruecker C. Streak Formation in Flow Over Biomimetic Fish Scale Arrays. Journal of Experimental Biologists. 2019; 222.

[9] Hamilton B., Churchill-Baird J., Tutunea-Fatan O., Bordatchev E., Parametric Simulation and Analysis of Self-Cleaning and Antifouling Functional Surfaces with Trilateral Geometry. ASPE Spring Topical Meeting. 2021, virtual event.

[10] Martin S., Bhushan B. Fluid Flow Analysis of a Shark-Inspired Microstructure. Journal of Fluid Mechanics. 2014; 756: 5-29.

[11] Wu L., Jiao Z., Song Y., Liu C., Wang H., Yan Y., Experimental Investigations on Drag-Reduction Characteristics of Bionic Surface with Water-Trapping Microstructures of Fish Scales. Scientific Reports. 2018. 8:12186.

[12] Walker J, Dixon B, Machining Fundamentals, Goodheart-Willcox Publisher; 9th edition (Aug. 29 2013)

A SET OF TURING COMPLETE MECHANICAL LOGIC ELEMENTS AND A SIMPLE LOGIC CIRCUIT

Frederick Sun, Robert M. Panas, Logan Bekker, Andrew J. Pascall
Lawrence Livermore National Laboratory
Livermore, California, USA

Amin Farzaneh, Jonathan B. Hopkins
University of California Los Angeles
Los Angeles, California, USA

INTRODUCTION

In this paper we present a set of additively manufacturable Turing complete micromechanical logic elements and a printed demonstration of a simple logic circuit consisting of several of these elements. While computation has been synonymous with electronics nowadays, there exist scenarios where mechanical computation is advantageous, such as harsh environmental constraints in high temperature, radiation, limited power supply, or minimal EM signature requirements.

Mechanical computation offers an alternative to traditional semiconductor electronics in specific applications where extreme condition unsuitable for semiconductor electronics needs to be met, such conditions include but are not limited to low energy consumption[1,2], passive data storage, data storage and computation under harsh environment such as extreme heat or high radiation where semiconductors are prone to failure [3].

The original computers of the 19th and early 20th century relied on mechanical logic systems to process information, most famously the difference and analytical engines by Babbage as early as in the 1830s. Recent advancement in 3D micro-additive manufacturing technology have provided fabrication techniques that allow us to build the printed micromechanical logic is presented in this paper.

The micromechanical logic elements included in this paper are the mechanical bit, the AND gate, OR gate, NAND gate, NOR gate and NOT gate, where all other gates can be achieved by a combination of these elements. The mechanical bit storing the digital signal is a bistable flexure system where one bistable state represents 1, and the other bistable state represents 0. The logic gates are displacement-based which read the logic states of mechanical bits connected to their input ports and outputs a displacement to mechanical bit connected to the output port according to gate function. This paper is the first to demonstrate a physical implementation of a simple logic circuit consisting of several displacement based logic gates and bistable mechanical bits, establishing the framework to construct more complex mechanical logic circuits.

THE MECHANICAL LOGIC BIT

Our mechanical logic bit is based on bi-stable flexure elements which use displacement to represent distinct logic states. Fig. 1 shows a physical implementation of a pair of mechanical logic bits connected via compliant connector links. Note that the principle of the design is independent of scale, the exact geometry or materials producing the compliance.

Degeneracy in the bistable states is required to ensure the logic performs equivalently for either signal, 0 or 1, where one bistable state represents the digital state of 1, and the other 0. The bit is constructed in an unloaded configuration, and energized into their bistable states by displacing a locking mechanism located on the right of the demonstration mechanism as can be seen in in Fig. 1. Digital information is stored in the mechanical bit while the bistable flexure system is energized.

Many useful digital logic circuits require that the output from one gate be fed into the input of one or more gates. While this is now trivial for electronic systems, mechanical logic gates need

to be “wired” with mechanical linkages. To that end, signal propagation is achieved via the compliant connector.

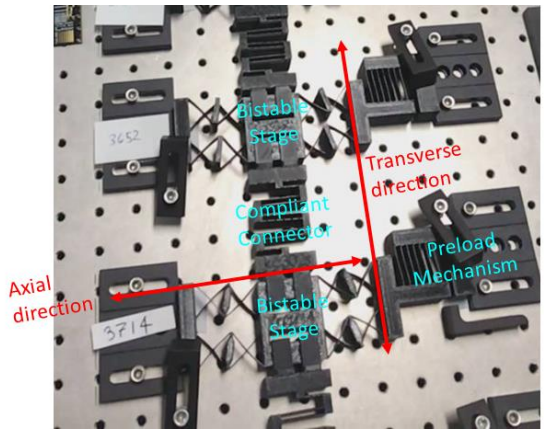

FIGURE 1: A pair of connected mechanical logic bits.

The digital signal is transported from one mechanical bit to the next as follows: An input signal displaces the mechanical bit from one bistable state to another, the coupling is momentarily compressed due to this displacement, storing the input kinetic energy into elastic potential energy. Stored kinetic energy is released onto the next mechanical logic element, pushing on and thereby propagating the signal to the next element. The compliant coupling allows a smaller input signal as opposed to flicking the entire circuit if the bits are rigidly connected.

To ensure signal propagation, we tune the compliance between bistable element nodes. The stiffness of the bistable flexure system is gradually decreased down the chain of mechanical logic elements, releasing the excess elastic potential energy to displace the downstream mechanical logic elements. The decreasing potential energy well within each successive mechanical logic element allows the input signal to traverse through a mechanical logic circuit consisting of many elements.

Bistbility in the mechanical bit and signal propagation can only be accessed in small regions of the full design space, such constraints guide the balance of compliance within and between bistable elements, regulated by the flexure stiffness in the transverse and axial direction of the mechanical bit as well as the stiffness of the compliant connector as labeled in Fig. 1.

Transverse stiffness provides a means to modulate the potential energy well of the bistable element. Bistability disappears when conventional stiffness of the transverse 4-bar parallelogram flexure mechanism exceeds negative stiffness generated by the axial direction compression of the structure. Connector stiffness provides a means to engineer pulse behavior. A weak connector linkage generates a short pulse profile extending across few nodes, an increasingly strong coupling linkage that extends the pulse length towards infinity. Consider in the most extreme case, when the coupling linkage is a rigid body, all node acts as one as if infinite pulse length. Having coupling too stiff or too compliant hampers the propagation of the pulse. A coupling too compliant may fail to displace the next mechanical logic element down the chain due to insufficient force, while a coupling too stiff may result in a pulse too long that does not properly displace a logic gate to the correct location in addition to the larger input force.

TURING COMPLETE MICROMECHANICAL LOGIC GATES

Fig, 2 shows a set of Turing complete mechanical logic gates. The AND gate is composed of two input ports and one output port. Mechanical bits are connected to the input and output tabs of the logic gates storing the signal. Fig.2(a) shows the core of the AND gate and Fig.2(b) shows the configuration with mechanical bits attached. In this figure, the input tabs are on the bottom and the output tabs are on top, the compliant connector is built into the parallel guide within each gate.

In Fig. 2(a) where the core of the AND gate is shown, when only one input tab is displaced, the intermediate stage rotates allowing the output tab remains in place as shown in Fig. 2(c). When both inputs tabs are displaced, shared transverse direction motion at the input suppresses rotation and directly passes the displacement to the output as shown in Fig. 2(d), fulfilling the function of the AND gate. The AND gate design is suited for bipolar, resettable requirements and is scalable as well as compatible with layer-based fabrication approaches. Two 90 degrees turns were achieved through flexure design to redirect the pulse direction and avoid interference of micro-fabricated parts.

Define the direction from the input to output as 1, and the other 0, the set of Turing complete logic

gates can be achievesd through simply reversing the direction of the 90 degrees turn transmission flexures as illustrated in figure 2(e-g). The reverse direction 90 degrees turn flexure essentially functions as a NOT gate. The pulse propagation characteristics are unaffected by resultant direction of the 90 degrees turn transmission flexures, a functional complete set of logic gates is thus obtained.

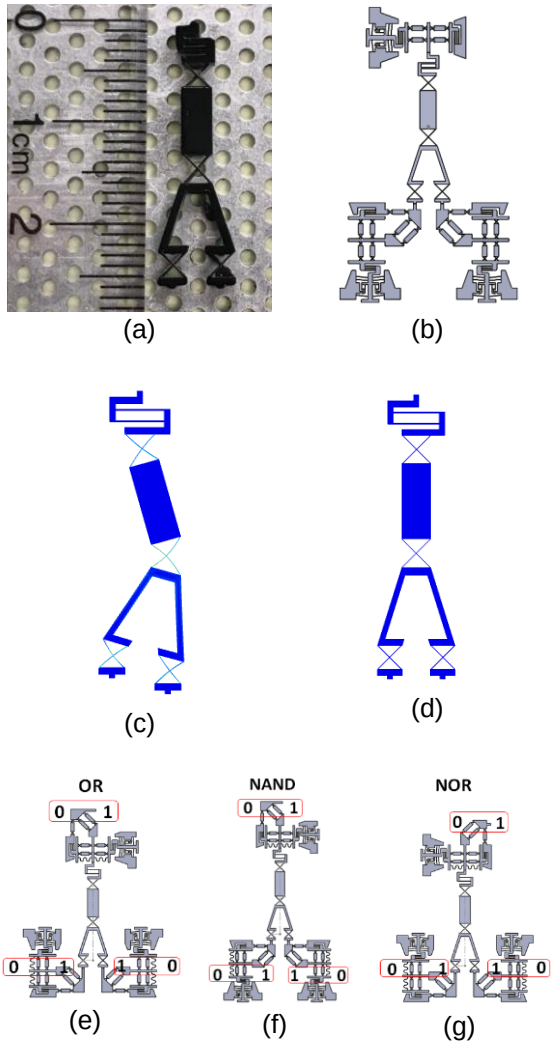

(a) (b) (c) (d) (e) (f) (g)

FIGURE 2: Mechanical logic elements: (a) Core of the AND gate, (b) AND gate, (c) AND gate with 1 input activated (d) AND gate with both inputs activated (e) OR gate, (f) NAND gate, (g) NOR gate

SIMPLE MICROMECHANICAL LOGIC CIRCUIT

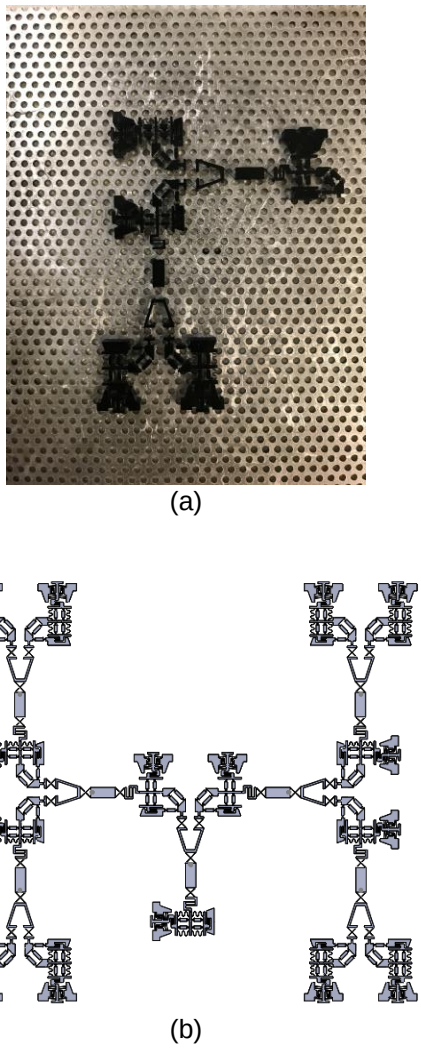

(a) (b)

FIGURE 3: A simple mechanical logic circuit with (a) 3 input bits (b) 8 input its

Finally, a simple circuit can be achieved by connecting several mechanical logic gates, as shown in Fig. 3(a) and Fig.3(b). The microfabricated simple circuit in Fig. 3(a) consists of two connected AND gates and built with printed resin, allowing simple Boolean operation. A hypothetical scenario where such a circuit is deployed is when multiple transducers are connected to the input tabs of the mechanical bits and a simple logical operation is required to check if all the transducers are activated. This simple mechanical logic circuit allows this logic operation to be performed on site all in an unpowered package.

A more sophisticated configuration that allows 8 inputs to be evaluated at once is shown in Fig

3(b), this design has yet to be fabricated due to the print window size limitation of the micro-fabrication equipment.

CONCLUSION

In summary, basic mechanical logic components including the mechanical bit and a set of Turing complete logic gates have been designed and constructed, and a simple circuit has been built with said components. By incorporating micro-mechanical logic circuits, environmental data collection capacity of multi-domain sensors and smart materials are enhanced by providing the capability to carry out basic logic operation in an integrated unpowered package. The technology is applicable to a wide range of where smart sensing is desired.

ACKNOWLEDGEMENTS

This work performed under the auspices of the U.S. Department of Energy by Lawrence Livermore National Laboratory under Contract LDRD-19-ERD-018. LLNL-CONF-826249.

REFERENCES

[1] C. Monroe, D. M. Meekhof, B. E. King, W. M. Itano, D. J. Wineland, 1995, “Demonstration of a Fundamental Quantum Logic Gate” Phys. Rev. Lett.

[2] R. Landauer, 1988 “Dissipation and noise immunity in computation and communication” Nature

[3] M. R. Werner, W. R. Fahrner, 2001 “Review on materials, microsensors, systems and devices for high-temperature and harsh-environment applications” IEEE Trans. Ind. Electron.

SELF-SENSING HYSTERESIS-TYPE BEARINGLESS MOTOR

Laura Homiller and Lei Zhou
Walker Department of Mechanical Engineering
University of Texas at Austin, TX, USA

INTRODUCTION

The development of high-speed machines is a growing trend in the electric machine industry. Increasing the speed decreases the volume and weight of the electric machine for the same power rating, which has advantages for electric transportation and portable power storage and generation applications. *Bearingless motors* are electric machines that apply torque and magnetic suspension forces on the rotor using a single stator assembly. These machines have demonstrated excellent performance for high-speed applications such as pumps [1] and flywheels [2] due to their frictionless operation and imbalance elimination. Additionally, the combined functionality of motor and bearing in a single assembly makes these machines compact and attractive for use in small devices [2, 3]. One major challenge that prevents wide usage of bearingless motors is the need for air-gap position sensors. The magnetic suspension of the rotor in a bearingless motor requires closed-loop feedback control for stabilization [4], but the required position sensors are typically expensive. If bearingless motors can operate without these sensors, system cost can be significantly reduced and these machines applied to a wider range of application areas.

This extended abstract presents a method for hysteresis-type bearingless motors to estimate the rotor's radial position without additional displacement sensors, aiming at enabling a new kind of self-sensing bearingless motor with lower cost and improved robustness. The key idea is to use the inductance variation of stator coils to estimate the rotor displacement, and use an injected high-frequency signal to amplify the sensitivity of winding impedance with respect to rotor displacement. We have carried out finite element (FE) simulations to demonstrate its feasibility, and are constructing a prototype self-sensing bearingless motor for experimental validations.

OPERATING PRINCIPLE

Bearingless Motor Operating Principle: The suspension control forces in a bearingless motor are generated by the superposition of two magnetic fields [4]. In our proposed motor design, a two-pole magnetic field is used for suspension, and a four-pole magnetic field is used for rotation. Figure 1 shows the winding diagram of our proposed motor, where the stator has 12 teeth, and each of the stator coils wrap around one stator tooth and carries an independently-controlled current to generate both the two-pole and four-pole magnetic fields [5]. In this way, the stator generate both thrust torque and suspension controlling forces to the rotor simultaneously.

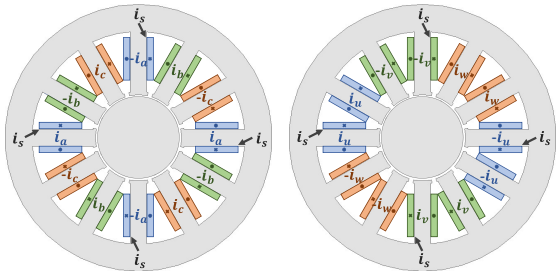

FIGURE 1. Winding pattern of prototype motor. i_s is the high-frequency air gap displacement sensing current. (a) 4-pole motor winding. (b) 2-pole suspension control winding.

In addition to the torque and force-generating currents, in order to enable the sensorless estimation for the air gap length, a high-frequency signal is injected to four stator coils's current as shown by i_s in Fig. 1. For each lumped coil, the inductance can be calculated as

$$L(g) = \frac{N^2 \mu_0 A}{2g}, \tag{1}$$

where g is the air gap length at the coil's position, N is the coil's number of turns, μ_0 is the free-space magnetic permeability, and A is the area of the stator tooth which the coil is wrapped around. The voltage across the coil is then related to the

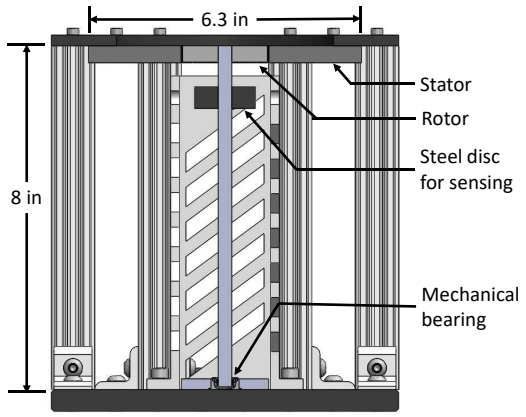

FIGURE 2. Cross-section view for the CAD design of self-sensing bearingless hysteresis motor prototype.

inductance of the coil according to:

$$v = Ri + L\frac{di}{dt} + E_b, \tag{2}$$

where v and i are the voltage and current in the coil, respectively, R is the coil's resistance, and E_b is the coil's back-electromotiveforce (back-EMF). In this work, since we are using a hysteresis motor, the back-EMF in the coils can be assumed to be small. Consequently, the voltage induced in each coil can be used to provide an estimate for the rotor's radial displacement.

HARDWARE OVERVIEW

We have designed a hysteresis-type bearingless motor testbed, and Fig. 2 shows a cross-section view of the CAD design. In this system, the rotor is on top of a vertical shaft, where the suspension forces of the motor are used to constrain the radial position of the shaft on the top end. In addition, a self-aligning mechanical bearing is used to constrain the radial position of the shaft at the bottom end. The self-aligning bearing is selected to allow angular movement of the shaft so that the position of the rotor is not mechanically constrained. Four inductive sensors (DW-AS-509, Contrinex) measure the rotor's radial position through a steel sensing disc mounted on the shaft, providing "ground truth" signals for the air gap length estimation problem. We will first test the magnetic suspension of the bearingless motor using the measured rotor's radial position, and the final system will use the estimated rotor position for the feedback control of the rotor's magnetic suspension.

We have constructed a prototype for the self-

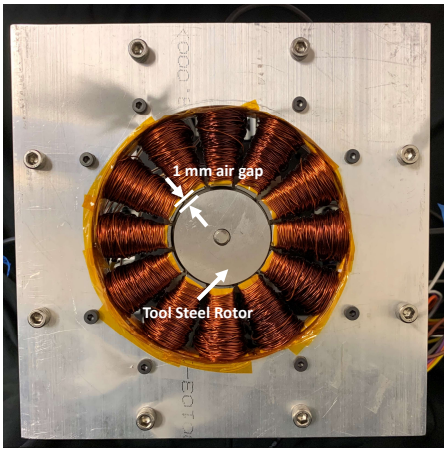

(a)

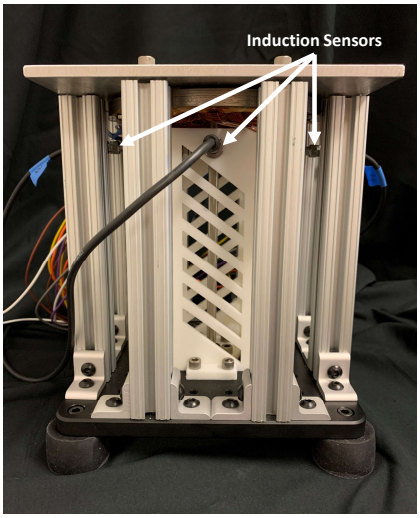

(b)

FIGURE 3. Photographs of motor prototype. (a) Top view showing the stator and rotor. (b) Side view of the structure showing sensors.

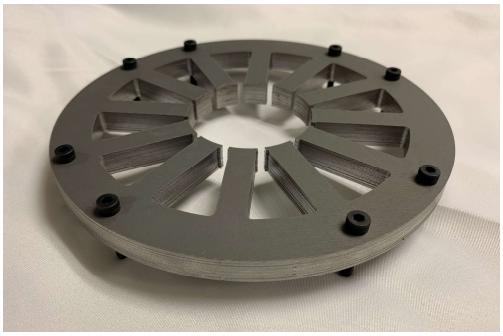

FIGURE 4. Photograph of stator laminations.

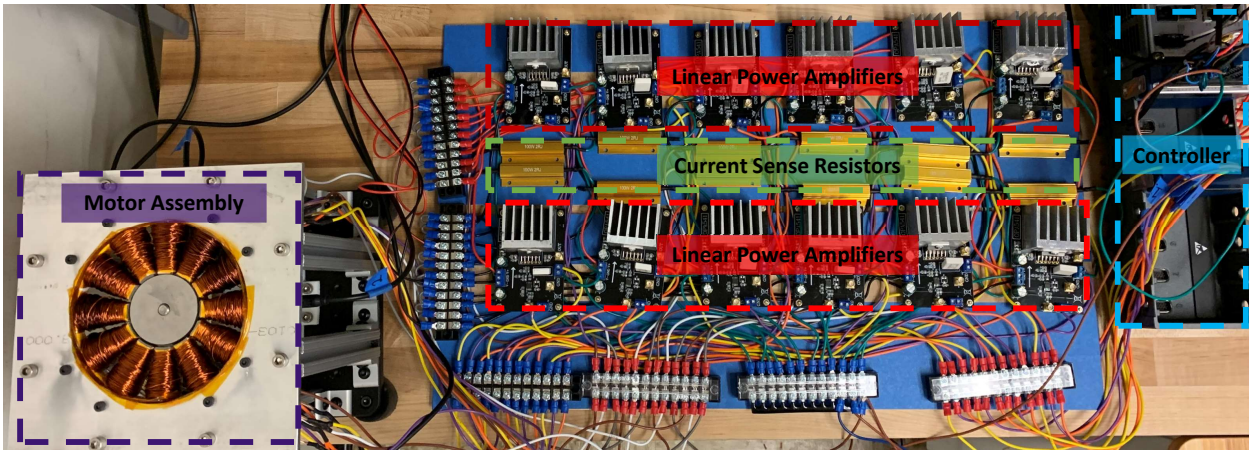

FIGURE 5. Photograph of motor setup. Each coil is individually controlled using NI CompactRIO, and 12 linear power amplifiers amplify the signal sent to the coils.

sensing bearingless motor testbed as shown in Fig. 3 and 5. In this setup, the rotor has a diameter of 49.5 mm and an axial length of 10 mm, and is made of D2 tool steel, which has large magnetic hysteresis and has been used in hysteresis motors as rotor materials [6]. Although hysteresis materials with better torque generation capability exist, in this work, we selected D2 tool steel as the rotor material due to its accessibility. The stator consists of lamination, insulation (Nomex 410 and KPT-1/2, DuPont), and winding coils. Figure 4 shows a photograph of the stator lamination, which is made of 20 layers of M19 steel of 0.5 mm thickness. The stator also uses a deep-slot configuration to allow larger winding volume. The stator coils are fabricated by magnetic wires of AWG22 (Epoxy Bondable MW, MWS). Each of the 12 stator coils is independently controlled and is driven by a linear power amplifier (OPA541, Texas Instruments). The coils are voltage controlled for initial testing, but analog current control will be implemented for future tests. The data acquisition of the sensor signals and realtime control uses NI compactRIO 9048.

Figure 6 shows a block diagram for the control system for the self-sensing bearingless motor. The difference between the voltages across coils 1 and 7, which are aligned with the positive and negative x-axis respectively, is multiplied by the high frequency carrier signal and then averaged using a moving average filter, givings an estimate for the x-directional displacement of the rotor $\hat{x}$. The estimate for the rotor's y-directional displacement $\hat{y}$ is calculated using the same process for the voltages across coils 4 and 10, which are located on the positive and negative y-axis. The estimate for rotor displacement is both compared with the displacements measured by the induction sensors x_{meas} and y_{meas} to give the error of the estimator and fed back for suspension control. The suspension controllers $C_x(s)$ and $C_y(s)$ take the error signals e_x and e_y and output the control efforts u_x and u_y. These control efforts are transformed d- and q-axis control efforts u_d and u_q, and then transformed to 3-phase suspension current commands i_u^*, i_v^*, and i_w^*. The suspension current commands are superimposed with the torque current commands and high frequency sensing signal according to the winding diagram in Fig. 1. These currents are passed to the power amplifiers, which drive the stator coils.

SIMULATION VALIDATION

We have conducted transient-time magnetic finite element simulations for the proposed air gap displacement sensing approach described in Figure 6 using Ansys Maxwell. Fig. 7 shows simulated demodulated voltages of the proposed motor with injecting a sensing current of 0.1 A at 2 kHz. The clear variation of signal with rotor radial displacement demonstrates the feasibility of the proposed approach.

CONCLUSION AND FUTURE WORK

The frictionless operation of bearingless motors makes the use of both the rotary and linear varieties of such machines attractive for a variety

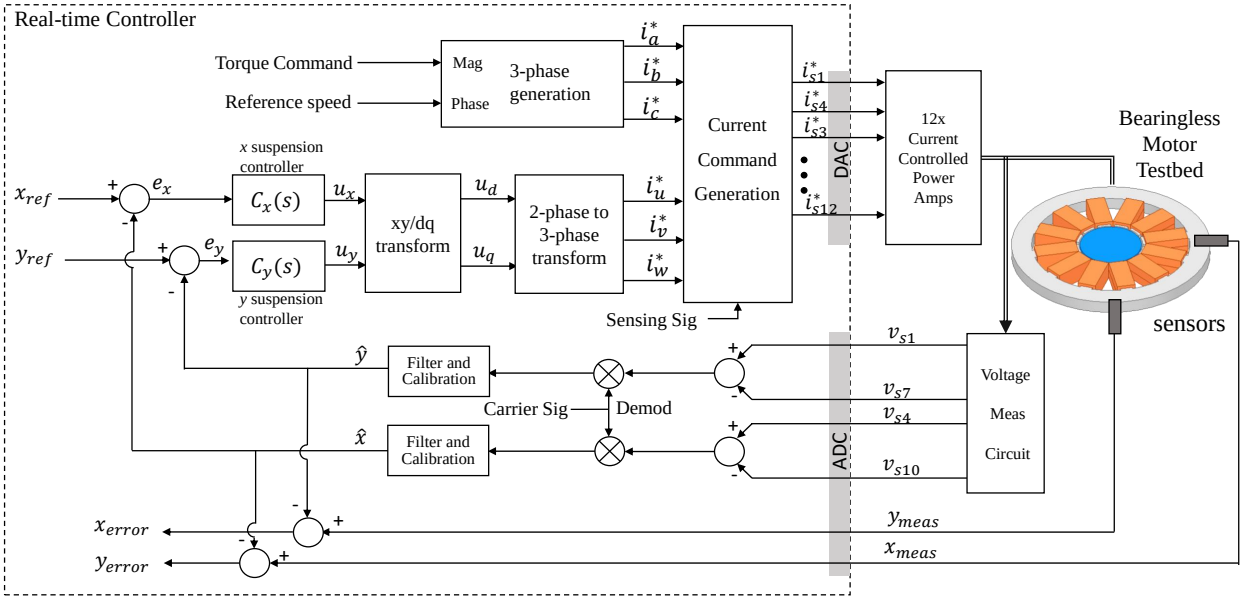

FIGURE 6. Control block diagram.

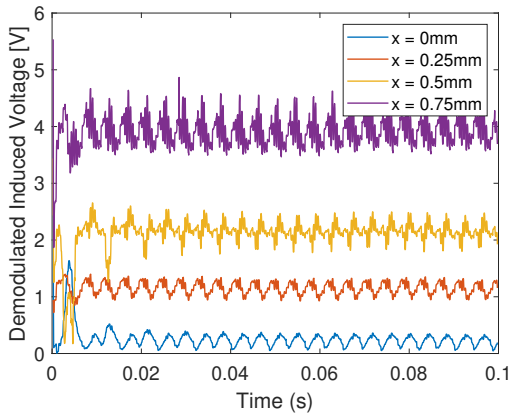

FIGURE 7. Simulated induced voltage results for varied rotor position.

of precision applications. Eliminating the need for position sensors in such systems improves robustness while reducing complexity and cost. Finite element simulation has confirmed the feasibility of estimating the position of the rotor using the voltage induced in the stator coils, amplified by the injection of a high frequency signal. A prototype has been constructed to test this approach.

After implementing and tuning the position estimation for the current setup, there are several opportunities for improving the performance of this motor design. We plan to test and experimentally evaluate different winding configurations and solutions for the systems' power electronics.

REFERENCES

[1] Schoeb R, Barletta N. Principle and application of a bearingless slice motor. JSME International Journal Series C Mechanical Systems, Machine Elements and Manufacturing. 1997;40(4):593–598.

[2] Ooshima M, Takeuchi C. Magnetic suspension performance of a bearingless brushless DC motor for small liquid pumps. IEEE Transactions on Industry Applications. 2010;47(1):72–78.

[3] Puentener P, Schuck M, Steinert D, Nussbaumer T, Kolar JW. A 150 000-r/min bearingless slice motor. IEEE/ASME Transactions on Mechatronics. 2018;23(6):2963–2967.

[4] Chiba A, Deido T, Fukao T, Rahman MA. An analysis of bearingless AC motors. IEEE Transactions on Energy Conversion. 1994;9(1):61–68.

[5] Raggl K, Nussbaumer T, Kolar JW. Comparison of separated and combined winding concepts for bearingless centrifugal pumps. J Power Electron. 2009;9(2):243–258.

[6] Zhou L, Gruber W, Trumper DL. Position Control for Hysteresis Motors: Transient-time Model and Field-oriented Control. IEEE Trans on Ind Appl. 2018;54(4):3197–3207.

TIME-DOMAIN BASED EARLY DETECTION OF CHATTER VIBRATIONS

Kaan Bahtiyar and Burak Sencer
School of Mechanical, Industrial and Manufacturing Engineering
Oregon State University
Corvallis, OR, USA

INTRODUCTION

Most machining processes suffer from unwanted vibrations in the form of forced and self-excited chatter vibrations that deteriorate the manufacturing quality. Once triggered, chatter vibrations may grow to be destructive, which may damage the tooling or the machine components. Therefore, early detection of onset of chatter vibrations and stopping the process or rapidly adapting to correct cutting parameters is up most critical for many machining applications. In particular, rapid detection of chatter in milling has been a long-standing issue [1].

Milling process is an intermitted cutting process, and thus it is prone to both forced and chatter vibrations at the same time. Figure 1 shows milling with a 4 fluted cutter on a flexible setup. Forced vibrations in milling originate due to the repetitive entry and exit (immersion) of rotating cutting edges of the milling tool into the workpiece. As a result, forced vibrations in milling is synchronized with the angular rotation speed of the cutter. The resultant cutting force profile is governed by the shape of the cutting edge, their immersion geometry, spindle's angular speed and structural dynamics of the machine tool. As a result, milling forces are wide spectrum and harmonic [2]. The frequency spectrum is controlled mainly by the spindle speed. In practice, overall force spectrum can be reconstructed accurately by summation several harmonics.

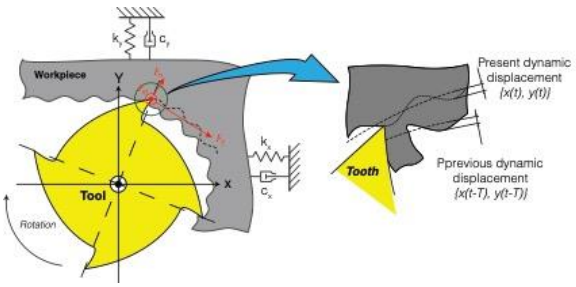

FIGURE 1. Milling kinematics and dynamic chip thickness

Unlike forced vibrations, chatter vibrations in milling are a type of self-excited vibrations that are triggered due to resonances in the machine tool/workpiece structure [3]. Chatter vibrations generally occur close the resonance frequencies of the tooling/workpiece structures, and once triggered they may grow to become destructive. Depending on the spindle speed and machine tool's structural dynamics, chatter vibrations may have a fundamental frequency and various side bands [4]. Figure 2 illustrates overall cutting force frequency spectrum. As shown, forced vibration harmonics are visible at integer multiples of the spindle speed $k\omega_s, k = 1...N$ and chatter frequency and its side bands (harmonics) $\omega_{CH,1}, \omega_{CH,2}, \ldots$ spread along the spectrum. Please also note that Figure 2 shows a frequency spectrum of a machining process that is suffering from chatter vibrations. If the process is stable, it would only exhibit forced vibration components (harmonics) at multiples of the spindle speed and the chatter frequency would not co-exist.

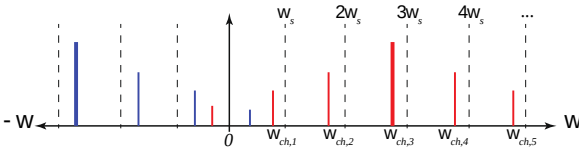

FIGURE 2. Spindle synchronized forced and chatter frequency harmonics.

As observed from Figure 2, one way to detect occurrence of chatter is to test if the frequency spectrum is corrupted with chatter components. Current state of the art typically utilizes frequency domain approaches where Fourier transform of vibration or sound signals recorded on the machine is processed. Since forced vibration occurs at the spindle speed and its harmonics, chatter vibration and its harmonics are sough in-between those frequency bands. Once all the chatter frequency components are detected, chatter energy is computed based on the total signal [5]. Finally, energy ratio between forced

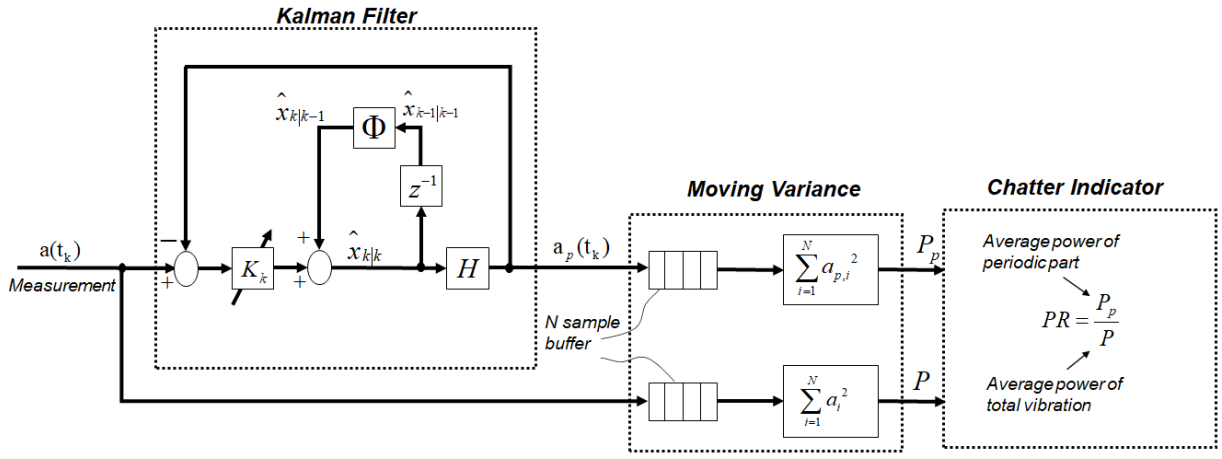

FIGURE 3. Block diagram of proposed chatter detection algorithm

and chatter vibration is considered to decide if chatter is onsetting or not. Typically, once 50% of the total machining energy is consumed by chatter, the process is identified as “chatter-ing”, or “chatter is onsetting”. Although this has become the standard procedure in online chatter detection [6], it has a major drawback. Frequency domain approach detects chatter vibrations only after the vibration has fully grown. This is due to the fact that Fourier analysis is not real-time as it requires a batch of data to accurately analyze power spectrum of vibration signals [4][7]. In particular, chatter may occur at various frequencies, $\omega_{CH,1}, \omega_{CH,2}, \ldots$ and to accurately capture chatter vibration energy, resolution of discrete Fourier transform (DFT) should be kept high. This demands larger batch sizes for DFT, which in return introduces larger delay in detecting the occurrence of chatter vibrations [4]. With such delay, the onset of chatter may be missed.

CHATTER DETECTION ALGORITHM

To address such practical deficiencies of frequency domain approaches, this work proposes a computationally efficient time-domain strategy to detect chatter in a timely manner. Acceleration signals acquired on the spindle housing is used in detecting occurrence of chatter. Figure 3 presents overall proposed chatter detection strategy.

Considering that milling process experiences both forced and chatter vibrations; total machining vibration energy is computed in time-domain based on the signal variance. Next, a Kalman filter is designed to track the forced vibration energy at spindle harmonics adaptively. To determine onset of chatter, the energy ratio approach is used, which evaluates forced vibration energy to the total signal energy. If it drops below a certain ratio, occurrence of chatter is identified. By using such a time-domain based approach accurate and early detection of chatter is achieved.

Variance-based Machining Energy Calculation

As shown in Figure 2, frequency spectrum of a milling process is dominated by both forced and chatter vibration components. The total energy of the process can be evaluated in frequency domain by integrating square of the entire magnitude spectrum by:

$$E(X) = \frac{1}{2\pi}\int_{-\pi}^{\pi} \left| X(e^{j\tilde{\omega}}) \right|^2 d\tilde{\omega} \qquad (1)$$

where $X(e^{j\omega})$ is the discrete time Fourier transform (DTFT) of the signal at a frequency ω. Notice that taking Fourier transform at high resolution along the entire frequency spectrum and evaluating Equation 1 is not viable in real-time.

Parseval’s theorem states that the energy of a signal can be computed by summing energy-per-sample across time [8] as well:

$$\sum_{n=-\infty}^{\infty} \left| x[n] \right|^2 = \frac{1}{2\pi}\int_{-\pi}^{\pi} \left| X(e^{j\tilde{\omega}}) \right|^2 d\tilde{\omega} \qquad (2)$$

The advantage of Equation 2 is that the total energy of a signal can be evaluated in time domain without evaluating its Fourier transform. However, it still requires the entire signal to be

processed all at once, which is still not practical. Instead, Equation 2 is evaluated in a limited window size by

$$\sum_{n=0}^{N-1}\left|x[n]\right|^2=\frac{1}{N}\sum_{k=0}^{N-1}\left|X[k]\right|^2 \tag{3}$$

where $X[k]$ is discrete Fourier transform (DFT) of $x[n]$. Notice that Equation 2 still holds since if energy of a signal is infinite, the signal is called power signal [9] where power (P) is defined as the energy consumed per unit time:

$$P=\lim_{N\to\infty}\left(\frac{1}{N}\sum_{n=0}^{N-1}\left|x[n]\right|^2\right) \tag{4}$$

Variance of a time domain signal presents its cumulative power spectrum [10] or overall energy except the static component as:

$$Var(x)=\frac{1}{N}\sum_{n=0}^{N-1}(x[n]-\mathbb{E}[x])^2 \tag{5}$$

where n is sample counter, N is signal length, and $\mathbb{E}$ is its expected value. As expressed in Equation 4 and 5, it should be noted that the power expression of a signal is similar to that of variance. Particularly variance is calculating the power of a signal by removing its mean. Since the vibration in milling is composed of sinusoidal components, the DC term of the measurement is not taken into account so that unwanted offsets do not affect the detection. Besides, for zero-mean signals, the variance is equal to the signal power. Therefore, it can be used to calculate the power of vibration in milling process measurements (acceleration, sound, current, etc.). To calculate its variance, the signal is buffered for a limited batch size. As the buffer size increases, the computational cost gets higher.

Calculations at each time step can be reduced by evaluating variance in a sliding windowed fashion. This can be interpreted as first in, first out logic. When the window slides one sample, the effect of the removed sample is subtracted from the variance calculation, instead the effect of the new sample is added. For a discrete signal $x[n]$ windowed with length N, the variance calculation becomes as follows:

$$Var(x)=\frac{1}{N}\sum_{i=n}^{n+N-1}(x[i]-\mathbb{E}[x])^2 \tag{6}$$

$$\begin{aligned}Var(x)=&\frac{1}{N}\sum_{i=n}^{n+N-1}x(i)^2\\&-2\frac{1}{N}\sum_{i=n}^{n+N-1}x(i)\mathbb{E}[x]+\frac{1}{N}\sum_{i=n}^{n+N-1}\mathbb{E}[x]^2\end{aligned} \tag{7}$$

$$Var(x)=\mathbb{E}[x^2]-\mathbb{E}[x]^2 \tag{8}$$

This shows that the variance can be calculated by the difference between mean of square and square of mean values of that signal. The expected values from the previous window is kept in the memory. Then, variance of the shifted window can be updated as following:

$$\begin{aligned}Var(x_{cur})=&Var(x_{prev})+\frac{x(n+N+1)^2}{N}\\&-\frac{x(n)^2}{N}-\left(\frac{x(n+N+1)}{N}-\frac{x(n)}{N}\right)^2\end{aligned} \tag{9}$$

where $x(n+N+1)$ is the new sample, $x(n)$ is the removed sample from the buffer, N is the window length.

Kalman Filter-based Forced Vibration Estimation

Previous section presented a time-domain approach to compute total vibration energy in cutting, which contains both stable forced and unstable chatter vibrations. This section focuses on extracting the stable forced vibrations components from the total signal energy.

Cutting forces excite the structure and generate forced vibrations that can be constructed by their harmonics at the spindle speed. A Kaman filter is designed to track amplitude of forced vibration harmonics to evaluate total forced vibration energy. The sampled forced vibration signal can be composed of $n = 1…N$ harmonics of spindle speed ω as:

$$x_f(kT)=\sum_{n=1}^{N}A_n(kT)\cos(n\omega kT+\phi_{f,n}) \tag{10}$$

where A_n is amplitude of each harmonic, with k being the sample counter and T is the sampling time. As proposed in [4], Equation 10 can be postulated in state space form:

$$\begin{bmatrix}q_1\\q_2\\\vdots\\q_{2N}\end{bmatrix}_{k+1}=\begin{bmatrix}\Phi_1&0&\cdots&0\\0&\Phi_2&&0\\\vdots&&\ddots&\vdots\\0&\cdots&&\Phi_N\end{bmatrix}\begin{bmatrix}q_1\\q_2\\\vdots\\q_{2N}\end{bmatrix}_k+\begin{bmatrix}w_1\\w_2\\\vdots\\w_{2N}\end{bmatrix}_k$$

$$y(kT)=\begin{bmatrix}1&0&\ldots&1&0\end{bmatrix}\begin{bmatrix}q_1\\q_2\\\vdots\\q_{2N}\end{bmatrix}_k+v_k \tag{11}$$

where w_k is the process noise, v_k is the observation noise, and Φ_n is the state transition matrix for each harmonics modeled as:

$$\Phi_n = \begin{bmatrix} \cos(n\omega T) & -\sin(n\omega T) \\ \sin(n\omega T) & \cos(n\omega T) \end{bmatrix} \quad (12)$$

with the states chosen as:

$$\left.\begin{aligned} q_{n,k} &= A(kT)\cos(n\omega kT + \phi_n) \\ q_{n+1,k} &= A(kT)\sin(n\omega kT + \phi_n) \end{aligned}\right\} \quad (13)$$

for $n = 1,3,5,..,2N-1$. Notice that the states of Φ_n (Equation (13)) is sought harmonic signal given by in-phase and phase-quadrant form. A conventional Kalman filter can be employed to observe those signals from [11]:

$$\begin{aligned} \hat{q}_{k|k\text{-}1} &= \Phi \hat{q}_{k\text{-}1|k\text{-}1} \\ P_{k|k\text{-}1} &= \Phi P_{k\text{-}1|k\text{-}1}\Phi^T + Q \\ S_k &= HP_{k|k\text{-}1}H^T + R \\ K_k &= P_{k|k-1}H^T S_k^{-1} \\ \tilde{y}_k &= x_k - H\hat{q}_{k|k\text{-}1} \\ \hat{q}_{k|k} &= \hat{q}_{k|k\text{-}1} + K_k\tilde{y}_k \\ P_{k|k} &= I - K_k H \; P_{k|k-1} \end{aligned} \quad (14)$$

where $\hat{q}$ is the state estimate vector, P is the error covariance matrix, K is the adaptive Kalman gain matrix, $\tilde{y}$ is the measurement pre-fit residual, x_k is the measurement, Q and R are diagonal process noise covariance matrix and covariance of the observation noise respectively. Then, the estimated forced vibration part of the measurement can be calculated from

$$\hat{x}_f(kT) = H\hat{q}_k \quad (15)$$

Chatter Indicator

Lastly, power ratio of the total measured vibration signal and the forced vibration component are compared as indicator of chatter onset. Notice that in the proposed approach, total energy of the signal and energy of the forced vibration are calculated separately. Therefore, the power ratio is defined as:

$$PR(n) = \frac{Var(\hat{x}_f)}{Var(x)} \quad (16)$$

where $\hat{x}_f$ denotes the estimated forced vibration part of the measured signal. The variance of those can be calculated as expressed in the Equation 10 to reduce the computational cost of the calculation. The power ratio changes between 0 and 1 with time, where 0 means the process is fully unstable, and it is fully stable at 1. It should be noted that when chatter occurs, both forced and chatter vibrations become apparent at the same time. Therefore, power ratio of *PR = 0.5* is selected as the threshold to detect the chatter. If PR drops below it, it indicates that chatter has occurred.

EXPERIMENTAL VERIFICATION

The proposed algorithm is verified in low immersion milling using an acceleration signal recorded on the spindle housing at a sampling rate of 10 kHz. A 10 mm cutter with 4 flutes is used, and a tapered shape AL6061 workpiece shown in Figure 4 is cut. Spindle speed is set to 6600 rev/min with a radial immersion of 2 mm, and the constant feed rate is set to 0.03 mm/tooth. As shown in Figure 4a, as the tool is fed, due to the tapered shaped of workpiece axial depth of cut increases gradually and chatter onsets midway through the cutting operation. Figure 4b presents the surface finish of the workpiece. Measured acceleration signal and estimated forced vibration part can be seen in Figure 4c which is zoomed in Figure 4d for stable and chatter onset zones. Figure 4e shows the power spectrum of the signals in Figure 4d. It is shown that Kalman filter estimates the periodic component of the measured acceleration signal successfully. As can be seen in Figure 4f, the power ratio drops when chatter onsets. In this experiment, the buffer size is set to 1024 samples, and the parameters of the Kalman filter are *R = 2* and $Q = R \times 10^{-5}$. As shown, the power ratio drops below 50% right when the chatter marks are observed on the part surface. This validates that the proposed algorithm can detect chatter onset timely. Notice that, *PR = 0.5* is an objective parameter. It can be set slightly lower to detect chatter even faster.

CONCLUSION

This paper presented a computationally efficient chatter detection algorithm for milling process. The forced vibration part in milling process is modeled as the sum of periodic components, and it is estimated by a Kalman filter specifically modeled to track a sinusoidal signal with known frequency. The signal power is computed using moving variance approach, which allows computationally real-time implementation. Chatter is detected by monitoring the power ratio.

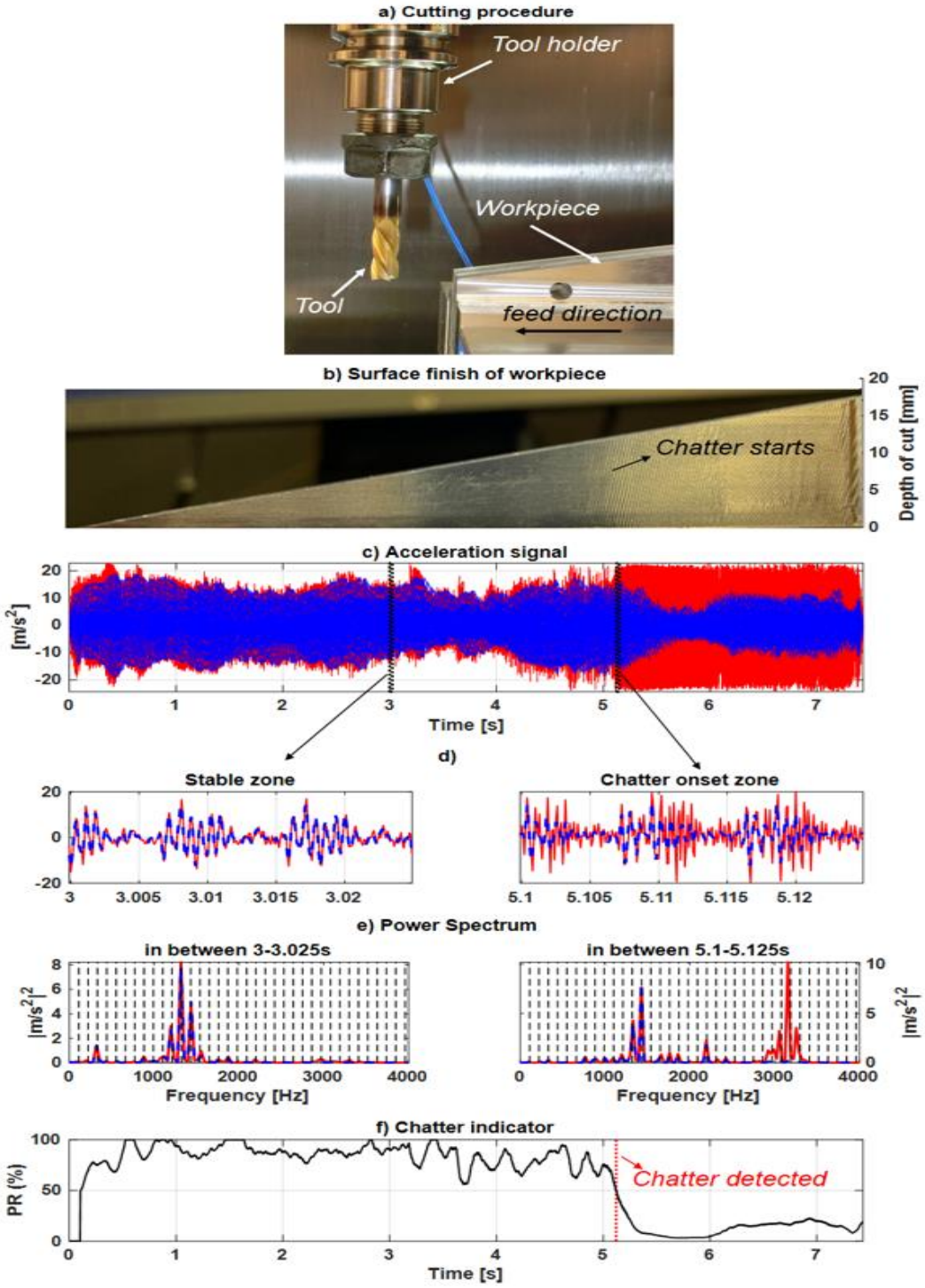

FIGURE 4. Experimental validation of the proposed algorithm. Solid red lines show measurement while dashed lines indicate estimated periodic part of the vibration.

The method has been applied on acceleration data, and results show that chatter is detected successfully.

REFERENCES

[1] Chen D, Zhang X, Zhao H, Ding H. Development of a novel online chatter monitoring system for flexible milling process. Mechanical

Systems and Signal Processing. 2021 Oct 1;159:107799.
[2] Altintas Y. Manufacturing automation: metal cutting mechanics, machine tool vibrations, and CNC design. 2nd ed. Cambridge: Cambridge University Press; 2012.
[3] Altintas Y, Budak E. Analytical prediction of stability lobes in milling. CIRP annals. 1995 Jan 1;44(1):357-62.
[4] Caliskan H, Kilic ZM, Altintas Y. On-line energy-based milling chatter detection. Journal of Manufacturing Science and Engineering. 2018 Nov 1; 140(11):111012.
[5] Al-Regib E, Ni J. Chatter detection in machining using nonlinear energy operator. Journal of dynamic systems, measurement, and control. 2010 May 1;132(3).
[6] Tran MQ, Liu MK. Chatter Identification in End Milling Process Based on Cutting Force Signal Processing. InIOP Conference Series: Materials Science and Engineering 2019 Oct 1 (Vol. 654, No. 1, p. 012001). IOP Publishing.
[7] Ma L, Melkote SN, Castle JB. A model-based computationally efficient method for on-line detection of chatter in milling. Journal of manufacturing science and engineering. 2013 Jun 1;135(3).
[8] Oppenheim AV. Discrete-time signal processing. Pearson Education India; 1999.
[9] Grami A. Introduction to digital communications. Academic Press; 2015 Feb 25.
[10] Koike R. Realtime monitoring and stability diagnosis of cutting process by applying disturbance observer [dissertation]. Tokyo. Keio University; 2016.
[11] Brown RG, Hwang PY. Introduction to random signals and applied Kalman filtering: with Matlab. 4th ed. Hoboken: Wiley; 2012.

VOLUMETRIC TWO-PHOTON POLYMERIZATION BASED ON COMPUTER-GENERATED HOLOGRAMS

Zhiqiang Fu[1], Kexuan Liu[3], Yintao Wang[1,2], Liangcai Cao[3*] and Shih-Chi Chen[1,2*]
[1] Department of Mechanical and Automation Engineering
The Chinese University of Hong Kong
Shatin, N.T., Hong Kong SAR, China
[2] Centre for Perceptual and Interactive Intelligence (CPII) Ltd, Hong Kong Science Park, N.T., Hong Kong SAR, China
[3] State Key Laboratory of Precision Measurement Technology and Instruments, Department of Precision Instruments,
Tsinghua University,
Beijing, China
[*]Email: scchen@mae.cuhk.edu.hk; clc@tsinghua.edu.cn

In this paper, we present a fast 3D printing method based on a 3D holographically shaped femtosecond laser amplifier and two-photon polymerization (TPP), where a liquid crystal-based spatial light modulator (LC-SLM) is used to encode and project the computer-generated holograms (CGHs) of the designed 3D objects. As such, complex 3D structures, e.g., woodpiles, can be fabricated via a single exposure without scanning achieving submicron-level resolution. Notably, the typical speckle issues in CGH are suppressed by sequentially displaying nine CGHs on the LC-SLM with different initial random phases. Mathematical models have been derived; fabrication experiments have been performed to verify the predicted performance. The new method will address the low fabrication rate issue in previously reported TPP systems.

PRINCIPLE OF CGH

CGHs have been widely implemented and used for the 3D holographic display. With the development of LC-SLMs, various 3D structures can be encoded as phase-only CGHs from different algorithms. Presently, most CGH generation algorithms are physically based algorithms, such as point-based algorithm or polygon-based algorithm [1]. In these methods, complex 3D structures are first decomposed into point or polygon clouds; next, an optical transmission model is applied to generate the hologram to be displayed on an LC-SLM. However, the calculation for a large point or polygon cloud requires extremely high computation power. To address this issue, we have proposed an angular-spectrum layer-oriented algorithm [2]. As shown in Fig. 1, the angular-spectrum algorithm slices a complex 3D structure along the depth direction (i.e., z-axis) and the angular spectra from each slice L_i are superposed as a sub-hologram H_i based on fast Fourier transform (FFT), which effectively reduces the computation time and cost. Specifically, the transfer function of the angular spectrum can be expressed as:

$$H_F(u,v,z) = \exp[jkz\sqrt{1-\lambda^2u^2-\lambda^2v^2}] \quad (1)$$

where u and v represent the spatial frequencies; k and z represent the wave number and the transmission distance respectively. The i^{th} sub-hologram H_i, which is related to the i^{th} slice, can be calculated as:

$$H_i = F^{-1}(H_F \cdot F(L_i)) \quad (2)$$

$$L_i = A_i\exp[j\phi_i(x,y)] \quad (3)$$

where F and F^{-1} represent FFT and inverse FFT respectively; A_i and ϕ_i represent amplitude and random phase of the i^{th} slice respectively. Lastly, the final hologram is the phase information extracted from the sum of the sub-holograms from all sliced layers.

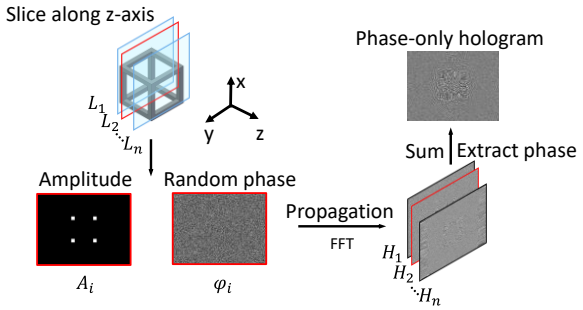

FIGURE 1. Schematic diagram of the angular-spectrum based layer-oriented algorithm [2].

CGH-BASED VOLUMETRIC TPP SYSTEM

TPP is known as the most precise additive manufacturing technique for fabricating complex 3D objects at submicron-level precision, where a femtosecond laser is focused in photoresists to induce a highly localized nonlinear absorption process for photopolymerization at the focal region. 3D structures are typically fabricated by raster-scanning the laser focus [3]; to improve throughput, new laser scanning methods have been developed, such as multi-focus parallel writing shaping [4], or layer-by-layer fabrication via programmable light sheets [5, 6].

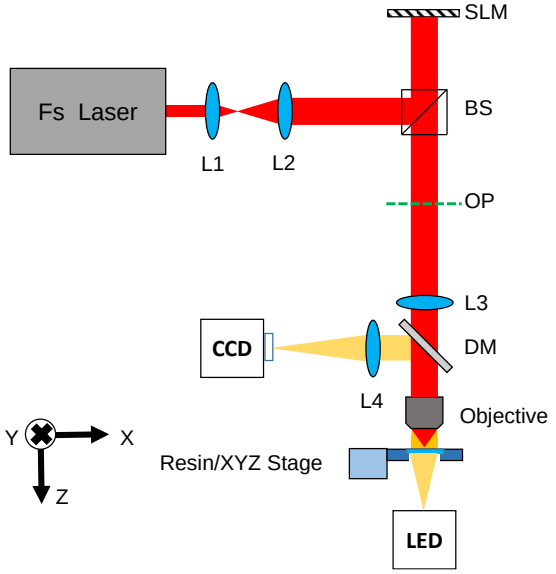

FIGURE 2. Optical configuration of the CGH-based TPP fabrication system. BS: beam splitter; DM: dichroic mirror; OP: object plane; L1 – L4, lenses (f_{L1}, f_{L2}, f_{L3}, f_{L4} = 50, 150, 400 and 200 mm, respectively).

To further improve the fabrication rate, we present a CGH-based volumetric TPP system, where arbitrary 3D structures can be printed with a single exposure. Figure 2 presents the optical configuration of CGH-based TPP system. The light source is a Ti: sapphire regenerative laser amplifier (Spitfire Pro, Spectra-physics Inc.) with a repetition rate of 1 kHz and an average power of 4.0 W. First, the laser beam is expanded via a 4-f system, i.e., L1 and L2, to fully fill the aperture of the LC-SLM (LCOS-X10468-2, Hamamatsu), which displays a CGH that encodes the designed 3D structure based on the angular spectrum algorithm. To suppress the unwanted laser interference and speckles, nine CGHs are sequentially displayed on the LC-SLM with randomly selected initial phases. The modulated laser beam then generates the designed 3D optical field in the object plane (OP). Lastly, the 3D optical field is relayed to the write field via a 4-f system, i.e., L3 and objective lens (Nikon CFI S Fluor 40× Oil). The resin used in the fabrication experiments is IP-Dip (Nanoscribe GmbH). An epi-illumination light source is coupled into the system for sample illumination; the CCD camera after the dichroic mirror (DM) monitors/records the fabrication process in situ.

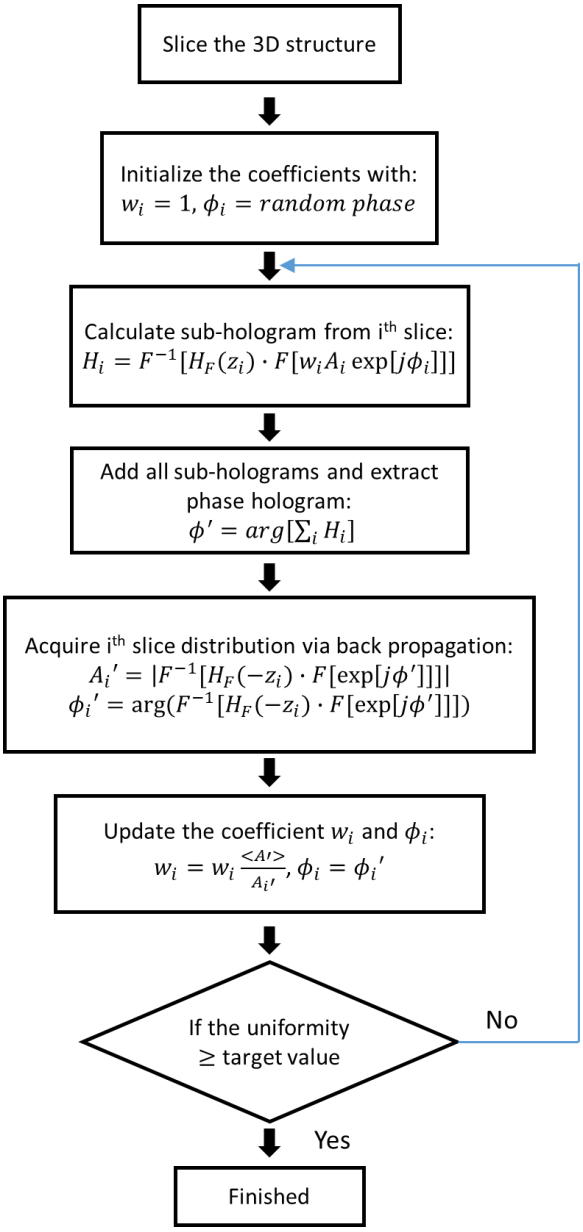
Slice the 3D structure
Initialize the coefficients with:
$w_i = 1, \phi_i = random\ phase$
Calculate sub-hologram from ith slice:
$H_i = F^{-1}[H_F(z_i) \cdot F[w_i A_i \exp[j\phi_i]]]$
Add all sub-holograms and extract phase hologram:
$\phi' = arg[\sum_i H_i]$
Acquire ith slice distribution via back propagation:
$A_i' = |F^{-1}[H_F(-z_i) \cdot F[\exp[j\phi']]]|$
$\phi_i' = \arg(F^{-1}[H_F(-z_i) \cdot F[\exp[j\phi']]])$
Update the coefficient w_i and ϕ_i:
$w_i = w_i \frac{<A_i'>}{A_i'}, \phi_i = \phi_i'$
If the uniformity ≥ target value
No
Yes
Finished

FIGURE 3. Flow chart of the WGS method applied to the angular-spectrum layer-oriented algorithm.

PHASE-ONLY HOLOGRAM

In the previous section, we have introduced the principle of angular-spectrum layer-oriented algorithm [2]. For volumetric printing, we further adopt the weighted Gerchberg-Saxton algorithm (WGS) [7] to ensure that the generated 3D holographic volume has a uniform intensity distribution. Figure 3 presents a flow chart of implementing the WGS algorithm to the angular-spectrum layer-oriented algorithm. Specifically, a coefficient w_i is introduced to the phase equation for adjusting the weight of the i^{th} slice. In the first round, the phase hologram ϕ' is calculated by extracting the results from the angular-spectrum method. A back-propagation method is applied to obtain the intensity distribution, i.e., amplitude A_i' and phase ϕ_i' at different slices (i.e., z_i). Next, the intensity weight w_i and initial phase ϕ_i are updated. In each iteration, the coefficients w_i and ϕ_i are optimized to reduce the deviations of intensity distribution. The loop repeats until the uniformity reaches the target value. With the advantage of FFT process in the angular-spectrum-based method, the total iteration time is greatly decreased, i.e., 5 seconds for 15 iterations.

To verify the effectiveness of CGH-based angular-spectrum method for projecting a 3D intensity field, we first perform simulated experiments with different intensity distribution at different depths. The results are presented in Fig. 4. Figures 4A and 4B present the reconstructed intensity distribution at a distance of 300 mm and 500 mm from the SLM aperture, respectively; Figures 4C and 4D present the ground truth of the pattern. In the simulation, the iteration number is set to 5. From the results in Fig. 4, one can clearly observe that the reconstructed patterns at different depths achieve a highly uniform intensity distribution, which meets the requirements for TPP fabrication.

FABRICATION RESULTS

We have devised and performed fabrication experiments via the CGH-based volumetric TPP system. First, we fabricate a free-standing nanowire structure via a single exposure (exposure time = 100 ms; laser power = 40 mW) to experimentally determine the resolution of the system. The results are presented in Fig. 5. By observing the top (Fig. 5A) and isometric views (Fig. 5B) of the nanowire SEM images, we find the minimum width and height of the printed nanowire to be 0.80 and 1.75 μm respectively. Notably, in Fig. 5 one can observe the negative effects of speckles as random spikes or thorns producing from the nanowire.

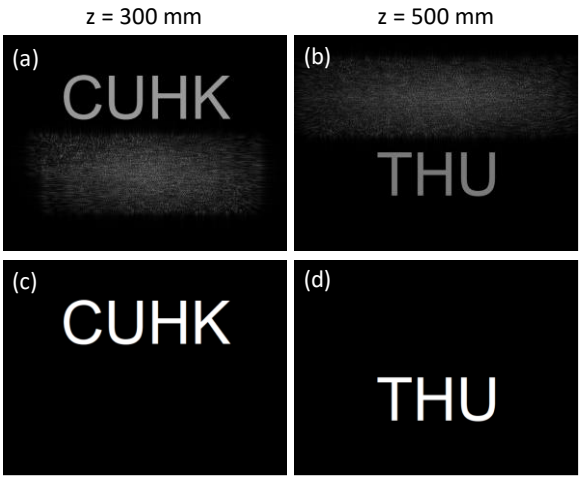

FIGURE 4. Simulated intensity distribution based on WGS-based angular-spectrum method. A and B. Intensity distribution at z = 300 and 500 mm, respectively. C and D. Designed ground truth at z = 300 and 500 mm, respectively.

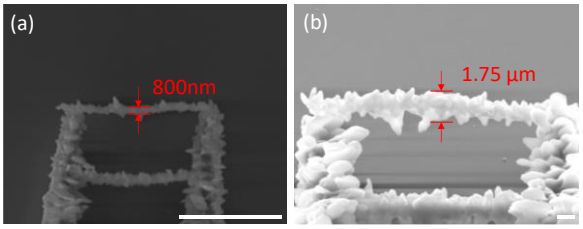

FIGURE 5. Printed nanowires demonstrating the lateral and axial resolution of the CGH-based TPP system. A and B. SEM images of the suspended nanowire feature. Scale bar: 10 μm and 1 μm in A and B respectively.

In order to demonstrate capability of printing arbitrary 3D structures and suppress the speckle effect, we next fabricate a 3D tripod structure (size ≈ 40 × 40 × 40 μm^3) with a single exposure (exposure time = 150 ms; laser power = 35 mW); and during the fabrication, nine holograms which are generated with different initial random phases are sequentially applied to the LC-SLM in order to average out the laser interference and speckles. The results are presented in Fig. 6, where one may find that the speckle effect has been moderately suppressed. The total fabrication time for the tripod structure is 200 ms, which is substantially faster than the conventional point-scanning or layer-by-layer fabrication systems.

With the 40× objective lens, the work volume of the CGH-based TPP system is calculated to be

50 × 50 × 40 μm^3 for single exposure fabrication. To perform large-area 3D fabrication, a precision XYZ stage is employed to maneuver the sample holder for 3D stitching. Figure 7A and 7B present the top and isometric views of a printed two-layer woodpiles structure, which serves as a repeating building block for constructing large-scale 3D structures. Figure 7C and 7D present three different large-area structures consisting of the woodpile building blocks. The fabrication time (i.e., exposure time) for each building block is 150 ms (laser power = 50 mW); and the total fabrication time for the large-scale structures is 3 - 5 seconds. From the SEM image, one may confirm again that the structures achieve submicron-level resolution.

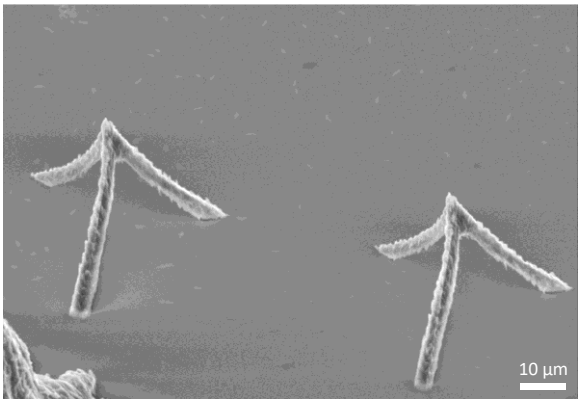

FIGURE 6. Printed 3D tripod structure array by sequentially displaying nine holograms on the LC-SLM. Scale bar = 10 μm.

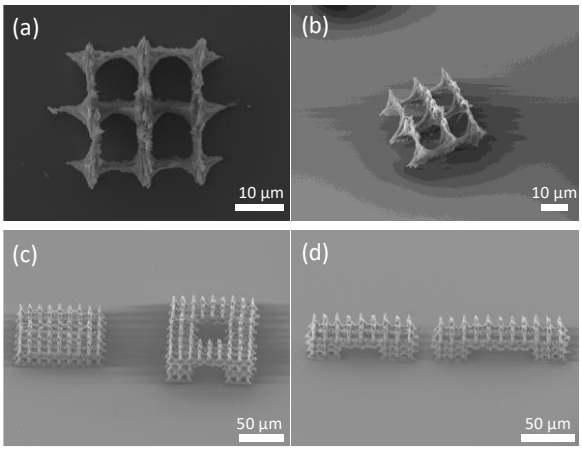

FIGURE 7. Printed 3D woodpile structure: A and B. Two-layer woodpile structure as a repeating unit; C and D. Large-area 3D structure fabricated by stitching the unit cell. Scale bar: 10 μm in A and B; 50 μm in C and D.

CONCLUSION

We have presented a new CGH-based volumetric TPP fabrication system that effectively applies CGH to realize high-throughput TPP fabrication. Specifically, WGS algorithm is applied to ensure that the projected 3D structure has a highly uniform intensity distribution. During fabrication, multiple holograms are averaged to suppress the laser interfence and speckle effects. The experimental results show that the lateral and axial resolution of the CGH-based TPP fabrication system are 0.8 and 1.75 μm respectively. Fabrication of complex 3D structures, including a 3D tripod and two-layer woodpile structure, have been demonstrated with single exposure. Lastly, large-scale structures with submicron resolution have been fabricated by stitching within a few seconds' time. The volumetric TPP fabrication system shows greatly enhanced fabrication rate, which may find important applications in the fields of nanotechnology and photonics.

ACKNOWLEDGMENT

This work partially supported by the Centre for Perceptual and Interactive Intelligence (CPII) Ltd under the Innovation and Technology Fund; HKSAR Research Grants Council (RGC), General Research Fund (GRF), 14203020; National Nature Science Foundation of China (NSFC), 61775117.

REFERENCES

[1] Zhao Y, Cao L. Zhang H, and He Q. Holographic Display with LED Illumination based on Phase Only Spatial Light Modulator. Proc. SPIE. 2012; 8559, 85590B.

[2] Zhao Y, Cao L, Zhang H, Kong D, and Jin G. Accurate Calculation of Computer-generated Holograms using Angular-spectrum Layer-oriented Method. Optics Express. 2015; 23(20): 25440-25449.

[3] Farsari M, and Chichkov BN. Two-photon Fabrication. Nature Photonics. 2009; 3(8): 450-452.

[4] Manousidaki M, Papazoglou DG, Farsari M, and Tzortzakis S. 3D Holographic Light Shaping for Advanced Multiphoton Polymerization. Optics Letters. 2020; 45(1): 85-88.

[5] Saha SK, Wang D, Nguyen VH, Chang Y, Oakdale JS, and Chen S. Scalable Submicrometer Additive Manufacturing. Science. 2019; 366(6461): 105-109.

[6] Yang D, Liu L, Gong Q, and Li Y. Rapid Two-photon Polymerization of an Arbitrary 3D

Microstructure with 3D Focal Field Engineering. Macromolecular Rapid Communications. 2019; 40(8): 1900041.
[7] Stuart D, Barter O, Kuhn A. Fast Algorithms for Generating Binary Holograms. arXiv preprint arXiv. 2014; 1409.1841.

PARALLEL 3D NANOFABRICATION USING 1000 PROGRAMABLE LASER FOCI

Wenqi Ouyang[1], Fei Han[1,2], and Shih-Chi Chen[1,2*]
[1]Department of Mechanical and Automation Engineering
The Chinese University of Hong Kong,
Shatin, N.T., Hong Kong
[2]Oxford-CityU Centre for Cerebro-Cardiovascular Health Engineering (CoCHE),
Hong Kong Science Park, N.T., Hong Kong SAR, China
[*]Email: scchen@mae.cuhk.edu.hk

In this paper, we present a multi-focus 3D printing solution based on the digital micromirror device (DMD) two-photon polymerization (TPP) fabrication system. By combining a femtosecond regenerative laser amplifier with the DMD scanner, up to 1000 laser foci can be simultaneously generated for parallel nano-fabrication. Note that the amplitude, phase, and position of each laser focus can be individually controlled for random-access scanning, allowing advanced trajectory planning for structural optimization. Complex 3D structures and functional micro-devices have been printed to demonstrate the resolution and quality of the system at a printing speed of 10^5 - 10^6 voxels/sec. Importantly, we find that the photopolymerization mechanism from the ultrahigh energy laser pulses are different from the typical two-photon absorption process, where improved fabrication results can be achieved by using a combination of less laser pulses and higher laser energy.

INTRODUCTION

Two-photon lithography, as one of the most promising high-resolution additive manufacturing methods, has been used to create complex 3D nano-/micro-structures for applications in photonics and micro-robotics etc. Conventionally, 3D structures are printed by serially scanning the laser focus in liquid photoresins, which limit the fabrication rate to ~0.1 mm^3/hour when performing high-resolution writing, i.e., ~150 nm. The low writing speed also constrains the use of two-photon lithography for fabricating large-scale structures or devices. To improve the throughput, various multi-focus scanning methods that split a laser beam into multiple foci for parallel printing have been developed. For example, multi-beam diffraction [1], micro-lens array [2] and diffractive optical element (DOE) [3] have been applied to perform multi-focus printing; however, these approaches can only effectively write periodic structures. To dynamically control each laser focus, liquid crystal-based spatial light modulators [4] have been adopted with a limited scanning speed, i.e., 100 Hz. Recently, our team developed a DMD-based TPP fabrication system based on binary holography, demonstrating fast parallel writing at 22.7 kHz using four laser foci [5]

In this work, we further increase the number of laser foci to 1000 with high resolution. This is achieved by combining our multi-focus TPP system, which now uses a regenerative femtosecond laser amplifier as the light source, with custom-designed photoresist. The improved fabrication rate will make TPP a useful tool for various applications, such as cell culture [6], drug delivery [7] and precision optics [8].

OPTICAL DESIGN

Figure 1 presents the optical configuration of the DMD TPP fabrication system, where the light source is a regenerative laser amplifier (Spitfire, Spectra-Physics; average power: 4 W; pulse width: 100 fs; repetition rate: 1 kHz). First, a half wave plate and a polarizing beam splitter are used to control the laser power. Next, a grating and a 4-f system (i.e., L1 and L2) are introduced to pre-compensate the angular dispersion from the DMD (DLP 6500, 1920 × 1080 pixels, Texas Instrument). Next, a filter spatially selects the -1st beam, which contains the designed scanning wavefront information in the binary hologram, which is optimized by the weighted Gerchberg-Saxton algorithm for enhanced multi-focus intensity control. Lastly, the generated foci are relayed to the focal region for fast 3D fabrication using up to 1000 laser foci, i.e., printing at 10^6 voxels/s. To monitor the fabrication process in situ, a backlighting microscope system is developed and integrated with the sample positioner (H-811.I2 6-Axis Miniature Hexapod, Physik Instrumente), which allows for fine

position control. An oil immersion objective (CFI S Fluor 40×, NA = 1.3, Nikon), which matches the refractive index of the custom-developed photoresin, is used for the fabrication experiments. The system work volume is calculated to be 310 × 560 × 150 μm^3 in x, y and z directions based on the 40× objective lens.

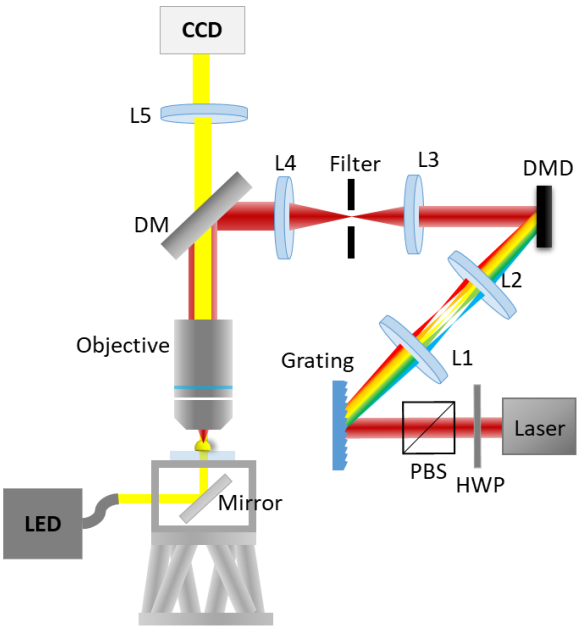

FIGURE 1. Optical configuration of the DMD-based TPP fabrication system. HWP: half-wave plate; PBS: polarizing beam splitter; DM: dichroic mirror; L1–L5: lenses (f_{L1}, f_{L2}, f_{L3}, f_{L4}, f_{L5} = 225, 250, 150, 200,100 mm, respectively).

DEVELOPMENT OF PHOTORESIN

As each laser pulse from the amplifier contains extremely high pulse energy (2 - 10 nJ for single-exposure, which is three orders of magnitude larger than typical TPP process), commercial photoresins, which typically have high writing thresholds and small dynamic ranges, are not suitable for this system. Previous studies on reaction mechanisms between extremely high energy pulses and photoresist indicate that under high irradiance (i.e. 10 - 100 TW/cm^2) the ionization rate is dominated by the effect of direct multi-photon ionization, followed by avalanche multiplication [9,10].

To this end, we have custom-developed an acrylate-based photoresin, which consists of PETA (35% wt.), BPADA (65% wt.), and CAS 55035-43-4 (0.2% wt.), with significantly lowered polymerization threshold, i.e., 1.35 nJ, such that a single laser pulse can induce photo-polymerization, making it suitable for high-resolution and high-speed writing. In other words, in our system better printing resolution is realized with less laser pulses; and the finest features are written with single exposures, as demonstrated in Fig. 2A and 2B, where the lateral and axial resolutions are measured to be 90 nm and 141 nm respectively with a voxel aspect ratio of 1.57. This counter-intuitive result substantially improves the fabrication rate, i.e., fabrication rate (voxels/sec) = laser repetition rate (1000 Hz) × number of foci. When 1000 laser foci are used for parallel writing, the fabricate rate is 10^6 voxels/s or 5 mm^3/hour.

To improve the functionality of the printed devices, we have further prepared a magnetic photoresin by mixing magnetic nanoparticles in this photoresin for micro-robotic applications.

FABRICATION EXPERIMENTS

Multi-focus parallel fabrication was performed via the DMD-TPP system and the custom-developed photoresist. Figure 2C - 2E present a large-scale 3D mechanical metastructure (0.3 × 0.3 × 0.5 mm^3) fabricated via 100 laser foci at a printing speed of 10^5 voxels/sec. The total print time is ~20 min. From the result, one may observe that the metastructure is highly uniform with a minimum feature size of 90 nm, indicating good intensity distribution among the laser foci over the entire DMD work field as well as the effectiveness of the weighted Gerchberg-Saxton algorithm. Figure 2F presents a 1-mm^3 cube with the same metastructure, written with 100 laser foci. Next, we applied a load of 0.3 N to the metastructure via a plastic tip and compressed the structure for 0.4 mm. Upon unloading, one may find the metastructure is fully restored, demonstrating the super-elasticity nature of metastructures. The modulus of the metastructure is measured to be 7.5 × 10^5 Pa.

To investigate the relationship between feature resolution and the number of foci for parallel writing, we printed octahedron trusses using 64, 100, 400 and 1024 laser foci, the SEM results are presented in Fig. 3A - 3D respectively. From the results, we can conclude that the feature resolution will not be compromised when less than 100 laser foci are used; the resolution will be slightly compromised with increasing laser foci when more than 100 foci are used due to the limited DMD pixels. This finding is consistent with our previous study on binary masks [11]. From Fig. 3D, we can observe submicron feature

resolution and high structural uniformity is still achieved with 1000 laser foci. Figure 3E and 3F present different TPP printed structures using 1000 laser foci, including a hydrophobic eggbeater array and annular wood-pile, demonstrating the high-resolution 3D random-access writing capability of our system.

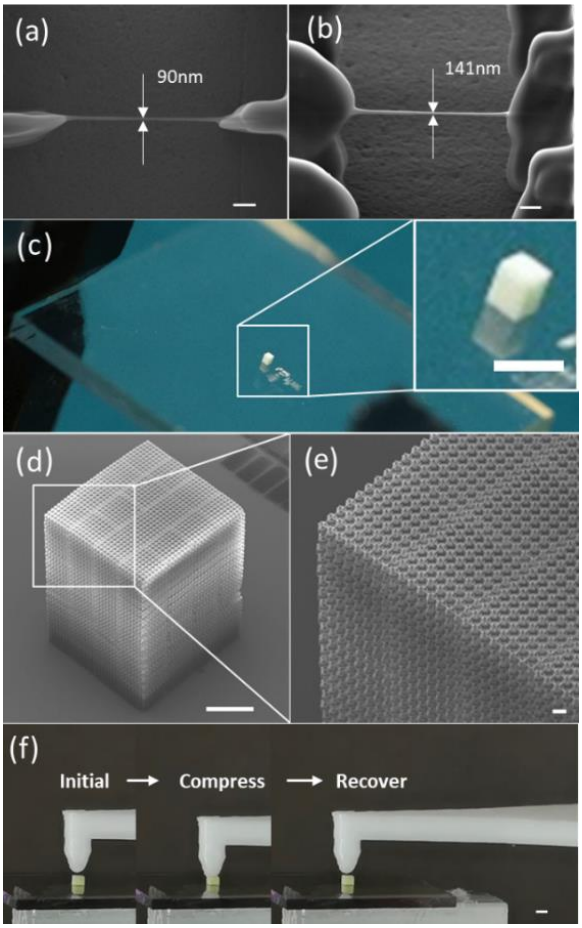

FIGURE 2. A. and B. Width and height of a printed nanowire measured from the SEM images; scale bars = 1 μm; C-E. Optical Image and SEM images of 3D metamaterial structure printed via 100 laser foci; scale bars = 0.5 mm, 100 μm and 10 μm respectively. F. Process of loading and recovering of the metamaterial structure; scale bar = 1mm.

It is worth to note that in the multi-focus writing process, the minimum distance between any two laser foci should be larger than 3 μm to avoid proximity effect and ensure best writing results can be achieved. On the other hand, a common issue for multi-focus writing is the accumulation of laser doses due to the projected laser foci, causing unwanted photopolymerization in the center of the work field. This can easily occur when writing with more than 100 laser foci and high exposure energy. We address this issue by staying below the threshold total light intensity as well as to generate highly uniform laser foci via the weighted Gerchberg-Saxton algorithm.

Comparing with other parallel fabrication methods, our DMD TPP system has unique advantages in speed especially when printing porous structures and structures with low duty cycles owing to the random-access scanning capability. Although the DMD holographic scanner has relatively low power efficiency (~5%), it is overcome by the 4W laser amplifier and the highly efficient photoresist. In the experiments, the required laser power for 1000 foci is 200 mW.

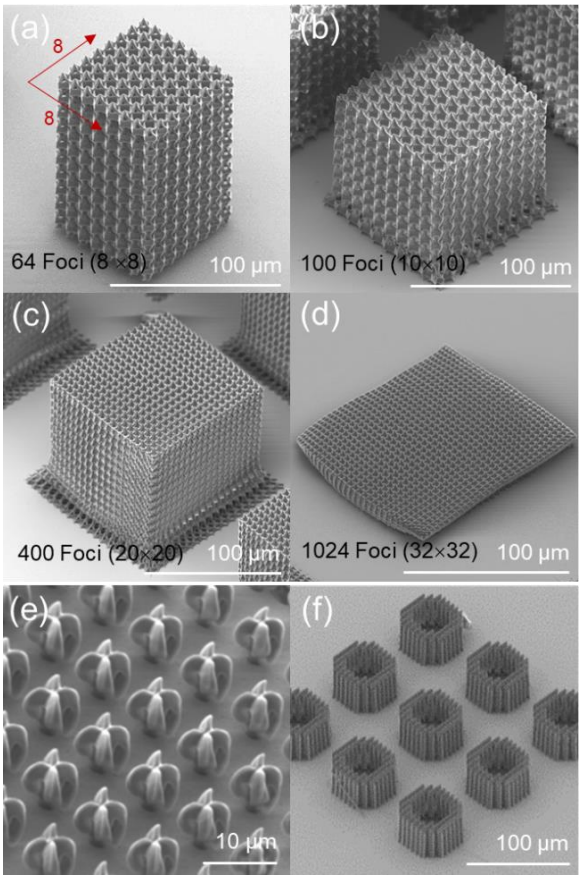

FIGURE 3. A- D. SEM images of metamaterial printed via 64, 100, 400 and 1024 laser foci respectively. E. and F. Optical Image and SEM image of micro-dot array. G. and H. SEM images of microstructrure.

Lastly, we demonstrate the fabrication of functional devices using the DMD TPP system.

As discussed before, the custom-developed magnetic photoresist, prepared by adding 3% weight of Fe_3O_4 powder, was applied for multi-focus TPP fabrication. Figure 4 presents the printed gear-shaped magnetic micro-robot using 100 laser foci; and one hundred micro-robots were printed via the parallel printing process within 1 minute. It is worth to note that the magnetic particles in the photoresins can substantially increase the laser writing threshold (e.g., 8 - 10 times) due to the scattering of light, which is a common drawback of such composite photoresins; while our system can effectively avoid such problem by exploiting the low polymerization threshold nature of our photoresin as well as the ultrahigh energy laser pulses. To control and manipulate the micro-robot, a custom-built magnetic coil array with a 10 mT magnetic field has been developed to realize multi-axis motion control. Specifically, we have demonstrated moving the micro-robot along a straight line, rotating the robot clockwise at a frequency of 5 Hz (Fig. 4B), and flipping the robot at 1 Hz (Fig. 4C).

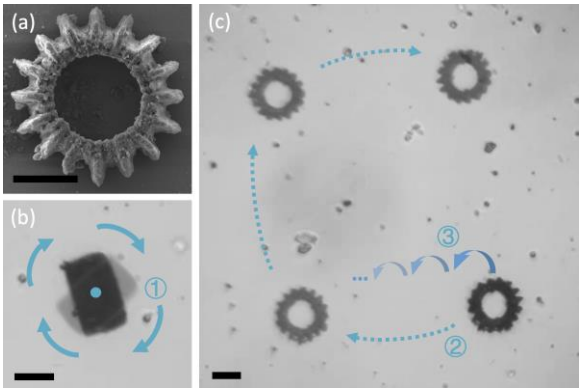

FIGURE 4. Fabrication and manipulation of gear-shaped micro-robots. A. SEM image of the TPP printed micro-robot; B. & C. Demonstration 3D motion control via the magnetic coil array. Scale bars = 20 μm.

CONCLUSION

We have presented a high-speed TPP fabrication solution using up to 1000 laser foci for parallel writing. This is achieved by combining the DMD holographic scanner, regenerative femtosecond laser amplifier, and the custom-designed photoresist. The photoresist includes custom-designed photo-initiators to achieve low polymerization threshold, high dynamic range, and high printing resolution, and is thus suitable for unique laser system with 1 kHz repetition rate. In the experiment, we demonstrated high resolution nano-printing (90 nm) via single-shot exposures, i.e., the voxel is polymerized by a single laser pulse at 1 kHz, which allows a maximum writing speed of 10^6 voxels/sec or 5 mm^3/hour. Various 3D micro-structures have been fabricated to verify the performance of the DMD TPP system, which may generate great impact in fields of nanotechnology, biotechnology, and photonics etc.

ACKNOWLEDGMENT

This work partially supported by the Oxford-CityU Centre for Cerebro-Cardiovascular Health Engineering (CoCHE) under the Innovation and Technology Fund; HKSAR Research Grants Council (RGC), General Research Fund (GRF), 14203020.

REFERENCES

[1] Dong XZ, Zhao ZS, Duan XM. Micronanofabrication of Assembled Three-dimensional Microstructures by Designable Multiple Beams Multiphoton Processing. Applied Physics Letters. 2007; 91(12): 124103.

[2] Kato JI, Takeyasu N, Adachi Y, Sun HB, Kawata S. Multiple-spot Parallel Processing for Laser Micronanofabrication. Applied Physics Letters. 2005; 86(4):044102.

[3] Hahn V, Kiefer P, Frenzel T, Qu J, Blasco E, Barner‐Kowollik C, Wegener M. Rapid Assembly of Small Materials Building Blocks (Voxels) into Large Functional 3D Metamaterials. Advanced Functional Materials. 2020; (26):1907795.

[4] Vizsnyiczai G, Kelemen L, Ormos P. Holographic Multi-focus 3D Two-photon Polymerization with Real-time Calculated Holograms. Optics Express. 2014; 22(20):24217-23.

[5] Geng Q, Wang D, Chen P, Chen SC. Ultrafast Multi-focus 3-D Nano-fabrication based on Two-photon Polymerization. Nature Communications. 2019; 10(1):1-7.

[6] Zandrini T, Shan O, Parodi V, Cerullo G, Raimondi MT, Osellame R. Multi-foci Laser Microfabrication of 3D Polymeric Scaffolds for Stem Cell Expansion in Regenerative Medicine. Scientific Reports. 2019; 9(1):1-9.

[7] Gittard SD, Ovsianikov A, Chichkov BN, Doraiswamy A, Narayan RJ. Two-photon Polymerization of Microneedles for Transdermal Drug Delivery. Expert Opinion on Drug Delivery. 2010; 7(4):513-33.

[8] Zhu X, Fang W, Lei J, Li Z, Xie F, Cao Y, Zhang Y, Qin F, Li X. Supercritical Lens

Array in a Centimeter Scale Patterned with Maskless UV Lithography. Optics Letters. 2020; 45(7):1798-801.
[9] Baldacchini T, Editor. Three-dimensional Microfabrication Using Two-photon Polymerization: Fundamentals, Technology, and Applications. William Andrew. 2015.
[10] Skliutas E, Lebedevaite M, Kabouraki E, Baldacchini T, Ostrauskaite J, Vamvakaki M, Farsari M, Juodkazis S, Malinauskas M. Polymerization Mechanisms Initiated by Spatio-temporally Confined Light. Nanophotonics. 2021; 10(4):1211-1242.
[11] Chen D, Gu S, and Chen S. Study of Optical Modulation based on Binary Masks with Finite Pixels. Optics and Lasers in Engineering. 2021; 42:106604.

HARDWARE AND CONTROL CO-DESIGN TOWARDS LIGHTWEIGHT PRECISION STAGES FOR HIGH-THROUGHPUT MANUFACTURING

Jingjie Wu and Lei Zhou
Walker Department of Mechanical Engineering
University of Texas at Austin, TX, USA

INTRODUCTION

Driven by the exponentially increasing adoption of Internet of Things, the global demand for integrated circuits (ICs) is rapidly growing, which calls for next-generation semiconductor manufacturing equipment with improved productivity. The acceleration capability of wafer and reticle scanning stages is critical to enhance the manufacturing throughput, which necessitates the development of next-generation precision motion stages with unprecedented acceleration capability. Developing lightweight motion stages is critical to achieve this goal, which brings other benefits such as reducing the system volume and energy consumption. However, the reduction of stages' mass tend to lower the stage's structural resonance frequencies, which can limits the stage's achievable control bandwidth, accuracy under high acceleration, and even stability [1]. It is long recognized that the active control for flexible structures must be designed with the plant dynamics and controller design considered in synergy. However, presently available stage design techniques typically take a sequential approach to design the hardware and then followed by control, where a rule-of-thumb with "first resonance being three-times of the closed-loop control bandwidth" is typically applied [2]. Although such an approach is well-developed for today's motion systems, it can lead to design conservatism and limits the stage's achievable overall performance.

Hardware and control co-design, (often referred as control co-design, or CCD) is a numerical design approach which formulates an optimization problem with hardware parameters and control policy considered in a uniform framework [3]. Compared to traditional sequential design where the physical plant is designed first followed by controller design, the CCD approach provides more design flexibility and larger feasible design space, thereby leading to designs with improved performance. CCD has demonstrated excellent potential to address the design coupling between hardware and controller, and has been applied to various fields such as in thermal-fluid systems [4], wind turbine [5] and mechatronic systems [6, 7]. However, existing CCD formulations typically cannot optimize for frequency-domain design specifications of the closed-loop system such as control bandwidth and maximum sensitivity, which limits their applications for precision motion systems. In addition, most prior CCD efforts use analytical plant model for the design optimization, which is not enough to characterize the continuum flexible structural dynamics of the moving stages with complicated geometry. These facts limits the application of CCD in precision motion systems.

Aiming at the aforementioned challenges, in this paper, we present a new formulation of nested hardware- and control- co-design framework for a magnetically levitated (maglev) precision motion stage, aiming at pushing for improved acceleration and accuracy performance in precision motion systems. The key contribution of this paper is the development of a new gradient-based nested-CCD-algorithm that: (a) explicitly optimizes for the closed-loop control bandwidth in both outer and inner loop, and (b) presents the inclusion of finite element (FE) simulated continuum structural dynamics to accurately model a stage with complicated geometry. The proposed approach is evaluated on a case study motion stage and demonstrated a 42% of weight reduction and 28% band with improvement comparing with a baseline sequential design approach, which showcase the potential of CCD to effectively reduce design conservatism in precision motion systems.

DYNAMIC MODELING OF MOVING STAGE

Figure 1 shows a diagram for the magnetically levitated linear stage being considered in this work. Here, only the vertical directional displacements and vibration are considered. Position control in x-, y-, and θ_z-directions will be added in the future. Four electromagnetic reluctance actuators are used to levitate the stage and control its position, and four displacement sensors are used to measure the stage's displacement. In this work,

all the actuator and sensor positions are fixed as shown in the Figure 1. We will evaluate the placement of actuators and sensors as design parameters in the hardware design.

Figure 2 shows a CAD model for the rib-reinforced linear stage built in COMSOL Multiphysics with the design parameters labeled. Three design variables, including rib width, rib height and base height, are being optimized in CCD framework. Figure 3 shows the first four FE-simulated resonance mode shapes and their corresponding natural frequencies. A motion state-space dynamic model for the system is derived from the FE results as

$$\begin{cases} M(\theta)\ddot{x} + K(\theta)x &= B_{FE}(\theta)u, \\ y &= C_{FE}(\theta)x, \end{cases} \tag{1}$$

where θ is a vector for the hardware design parameters. M, $K \in \mathbb{R}^{n\times n}$ are the mass and stiffness matrices, respectively. Here M and K are computed via FE simulations.$x \in \mathbb{R}^n$ is a vector for the state variables representing the displacement of the nodes, n is the number of nodes determined by the FE mesh setting. B_{FE} and C_{FE} are input and output matrices distributing actuator forces u and measurements y over nodes.

Note that the system dynamics (1) has a dimension of n. When using a fine mesh in the FE simulations, the value of n is typically very large, consequently directly solving (1) is computationally expensive. To address this issue, we transformed the dynamics (1) into decoupled modal coordinates and then conducted model reduction by truncating the high-frequency modes. The mode-decoupling coordinate transformation are computed as

$$M\Phi\Omega^2 = K\Phi, \tag{2}$$

$$x = \Phi q, \tag{3}$$

where $\Omega = \mathrm{diag}(\omega_1, \cdots, \omega_n)$ is a diagonal matrix of n natural frequencies, and $\Phi = [\phi_1, \cdots, \phi_n]$ is an $n \times n$ matrix where each column represents a vector of the mode shape, and q is the modal coordinate vector. By substitute (2) and (3) into (1), we can find the decoupled dynamic equation of the system as

$$\begin{cases} M^{'}\ddot{q} + 2\zeta\Omega\dot{q} + K^{'}q = \Phi B_{FE}(\theta)u, \\ y = \Phi C_{FE}(\theta)q, \end{cases} \tag{4}$$

where $M^{'}, K^{'} \in \mathbb{R}^{n\times n}$ are the model mass and stiffness matrices, and ζ is the damping ratio which we use 0.01 in this paper.

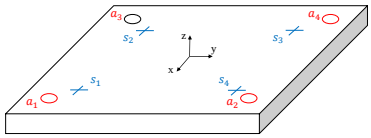

FIGURE 1. Diagram for actuator and sensor configuration for magnetically levitated stage.

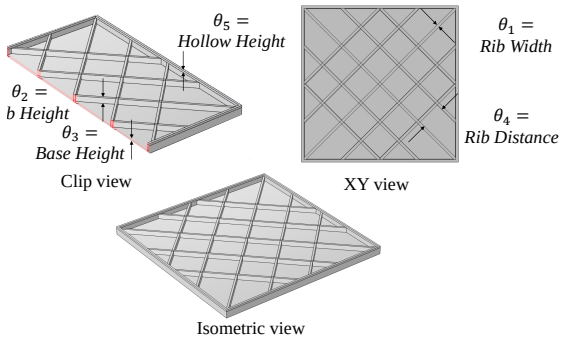

FIGURE 2. Diagram for parameterized rib-enhanced stage model.

With the model coordinates decoupled, we then reduce the system order by truncating the high-frequency flexible modes. In this work, we decided to model the three rigid-body modes (tip, tilt, and vertical translation) and the first 10 vibration modes, and all high-frequency modes are truncated. With nominal design parameters, this model is able to describe the system dynamics accurately up to approximately 1400Hz, which is sufficient for the control design. Next, a state-space model of the stage dynamic for controller design can be derived from (4).

In our design, there are only 3 rigid body modes but there are 4 actuators and sensors, which is called over-actuation and over-sensing, to increase the control bandwidth in the sense that the first vibration mode can be actively controlled. We are currently validating the feasibility of the CCD approach by optimizing only 3 parameters like in Fig. 2 and later will be testing the use of topology optimization where the number of hardware decision parameters is significantly larger which can further exploit the potential of the structure dynamics and push for better performance.

CONTROL CO-DESIGN FORMULATION

Aiming at reaching optimal overall system performance and thus remove the design conservatism in typical sequential design procedures, in this work, we proposed a nested CCD formulation for

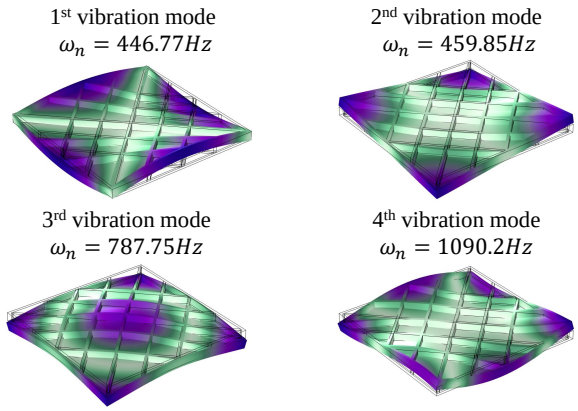

FIGURE 3. The first four vibration modes of the moving stage being considered simulated via COMSOL Multiphysics.

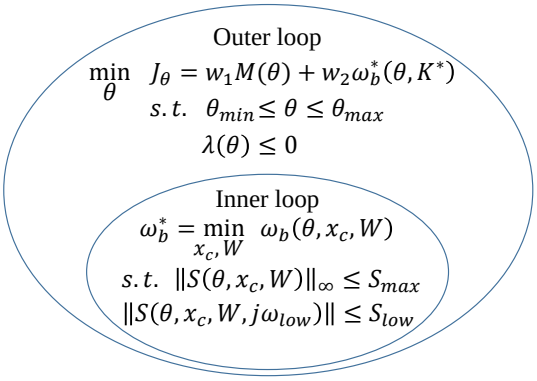
Outer loop
$\min_{\theta} \quad J_\theta = w_1 M(\theta) + w_2 \omega_b^*(\theta, K^*)$
$s.t. \quad \theta_{min} \le \theta \le \theta_{max}$
$\lambda(\theta) \le 0$
Inner loop
$\omega_b^* = \min_{x_c, W} \ \omega_b(\theta, x_c, W)$
$s.t. \ \|S(\theta, x_c, W)\|_\infty \le S_{max}$
$\|S(\theta, x_c, W, j\omega_{low})\| \le S_{low}$

FIGURE 4. Diagram for nested hardware-control co-design algorithm for linear stage with reduced weight.

the maglev moving stages as shown in Figure 4. Here, the outer loop optimizes the hardware design parameters, and the inner loop solves an optimal control problem with the hardware design parameters fixed. J_θ is the co-design objective function, which is a weighted sum of the moving stage's mass M and the control bandwidth ω_b^*. $w_1 > 0$ and $w_2 < 0$ are the weights for the objective function. Such an objective function sets the design target to maximizes the control bandwidth while minimizing the moving stage's weight. The following sections discusses the design for the inner and outer loops.

A. Inner loop optimization

The inner control optimization loop in Fig. 4 maximizes the control bandwidth of the problem while satisfying robustness requirements through limits on the closed-loop sensitivity function, which is solved at each iteration of the

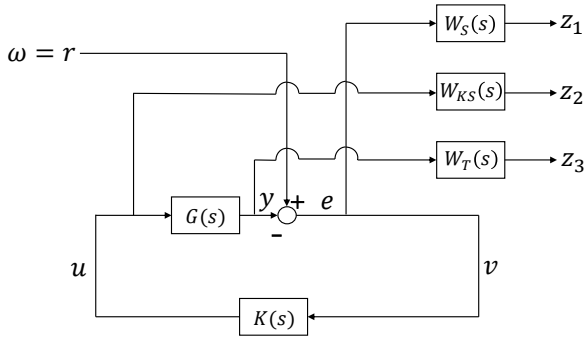

FIGURE 5. Diagram for mixed sensitivity $S/KS/T$ H_∞ controller design formulation.

outer loop given fixed plant parameter θ. Herein, as in Fig. 4, the state space model for inner loop controller design is derived from the FE Model given fixed plant parameter. A systematic mixed sensitivity H_∞ loop shaping (mix-syn H_∞) controller design [8] as shown in Fig. 5 is adopted to guarantee the closed-loop stability and to shape the sensitivity function for robustness and performance by designing weighting filters W_S, W_{KS} and W_T. The weighting filters are all made up of diagonal SISO filters defined in (5) as $W_S(s) = \mathrm{diag}(W_1(s), \cdots, W_1(s))$, $W_{KS}(s) = \mathrm{diag}(W_2(s), \cdots, W_2(s))$, and $W_T(s) = \mathrm{diag}(W_3(s), \cdots, W_3(s))$, where

$$
\begin{aligned}
W_1(s) &= \frac{s/M_S + \omega_S}{s + \omega_S A_S}, \\
W_2(s) &= \frac{c_K(s + \omega_K)}{M_K(s + c_K\omega_K)}, \\
W_3(s) &= \frac{s + (1/A_l)\omega_T}{A_u s + \omega_T},
\end{aligned}
\tag{5}
$$

where M_s, ω_s, ... are the design parameters for the filters. Our selection for the filter parameters follows reference [9]. Here, M_S is chosen to impose a reasonable upper bound on maximum peak of sensitivity function and A_S to limit steady state tracking error. M_K is determined by the actuator capability while c_K is a fixed large number and ω_K is fixed to be reasonable frequency for robust stability against additive uncertainty at high frequency. A_l is determined by the fact that maximum singular value of complementary sensitivity function at low frequency must be close to 1 for good tracking performance while A_u is set to be a small number for roll-off at high frequency and thus guarantee the robust stability against multiplicative uncertainty. All filter parameter values are listed in Table. 1. Consequently, there are only two decision variables ω_S and ω_T for the inner-loop optimization problem.

TABLE 1. Mixed sensitivity H_∞ synthesis filter parameters.

	M_S	A_S	c_K	ω_K	M_K	A_l	A_u
value	2	10^{-4}	10^4	100 Hz	4.5×10^4	1	10^{-2}

The objective function for the inner loop is defined to be the bandwidth frequency where the maximum singular value of the sensitivity function reaches -3 dB for the first time from below as (6).

$$\|S(\theta, \omega_b, K)\|_2 = -3 \text{ dB}, \tag{6}$$

where K is a controller synthesized via the mix-syn H_∞ design. Since there is not a closed-form expression for the gradient of the objective and constraints, to search for the controller design with maximum bandwidth, we conduct a parameter sweep for ω_S and ω_T for every given plant parameter θ. The optimal controller design and the bandwidth are passed to the outer loop for hardware design optimization in the next iteration.

B. Outer loop optimization

The outer plant optimization objective function contains the weighted sum of moving stage's weight M and the optimal control bandwidth ω_b^* solved in the inner loop. In our formulation, the outer loop is solved via a gradient-based approach. Below we discuss the computation of the gradients.

The gradient of the objective function J_p with respect to the plant design parameter θ can be derived as

$$\frac{\partial J_\theta}{\partial \theta} = w_1 \frac{\partial M(\theta)}{\partial \theta} + w_2 \frac{\partial \omega_b^*(\theta, K^*)}{\partial \theta}, \tag{7}$$

where $\partial M(\theta)/\partial\theta$ is directly available from COMSOL sensitivity analysis, and the second term can be found by applying the implicit function theorem [10] on (6) as

$$\frac{\partial \omega_b}{\partial \theta} = -\frac{\partial \|S(\theta,\omega_b,K)\|_2}{\partial \theta} \Big(\frac{\partial \|S(\theta,\omega_b,K)\|_2}{\partial \omega_b}\Big)^{-1}, \tag{8}$$

where $\partial\omega_b/\partial\theta \in \mathbb{R}^m$ is the gradient of bandwidth w.r.t. the hardware parameter θ. (S, G, K below are all considered as a function of θ, ω_b.) To compute $\partial\|S\|_2/\partial\theta$ and $\partial\|S\|_2/\partial\omega_b$, the following relationship is introduced [11]

$$\frac{\partial \sigma_i}{\partial p} = \text{Real}\big[u_i^* \frac{\partial G}{\partial p} v_i\big], \tag{9}$$

where u_i and v_i are the i-th column of the unitary matrices U and V from singular value decomposition (SVD), i.e., $G = U\Sigma V^*$. Applying (9) to (8), we can find

$$\frac{\partial \|S\|_2}{\partial \theta_i} = \text{Real}\big[u_1^* \frac{\partial S}{\partial \theta_i} v_1\big], \tag{10}$$

where $S = (I + GK)^{-1}$, u_1 and v_1 are the $1st$ column of U and V corresponding to the maximum singular value σ_1. Considering

$$\frac{\partial U^{-1}}{\partial x} = -U^{-1} \frac{\partial U}{\partial x} U^{-1}, \tag{11}$$

we have

$$\frac{\partial S}{\partial \theta} = -(I + GK)^{-1} \frac{\partial G}{\partial \theta} K (I + GK)^{-1}, \tag{12}$$

where $\partial G/\partial\theta$ can be found from the system's dynamics. In this work, a finite difference method is used to compute $\partial G/\partial\theta$ from the FE simulations. This method is effective for systems considering a small number of hardware design variables. For system with large number of hardware design parameters, the gradient of system matrices should be computed. Finally $\partial\|S\|_2/\partial\theta$ can be found by combining (10) and (12).

The gradient $\partial\|S\|_2/\partial\omega_b$ can be found as

$$\frac{\partial \|S\|_2}{\partial \omega_b} = \text{Real}\big[u_1^* \frac{\partial S}{\partial \omega_b} v_1\big]. \tag{13}$$

Applying (11) to (13), we have

$$\frac{\partial S}{\partial \omega_b} = -(I + GK)^{-1} \Big(\frac{\partial G}{\partial \omega_b} K + G \frac{\partial K}{\partial \omega_b}\Big)(I + GK)^{-1} \tag{14}$$

where both $\partial G/\partial\omega_b$ and $\partial K/\partial\omega_b$ can be readily computed by using state space matrices and (11). Finally, combining (13) and (14), we can obtain the values of $\partial\|S\|_2/\partial\omega_b$. With these aforesaid relationships, the gradient of the outer-loop objective function can be computed.

C. Overall nested CCD algorithm

The overall nested CCD algorithm is shown in Fig. 6. In this process, the plant parameters are first initialized by the FE simulations. Through the aforementioned modal decomposition approach, a state-space model is derived and then conveyed into the inner loop for the mix-syn H_∞ controller design to search for the controller design that maximizes the control bandwidth. Next, the optimal controller is sent to outer loop, where the plant parameters are updated via a steepest gradient descent algorithm until convergence.

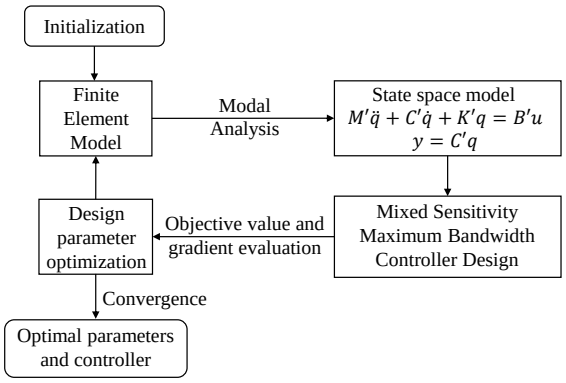

FIGURE 6. Flowchart of the proposed nested algorithm.

RESULTS AND DISCUSSION

We simulated two test cases to evaluate the performance of the proposed of CCD framework as discussed below:

We first performed the system design using a baseline sequential design approach. In this design method, the plant, or hardware, parameters are determined via shape optimization in COMSOL Multiphysics, where the weight of the stage is being minimized as the objective function, and the natural frequency of the stage's first vibration mode is constrained above 250 Hz according to rule of thumb. The optimal bandwidth controller is then designed for the given model using the same mix-syn controller synthesis method.

Next, we conducted the optimal design for the same system using the proposed CCD approach, where the formulation follows the algorithm shown in Fig. 4 and Fig. 6, and the weights in the objective are selected as $w_1 = 0.9994$ and $w_2 = 0.0333$. Fig. 8 show the history profile of parameters convergence, J_θ value, stage's weight, and closed-loop control bandwidth. It takes 25 iterations to converge.

The performance of the optimal designs of both design approaches are compared in Fig. 7 and Table 2. From data in Table 2, it can be observed that stage mass of the CCD case is reduced by 42% compared to the baseline design, and the closed-loop control bandwidth in the CCD case is 28% higher than that of the baseline case. These results demonstrate that the proposed CCD approach can successfully optimize the hardware and controller parameters in a unified process, and can enable system designs with improved overall performance compared to the optimal design using the conventional sequential design method.

TABLE 2. Comparison between the optimized system performance using the baseline sequential design and the proposed CCD framework.

	Stage Weight	Bandwidth	Obj. value	1st res. freq.
Baseline	1.02 kg	55.7 Hz	-10.65	250.0 Hz
CCD	0.59 kg	71.6 Hz	-14.40	110.5 Hz

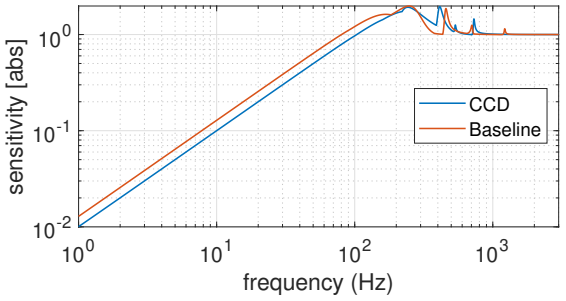

FIGURE 7. Maximum singular value of closed-loop sensitivity functions of the CCD and baseline optimal designs.

CONCLUSIONS AND FUTURE WORK

In this work, we have created a new CCD framework with the flexible structure's spatial-temporal dynamics considered via FE simulations, and also proposed a CCD approach that is explicitly optimizing for control bandwidth. With the aforesaid advances, this work effectively enable the CCD formulations for the design optimization for precision motion systems. The performance of the proposed CCD framework is evaluated via simulations, and has demonstrated a 42% weight reduction and a 28% bandwidth improvement comparing to a baseline sequential optimal design and optimal contro approach. The significant performance gain shows the potential of CCD for precision motion systems.

In future, we will work on the experimental evaluation of the proposed CCD framework's performance. We will also study how to formulate the CCD problem with the stage's flexible modes under active control. In addition, by enabling CCD formulations using FE structural models, which paves the way to the use of computational tools such as topology optimization to further optimize the stage structures and reduce weight. We envision these advances can significantly improve the performance of CCD for precision stages, and thus enable the next-generation motion sys-

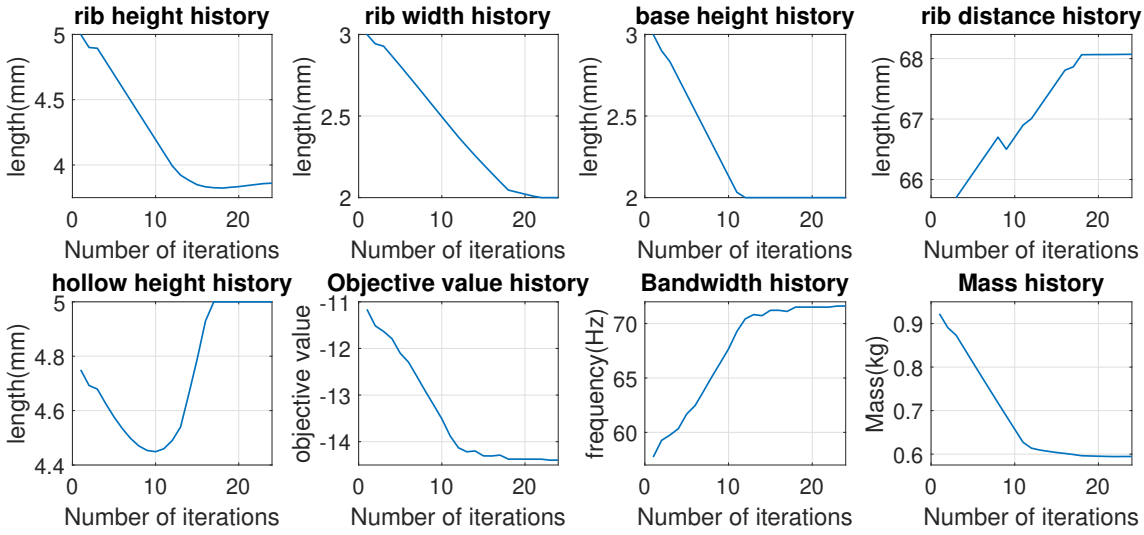

FIGURE 8. History of parameters value during CCD optimization.

tems with high speed, high precision, and low power consumption, thereby benefiting various applicaiton areas.

REFERENCES

[1] Oomen T, van Herpen R, Quist S, van de Wal M, Bosgra O, Steinbuch M. Connecting system identification and robust control for next-generation motion control of a wafer stage. IEEE Transactions on Control Systems Technology. 2013;22(1):102–118.

[2] Yong YK, Bhikkaji B, Moheimani SRR. Design, modeling, and FPAA-based control of a high-speed atomic force microscope nanopositioner. IEEE/ASME Transactions on Mechatronics. 2012;18(3):1060–1071.

[3] Garcia-Sanz M. Control Co-Design: an engineering game changer. Advanced Control for Applications: Engineering and Industrial Systems. 2019;1(1):e18.

[4] Nash AL, Jain N. Combined plant and control co-design for robust disturbance rejection in thermal-fluid systems. IEEE Transactions on Control Systems Technology. 2019;28(6):2532–2539.

[5] Deshmukh AP, Allison JT. Multidisciplinary dynamic optimization of horizontal axis wind turbine design. Structural and Multidisciplinary Optimization. 2016;53(1):15–27.

[6] Wang YS, Wang Y. A gradient-based approach for optimal plant controller co-design. In: 2015 American Control Conference (ACC). IEEE; 2015. p. 3249–3254.

[7] van der Veen G, Langelaar M, van der Meulen S, Laro D, Aangenent W, van Keulen F. Integrating topology optimization in precision motion system design for optimal closed-loop control performance. Mechatronics. 2017;47:1–13.

[8] Skogestad S, Postlethwaite I. Multivariable feedback control: analysis and design. vol. 2. Citeseer; 2007.

[9] Ortega M, Rubio F. Systematic design of weighting matrices for the H mixed sensitivity problem. Journal of Process Control. 2004;14(1):89–98.

[10] Krantz SG, Parks HR. The implicit function theorem: history, theory, and applications. Springer Science & Business Media; 2012.

[11] Mukhopadhyay V, Newsom J. Application of matrix singular value properties for evaluating gain and phase margins of multiloop systems. In: Guidance and Control Conference; 1982. p. 1574.

STUDY ON NON-AXSYMMETRIC 3D CURVED SURFACE TURNING BY DRIVEN-TYPE ROTARY TOOL SYNCHRONIZED WITH SPINDLE

Akane Ishizuka[1], Yoshitaka Morimoto[2], Akio Hayashi[2],
Yoshiyuki Kaneko[3], and Naohiko Suzuki[3]
[1]Graduate School of Mechanical Engineering
Kanazawa Institute of Technology
Ohgigaoka Nonoichi Ishikawa, Japan
[2]Department of Mechanical Engineering
Kanazawa Institute of Technology
Ohgigaoka Nonoichi Ishikawa, Japan
[3]Takamaz Machinery CO., LTD
Hakusan Ishikawa, Japan

INTRODUCTION

The target workpiece is shown Figure 1. The outer profile consists of cylindrical part and the 7th-order function curved surfaces. When these curved surface are machined by the conventional machining center and the grinding machine, it takes lot of times to complete with enough accuracy [1]. This target workpiece has a rotation center and non- axisymmetric complex three-dimensional curved surfaces. Because it is possible to machine by milling process with 5-Axis machining center, which has three translational motions three orthogonal axes and two rotational axes, is the most conventional and suitable for the complex profile machining. On the other hand, turning has another possibility to realize machining this workpiece. However, as the hardness of the target workpiece often shows over 60 HRC, the single point cutting leads to the tool wear even during cutting one workpiece. This machining process cannot avoid the profile error of the target workpiece. As a same reason, the tool wear has to be considered during the machining of workpiece, even if the CBN cutting tool tip is used. Moreover, it is required to set an offset position kept the constant distance from the tool path on the target profile [3]. In this case, because the tool position without the tool interference has to be calculated for 5-Axis machining, the tool path becomes complex and the machining efficiency decreases. In addition, during grinding process, as a method of machining 3D surfaces, precision grinding using grinding wheel with an arc section is required. However, since profile errors occur during truing of grinding wheel, which greatly affects the profile accuracy of the workpiece [4]. Therefore, the improvement of machining efficiency and the improvement of the profile accuracy become issues.

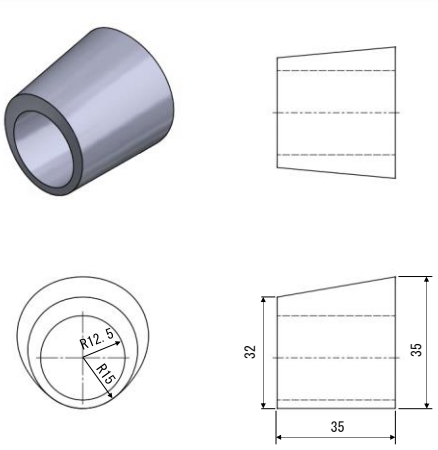

FIGURE 1: TARGET WORKPIECE WITH CURVED SURFACE

From such a background, to solve this problem, we decide to machine this with the hard-turning method [2]. Furthermore, we try to apply the driven type rotary cutting tool for the reason of long tool life. We have developed the CNC lathe for high-speed and high-efficiency machining in previous study. This CNC lathe is a structural design based on NACS-Turning [5]. This enables a non-circular machining method in which the rotational motion of the spindle and the high-speed translational machining operation of the tool synchronizing with the rotational motion of the spindle. In the previous research, we have proposed an on-machine measurement method using the line laser displacement sensor, with a non-contact method.

In this study, a new tool rotation axis (B-Axis) is added to overcome the present accuracy, it is

controlled to rotate with synchronizing to the rotational position of the spindle (C-axis) holding the workpiece, the X1-, X2-, and Z-Axis are positioned simultaneously in total. In this paper, the on machine compensated machining results based on the proposed method by a new hardware configuration developed is proposed to improve the machined profile accuracy.

EXPERIMENTAL APPARTUS

Figure 2 shows a schematic diagram of the lathe developed for this study. Table 1 shows the specifications of the CNC lathe. This CNC lathe has introduced a non-circular machining method by NACS-Turning in order to machine three-dimensional curved surface with enough high productivity. The non-circular machining method is based on the conventional turning process that machine a non-circular and/or non-axisymmetric curved surface by control the tool post motion in the radial direction at high speed. The Z-Axis is controlled with the constant feed rate to the workpiece spindle [5]. The developed CNC lathe in the previous study equipped the spindle and the linear motor driven moving table units on its bed. In addition, the moving table with tool post and the opposite tandem table are aligned on the X-Axis. This has the effect of mutually canceling the inertial force generated when the machining operation is performed at high acceleration by the inertial force of the opposing table. Also, this table performance to make the tool follows at high speed. In order to enable high-speed and high-precision machining motion, linear encoders for the table position detection are attached to the X1-, X2-, Z-Axis. This linear encoder has a resolution of 5 nm and detects positions at

TABLE 1: DEVELOPED 5-AXIS CNC LATHE

Items of specification			Eng. Unit
Head sock	Max, spindle speed	10000	min^{-1}
	Power of main motor	1.0/2.64	kW
	Stroke	200	mm
	Max. acceleration	12.1	m/s^2
	Max. speed	90	m/min
Carriage	Max. load	1674	N
	Power facility capacity	3.5	kVA
	Continuous thrust	600	N
	Max. thrust	1800	N
	Stroke	90	mm
	Max. speed	2	m/s
	Max. acceleration	133	m/s^2
	Magnetic attraction force	4500	N
	Mass of coil and LM block	10.1	kg
	Mass of CFRP table	2.3	kg
	Size of CFRP table	200X498X13	mm
Driven tool	Tool servomotor	200	W
Bed	Size	720X498X13	mm
	Resolution	5	nm
Positioning control	Sampling period	0.222	ms

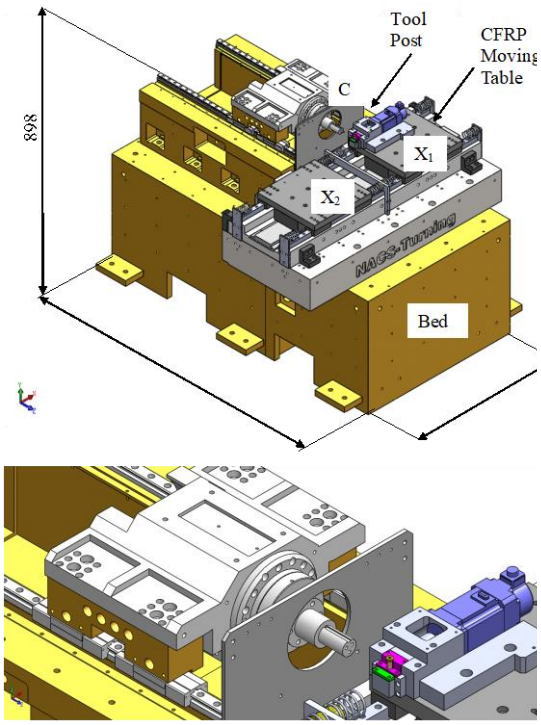

FIGURE 2: SCHEMATIC PICTURE OF DEVELOPED 5-AXIS CNC LATHE

sampling intervals of 0.222 ms. Each axis can be numerically controlled by the NC controller and operates by the maximum acceleration of 133 m/s^2, and has sufficient numerical coordinate's resolution. It is possible to realize the position feedback and memorize the motion in the NC device by not only the linear scale pulses but also the inner servo motor motion.

MACHINING RESULT

Figure 3 shows the designed profile near the end of the highest lift of the cam using the 7^{th} order function curve. It takes 36 seconds to machine by one pass. At first, the tool is positioned away from the workpiece and the machining motion is given from there. The machining path is calculated so as to extend the inclination of the machining profile, the motion of the tool increases in the time domain. Also, because of the tool radius offset, the program continued to operate after reaching at the end of the machined profile, and was controlled to move to a position completely away from the machined surface and to stop finally. The maximum stroke (oscillation) of the tool is about 6 mm in diameter, and the acceleration at this time is about 9.0 m/s^2 at the maximum. This satisfies the allowable acceleration of 133 m/s^2 of the linear drive moving table unit, and stable machining can be expected.

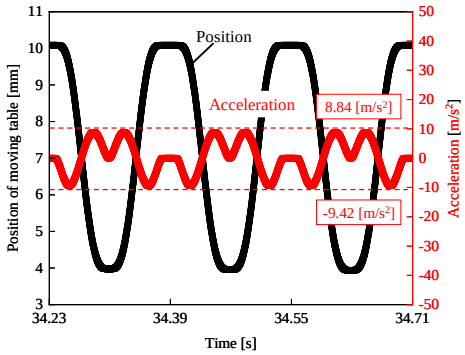

FIGURE 3: POSITION AND ACCELERATION OF MOVING TABLE

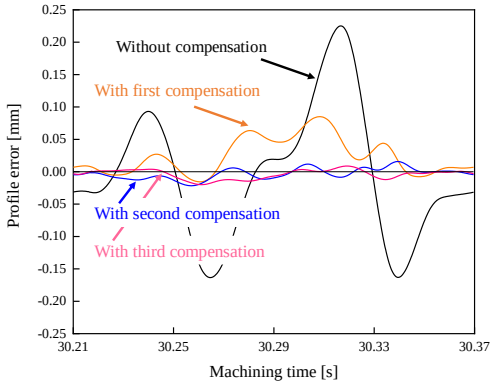

FIGURE 4: PROFILE ERROR MEASURED BY LASER LINE SENSOR

Figure 4 shows the results of machining experiments using the measurement method proposed in the previous study [9]. In this experiment, it is difficult to compare the whole profile because the number of machining points exceeds hundred thousand points. Therefore, one rotation profile of the workpiece where the lift is the highest is extracted and the machining profile is evaluated. Also, the profile evaluation is performed by applying the least squares method to the measurement results. From this figure, the error from the designed profile appears largely at the part where the curvature increases. This error is observed at every rotation, and as the lift increases, the error increases. Also, from Figure 3, the overcutting occurs when the error value is negative, and undercutting occurs when the error value is positive. The RMS (Root Mean Square) of the machining error of the normal machining surface is 88.8 μm. This error is compensated by the following NC program by adding the compensated data. In this figure, the profile error between the designed profile and the measurement results by the input command shows the maximum error of 26.9μm with the black solid line.

In order to reduce the machining error, the repetitive control for compensation for the machining tests was applied in this study and the experimental procedure was performed. In Figure 3, the machining error by compensation machining. The RMS of the first compensated machining was 7.6μm, and after the second compensated machining, it was 6.14μm, and the error decreased by about 13.7%. However, in the range of 30.29 to 30.33 s, the machining error reverses against the previous machining error was appeared. The cause is considered that the motion delays at the long stroke and that the tool operation reverses in this time range. Also, it is thought that the tool motion in the cutting direction is prevented by the thrust cutting force. Therefore, the profile accuracy will be further improved by applying the new compensation method depending on the rotational positions of both the rotary tool and the spindle.

NEW CONFIGRATION OF 5-AXIS CNC LATHE

Figure 5 shows the radial and angular errors when the driven type rotary tool is installed and rotating. In addition, since cutting force acts during machining, two similar types of errors are added to the error on the rotary tool.

Since this error varies depending on the rotational speed and rotational position of the rotary tool, the tool alignment error at the machining point is expressed by the following formula using the spindle rotational position θ_i

$$R_{\theta_i} = \Delta Rr_{\theta_i} + \Delta Ra_{\theta_i} \quad (1)$$

Therefore, by applying the control method that synchronizes the rotational position of the rotary tool with the rotational position of the spindle, the alignment error for each rotational position of the rotary tool always cuts a specific position on the workpiece surface even if the cutting force is applied. Therefore, we have developed the spindle synchronous driven type rotary tool post shown in Figure 6. Figure 7 explains a synchronizing machining method to consider the motion error that occurs in the rotary tool. Data acquired every time during the workpiece rotation every 0.5 degrees and the total of 720 data are acquired during cutting. By repeating this process, data for the total cutting length of the workpiece

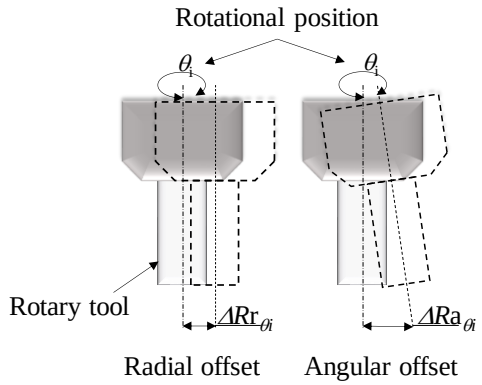

FIGURE 5: ROTARY TOOL ALIGNMENT WITH GEOMETRICAL ERROR

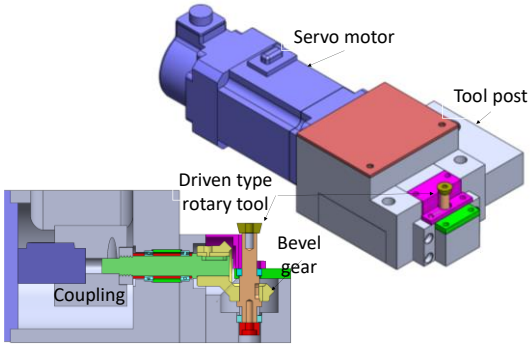

FIGURE 6: DEVELOPED SYNCHRONOUS DRIVEN TYPE ROTARY TOOL CONTROLED BY SERVO MOTOR

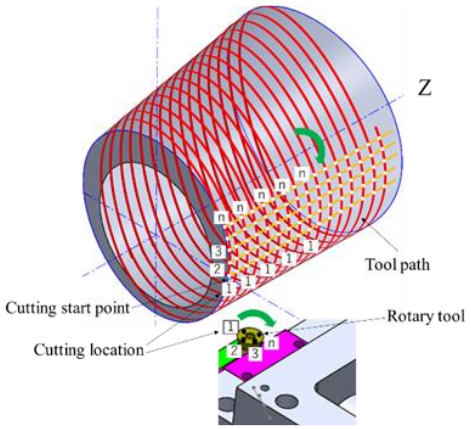

FIGURE 7: INTERSECTION OF X-Z PLANE AND WORKPIECE SURFACE INTERSECT

is acquired and calculated. Every cutting points of the workpiece and the tip of cutting tool along with Z-Axis are synchronized such as point 1 on the workpiece and point 1on the cutting tip. These are repeated as same as point 2 for point 2, point 3 for point 3, and point n for point n. Here, point n indicates an arbitrary point in the workpiece. By this process, the cutting is completed as if the single point cutting by the conventional turning process is executed.

As a result, the command value for repetitive control must not take into account the dynamic variation of the depth of cut included in the workpiece profile measured by the on-machine laser line sensor, but includes the average error component shown in equation (1). In this operation, a specific machining point of the rotary tool passes through the ridge line where the X-Z plane and the workpiece surface intersect determined by the spindle rotation position.

MACHINING RESULT WITH ROTARY TOOL

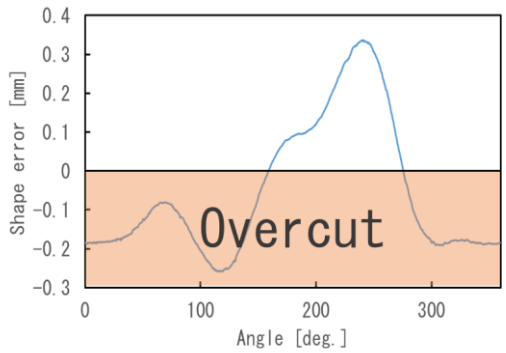

FIGURE 8: SHAPE ERROR IN MACHINING ROTARY TOOL

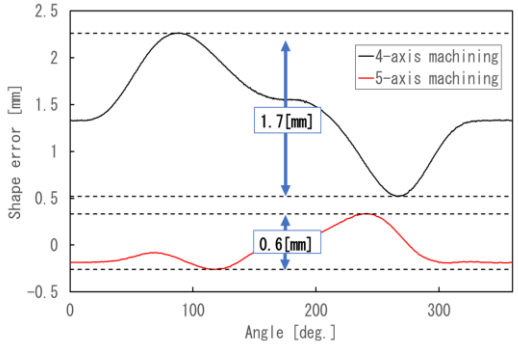

FIGURE 9: COMPARING SHAPE ERROR

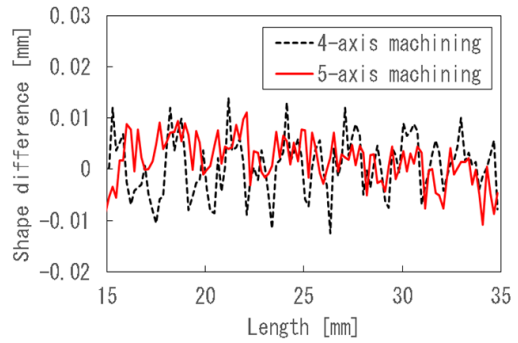

FIGURE 10: SURFACE ROUGHNESS

Figure 8 shows the shape error when machining with B-Axis synchronizing with the spindle. Comparing the target shape and the shape of the machined workpiece, there often existed overcutting part of workpiece. Figure 9 shows comparison of shape error between the 4-Axis machining and the 5-Axis machining. The difference between the maximum and minimum values of the shape error of 4-Axis machining is 1.7 mm, and the difference from the maximum to the minimum values of the shape error of 5-Axis machining is 0.6 mm, which is 30% less than that of 4-Axis machining. As a result, it was possible to reduce the shape error in 5-Axis machining. To improve the shape accuracy, it is necessary to correct the overcut portion by using the synchronization with B- and C- Axis.

Figure 10 shows surface roughness of 4- and 5-Axis machining. While the surface roughness with the fixed tool was 22.7μm, the surface obtained with a rotary tool is 11.1μm. 5-Axis machining succeeds reducing surface roughness 50% than 4-Axis machining. The factors that affect the surface roughness in machining with the rotary tool are considered to be the change in the depth of cut and the effect of tool wear. Comparing the fixed tool to the rotary tool, the rigidity of the shaft of the rotating part is weaker than the fixed tool. On the other hand, in a rotary tool, the cutting point of the cutting tool changes with each angle, so that the tool wear is reduced. It is thought that these factors reduced the surface roughness. Moreover, since the depth of cut reduced, the processing time becomes long. Therefore, to shorten the machining time, it is necessary to improve the rigidity of the rotating shaft of the rotary tool.

CONCLUSION

The following results has been obtained:

1) The proposed compensated machining method decreased the RMS of the machined profile from 64.6 μm to 6.14 μm.
2) As a result of comparing machining centers with CNC lathe, the machining method of CNC lathe has enabled high profile accuracy and short machining time.
3) We have developed the spindle synchronous drive type rotary tool post to suppress the geometrical error of the rotary tool during cutting.
4) The surface roughness improved from 22.7 μm with the fixed tool to 11.1 μm with the rotary tool.
5) It is possible to reduce the effect of tool wear using the rotary tool. However, since the rotary tool cannot withstand a large cutting force, the tool post and tool shaft should be improved.

ACKNOWLEDGEMENTS

The authors express their gratitude to Takamaz Machinery Co., Ltd for their cooperation in this study. This study was supported by JSPS KAKENHI Grant Number 15H03905 (Grant-in-Aid for Scientific Study (B)).

REFERENCES

[1] I Taki, M. Nakamura, et al, “Development of a motorcycle engine with a three-dimensional cam for continuous variable valve lift and timing mechanism”, SAE International Journal of Engines, Vol.1, pp1357-1365, 2009.

[2] Yoshitaka Morimoto, “Non-circular machining method by turning”, Japanese patent disclosure 5413913, 2013.
Kanda, T., Morishige, K., “Tool Path Generation for Five-Axis Controlled Machining with Consideration of Tool and Structure Interference,” Journal of the Japan Society for Precision Engineering, Vol. 81, No.10, pp.969-973, 2015.

[3] Morimoto, Y., Emoto, S., Moriyama, T., Kaneko, Y., and Nakagaki, K., “Realization of 3D Surface Machining by Turning,” Proceedings of the Annual Conference of the Precision Engineering Society Spring Conference, (2013), pp.719-720.

[4] Kanda, T., Morishige, K., “Tool Path Generation for Five-Axis Controlled Machining with Consideration of Tool and Structure Interference,” Journal of the Japan Society for Precision Engineering, Vol. 81, (2015), No.10, pp.969-973.

[5] Hino, R., Shamoto, E., and Moriwaki, T., “Tool Path Generation by Immediate Offset Method (1st Report) Proposal of Fundamental Procedure,” Journal of the Japan Society for Precision Engineering, Vol. 69, (2003), No.6, pp.781-787.

[6] Morimoto, Y., “Non-circular machining method by turning,” Japanese patent disclosure 5413913 (2013).

[7] Ito, S., Matsuura, D., Meguro, T., Goto, S., Shimizu, Y., Gao, W., Adachi, S., and Omiya, K., “On-machine form measurement of high precision ceramics parts by using a laser displacement sensor, ” The Japan Society of Mechanical Engineers, Vol. 8, (2014), No.4, pp.1-12.

[8] Kensuke Nakagawa, et al., “Study on Turning of Non-axisymmetric Three-Dimensional Curved Surface”, Proceedings of the ASME IMECE2019, IMECE2019-11100, 2019

DEEP LEARNING WORKFLOWS FOR DIMENSIONAL METROLOGY WITH HIGH-RESOLUTION X-RAY COMPUTED TOMOGRAPHY

Aniket Tekawade[1], Herminso Villarraga-Gómez[2], Matthew Andrew[3], Brandon A. Sforzo[4], Alan L. Kastengren[5], Christopher F. Powell[4]
[1]Data Science and Learning Division, Argonne National Laboratory, Lemont, IL, USA
[2]Carl Zeiss Industrial Metrology, LLC, Wixom, MI, USA
[3]Carl Zeiss X-ray Microscopy, Inc., Dublin, CA, USA
[4]X-ray Science Division, Argonne National Laboratory, Lemont, IL, USA
[5]Energy Systems Division, Argonne National Laboratory, Lemont, IL, USA

Industrial X-ray computed tomography (CT) has evolved into a popular solution for dimensional metrology in modern quality control applications. Prior work by the authors has shown its efficacy in geometric dimensioning and tolerancing of metallic components [1, 2]. A typical CT metrology workflow starts with scanning a sample to acquire projections around a 180/360 spin and is followed by image processing steps involving CT reconstruction, surface determination (segmentation or thresholding) and dimensional measurements. Depending on the (1) resolution demanded, (2) keV energy of source, and (3) attenuation characteristics of the sample material, the total exposure time can increase dramatically to achieve adequate signal-to-noise (SNR) ratio for high-precision dimensional metrology. Scanning time is the sum of total exposure (number of projections times the exposure time per projection) and instrument overhead (e.g., sample rotation speed). Hence, the applicability of this tool to in-line (or online) metrology can be challenging for mm-sized metallic components (e.g., automotive fuel injectors) demanding high (< 5 µm) surface resolution due to low photons/pixel ratio.

The authors previously reported a surface determination workflow using deep learning (DL) with surface resolution under 5 micrometers on synchrotron CT [3]. The nominal diameter of the holes in this injector is 165 µm. These holes are not accessible to traditional measuring methods such as tactile or optical coordinate measuring machines (CMM). Furthermore, the attenuation through steel walls of approximately 5 mm thickness create poor contrast and beam hardening effects. While scan times to achieve reasonable contrast for such a gasoline fuel injector in synchrotron CT can be under 15 minutes, a scan using Zeiss Versa 620 would take up to 6 hours to achieve similar resolution.

Here, we evaluate two DL-based software packages – CTSegNet and DeepRecon for the challenging use case reducing scanning time for measurements of the internal orifices of a steel fuel injector in a Zeiss Versa 620. CTSegNet was developed by the first author (A. Tekawade) at the Argonne National Laboratory for direct segmentation of noisy CT scan volumes. DeepRecon was developed by ZEISS as a reconstruction engine for denoising volumes obtained from low-dose scans. The main purpose of this paper is to analyze potential reductions in scanning time when DL-based workflows are used to augment image-quality.

For the evaluation, the research fuel injector (Spray G) contributed by the Engine Combustion Network (ECN) was scanned using a ZEISS Versa 620 instrument by acquiring a total of 3600 X-ray projections with 6 seconds exposure per projection (total 6 hours). Then, this data was reconstructed using equally spaced subsets of those projections (e.g., 2X, 4X, 6X, 8X, 10X; where 4X means 900 projections) to mimic reduced scan time. Each subset was reconstructed using DeepRecon Pro (DRPro, the latest version of DeepRecon) as well as a traditional Feldkamp–Davis–Kress (FDK) reconstruction algorithm and then thresholded to determine the surface. The data reconstructed by FDK was directly segmented (or binarized) using CTSegNet which utilizes multiple passes of 2D fully convolutional neural networks (fCNN) to perform 3D segmentation [3], resulting in a binarized volume which implicitly determines the surface (see Figure 2).

MEASUREMENT ACCURACY EVALUATION

The final surfaces computed from FDK, DRPro and CTSegNet were analyzed using a dimensional metrology workflow. A cylindrical fit was applied to the orifices of each of the 8 holes and their cylindricity was measured. We assume the cylindricity from the 1X case (full 6-hour exposure) as the reference data and track the deviation from reference as scan time is reduced (see Figure 1). Both CTSegNet and DRPro limit the maximum deviation to less than 2 µm for reduction factors of

up to 10X for cylindricity. While DRPro retains accuracy up to 10X for deviation in diameter, the accuracy of direct segmentation using CTSegNet is accurate only up to 6X. This is expected, since segmentation is a post-reconstruction step, and some information may be lost during reconstruction. Effectively, this means that reducing scan times by 10X and applying a DL-based workflow could provide the same level of accuracy as a 2X reduction when obtaining the surface directly from FDK.

MODEL TRAINING WORKFLOW

In both CTSegNet and DRPro, the respective segmentation and denoising models are trained with pairs of noisy (low-dose) and high-quality (high-dose) data, which requires at least one full exposure scan to be performed as a sort of calibration need. While well trained DL models should be generally applicable to new data, accuracy improvements are observed when models are retrained with new data that show morphological similarities to the sample being imaged. To avoid collecting full exposure data, we integrate a forward simulation into the training workflow. This section will report our findings on training data needs when simulation data is used. (Further analyses will be presented in the extended abstract.)

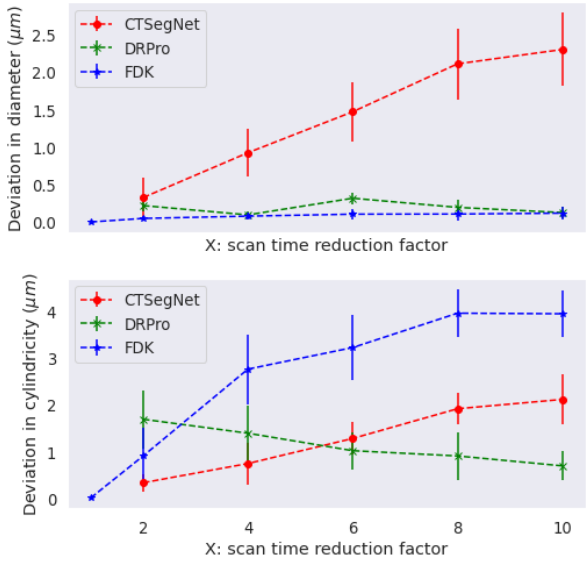

Figure 1: Deviation in diameter and cylindricity with the full-exposure scan used as reference surface for different throughput reduction factors (2X, 4X, 6X, 8X, and 10X). The error bars indicate the standard deviation in hole-to-hole variability of diameter measurements.

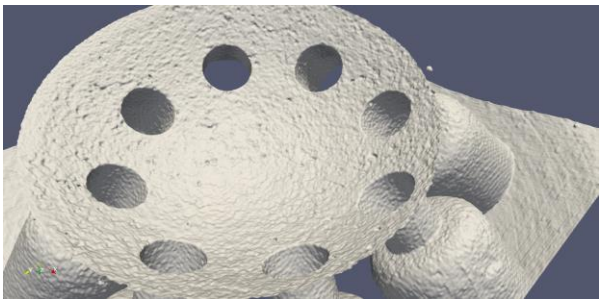

Figure 2: Geometry of the 8-hole gasoline injector (ball is removed). Nominal diameter of the small holes is 165 μm. Surface was computed directly through voxel binarization using CTSegNet.

CONCLUSIONS

Scan times in X-ray CT dimensional metrology can be prohibitively high in small components (e.g., with sizes in the range 1–10 mm) that require micrometer-sized feature resolution due to the low photon/pixel ratio. When DL-based elements such as denoisers (DRPro) or segmenters (CTSegNet) are incorporated into the workflow, the same metrological resolution could be achieved with a more than 5X throughput bump that substantially reduces the scanning time. Whereas FDK reconstruction algorithms reduce the CT data quality and the accuracy of dimensional information in such data, DRPro and CTSegNet can be used as alternatives to reduce measurement acquisition time without major accuracy loss in the dimensional data. This is especially true for measurements of diameter. For form measurements (e.g., cylindricity), variations are expected to be in the order of 2 μm or less when using DRPro and CTSegNet with a 10X throughput factor. In contrast the deviations produced by the FDK method are larger than 2 μm and produce more noisy data (see Figure 3). Thus, DL-based methods are advantageous to increase the throughput of CT acquisition while minimizing accuracy loss in dimensional data.

REFERENCES

[1] H. Villarraga-Gómez, E. L. Herazo and S. T. Smith, "X-ray computed tomography: from medical imaging to dimensional metrology," Precision Engineering, vol. 60, pp. 544-569, 2019.
[2] H. Villarraga-Gómez, C. Lee, and S. T. Smith, "Dimensional metrology with X-ray CT: A comparison with CMM measurements on internal features and compliant structures," Precision Engineering, vol. 51, pp. 291-307, 2018.
[3] A. Tekawade, B. A. Sforzo, K. E. Matusik, A. L. Kastengren, C. F. Powell, “High-fidelity geometry generation from X-ray CT data using convolutional neural networks”, in Developments in X-Ray Tomography XII. Vol. 11113. International Society for Optics and Photonics, 2019.
[4] D. Duke et al, “Internal and near nozzle measurements of Engine Combustion Network Spray G gasoline direct injectors.”, Experimental Thermal and Fluid Science, vol. 88, pp. 608-621, 2017.

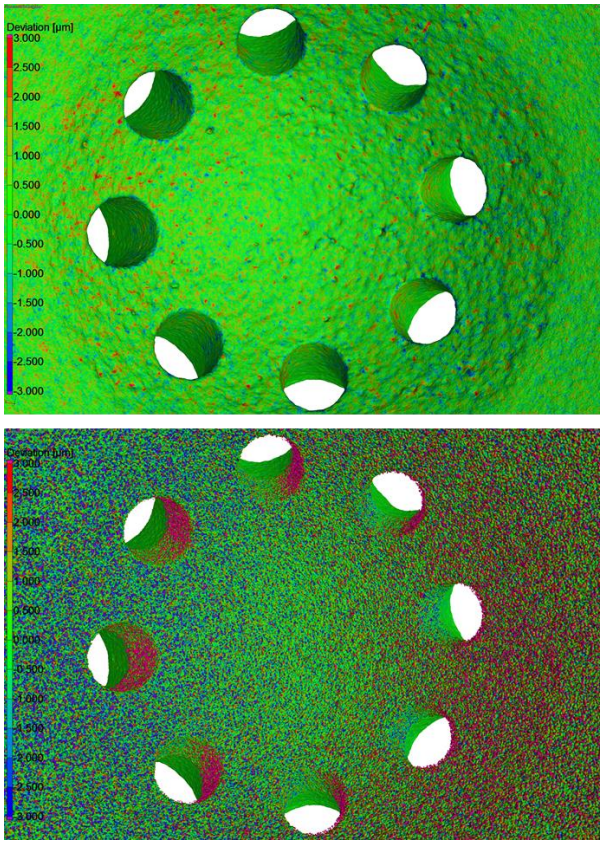

Figure 3: Comparison between thresholded surfaces at 10X reduction from DRPro (above) and traditional FDK (below). The colormap indicates deviation form the reference (1X) surface.

IMPROVING SCAN TIME AND IMAGE QUALITY IN 3D X-RAY MICROSCOPY BY DEEP LEARNING RECONSTRUCTION TECHNIQUES

Herminso Villarraga-Gómez[1], Andriy Andreyev[2], Matthew Andrew[2], Hrishikesh Bale[2], Ravikumar Sanapala[2], Masako Terada[2], Allen Gu[2], Bruce Johnson[2], Lars Omlor[3], and Christoph Graf vom Hagen[2]
[1]Carl Zeiss Industrial Metrology, LLC, Wixom, MI, USA
[2]Carl Zeiss X-ray Microscopy, Inc., Dublin, CA, USA
[3]Carl Zeiss, Inc., White Plains, NY, USA

Applications of 3D X-ray imaging techniques have expanded from their initial and most popular field of application, medical diagnostics, to industrial measurements [1]. Recent developments in image acquisition, electronics, computational power, and computed tomography reconstruction algorithms have made X-ray based technologies suitable for broad academic and industrial utilization. However, for imaging applications requiring high-resolution capabilities, down to a few micrometers and even at nanometer level, the cost of 3D X-ray measuring services can still be one of the main roadblocks for wider adoption of X-ray based technologies in industrial environments. Computed tomography (CT) reconstruction is the mathematical process that, based on 2D radiographic projection data captured from different angular positions around an object, generates a 3D volumetric density map of that object that reveals its internal and external features (Figure 1). In high-resolution X-ray CT, also known as 3D X-ray microscopy (XRM), long data acquisition times (in the order of hours) are required to overcome low photon counts for dense samples. Reducing the number of radiographic projections (N_p) acquired for CT reconstruction, while maintaining image quality, can be effective to decrease measurement cost, depending on the reconstruction approach. With traditional filtered-back-projection based reconstruction techniques, e.g., Feldkamp-Davis-Kress (FDK) algorithm [2], reducing N_p can cause a significant loss in image quality. This would reduce measurement accuracy and repeatability [3]. Typical N_p thresholds for a faithful 3D image reconstruction, defined by the Nyquist-Shannon sampling theorem, are in the order of two thousand projection views with modern XRM instruments. As an alternative, Deep learning (DL) based image reconstruction is an emerging technology for reducing N_p further, even down to a few hundred projections, without a significant loss of image quality. DL-based algorithms for CT reconstruction improve the scan time (throughput) and image quality capabilities of XRM. This paper presents the integration of DL-based techniques into 3D XRM workflows, illustrated by several application examples (using scan data from a ZEISS Xradia 620 Versa X-ray microscope). The benefits of employing DL-based reconstruction techniques to improve 3D XRM measurement performance by reducing data acquisition time and increasing signal-to-noise ratio (enhancing image quality) are highlighted and discussed.

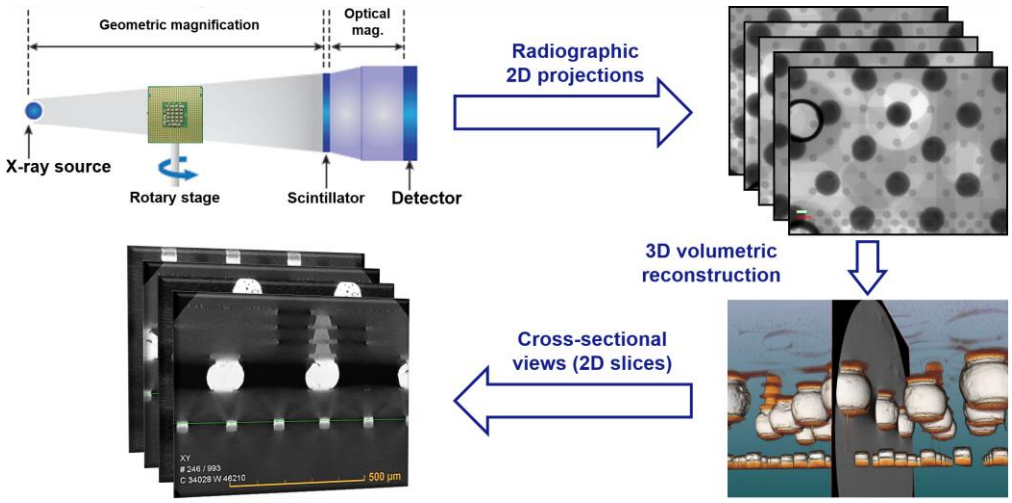

Figure 1: Schematic workflow of the 3D XRM measurement process. After CT reconstruction, false colors can be used to represent 3D volume density maps of an object (e.g., electronic circuit board) and segment it into its different components. Cross-sectional images (2D slices) extracted from the 3D volume can be used to inspect the object's internal features.

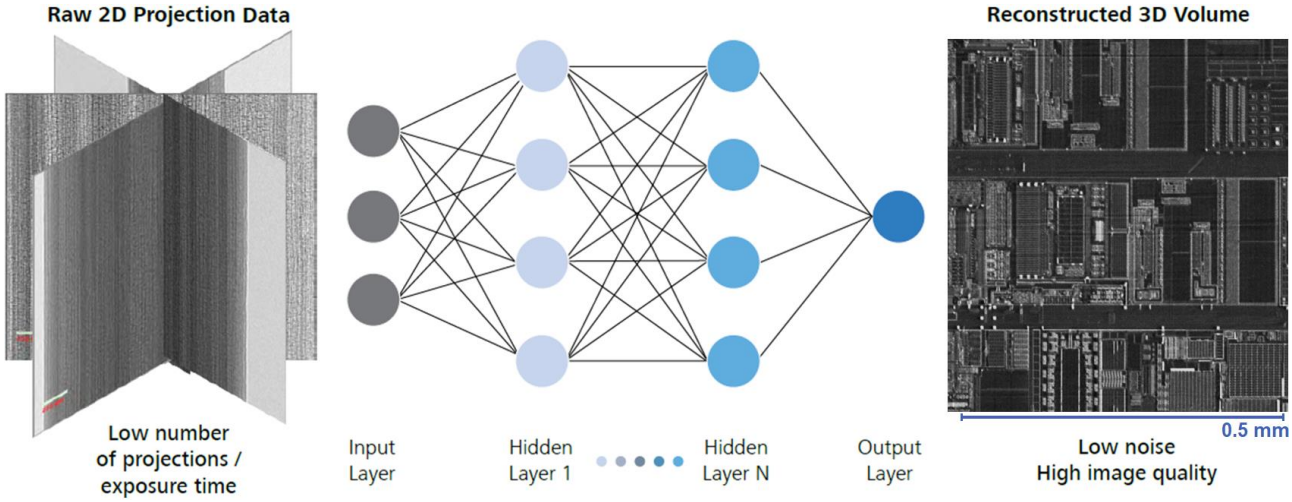

Figure 2: By integrating a pre-trained neural network between radiographic projection data and CT reconstructed data, high quality reconstructions can be achieved with low number projection views N_p, or short time exposures.

DEEP LEARNING WORKFLOW

Most of the machine learning applications in the field of 3D X-ray imaging, to date, have been focused on post-reconstruction methods for image segmentation, feature classification, and feature recognition [4, 5, 6]. DL-based algorithms have not been integrated deeply inside an instrument workflow, especially in one as complex as 3D XRM. This paper presents a DL-based reconstruction workflow developed by ZEISS, hereafter referred to as DeepRecon. This technology is integrated in the CT reconstruction phase of XRM measurement through a software interface that has a user input reduced to the specification of a desired application result (i.e., to improve image quality, or throughput time). DeepRecon introduces trained convolutional neural networks between the X-ray projections (or radiographs) and the final reconstructed volume. This has the effect of considerably denoising the 3D XRM data, as well as reducing sampling effects that are typically present in CT reconstructions performed by FDK, e.g., aliasing artifacts (shadow bands and dark streaks, or noise-like distortions), when insufficient X-ray projection data are used. With DeepRecon, the measurement workflow enables image processing, interpretation, and retrieval to be performed using an on-demand trainable neural network, allowing for high quality reconstructed data to be achieved despite rapid acquisitions using a small N_p value for data reconstruction (Figure 2).

Using ZEISS proprietary cost functions and training procedures, DeepRecon can produce image reconstructions from a set of data acquired with a low N_p (training input), when an FDK reconstructed image produced with a large N_p is used as the reference "ground truth" (training target) data. The DL network training is performed for a particular set of XRM data acquisition settings and a given sample class (defined as a set of samples which share the same or similar X-ray attenuation and scan recipe parameters). A trained network can be applied to data sets belonging to the same sample class. If the sample class differs, or if the XRM acquisition parameters are modified, the network must be retrained. Training a DL network with DeepRecon does not require prior information of the type of sample. Users can create custom networks in any application, without the need for machine learning expertise. The automated training scheme is built into a software interface with a couple of selectable options in a drop-down menu.

DEEP LEARNING vs. STANDARD FDK

DeepRecon reconstruction enables throughput and image quality improvements of 3D XRM measurement, with potentially up to 10X reduction in measurement time, when compared with standard FDK reconstruction. Figure 3 shows the example of data reconstruction for a section of an additively manufactured Inconel lattice, scanned with a voxel size V_x = 1.5 µm, using both FDK and DeepRecon when N_p = 1600 (scan time t = 10 h). The image quality of the DeepRecon data is better than the FDK reconstruction in terms of noise reduction and preservation of surface features. As observed in the bottom section of Figure 3, DeepRecon is able to preserve finer morphological details of voids and unsintered powder, which can provide key insights into the process optimization

of the laser sintering process. Some of the smaller voids that are usually not well discerned with FDK reconstruction, due to low contrast-to-noise ratio and other artifacts caused by the high attenuating density of these lattice materials, were successfully restored in the DeepRecon reconstructed data.

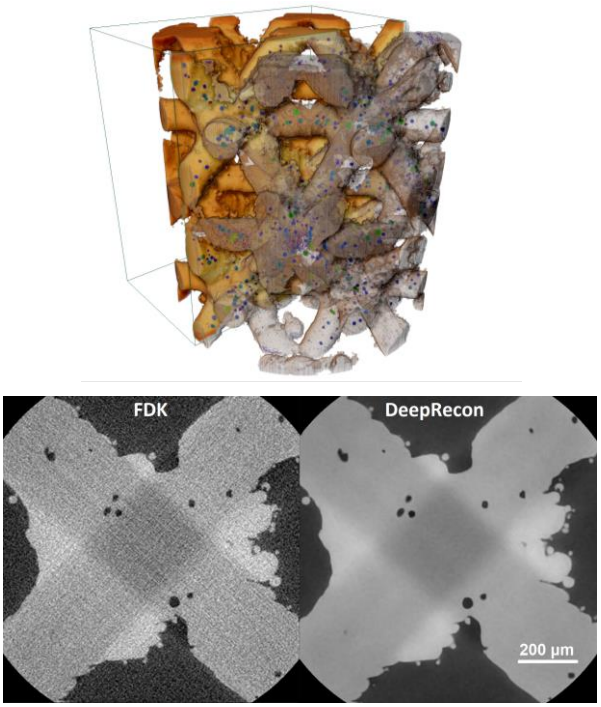

Figure 3: 3D XRM volume rendering of an Inconel 3D printed lattice highlighting porosity distribution (top); and a cross-sectional view (bottom), reconstructed with both FDK and DeepRecon, when N_p = 1600 (V_x = 1.5 µm).

Figure 4 shows data reconstructions for a portion of a cast aluminum part, when N_p = 2880 (t = 8 h, V_x = 3.7 µm). Compared to FDK, DeepRecon reduces noise levels in the data and eliminates streak artifacts (gray value distortions typically caused by multiple mechanisms including beam hardening, photon starvation, and scattering radiation effects), making easier the identification and quantification of porosity in the data. But in addition to improving image quality, DL-based reconstruction workflows reduce XRM scan time, as illustrated in Figure 5 (for the same aluminum casting), where data acquisition was reduced by a factor of eight with N_p = 360. DeepRecon preserves fine details in the data, revealing voids that get lost in the noise of the FDK reconstruction and defining a clear boundary separation between air and material. The latter facilitates the use of thresholding algorithms for the evaluation of the internal porosity in metal castings, with about an 8X throughput time improvement (FDK would require N_p > 2800, as shown in Figure 4, if V_x = 3.7 µm).

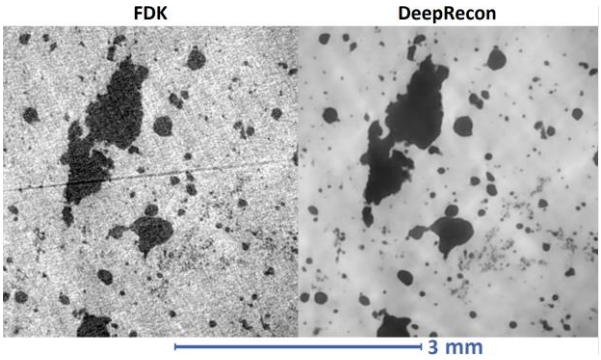

Figure 4: An XRM cross-sectional slice view of an aluminum casting, reconstructed with both FDK and DeepRecon, when N_p = 2880 (V_x = 3.7 µm, t = 8 h).

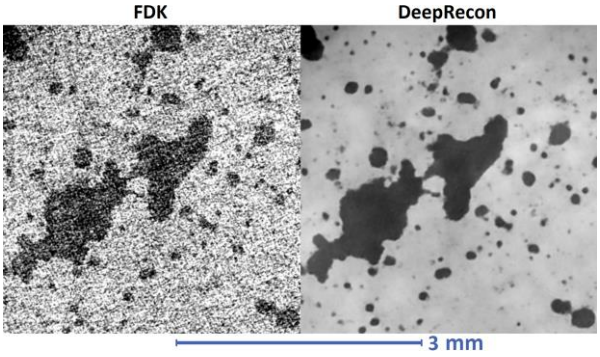

Figure 5: Another cross-sectional view of the 3D XRM data for the aluminum casting, reconstructed with both FDK and DeepRecon, when N_p = 360 (t = 1 h).

Figure 6 shows high-resolution XRM images (V_x = 2.8 µm) for the corner of an injection-molded plastic connector, corresponding to two different settings, N_p = 1800 (t = 60 min) and N_p = 180 (t = 6 min), reconstructed with both FDK and DeepRecon. Though the FDK data at N_p = 1800 do not seem to be affected by aliasing effects, the DeepRecon data are still of better quality in terms of contrast-to-noise ratio. When N_p = 180, the FDK reconstruction is undersampled, and the imagery data are affected by streak artifacts and noise from the stochastic nature of the X-ray imaging process. In contrast, the DL-based reconstructed data reduce noise and eliminate aliasing effects, thus preserving the high contrast definition of the plastic connector surfaces (even at N_p = 180). This is particularly important for dimensional measurements [1, 7]; an accurate surface determination (edge detection) is crucial for CT dimensional metrology [8, 9]. With N_p = 180, the

FDK data would present challenges during the surface determination step given the low signal-to-noise ratio, limited contrast around the edges of the plastic material, and other gray value distortions in the data (e.g., cupping and streaking artifacts). Overall, by reducing N_p by a factor of ten, DeepRecon was able to speed up the XRM measurement process up to approximately six minutes per sample piece for the plastic connector, i.e., about a 10X throughput time improvement as compared to FDK optimized parameters (t = 60 min if N_p = 1800, when V_x = 2.8 µm). Furthermore, from the results shown in Figure 6, it is apparent that the use of DL-based reconstruction algorithms could be beneficial in the field of dimensional surface metrology.

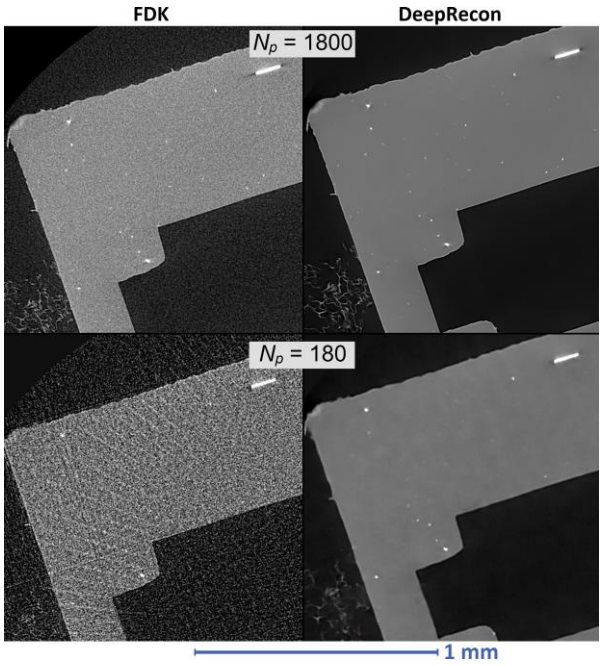

Figure 6: XRM cross-sectional views of the corner of a plastic connector, reconstructed with both FDK and DeepRecon, with two different values of N_p (V_x = 2.8 µm).

Another application example for using DeepRecon would be to speed up assembly inspection of small camera lens modules, such as those used in smartphones. The optical lenses of modern cell phone cameras are made of multi-layer stacked polycarbonate lenses. The optical axis of each layer in the stack must be precisely aligned to ensure light reception from a complementary metal oxide semiconductor (CMOS) sensor is in focus. Lens thickness, gaps, de-centricity and tilt must be inspected and measured during and after the lens assembly by nondestructive techniques [7]. Figure 7 shows XRM images revealing internal features of a smartphone camera lens stack, including a comparison between images reconstructed with both FDK and DeepRecon, for N_p = 1200. The DeepRecon reconstruction resulted in better image quality, in terms of contrast-to-noise ratio, allowing subsequent surface segmentation and assembly inspection.

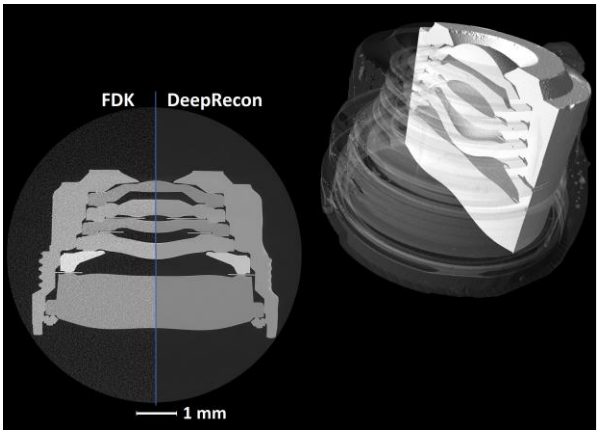

Figure 7: An XRM cross-sectional view of the inside of a smartphone camera lens assembly. On the upper-right corner there is a 3D rendered image that shows a solid view in a portion of the assembly with a semi-transparent view for the other portion (N_p = 1200, V_x = 7.5 µm).

Figure 8 shows cross-sectional views from the 3D image reconstruction of the smartphone camera lens module, using a voxel size V_x = 7.5 µm. An FDK reconstruction performed with N_p = 1200 (t = 90 min) is compared to reconstructions of FDK and DeepRecon data using N_p = 120 (t = 9 min). It is observed that FDK data reconstructed with N_p = 120 are significantly affected by aliasing artifacts and noise, thus showing the effects of undersampling. By contrast, the DeepRecon data, still using N_p = 120 (t = 9 min), show significantly better contrast-to-noise ratio and these data can enable faster dimensional measurement inspection and assembly verification of cell phone camera lens stacks. This case study further demonstrated the effectiveness of the new DeepRecon method to reduce the data acquisition time by a factor of ten.

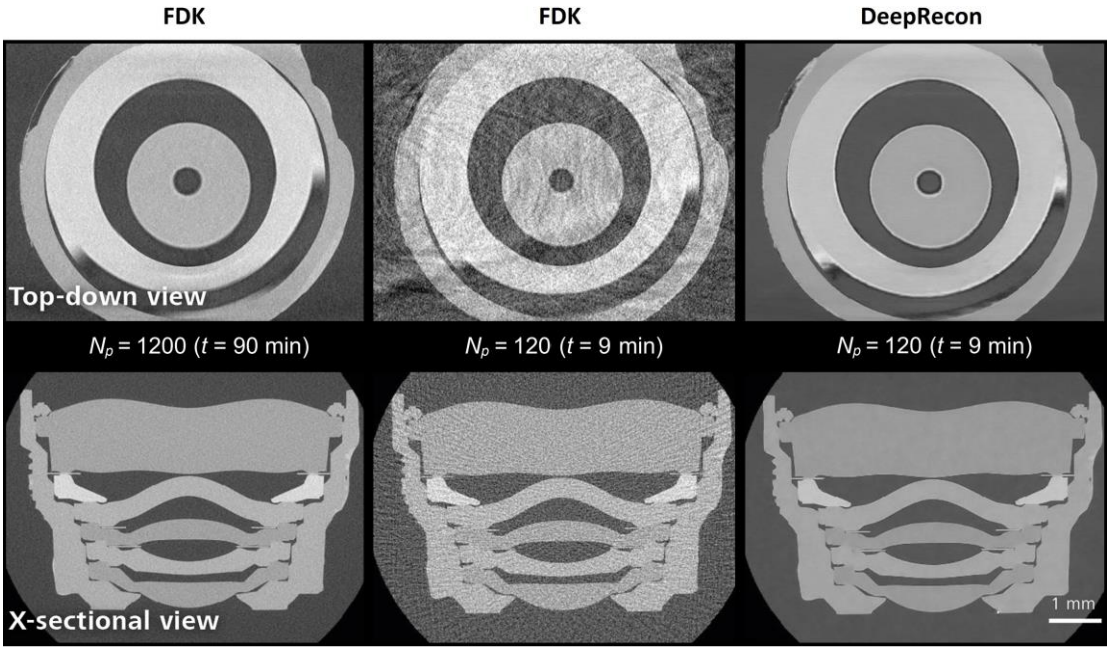

Figure 8: Comparison of XRM data reconstructions for a commercial camera lens assembly (V_x = 7.5 µm). Data reconstructed through FDK using N_p = 1200 (t = 90 min) are compared with FDK and DeepRecon data that use N_p = 120 (t = 9 min). Images on the top row are the top-down views, side cross-sectional views are shown on the bottom row.

CONCLUSIONS

Data reconstruction using traditional filtered-back-projection algorithms (e.g., FDK) require a number of projections (N_p) in the order of thousands for a faithful 3D XRM image representation. This means that, even with state-of-the-art instrumentation, XRM (X-ray microscopy or high-resolution X-ray CT) acquisition times can be in the order of several hours, which may not be cost effective for industrial measurement tasks. Reducing the time required for data acquisition is desirable to improve time-to-data and the cost of the measurement or inspection process. To tackle this issue, DL-based algorithms can be used for optimization of the reconstruction process with a reduced N_p. This was demonstrated in this paper with the integration of DL-based techniques into XRM measurement through ZEISS DeepRecon. Using specific application examples, DeepRecon was shown to significantly improve the 3D XRM measurement performance, producing significant improvements in scan time and image quality. Reconstructions of XRM data produced by DeepRecon can provide up to a 10X throughput time improvement, i.e., a scan time reduction by a factor of ten, at similar or better image quality compared to standard FDK data reconstructions that require long scans with large N_p values (in the thousands). Thus, DL-based data reconstructions allow for XRM industrial workflows to be applied much more economically.

In addition to alleviating one of the most significant obstacles preventing the wider adoption of 3D XRM in industrial environments, namely ‘data acquisition time’, DL-based X-ray inspection technologies will have a major impact on testing and failure analysis of advanced semiconductor packages [10, 11] (where nondestructive imaging is often required down to sub-micrometer resolution levels). Since DeepRecon has an automated training scheme built into a software interface that operates with user-selected options from a drop-down menu, DL custom networks can be easily created without the need for machine learning expertise (thus overcoming one of the main hurdles to a broad use of DL technologies).

REFERENCES

[1] H. Villarraga-Gómez, E. L. Herazo and S. T. Smith, "X-ray computed tomography: from medical imaging to dimensional metrology," *Precision Engineering,* vol. 60, pp. 544-569, 2019.

[2] L. A. Feldkamp, L. C. Davis and J. W. Kress, "Practical cone-beam algorithm," *J. Opt. Soc. Am. A,* vol. 1, no. 6, pp. 612-619, 1984.

[3] H. Villarraga-Gómez and S. T. Smith, "Effect of the number of projections on dimensional measurements with X-ray computed tomography," *Precision Engineering,* vol. 66, pp. 445-456, 2020.

[4] M. Andrew, "A quantified study of segmentation techniques on synthetic geological XRM and FIB-SEM images," *Computational Geosciences,* vol. 22, no. 6, pp. 1503-1512, 2018.

[5] A. Tekawade, B. A. Sforzo, K. E. Matusik, A. L. Kastengren and C. F. Powell, "High-fidelity geometry generation from CT data using convolutional neural networks," in *Proc. SPIE Vol. 11113*, San Diego, California, USA, 2019.

[6] W. Yao, L. Chen, H. Wu, Q. Zhao and S. Luo, "Micro-CT image denoising with an asymmetric perceptual convolutional network," *Physics in Medicine & Biology,* vol. 66, no. 13, p. 135018, 2021.

[7] H. Villarraga-Gómez, N. Kotwal, V. Ninov, L. Omlor, B. Johnson, R. Zarnetta, D. Weiss, W. Kimmig, M. Krenkel and C. Graf vom Hagen, "High-precision metrology with high-resolution computed tomography using 3D X-ray microscopes," in *Proc. 35th ASPE Annual Meeting*, Vol 73, pp.174-178, 2020, 2020.

[8] H. Villarraga-Gómez, C. Lee and S. T. Smith, "Dimensional metrology with X-ray CT: A comparison with CMM measurements on internal features and compliant structures," *Precision Engineering,* vol. 51, pp. 291-307, 2018.

[9] H. Villarraga-Gómez, J. Thousand and S. T. Smith, "Empirical approaches to uncertainty analysis of X-ray computed tomography measurements: A review with examples," *Precision Engineering,* vol. 64, pp. 249-268, 2020.

[10] A. Gu, A. Andreyev, M. Terada, B. Zee, S. Mohammad-Zulkifli and Y. Yang, "Accelerate your 3D X-ray failure analysis by deep learning high resolution reconstruction," in *Proc. 47th International Symposium for Testing and Failure Analysis*, Phoenix, AZ, USA, 5p, 2021.

[11] H. Villaraga-Gómez and J. D. Bell, "Modern 2D & 3D X-ray technologies for testing and failure analysis," in *Proc. 45th International Symposium for Testing and Failure Analysis*, Portland, OR, USA, pp. 14-19, 2019.

DESIGN OF A POLARISCOPE TOOL FOR THE EVALUATION OF STRAIN IN ROLL-TO-ROLL NANOFABRICATION

Groh, Barbara T.[1]; Connolly, Liam G.[1]; Cullinan, Michael[1]
[1]University of Texas at Austin, Walker Department of Mechanical Engineering, Austin, TX, USA

ABSTRACT

While roll-to-roll (R2R) manufacturing has the potential to lower costs in producing unique, flexible products, it faces major hurdles in the advancement of processing nano-featured products. Process development and control for nanofabrication requires exceptionally precise metrology in order to resolve individual features. Reducing measurement uncertainty is a necessary advancement to R2R manufacturing technology if this method is to usurp more traditional rigid-substrate processes.

One challenge is that the necessary tension in the web (substrate) for most R2R processes results in non-insignificant deformation which can vary due to a variety of process effects, thickness nonuniformity, and jitter in the applied tensioning torque. This inevitably leads to deformation in any fabricated structures along with the substrate, necessitating a correction if using in-line metrology.

This research serves to design and construct a tool capable of non-contact metrology of web deformation. As many of the flexible substrates used in R2R manufacturing are transparent polymers which experience the photoelastic effect while under tension, the proposed tool is will map the change in polarization due to this effect at the microscale across the web.. This data will enable the real-time calculation of deformation across the web and the creation of models to correct for errors in measured structures due to pattern deformation for a variety of in-line measurement.

1. INTRODUCTION

In R2R additive manufacturing, a flexible substrate is tightly stretched between two primary rollers – unwind and rewind – with any processing steps or additional web regulation taking place between the two. Consequently, the material undergoes stress across the stretched-out substrate, otherwise known as the web. For most macro-scale features, this is not a problem because the deformations are typically on the order of hundreds of nanometers. However, as critical dimensions continue to get shrink, the deformations cannot be ignored. This becomes particularly problematic when the fabrication process requires more than one patterned layer. It is imperative that all layers align as any error between features, or overlay error, may significantly effect manufacturing yield. Figure 1 shows how registration error can cause misalignment which changes the function of an example device.

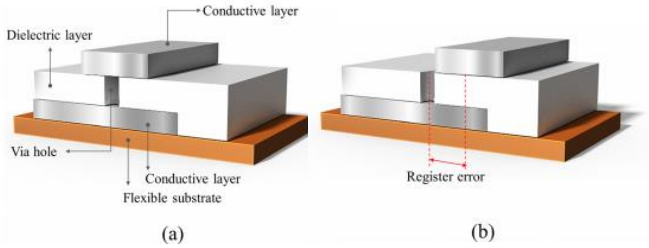

FIGURE 1. a) A nanoscale feature with multiple layers. b) features are misaligned due to registration error [1]

2. TOOL DESIGN

The proposed polariscope metrology tool leverages the unique optical properties of transparent flexible substrates used in many R2R systems to measure deformation in the tensioned web. The specific property of interest is the photoelastic effect.

The photoelastic effect occurs when polarized light passes through a transparent, often mostly amorphous material, particularly one that is optically isotropic under no stress, but optically anisotropic under stress [4]. This material, under stress, then has the ability to refract light similar to a crystalline material, resulting in polarization changes that can make images like the one seen in Figure 2.

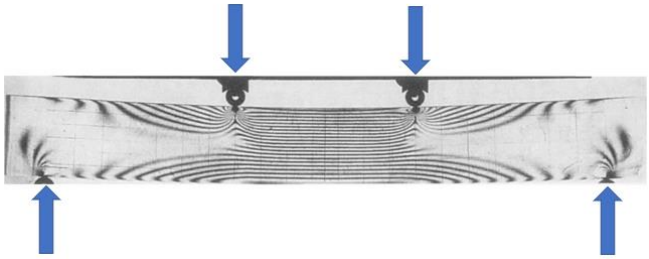

FIGURE 2. Stress lines in a thin film under a bending load [3]

Therefore, by measuring the change in polarization of light through the stressed substrate, it is possible to create a map of the local strain and account for the deformation when adding features to the material or measuring fabricated patterns. This is done by building a plane polariscope, which is made using a polarizer to polarize the incident light source, followed by the

material to be analyzed, and then a second polarizer at 90 degrees offset to the original for analyzing the change in polarization after the light has passed through the material. This basic setup can be seen if Figure 3.

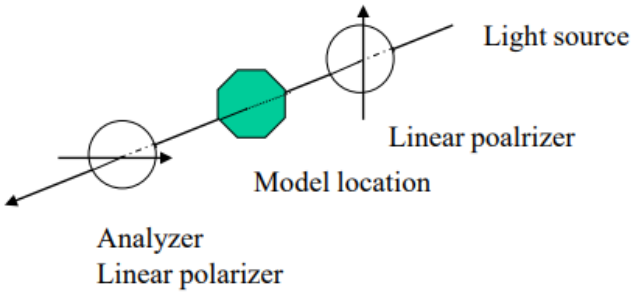

FIGURE 3. Progression of light through a plane polariscope [4]

The tool consists of a light source, a polarizer to polarize the laser light, another polarizer to analyze the light that has been changed by passing through the substrate, and an optical column with an objective lens and a camera to magnify and capture the results. A pair of stages move the polarizers and optical column to scan across the substrate to capture measurements over the entire web. Figure 4 illustrates the full polariscope tool design such that the web may be tensioned between the stage containing the majority of the optical devices and the lofted stage containing the camera and optical column.

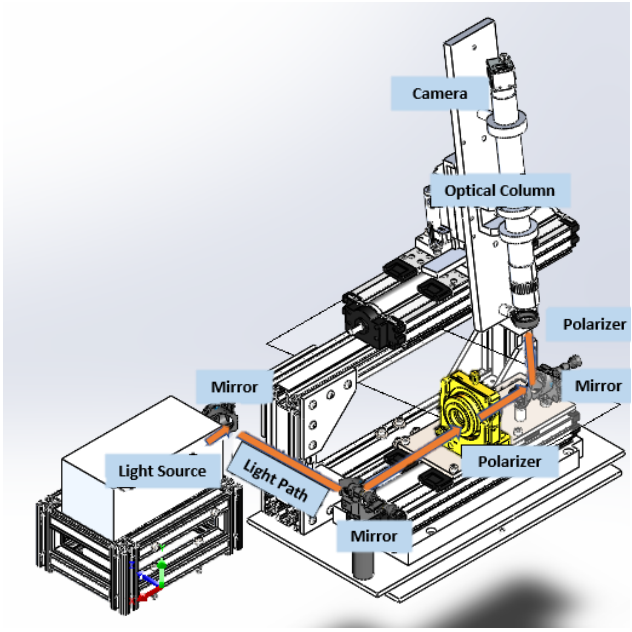

FIGURE 4. Full Polariscope Tool Design

Completing the tool design involves finalizing the setup such that it is able to take polariscopic images of the substrate as well as synchronizing both stages to collect images across the whole substrate. Additionally, the proposed design requires a white light source to allow for the most efficient imaging. Once the tool is able to capture images, the stages may be incorporated to raster across the substrate, and the images must be compiled to create an accurate map of the whole web.

3. FUTURE WORK

The images captured by the polariscope will be visual representations of the stress across the web. These will be generally composed of fringes of varying intensity of light that can be counted and analyzed to determine the amount of strain that the web undergoes during R2R-typical tension. The proposed method of analysis is a computer-vision-based approach that will employ image segmentation to identify and count fringes in each image.

Upon the completion and optimization of the tool construction and the necessary image analysis methods, the setup will be able to output reliable deformation measurements of the web on the R2R system. With these measurements, it will be necessary to begin working on a reliable method of adjusting manufacturing parameters in order to correct for the measured displacement and begin manufacturing multilayer devices with minimal register error.

ACKNOWLEDGMENTS

This research is based upon work supported primarily by the National Science Foundation under Cooperative Agreement No. EEC-1160494 and Graduate Research Fellowship Program Grant No. 2017251210.

REFERENCES

[1] J. Lee, S. Park, K. H. Shin, and H. Jung, “Smearing defects: a root cause of register measurement error in roll-to-roll additive manufacturing system,” *Int. J. Adv. Manuf. Technol.*, vol. 98, no. 9–12, pp. 3155–3165, 2018, doi: 10.1007/s00170-018-2465-0.

[2] W.-C. Wang, “Photoelasticity,” p. 66.

[3] G. Cloud, *Optical Methods of Engineering Analysis*, vol. 34. Cambridge University Press, 1995. Accessed: Jul. 26, 2021. [Online]. Available: http://doi.wiley.com/10.1111/j.1747-1567.2009.00611.x

OPTICAL FIBER SURFACE PROBE USING MECHANICALLY MODULATED FABRY-PEROT INTERFEROMETRY

Farzaneh Shabahang, Dr. Stuart Smith
Center of precision metrology
University of North Carolina at Charlotte
Charlotte, North Carolina, USA

ABSTRACT

This paper presents a fiber based Fabry-Perot surface probe that currently comprises a 1.8 mm diameter GRIN lens protruding from a cylindrical body of diameter 5 mm. quadrature signals for phase unwrapping are achieved by mechanically modulating the GRIN lens assembly. To demonstrate operation, sinusoidal profiles on a diamond-turned aluminum reference surface each having an amplitude of 2 μm and spatial wavelengths ranging from 0.15 to 0.5 mm have been measured. A comparison between these measurements and results from a stylus profilometer is presented.

INTRODUCTION

Conventional optical methods for the quantitative measurement of surface topography are mostly lens- based systems [3-6,8,9]. A drawback of such systems is the large volume of the optics and short working distance that precludes measurements in confined spaces. There have been a large number of research studies reporting fiber-based probe systems [1-3,7,10-18]. some of the examples of fiber-based probes are optical coherence tomography, Fabry-Perot interferometer probes, optical coherence scanning interferometry and confocal probes.

The goal of this work is to realize metrological optical probing using fiber- based probes to increase the range and overcome space limitations to create a fiber optic probe to measure a broad range of hard-to-reach surfaces. The design shown here uses Fabry-Perot interferometry for displacement sensing and a fiber probe GRIN lens to increase lateral resolution.

OPTICAL SYSTEM DESIGN

Referring to figure 1, the Fabry-Perot fiber-based interferometer comprises a two by one, single mode 630nm fiber optic coupler/splitter, a fiber coupler photo detector and coherent fiber coupled laser diodes with 633-650 nm wavelengths. Major tasks involved with fabrication and automation include:

- Focusing of the laser spot (using a GRIN lens) onto test surfaces that are then traversed laterally with respect to the probe.
- Stabilization of the diode laser system.
- Creation of a mechanical modulation system using piezo electric actuators to modulate phase and extract the phase of light returning into the fiber with a short optical path.

Currently this probe design has been extended to enable measurements in both the axial and radial directions and is briefly discussed at the end of this paper.

EXPERIMENTS & RESULTS

Figure 1 shows a schematic diagram of the optical probe that currently uses a diode laser coupled into single mode 630 nm fiber fastened at its end with a tip-tilt aligner. Detection of the surface location is achieved by measuring the interference of the small amount of light reflected from the end of the probe and the light reflected from the surface of the specimen, called a Fabry-Perot (FP) cavity. After detecting the interference of light coming out of the Fabry-Perot cavity between fiber surface and object mirror, it is necessary to extract phase information to measure displacement corresponding to the location of the surface. Frequency modulation is used to create harmonics for phase unwrapping. In early studies the FP cavity comprises a bare fiber (200 μm diameter) and specimen surface.

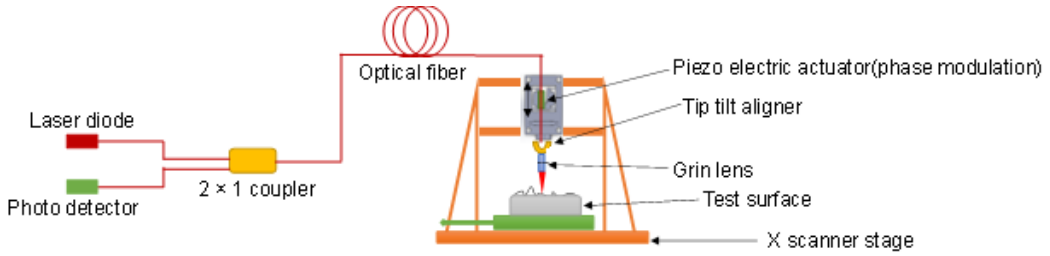

Figure 1. Schematic representation of the fiber optic Fabry Perot prob using mechanical modulation of light.

A second fiber probe and specimen traverse stage have been fabricated and tested with major performance parameters listed in Table 1. A photograph of the experimental apparatus showing the GRIN lens-based fiber probe measuring the central portion of the test specimen is shown in Figure 2.

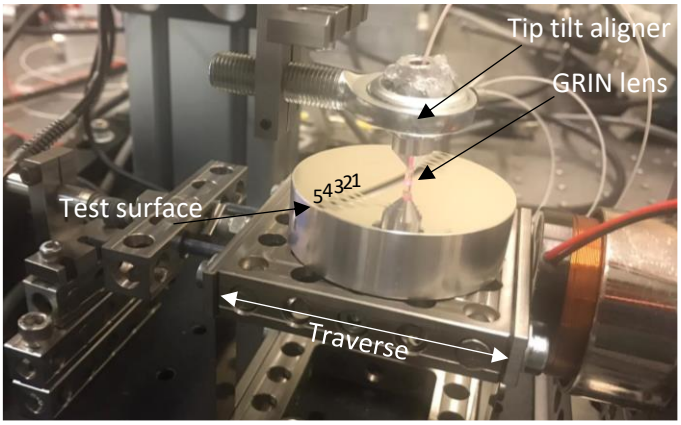

Figure 2, Photograph of experimental apparatus showing fiber probe measuring the central portion of the test specimen with sinusoidal regions 1, 2, 3, 4 and 5 indicated on the surface.

Table 1 Fiber optic Fabry Perot probe performance specifications

specification	Working distance	Vertical resolution	Lateral resolution	Vertical range	Lateral range	speed
value	0-1 mm	3.25 nm	17.5 µm	3-300 µm	10 mm specimen travel range	0.1 mm/sec

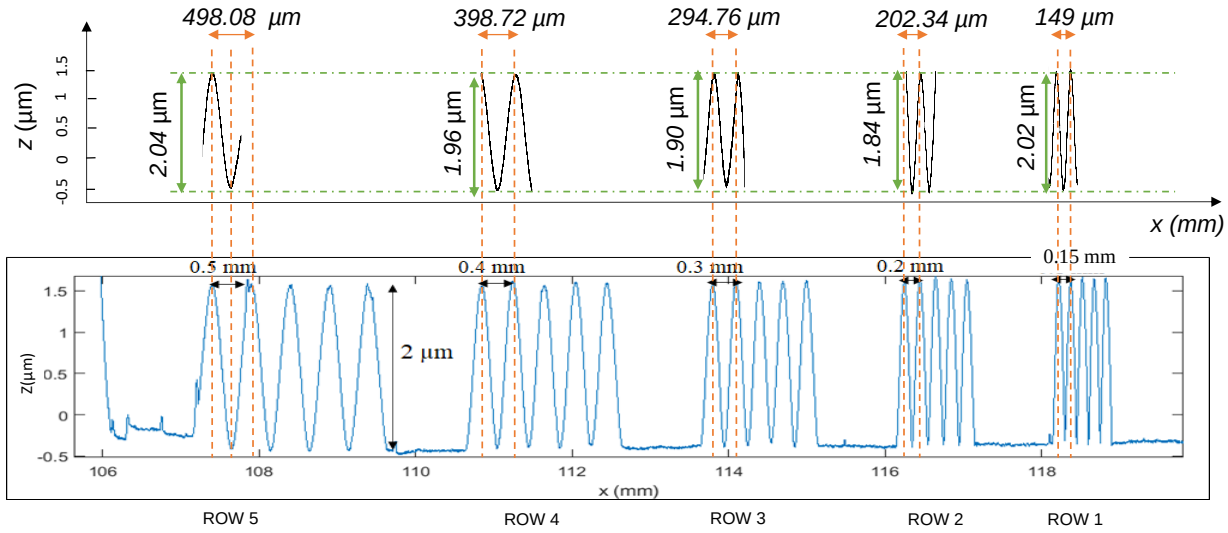

Figure 3 Results for optical measurement of the sinusoidal test sample (top) with stylus profilometer scanning data (bottom).

To evaluate performance, a diamond turned aluminum test specimen with a variety of sinusoidal profiles having wavelengths ranging from 0.1 to 0.5 mm has been produced. Figure 2 (top part) shows preliminary measurements of a profile on a section containing a sinusoidal profile with peak to valley amplitude 2 µm and 0.15, 0.20, 0.30, 0.4 and 0.5 mm lateral spacing (wavelength). For comparison, measurement in a similar region using a stylus profilometer (Mahr LD260) is also shown in Figure 2 (bottom part). AS of writing, the deviations between the measurements are comparable to the expected uncertainties of the two profilometers.

Table 2 Fiber Fabry Perot probe and stylus profilometer measurements of a test surface (PP spacing)

Region number on the test specimen	Flat surface	1	2	3	4	5
PP (spacing between ripples) (Number of datapoints in FPGA LabVIEW program)	51500	9318	12654	18434	24936	31150
Equivalent measurement in µm	776 µm (range of scan)	149 µm	202.34 µm	294.76 µm	398.72 µm	498.08 µm
PP (Stylus measurement)	-	150 µm	200 µm	300 µm	400 µm	500 µm

Table 3 Fiber Fabry Perot probe measurements of a test surface (PV amplitude). PV value from stylus profilometer is reported as 2 µm.

Region number on the test specimen	1	2	3	4	5
PV (amplitude of each ripple) in µm	2.02 µm	1.84 µm	1.9 µm	1.96 µm	2.04 µm

FUTURE WORK

As a further development, a new fiber optic probe has been fabricated and fastened to a 120 mm × 50 mm positioning stage as shown in Figure 4. This stage uses a piezoelectric stack actuator with 20 µm range and nanometer resolution with displacement being measured using a Lion Precision capacitance probe. The bandwidth of modulation frequency is currently limited to 1.2 kHz that is capable of profiling speeds of 0.1 mm per second. Current efforts have reduced the size of the probe to less than 10 mm × 5 mm × 5 mm volume with modulation being provided by an actuator at the fiber tip, results from which will be presented at the conference. This new design currently provides a modulation bandwidth of around 10 kHz and will potentially increase the profiling speed to greater than 1 mm per second.

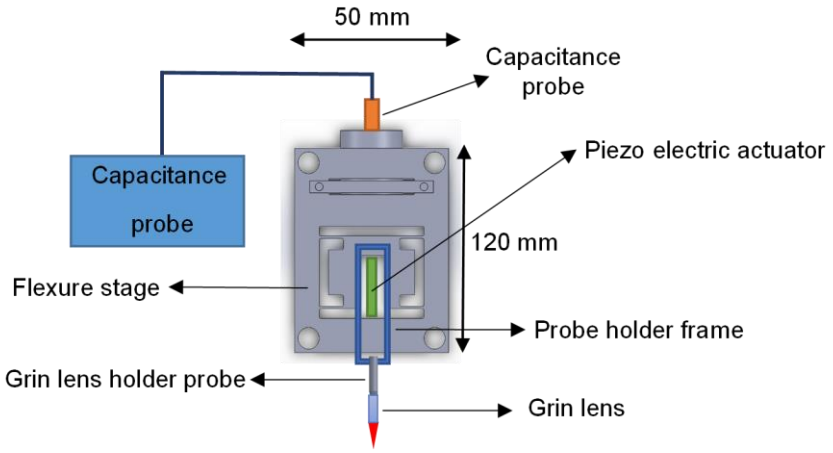

Figure 4 piezo electric GRIN lens modulator

REFERENCES

[1] Byeong Ha Lee, Young Ho Kim, Kwan Seob Park, Joo Beom Eom, Myoung Jin Kim, Byung Sup Rho and Hae Young Choi. “Interferometric Fiber Optic Sensors.” Review of Sensors 12, 2467-2486 (2012).

[2] S. W. Harun, M. Yasin, H. Z. Yang, Kusminarto, Karyono, H. Ahmad. “Estimation of Metal Surface Roughness Using Fiber Optic Displacement Sensor.” Laser Physics Vol. 20, No. 4, pp. 904–909 (2010).

[3] J. Plucinski, R. Hypser, P. Wierzba, M. Strakowski, M. Jedrzejewska-Szczerska, M. Maciejewski, and B.B. Kosmowski. “Optical low-coherence interferometry for selected technical applications.” Bulletin of the polish academy of sciences Vol. 9554, I-6 (2008)

[4] Peter de Groot. “Principles of interference microscopy for the measurement of surface topography.” Zygo Corporation, Laurel Brook Road, Middlefield, Connecticut 06455, USA Vol. 7, pp. 1-65(2015)

[5] Stahl, H. Philip. “White-light moire phase-measuring interferometry.” 34th Annual International Technical Symposium on Optical and Optoelectronic Applied Science and Engineering Vol. 1332 ,720-730(1990)

[6] Davidson, Mark, Kaufman, Kalman, Mazor, Isaac, Cohen, Felix. “An Application of Interference Microscopy to Integrated Circuit Inspection and Metrology.” Integrated Circuit Metrology, Inspection, & Process Control Vol. 775, 233-247(1987)

[7] Byron S. Lee and Timothy C. Strand. “Profilometry with a coherence scanning microscope.” Applied Optics vol. 29, pp. 3784-3788(1990)

[8] Artigas R. (2011) Imaging Confocal Microscopy. In: Leach R. (eds) Optical Measurement of Surface Topography. Springer, Berlin, Heidelberg. https://doi.org/10.1007/978-3-642-12012-1_11

[9] Blateyron, F., 2011. Chromatic Confocal Microscopy, pp. 71–106.. doi:10.1007/978-3-642-12012-1_5

[10] Joseph A. Izatt, Manish D. Kulkarni, Hsing-Wen Wang, Kenji Kobayashi, and Michael V. Sivak, Jr.

“Optical Coherence Tomography and Microscopy in Gastrointestinal Tissues.” IEEE journal of selected topics in quantum electronics, Vol. 2, 1017-1027 (1996).

[11] Joseph M. Schmitt. “Optical Coherence Tomography (OCT): A Review” IEEE journal of selected topics in quantum electronics, vol. 2, 1205-1215 (1999).

[12] Dan P. Popescu & Lin-P’ing Choo-Smith & Costel Flueraru & Youxin Mao & Shoude Chang & John Disano & Sherif Sherif & Michael G. Sowa. “Optical coherence tomography: fundamental principles, instrumental designs and biomedical applications.” Biophysics, vol.3, 155–169 (2011)

[13] Adam M. Zysk, Freddy T. Nguyen, Amy L. Oldenburg Daniel L. Marks, Stephen A. Boppart. “Optical coherence tomography: a review of clinical development from bench to bedside” Journal of Biomedical Optics, vol. 12, 5 (2007)

[14] Ankesh Tiwari, Pradeep Kumar Yadav, Richa Srivastava and Navin Chaurasiya. “Optical Fiber Sensor: Review and Applications.” Optical Fiber Sensor: Review and Applications, vol.6, 1358-1362 (2018).

[15] Garry Berkovic and Ehud Shafir. “Optical methods for distance and displacement measurements.” Advances in Optics and Photonics, vol.4, page 441 (2012).

[16] Y. Alayli, D. Wang and M. Bonis. “Optical fiber profilometer with submicronic accuracy” SPIE Conference, Vol. 3509, page 84-87 (1998).

[17] Zhu Nan-nan, Zhang Jun. “Surface roughness measurement based on fiber optic sensor.” ScienceDirect measurements, vol.86, Pages 239-245 (2016).

[18] Byeong Ha Lee 1, Young Ho Kim, Kwan Seob Park, Joo Beom Eom, Myoung Jin Kim, Byung Sup Rho and Hae Young Choi. “Interferometric Fiber Optic Sensors.” Sensors, vol. 12, 2467-2486 (2012).

.

RELAXED UNCERTAINTY DIMENSIONAL METROLOGY FOR ASSEMBLY VIA PHOTOGRAMMETRY USING OPEN-SOURCE LIBRARIES

Rahma Nawab[1], Angela Davies Allen[1], and Nien Lee[2]
[1]Center for Precision Metrology
University of North Carolina at Charlotte
Charlotte, North Carolina, USA
[2]Caterpillar Inc
USA

ABSTRACT
Current non-contact technologies used for assembly line quality inspection utilize laser scanners and video-based data. The former requires expensive equipment and does not provide dense point cloud data, while the latter does not provide quantitative data and typically relies on human interpretation and experience. This paper discusses a cost-effective open-source-library approach that combines dimensional metrology with digital reconstruction for assembly quality inspection. The proposed method allows dimensional analysis – millimeter-scale positioning/assembly error estimation - and visualization using non-contact metrology via photogrammetry.

INTRODUCTION
A thorough review on machine vision techniques in industrial environments (1) explored different vision techniques, such as laser scanners, photogrammetry, structured light and laser triangulation. Laser techniques are often used for scanning but are expensive and come with safety considerations. Geometric information acquired using these laser scanners is of high resolution and accuracy, but costly because of expensive scanning equipment and the need for skilled manpower to obtain initial basic data (2). Added to the equipment cost, is the time and money needed for specialized programs to process the initial basic data.

Photogrammetry on the other hand requires minimal manpower and low-cost equipment. Offering fast measurements with high density 3D point cloud data, photogrammetry can cover an extensive area in terms of object volume and accuracy at a low cost (3).

Industrial assembly features often consist of highly textured surfaces, with contrasting colors and features, making it an ideal application of feature detection-based photogrammetry without the need of coded or non-coded targets. The use of coded targets reduces measurement uncertainty, but for assembly-line positioning error detection on the millimeter scale, feature detection alone is likely sufficient. Feature detection algorithms in photogrammetry follow finding edges and defining features using difference of Gaussians or using a hessian matrix-based blob detector in popular algorithms like SIFT (scale-invariant feature transform) and SURF (speeded-up robust features). These rely on visual properties of the surface and show significantly less noise for these surfaces than LIDAR based sensors (4).

PROPOSED METHOD
Similar to traditional non-contact methods, the proposed method is a two-part inspection process consisting of data acquisition and data analysis.
The following components comprise the method proposed:

- Photogrammetry is used to obtain dimensional information in the form of a 3-D point cloud of the actual scene. Data can be acquired with a commercially available handheld camera device such as a smartphone camera. The object or body of interest is photographed from a range of directions, so that all significant areas are captured. It is not necessary to place coded targets in the scene.
- The images obtained are then converted to a 3-D point cloud using open-source

photogrammetry and point cloud reconstruction libraries.
- The obtained 3-D point cloud is compared with the relevant computer aided design (CAD) model, using open-source library registration algorithms, to obtain dimensional or positional errors on the millimeter scale with a sub-millimeter uncertainty goal. The CAD model comparison is performed by using CAD models of the individual components in the assembly, performing coarse and then fine registration of these models to the point cloud to estimate where the component is on the assembly to estimate a positioning error.

This allows cost-effective ease-of-use digital reconstruction of the assembled system with the necessary dimensional information for quality control assessment of the assembly process. Potential applications include assembling combustion engines, vehicle parts, aerospace, and packaging industries.

Experiment

A custom test target artifact was designed and fabricated to test the approach. The artifact is 300 mm high and 300 mm wide, featuring nuts, bolts, blocks, and posts welded onto a steel plate. The target was designed to resemble mechanical assemblies in automotive applications. Figure 1 shows the artifact mounted on an optical bench.

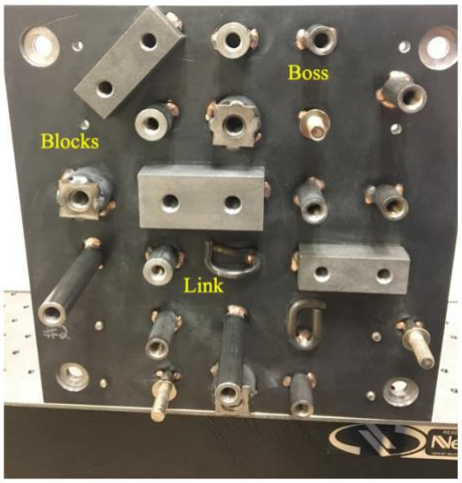

FIGURE 1 : Artifact simulating industrial features of interest

For data acquisition, keeping with our goal of an inexpensive and accessible system, we use a smart phone camera. The focal length is fixed and 60 images from different camera angles and distances around the plate are captured.

A 3-D point cloud is obtained from 2-D images using the open source library, openMVG (5). The library allows us to follow a structure from motion (sfM) pipeline. Instead of using coded or non-coded targets that are commonly used in industry, we used the SIFT (scale-invariant feature transform) algorithm to detect features on the images, this also makes the process more automated. Features extracted using SIFT have shown to be robust with images with noise, change in illumination, and across a range of affine distortion (6).

Another open source library openMVS (7) is used to perform a depth-map merging method, which works well on large scale objects (8). This is used to obtain a dense point cloud.

Positioning Error Determination

To perform quality check on a feature of interest, the feature needs to be detected in the data set and its displacement from reference calculated. We followed a two-tier process to perform this:
- Information about the coordinates of the feature, from the CAD model, was used to select an approximate area in the data set to isolate the feature of interest.
- ICP was used to register the isolated feature and it's CAD model to find a transformation relative to the global coordinate frame. The transformation matrix was then used to extract the positioning error.

RESULTS

Figure 2 shows the sparse point cloud obtained using an incremental sfM pipeline to perform photogrammetry. In this step, the camera poses and 3-D shape using feature detection were calculated. As can be seen in the figure, part of the optical bench was also reconstructed. Figure 3 shows the dense point cloud obtained after performing dense reconstruction on the sparse point cloud.

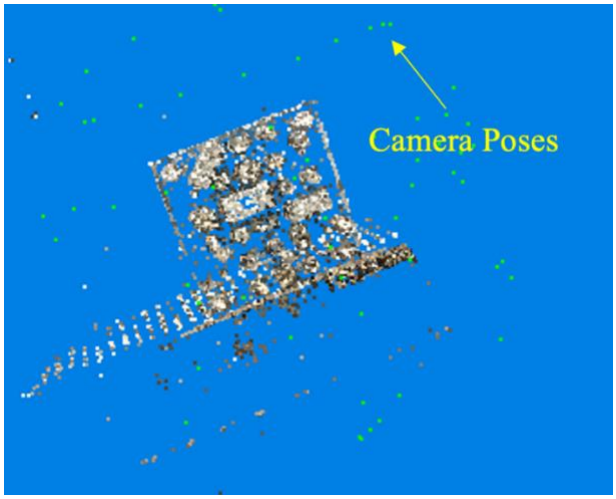

FIGURE 3: Sparse point cloud of the artifact

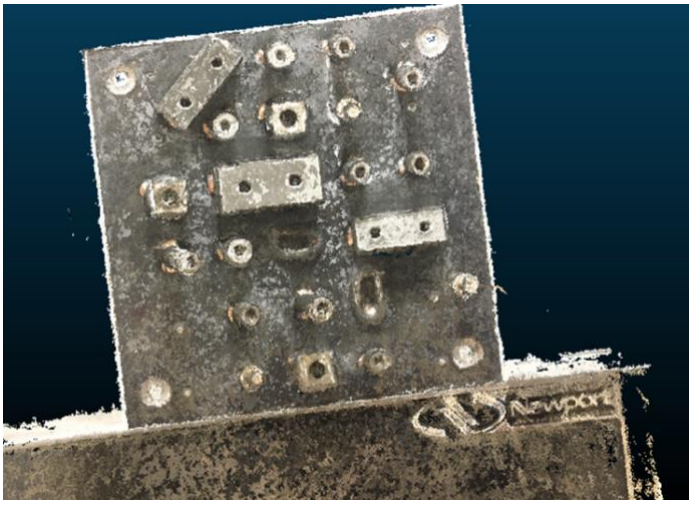

FIGURE 3: Dense point cloud

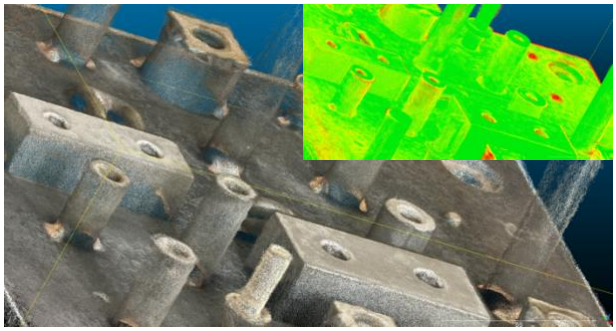

FIGURE 4: Dense point

As can be seen in figure 4, the individual features on the plate have been reconstructed relatively well. The insert in figure 4 shows a distance map relative to the CAD, the deviations from the reference were found to lie between -0.75mm to 0.75mm (9).

To study how well our method is working to calculate positioning errors in a feature of interest, we first tested the algorithm on a simulated data set. Figure 5(a) shows a post as our feature of interest, Figure 5 (b) and (c) show the posts before and after ICP registration respectively.

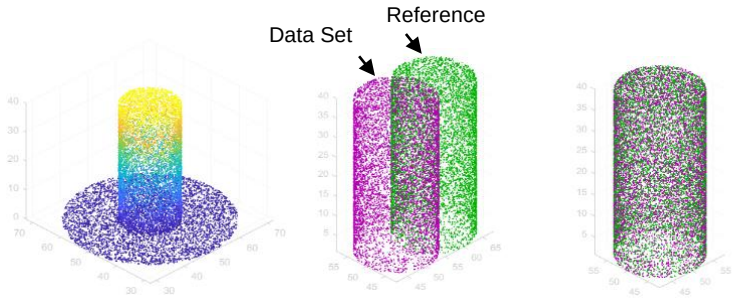

(a) *(b)* *(c)*

FIGURE 5: Simulated data set (a) Post as a feature of interest, (b) Posts before registration, (c) Posts after ICP registration

Positioning errors were simulated by displacing the post relative to the global coordinate frame on the plate. Fig 6 (a) shows the actual positioning error in the post and the measured positioning error using the above method with ICP. Fig 6 (b) shows the error in our measurement of the position. As seen the position is measured with an accuracy of ± 0.4 mm, for positional errors as large as 10 mm.

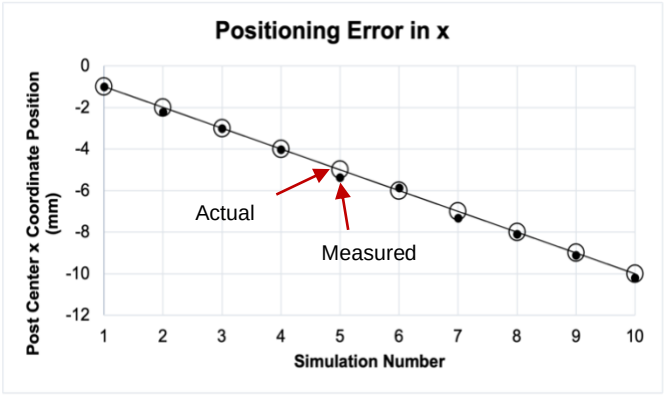

(a)

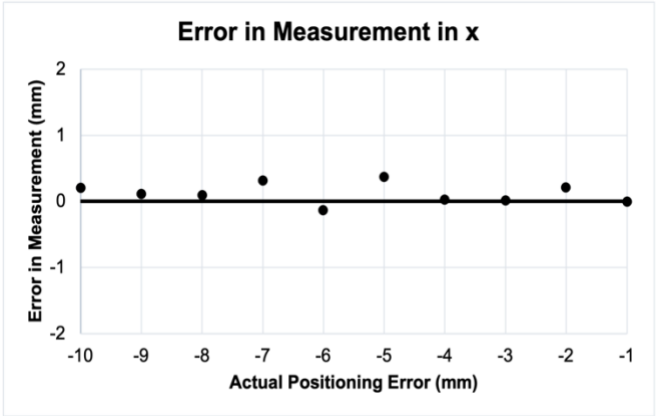

(b)

FIGURE 6: Simulated data set, positioning error estimation

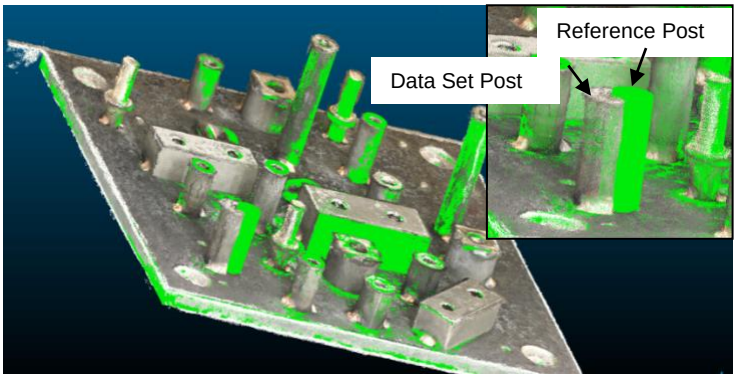

FIGURE 7: Photogrammetry data superimposed with the CAD

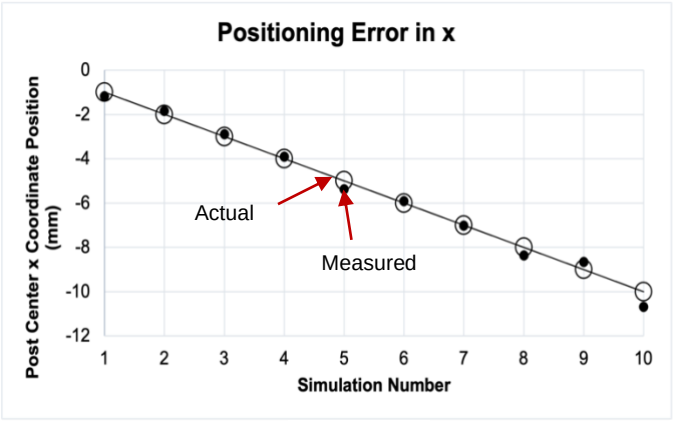

(a)

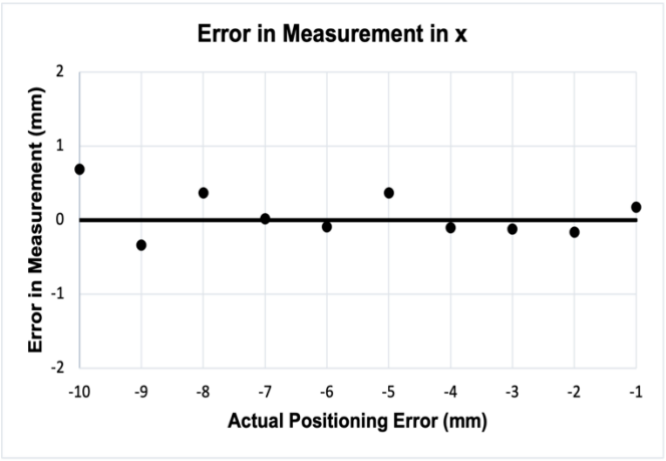

(b)

FIGURE 9: Photogrammetry data set, positioning error estimation

Figures 7 and 8 show the Photogrammetry data, registered with the CAD as a reference model and the feature of interest isolated using information of the coordinates from the CAD. ICP was then performed, and the positioning error calculated for a range of different simulated reference data sets, with positional errors

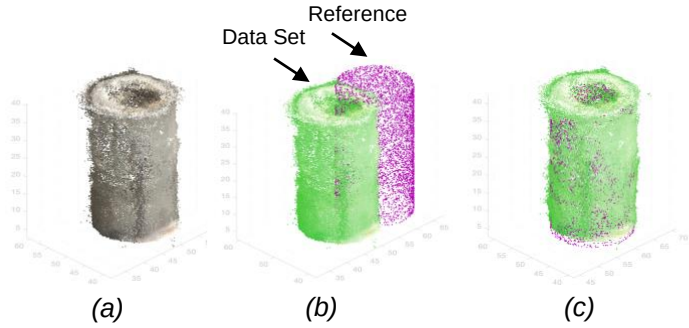

FIGURE 8: Photogrammetry data (a) Post as a feature of interest, (b) Posts before registration, (c) Posts after ICP registration

ranging from 1 – 10 mm. The results are shown in figure 9. As seen in figure 9(b) the error in our measurement of the position falls within ± 0.6 mm.

CONCLUSION AND FUTURE WORK

In conclusion we have demonstrated an inexpensive and easily accessible quality inspection, using open-source software, smart phone cameras and easily accessible programs. The method was tested with both simulated and photogrammetry data and was able to calculate a positioning error accurately within the sub millimeter range, with an accuracy of ± 0.6 mm.

Future work includes, incorporating an augmented reality component to display the error deviations, studying noise levels in the point cloud, defining measurands for complex shaped objects, like a link and doing an uncertainty analysis.

REFERENCES

1. Pérez L, Rodríguez Í, Rodríguez N, Usamentiaga R, García D. Robot Guidance Using Machine Vision Techniques in Industrial Environments: A Comparative Review. Sensors. 2016 Mar 5;16(3):335.
2. Moon D, Chung S, Kwon S, Seo J, Shin J. Comparison and utilization of point cloud generated from photogrammetry and laser scanning: 3D world model for smart heavy equipment planning. Automation in Construction. 2019 Feb 1;98:322–31.
3. Wang Q, Kim M-K. Applications of 3D point cloud data in the construction industry: A fifteen-year review from 2004 to 2018. Advanced Engineering Informatics. 2019 Jan;39:306–19.
4. Aldao E, González-Jorge H, Pérez JA. Metrological comparison of LiDAR and photogrammetric systems for deformation

monitoring of aerospace parts. Measurement. 2021 Apr 1;174:109037.
5. OpenMVG (open Multiple View Geometry) [Internet]. openMVG; 2021 [cited 2021 Aug 31]. Available from: https://github.com/openMVG/openMVG
6. Lowe DG. Distinctive Image Features from Scale-Invariant Keypoints. International Journal of Computer Vision. 2004 Nov;60(2):91–110.
7. cDc. OpenMVS: open Multi-View Stereo reconstruction library [Internet]. 2021 [cited 2021 Aug 31]. Available from: https://github.com/cdcseacave/openMVS
8. Shen S. Depth-map merging for Multi-View Stereo with high resolution images. In: Proceedings of the 21st International Conference on Pattern Recognition (ICPR2012). 2012. p. 788–91.
9. CloudCompare - Open Source project [Internet]. [cited 2021 Sep 24]. Available from: https://www.danielgm.net/cc/
10. Luhmann T. Close range photogrammetry for industrial applications. ISPRS Journal of Photogrammetry and Remote Sensing. 2010 Nov;65(6):558–69.
11. Register two point clouds using ICP algorithm - MATLAB pcregistericp [Internet]. [cited 2021 Sep 24]. Available from: https://www.mathworks.com/help/vision/ref/pcregistericp.html

PRECISION DESIGN AND ERROR ANALYSIS OF VARIABLE VOLUTE MECHANISM FOR A CENTRIFUGAL PUMP

Hilary A. Johnson[1] and Alexander H. Slocum[1]
Department of Mechanical Engineering
Massachusetts Institute of Technology
Cambridge, MA, 02139, USA

INTRODUCTION

Centrifugal pumps are comprised of a rotating impeller and a spiral volute casing. The performance and efficiency of a centrifugal pump is controlled by the geometry of the spiral volute as well as the impeller radius and rotational speed. It is well established in literature that there is an optimal volute spiral geometry, calculated according to conservation of angular momentum, to maximize efficiency for a particular desired operating point. [1] However, pump applications require operation over a range of pressures and flow rates, and so a fixed volute shape cannot be optimal for all operating conditions. A new category of pump, a variable volute, enables operators to control the volute volume to match particular operating conditions.

This work demonstrates the precision design and experimental mechanical test of a controllable variable volute mechanism. A spiral piston face translates linearly within the casing to changes the height and hence the volume of the volute. The efficiency and operation of the pump is sensitive to the matching of the volute volume and flow rate. Based on the machine design of the pump, error analysis compared with experimental data demonstrates the ability of the mechanism to accurately and repeatably control the volute height.

OVERVIEW OF THE DESIGN

The variable volute mechanism is comprised of a worm gear, which drives a worm wheel with a multi-start internal thread that engages a corresponding thread emanating from the backside of a spiral volute piston. The large diameter leadscrew is a five start thread to achieve a lead of 40mm with 8mm pitch. The multi-start thread was also chosen to reduce tip-tilt of the piston face during translation. The piston face matches the volute spiral and linearly changes the height and hence the volume of the volute.

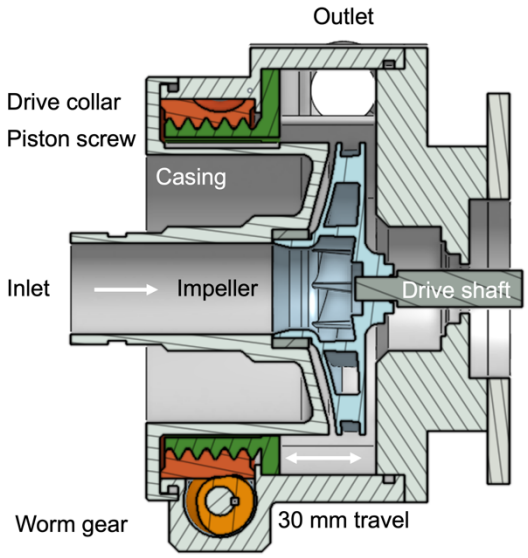

FIGURE 1. Cross-sectional model of the variable volute mechanism in a centrifugal pump at the largest position.

TABLE 1. Functional requirements

Functional requirement	Design parameter
30 mm of travel (10-40 mm)	5 start leadscrew, 8mm pitch, 40 mm lead
Volute height controllable +/- 1.5 mm	75 tooth worm gear gives 0.11 mm/deg
Non-backdrivable B>1, self-locking	Worm gear ratio B = 2.758 [2]

In order to reduce the torque to actuate the piston, the working fluid is allowed to pressure balance in front and behind the piston such that it does not have to overcome the pressure in the volute. Non-backdrivability is established based on the thread mean diameter, the coefficient of friction, the lead and cosine of the thread angle.

Tooth size and worm selection was based on the Von Mises stress at the root of each gear tooth, yielding a 0.041 yield stress to tensile strength ratio. The worm gear teeth were designed using GearTraxPro-2021 [3] using a normal pressure angle of 20 deg, 6.65mm pitch and 158.75mm reference diameter. The resulting worm to gear ratio is 75:1.

The volute casing, drive collar and piston screw were additively manufactured using Nylon PA-12 with a 40% glass fill in a selective laser sintering process [4]. Dimensions were within a 50 thousandths tolerance. Post-processing included boring and machining precision surfaces and scraping and wearing in the screw threads with lapping compound. One would expect that in volume manufacturing, the threads would be milled and would achieve equivalent or better accuracy.

ERROR BUDGET

Sources of geometric error in the variable volute height include tip-tilt in the piston stage as well as backlash in the screw threads, backlash in the worm to gear mating, backlash in the motor couplings and in the motor, and sinusoidal error in the shaft coupling. Error budgeting and estimation drove design decisions in the most critical modules.

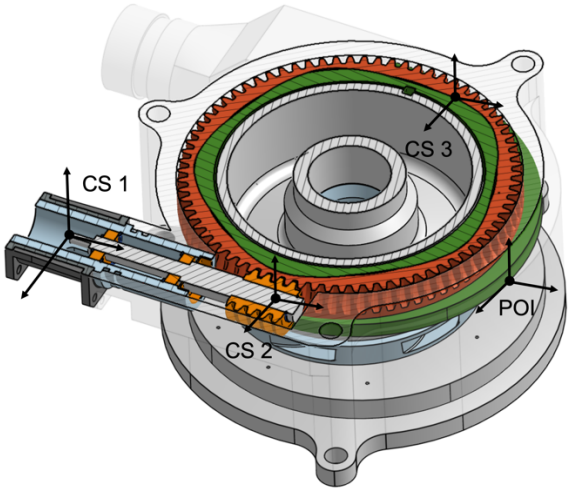

FIGURE 2. *Coordinate systems labeled at the intersection between parts in the force loop for error apportionment. Point of interest labeled at the piston surface facing the volute.*

TABLE 2. Error apportionment

CS	Error Source	Local Error		Volute Error	
1	Motor coupling backlash	3	deg	0.004	mm
2	Worm-gear backlash	1	deg	0.11	mm
3	Keyed piston backlash	1	deg	0.22	mm
POI	Piston stage tip-tilt	0.015	deg	1.33	mm
Total Est. Error		Linear sum		1.66	mm
		Root sq sum		1.35	mm
		Average		1.51	mm
Allowable Error				1.5	mm

The original error budget showed that the backlash in the piston screw threads was 15 deg without a rotational constraint, resulting in 1.67 mm in volute error. This motivated the decision to include a machine key between the piston and casing for rotational constraint, thereby reducing the backlash estimate to 2 degrees and 0.22 mm in volute error. This highlights the utility of error budgeting to prioritize design decisions.

The predicted error budget shows that the estimated error, calculated as the average of the linear and root square sums, is less than the allowable error.

EXPERIMENT

The experimental setup as shown in Figure 2. uses three dial indicators with +/- 0.025mm accuracy to measure the translation and tip-tilt of the piston over 30 mm of travel. The volute casing was positioned on a level mill table on three pin contacts and was secured using fixturing step blocks. Three dial indicators were positioned approximately equidistant to measure points in a plane on the piston surface over the travel of the lead screw.

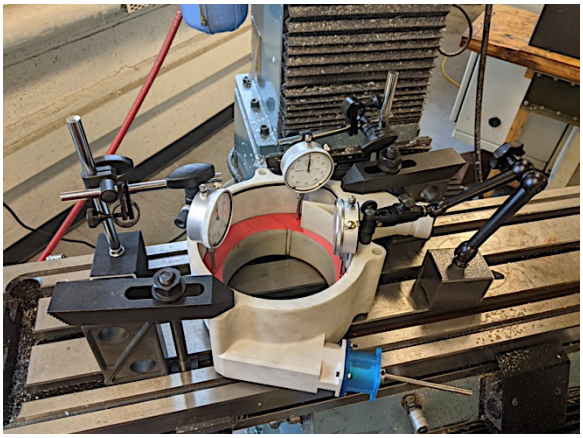

FIGURE 3. Experimental setup showing 3 dial indicators positioned on the piston surface. A motor was used to rotate the worm shaft protruding from the blue motor mount.

Thirty discrete height increments for each of the three dial indicators (z_1, z_2, z_3), were measured and repeated for six trials. The heights, z, were combined with the dial indicator locations, x and y, to form points (x, y, z). The difference between the points was taken to construct two vectors (v_1, v_2), defining the plane. The cross product of the vectors yields the normal vector, *n*, to the plane $v_1 \times v_2 = (a, b, c)$. The equation for each plane was defined in the form: $ax + by + cz = d$, where *d* is the dot product of the normal vector and a point on the plane.

The angular difference from the previous point and the angular difference from a zero reference plane were calculated using the angle between two vectors formula $\cos\alpha = \overline{n_1} \cdot \overline{n_2} / |\overline{n_1}||\overline{n_2}|$.

The number of worm gear rotations and the direction was recorded for each point.

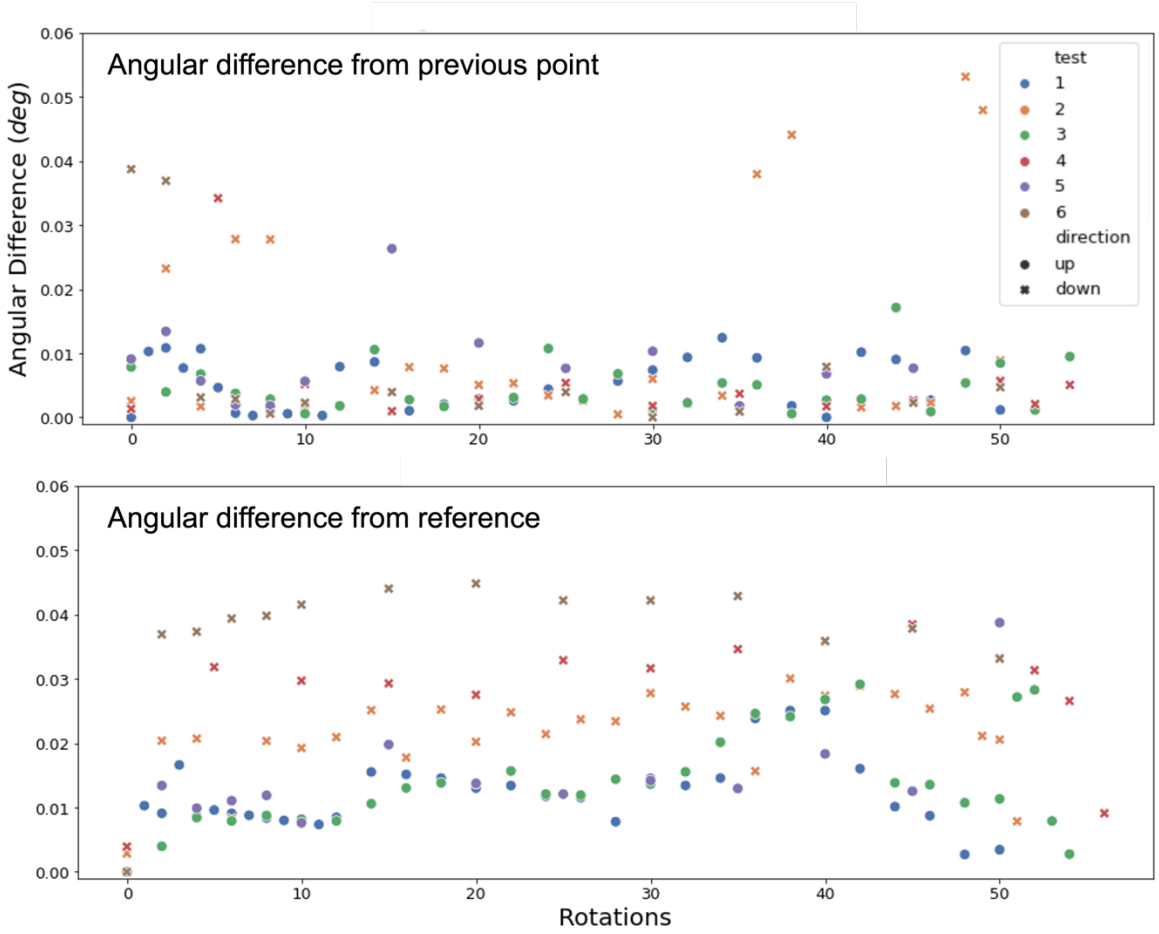

Figure 3. *Plots showing the calculated angular difference from the previous point and from the zero reference plane.*

Potential sources of measurement error were assessed and countermeasures implemented. The local uncertainty in measuring the worm gear rotation is estimated at +/- 5 deg, translating to a negligible corresponding volute uncertainty of 0.007 mm. The dial indicator positions were marked on the piston surface for repeatable placement. A machinist square was used to orient the dial indicators with respect to the piston surface at the reference plane, reducing cosine errors.

RESULTS

Results for the angular difference from the previous point showed no more than 0.053 deg of tip-tilt, with a mean of 0.0079 and standard deviation of 0.010 degrees. Results for the angular difference from the reference plane show a max tip-tilt of 0.045 deg, with a mean and standard deviation of 0.019 and 0.011 respectively.

However, there is a significant difference in the angular difference from the reference between the up and down trials. From observation, on the down trials there was an initial backlash of approximately 4-8 deg before translation of the piston. The data supports this observation, as trials 2, 4, and 6 seem to have a step offset between rotations 0 and 1. In the fully assembled pump this rotation is constrained with a machine key. In this configuration, backlash is limited by the wedging of the spiral into the casing and is sensitive to the gap between the spiral and casing surfaces. On the upwards trials, the piston is rotationally constrained by contact at the cutwater. Selecting only the up trials gives a mean angular error of 0.013 from the reference, a significant improvement.

The mean degree of tip-tilt results is a mean sine error at the center of the throat of the spiral volute piston, at a radius of 88 mm. This error results in 1.67 mm in the volute height, when considering all the data. When considering only up data, sine error results in 1.14 mm of error.

Comparing the experimental results with the error budget, in Table 2, the mean values for tip-tilt are greater than the 0.015 deg of allowable error. However, the up only data is within the allowable range. The tip-tilt error is the most significant contributor to error in the volute height, because the sine error magnifies angular error over distance.

The height of the volute linearly impacts the volume of the volute. However, error in the height disproportionately impacts the accuracy more at smaller flow-rates than it does at higher flow-rates. The mean sine error calculated of 1.67mm offset results in 4% and 17% errors at the maximum 40mm and minimum 10mm volute heights respectively.

The gauge height to rotations results, shown in Figure 4, show close agreement between the linear fit and theoretical calculated slope. The theoretical calculated slope, based on the motor to gear to screw ratio, is 0.0210 while the linear fit is 0.0205 with an offset of -0.028. The difference between the theoretical and linear fit is the accuracy of the mechanism.

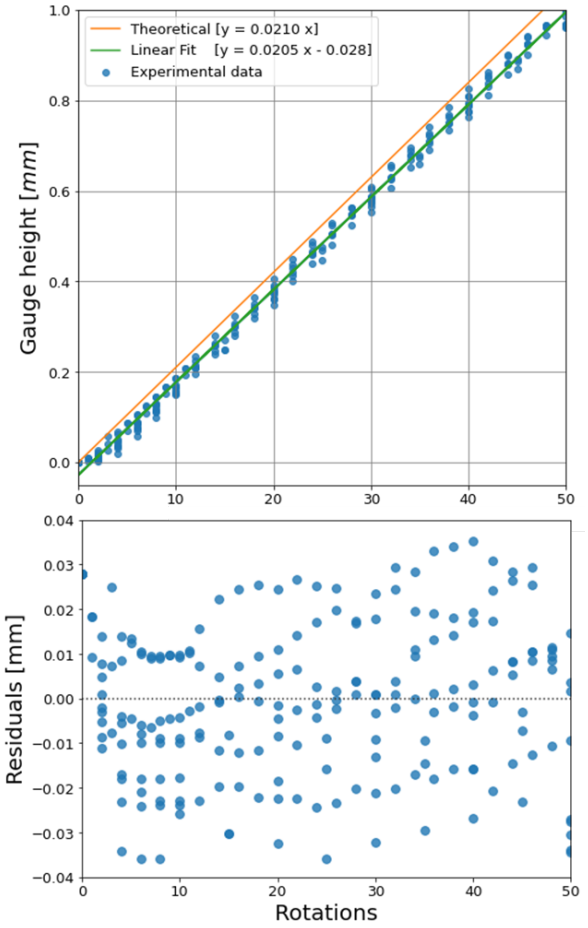

FIGURE 5. *Comparing experimental data, the linear regression, and the theoretical slope*.

The residuals plot shows that the data is distributed within a range of +/- 0.04 about the linear best fit line. This is the range of repeatability of the process.

CONCLUSION

This paper presents a variable volute mechanism consisting of a worm driving a worm gear integrated with a lead screw collar which drives a linear piston stage. The spiral piston face translates around the impeller and changes the volume of the volute. The designed variable volute mechanism meets most key functional requirements including self-locking, and range of travel greater than 30 mm. Features such as the five start thread and the machine key to constrain a rotational degree of freedom were implemented as a result of error apportionment. Experimental results show that the mechanism is close to the 0.015 deg of allowable tip-tilt error, especially when considering up trials only. The linear best fit of the data is close to the theoretical calculated slope and could be used to directly drive the mechanism.

Error apportionment compared with experimental data demonstrates the ability of the mechanism to fairly accurately and repeatably control the volute height close to the allowable error. The ability to match the volute volume to the flow rate allows for optimization of centrifugal pump efficiency and operation.

ACKNOWLEDGEMENTS

This work was supported by Xylem, Inc., through the MIT Abdul Latif Jameel Water and Food Systems Lab. Thank you to Daniel Gilbert for his help with fabrication in the MIT Laboratory for Manufacturing and Productivity.

REFERENCES

[1] Gülich, J. F., 2014, *Centrifugal Pumps*, Springer-Verlag, Berlin Heidelberg.

[2] Slocum, A. H., 1992, *Precision Machine Design*, Society of Manufacturing Engineers.

[3] *Gear Trax Pro Software*, Camnetics.

[4] *SLS Datasheet PA12 Glass Filled*, Protolabs.

INTERFERENCE FIT, SUB-MICRON PILOTED TOOL HOLDER

Dave Arneson
Professional Instruments Company
Hopkins, Minnesota, USA

ABSTRACT
Deterministic micro-cutting processes such as diamond micro-milling require stiff, repeatable toolholders. Common solutions such as collets, while convenient, have drawbacks that become apparent when used in optics manufacture where results are measured in nanometers [1]. The interference fit piloted toolholder described here features high stiffness and provides micron-level repeatability without adjustment. To achieve ¼ micron centering, a selective screw torqueing technique can be used.

FIGURE 1. Optional chucking system for a high speed spindle with sub-micron repeatability.

BACKGROUND
This tool holder uses two techniques developed at Professional Instruments over the years to tackle difficult jobs. The first is our spherical piloting system which uses a unique cylindrical flexure mated to a spherical pilot where the spherical pilot is actually 1 micron bigger than the hole it gets inserted into, both the spherical pilot and the cylindrical flexure are made of steel bonded titanium carbide called Ferro-TiC®, which is a machinable carbide with phenomenal wear characteristics [2]. This along with an extremely flat mounting flange allows for incredible repeatability [3]. The second uses the ability to insert a carbide shaft that is 6 microns larger than a hole, without the use of heat. This only works if you make your tool holder out of a tough, hard steel like 440C stainless steel, and you hold your tolerances to levels not available to standard machine shops. Another advantage is since there are no moving parts the balance remains rock solid from initial installation to re-installation, in some cases eliminating the need to re-balance the tool on the work spindle [4].

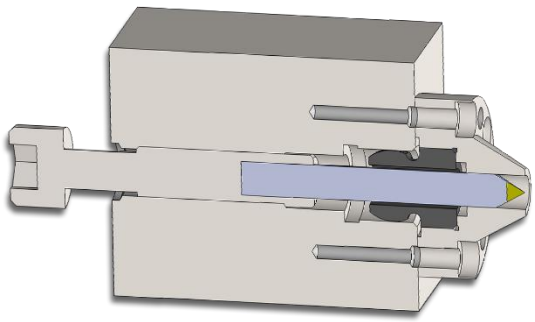

FIGURE 2. Sectioned view of the tooling to insert the carbide shank diamond end mill.

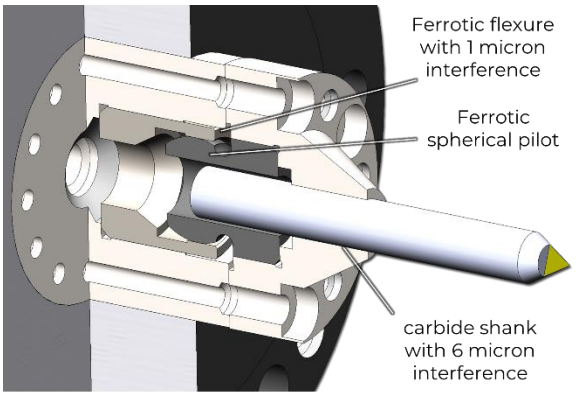

FIGURE 3. Sectioned view of piloted tool holder with carbide shank diamond end mill installed.

FIGURE 4. The carbide shank diamond end mill is inserted into the tool holder with a simple, screw actuated fixture.

RESULTS

One of the interesting things the interference tool holder allows is to micro-adjust how far the tool sticks out from the tool holder. In one quick test, we were able to adjust the “stick-out” in 2 micron increments. Another advantage to this toolholder is its compactness. Since there are no moving parts as you have in a collet the balance won’t change significantly when you change tools. At 20 mm overall length, it’s significantly shorter than a comparable tool holder resulting in a stiffer structural loop.

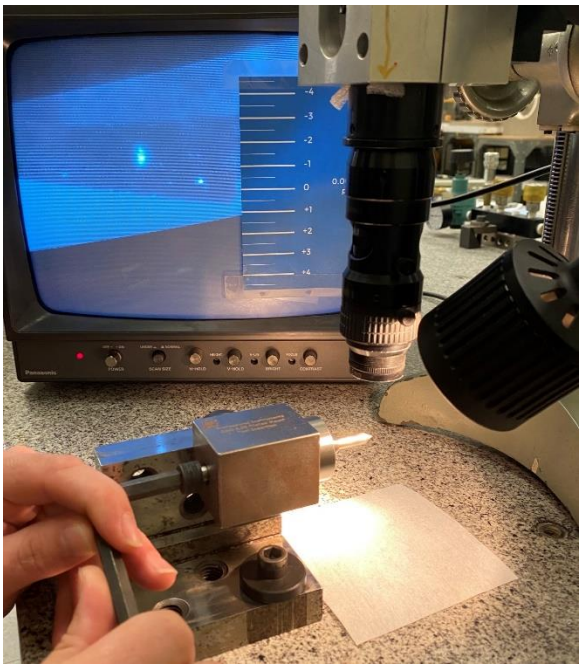

FIGURE 5. Microadjusting the tool using tool insertion fixture.

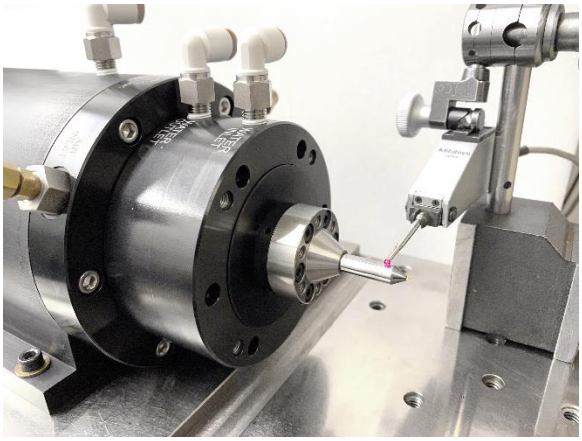

FIGURE 6. Repeatability tests demonstrate sub-micron repeatability. Even better results are possible using the shadetree mechanic’s technique of selective torqueing.

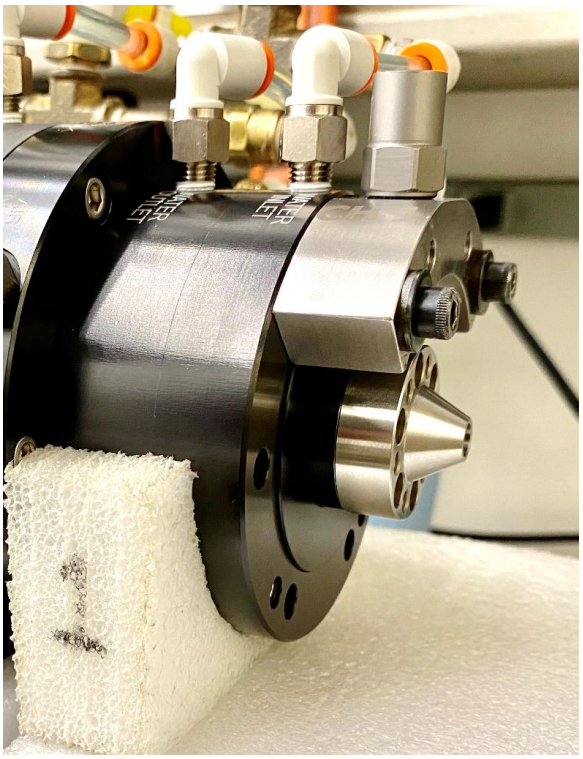

FIGURE 7. Setup for balancing the tool holder allows for ISO 1940 Grade 0.4 and better.

CONCLUSIONS

Tool holders are an extremely important, but often overlooked, component of ultraprecision optics manufacturing. Using interference tool holders goes way back at Professional Instruments to a job grinding extreme aspect ratio holes for a fuel injector body. Grinding wheels held in traditional collets just wouldn't grind because they would instantly chatter. While interference tool holders like this are difficult to make and not particularly convenient to use, they are critical in cases where one is looking for the ultimate in accuracy.

REFERENCES

[1] Hui LI, et al. "Micro-optical fabrication by ultraprecision diamond machining and precision molding." Front. Mech. Eng. 12(2): 181-192. 2017.

[2] https://www.psmindustries.com/ferro-tic/

[3] Liebers MJ, et al. "Repeatability of a chucking system based on centralizing with a sphere and locating axially on a flange." euspen Annual Proc. Stockholm, Sweden. 2012.

[4] Knapp BR, et al. "The importance of spindle balancing for the machining of freeform optics." Proc. ASPE Spring Topical on Structured and Freeform Surfaces. Charlotte, NC. 2011.

Authors Index

Authors Index

Agrawal, Aman R. 16, 260
Aguirre, Gorka 102
Ahn, Seong-Hyo 276
Aksyuk, Vladimir A. 215
Allen, Angela D. 360
Ambaum, N. 89
Andrew, Matthew 344. 347
Andreyev, Andriy 347
Anthis, Austin F. ..... *
Arneson, David 370
Arnold, Ian J. 211
Artusio-Glimpse, Alexandra 1
Bahtiyar, Kaan 316
Baines, Josh 83
Bale, Hrishikesh 347
Bartlett, Graham ..... *
Behera, Dipankar 78
Bekker, Logan 308
Bendiksen, Aage 254
Betters, Emma 220
Bhushan, Brij M. ..... *
Birckigt, Pascal 21
Bleicher, Friedrich 266
Blevins, Tyler 220
Blue, Craig 220
Bordatchev, Evgueni V. 183, 302,
Branson, David 155
Brouwer, Dannis M. 45
Cao, Liangcai 322
Carter, Jonathan J. 21
Cates, Nichole 130
Chalifoux, Brandon D. 171, 211
Chandrasekaran, Swetha 58
Chao, Leon 27
Chen, Shih-Chi 67, 322, 327
Chen, Yang 136
Chowdhury, Mitul D. 16
Chun, Heebum 298
Colinas-Armijo, Natalia 102
Comden, Zane 27
Compton, Brett 32, 248
Connolly, Liam G. 353
Cornelius, Aaron 220, 242
Corson, Gregory 242
Cortes, John 58, 271
Cullinan, Michael A. 78, 353
Da, Li 178
Daneshkhan, Behrooz 133
de Jong, Jan J. 45
de Vries, Jorrit 142
Ding, Zin ..... *
Dumanli, Alper 120
Dvorak, Jake 220, 242, 248
Eaton, Parker 130
Ensinger, Wolfgang 205, 282
Epping, L.J. 45
Fai, Cheung Chi 178
Fan, Chunjie 72
Farzaneh, Amin 308
Felius, Mario 142
Fritz, Matthias 205, 282
Fu, Zhiqiang 322
Furst, Stephen J. 130
Furutani, Katsushi 294
Gerberding, Oliver 21
Gilpin, Richard 83
Goldstein, Barbara 27
Gomez, Michael 32, 189, 221, 232, 238, 288
Graf vom Hagen, Christoph 347
Groeb, Johann 205, 282
Groeb, Marvin 205, 282
Groh, Barbara T. 353
Gu, Allen 347
Guo, Ping 114
Guo, Xiangyu 161
Guzman, Felipe ..... *
Haddad, Darine 54
Haliday, H. Scott ..... *
Hamel, William R. 50
Hamer, Tyler T. ..... *
Hamilton, Benjamin W. 302
Han, Fei 327
Hannot, Stephan 142
Harmon, Joannie 220
Hayashi, Akio 338
He, Chuan 97
Hegde, Himanshu 37
Heilmann, Ralf K. 171
Hendricks, Jay 27
Heyman, Ian 108

***No Abstract Available**

Hii, King-Fu 136
Hijkoop, Erik G. ..... *
Homiller, Laura 312
Hopkins, Johnathan B. 41, 220, 308
Ibabe, Beñat Iñigo 102
Ibrahim, Malek 108
Ilic, Robert 215
Isa, Mohammed A. ..... *
Ishizuka, Akane 338
Jacobs, Leah 242
Jain, Anant 83
Jared, Bradley H. 50
Jiangxin, Yang 178
Johnson, Bruce 347
Johnson, Hilary A. 365
Johnstone, Rollin 136
Kaneko, Yoshiyuki 338
Karandikar, Jaydeep 193, 266
Kastengren, Alan L. 344
Keck, Lorenz 10, 54
Kim, Hyo-Young 37
Kim, Jungsub 37
Knapp, Byron ..... *
Koehlenbeck, Sina M. 21
Laverty, Kevin A. 211
Leach, Richard K. 155
Lee, ChaBum 37, 152, 161, 298
Lee, Nien ..... *
Lehman, John 11
Leitner, David 266
Li, Qingfeng 21
Liao, Aaron 78
Lifel, Ren ..... *
Liu, Kexuan 322
Liu, Yuxiang 125, 215
Loke, Corey 254
López de Lacalle, Luis N. 102
Lu, Wanping 67
Marshall, Erin 248
Mettry, Magi 58, 271
Micklow, Lauren 130
Miramontes, Eduardo 50
Mokrani, B. 89
Montano, Joshua D. ..... *
Morgan, Winter ..... *
Morimoto, Yoshitaka 338
Morrison, Mark 220
Munden, Ryan 254
Nahata, Sudhanshu 165
Naples, Neil 146
Nawab, Rahma 360
Nazario, Jose 220
Newell, David 11, 27, 54
No, Timothy 288
Okwudire, Chinedum E. 97
Omlor, Lars 347
Oss, Dan ..... *
Ouyang, Wenqi 327
Overschie, Peter 142
Ozdoganlar, O.B. 165
Panas, Robert M. 58, 271, 308
Pandya, Parth N. 83
Pankow, Mark 130
Papadakis Ktistakis, Iosif 254
Pascall, Andrew J. 308
Patterson, Matthew R. 248
Pawlowski, Michal E. 254
Penney, Joshua 50, 242
Perera, Charles W. 27
Piano, Samantha 154
Pluchar, Christian M. 16
Powell, Christopher F. 344
Pratt, Jon R. 260
Raby, Alison ..... *
Ramani, Keval S. 97
Ramsauer, Christoph 266
Rangel, Otoniel F. 183
Robbins, Joshua 50
Roblee, Jeff 199
Rogers, Kyle 11
Romani, Monsuru ..... *
Romberg, Stian 248
Roux, Steve 254
Sanapala, Ravikumar 347
Schlamminger, Stephan 11, 27, 54, 260
Schmitz, Tony L. 32, 50, 189, 193, 220, 221
..... 232, 238, 242, 248, 266, 288
Schulze, Sven 11
Seifert, Frank 11, 27, 54
Sencer, Burak 120, 316
Sforzo, Brandon A. 344
Shabahang, Farzaneh 355
Shanmugam, Ragavanantham ..... *
Shao, Qi 67
Shattenburg, Mark L. 171
Shaw, Gordon 11
Shen, Jing-Jing 248
Simonds, Brian 11
Slocum, Alexander H. 365

***No Abstract Available**

Smith, Scott 220
Smith, Stuart T. 72, 355
Sohn, Alexander 146
Spaan-Burke, Theresa M. 142
Spero, Robert ..... *
Sreenivasan, S.V. 83
Strüning, Rick 21
Sun, Frederick 308
Suzuki, Naohiko 338
Tekawade, Aniket 344
Terada, Masako 347
Theans, S. 45
Theska, René 11, 54
Trumper, David L. ..... *
Tsuchiya, Takahiro 294
Tutunea-Fatan, Remus 183, 302
Ullsperger, Tobias 21
Valdez, Mario O. ..... *
Vallance, Ryan R. 136
van den Beucken, Nick 63
van den Braber, Rens ..... *
van der Nolle, Rens 142
van Swaaij, Stijn ..... *
Verbaan, Kees ..... *
Vermeulen, J.P.M.B. 89
Villarraga-Gomez, Herminso 344, 347
Walsh, James 254
Wang, Mingkang 215
Wang, Yaoke 114
Wang, Yintao 322
Wang, Zhikun 152
Whalen, Mallory M. 171
Williams, Paul 11
Wilson, Dalziel J. 16, 260
Wilson, Wynona ..... *
Wisniewski, Hayden J. 171
Worthington, Matthew 58, 271
Wu, Jingjie 332
Yang, Zhidi 41
Yanlong, Cao 178
Yazzie, Joel ..... *
Zameroski, Ross 221, 242
Zhang, Rui 215
Zhou, Lei 108, 276, 312, 322

***No Abstract Available**